University of Southampton

FACULTY OF NATURAL AND ENVIRONMENTAL SCIENCES

Ocean and Earth Science

An integrated geophysical analysis of rifting evolution and gas hydrate occurrence in the Eastern Black Sea Basin

by

Vanessa Monteleone

A thesis submitted to the University of Southampton in accordance with the requirements for the degree of Doctor of Philosophy

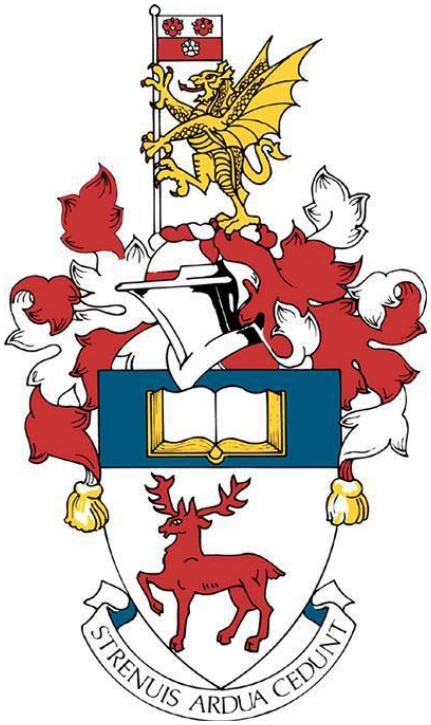

June 2021

University of Southampton

Abstract

FACULTY OF NATURAL AND ENVIRONMENTAL SCIENCES
SCHOOL OF OCEAN AND EARTH SCIENCE

Doctor of Philosophy

AN INTEGRATED GEOPHYSICAL ANALYSIS OF RIFTING EVOLUTION AND GAS HYDRATE OCCURRENCE IN THE EASTERN BLACK SEA BASIN

by

Vanessa Monteleone

One of the key elements in passive continental margins and basins research is the understanding of how extensional processes initiate and evolve from rifting to breakup stage. These processes may vary spatially and temporally as result of the complex trade-off between spreading rates, lithospheric compositional variations, and along-axis changes in melt supply. Thus, extension may focus over one conjugate margin resulting in an along-axis change in rifting style. Lower crust and/or mantle exhumation may occur at hyper-extended areas, and along-axis changes in melt supply during spreading may result in varying amounts of magmatic intrusions within a highly extended continental crust. The resulting crustal structure and composition at rifted margins may therefore present a geophysical signature differing from what is normally expected for continental and oceanic crust, making it difficult to define the transition from the late stages of continental rifting to initial oceanic accretion. Nevertheless, a clear understanding of the stages defining passive continental margins and extensional basins evolution is key to unravel the mechanisms driving lithospheric extension, as well as the present-day configuration at these settings. Sedimentary basins formed in continental rifts and rifted margins also contain some of Earth's major hydrocarbon fields. Constraining the evolution and dynamics of these fields gives insight into the timing of basin formation, sedimentation, trap formation, and heat-flow evolution, which are crucial for efficient hydrocarbon exploration. Passive continental margins are also relevant to the study of gas hydrates deposits, which are of interest not only for their potential as a future energy resource, but also for their implications on seafloor stability and their contribution to climate change. However, the dynamics driving their formation and evolution along passive margins is yet to be fully understood.

This study provides an integrated geophysical investigation at one of the currently most debated extensional regions, the Eastern Black Sea Basin (EBSB). Here, the timing and dynamics of rifting and breakup processes and the resulting crustal configuration are still poorly constrained. This is due to the deep water setting and thick sedimentary infill, limiting direct sampling of deep sedimentary units and the ability of imaging the deep basin structures using conventional seismic imaging. The EBSB is also a frontier for oil and gas exploration due to the presence of a regional source-rock, the Oligocene-lower Miocene Maykop Formation. Thus, untangling the stages in basin evolution and defining the extent of different crustal basements is essential for modelling the maturity of the hydrocarbon systems in place. This study uses high-resolution, 2D long-offset seismic reflection data by *Geology Without Limits* (GWL) to investigate the deep tectono-stratigraphic elements of the basin and the morphological character of its basement. Magnetic

anomaly data are integrated to complement and guide seismic interpretation, defining the magnetisation character of morphologically different crustal domains. The combined analysis of tectono-stratigraphic and magnetic anomaly results provides new insights on the present-day crustal configuration, and on the timing and kinematics of rifting and breakup processes across the EBSB.

The Black Sea is characterised by thermo-dynamic conditions which make this area favourable to gas hydrate formation. Gas hydrates have long been known in this area, with related evidence for Bottom Simulating Reflectors (BSRs) predominantly found in the western part of the basin (WBSB). Seismic data used in this study reveal new evidence for multiple BSRs along the NE margin of the EBSB, thus providing a new case study to investigate the physical nature of the identified BSRs, the presence and distribution of gas hydrates and/or free gas zones, and the mechanism(s) driving multiple BSRs generation. The long-offset nature of the seismic acquisition provides both reflected and refracted travel-time information that can be used in a tomographic approach, aiming to define a 2D velocity model within the shallow sedimentary section. To improve refracted arrivals, downward continuation is also applied to the seismic data. Results help to constrain velocity changes in sediments across the BSRs, which are interpreted as indicative for the presence of free gas and gas hydrate in the area. Velocities defined form travel-time analysis are also used to provide estimates of free gas and gas hydrate saturation in sediments using a forward effective-medium modelling approach.

Results from this thesis contribute to the understanding of rifting evolution on both small-scale basins, such as the Black Sea, and fully developed passive continental margins. Similarly, results also contribute to the general understanding of gas hydrate evolution in the Black Sea as well as along other well-known gas hydrate regions.

Table of Contents

Table of Tables

Table of Figures

Table of Figures

Table of Figures

Research Thesis: Declaration of Authorship

I, Vanessa Monteleone, declare that this thesis and the work presented in it are my own and has been generated by me as the result of my own original research.

Title of thesis: "An integrated geophysical analysis of rifting evolution and gas hydrate occurrence in the Eastern Black Sea Basin"

I confirm that:

1. This work was done wholly or mainly while in candidature for a research degree at this University;
2. Where any part of this thesis has previously been submitted for a degree or any other qualification at this University or any other institution, this has been clearly stated;
3. Where I have consulted the published work of others, this is always clearly attributed;
4. Where I have quoted from the work of others, the source is always given. With the exception of such quotations, this thesis is entirely my own work;
5. I have acknowledged all main sources of help;
6. Where the thesis is based on work done by myself jointly with others, I have made clear exactly what was done by others and what I have contributed myself;
7. Parts of this work have been published in peer-reviewed scientific journals:
    - **Chapter 3** has been published as: Monteleone, V., Minshull, T. A., & Marín-Moreno, H. (2019). "Spatial and temporal evolution of rifting and continental breakup in the Eastern Black Sea Basin revealed by long-offset seismic reflection data". *Tectonics*, 38(8), 2646-2667. DOI: https://doi.org/10.1029/2019TC005523
    - **Chapter 4** has been published as: Monteleone, V., Minshull, T. A., & Marín-Moreno, H. (2020). "Integrated geophysical characterization of crustal domains in the eastern Black Sea". *Geology*, 48(4), 405-409. DOI: https://doi.org/10.1130/G47056.1
    - **Chapter 5** is to be submitted for publication in the *Journal of Geophysical Research (JGR): Solid Earth* as: Monteleone, V., Minshull, T. A., & Marín-Moreno, H. "Seismic characterization of multiple BSRs in the Eastern Black Sea Basin".
8. I suspended my research degree candidature to undertake a nine-month placement within the National Oceanography Centre (NOC), working on a project relevant to the gas hydrate study performed in Chapter 5 of this thesis. The results of this work will be submitted for publication in *Marine and Petroleum Geology (Elsevier)* as: Monteleone, V., Marín-Moreno, H., Bayrakci, G.

& Best, A. “Seismic characterization and modelling of gas hydrate occurrence in the northern Bay of Bengal, offshore Bangladesh”.

Signature: .....Date:.....

Acknowledgements

I would like to thank both my supervisors, Tim Minshull and Héctor Marín-Moreno, for guiding me throughout my time as PhD student at the University of Southampton, for their continuous support and useful inputs, and for keeping me always on track and focused during my project. I feel extremely lucky to have had them as supervisors, as they have both always showed their presence and dedication to the project, shared their expertise, and they have had a fundamental role in encourage me during all the steps of my PhD. Tim always ensured that I maintained a strong focus throughout my PhD and gave me the possibility to gain experience and to acquire new skills participating in scientific cruises, attending workshops and courses, and presenting at several international conferences. Héctor always provided me with straight feedback on my research and with useful suggestions on how to improve results, and I thank him for all the time he made available for explanations and discussions. I also thank Tim Henstock and Jon Bull for the inputs provided during my PhD milestones, and for the expertise shared during the scientific cruises. A special thanks goes to my examiners, Lisa Mcneill and Gareth Crutchley, for the usefull inputs provided during the Viva and for their suggestions on how to improve this thesis.

I am grateful to the Environment Research Council (NERC) Centres for Doctoral Training (CDTs) in Oil and Gas for sponsoring my PhD, for the training provided, and for the fantastic collegues that I have met during the training academy. Among them, I thank Panayiota and Raquel for their friendship, support, and great moments spent together. I am also grateful for the placement experience that was offered to me at NOC, which allowed me to work on a relevant research project getting useful insights on a subject that became fundamental in the last part of my thesis. I thank Héctor, Gaye Bayrakci and Angus Best for the collaboration and support given me during this placement, which revealed to be a great personal and professional experience.

I would also like to thank all the PhD students, postdocs and researchers that helped me at different stages of my project, particularly Gaye, Mark Vardy, Adnan Djeffal, Tanner Acquisto, Robert Allen and Louise Watremez for the help they provided me during my challenging time with seismic data and tomographic techniques.

Thanks to my friends and officemates, particularly Bhargav, David, Naima and Giuseppe, for the time spent together and for the funny moments that made my time as PhD student an enjoyable experience.

Finally, a special thank goes to my family for the support and encouragement during the ups and downs of PhD life, and to Marco, who has constantly been on my side during these four and a half years. To them, I dedicate this thesis.

Definitions and Abbreviations

2D ..... Two-dimensional

3D ..... Three-dimensional

A/m ..... Ampere/meter

AGC ..... Automatic Gain Control

(B)GHSZ ..... (Base of) Gas Hydrate Stability Zone

BP ..... British Petroleum

BSR(s) ..... Bottom-Simulating Reflector(s)

COB..... Continent-Ocean Boundary

COT..... Continent-Ocean Transition

EBSB ..... Eastern Black Sea Basin

EMAG2-v3 ..... Earth Magnetic Anomaly Grid 2 (version 3)

F-K ..... Frequency-Wavenumber

GEBCO ..... General Bathymetric Chart of the Oceans

GH ..... Gas Hydrate

IGRF ..... International Geomagnetic Reference Field

LGM..... Last Glacial Maximum

m/s ..... meters per second

ms..... milliseconds

MBSH..... Mid Black Sea High

Moho..... Mohorovičić discontinuity

NMO..... Normal Move-Out

nT ..... nano Tesla

OBS..... Ocean Bottom Seismometer

P-T ..... Pressure-Temperature

RMS ..... Root Mean Square

SEGY ..... Society of Exploration Geophysicists digital recording standard Y

TPAO ..... Türkiye Petrolleri Anonim Ortaklığı (Turkish Petroleum Company)

TWTT..... Two Way Travel-Time

V_P ..... Compressional (P-wave) velocity

WBSB ..... Western Black Sea Basin

Chapter 1 Introduction

1.1 Overview and rationale

Passive continental margins and extensional basins are subjects of great interest for both academic research and the energy industry, the former trying to unravel how extensional processes initiate and evolve through time and the latter, based on the understanding of the geodynamics shaping these areas, primarily interested in exploiting their hydrocarbon resources.

Continental rifting is the first-order mechanism driving the formation of passive continental margins and extensional basins and is the result of extensional forces stretching and thinning the continental lithosphere. As a natural consequence, lithospheric breakup may occur followed by the emplacement of new crust through surface volcanism and subsurface intrusions, resulting in the formation of new ocean basins bordered by passive continental margins. Classical models of rifted margins are based on the idea that seafloor spreading directly follows rifting and that continental breakup is a process well defined in time and space. Consequently, each stage in basin evolution is identified by well defined sedimentary sequences recording pre-, syn- and post-kinematic (i.e., thermal subsidence) phases, separated by stratigraphic unconformities, i.e., breakup unconformity (Driscoll et al., 1995). However, results from deep-water drilling (e.g., Ocean Drilling Program, ODP) and observations from refraction surveys and higher quality 2D/3D geophysical data have shown that the tectono-sedimentary architecture at rifted margins records intermediate and complex deformation phases, which relate to the fact that rifting and continental breakup are more variably distributed in time and space (e.g., Tucholke and Sibuet, 2007; Alves and Cunha, 2018; Muirhead et al., 2016; Nixon et al., 2016; Péron-Pinvidic et al., 2007; Gillard et al., 2015; Soares et al., 2012; Alves et al., 2021). Evidence of a poly-phase rifting evolution and/or of a complex breakup history along the margin have been presented by numerous studies (e.g., Tucholke et al., 2007; Muirhead et al., 2016; Nixon et al., 2016; Gillard et al., 2015; Franke, 2013; Soares et al., 2012). Extension may focus over one conjugate margin resulting in an asymmetric rift structure and, along the same margin, change in rifting style may also occur. Similarly, a focused breakup and oceanic spreading may occur, which progressively migrates along-axis accompanied by changes in melt supply. Where melt supply is low, lower crust and/or mantle exhumation at hyper-extended areas, as well as varying amounts of magmatic intrusions within a highly extended continental crust, may occur (e.g., Pickup et al., 1996; Sibuet et al., 2007; Sauter et al., 2018) (Figure 1-1).

Distinct architectures, associated with specific deformation and/or magmatic processes, generally characterise continental margins from proximal to distal and oceanic domains (e.g., Peron-Pinvidic

and Osmundsen, 2018) (Figure 1-1). Nevertheless, deformation processes may overlap in time and space reflecting the complex trade-off between spreading rates, lithospheric compositional variations, and along-axis changes in mantle and lithospheric properties, making boundaries between rift domains diffuse (e.g., Tucholke et al., 2007; Tugend et al., 2015). The variability in deformation processes and the resulting complexity in architectural elements identified at extended margins, has brought about a relatively wide range of rift domain definitions, and criteria for the identification of their limits may differ (e.g., Peron-Pinvidic et al., 2013; Sutra et al., 2013; Stanton et al., 2019) (Figure 1-1).

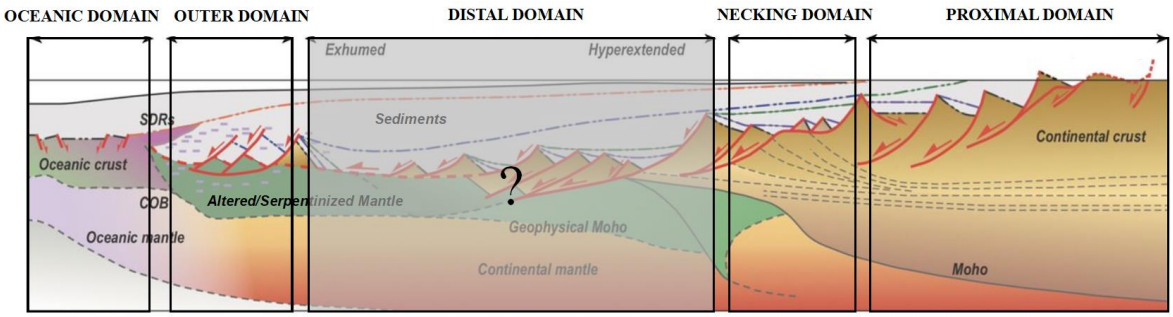

Figure 1-1. Schematic representation of margin's domains. Proximal domain: fault systems with syn-rift sediments in hanging-wall basins. Necking domain: greater extension and rotation of crustal fault blocks, ductile stretching in the lower crust. Distal domain: migration and localisation of deformation can result in ambiguous crustal configurations (?); in the shaded box, the case shown is a hyperextended magma-poor distal margin (section 1.2.3) characterised by highly extended and rotated crustal blocks with low angle to horizontal detachment faults and large displacements with highly thinned lower crust (hyper-extended domain), partly riding on exhumed continental mantle (exhumed domain). Outer domain: breakup zone with igneous intrusions (dykes and sills) and seaward-dipping reflectors (SDRs) formed by lava flows and volcanoclastic wedges dipping oceanward. Continent–ocean boundary (COB). Oceanic domain: thin high-velocity oceanic crust commonly with a well-defined seismic Moho (modified from McClay and Hammerstein, 2020).

Besides the impact on the structural elements and basement configuration, the extreme variability of the processes controlling margin evolution often complicates the identification and age definition of syn-kinematic (or syn-rift) and early post-kinematic (or post-rift) sedimentary infills. This is particularly true in deep water settings and where thick sedimentary infills mask the early syn- and post-kinematic units, limiting both direct and indirect investigations. Similarly, the crustal structure and composition of a basin is often difficult to constrain by direct sampling (e.g., ODP; Boillot et al., 1988). A variety of indirect geophysical methods (i.e., seismic reflection and refraction,

potential fields) are used to overcome these limitations (e.g., Gillard et al., 2015). However, the basement underlying extensional basins may also present a geophysical signature differing from what is typically expected for continental and/or oceanic crust, resulting in a difficult definition of the transition from the late stages of continental rifting to initial oceanic accretion (see section 1.2.4). Despite these challenges, understanding the different stages in passive continental margins and extensional basin evolution is key to unravel the mechanisms driving lithospheric extension, as well as the present-day structural configuration at these settings.

Sedimentary basins formed on passive continental margins and rifted basins also host some of Earth's major hydrocarbon fields. Thus, a clear definition of the extent of continental versus oceanic crust and of the presence, if any, of intermediate or *transitional* crust is fundamental to reconstruct their thermal history, which is key for models of heat flow and, hence, of hydrocarbon maturation (e.g., Fraser et al. 2007). Beside conventional hydrocarbon resources, there has been growing interest over the last few decades in un-conventional hydrocarbons such as gas hydrates. This type of deposit, which is stable within a limited range of pressure and temperature conditions present in sediments few hundred meters below seafloor (Kvenvolden and Lorenson, 2001), has attracted considerable interest for its potential as a future lower-carbon energy source; furthermore, given the big amounts of gas that can be released upon their dissociation, interest in gas hydrate has also been driven by their potential impact on seafloor sediments stability and on climate change (e.g., Kvenvolden, 1993; Grauls, 2001; Boswell and Collett, 2011; Ruppel and Kessler, 2017; Minshull et al., 2020). Several studies have therefore focused on the investigation of gas hydrate formation and dynamics, which are yet not fully understood.

This thesis presents a case study of the Eastern Black Sea Basin (EBSB). Here, the deep water (2.0-2.2 km) setting and the thick sedimentary infill (up to 9 km-thick) limit the ability to sample and image the deep basin stratigraphy and underlying basement. This, in turn, makes difficult to constrain the timing and mechanisms driving extension, and to define whether breakup and oceanic spreading has occurred in the central basin. The whole Black Sea basin is also a frontier in hydrocarbon exploration due to the presence of a regional source-rock, the Oligocene-lower Miocene Maykop Formation (e.g., Robinson et al., 1996; Tari and Simmons, 2018). Thus, untangling basin evolution and dynamics is essential for modelling the maturity of the hydrocarbon systems in place. The basin is a well-known area for gas hydrate studies, with thermodynamic conditions and high organic content of sediments making up to 91 % of the deep-water part of the basin favourable for gas generation and hydrate formation (Vassilev and Dimitrov, 2002). Most studies have focused on the Western Black Sea Basin (WBSB), particularly in areas where seismic Bottom-Simulating Reflectors (BSRs), generally associated with the base of the gas hydrate stability zone (BGHSZ), have been identified. Seismic data along the Danube deepwater fan and in the central Black Sea have

also shown the presence of multiple BSRs, whose controversial nature has spurred great research interest (Popescu et al., 2006; Zander et al., 2017; Riedel et al., 2020; Bialas et al., 2020). While single BSRs have been observed at few locations in the EBSB (Vassilev and Dimitrov, 2002; Minshull and Keddie, 2010), there is no evidence, to date, for the occurrence of multiple BSRs in the EBSB. This part of the basin therefore provides a new case study to investigate the presence of such controversial features, determine their hydrate-related nature and, based on that, define hydrate accumulation and formation dynamics.

The main dataset for this study consists of 2D long-offset seismic reflection profiles, acquired as part of a regional survey by *Geology Without Limits* (GWL) and ION GXT in 2011. Seismic profiles are used to interpret the deep tectono-stratigraphic elements of the basin and to analyse basement morphological variations as a proxy for crustal type. Forward magnetic anomaly modelling is used to complement and guide seismic interpretation of crustal domain. Results are compared with previous studies from a 2005 wide-angle seismic experiment showing a NW to SE transition from a 7-9 km thick crust with continental lower crustal velocities (6.4-6.6 km/s), to an anomalously thick crust of 11-13 km with oceanic lower crustal velocities (6.8-7.2 km/s) (Shillington et al., 2009). Based on this integrated analysis, this study aims to provide insights on (i) how rifting deformation is accommodated in space and time, (ii) how stratigraphic and structural elements record strain distribution and localization during the process of continental extension and lithospheric breakup and (iii) how the spatial and temporal distribution of rifting and breakup processes in the area translate in terms of resulting crustal configuration (Chapter 3 and Chapter 4).

The same seismic data show new evidence for the presence of up to four vertically stacked BSRs along the NE margin of the EBSB. Multiple BSRs are uncommon features identified in few other gas hydrate provinces, where their presence has been variably interpreted to result from hydrate dynamics controlled by climatic/sea-level changes, tectonic uplift, high sedimentation rates, changes in the hydrate-forming gas composition, or as defining the boundaries between different zones of fluid overpressure (e.g., offshore Peru, Auguy et al., 2017; offshore Oregon, Bangs et al., 2005; Nankai margin, offshore Japan, Foucher et al., 2002; North Atlantic margins, Posewang and Mienert, 1999; offshore SW Taiwan, Kunath et al., 2020; WBSB, Bialas et al., 2020). To constrain the physical nature of the EBSB BSRs, seismic data are used to derive a 2D velocity model of the sediments. A travel-time analysis approach is applied to streamer data, which are also pre-conditioned using downward continuation to improve refracted travel-time picking. The defined seismic velocity model is then compared with seismic velocity estimates from a forward modelling approach based on the effective-medium theory, which is used to estimate gas and/or gas hydrate saturation in sediments. Results from this study aims to: (i) show the benefits and limitations of downward continuation technique, generally used to improve the refracted wavefield before

travel-time analysis applied for deeper targets, (ii) define the physical nature of the EBSB multiple BSRs, providing an estimate for the free gas and gas hydrate saturation in sediments and (iii) propose the mechanism(s) explaining multiple BSR generation (Chapter 5).

The research background for Chapters 3, 4 and 5 of this thesis is provided in the following sections. Section 1.2 focuses on the main concepts, terminology, end-members and kinematic models defined in the context of continental rifting, providing a reference for the content of Chapters 3 and 4. Section 1.3 introduces the subject of gas hydrates, which provides a contextualisation for the content of Chapter 5. Finally, Section 1.4 provides the background to the EBSB geological settings and hydrocarbon exploration studies, and discusses the open questions ultimately motivating this study.

1.2 Continental rifting

Continental rifting results from extensional forces that cause the continental lithosphere to stretch and thin. Regional extension can be caused by far-field plate movements (e.g., breakup of Pangea; Olsen 1997), back-arc extension (e.g., Aegean; Jolivet et al. 2010), post-orogenic extension (e.g., Basin and Range; Jones et al. 1992), or mantle plumes or hotspots (e.g., Ethiopian rift; Chorowicz 2005). If rifting continues up to continental breakup, new oceanic lithosphere may be emplaced during seafloor spreading, leaving the two sides of the continental rift behind as conjugate rifted continental margins and developing a new ocean basin in between them (e.g., Wilson, 1966; Brune, 2016).

Early studies on rifted margins focused within shallow water, proximal margin domains and intracontinental rift basins, and data acquisition was limited to sedimentary infill down to the basement in areas prospective for hydrocarbons (e.g., Levell et al., 2010). Since little was known about the structure of the more distal settings and on the deeper crustal configuration, simple conceptual models were developed to explain the formation of rifted margins (e.g., McKenzie, 1978; Wernicke, 1985).

Expeditions funded by international science bodies such as DSDP (Deep Sea Drilling Project), ODP (Ocean Drilling Project) and IODP (International Ocean Drilling Project), together with improved geophysical techniques, brought to the discovery of new structural settings such as wide zones of exhumed subcontinental mantle and large offset normal faults (e.g., Boillot et al., 1987), and led to key observations about rifting evolution along a margin such as the progressive localisation of rifting into the area of future breakup as well as its propagation along the margin (e.g., Peron-Pinvidic et al., 2007). The migration and localisation of deformation towards more distal parts of the margin is associated with a change in the mode of extension, resulting in a different structural evolution of proximal and distal margins. Thus, significant along-strike variations in terms of basement structure, stratigraphy, subsidence and thermal and magmatic evolution can be observed along margins (i.e., Møre - Vøring - Lofoten segment of the mid-Norwegian margin; Faleide et al., 2008; Iberia-Newfoundland; Peron-Pinvidic et al., 2007; Soares et al., 2012). Structural and stratigraphic elements, recording the history of rifting, breakup and oceanic spreading, and the post-rift evolution in these settings, also reveal the complex timings, dynamics, and processes contributing to the shaping of new ocean basins and passive continental margins which make every rift unique (e.g., Bradley, 2008; Brune, 2016). All these new observations show that rifting is fundamentally multiphase and results from the interaction of crustal and mantle processes, requiring a revision of the simple models originally used to describe margin's evolution, and to the development of new

terminology and definitions (i.e., poly-phase rifting, sequential faulting, rift migration; Peron-Pinvidic and Manatschal, 2019).

Several key parameters strongly influencing rift evolution and the final geometry of rifted margins have been defined: lithospheric thermal state, compositional variations in the crust and mantle, the presence of fluids, and the temporal and spatial variations in strain rate. These parameters all serve to control the rheology of the extending lithosphere (e.g., Pérez- Gussinyé et al., 2006; Rupke et al., 2013; Jammes et al., 2015). Other parameters include rift obliquity, structural inheritance, and sedimentary and magmatic input during rifting (e.g., Burov and Poliakov, 2001; Bialas et al., 2010; Jeanniot and Buiter, 2018). Modeling techniques are now widely used to explore the impact of these parameters on rift evolution, some of them providing a description of the 3D strain distribution and of the tectonic, magmatic, isostatic, and thermal evolution at rifted margins (e.g., Corti et al., 2003; Huismans and Beaumont, 2007; Brune et al., 2017; Le Pourhiet et al., 2018; Zwaan and Schreurs, 2020).

Nevertheless, end-members are still used to describe extensional margins and basins, summarising key differences in geometry and mechanism of extension, which are the result of the properties and thus the behaviour of the lithosphere. The mechanism of extension will also influence the amount of magmatism accompanying and following extension, which is also described according to different models. Below, some of these end-members together with new definitions accounting for the complex dynamics identified at extensional settings are discussed. Terminology and definitions from this section are relevant to the content of Chapters 3 and 4.

1.2.1 Narrow vs. wide rift

It is generally accepted that the final geometry of the rift (i.e., the character of lithospheric thinning, distribution of normal faults, the exposure of lower crust and/or upper mantle lithosphere, and the symmetry) depends largely on rheology and temperature of the lithosphere. *Hot*, weak, or thick continental crust is dominated by ductile deformation and often extends symmetrically into a wide rift system (e.g., Huismans and Beaumont, 2007). On the contrary, extension in *cold*, strong, or thin crust is accommodated by brittle faults and ductile shear zones that facilitate narrow rifts with asymmetric fault geometries (Buck et al., 1999; Brune et al., 2017) (Figure 1-2).

Wide continental rifts exhibit broadly distributed deformation accommodated by regularly spaced, near-parallel, normal faults (e.g., Huismans and Beaumont, 2007). The majority of these faults accommodate only a small amount of extension (< 10 km; Jones et al., 1992). The rest of the extension may be accomplished by large-scale detachment faults that can have a displacement of up to 50 km (Wernicke, 2009) (Figure 1-2). Thus, wide margins exhibit gradually thinning continental

crust over a distance of > 100 km (i.e., Gabon margin; Blaich et al., 2011). On the other hand, narrow continental rifts consist of an elongated series of asymmetric rift basins flanked on one side by steeply dipping normal faults (i.e., Gulf of Corinth, Nixon et al., 2016). Thinning and weakening of the lithosphere is focused at the rift axis, as evidenced by the shallowing of the seismogenic layer (at ~ 12-15 km) at the rift axis. A narrow necking zone (the boundary between the proximal and distal margins; Figure 1-1) is present, where the crust thins abruptly from a normal thickness (~ 30 km) to less than 5 km over a distance of approximately 50 km (i.e., Flemish Cap margin - Bassi et al., 1993; Welford et al., 2012; West Greenland margin - Chalmers and Pulvertaft, 2001; Skaarup et al., 2006).

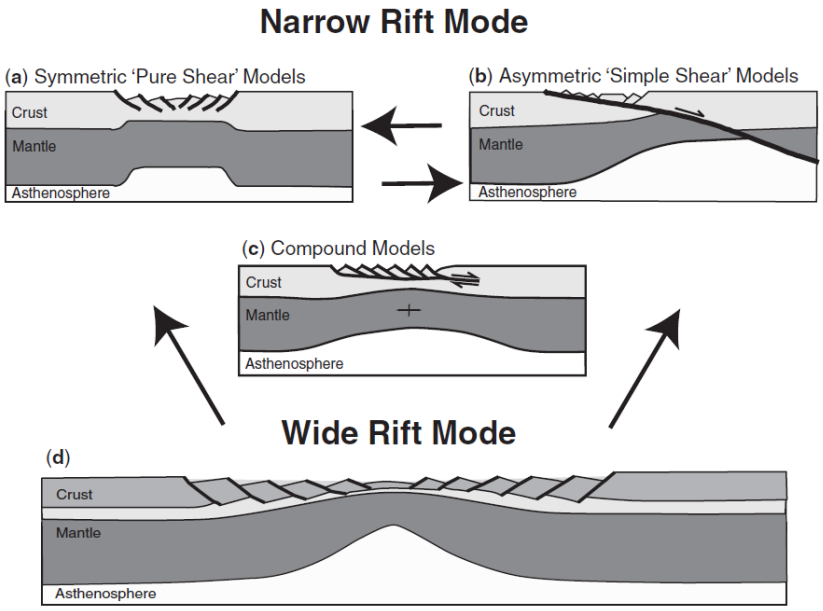

Figure 1-2. End-member styles of rifting. (a) Symmetric, (b) asymmetric and (c) compound narrow models, and (d) the wide rift model. Arrows in the diagram indicate that both narrow and wide rifts can ultimately result in symmetric or asymmetric conjugate margins (from Huismans and Beaumont, 2007).

However, as more data have become available it is clear that rifted margins and continental rifts can be very diverse, and their width is far from constant along their strike (e.g., Ziegler and Cloetingh, 2004; Reston, 2009; Mohriak and Leroy, 2012). As such, asymmetric conjugate margin pairs can have a narrow margin facing a wide margin as its conjugate (i.e., Camamu-Gabon - Blaich et al., 2011; Labrador-SW Greenland - Chian et al., 1995). This change in distribution of deformation along the rift has been explained by changes in the temperature of the pre-rift lithosphere, changes in the direction of extension, and the diachronous nature of rifting (e.g., Ziegler and Cloetingh, 2004; Reston, 2009; Brune et al., 2017). Another observation is the time-dependency of deformation. While in wide rifts the margin is formed by continuous stretching of the entire margin area, narrow rifts can also generate wide margins by diachronous stretching during lateral rift

migration (Brune et al., 2014). In addition, the boundary between narrow and wide rift zones can be linked to a change in geological setting. An example is the northern Rio Grande rift which is located between the strong and tectonically stable Great Plains and Colorado Plateau (e.g., West et al. 2004). The northern rift is < 100 km wide and has characteristics of a narrow rift, whereas the southern region shows distributed deformation and has similar characteristics to the wide and hot Basin and Range (Keller and Baldridge, 1999; Wilson et al., 2005).

Although these two end-members provide the standard framework to understand initial rift geometry, they don't account for the dynamics at intermediate and late rift stages shaping the final margin architecture, where both narrow and wide rifts can ultimately result in highly asymmetric conjugate margins (Brune et al., 2017).

1.2.2 Symmetric vs. asymmetric rift

Kinematic models are used as templates for the interpretation of observations along passive margins. The widely accepted end-member styles of lithospheric extension, and their associated geometries, are represented by the "*pure shear*" or symmetric model (McKenzie; 1978) (Figure 1-2a), and the "*simple shear*" or asymmetric model (Wernicke, 1985) (Figure 1-2b).

Symmetric models show similar structural evolution on both margins with the rift axis as the centre of symmetry (McKenzie, 1978), whereas asymmetric models assume significant deformation along a single, low-angle normal fault (detachment) that cuts through the crust and lithospheric mantle (Wernicke, 1985; Boillot et al., 1992). These faults can accommodate tens of kilometres of offset and eventually develop into high-angle shear zones extending into the upper mantle and leading to the exposure of lower-crust/mantle material at the surface (e.g., Whitmarsh et al., 2001). The two conjugate margins, representing the upper and lower plate of a detachment fault, show fundamentally different geometries (Nagel and Buck, 2004). Combinations of these geometries are also presented (Lister et al., 1986; Huismans and Beaumont, 2007) (Figure 1-2c).

1.2.3 Magma-poor vs. magma-rich

Based on the volumes of extension-related magmatism and on the amount of magma present during breakup two end-members are defined: "*magma-rich*" (or volcanic) and "*magma-poor*" margins (Planke et al., 2000; Franke, 2013; Geoffroy et al., 2015; Péron-Pinvidic et al., 2013; Tugend et al., 2020; Gallahue et al., 2020) (Figure 1-3).

At magma-rich (volcanic) rifted margins, the lithospheric mantle breaks before (or at the same time as) the crust to produce large volumes of syn-rift igneous rocks (Geoffroy, 2005). Voluminous

intrusive and extrusive magmatic emplacement develops over short time periods, facilitating and resulting from continental rifting and breakup.

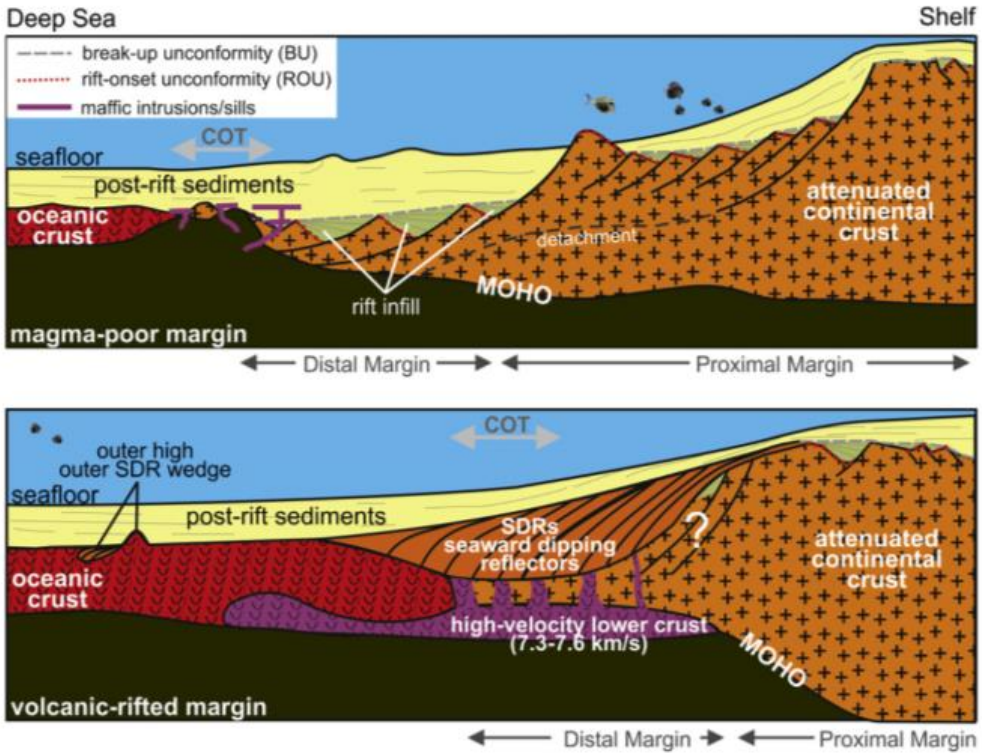

Figure 1-3. Schematic sketch of the magma-poor (top) and magma-rich (bottom) end-member extremes of passive continental margins (Franke, 2013).

Flood basalts are generally emplaced during the pre- and/or syn-rift stages, and this is typically manifested in reflection seismic data by the presence of seaward-dipping reflectors (SDRs) at the proximal domain (e.g., Geoffroy, 2005; Franke, 2013; Marzoli et al., 2018) (Figure 1-3). Additionally, focused magmatism expressed as volcanic flows, mafic intrusions, and/or igneous underplating occurs during continental breakup and the transition to seafloor spreading (White et al., 1987; Bastow and Keir, 2011; Geoffroy et al., 2015). Thus, widespread high-velocity lower crust may be present as a result of igneous underplating, showing velocities above 7.2 km/s (e.g., White et al., 1987; Talwani and Abreu, 2000) (Figure 1-3). Such high-velocity lower crust is typically confined within a narrow zone in the range of about 50 km from the rift, whereas “normal” oceanic crust with lower-crustal velocities associated with basalt flows is visible up to 200 km away from the rift (White et al., 2008). There are several hypotheses regarding the origin of the high-velocity lower crust, including massive intrusions, mafic underplating, partially serpentinized mantle beneath extremely stretched margins, and inherited high-grade metamorphic rocks (Ebbing et al., 2006; Gernigon et al., 2006). Examples of magma-rich rifted continental margins include the East North American Margin (ENAM) in the Central Atlantic (Austin et al., 1990; Whitmarsh et al., 2001), portions of the conjugate margins of the South Atlantic (Franke et al., 2007; Koopmann et al., 2014)

and North Atlantic (Eldholm and Grue, 1994), the margin of the Canadian Arctic (Funck et al., 2011), the margin of East Antarctica (Gupta et al., 2017), the north-western Australian Margin (Hopper et al., 1992), and the Southwest Indian Margin (Ajay et al., 2010).

At magma-poor rifted margins, little or no magmatism accompanies extension. These margins typically exhibit extreme crustal thinning (hyper-extension) along a main detachment fault (Figure 1-1; Figure 1-3). Also, mantle and/or lower lithosphere exhumation may occur and precede the onset of steady-state seafloor spreading (e.g., Franke, 2013; Mortimer et al., 2020). As a result, magma-poor margins often show wide domains of extended crust with wide-ranging extensional features as rotated faults blocks and detachment surfaces near the base of the continental crust, but limited magmatism which seems to be delayed to post-breakup (Franke, 2013) (Figure 1-3). Some of the best-known examples of magma-poor margins are the Brazil-Angola margin (e.g., Contreras et al., 2010; Contrucci et al., 2004), the NW Australian margin (e.g., Discroll and Karner, 1998), the Iberia-Newfoundland margin (e.g., Whitmarsh et al., 2001; Sibuet and Tucholke, 2013) and the Gulf of Aden (e.g., Autin et al., 2010).

The magmatic budget and the timing of magma emplacement relative to breakup can change along the same extensional margin, thus intermediate examples also exist. For instance, along the extended margins of the South China Sea (e.g., Franke, 2013; Peng et al., 2020), the Norwegian margin (e.g., Jakob et al., 2019) and the Gulf of California (e.g., Lizarralde et al., 2007), elements of both end-members are present as a result of an along-axis variation in the amount of magmatism. Changes in crustal geophysical expression, i.e., seismic velocity structure and crustal thickness, may be therefore identified at these locations. These changes may be representative for the transition from magma-poor to magma-rich margins, reflecting the mechanisms driving extension, the presence of inherited tectonic structures, the nature and composition of the lithosphere affected by extension, and the presence of focused thermal anomalies (Nemčok and Rybár, 2017, and references therein). Therefore, observations along extensional margins show the complexity in clearly distinguishing between end-members, highlighting the reality of a transition between the two end-members rather than a distinct separation. This is in contrast with classical models assuming that seafloor spreading directly follows rifting and that continental breakup is a process well defined in time and space. In this classical view, a Continent-Ocean Boundary (COB) is defined as the sharp boundary between fully continental and oceanic basement (e.g., Mjelde et al., 1992; Maillard et al., 2006). Observations from geophysical data have instead revealed the presence of features that might plausibly be assigned to either continental or oceanic crustal type (e.g. Ball et al., 2013). This led to the definition of a finite-width Continent-Ocean Transition zone (COTZ, COT or OCT), instead of a linear COB (e.g., Eagles et al., 2015) (Figure 1-3). The COT accounts for the presence of a *transitional* zone characterised by neither clearly continental nor oceanic crust, which

results from the complex interaction between along-axis variations in lithosphere and mantle properties, the timing and kinematics of extension, the strain rates and the amount of magmatism (e.g., Franke, 2013). Crustal structure and composition at the COT may vary from one location to another, thus the nature of the transition is often debated. Both magma-rich and magma-poor COT have been interpreted as the equivalents of oceanic crust generated under unusual melting conditions (Williams et al., 2011; Scott, 2000, Gillard et al., 2015) or as the products of extreme volcanic or mechanical alteration of continental crust and mantle occurring prior to the onset of seafloor spreading (Eldholm and Grue, 1994, Lundin and Doré, 2011; Nirrengarten et al., 2014). Thus, the COT can describe either the highly-thinned continental crust sometimes bearing small amounts of volcanic intrusions (e.g., Colwell et al., 2006), or a domain of exhumed lower crust and/or mantle (sometimes altered by hydration and serpentinised) followed by non-steady state proto-oceanic lithosphere (e.g., Gillard et al., 2015), or the anomalously thin oceanic crust lying between proper continental and oceanic domains (e.g., Franke et al., 2011). At some locations, the COT may be defined as a narrow zone ≤ 30 km-wide (i.e., Newfoundland margin – Sutra et al., 2013; Campos Basin - Stanton et al., 2019; Gulf of Aden – Leroy et al., 2010). At some of these locations, magmatic segmentation guided by the presence of transform faults which may be inherited from pre-existing structure in the continental lithosphere and may control the evolution at spreading segments, is used to explain such a narrow transition (e.g., Collier et al., 2017; Hammond et al., 2013). Along other margins, the COT may be a wide segment extending for 50-100 km (i.e., Australia-Antarctic margins; McCarthy et al., 2020) or more (e.g., Eagles et al., 2015).

1.2.4 Oceanic domain

The identification of oceanic crustal domains, and their lateral extent and structure, is key for constraining breakup and oceanic spreading stages at extensional settings.

In the early 1970s, a layer-cake ("*Penrose-type*") model was proposed to define the oceanic crustal structure based on ophiolite studies, marine geophysical and dredging data (Vine and Moores, 1972) (Figure 1-4a). Velocity-depth structure coming from seismic refraction experiments then provided valuable information on the structure of the oceanic crust, which is generally subdivided into three distinct layers. "Layer 1" consists of the sedimentary layer accumulated over the igneous basement, whereas the igneous basement is divided into the upper oceanic crust or "Layer 2", and the lower crust or "Layer 3" (Raitt, 1963; Grevemeyer et al., 2018). Layer 2 is generally ~ 1.5-2 km-thick, with a region of strong velocity gradients and velocity increasing from ~ 3 km/s to ~ 6.7 km/s towards its base (White et al., 1992; Grevemeyer et al., 2018). The boundary between Layer 2 and Layer 3 shows primarily a decrease in vertical velocity gradient from > 1 km/s per km to 0.1 km/s per km, with velocity increase within layer 3 from ~ 6.7 km/s at the transition zone to ~ 7.0-7.2 km/s

near the crust-mantle boundary (Carlson and Miller, 2004). This observation suggested that the physical properties of Layer 3 are relatively homogeneous at a seismic scale. Layer 3 is often referred to as "oceanic layer" because it includes more than two-thirds of the igneous crust, and oceanic crustal thickness changes seem to be predominantly dominated by changes in Layer 3 accretion (e.g., White et al., 1992; Grevemeyer et al., 2018) (Figure 1-4).

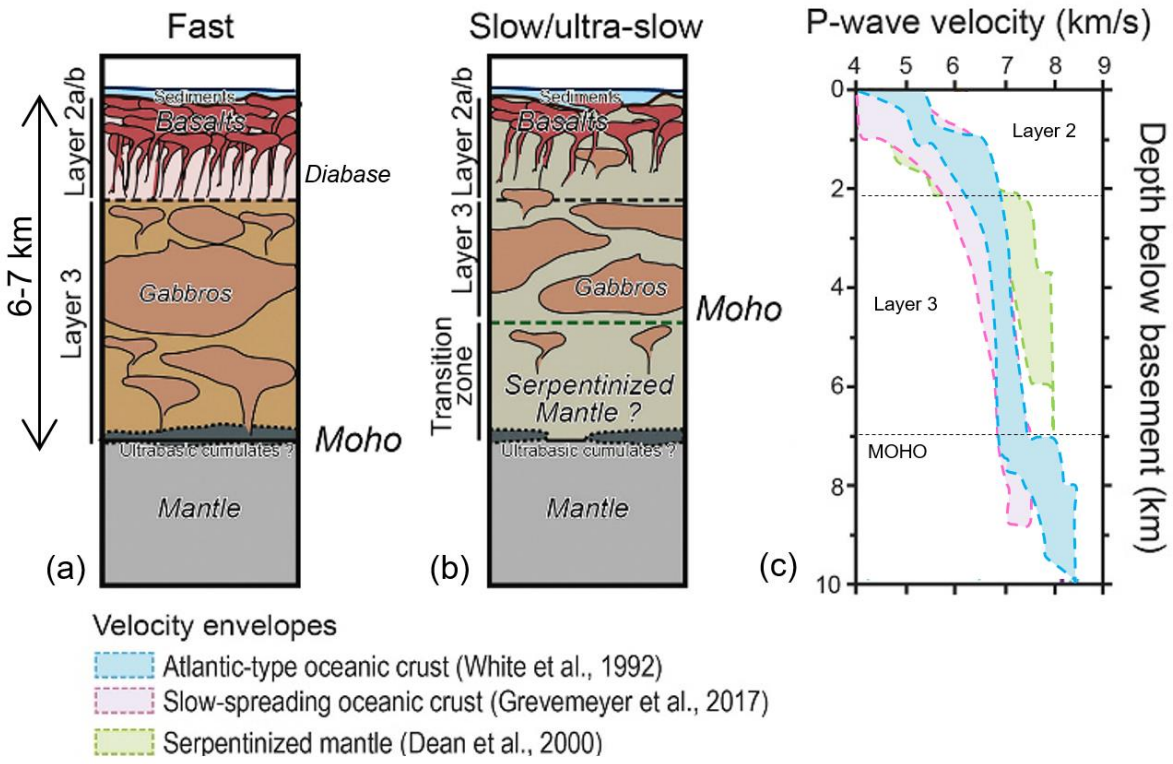

Figure 1-4. The structure of the oceanic crust at fast- versus slow-/ultra-slow spreading rates. Oceanic layer 3 shows different morphologies affecting oceanic crustal thickness and velocity structure. (a) A continuous gabbro layer ("Penrose-type" oceanic crust; Vine and Moore, 1972) accreted at fast- and intermediate-spreading. (b) A layer of serpentinized mantle peridotites (Hess, 1962). (c) 1D velocity-depth envelopes through oceanic lithosphere showing changing velocity trends for normal oceanic crust (White et al., 1992), slow-spreading oceanic crust (Grevemeyer et al., 2017) and the case of serpentinized mantle (Dean et al., 2000). Image modified from Tugend et al. (2019).

Although oceanic crust average thickness is estimated to be 6.57 ± 1.61 km (Raitt, 1963), ~ 6 km (Chen, 1992), or more commonly 7.08 ± 0.78 km (White et al., 1992), a large degree of variability has also been observed (i.e., at magma-poor versus magma-rich, transform margins) suggesting that crustal accretion itself is highly variable in time and space (Van Avendonk et al., 2017). Key factors controlling the variability of oceanic crustal accretion include mantle composition, water content and temperature (Dick and Zhou, 2015; White et al., 1992; Korenaga et al., 2002), and slow (20-50 mm/yr) and ultraslow (< 20 mm/yr) spreading rates versus intermediate and fast-spreading

rates (Grevemeyer et al., 2018; White et al., 2001). At fast- and intermediate-spreading rates magma supply is relatively constant, axial melt is present in the upper crust, the thermal structure is warm, and crustal thickness is fairly uniform (e.g., Canales et al., 2003; Carbotte et al., 2013; Kent et al., 1993) (Figure 1-4a). At slow-spreading rates, magma supply is variable both spatially and temporally, axial melt is rarely observed, the thermal structure is relatively cool, oceanic core complexes and detachment faults are common, and crustal thickness is highly variable (e.g., Escartín et al., 2017; Hooft et al., 2000) (Figure 1-4b). At slow-spreading rates, crustal thickness may also vary as a function of segmentation, supporting focused mantle upwelling at the centre of the segments (e.g., Tolstoy et al., 1993). Thus, the thickness of the crust is 7-9 km in the middle of the spreading segment, while it is much thinner (4-6 km) at the end of the spreading segments (e.g., Canales et al., 2000; Hooft et al., 2000; Dannowski et al., 2011). At ultraslow-spreading rates an abrupt decrease in the amount of melt generated may also occur (White et al., 2001). The formed crust may undergo tectonism and core-complex formation, un-roofing lower crust and upper mantle to the seafloor and hence causing alteration and hydration (serpentinisation) (e.g., Cann et al., 1997; Reston and Ranero, 2011). However, even at ultra-slow spreading rates, crustal thickness may range from < 3 km (Jackson et al., 1982; Jokat and Schmidt-Aursch, 2007) to > 9 km (e.g., Niu et al., 2015). Despite the strong variability in crustal thickness, ultraslow-spreading crust seems to be on average thinner than crust formed at higher spreading rates (Grevemeyer et al., 2018).

Spreading rates, the amount of melt generated during spreading, and the presence of transform segmentation can affect not only the thickness and velocity structure of the newly formed crust (Figure 1-4), but also its morphology (e.g., Dunn and Martinez, 2011; Cannat et al., 2003) (Figure 1-5, Figure 1-6). Typically, 'normal' oceanic crust on seismic reflection data is characterised by a smooth top basement with highly reflective upper crust and a relatively acoustically transparent lower-crust, a well-marked reflector at the base of the crust interpreted as the Moho, commonly observed at ~ 9-10 s TWTT, and a passive sediment infill directly overlying the basement (Figure 1-5). However, such unambiguous oceanic crust in not often imaged on seismic reflection profiles and, similarly, a well-marked reflector that could be interpreted as the Moho is rarely observed, while the seismic texture within the basement is often confusing (Sauter et al., 2018) (Figure 1-6). When other evidence (i.e., drilling, seismic tomography) is missing, crustal domains are qualitatively assessed based on morphological changes of the top of the basement reflector.

Changes in the character of acoustic basement from '*rough*' to '*smooth*', is one of the earliest observations of seafloor structure (i.e., western North Atlantic, Windisch et al., 1965). Such change was initially linked to the contrasting morphologies resulting from fast- and slow-spreading ridges (Menard 1960; Heezen 1960). The transition from a magma-poor to magma-rich margin has also

been considered to explain changes in basement morphology, as well as crustal velocity structure (e.g., Keen and Potter, 1995; Shillington et al., 2009).

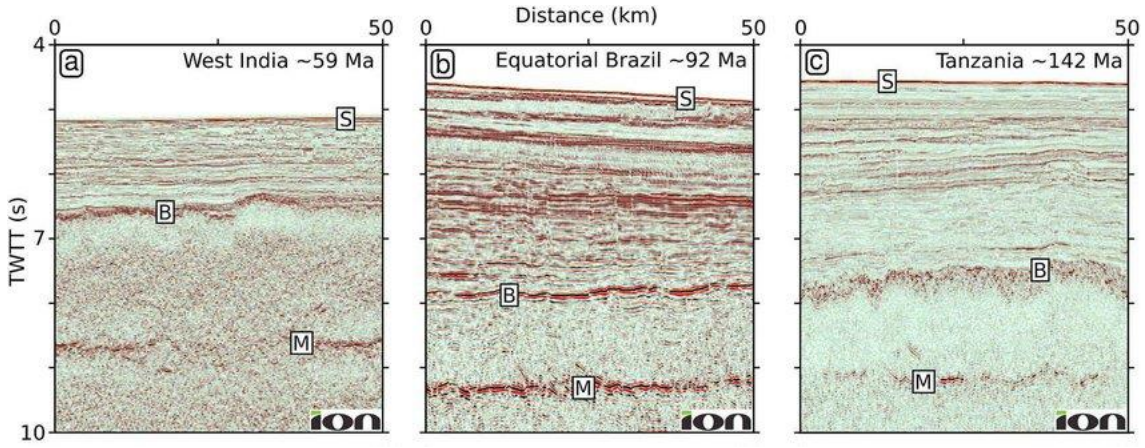

Figure 1-5. Smooth basement morphology. (a) W-India, (b) Offshore Brazil, and (c) Tanzania. S = seafloor, B = basement and M = Moho reflections. The vertical scale is in two-way travel-time (TWTT) and is expressed in seconds (s) (modified from Hoggard et al., 2017).

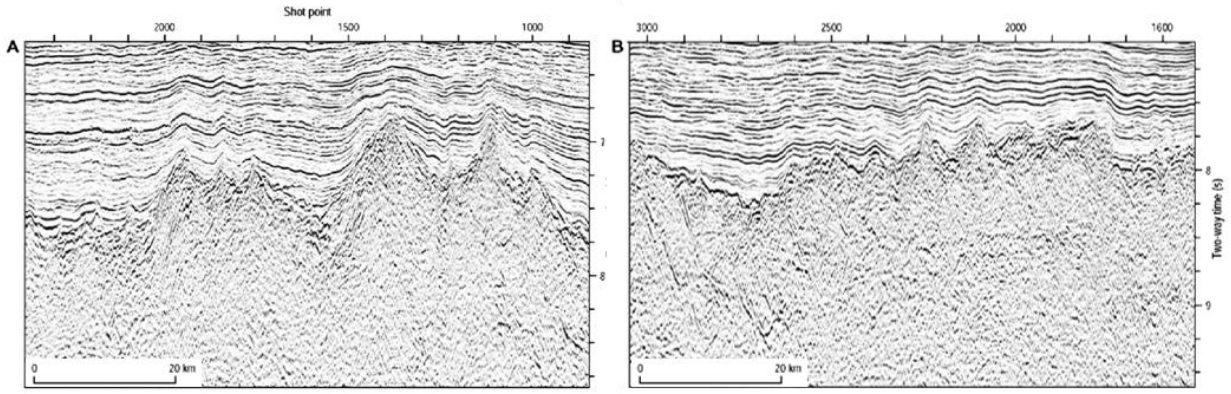

Figure 1-6. Rough oceanic crust along-strike of the Antarctic margin (modified from Whittaker et al., 2010).

It is commonly inferred that seafloor roughness (i.e., the root-mean square deviation of residual basement relief) increases dramatically for full spreading rates <40 mm/yr (e.g., Malinverno 1991; Ehlers and Jokat 2009). Top basement roughness is therefore considered to indicate large tectonic extension and low/intermediate magma supply at either slow- or ultraslow-spreading rates (i.e., Iberia and Newfoundland margins, Flemish Cap and Goban-Spur margins; Sauter et al., 2018; Australian and Antarctic margins, Whittaker et al., 2010; Davis et al., 2019) (Figure 1-6). Roughed and faulted crust has also often been imaged at ultra-slow/slow mid-oceanic ridges (e.g., Dick et al., 2003; Niu et al., 2015). At some locations, enhanced topography visible within the oceanic crustal domain has been associated with mantle exhumation processes and intense faulting caused by the slow rates of igneous production (i.e, Nova Scotia rifted margin, Keen and Potter, 1995; Porcupine Basin, Reston and McDermott, 2011). Therefore, a rough basement morphology may

result from slow and ultra-slow seafloor spreading rates, mantle exhumation processes at magma-poor settings, and polyphase tectonism and magmatism during and after spreading (e.g., Malinverno, 1991; Sauter et al., 2018). However, examples exist where smooth seafloor is generated at ultra-slow spreading rates where detachment tectonics is taking place (i.e., SW Indian Ridge, Sauter et al., 2013; Porcupine Basin, Reston and McDermott, 2011). Normal to fast seafloor spreading rates and/or high melt supply (volcanic margins) promote the generation of sufficient magmatic melt to accrete a normal oceanic crust (e.g., Sibuet et al., 2007; Pérez-Gussinyé, 2013), thus generally result in a smooth basement morphology (i.e., Northern South China Sea, Yu et al., 2021). Nevertheless, a smooth oceanic basement may even occur at slow-spreading ridges, if these are affected by long-lasting mantle thermal anomalies (i.e., Reykjanes Ridge; Malinverno, 1991).

Both melt supply and spreading rate may vary along the margin, promoting a gradual transition rather than a distinct separation between morphologically different domains (e.g., Malinverno, 1993; Small and Sandwell, 1994). Thus, the transition from rough to smooth oceanic basement is often observed along the same margin. This is the case for the rough to smooth boundary in the igneous basement of the Western North Atlantic, which was correlated with a change in spreading rate (Sundvik et al., 1984). At some margins, i.e., Newfoundland, relatively smooth basement associated with exhumed mantle is adjacent to a much rougher basement (Sauter et al., 2018). In contrast, the Iberia margin shows a rough basement generated by high relief peridotite ridges resulting from successive faulting episodes (e.g., Reston and McDermott, 2011). These examples illustrate the fundamental difference between incipient oceanic crust, exhumed mantle domain and steady state oceanic crust, which complicates the definition of the COT. Furthermore, multiple tectonic and magmatic episodes may have affected the whole proto-oceanic/exhumed mantle domains leading to highly variable top basement roughness. Therefore, the nature of the oceanic basement must be inferred from a conjunction of observations from seismic (refraction and/or reflection) and potential field data (i.e., Iberia– Newfoundland, Goban Spur–Flemish Cap, Australia–Antarctic margin, Sauter et al., 2018; Labrador-West Greenland, Keen et al., 2018), none of these being conclusive on its own.

1.2.5 Back-arc basins and active rifts

Back-arc basins are associated with island arcs and subduction zones and they are found at some convergent plate boundaries, presently concentrated in the western Pacific Ocean (Figure 1-7). Their formation is generally associated with tensional forces caused by migration or "*roll-back*" of a subduction hinge; if roll-back is faster than the plate convergence, extension will take place in the overriding plate, causing rifting of the lithosphere behind the volcanic arc as a result of the sinking of the subducting slab (e.g., Dewey, 1980; Schweller, 1987). Despite being considered small ocean

basins, back-arc rifts can show a great deal of variability both in rifting structures and geometries and in terms of crustal configuration. This is evidenced, for instance, by changes in extension rate, magmatic addition and resulting crustal structure over short distances along the South China Sea margins (e.g., Brune et al., 2017), and by the N-S change in crustal domains in the central Yamato Basin, Japan Sea (e.g., Sato et al., 2020). In some cases, changes in crustal structure and in magmatic addition during seafloor spreading are controlled by transform faults bounding different spreading segments (e.g., Okinawa Trough – Sibuet et al., 1995; Woodlark Basin – Taylor et al., 1995), similar to spreading centre segmentation occurring at well-developed ocean basins (i.e., Atlantic margins).

Studies have therefore highlighted the fact that back-arc basins share common structural characteristics and intrinsic dynamics to the widely rifted continental margins. Nevetheless, the small scale of the problem and the relative proximity of the conjugate margins can ease geodynamic reconstructions, as the 3D distribution and geometry of the tectono-sedimentary elements of the basin are more easily defined. Therefore, studies at back-arc basins can provide valuable insights into the mechanisms driving the formation of passive continental margins worldwide.

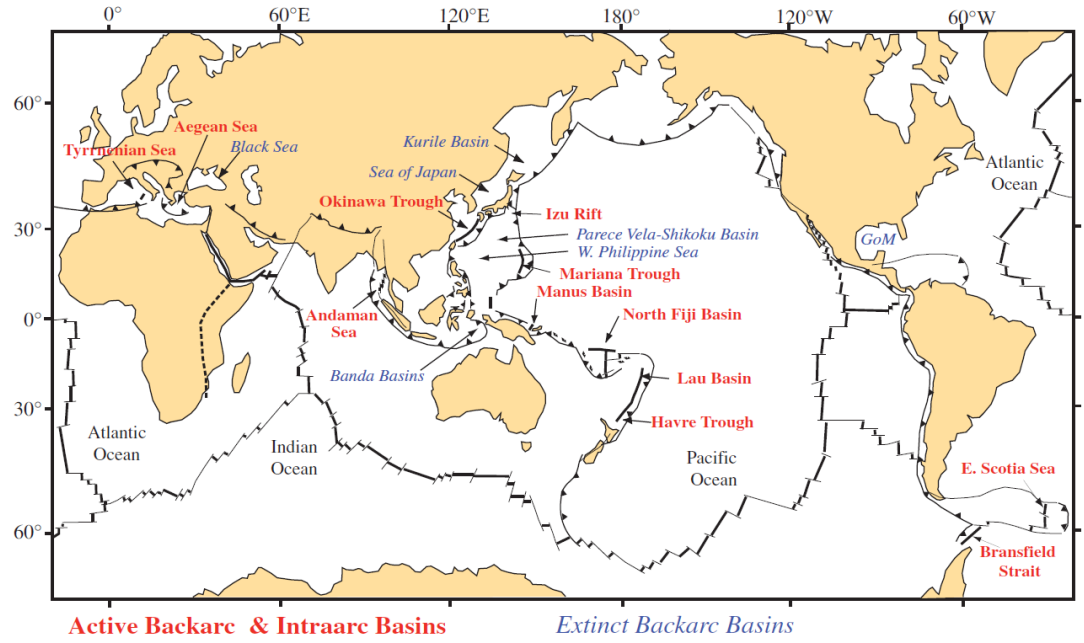

Figure 1-7. Map of the Active (red) and Inactive (blue) back-arc basins (Stern and Dickinson, 2010).

Other key areas for the study of the complex dynamics shaping passive margins and rift basins are active continental rifts, including the East African Rift (e.g., Ebinger and Casey, 2001), the Gulf of Corinth (e.g., Nixon et al., 2016) and the Woodlark Basin (e.g., Taylor et al., 1995), along with the recent or ongoing seafloor spreading locations such as the Red Sea (e.g., Almalki et al., 2016) and the Gulf of California (e.g., Lizarralde et al., 2007). Studies in these locations have recognized progressive strain localization as an important process in rift evolution on a variety of temporal and spatial scales (e.g., Goldsworthy and Jackson, 2001; Nixon et al., 2016). Evidence from these areas,

similar to observations along failed rifts such as the North Sea, indicate that rifting develops an initially broad zone of complex deformation characterised by closely spaced high-angle normal faults (35-60˚ angles). These faults progressively migrate towards the future basin area in a "domino-style" fashion (i.e., sequential faulting, Ranero and Perez-Gussinye, 2010) leaving inactive fault systems behind and becoming progressively localized onto a smaller number of discrete and increasingly larger faults characterised by lower-dip angles (e.g., Walsh et al., 2001; Cowie et al., 2005). Fault migration also has an effect on the evolution of syn-rift sediment patters, with sedimentation initially occurring within sparse and small deposcenters, and becoming then focused into fewer and larger depocenters. Furthermore, it has been shown that active faulting and strain migrate toward the rift axis with increasing extension, resulting in rift narrowing (Gawthorpe et al., 2003; Cowie et al., 2005). These types of observations are key for the understanding of the three-dimensional evolution of rifted basins and margins and represent a fundamental basis for kinematic model reconstructions (section 1.2.6).

Structural processes observed at back-arc basins and active rifts can therefore provide insights into the initial stages of evolution that have shaped fully developed passive margins, thus overcoming the difficulty in clearly resolving the deep tectonic and stratigraphic elements related to their syn- and early post-kinematic evolution that leaves their rift history unresolved.

1.2.6 Kinematic models

In order to reconstruct rigorously the kinematic evolution of basins it is important to constrain the third dimension of tectonic systems. Thus, it has been revealed necessary to investigate the three-dimensional distribution of stratigraphic sequences which bear a record of the rift geometry. Although seismic reflection and refraction data, potential field (gravity and magnetic) data, well logs and geochemical data can provide valuable information over specific locations and/or the regional settings investigated, they may lack a comprehensive, 3D overview. Constrained by these datasets, many kinematic, analogue and simple dynamic modelling studies have been defined to explain the sparse observations from continental rifts and rifted margins (e.g., Buck, 1988; Huismans and Beaumont, 2002; Nagel and Back, 2004; Le Pouriet et al., 2018; Zwaan et al., 2020). These models provide insights into the lithosphere and mantle behaviour during the dynamics of rifting (e.g., Nagel and Buck, 2004), helping to understand changes occurring during extension and breakup as a consequence of any inherited lithospheric thermal, rheological, or thickness contrasts between different terranes (i.e., transform margins; e.g. Koopmann et al., 2014; Le Pourhiet et al., 2018). Thus, they provide constrained models explaining observations from other datasets.

Traditionally, continents were considered to rift instantaneously under constant along-strike extension conditions. However, studies started to recognise that rifting is not instantaneous but rather progressive, and that continents open by a propagating rift which shows variable amounts of continental extension (e.g., Vink, 1982). Based on this idea, more recent models imply a propagation of the tipping point of rifting, resulting in a V-shaped basin (Figure 1-8). Rift propagation may be explained by models assuming continuous extension rates along-strike (Figure 1-8a), or by models implying an along-strike variation in extension due to motion about a rotation axis or about an Euler pole, with associated propagation of rift structures or oceanic basins (e.g., Martin, 1984; Augustin et al., 2014) (Figure 1-8b). Examples of rotational extension are found in the Red Sea region (Bellahsen et al., 2003), and along the NE Atlantic continental margin, with various V-shaped basins having formed during continental breakup (i.e., Porcupine Basin; Peron-Pinvidic and Manatschal, 2010). Different kinematic evolutions may also occur at rift propagation and break-up for rotational tectonic settings (i.e., simple, delayed, node and segmented propagation; Zwaan et al., 2019, and references therein) (Figure 1-8b). These may be used to describe distributed rifting and oceanic spreading centres entering a continental domain by segmented propagation as observed in the Woodlark Basin, Gulf of Aden and the Laptev Margin (Manighetti et al., 1997, Taylor et al., 1999; Franke and Hinz, 2009)

Rotational extension has commonly been referred to as “scissor-like” extension (e.g., Zhou et al., 1995; Le Pourhiet et al., 2018), which implies extension on both sides of the rotation axis. Other studies introduced the concept of “laundry peg” motion, describing a simultaneous opening and closing on opposite sides of the rotation axis (Figure 1-8d). This model implies a transition from extension to contraction which may also develop in back-arc systems due to rotational motion between the down-going and overriding plate, as seen in various basins (Seebeck et al., 2014; Wallace et al., 2009).

Numerical and analogue models are used to simulate crustal scale strain distribution during extension, together with the behaviour of the uppermost mantle. These models, predicting the evolution of continental extension, have been widely used to define the fault pattern generating during rift migration and hyper-extension (e.g., Ellis and McClay, 1988; Brun et al., 2002; Nagel and Buck, 2004), consequently helping to discern between different mechanism (i.e., kinematic models) of extension. The effect of discontinuities and/or transform faults controlling magma supply along spreading segments are also considered (e.g., Georgen and Lin, 2003; Koopmann et al., 2014). Models show that thermal perturbation by transform faults results in a reduction in crustal thickness near the transforms, producing an anomalous oceanic crustal structure (e.g., Dunn and Martinez, 2011). Transfer/transform faults can act as rift propagation barriers delaying the opening of consecutive rift segments (Koopmann et al., 2014). Rift delay can affect both mantle and melt

flow between segments, limiting the propagation of low-viscosity mantle across the segment boundary, and favoring melt accumulation at the opening segment. The model predicts rift-parallel flow and concomitant magmatic peaks near the propagation barrier caused by the lateral pressure gradient between sequentially opening segments (Koopmann et al., 2014).

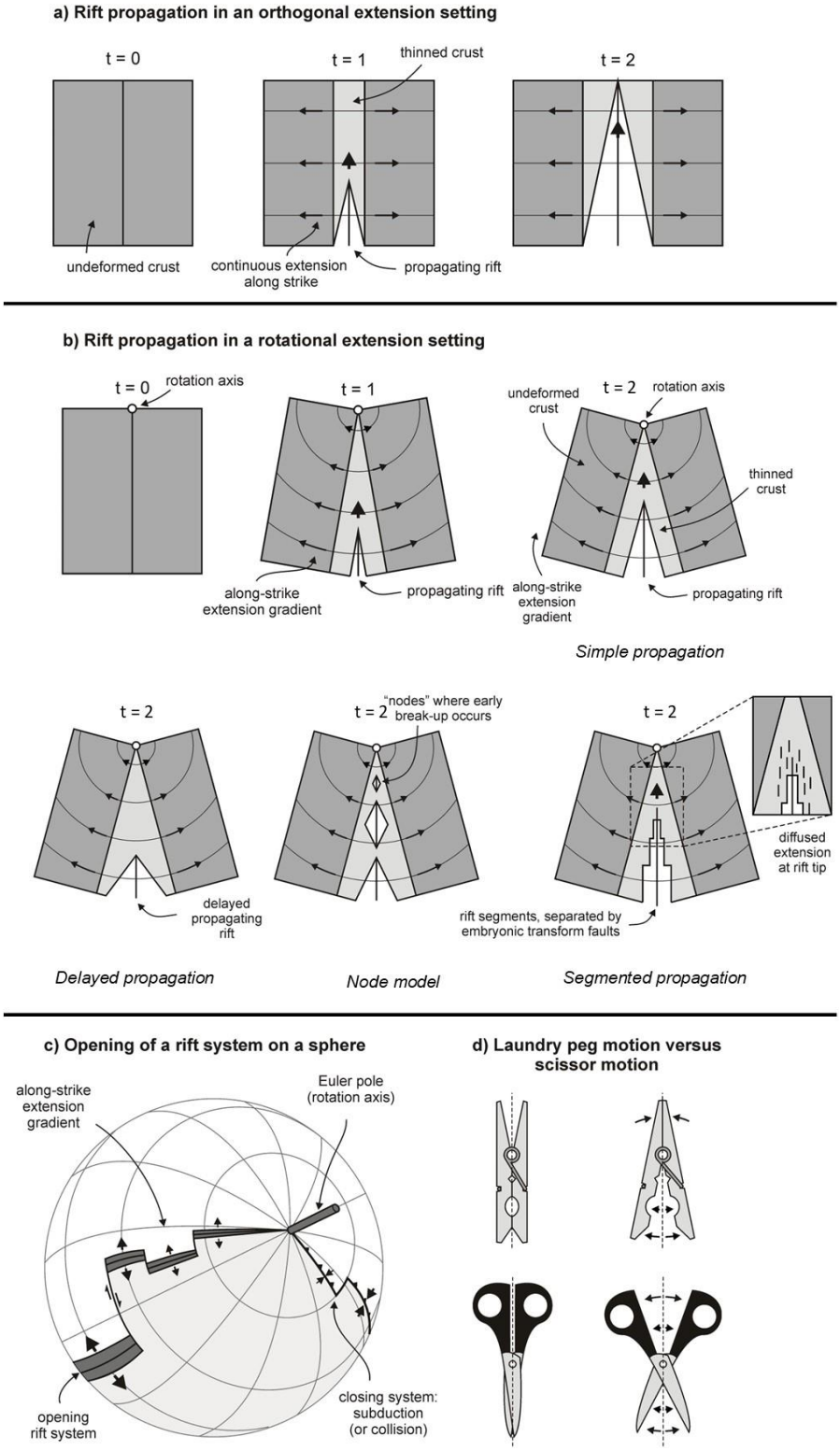

Figure 1-8. Different rift propagation and breakup models. (a) Orthogonal extension; extension rates are uniform along-strike. (b) Rotational extension; along-strike extensional

gradients and a rotation axis are involved. This model explains the opening of a rift system on a global scale (c). (d) "Scissor-like" versus "laundry peg" tectonics, the first involving simultaneous extension on both sides of the rotation axis, the second describing the simultaneous opening and closing on opposite sides of the rotation axis (modified from Zwaan et al., 2019; see references therein).

1.3 Gas hydrate

Gas hydrate is an "ice-like" crystalline solid comprising hydrogen-bonded water molecules with trapped gas molecules, mostly methane (CH_4), that is stable at medium-high pressures and low temperatures (Sloan and Koh, 2008) (Figure 1-9).

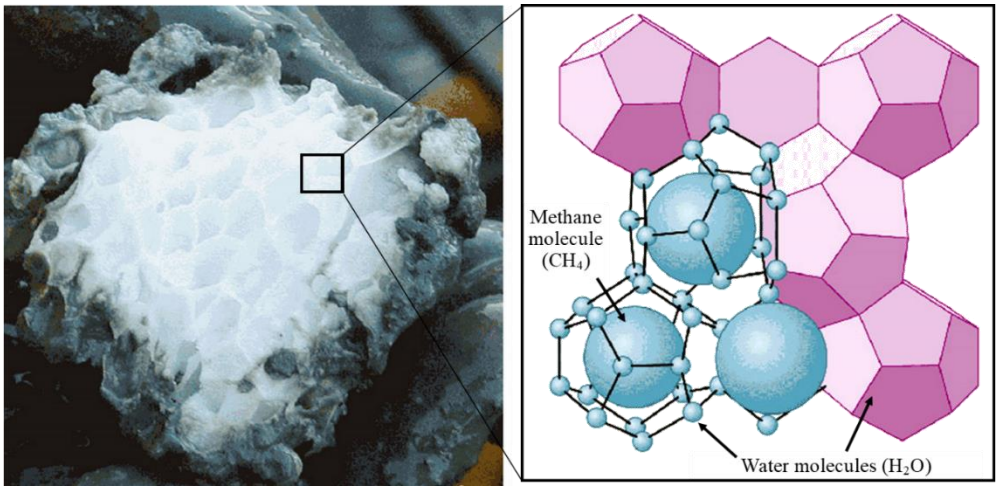

Figure 1-9. Gas hydrate. Left) Ice-like block of methane hydrate (offshore Oregon). Right) Molecular structure of methane hydrate, with methane gas molecules tightly enclosed in cages composed of water molecules. Each node of a pentagonal face represents a water molecule (after GEOMAR; https://www.geomar.de/en/centre/central-facilities/bibliothek/publications-at-geomar/ifm-geomar-reports).

The chemical formula of a methane hydrate compound is:

$$CH_4 + n \cdot H_2O \rightarrow CH_4 \cdot n \cdot H_2O \qquad (1\text{-}1)$$

where the hydration number (n) changes with the type of gas, pressure, temperature, salinity, and pH (Klapp, 2009; Hesse and Schacht, 2011; Ye and Liu, 2013). Gas hydrate formation is a reversible process, meaning that solid hydrate can form when favourable thermodynamic conditions are present, and dissociate releasing gas and water as separate fluid phases when these conditions are altered (Sloan and Koh, 2008).

Gas hydrate deposits have attracted considerable interest over the last few decades because of the high amount of methane gas stored in the hydrate phase, with 1 m^3 of solid hydrate containing approximately 164 m^3 of CH_4 gas at standard pressure and temperature (e.g., Boswell and Collett, 2011; Kvenvolden, 1998), which makes them a potential future lower-carbon energy source (Kvenvolden, 1993; Grauls, 2001; Boswell et al., 2020). Vast research programs have been undertaken by countries like the United States, Canada, Japan, India, Korea, and China in order to

explore the long-term goal of exploiting gas hydrates as an energy resource in a cost effective and safe manner (e.g., Collett et al., 2014; Arora et al., 2015). Gas hydrate exploration also involves the study of hydrate phase transformation, mass transfer, sediment deformation, gas expansion etc., that relate to hydrate dissociation and its impact on the surrounding environment (Ruppel, 2011). Hydrate dissociation may occur in response to hydrostatic pressure reduction caused by sea-level decrease and deglaciation (Maslin et al., 2004), temperature increase by ocean warming (Marin-Moreno et al., 2013) or salinity increase (Riboulot et al., 2018). Hydrate dissociation affects the mechanical properties of the hydrate-bearing sediment and releases large amounts of gas and water that can trigger profound changes in fluid pressure, temperature, and stress. Hence, it can play some role in the evolution of various natural processes such as large-scale seafloor instabilities i.e., subsidence and landslides (Sultan et al., 2004; Brown et al., 2006; Yang et al., 2018), and also may represent a potential drilling and infrastructure hazard (Sultan et al., 2004; McConnell et al., 2012; Merey, 2016). Furthermore, the gas released into the sediment upon hydrate dissociation may reach the water column and ultimately the atmosphere, contributing to both ocean acidification (Valentine et al., 2001) and global warming (Nisbet, 1990; Dickens et al., 1997; Ruppel and Kessler, 2017). Therefore, studies at different locations have focused on understanding the gas hydrate response to environmental change to enhance our capacity to quantify the free gas released from hydrate destabilisation (e.g., Krishna-Godavari Basin; Joshi et al., 2014; Lake Baikal, De Batist et al., 2002; U.S. Beaufort margin, Hornbach et al., 2020; offshore Svalbard, Marin-Moreno et al., 2013).

In the following sections, gas hydrate distribution and morphology (1.3.1), direct and indirect evidence for gas hydrates along continental margins (1.3.2), and the main physical parameters of hydrate-bearing sediments (1.3.3) are discussed. This information constitutes the background for Chapter 5.

1.3.1 Gas hydrate occurrence

The majority of natural gas hydrates occurs in marine environments (~99%), with a small proportion (~1%) occurring in permafrost environments (Ruppel, 2015; Boswell et al., 2020). Gas hydrate formation relies on factors such as the availability of low molecular weight gas and water, pore-size distribution, pore-water salinity, geothermal gradient and seafloor temperature (Dickens and Quinby-Hunt, 1997; Moridis and Collett, 2003) (Figure 1-10). Hydrocarbon molecules such as methane (CH_4), ethane (C_2H_6), propane (C_3H_8) and i-butane (i-C_4H_{10}), and other gases such as carbon dioxide (CO_2), hydrogen sulfide (H_2S), nitrogen (N_2) and oxygen (O_2) can form their own hydrate (simple or pure hydrate), at their pressure-temperature equilibrium conditions and given enough water in the system (Giavarini and Hester, 2011). There are three main types of hydrate structures

in nature: Structure I (sI), Structure II (sII) and Structure H (sH) (Sloan, 1998). Depending on the molecular diameter of the gas, different types of hydrate structure can form. Simple hydrates of CH_4, C_2H_6, CO_2, H_2S, are sI type of gas hydrate. C_3H_8, i-C_4H_{10}, N_2 and O_2 form sII type of gas hydrate (e.g., Rogers, 2015). Different from sI and sII hydrates, sH hydrates are formed by one gas such as CH_4 and other larger molecules. sI and sII hydrates are common all over the world, whereas sH hydrates are rare and have only been found in a few areas such as the Gulf of Mexico, the Cascadia margin, and the Caspian Sea (Hester and Brewer, 2009).

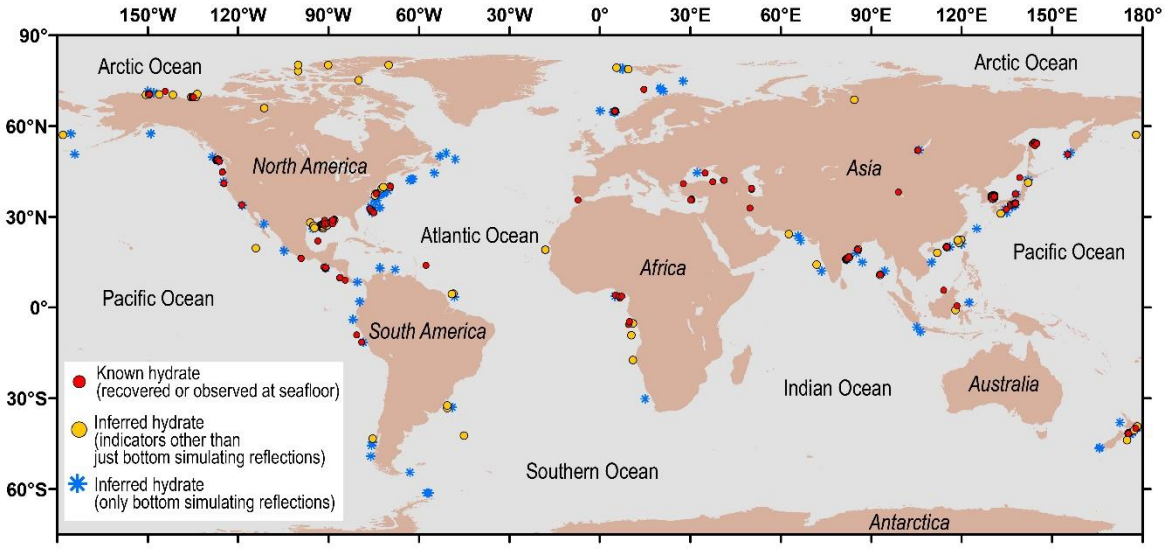

Figure 1-10. Global distribution of recovered or observed gas hydrate (red circles) and inferred gas hydrate (yellow circles and blue symbols) (from the U.S. Geological Survey database; Waite et al., 2020).

The most abundant hydrate-forming gas in marine sediments is methane (CH_4) with small amounts of hydrogen sulfide (H_2S), carbon dioxide (CO_2), and other small molecule gases (i.e., ethane, C_2H_6 and propane, C_3H_8). The carbon isotopic values of the hydrate samples obtained by drilling have revealed that the hydrate-forming gas is normally related to the bacterial breakdown of organic matter within the shallow sediments (e.g., Kvenvolden, 1993; Sloan and Koh, 2008; Max and Johnson, 2016). However, deeper biogenic sources associated with longer migration pathways and methane migration sourced by biodegradation or leakage from deeper thermogenic hydrocarbons are being increasingly reported (e.g., Lorenson and Collett, 2018; Paganoni et al., 2019).

The organic carbon is delivered to the marine sediment both by the rain of phytoplankton to the seafloor in highly productive continental margin waters and by export of terrestrial sediment from the continents (e.g., Rupper and Kessler, 2017). Re-mineralisation of sedimentary organic carbon produces CO_2, and most CH_4 formed in sediments by microbial processes is the result of reducing this CO_2 (e.g., Wallmann et al., 2012). Therefore, owing to the concentration of organic carbon on

continental margins, these locations are where most gas hydrates occur (Figure 1-11). The presence of heavier hydrocarbons beside methane (i.e., ethane, propane) is less common, and is associated to thermo-catalytic production at depth via heating of buried kerogen (e.g., Sloan, 2003; Bourry et al., 2009) (Figure 1-11).

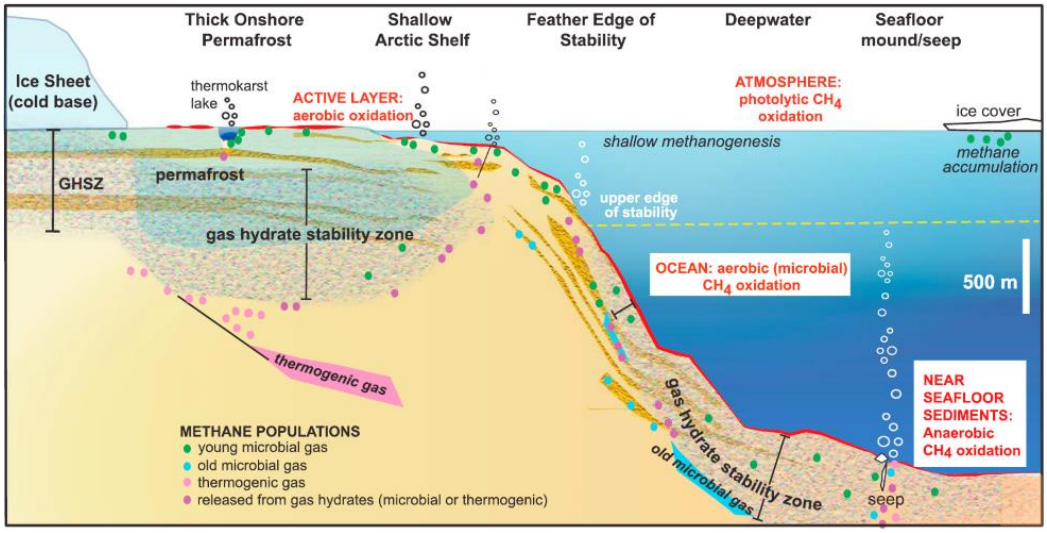

Figure 1-11. Schematic of methane hydrate dynamics and methane distributions in different physiographic provinces (from Ruppel and Kessler, 2017).

In marine environments, gas hydrates are stable at seafloor depths greater than about 500 m in temperate latitudes and greater than about 300 m at high Arctic latitudes, where bottom water temperature is colder (Ruppel and Kessler, 2017). In sub-seafloor sediments, the temperature increases with depth depending on the heat-flow from below and the thermal conductivity of sediments at that specific site. The requirements of low temperature and high pressure for gas hydrate formation is therefore met within a certain depth range below the seafloor (Figure 1-11, Figure 1-12). Below this depth, the increase in pressure is not able to compensate for the increase in temperature in sediments (Sloan, 1998). Free gas is generally present below the gas hydrate stability zone (GHSZ). Gas hydrates can also act as an efficient obstacle for gas migration in sediments since they trap gas under the right conditions and decrease the absolute permeability in sediments (e.g., Wang et al., 2020).

By integrating data of pressure, temperature and salinity conditions of the sub-seafloor sediments with the phase boundary of gas hydrate, the GHSZ can be predicted (Figure 1-12). To predict the GHSZ in the marine environment, if there are no data to constrain the pore water pressure and salinity, pore size distribution, and gas type, the following assumptions are typically made: seawater salinity of 3.5 wt% (particularly for shallow marine gas hydrate accumulations), pure methane hydrate, hydrostatic pressure, and the bulk methane hydrate phase boundary (no pore size effects).

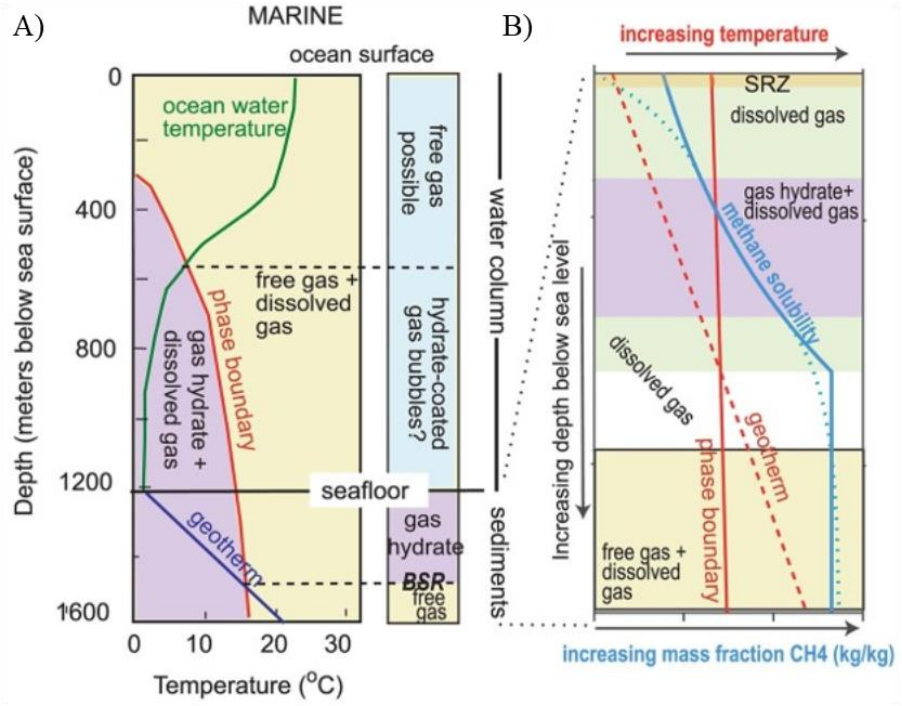

Figure 1-12. Gas hydrate stability, considering fully equilibrium conditions in (A) deepwater marine settings. Purple zones = gas hydrate with dissolved gas; yellow regions = coexisting dissolved gas and gas bubbles. (B) Expanded plot within the sub-seafloor sediments in (a), showing the relationship between the GHSZ and the zone where gas hydrate actually occurs based on pressure-temperature and methane solubility. Blue solubility curves are read on the bottom axis and red temperature curves on the top axis. Green areas = dissolved methane gas within the theoretical GHSZ. White region = dissolved gas beneath the base of the GHSZ. The bottom-simulating reflector (BSR) marks the boundary between free gas and overlying hydrate-bearing sediments. SRZ = nominal sulfate reduction zone, where methane is consumed via anaerobic oxidation of methane (modified from Ruppel and Kessler, 2017).

Gas hydrates can occur in sediments anywhere within the GHSZ. However, they tend to show a heterogeneous distribution as their formation depends on the availability of hydrocarbon gas and pore water, salinity, permeability, porosity, etc. apart from the pressure, temperature and salinity requirements (Duan et al., 2011; Klauda and Sandler, 2005; Xu and Ruppel, 1999; Zatsepina and Buffett, 1998). The zone where gas hydrate can potentially occur will have both a top and a bottom that are controlled by the local solubility of CH_4 in the pore space and the availability of CH_4 at each location in the sedimentary section (Ruppel and Kessler, 2017) (Figure 1-12). Therefore, when considering the vertical distribution of gas hydrates in marine sediments, a critical distinction is made between the GHSZ and the zone of actual gas hydrate occurrence, also defined as gas hydrate zone (GHZ) (Zatsepina and Buffett, 1998; Wood and Ruppel, 2000) or gas hydrate occurrence zone (GHOZ) (Riedel and Collett, 2017).

Structural and stratigraphic aspects of a geological setting control the distribution of methane and other fluids in the sediment. For instance, faults and fractures can provide preferential migration pathways controlling the upward migration of fluids (Jain and Juanes, 2009). Permeability and porosity within different formations can induce a stratigraphic control that regulates the upward and lateral migration of fluids (Nimblett and Ruppel, 2003; Dai et al., 2012). All these factors (permeability, porosity, faults, fractures, total organic content, salinity, heat-flow, etc.) are highly variable within different geological settings, and so gas hydrate can occur in a very wide range of sedimentary environments. Additionally, it is important to constrain the geological evolution of a sedimentary basin to understand the evolution of the gas hydrate system in place (Max and Johnson, 2014).

The morphology of gas hydrate in sediments can vary at both macroscopic and microscopic scale (Ecker et al., 1998; Clennel et al., 1999). At a macroscopic scale, hydrate can be described as either *pore invasive* or *grain–displacing* (Collett et al., 2008; Holland et al., 2008; Riedel et al., 2006). Hydrate morphology and distribution in the host sediments is determined by the state of effective stress (the difference between lithostatic pressure and pore pressure in sediments) and the host sediment grain size (Dai et al., 2012).

In coarse-grained sediments (i.e., sands) the main type of hydrate morphology is *pore-invasive* or disseminated. This means that hydrate forms in the pore space of the host sediment, replacing the pore fluid without displacement between particles occurring during hydrate growth, thus leaving the sediment grain matrix relatively intact (Collett et al., 2008; Ren et al., 2020). At the microscopic scale, pore invasive hydrates can form different habits including cementing, grain coating, pore-floating and load-bearing (Ecker et al., 1998; Dai et al., 2012; Sava and Hardage, 2006; Dangayach et al., 2015) (Figure 1-13). Pore-scale observations show that hydrate pore habits are mainly grain-coating and cementing in excess-gas environments and pore-floating in excess water environments, and could shift as environmental conditions change (Lei et al., 2019).

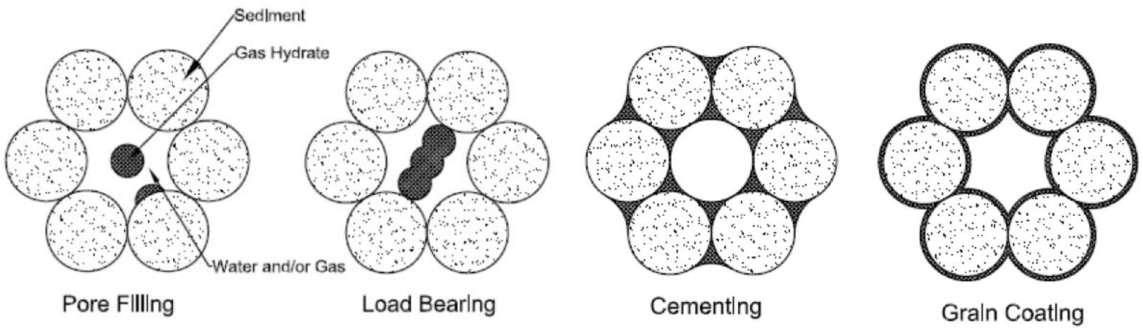

Figure 1-13. Conceptual diagram showing different hydrate morphologies (modified from Dangayach et al., 2015).

In fine-grained sediments (i.e., clays), the smaller pore sizes, associated capillary actions, and water-mineral interactions can inhibit hydrate nucleation in the pore space. Consequently, the growth of hydrate crystals acts to displace the particle (Lei, 2017; Park et al., 2018). A particle-displacive hydrate forms morphologies such as discrete nodules, layers, veins and lenses of pure hydrate (Holland et al., 2008; Collett et al., 2014; Dai et al., 2012; Zhang et al., 2015).

The impact that different non-grain displacing hydrate morphologies and saturations have on the physical properties of sediments is discussed in section 1.3.3.

1.3.2 Gas hydrate exploration

Multidisciplinary investigations using geophysical techniques such as seismic reflection and refraction methods, electromagnetic methods, and geochemical analysis with support from logging (i.e., sonic, resistivity, and mud gas logs) have been used extensively to explore the occurrence and character of gas hydrate accumulations on continental margins and permafrost regions (e.g., Collett et al., 2019; Boswell et al., 2020; Minshull et al., 2020).

Seismic reflection data are often used to identify the base of the gas hydrate stability zone (BGHSZ) beneath the seafloor, which is manifested by a high amplitude seismic reflector generally characterised by a negative impedance contrast, known as a Bottom Simulating Reflector (BSR) (Shipley et al., 1979; Andreassen et al., 1997; Hyndman and Dallimore, 2001) (Figure 1-14). When the BSR depth coincides with the BGHSZ, its position marks approximately an isotherm. Thus, it roughly parallels the seafloor often crosscuts the background stratigraphy (e.g., Grevemeyer and Villinger, 2001; Hyndman and Dallimore, 2001).

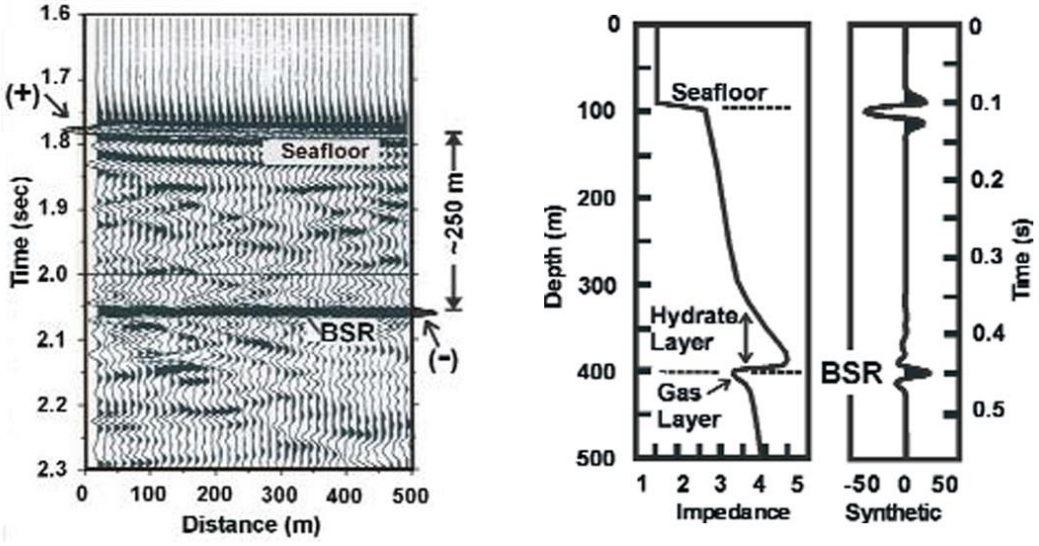

Figure 1-14. Example of BSR showing a reflection polarity opposite to that of the seafloor. To the right, a plot of the impedance contrast versus depth. Seismic velocities increase in

proximity of the BSR, while a low-velocity zone beneath the BSR is associated with a free gas zone. To the left, a synthetic seismogram reproduces the signal polarity of seafloor and BSR. The seafloor reflection results mainly from the density contrast, while the BSR reflection results mainly from the velocity contrast (offshore Vancouver Island; Hyndman and Dallimore, 2001).

The BSR is usually considered a direct indicator for the presence of hydrate (Minshull et al., 2020), although it should be noted that there are non-hydrate BSRs in nature that come from lithological and/or geochemical changes (e.g., Berndt et al., 2004; Cook and Tost, 2014). The BSR reflection generally arises at the boundary between a hydrate-bearing layer with higher seismic velocity overlaying a low-velocity zone, typically a few meters to many tens of meters thick, in which there is free gas within the pore space (Singh et al., 1993; MacKay et al., 1994; Hovland et al., 1997).

The lack of a seismic BSR in an area with the right hydrate stability conditions does not necessary imply the absence of hydrate (e.g., Chabert et al., 2011; Riedel et al., 2011). Also, drilling, coring, and geophysical logging at different locations of the Danube Fan, where seismic BSRs were observed, showed no evidence for the presence of any significant gas hydrates within the drilled/cored sequences (Riedel et al., 2020), and/or only evidence for gas bubble expulsion from the borehole at BSR depth (Bohrmann et al., 2018). Therefore, although BSRs are considered as a strong evindence for the presence of hydrates, their nature can be controversial. Other evidence of gas accumulations and migration pathways within and above the GHSZ (i.e., gas chimneys, pipes, bright-spots, mud-volcanoes) are considered indirect indicators for the presence of gas hydrates, as they show the availability of gas for hydrate formation (Minshull et al., 2020).

In some cases, the BSR can be inconsistent with the predicted BGHSZ, or it may be observed at locations where hydrate should no longer be present according to modelling (e.g., Bangs et al., 1993; Ruppel, 1997; Ker et al., 2019). Many processes can explain the disparity between model and observation, such as localized heat-flow anomalies (e.g., De Batist et al., 2002; Suess et al., 1999), bottom water pressure and temperature variations at glacial-interglacial cycles (e.g., Phrampus et al., 2014; Foucher et al., 2002) and/or heat conduction from below the GHSZ following geothermal gradient re-equilibration due to rapid sediment deposition (e.g., Zander et al., 2017), inducing a vertical migration of the BGHSZ and of the associated BSR (e.g., Delisle et al., 1998). As a result of vertical changes in the BGHSZ, a diagenetically induced permeability barrier may form in place of the BSR when this was active and existed stably at the level for an extended period (e.g., Clennell et al., 1999).

At some areas, i.e., the Nankai margin, Hydrate Ridge, the Storegga slide, the presence of two or more vertically stacked BSRs have also been recognized (e.g., Bangs et al., 2005; Foucher et al.,

2002; Posewang and Mienert, 1999; Tréhu et al., 1999). Multiple BSRs are unusual features that have become a focus of interest in gas hydrate research as their study can provide useful insights into the hydrate system sensitivity to environmental changes triggering their dissociation and a release of free gas and water (e.g., Kretschmer et al., 2015; Ruppel, 2011; Ruppel and Kessler, 2017). The existence of multiple BSRs has triggered several questions, for example, how long a residual BSR can last or how fast a new BSR gains reflectivity (Foucher et al., 2002). The different interpretation of multiple BSRs origin are further discussed in Chapter 5.

1.3.3 Gas hydrate and seismic velocities

Hydrate-bearing sediments show different physical properties compared to non-hydrate bearing sediments. These include thermal properties, permeability, electrical conductivity and permittivity, elastic P- and S-wave velocities (V_P and V_S), shear strength, and volume changes resulting from hydrate dissociation. Compressional P-waves and shear S-waves are extensively used for mapping hydrate occurrences and estimating the hydrate saturation within those occurrences (Waite et al., 2009; Westbrook et al., 2008). This is possible because the presence of hydrate stiffens the host sediment, increasing the P- and S-wave velocities, as demonstrated in hydrate-bearing clay, silt, and sand at different effective stress and hydrate saturation levels (Lee, 2007; Lee et al., 2009).

The propagation of P-waves and S-waves produces longitudinal and shear strains with particle motion, which propagate longitudinal and perpendicular to the direction of wave propagation, respectively. Their propagation speeds are controlled by the sediment's bulk modulus (K), a measure of compressive strength and thus of the sediment's resistance to a uniform compression, and by the shear modulus (μ or G), a measure of the material's shear strength (Sheriff and Geldart, 1995). When considering an isotropic elastic medium, the relationship between P- and S-wave seismic velocities, compressive and shear strength (bulk modulus K, and shear modulus μ), and the bulk (or effective) rock density (ρ) of a medium is given by (Mavko and Mukerji, 1998):

$$V_P = \sqrt{\frac{K+\frac{4}{3}\mu}{\rho}}, \tag{1-2}$$

$$V_S = \sqrt{\frac{\mu}{\rho}}, \tag{1-3}$$

where $\rho = \rho_f \varphi + \rho_{min}(1-\varphi)$, with φ being the medium porosity, and ρ_f and ρ_{min} the fluid and mineral density, respectively. Differences in P- and S-wave propagation modes mean that they are sensitive to different properties of the sediment. The bulk modulus (K) is determined by both the grains and pore fluid properties, whereas the shear modulus (μ or G) is only controlled by the shear

stiffness of the granular skeleton, assuming that the fluid has negligible shear modulus (Biot, 1956; Waite et al., 2009).

Gas hydrates have a high bulk modulus ($K = 7.9\,GPa$) and shear modulus ($\mu = 3.3\,GPa$) compared to water that has low bulk modulus ($K = 2.17\,GPa$) and no shear strength ($\mu = 0$) (Best et al., 2013). Seismic velocity estimates from synthetic pure gas hydrate show high P- (3.65 km/s) and S-wave (1.89 km/s) velocities for pure hydrates (Waite et al., 2000). Thus, replacement of pore water by gas hydrate increases the P-wave velocity (Lee, 2007; Lee et al., 2010) (Eq. 1-2) as the density of water and hydrate is similar. The S-wave velocity also increases due to the presence of gas hydrates and the amount of increase in the S-wave velocity depends on the contribution of gas hydrates to the granular skeleton of the composite (Eq. 1-3). The presence of gas hydrates increases the bulk and shear moduli of a medium depending on morphology (Dvorkin and Nur, 1993; Ecker et al., 1998; Priest et al., 2009; Dai et al., 2012). When gas hydrate is present in the form of load bearing or cementing hydrate, it increases the shear modulus of a medium, whereas the increase in shear modulus is negligible in cases where gas hydrates form away from grain contacts (Ecker et al., 1998; Yun et al., 2005; Waite et al., 2009). Thus, the increase in bulk and shear modulus is much higher for cementing hydrate and slightly higher for load bearing gas hydrate morphologies, compared to the pore-floating gas hydrate morphologies (Waite et al., 2009; Dai et al., 2012). The presence of gas in pore space affects P- and S-wave velocities differently. A reduction in P-wave velocity is produced by the fact that gases do not shear ($\mu = 0$) and they have a very low bulk modulus ($K = 100 - 150\,kPa$), whereas S-wave velocities may increase at high gas saturations as gases tend to reduce the density of the composite.

Thus, the P- and S-wave velocity of gas hydrate-bearing sediments is a function of mineral composition, porosity, pore fluid, gas and gas hydrate saturation, gas hydrate morphology, grain connectivity, degree of consolidation or lithification, pore pressure, stress state, etc. (Berryman, 1992; Jakobsen et al., 2000). The relationship between physical properties of the sediment and seismic velocities can be explained by the effective-medium theory (Mavko et al., 2009). Effective medium theory is based upon different rock physics models that predict the response of gas hydrate-bearing sediments to a seismic input, and from that, constrain hydrate and gas saturation in sediments (Chand et al., 2004). Effective-medium modelling principles are further discussed in section 2.4.2, and their application is shown in Chapter 5 of this thesis.

1.4 Geological setting

1.4.1 The Black Sea

The Black Sea is a deep-water basin located between the Pontide Mountains in Turkey to the South, the Caucasus Mountains to the East, and the relatively low coastal regions of Ukraine and Balkan countries to the West (Figure 1-15). The basin is underlain by a flat, 2.0-2.2 km-deep abyssal plain that obscures two separate depocenters, named the Western Black Sea Basin (WBSB) and the Eastern Black Sea Basin (EBSB). The WBSB and EBSB are separated by a continental ridge called the Mid-Black Sea High (MBSH), which includes the Andrusov and Arkhangelsky ridges (Figure 1-15).

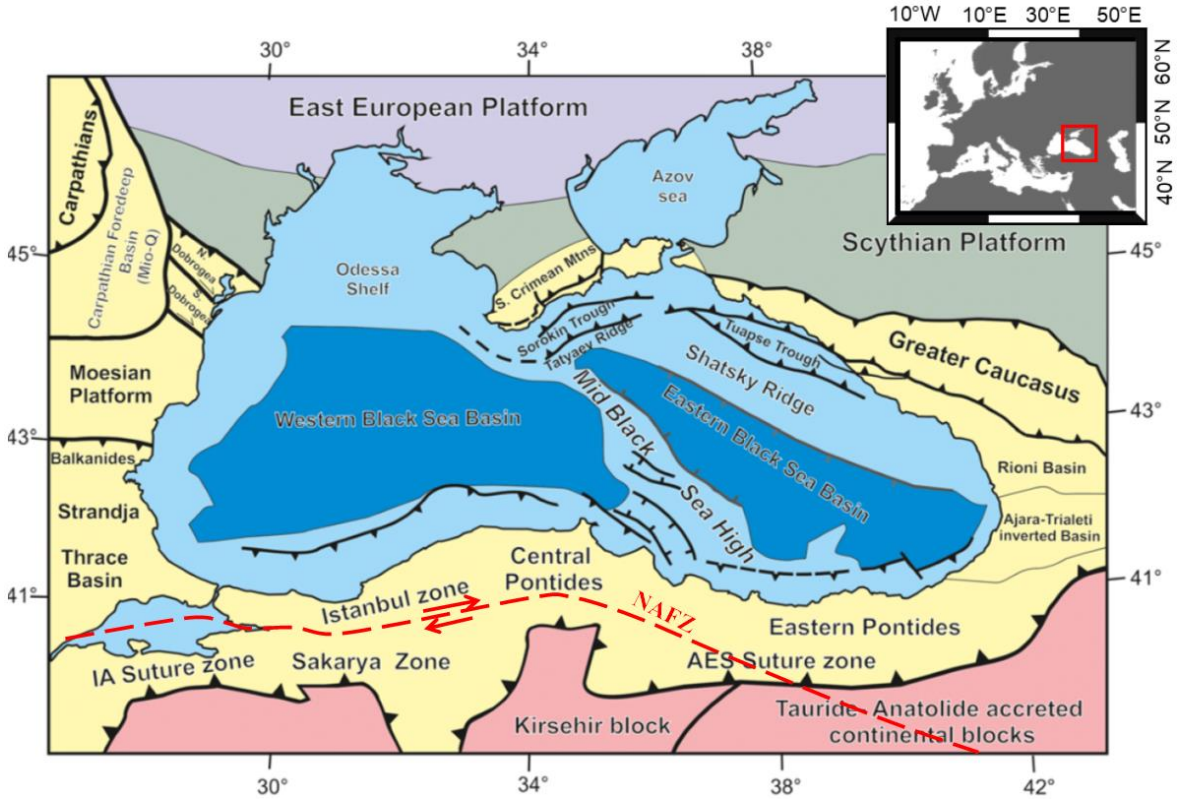

Figure 1-15. Simplified structural map of the Black Sea domain. The North Anatolian dextral strike-slip Fault Zone (NAFZ) is also shown on map, which respresents the boundary between the Eurasian and the Anatolian plates (modified from Sheremet et al., 2017, Robinson et al., 1996, Okay et al., 1994 and Nikishin et al., 2015c).

The formation history and dynamics of the Black Sea have been discussed by several studies based on multichannel seismic reflection and refraction, gravity and magnetic data, providing different interpretation of the structural features present in the western and eastern halves of the basin (e.g., Adamia et al., 1974; Letouzey et al., 1977; Tugolesov et al., 1985; Finetti et al., 1988; Okay et al.,

1994; Spadini et al., 1996; Rangin et al., 2002; Egan and Meredith, 2007; Edwards et al., 2009; Shillington et al., 2009; Sheremet et al., 2016; Sydorenko et al., 2017).

The whole basin developed within a continental lithosphere that is made up of a mosaic of fragments accreted during several tectonic events from the Precambrian to the Lower Mesozoic (e.g., Sheremet et al., 2017, Robinson et al., 1996, Okay et al., 1994; Stephenson and Schellart, 2010; Nikishin et al., 2015b, c) (Figure 1-15). Throughout the Lower Mesozoic, the Caucasus-Arabian segment underwent convergent motion due to the northward subduction and closure of the Tethys Ocean. This geological event is recorded in the area south of the Black Sea by the presence of the Pontides magmatic arc (Figure 1-15). Following this compressional stage, during Upper Mesozoic time, the area in the hinterland of the Pontides magmatic arc was affected by extensional forces resulting from the "roll-back" of the Neotethyan lithosphere subducting below the southern part of the Eurasian continental margin (e.g., Okay et al., 1994; Nikishin et al., 2003; Stephenson and Schellart, 2010).

Back-arc rifting is therefore considered the first-order geodynamic process responsible for the tectonic evolution of the two sub-basins. However, the kinematics and timing (i.e., age of the oldest sediments) for their relative opening remains controversial (e.g., Verzhbitsky et al., 2002; Sydorenko et al., 2017). The WBSB is thought to have formed during Lower to Upper Cretaceous time following the detachment of a continental terrane (the Istanbul zone) from the Eurasian Plate (Odessa shelf), as consequence of the extensional forces generated by the roll-back of the subducting Neotethyan lithosphere (Okay et al., 1994). The resulting N-S opening is considered to have evolved until breakup and oceanic crust emplacement in the central basin (e.g., Okay et al., 1994; Kazmin et al., 2007) (Figure 1-16). In the EBSB, paleo-magnetic data have suggested an anti-clockwise rotational opening around a rotational pole located in Crimea, following the separation of the Shatsky Ridge from the MBSH (Galushkin et al., 2006, Westphal et al., 1986). This type of opening mechanism resulted in a NE-SW extension increasing towards the SE (e.g., Finetti et al., 1988, Edwards et al., 2009). Stephenson and Schellart (2010) argued that the orientation and structure of the MBSH is consistent with a single opening phase of the basin, which occurred in a back-arc settings as a result of asymmetric slab roll-back. Other studies also agree on the synchronous opening of EBSB and WBSB (e.g., Verzhbitsky et al., 2002; Nikishin et al., 2015a) (Figure 1-16), whereas other evidence seems to suggest a later opening phase for the EBSB, potentially during Upper Cretaceous and/or during Palaeocene-Eocene time (e.g., Kazmin et al., 2007; Hyppolite et al., 2010; Shillington et al., 2008). Furthermore, while it is commonly accepted that the centre of the WBSB is underlain by oceanic crust, it is still debated whether the EBSB reached breakup and magmatic spreading, and thus, whether the central basin overlies a crustal basement

of oceanic affinity or if it is characterised only by highly thinned continental crust (e.g., Verzhbitsky et al., 2002; Graham et al., 2013; Nikishin et al., 2015a, b; Shillington et al., 2009).

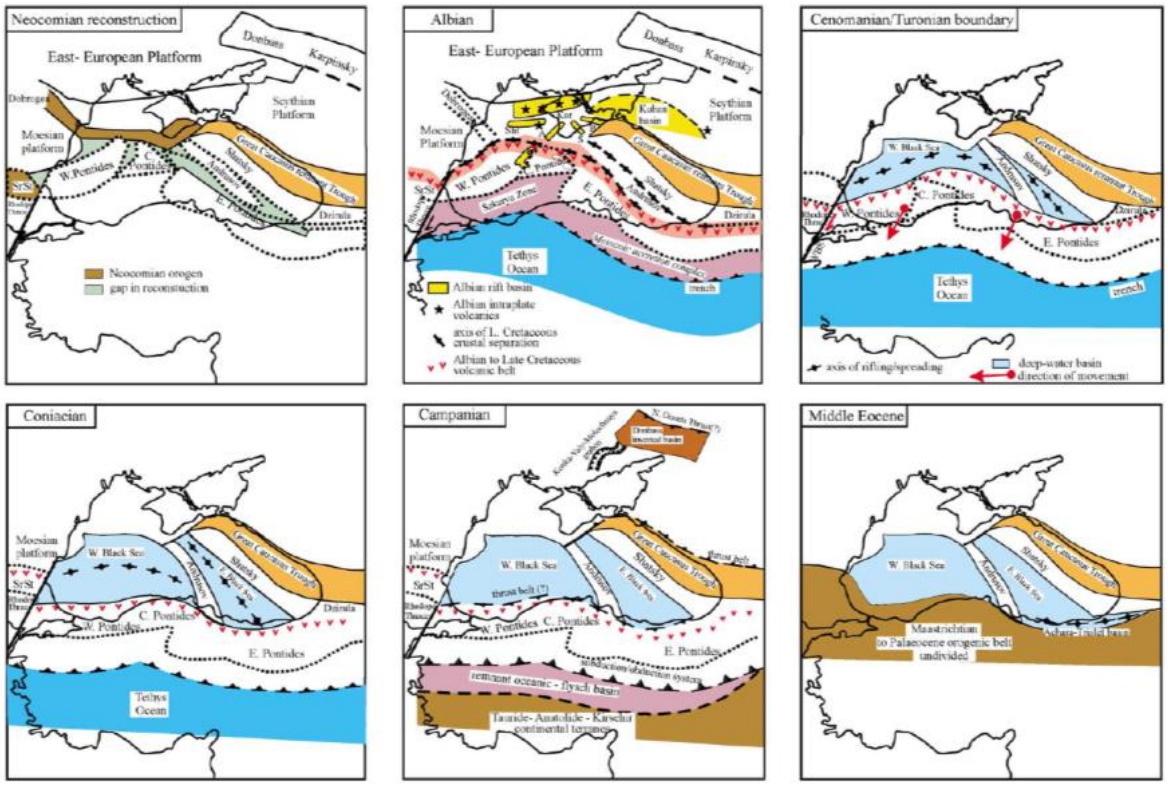

Figure 1-16. Paleo-tectonic reconstructions of the Black Sea region (from Nikishin et al., 2015b).

Following rifting, the Black Sea underwent rapid thermal subsidence accompanied by high sedimentation rates, which resulted in the deposition of thick sequences of mainly Tertiary sediments reaching up to 14 km in the central WBSB and up to 8-9 km in the central EBSB (e.g., Okay et al., 1994; Nikishin et al., 2003; Shillington et al., 2008).

At present, the Black Sea is undergoing compressional deformation that has been active since the Eocene (Saintot et al., 2006), or possibly the Palaeocene (Sheremet et al., 2016) time, and is related to the convergence of the Eurasian and Arabian plates. The Oligocene period is traditionally considered as the beginning of the syn-collisional (orogenic) stage forming the Caucasus mountain range to the east of the Black Sea basin, causing the uplift of some areas as well as the reactivation of older fault systems and the formation of inverted structures (e.g., Stovba et al., 2009). This time also represents the onset of deposition of the Oligocene-lower Miocene organic-rich shale, the regional source-rock of the Black Sea basin: the Maykop Formation (e.g., Tari and Simmons, 2018). Compressive deformation has predominantly concentrated around the edges of the EBSB, as shown by seismic reflection data and earthquake locations (Reilinger et al., 2006). This deformation has resulted in the folding of the Oligocene to Quaternary infills of the Tuapse and Sorokin troughs

(Figure 1-15), which have been thrusted over the shoulders of the Shatsky Ridge in the EBSB, favoured by the presence of the underlying ductile Maykopian units.

1.4.2 Previous geological studies in the EBSB

The origin and kinematic evolution of the EBSB has been under investigation since the publication of regional seismic lines for the entire Black Sea area in the 1980's (Tugolesov et al., 1985; Finetti et al., 1988; Belousov et al., 1988). From that moment, numerous studies have attempted to unravel the timing and kinematics of EBSB opening (e.g., Finetti et al., 1988; Görür, 1988; Graham et al., 2013; Nikishin et al., 2003; Okay et al., 1994; Rangin et al., 2002; Robinson et al., 1996; Shillington et al., 2008; Stephenson and Shellart, 2010; Sydorenko et al., 2017). However, the limited constraint over the deep, syn-kinematic and early post-kinematic stratigraphic record of the basin complicates geodynamic reconstructions. This is also due to the lack of deep wells in the central basin, where direct sampling generally stops at relatively shallow depths (post-Eocene time) in the sedimentary sequence (e.g., Ross, 1978). Wells located onshore and along the basin's margins (i.e., Georgia and Crimea) and wells drilled in the WBSB have been integrated by several studies, but correlations with the central EBSB stratigraphy are difficult (e.g., Sydorenko et al., 2017). Most of the stratigraphic interpretations also rely on correlation from uplifted and exposed onshore stratigraphic sequences (e.g., Nikishin et al., 2015b) which, again, are difficult to correlate with the deep basin stratigraphic record. Nevertheless, outcrop analysis and well correlation from Crimea, Georgia, and Turkey coastlines and onshore areas have been performed to define the timing of rifting and potential breakup in the basin (e.g., Sydorenko et al., 2017; Hippolyte et al., 2018). Although the thick sedimentary infill of the basin contains important information on the rifting and post-rift evolution of this area, it also limits the ability of conventional seismic acquisition to image the deep sedimentary units and tectonic structures. All these limitations led to the definition of different structural and geodynamic models to explain the back-arc evolution and the present configuration of the EBSB leaving disagreement within the scientific community over the timing and kinematics of basin opening (e.g., Spadini et al., 1996; Starostenko et al., 2004; Galushkin et al., 2006; Egan and Meredith, 2007; Maden, 2013; Yegorova et al., 2013; Espurt et al., 2014; Nikishin et al., 2015a, b).

Great disagreement also exists on whether the basin's stretched lithosphere reached breakup with subsequent seafloor spreading. Therefore, it is still questioned whether the EBSB is underlain by oceanic crust, or by a thinned continental crust, or by a mixture of the two, and on the extent of the different crustal domains (e.g., Shillington et al., 2009; Graham et al., 2013; Nikishin et al., 2015a, b). Different geophysical techniques have been used to constrain the crustal structure of the EBSB and surrounding regions (e.g., Yegorova and Gobarenko, 2010, Çınar and Alkan, 2016, Egan

and Meredith, 2007, Yegorova et al., 2013, Stephenson and Schellart, 2010, Vincent et al., 2016). A local seismic tomography study in the northern-central part of the EBSB, defined three-dimensional P- and S-wave velocity models which have been interpreted to show a highly extended and intruded continental crust, referred to as "suboceanic" crust, in the central part of the basin (Gobarenko et al., 2015). This tomographically defined suboceanic crustal domain was interpreted to show serpentinized mafic lower crust or upper mantle lithosphere exhumed during Cretaceous rifting and lithospheric hyperextension (Gobarenko et al., 2015). Seismic interpretation of "*hummocky*" morphologies at the EBSB crustal basement has been interpreted by Nikishin et al. (2015a) as evidence for oceanic crust. Results from an Ocean Bottom Seismometer (OBS) experiment conducted in 2005 along the Turkish sector of the EBSB have provided fundamental insights into the crustal structure in that part of the basin (Shillington et al., 2009). Results have shown the presence of a sharp transition from a thin crust (7-9 km-thick) with continental lower-crustal velocities (6.2-6.6 km/s) in the NW to a thick crust (11-13 km) with oceanic-like lower-crustal velocities (6.8-7.2 km/s) in the SE (Shillington et al., 2009) (see Chapter 4). The authors interpreted this sharp transition, occurring over a distance of ~ 30 km and bounded to the SE by a transform fault which is interpreted to control the thermal state of the lithosphere, as a magma-poor to magma-rich transition. Another study combined seismic data interpretation, looking at basement morphology, with gravity anomaly modelling to define crustal thickness and density, and results have been interpreted to show the presence of oceanic crust in the central basin, with a narrow COT in between continental and ocean domains (Graham et al., 2013). The variety of interpretation on the crustal composition and relative extent coming from different datasets shows the still poor understanding of the central basin structure. The Black Sea has therefore raised important questions and considerations about the crustal affinity of deep marine basins formed in back-arc settings, particularly on whether these are underlain by highly deformed and intruded lithosphere of continental affinity or whether they are the locus of oceanic crustal accretion.

Some studies have also focused on understanding the EBSB opening mechanism (e.g., Okay et al., 1994; Nikishin et al., 2015). The basin opening kinematic history has generally been compared with a "scissor-like" rotational opening, similar to other back-arc basins such as the Lau Basin, the Okinawa Trough, the Tyrrhenian Sea, and the Aegean Sea. However, depending on the timing of the deepest stratigraphic record, and on the tectono-stratigraphic contacts, the opening dynamic may be different. Studies have also tried to define the symmetric versus asymmetric rift structure. Nikishin et al. (2015a) inferred that the WBSB has a distinct asymmetry characterised by the presence of a single gently-dipping main detachment fault along the southern sidewall of the basin, with the northern sidewall bounded by a larger number of normal faults characterised by smaller displacement. In contrast, Nikishin et al. (2015a) suggested that the EBSB is a rather symmetrical

rift that opened within a weak and hot lithosphere (Nikishin et al., 2003) with normal faults along both sidewalls and a neck-shaped thinning of the lithosphere (Ziegler and Cloetingh, 2004). Some recently published studies (e.g., Bilim et al., 2021; Maynard and Erratt, 2020), show that interest in unravelling the Black Sea crustal and sedimentary structure is still ongoing. A more detailed analysis of the published studies and results is provided in Chapter 3.

1.4.3 A frontier in hydrocarbon and gas hydrate exploration

The Black Sea represents the world's largest anoxic intercontinental basin (Finetti et al., 1988; Nikishin et al., 2003), and it has long been known to host significant oil and gas potential (e.g., Stovba et al., 2009; Kitchka et al., 2014). Abundant seepage, outcrops of potential source rocks around its margins, large potential traps imaged on seismic data, and a variety of potential reservoir and play concepts point towards the considerable potential to reward the successful explorer (Simmons et al., 2018). Due to this potential, several studies have focused on understating the mechanisms that control the formation of the Black Sea regional basin structure, although very few wells have been drilled in its deep-water sector (Kitchka et al., 2014).

Of great interest in the Black Sea basin is an Oligocene-lower Miocene, organic-rich unit, and potential source-rock: the Maykop Formation (Tari and Simmons, 2018). The Maykopian sequence is present throughout the basin and is associated with a number of fluid escape and accumulation features, also visible on seismic profiles. Major hydrocarbon discoveries are located in the northern part of the basin (south of Crimea) and within the Danube and Dnieper deep-water fans in the WBSB. Other promising areas are represented by the thrust anticlines with Maykop cores in the Sorokin Trough, and by the structural traps of the northwestern continental slope/toe (Kitchka et al., 2014).

The Oligocene to Recent deep-water sedimentation in the Black Sea is dominated by pelagic shales, consisting of organic rich material sourced by river systems and deposited within a rapidly subsiding basin (Tari and Simmons, 2018). This translates to the presence, beside deeply sourced gas (thermogenic) from the Maykop Formation, of biogenically degraded gas formed within shallower sedimentary units (e.g., Merey and Sinayuc, 2016). Part of these units have been deformed along the margins of the EBSB following the post-Eocene compressional reactivation (e.g., Saintot et al., 2006). Within these deformed units, widespread evidences of fluid escape features (i.e., mud volcanoes and gas seeps) has been identified, together with seismic evidence for fluid accumulation and migration pathways (e.g., Vassilev and Dimitrov, 2002; Krastel et al., 2003; Starostenko et al., 2010; Xing and Spiess, 2010). In recent years, gas hydrate deposits have also been under investigation in these same areas (e.g., Popescu et al., 2006; Zander et al., 2020; Bialas et al., 2020;

Riedel et al., 2021). As for conventional hydrocarbons, most of the gas hydrate occurrences are also primarily found within the deep-water fan systems (Danube and Dnieper Fans) of the WBSB and in the central Black Sea off Crimea. Here, several indicators for the presence of hydrates come from drilling and coring, geochemical analysis of seeps and mud volcanoes, and from seismic BSRs (e.g., Popescu et al., 2006; Zander et al., 2017; Dinu et al., 2018). Consequently, studies on gas hydrate systems have primarily been focused in the WBSB area, with only few studies identifying and studying the presence of gas hydrate systems in the EBSB (Vassilev and Dimitrov, 2002; Minshull and Keddie, 2010) (see Chapter 5).

Nevertheless, the whole Black Sea basin bears a high potential for the formation of hydrates. Beside the presence of some amounts of deeply sourced gas (e.g., Merey, 2017; Limonov et al., 1997; Kruglyakova et al., 2004; Mazzini et al., 2004), the 99% of gas (methane) in the Black Sea is linked to biogenic degradation within the shallow sediments (e.g., Ginsburg and Soloviev, 1998; Vassilev and Dimitrov, 2002; Poort et al., 2005; Merey and Sinayuk, 2016). The formation of such large amounts of biogenically derived methane in the Black Sea is favoured by (i) the semi-isolated basin conditions, (ii) the rapid and conspicuous sediment supply from major river systems and (iii) the anoxic deep-water settings (Minshull et al., 2020, and references therein). Given the availability of large amounts of gas, its transformation into a hydrate phase is particularly favoured by the low pore-water salinity of sediments and the deep-water settings translating into high-pressure conditions.

The favourable Black Sea conditions are related to the unique hydro-chemical structure of the basin, which is the result of its past (post-rifting) history. The basin was a freshwater lake from 22,000 to 9,000 year B.P. After the rise of the sea-levels, the warm saline waters of the Mediterranean Sea flowed through the Black Sea via the Bosphorus. Then, the denser saline water sank and less dense water rose to the top, resulting in the present-day vertical temperature gradient of the Black Sea water column, showing relatively warm deep water (8.9-9.1˚C), with a shallow, cold intermediate level separating the deep warm water from the surface cold water (e.g., Klauda and Sandler, 2003; Stanev et al., 2014). The strong density gradient forced by the halocline means that there is little vertical mixing in the Black Sea waters (Stanev et al., 2014). Thus, little atmospheric O_2 reaches deep waters, which are consequently markedly anoxic (Muratov et al., 1978). Water salinity in the Black Sea is much lower than typical seawater, increasing from 1.75 to 2.23% (17.5-22.3 ppt) between sea-level and 200 m below sea-level (bsl), and being almost constant from 200 m below sea-level to seafloor (Railsback, 2010; Stanev et al., 2014). Cores recovered at DSDP Hole 379A, located in the central Black Sea, shows sea surface chlorinity and salinity of 1.144% and 2.02%, respectively (Ross, 1978; Shishkina, 1978). At the borehole location it was observed that chlorinity drops to 0.27% at 32.4 mbsf, and salinity stays low up to 268 mbsf depth, fluctuating

between 0.18 and 0.33%. The difference in salinity and chlorinity in sediments below seafloor from seawater at seafloor was interpreted as the freshening of the basins during late Pleistocene in the Black Sea (Shishkina, 1978). Similarly, low pore-water salinity of 0.5% was measured at the DSDP Leg 42B Hole 379A in the central Black Sea (Ross, 1978). This low salinity is due to dominant freshwater stages in the Quaternary deposits, corresponding to phases of isolation of the Black Sea (Popescu et al., 2006). Soloviev and Ginsburg (1994) stated that the water responsible for gas hydrate formation is of a lower salinity than the Black Sea water. All these characteristic elements of the Black Sea basin play an important role in methane generation, accumulation, and transformation into hydrate whenever pressure and temperature (P-T) conditions are met.

Various forms of evidence for the presence of gas and gas hydrates are visible in the Black Sea (Figure 1-17). A large number of vigorous methane-rich seeps fields have been found on the shelf of the Black Sea, releasing gas high into the water column (Hillman et al., 2018; Naudts et al., 2006; Römer et al., 2012; Schmale et al., 2011). These seeps, which are the major methane source responsible for the high concentrations measured in the water column (Greinert et al., 2010; Reeburgh, 2007), are mostly located in the transitional zone between shelf and continental slope (i.e., Sorokin and Kerch-Taman troughs, Batumi, Shatsky and Arkhangelsky ridges and Giresuan basin; Egorov et al., 2011; Naudts et al., 2006; Schmale et al., 2011; Riboulot et al., 2018) (Figure 1-17). The pattern of seep distribution has been linked with the uppermost limit of the GHSZ within subseafloor sediments (Riboulot et al., 2017). Numerous mud volcanoes are also associated with the presence of gas coming from dissociated hydrates (e.g., Shnyukov, 2013; Xing and Spiess, 2015) (Figure 1-17). Other indicators for hydrate occurrence, such as BSRs, high resistivity anomalies, and gas chimneys are widespread along the margins of the basin and in its central part, as summarised in a map presented within the framework of the COST Action “Migrate: Marine gas hydrate – an indigenous resource of natural gas for Europe” (Minshull et al., 2020; https://www.migrate-cost.eu/wg1-reports). Other maps showing the location of mud volcanism, intense gas seepage and cold vents, potentially associated with gas hydrate systems, are presented by several studies (e.g., Haeker et al., 2015; Schmale et al., 2011; Starostenko et al., 2016).

Gas hydrates have also been cored in the sediments from various locations around the Black Sea, such as mud volcanoes in the Sorokin Trough (Bohrmann et al., 2003), cold vent areas in Batumi, Colkheti, Kerch, and Pechori (Pape et al., 2010; Reitz et al., 2011; Römer et al., 2012; Zander et al., 2020) and in the Danube paleo delta (Bohrmann et al., 2018; Ruffine et al., 2021) (Figure 1-17). Gas hydrates recovered by gravity corer in Batumi Region of the EBSB have shown that the recovered gas hydrate samples contain 99.96 % CH_4 gas, which is an indication of sI type hydrate (Heeschen et al., 2011). Other hydrate-bearing cores retrieved in the WBSB and in Georgia, using a long piston

corer, have shown that hydrate sediments are mainly composed of lacustrine sediment deposited during the Holocene (Ross and Degens, 1974; Pape et al., 2010).

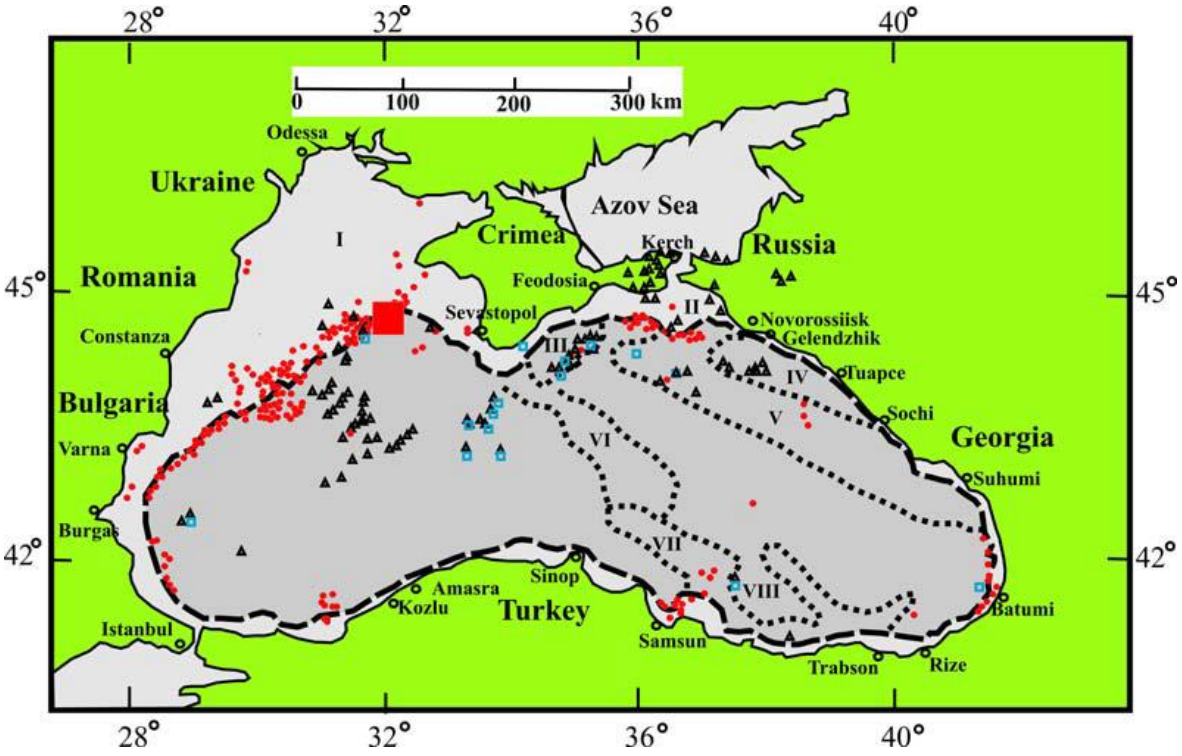

Figure 1-17. Gas and gas hydrate-related evidence in the Black Sea, including mud volcanoes (black triangles), gas seeps (red circles) and gas hydrates (blue squares). Bold dashed lines indicate the shelf edge, and bold squared lines show the boundaries of tectonic units. Roman numbers indicate different tectonic units (I, NW Shelf; II, Kerch-Taman trough; III, Sorokin trough; IV, Tuapse trough; V, Shatsky ridge; VI, Andrusov ridge; VII, Arkhangelsky ridge; VIII, Giresuan basin) (from Starostenko et al., 2010).

Seismic evidence for gas hydrates, in the form of BSRs, is observed at several locations in the Black Sea and particularly in the Danube and Dnieper fan areas and in the central basin. Here, multiple BSRs are also identified (e.g., Popescu et al., 2006; Küçük et al., 2015; 2016). Some studies infer that the present-day gas hydrates of the Black Sea basin are in a steady-state conditions, meaning that the observed upper BSR represents the present-day BGHSZ. Other studies, instead, support the hypothesis that the upward migration of the BGHSZ is a long-lasting process, and that the WBSB gas hydrate system is still in a transient state (e.g., Poort et al., 2005; Zander et al., 2017; Ker et al., 2019; Colin et al., 2020). Evidence for irregular BSRs are also associated with this transient state condition, although such heterogeneities could result from different sediment permeability, variable gas hydrate concentration, or a combination of both (Colin et al., 2020). In sedimentary layers with higher gas hydrate concentration, the dissociation can produce more free gas and higher pore overpressure. In these layers, the overpressure can delay hydrate dissociation. Modelling of the steady-state BGHSZ by Sultan et al. (2010) shows that the observed BSR is currently shallower

than the LGM modelling, yet deeper than the present-day modelling. The intermediate depth of the BSR is considered to support the hypothesis of a transient state of the hydrate system (Zander et al., 2017; Colin et al., 2020).

Some evidence for seismic BSRs come from the EBSB, i.e. offshore Crimea, Georgia and Turkey, and these are associated with the presence of a single BSR (e.g., Vassilev and Dimitrov, 2002; Minshull and Keddie, 2010). However, no study clearly identifies and discuss the presence of BSRs and/or gas hydrate systems in the Tuapse Trough, thus leaving this area open to further investigation.

1.5 Aims of this study

This thesis contributes to the understanding of two main subjects: the first one being the timing and mechanisms of rift and breakup processes and the resulting tectono-magmatic configuration in the EBSB (Chapters 3 and 4), and the second one being an investigation of new seismic evidence showing multiple BSRs along the NE margin of the EBSB (Chapter 5). A common element to both topics is the geophysical nature of the investigation, which mainly relies on 2D long-offset seismic reflection profiles acquired in the Black Sea during 2011-2012. The three fundamental questions addressed by this thesis concern the followings:

1) A clear definition of the timing and kinematics for the opening of new ocean basins and the development of passive continental margins is often uncertain. Geodynamic reconstructions are complicated because the tectono-stratigraphic elements recording the basin evolution often show a high degree of variability along the basin axis. Thus, classically defined pre-, syn- and post-rift sedimentary units are often difficult to identify and cannot be used to recognise well-defined rifting and breakup domains at extensional settings. Furthermore, tectono-stratigraphic features are often poorly or sparsely imaged using 2D geophysical datasets, so little constraint is provided on their 3D variability across the study area, especially if focused along big passive continental margins and basins (i.e., Atlantic margins). A way to overcome such limitations, helping to understand how rifting and breakup have evolved trough time and space, is to study smaller scale basins (i.e., failed rifts, active rifts and back-arc basins), which have proved that these areas present similar complexity and forming mechanisms to bigger scale passive continental margins and basins (i.e., Atlantic margins) (e.g., Taylor et al., 1995; Franke, 2013). This thesis contributes to the understanding of extensional basin and passive margin evolution by discussing the case study of the Black Sea back-arc basin, and addresses the following question: What is the timing and kinematic history of back-arc extension in the EBSB? Several studies have tried to constrain the age of basin opening based on a variety of direct and indirect evidence. However, big discrepancies still exist. It is generally believed that the basin may have formed anytime from Lower Cretaceous to Eocene time. Also, independent of the exact timing, basin opening is generally considered to have occurred synchronously along the EBSB, thus leading to the idea of an instantaneous along-axis event related to a “scissor-like” opening kinematics. Discrepancies in the estimated timing of rifting at different locations along the EBSB, and based on different datasets, suggest a non-uniform or diachronous timing of rifting along the basin axis, thus indicating that the instantaneous “scissor-like” kinematic model may be not representative for the EBSB opening. The deep

stratigraphic and structural elements of the basin are investigated using high resolution seismic data, and are correlated with published litho-stratigraphy, where possible. This analysis provides new insights into the temporal and spatial evolution of rifting and breakup processes in the basin. Results are comparable to observations from other well-developed, large-scale passive continental margins, supporting the idea of a complex and diachronous along-axis rifting and breakup history.

2) The presence, extent and nature, if any, of oceanic basement at extensional settings is often difficult to define when using indirect geophysical methods (i.e., seismic data and/or potential field data). Elements such as the amount of magmatism, the spreading rate, the mantle temperature, and the presence of transform faults controlling the distribution of melt often interact affecting the resulting basement structure. Thus, the emplaced crust may result in a morphology and/or a geophysical signature differing from what normally expected at either continental or oceanic settings. Crustal basement resulting from mantle exhumation processes and/or with an intermediate composition between continental and oceanic crust have also been identified (e.g., Franke, 2013), landward of "normal" oceanic basement at the distal parts of a margin. This basement, often referred to as the Continent-Ocean Transition (COT), is interpreted as the transition from "normal" continental to oceanic crust. Although the nature and extent of the COT, as well as of the proper oceanic crust, are difficult to define, their identification is key to understanding the mechanisms driving extension and the behaviour of the lithosphere under extension. Where direct evidence (i.e., well data) is lacking, geophysical data integration and comparison is key to define the often uncertain nature of the crustal basement. This thesis investigates the presence and distribution of oceanic and/or transitional crust in one of the most debated areas, the EBSB, addressing the following question: Did the basin reach the breakup stage and, if so, what is the crustal composition and distribution in the central part the basin? Defining the composition of the crust at extensional settings is important to unravel the mechanisms of extension, the behaviour of the lithosphere under extension, and to reconstruct the thermal history of a basin. Studies from the EBSB mostly disagree on the presence, character and distribution of a basement related to spreading processes, which may also be a consequence of the type of dataset used and of the interpretation given to the observations. Studies have inferred that the basin may be underlain by stretched continental crust, highly stretched continental crust intruded by volcanics, exhumed and serpentinized mantle, or by oceanic crust, with no clear definition of the boundaries between different crustal domains. This thesis introduces the application of magnetic anomaly modelling, often used to constrain the presence and extent of oceanic crust, in an area where this technique has not been tested yet. Seismic interpretation (point 1) is used

to provide initial constraint to the magnetic anomaly modelling to define crustal domains and their boundaries. Results are then compared with previous observations providing a new interpretation that reconcile discrepancies.

3) Bottom-Simulating Reflectors (BSRs) visible on seismic reflection data are often interpreted to represent the present-day base of the gas hydrate stability zone (BGHSZ) in sub-seafloor sediments. Multiple BSRs have been recognised along few continental margins (i.e., Gulf of Mexico; Nankai margin; etc), raising questions about their formation mechanisms, since only one of them can represent the present-day BGHSZ. This thesis shows new evidence for multiple BSRs in the NE part of the EBSB, and addresses important questions, such as: what is the physical nature of these multiple BSRs, i.e., are they related to the presence of gas/gas hydrate? and, if so, what is their distribution and saturation in sediments? and, which are the mechanisms responsible for multiple BSRs generation? To answer these questions, it is important to define the physical properties of sediments linking them to the presence of hydrate and/or free gas bearing zones. Due to the lack of direct information on the investigated sedimentary section, seismic tomography is applied to the dataset to extract velocity information. Downward continuation is used, first, to improve refracted travel-times aiming to extract BSR-related arrivals. Combined reflection and refraction travel-time modelling is then used to determine the velocity structure of sediments. The depth of the interpreted BSRs is compared with the calculated BGHSZ. An effective-medium modelling approach is used to provide estimates of hydrate and gas saturation based on the seismic velocities obtained from travel-time analysis. Results from this study are used to assess the potential and limitation of downward continuation and travel-time tomography when applied to shallow (i.e., gas hydrate) studies, and to define the nature and formation mechanism(s) for multiple BSRs in the EBSB, comparing them with the better-known gas hydrate system in the WBSB and at other continental margins.

1.6 Thesis outline

The EBSB represents a natural laboratory to study both rifting processes and gas hydrate systems, especially given the limited number of studies that have focused on this part of the basin leaving many questions still open to debate. Seismic interpretation of the 2D long-offset profiles provides the background information to this study. This is then integrated and supported by other techniques generally used at extensional settings and gas hydrate regions, but not yet applied to this specific area. Results from this study aim not only improve the understanding on the EBSB rifting evolution, present-day configuration, and gas hydrate distribution and dynamics, but also to contribute to the more generally understanding of passive margin evolution and gas hydrate systems along them. Based on this preface, the thesis outline is as follow:

Chapter 2 describes data and methodology used in this study. Section 2.1 introduces the long-offset seismic reflection profiles, providing information on the data acquisition and geometries and introducing the principles of tectono-stratigraphic interpretation, the time-depth conversion steps applied to seismic profiles and related seismic interpretation (Chapter 3). Section 2.2 describes the seismic velocity modelling performed using downward continuation to pre-condition the data and travel-time tomography (Chapter 5). Section 2.3 defines main concepts related to geomagnetic field, the magnetisation of rocks, the global magnetic reference and anomaly grid models and the forward magnetic anomaly approach used to complement and support seismic interpretation in Chapter 4. Finally, section 2.4 focuses on the gas hydrate modelling approaches, including the modelling of the BGHSZ under steady-state conditions, and the effective-medium modelling used to estimate gas and gas hydrate content in the pore space (Chapter 5). Section 2.1.2 represents the supplementary material of Chapter 3.

Chapter 3 provides new insights on the time and kinematic of rifting and breakup processes in the EBSB. Seismo-stratigraphic and tectonic evidence related to syn-kinematic evolution of the basin are interpreted on seismic reflection data and correlated with published litho-stratigraphic information. The analysis reveals new insights onto the Upper Cretaceous to Cenozoic sequence recording extensional processes in the basin. Evidence discussed in this chapter show that extension have migrated along-axis from SE to NW, and continued for longer time than previously inferred, while breakup initiated and focused in the SE of the basin. These results highlight the diachronous character of rifting and breakup processes in the EBSB, similarly to what observed along other well-studied continental margins and rift basins by recent studies.

This chapter has been published on the peer-review journal *Tectonics*. The full reference is: Monteleone, V., Minshull, T. A., & Marin-Moreno, H. (2019). Spatial and temporal evolution of

rifting and continental breakup in the Eastern Black Sea Basin revealed by long-offset seismic reflection data. *Tectonics*, 38(8), 2646-2667. DOI: https://doi.org/10.1029/2019TC005523. VM performed the seismic interpretation and tectono-stratigraphic reconstruction with guidance and review from TM and HMM. The supplementary material from this paper is shown in Chapter 2 (section 2.1.2) of the thesis. Interpreted seismic profiles that are not shown in Chapter 3, are shown in Appendix A.

Chapter 4 investigates the presence of different crustal domains and their lateral extent in the central EBSB, based on the integrated analysis of seismic reflection data interpretation (Chapter 3) with magnetic anomaly modelling. Basement morphological variations are used to provide initial constraints on crustal domain type and distribution. The magnetisation character at the identified crustal domains is modelled from the regional magnetic anomaly data and is integrated to constrain crustal domain boundaries. Results are then compared with previous studies, and apparent contradictions are discussed and linked to fault-controlled changes in along-axis magmatic addition influencing the structure and geophysical character of the emplaced crust.

This chapter has been published on the peer-review journal *Geology*. The full reference is: Monteleone, V., Minshull, T. A., & Marin-Moreno, H. (2020). Integrated geophysical characterization of crustal domains in the eastern Black Sea. *Geology*, 48(4), 405-409. DOI: https://doi.org/10.1130/G47056.1. VM performed the magnetic anomaly modelling and tectono-magmatic reconstruction with guidance and review from TM and HMM. Supplementary material information from this paper has been added in a method section of Chapter4 (section 4.2). Fundamentals of magnetism are discussed in Chapter 2 (section 2.3). Additional images belonging to the supplementary material of the paper are shown in Appendix B.

Chapter 5 presents new evidence for multiple BSRs within the upper Miocene-Quaternary folded and thrusted sequences of the Tuapse Trough, to the NE margin of the EBSB. To constrain sediment's physical properties, thus providing insights on the presence and concentrations of gas and/or hydrate, travel-times from a single seismic profile are used. To overcome streamer data limitations in imaging the velocity structure of sediments, downward continuation is applied to inprove refracted signal quality in preparation to travel-time analisys. Reflected and refracted travel-times are used in a forward tomographic approach to define a 2D velocity model along the study region. Velocity information show changes in physical properties within sediments, where gas and gas hydrate concentration are estimated using an effective-medium modelling approach. Results are used to characterize the nature of the multiple BSRs in this part of the basin, discussing the possible mechanisms responsible for their formation.

VM performed the seismic interpretation, downward continuation, and travel-time analysis with guidance from TM. BGHSZ and elastic-medium modelling were also performed by VM with guidance from HMM. TM and HMM reviewed this work. Additional images belonging to the supplementary material of this chapter are shown in Appendix C, Appendix D and Appendix E.

Chapter 6 summarises and discuss the findings, the limitations of this study, their broader applicability, and future work.

Chapter 2 Data and methods

2.1 Seismic data

Twelve post-stack, time-migrated seismic reflection profiles have been used in this study (Figure 2-1). Seismic profiles were acquired as part of a regional survey in 2011-2012 by *Geology Without Limits* (GWL) and ION GXT, using an 816-channel hydrophone streamer with a maximum offset of 10200 m, a receiver spacing of 12.5 m, and a towing depth of 9 ± 0.5 m. A source of 5680 cubic inches array was towed at a depth of 8 ± 0.5 m, and the source interval was 50 m. Such configuration allowed the data to provide higher resolution than conventional seismic acquisition up to deep, basement levels. Table 2-1 summarises the acquisition parameters and the processing steps carried out by GWL.

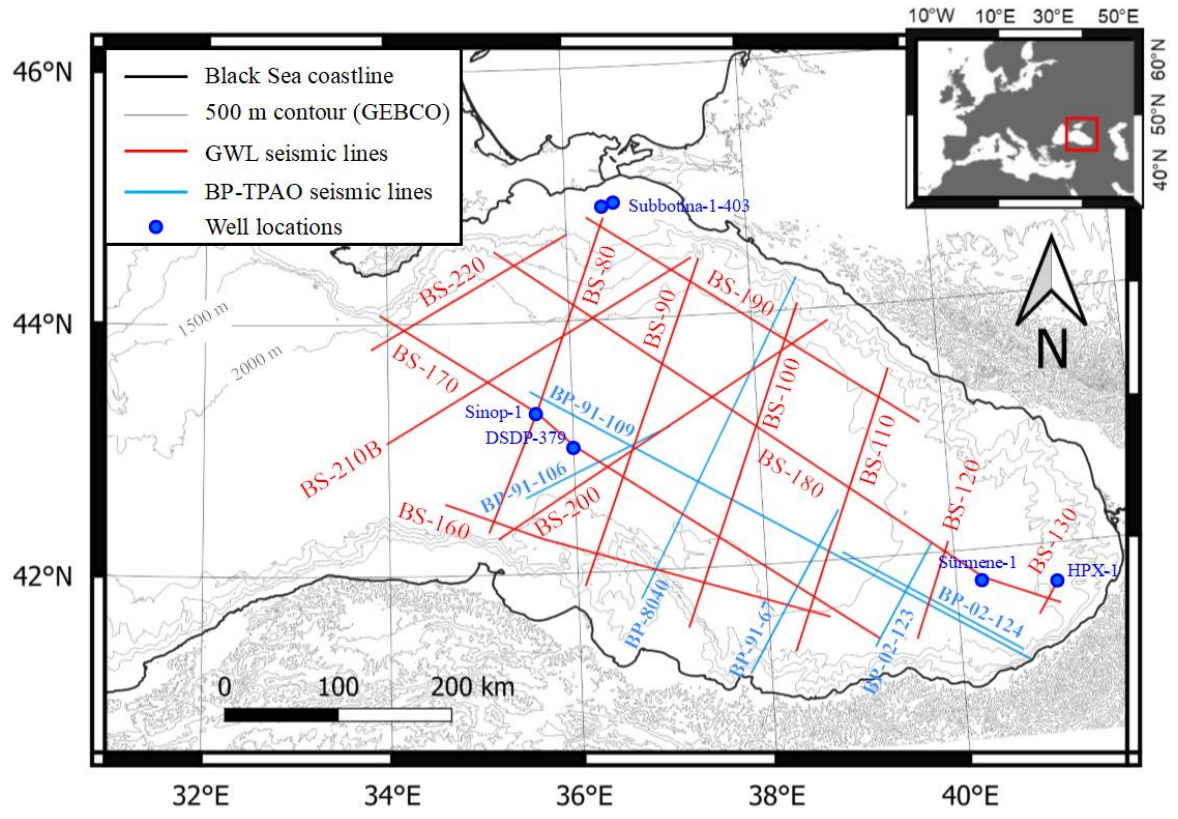

Figure 2-1. Map of the EBSB region showing the locations of the GWL seismic profiles (red) used in this study. Other seismic profiles from BP-TPAO (blue) have been integrated to better constrain seismic interpretation. Topographic and bathymetric contour from GEBCO is displayed at 500 m interval (www.gebco.net). Blue dots indicate offshore well locations after Stovba et al. (2009) and Tari and Simmons (2018).

The long-offset seismic dataset were integrated with other seismic profiles from a joint British Petroleum (BP) and Turkish Petroleum Corporation (TPAO) acquisitions in 1991-1992 and 2002 (e.g., Robinson et al., 1996; Shillington et al., 2008) (Figure 2-1). These seismic profiles show limited resolution at basement depths, nevertheless, stratigraphic sequences imaged above basement are used to trace horizons in continuity with the long-offset profiles, thus increasing the survey grid density and reducing interpretation gaps and related uncertainties between long-offset profiles.

Table 2-1. Summary of the 2D long-offset seismic reflection profiles acquisition parameters and GWL processing steps used to generate the post-stack time migrated profiles.

Acquisition parameters					
Source		Streamer		Recorder	
Array volume	5680 cu.in	Length	10200 m	Sampling rate	2.0 ms
Shot interval	50 m	Channels	816	Record length	18 sec
Depth	8 m ± 0.5 m	Receiver interval	12.5 m	Filters Low Cut	3 Hz
Pressure	2000 PSI	Depth	9 m ± 0.5 m	Filters High Cut	200 Hz
		Offset min	149.5 m		
		Offset max	10500 m		
Processing steps					
SEGY input and geometry application					
Spherical divergence correction					
Velocity analysis					
Predictive deconvolution 8 ms, 240 ms, whitening 1%					
Radon de-multiple					
Amplitude balancing					
Normal Move Out (NMO) muting and stacking					
Kirchhoff migration					
Band-pass filter 4-8-100-120 Hz					
Coherent filtering					
Amplitude balancing					

Seismic reflection profiles were used to document the geometrical relationships between tectonic and stratigraphic elements of the basin, and to define a link between deformation phases and distinct sedimentary units. Chapter 3 combines observations from changes in fault geometry and sedimentary architectures, linking them to the kinematics of basin opening. The stratigraphic contacts between sedimentary infill and the underlying basement, and changes in the basement morphological character, provide preliminary constraints for the definition of different crustal domains. These are then complemented by magnetic anomaly modelling (Chapter 4).

Part of a single long-offset seismic reflection profile, BS-200B (Figure 2-1), was downward continued to a datum close to seafloor, and travel-times corresponding to different seismic phases were used for a combined reflection and refraction tomographic analysis to define the velocity structure of the shallow sediments at the BSRs (Chapter 5).

2.1.1 Seismic interpretation

Tectono-stratigraphy

In Chapter 3, regionally distributed prominent reflectors, characterized by discordant stratigraphic contacts and variations in seismic character are used to identify the top and base of separate sedimentary sequences. Seismic sequence stratigraphic interpretation principles, defined by reflection terminations, are used to define sequence boundaries (Mitchum et al., 1977a, b) (Figure 2-2). Internal geometries and seismic facies variation occurring within each of the identified sequences, as well as their interaction with structural elements (i.e., faults), are used to map non conformable pre-, syn- and post-rift (or kinematic) packages. These distinct packages are described according to the classical definition of not time equivalent sequences separated by unconformity surfaces of fundamental importance in passive margins, including the base of the syn-rift infill and the base of the post-rift, passive infill (e.g., Williams, 1993; Falvey, 1974; Franke, 2013). Based on evidence showing the variable syn- to post-kinematic character of the identified units, depending on their location in the basin, classically defined sequences are discussed according to more recent definitions i.e., the "*breakup sequence*" by Soares et al. (2012).

Established stratigraphic analysis of the lateral continuity of sediments, super-imposition, and cross-cutting relationships between them and with the underlain basement (pre-rift) are used to understand their age relationships. These techniques assume that seismic reflections follow timelines in the stratigraphy (Vail et al., 1977). Fault planes are also interpreted, based on the identification of residual diffractions, on evidence for discontinuities along continuous seismic reflections and for kinematic sedimentary infill geometries. Faults geometry (i.e., dip angle) and distribution are mapped to define different extensional domains across the basin.

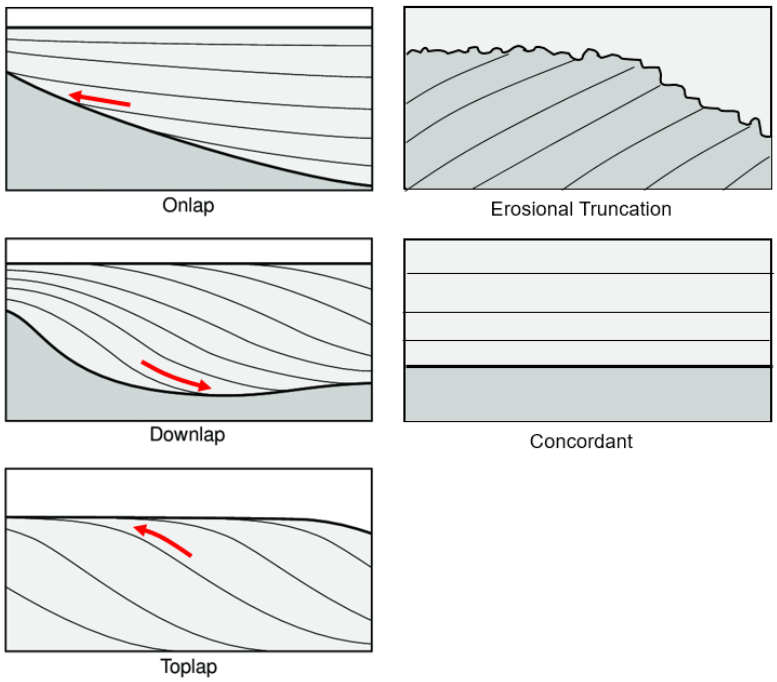

Figure 2-2. Angular relationship (concordant or discordant) between reflectors (thin lines) and bounding unconformities (bold lines) interpreted as sequence boundaries (modified from Mitchum et al., 1977a, b).

The timing of rifting (i.e., the age of the deeper sedimentary units) is constrained based on published litho-stratigraphy and well-correlated seismic interpretation from the EBSB region (e.g., Finetti et al., 1988; Robinson et al., 1996; Nikishin et al., 2003; 2015a, b; Shillington et al., 2008; Sydorenko et al., 2017; Tari and Simmons, 2018). The litho-stratigraphic identification and age definition for the basin sedimentary units on seismic data relies on the correlation with few deep-water wells in the area, although these generally never reach pre-Eocene stratigraphic units (e.g., Muratov et al., 1978; Ross, 1978; Sydorenko et al., 2017; Starostenko et al., 2011; Tari and Simmons, 2018), and onshore outcrops (e.g., Hippolyte et al., 2018; Nikishin et al., 2003, 2015c; Tari and Simmons, 2018).

Seismo-stratigraphic interpretation in this study refers to the conventional subdivision of the EBSB sedimentary infill, including the Mesozoic, the Palaeocene-Eocene, the Oligocene-lower Miocene Maykop, the middle and upper Miocene, and the Pliocene-Quaternary successions (e.g., Shillington et al., 2008; Sydorenko et al., 2017; Tari and Simmons, 2018). This subdivision is further discussed in Chapter 3. Here, a step forward is made in re-assessing the presence, distribution and age of the syn-rift and early post-rift deposits, whose presence and extent in the basin is still highly debated thus leading to a broad spectrum of interpretations for the age of basin opening.

Basement morphology

A qualitative assessment of the *rough* versus *smooth* basement morphological character is used to map boundaries between different crustal domains in the EBSB (Chapter 4). Rough basement morphology is discussed as potentially resulting from slow- or ultra-slow seafloor spreading (e.g., Malinverno, 1991) or mantle exhumation processes (e.g., Sauter et al., 2018). Smooth basement morphology is instead considered as potentially resulting from extrusive volcanic material related to anomalously thick and/or fast spreading oceanic crust (e.g., Small, 1994; Searle et al., 2010), exhumed mantle (e.g., Pickup et al., 1996; Sauter et al., 2013), or thinned continental crust overlain by basaltic flows (e.g., Zhao et al., 2016). Morphologically defined crustal domains are then modelled using magnetic anomaly data (see section 2.3) to constrain the petrological affinity of the basement and, from that, to narrow down the possible origin of its morphological character (Chapter 4).

2.1.2 Time-depth conversion

Interval velocities derived from stacking velocities provided by GWL have been used for time-depth conversion of the seismic data and related interpretation (Figure 2-3). Because the seismic reflection data were acquired with a 10 km-long streamer, these data cannot constrain the velocities of deeper strata ($\geq$ 10 km). Thus, to ensure an accurate time-depth conversion at deeper, basement levels, stacking velocities were compared with velocities from a 2005 wide-angle seismic experiment (Shillington et al., 2009*,* 2017) (Figure 2-3). The comparison between GWL velocities and those from wide-angle seismic profiles, which have a sufficiently large aperture to constrain the velocities of deep sediments, has shown that the two velocity functions are very similar in the shallow section (above basement reflection) whilst wide-angle seismic velocities are faster in the deeper section (Figure 2-3). Although shallow velocity trends are similar in both stacking and wide-angle velocities, stacking velocities have a better coverage across the study region, and they also show a more detailed and reliable match between velocity changes and geological variations. Wide-angle velocities are instead considered more reliable at depth, so these data have been used to estimate a mean velocity trend below basement. Therefore, the two velocity fields have been combined to provide the most accurate velocity model for time-depth conversion.

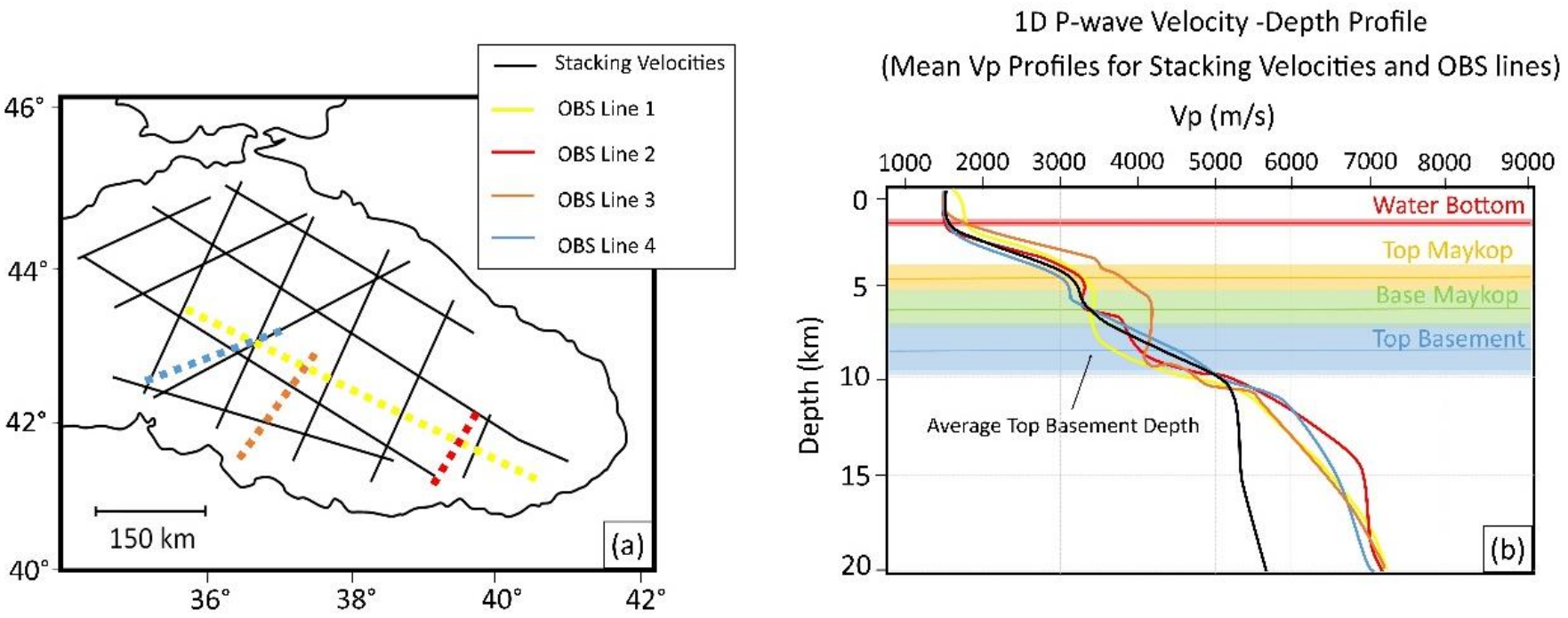

Figure 2-3. (a) Survey area map showing the location of the stack profiles used in this study and the OBS lines (Shillington et al., 2009). (b) 1D velocity-depth profiles comparing stacking velocities and OBS profiles. Black line— Mean velocity profile derived from stacking velocities. Coloured lines—Mean velocity profile derived from OBS lines (colour code for each line is shown in (a)). Mean depth ranges for the interpreted horizons and their standard deviations are highlighted in the coloured bands: Red - Water Bottom, Yellow - Top Maykop, Green - Base Maykop and Blue - Top Basement (see also Mean Depth Horizon (± error) column in Figure 2-4b). OBS velocities are faster below the basement compared to stacking velocities.

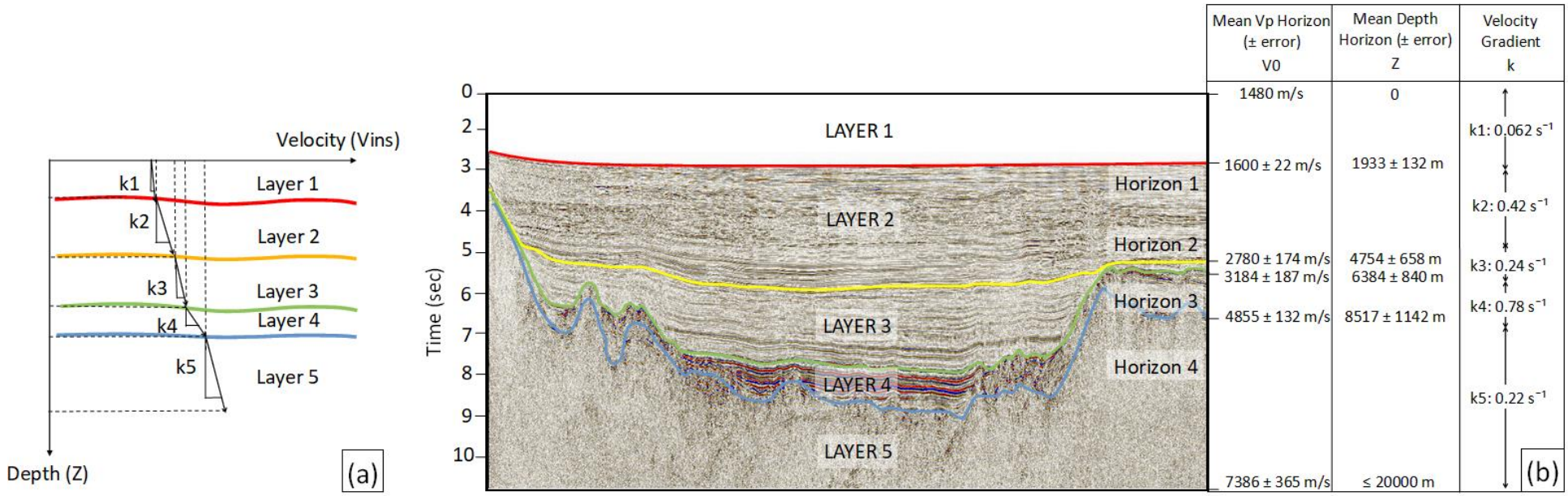

Figure 2-4. Velocity model building constrained by four time-interpreted seismic horizons (Water Bottom, Top Maykop, Base Maykop and Top Basement), the mean velocities (V_0) estimated along these horizons from the combined stacking and wide-angle velocity fields, and a defined velocity gradient (k). (a) Schematic representation of the linear velocity function applied for each layer. (b) Seismic section (BS-90) with the four-interpreted seismic horizons defining the velocity model layers shown in overlay. The values and uncertainties for the initial velocities (V_0) and the associated mean horizon depths (Z), and the values of constant velocity gradient (k) used are shown in the table to the right.

The velocity model building was generated using Petrel software. The model is constrained by four time-interpreted seismic horizons: Horizon 1 - Water Bottom, Horizon 2 - Top Maykop, Horizon 3 - Base Maykop, Horizon 4 - Top Basement. These horizons also correspond to major velocity changes, which define a five-layer velocity model (Figure 2-4). Mean velocities (V_0) estimated along these horizons from the combined stacking and wide-angle velocity fields are used as reference velocity at the top of their corresponding layer. V_0 is calculated by lateral staking of velocity information along each interpreted horizon (± 200 m from that horizon). For each layer, a constant velocity gradient (k) has been introduced in the model generation, to allow V_0 to increase with a linear function (Figure 2-4a), which is represented by the linear instantaneous velocity equation from Slotnick (1936) (Eq. 2-1):

$$V_z = V_0 + k\,(Z - Z_0) \qquad (2\text{-}1)$$

where V_z (in m/s) is the velocity at the base of the layer (Z), V_0 (m/s) is the velocity at the top of the layer (Z_0), k (s^{-1}) is a constant velocity gradient, Z (m) is the depth of the base of the layer at which V_z velocity is calculated, and Z_0 (m) is the depth at the top of the layer, associated with the initial velocity V_0. For each layer, the velocity gradient (k) allows V_0 to increase from the top of the layer to the base of the layer, depending on the thickness of the layer ($Z - Z_0$).

2.2 Seismic velocity modelling

Seismic methods are often used to obtain images of the sediments and crust and to map the variations in physical properties, particularly P-wave velocity (V_P), providing information on the subsurface geology. The most objective and widely used method to retrieve V_P models is seismic tomography, using either travel-time information only, as in travel-time tomography (e.g., Korenaga et al., 2000; Hobro et al., 2003), or a more complete set of waveform attributes including both phase and amplitudes as in full-waveform inversion (FWI) (e.g. Virieux and Operto, 2009).

There are different types of arrivals that can be identified in seismic data. Refracted arrivals travel along the steepest velocity gradient and turn within the sub-surface, thus they represent a good measure of the overall velocity gradient structure. Reflected arrivals also contain information on the velocity structure but, importantly, they place constraints on the depth and geometry of sub-surface interfaces. The combination of both travel-time types will provide a well constrained velocity model and reduces uncertainties. It is becoming more common to use multichannel seismic surveys for travel-time analysis, due to the density of shots and receivers compared to wide-angle surveys. However, conventional first arrival tomography is limited when using multichannel data. This is because the presence of a thick water layer makes refraction wave arrivals visible only to the far offsets of the shot gathers. Also, complex seafloor topography and sub-seafloor stratigraphy can cause 3D scattering noise that cannot be simulated by 2D wave propagation modelling, so this noise can pose difficulties in tomographic analysis. In order to overcome these limitations, thus improving refracted travel-time picking, downward continuation can be applied to extrapolate both shots and receivers from the sea surface to a datum closer to the seafloor (e.g., Berryhill, 1979, 1984; Arnulf et al., 2014; Qin and Singh, 2018).

The following sections introduce (i) the re-datuming of the recorded data closer to the seafloor by downward continuation (2.2.1) and (ii) the travel-time tomography performed on the original and downward continued data (2.2.2).

2.2.1 Wave equation datuming (downward continuation)

Downward continuation, like upward continuation, is a wave-equation procedure developed to change the datum of a collection of zero-offset seismic traces from one surface to another (Berryhill, 1979). This procedure was designated “wave-equation datuming”, and its applications to zero-offset data included a velocity-replacement “static” correction and multi-layer forward modelling. A form of Huygens’ Principle (Scales, 1995) is used to extrapolate seismic waves from one datum to another (Figure 2-5, Eq. 2-2).

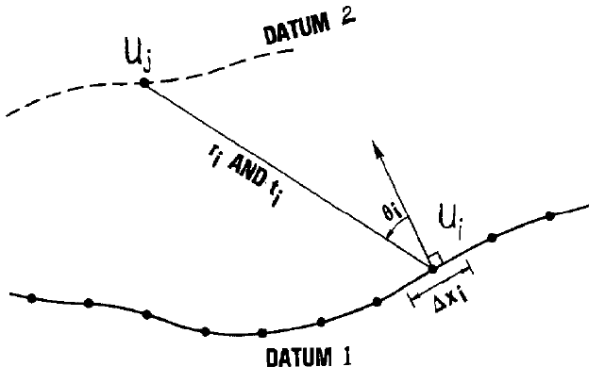

Figure 2-5. Huygens' Principle in the case of upward continuation from datum 1 to datum 2

$$Uj(t) = \frac{1}{\pi}\sum_i \Delta xi \ cos\theta i \frac{ti}{ri} \ [Ui\ (t - ti) * Fi] \qquad (2\text{-}2)$$

In Equation (2-2) and Figure 2-5, subscript *i* represents all the input seismic traces Ui referenced to datum 1, and $Uj(t)$ is the output seismic trace computed at some point on datum 2. ri is the distance between point Ui and the output location Uj, ti is the travel-time between the same two points, θi is the angle between ri and the normal to the datum surface, and Δxi is the spacing between input locations (trace spacing). The argument $(t - ti)$ indicates that Ui is delayed by travel time ti. Fi is a filter operator that has the practical function of preventing waveform distortion. The asterisk denotes convolution of Ui with Fi filter operator (Berryhill, 1979). Equation (2-2) as it stands describes the upward extrapolation of upcoming waves. To compute the downward extrapolation of upcoming waves, the input and output traces need to be reversed.

Berryhill (1984) extended this procedure to unstacked data. Since data are downward continued using a single-square-root operator (Reshef, 1991), meaning that extrapolation of the wave equation can be performed in a single domain, source and receiver need to be downward continued separately and their positions are interchanged alternately. Although no change was required in the mathematical algorithm, two passes through the data (common-source and common-receiver points; Figure 2-6) is required to change the datum of the entire seismic line (Berryhill, 1984). The rearrangement of the data is possible because of the reciprocity principle, so that if source and receiver have identical directional characteristics, meaning that the same seismogram should be recorded if the locations of the sources and geophone were exchanged (Wapenaar, 1996), then interchanging the positions of sources and receivers yields identical seismic traces. The seismic reciprocity principle is defined by the Green's function (Knopoff and Gangi, 1959), which describes the symmetry property of the wave field.

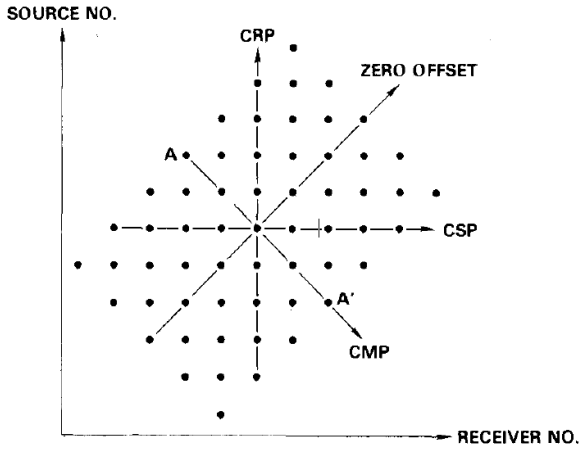

Figure 2-6. Schematic plot of source versus receiver coordinates. Common-source point (CSP), Common-receiver point (CRP), Common-mid point (CMP) and zero offset (Berryhill, 1986).

For moving both receivers and sources from one datum to another, we first need to operate on the line in (natural) common-source order, group by group, using Equation 2-2. Then, after sorting the resulting data into common-receiver points, the operation is performed in common-receiver point order, group by group, using Equation 2-2. The first pass moves the geophones and the second moves the shots. At the conclusion of step 2, all sources and receivers are effectively near or at the seafloor, compressing wave fronts and magnifying amplitudes (Berryhill, 1986). Although generally applied to wide-angle seismic refraction experiments, downward continuation of streamer data has been used in a number of studies to simulate a near-bottom refraction experiment, but with order of magnitude greater sampling (e.g., Arnulf et al., 2011). Using this method there is the advantage of exposing more of the shallow turning refractions as first arrivals that can be accurately picked for tomography, improving vertical resolution of the resulting velocity model (Arnulf et al., 2011; Harding et al., 2016).

The downward continuation method described in Berryhill (1979) is based on the strategy of solving the wave equation, i.e. finite-difference or Fourier Transform methods, in the time domain. This method uses Fourier Transform of the wave equation in a one-way form that defines a first-order derivative in the depth direction. Finite differences of the first and second order derivatives are then used to propagate the wave field. The Kirchhoff's integral extrapolation technique in the time domain is formulated by convolving the recorded wavefield at the water surface with the time lagged delta functions and summing these convolved results over all receiver locations for all shot gathers (Berryhill, 1984; Harding et al. 2007; Arnulf et al., 2011). The time lags are estimated by dividing the distance between the surface locations of the shot gathers and their extrapolated positions on seafloor by a constant water velocity.

In Chapter 5, the downward continuation technique is implemented using a MATLAB code (Harding et al., 2007). The data preconditioning and the parameters used for downward continuing the seismic field in this study are further described in the method section of Chapter 5.

2.2.2 Travel-time tomography

The travel-time tomography technique aims to reconstruct a model of the physical properties (i.e., seismic velocity structure) based on a set of measured data (i.e., seismic wavefield). The tomographic approach is an inverse geophysical problem, consisting of four main steps (Rawlinson and Sambridge, 2003):

1) Model parametrisation, i.e., the number of model parameters, the grid spacing and grid geometry and a starting model m_0.
2) Forward problem, consisting of the prediction of the set of observations or data (d) from a model (m) of the system, where the physical relationship between model and data is expressed as:

$$d = G\,[m] \tag{2-3}$$

3) Inverse problem, which tries to reconstruct a model (m) of the physical system from a set of observables (d), where G is a matrix defining the physical problem (i.e., ray theory). This involves an iterative procedure, where an initial guess of the model (m_0) is gradually modified to better fit the observed data.
4) Uncertainty analysis. It is never possible to obtain an exact model of a physical system. Therefore, to fully characterise the solution of the inverse problem it is necessary to estimate the uncertainty associated with each model parameter.

From ray theory, the relationship between an unknown model and the observed traveltimes is given by the path integral for the traveltime (T) for one source-receiver pair according to Equation 2-4:

$$T = \int_i u_0(s)ds \tag{2-4}$$

Where u_0 is the slowness (reciprocal of the velocity), *ds* is an infinitesimal length and i represents the raypath which is a function of u_0. The raypath itself is determined by the velocity structure using Snell's law, which assumes a known travel-time at the shortest path. To calculate the travel-time of a raypath (i), the model can be parametrised into blocks (j) of constant slowness (or velocity) (Figure 2-7).

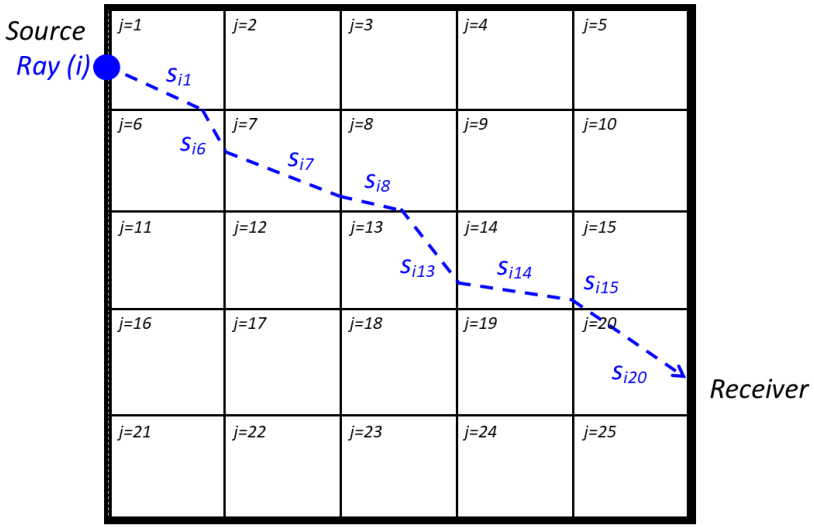

Figure 2-7. Model parametrisation into blocks (j) of constant slowness value. When a seismic wave crosses the model, the raypath (i) will be the sum of the distances travelled in each block (s_{ij}).

Considering this model parametrisation, the forward modelling step utilises Equation 2-4 to calculate a set of synthetic travel-times d_i for a given model m_j, and the Fréchet derivatives of the synthetic travel-times as a matrix G_{ij}. A perturbation in the travel-time data is related to a perturbation in the model by a scalar form of Equation (2-3), which can be written as:

$$d_i = \sum_{j=1}^{M} G_{ij}\, m_j \qquad (2\text{-}5)$$

$$i = (1,2,\dots,N);\; j = (1,2,\dots,M)$$

where subscripts i and j indicate the ith raypath and the jth block crossed by the ray, respectively, d_i is the observations/data (travel-times) to calculate for each block j, m_j is the model (seismic velocity/slowness) within a block j, *N* is the number of observations, *M* is the number of model parameters, and G is the physical problem (i.e., ray theory), which is expressed as a N x M matrix. G_{ij} is defined as the ratio between the distance travelled by a raypath i in a block j (s_{ij}), and the reference slowness (or velocity) of the starting model in that block (Figure 2-7). The mathematical relationship in Equation 2-5 shows that if N = M the problem is exactly determined, if N < M the problem is under-determined, and if N > M it is over-determined.

In a forward problem, the traditional method to calculate the arrival travel-times for reflection and/or refraction events from a defined model (i.e., seismic velocity model) is based on ray theory (e.g., Červený el al. 2001). Wavefront tracking schemes such as finite difference solutions of the eikonial equation (Vidale, 1990; Qin et al., 1992), or methods such as network/graph theory making direct use of Fermat's principle (Moser, 1991) have also been employed. For the inverse problem,

given a dataset d (travel-times), the model m is determined (earth velocity model), provided an initial model m_0 (e.g., Parker, 1994; Tarantola, 1987).

2.2.2.1 Forward travel-time analysis and velocity model parametrisation

Forward travel-time tomography relies on trial-and-error modifications of the initial velocity model in order to match the calculated and observed travel-times, aiming to obtain a model for which the misfit between calculated and observed travel-time data is minimal (Scales et al., 1994).

The velocity model presented in Chapter 5 was generated using RAYINVR forward ray-tracing algorithm presented in Zelt and Smith (1992). RAYINVR code is used in a layer-stripping approach, modelling from top to bottom. The model is defined as a series of layered, variable block size representation of 2D isotropic velocity structure (Zelt and Ellis, 1988; Zelt and Smith, 1992). Each layer boundary is specified by an arbitrary number and spacing of boundary nodes connected by linear interpolation. A single node may be used to represent a horizontal boundary, whereas detailed topographic relief may be specified by multiple nodes. Within each layer, the P-wave velocity field is specified by an arbitrary number and spacing of upper- and lower-layer velocity points. The complete velocity field within each layer is defined so that the velocity varies linearly with position along the upper- and lower-layer boundaries between the specified points and linearly between the upper and lower boundaries in the vertical direction. A constant velocity along an upper or lower layer boundary across the full length of the model is specified by a single velocity point, and a constant-velocity layer is specified by a single velocity value for the layer (Zelt and Smith, 1992).

Layer boundaries defined in this study represent real seismic events interpreted along the stacked seismic reflection profile. This is because a simple, flat-layered model (except for seafloor topography) was able to fit calculated and observed travel-times in areas with little geological complexity (flat-lying stratigraphy), but in areas with complex sub-seafloor stratigraphy unrealistic and sudden velocity variations had to be considered to fit the observed travel-times. As a result, a greater number of nodes was used to define layer boundaries within the geologically complex, fold and thrust area (see model depth nodes in Figure 5-8, Chapter 5), so that velocities could be specified within an acceptable range of values. Velocity nodes were initially set to be laterally uniform across defined layer, with small gradients allowed from top to bottom of the layer. Velocities were set based on values from stacking velocities provided by GWL along the same profile.

Once the initial model geometry was defined, depth and velocity values for each node were adjusted during layer modelling. Small variations were necessary for depth compared to velocity

values at the nodes. At satisfactory fit between calculated and observed travel-times, layer parameters were fixed, and modelling moved to the layer below.

The layer stripping approach relied on reflected travel-times from non-downward continued shot gathers. Refracted travel-times from downward continued shot gathers were introduced later to further constrain velocity nodes, finalising the model creation. A more detailed description of the velocity model definition, and the procedure for seismic phase identification and picking is presented in Chapter 5 (section 5.5.2).

2.2.2.2 Ray tracing

Rays are traced through the velocity model using zero-order asymptotic ray theory, numerically solving the ray tracing equations for 2D media using Runge-Kutta method (Sheriff and Geldart 1983) with error control to solve these systems as suggested by Červený et al. (1977). To complete the basic ray tracing algorithm, Snell's law is applied at the intersection of a ray with a layer boundary (Zelt and Smith, 1992). The ray step length is adjusted at each point along the ray path to avoid the inaccuracy of using large increments in the local partial derivatives when the ray bending is large, and the use of unnecessarily small step lengths when the ray bending is smaller. Within constant-velocity trapezoids, straight ray paths are used. A ray traced through the model is defined only at a series of points, the number and spacing of which is dependent on a user defined value. The travel-time at the endpoint of the ray is evaluated by numerical integration along the ray path using the trapezoidal rule (Zelt and Smith, 1992).

After the ray tracing procedure is complete, the code returns an RMS travel-time misfit between the travel-times along the calculated ray paths and those which are observed. Models are modified by trial-and-error with the aim of reducing this RMS travel-time misfit. A chi-squared χ^2 statistic value is also returned, which is used to quantify the fit between the observed and calculated distribution of travel-times, in the form:

$$\chi^2 = \frac{1}{n_{res}} \sum_{j=1}^{n_{res}} \left(\frac{r_j}{\sigma_j}\right)^2 \qquad (2\text{-}6)$$

where r_i is the element of the travel-time residual vector r corresponding to the jth travel-time datum, and σ_j is the picking error associated with that travel-time. Equation 2-6 expresses the difference between calculated travel-times and the observed data picks weighted by their assigned error, with a χ^2 value of 1.0 fitting the data within the error bounds.

2.3 Magnetic anomaly data

This section describes the fundamentals of the methodology used in Chapter 4, including: the origin and definition of the Earth's magnetic field (2.3.1), the magnetisation of rocks (2.3.2), the global reference model (2.3.3) and magnetic anomaly grid (2.3.4), and the forward magnetic modelling approach used in this study (2.3.5).

2.3.1 Earth's magnetic field

The Earth's magnetic field (or geomagnetic field) measured at any point on the Earth's surface is a combination of several magnetic fields generated by various sources derived from both within and outside the Earth. These vary spatially and temporally, causing field changes on different time scales from milliseconds to millions of years (Hinze et al., 2013). The main contribution to the Earth's geomagnetic field is generated by electromagnetic currents in the outer core of the Earth, which account for about 98% or more of the geomagnetic field (Merrill et al., 1996). This portion of the geomagnetic field is often referred to as the *Main Field*, and is the one defining the Earth's dipole with a negative pole in the northern hemisphere and a positive pole in the southern hemisphere, and magnetic field lines that extend out into space (Figure 2-8). Superimposed on the main and external fields are the relatively minor static effects from subsurface magnetisation contrasts that are of interest in exploration studies and are used to help determine the compositional, structural, and thermal properties, and thus the history of the Earth's crust and uppermost mantle (Hinze et al., 2013).

The Earth's magnetic field at any location on, above, or within the Earth is generally described by seven parameters: declination (D), inclination (I), horizontal intensity (B_h), vertical intensity (Z), total intensity (B) and the north (X) and east (Y) components of the horizontal intensity (Johnson et al., 2008; Hinze et al., 2013) (Figure 2-8). The dipole (B_h) is offset and tilted about 11° from the Earth's spin axis (X), thus the magnetic poles will differ from the Earth's poles by this offset (Johnson et al., 2008). By convention, declination is considered positive when measured east of north, inclination and vertical intensity positive down, X positive north, and Y positive east. Intensity also tends to decrease from the poles to the equator (e.g., Chulliat et al., 2015).

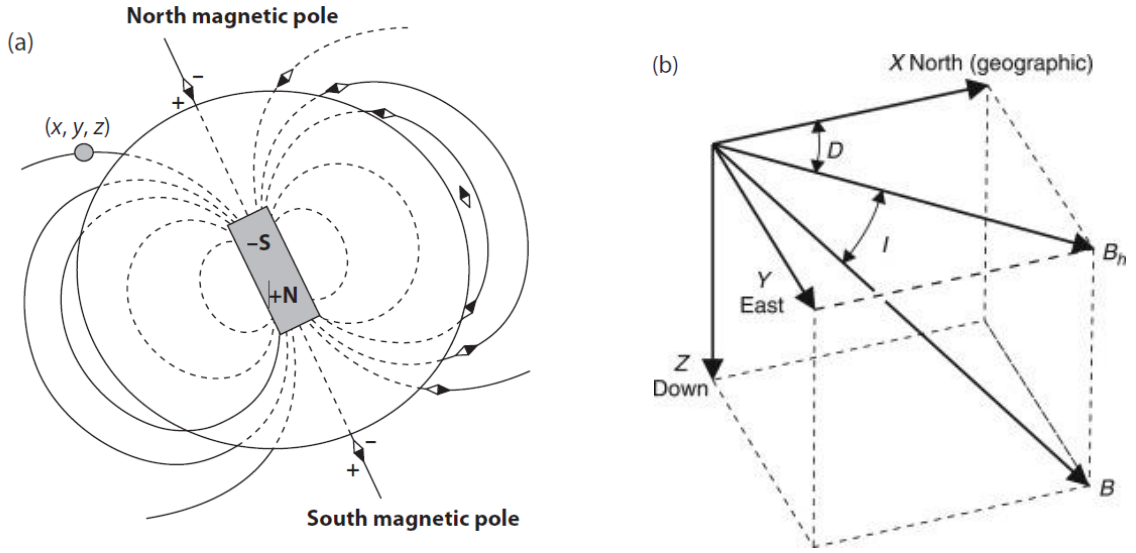

Figure 2-8. The Earth's normal magnetic field represented by (a) lines of force from a dipole located at the centre of the Earth (Hinze et al., 2013). (b) Diagram showing the magnetic field at any location on, above or within the Earth: B is the magnitude of the vector representing Earth's magnetic field, the declination (D) is the angle that the horizontal intensity (B_h) makes with respect to the geographic north (X) (positive angle clockwise), and the inclination (I) is the angle between B and the horizontal (B_h), which can vary between -90˚ and +90˚ positive angle down (Johnson et al., 2008).

Non-dipolar main field components originating within the outer core of the Earth, are also superimposed on the dipolar field. These fields are measured over thousands of kilometres, and they have magnitudes of the order of 10% of the main field. The most dominant portion of the non-dipolar field drifts westward at a rate of roughly 0.18˚/yr. This drift is observable on isomagnetic charts, which are contour maps of equal magnitude or direction of the Earth's field. These maps are prepared at intervals of 5 years, a span of time referred to as an epoch in geomagnetic studies. Long-term variations in both magnitude and direction are therefore observed in both dipole and non-dipole fields of the Earth and are termed *secular variations.* The Main Field and its secular variations are described by mathematical models, i.e., the International Geomagnetic Reference Field (IGRF) (section 2.3.3).

2.3.2 Magnetisation of rocks

When the Main Field is applied to Earth's materials (i.e., rocks) it causes them to become magnetised depending on the amount of magnetic minerals present within their structure. Magnetisation is the dipole moment per unit volume and is a vector quantity because a dipole has a strength and a direction. The relationship between the Earth's magnetic field strength $|B|$ (A/m) and the magnetisation M (A/m) of a material is given by:

$$M = \kappa |B| \quad (2\text{-}7)$$

where, considering a magnetically isotropic material, κ is a dimensionless constant that indicates the degree of magnetisation (M) of a material in response to an applied magnetic field (B). Thus, it is a value representing the volume of the magnetic susceptibility, where magnetic susceptibility is a measure of the magnetic response of a material to an external magnetic field (e.g., Hanna, 1977; Hunt et al., 1995). The magnetisation has the same direction as the Earth's field, and because the Earth's field is different at different locations on the Earth, the same object will get magnetized differently depending upon where it is situated (Johnson et al., 2008).

All materials have magnetic susceptibility, which can be either positive (paramagnetic; i.e., iron, titanium, chromium) generating a field aligned with the applied one, or negative (diamagnetic; i.e., quartz) generating a field that counteracts the Earth's field (Hunt et al., 1995). In ferro-magnetic material (i.e., ferrite in oceanic gabbro), the presence of magnetic minerals makes magnetic susceptibility temperature dependent. This means that when the material is above its Curie temperature (i.e., 580 ˚C for pure magnetite; Hunt et al., 1995), i.e., the temperature above which these minerals revert to a paramagnetic state, thermal agitation prevents the elementary dipoles from aligning with the ambient magnetic field. Instead, when the body with magnetic minerals cools through its Curie temperature, it acquires a remnant magnetisation which is parallel to the contemporary local geomagnetic field. If taken out of the original inducing field, these rocks will still possess a magnetic field like that of a dipole. Therefore, the magnetisation (M) in surveyed rocks can be described by the vector sum of induced (M_i) and remanent (M_r) magnetisation:

$$M = M_i + M_r \quad (2\text{-}8)$$

Minerals that are diamagnetic or paramagnetic show only induced magnetisation, whereas ferro-magnetic minerals (i.e., magnetite) carry a remanent magnetisation or remanence. This remanence can last for millions of years and it may be in a completely different/opposite direction from the present Earth's field, as it was acquired at the time the rock solidified recording its contemporary geomagnetic field. If a remanence is present, it is difficult to separate it from the induced magnetisation unless samples of the rock are measured. Generally, if values of remanence of rock materials are not known, and for magnetic anomaly modelling purposes (i.e., avoid using purely arbitrary values), the rock magnetisation may be assumed to be induced (e.g., Rippington et al., 2015).

Magnetic susceptibility values are useful in geophysical exploration, and in models of both crustal magnetisation and magnetic anomalies. Susceptibility values for different minerals are provided by Hunt et al. (1995) and Hinze et al. (2013). Sedimentary rocks are significantly less magnetic than

crystalline rocks, owing to the lack of ferro-magnetic minerals. Igneous rocks, which originate from the solidification of magma, make up a prominent part of the continental crust and the vast majority of the oceanic crust as well as underlying mantle. Thus, they are a significant source of magnetisation in the Earth where the temperature is below the Curie point of the constituent magnetic minerals (Hinze et al., 2013). The primary classification of igneous rocks is based on their mineralogy reflecting their bulk chemical composition. Those that are rich in silica are referred to as felsic (or acidic) with granite and rhyolite (the volcanic equivalent of granite) being the primary types. These rocks occur primarily in the upper crust of the continents. At the other end of the composition spectrum are mafic (or basic) rocks rich in iron and magnesium that make up the great majority of the oceanic crust and the lower continental crust. Ultramafic rocks, which are relatively higher in iron and magnesium and lower in silica, make up the upper mantle and occur only rarely in the crust. The magnetic properties of igneous rocks depend on the bulk rock composition, but also their oxidation state, hydrothermal alteration, and metamorphism. As a result, the magnetic properties are related in complex ways to the source of the igneous rocks, geological setting, and history of subsequent geochemical processes (Clark, 1999). Mafic rocks, which are the constituents of oceanic crust, contain greater amounts of iron and titanium oxides than felsic rocks (roughly 5% versus 1%), and thus commonly have greater magnetisations than felsic rocks, i.e., granitic rocks (constituents of continental crust). Typically, the integrated magnetisation of the roughly 6 km of mafic oceanic crust has an estimated induced magnetisation component ranging from 0.15 to 0.34 A/m and a remanence of 0.90 to 3.71 A/m (e.g., Harrison, 1987).

Metamorphism can profoundly affect the magnetic characteristics of the rocks, depending on the rock type. Haggerty (1979) noted that metamorphism usually decreases the magnetisation of igneous rocks. Hydrothermal alteration of ultramafic rocks such as peridotite and dunite leads to serpentinization and is normally accompanied by a marked change in magnetisation (Saad, 1969). Recent studies have shown that the magnetic behaviour of metamorphic rocks depends on the minerals present; considering abyssal peridotites, their contribution to marine magnetic anomalies can become significant (i.e., natural remanent magnetisation values > 5 A/m) when they are affected by a high degree of serpentinisation (>75%) (Oufi et al., 2002). Also, the remanent magnetization carried by these highly serpentinized peridotites can be similar to that of oceanic basalts, although their induced magnetization will generally be much higher than that of basalts (Oufi et al., 2002).

Long-wavelength magnetic anomalies observed in satellite magnetic measurements and low-pass filtering of regional and continental-scale magnetic data sets have focused attention on magnetic sources within the lower crust and in the lithosphere in general (e.g. Shive et al., 1992). Ferromagnetism is the most common form of magnetism causing magnetic anomalies. Analysis of

these anomalies, considering the best estimates of the thickness of the magnetic lithosphere, indicates overall magnetisations of the magnetic lithosphere ranging from 2 to 10 A/m, with 4 A/m a typical value (Hinze et al., 2013). These magnetisations are of the order of 10–100 times the average value of upper crustal rocks as well as uplifted lower crustal rocks. Accordingly, additional sources of magnetisation are required in the deep magnetic lithosphere. Studies of deep rock fragments (xenoliths) and uplifted lower crustal rocks as well as thermodynamic considerations have led most investigators to the conclusion that magnetite is probably the major source of magnetism in the lower crust (e.g. Kelso et al., 1993). The depth extent of this magnetism is controlled by the Curie temperature of magnetite, which is about 580-600˚C in the deep crust owing to pressure effects. This temperature generally is reached near the base of the crust at the Moho discontinuity in the continents and slightly below the Moho in the oceans (Hinze et al., 2013).

Extensive measurements of magnetic properties may be found in Carmichael (1982) and Clark (1966). For a more detailed description of magnetic units, conversions, rock magnetism and theory, see Shive (1986), Blakely (1995) and Hinze et al. (2013).

2.3.3 A global magnetic reference model

The Earth's field at any location is approximately provided by large-scale, time-averaged mathematical models of the Earth's field based on measurements from satellites, magnetic observatories, and other surveys. These mathematical models include: the World Magnetic model (WMM), the International Geomagnetic Reference Field (IGRF), the BGS Global Magnetic Model (BGGM), and the Model of the Earth's Magnetic Environment (MEME). This study refers to the IGRF model, describing the main field and its secular changes (Thebault et al., 2015) (Figure 2-9).

The secular variations in both the angular relationships and amplitude of the main magnetic field components have necessitated periodic updating of the charts representing the Earth's magnetic field. Each half decade, since 1965, the IGRF has been computed and internationally adopted, based on magnetic observatory and survey measurements plus, in recent years, observations of the Earth's field from satellites (e.g. Olsen et al., 2007; Thebault et al., 2015). Therefore, the IGRF describes the Earth's geomagnetic field components (i.e., I, Figure 2-9a, D, Figure 2-9b B, Figure 2-9c, B_h and Z), and provides estimates of their annual rate of change. Information on declination and inclination of the Earth's field can be applied to magnetic anomaly data as a correction i.e., reduction-to-pole (see sections 2.3.4, 2.3.5 and Chapter 4).

The IGRF represents a best fitting approximation to the field by a series of spherical harmonics of increasing degree. Harmonics of up to degree 13, approximately 3,100 km and longer at the Earth's surface, are dominated by the core field, whereas higher degrees are related to lithospheric

magnetisation anomalies. The IGRF accommodates the flattening of the Earth's shape and considers elevation relative to sea level, so that all components of the Earth's magnetic field can be computed from the equation at any altitude.

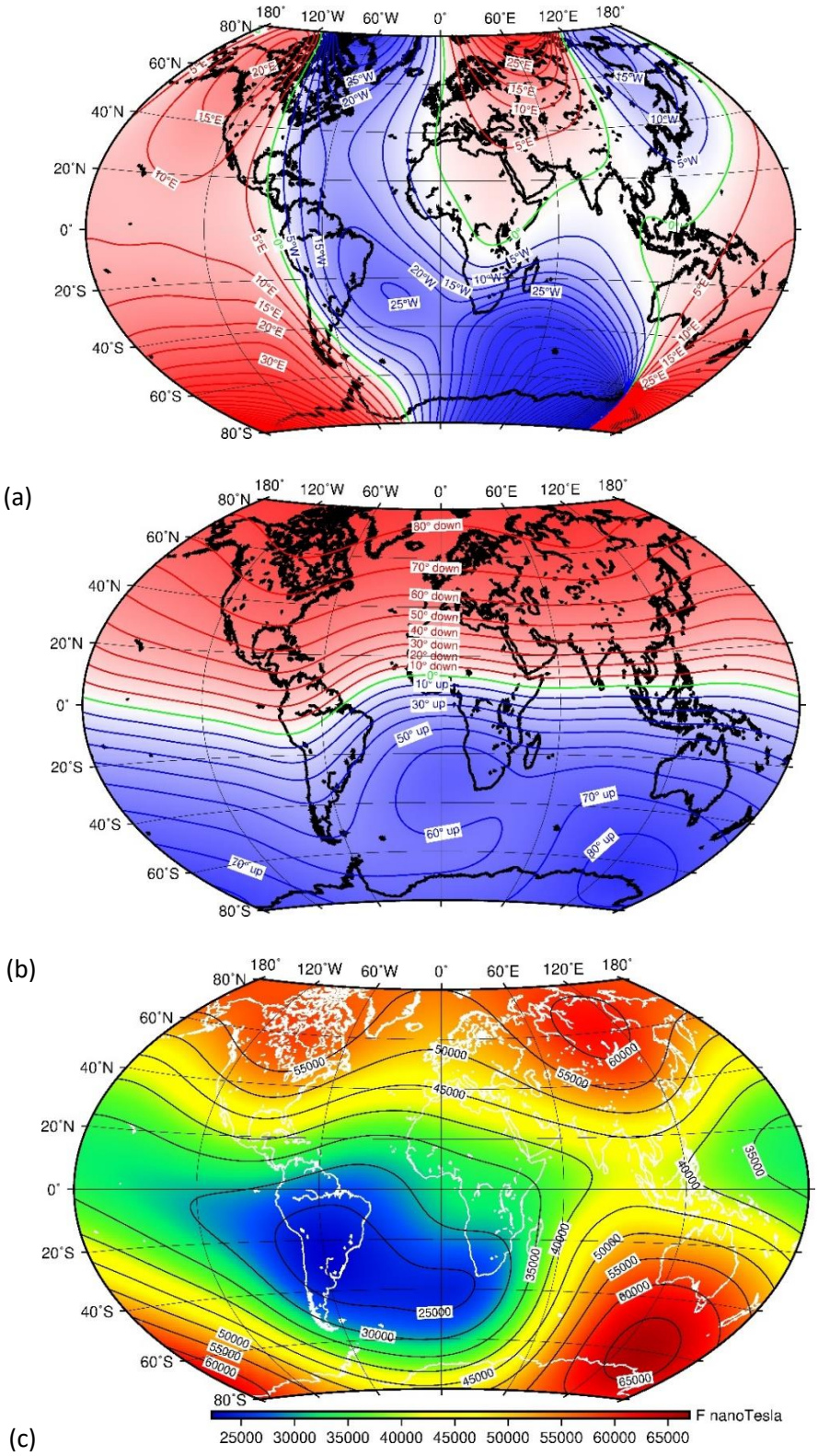

Figure 2-9. IGRF model of the Earth's Main Field. (a) Inclination, (b) Declination and (c) Total field intensity (from http://www.geomag.bgs.ac.uk/research/modelling/IGRF.html; Thebault et al., 2015).

2.3.4 Magnetic anomaly grid

Magnetic anomaly maps provide insight into the subsurface structure and composition of the Earth's crust. Distinct patterns and magnetic signatures can be attributed to the formation (seafloor spreading) and destruction (subduction zones) of oceanic crust, the formation of continental crust by accretion of various terranes to cratonic areas and large scale volcanism both on continents and oceans (Maus et al., 2009).

Magnetic anomalies are generally a small fraction of the total magnetic field, which ranges from 25,000 to 65,000 nanoteslas (nT) (Hinze et al., 2013) (Figure 2-9c). Ground-based, aeromagnetic, shipborne or spacecraft (i.e., CHAMP satellites) surveys can be used to measure these magnetic anomalies. A grid representing the total intensity magnetic anomaly of the Earth is the Earth Magnetic Anomaly Grid (EMAG2-v3, www.NOAA.gov), which is specified as a 2-arc-minute resolution grid at an altitude of 4 km above mean sea level, and it is compiled from satellite, marine, aero-magnetic and ground magnetic surveys (Meyer et al., 2017).

There are two main corrections that are applied to this grid to obtain the magnetic anomaly for magnetic measurements. The first is removing short-term variations in the field from external sources. Their contribution can be measured by returning to a base station repeatedly or by having another magnetometer that periodically measures the field at a fixed location. Second, since the anomaly is the local contribution to the magnetic field, the main geomagnetic field represented by the IGRF must be subtracted from it (Hinze et al., 2013).

When looking at the magnetic anomaly field at a specific location of the Earth, a reduction-to-pole (RTP), or reduction-to-equator (RTE), transform can be applied to the magnetic anomaly grid. RTP reduces the magnetic anomalies to the pole and corrects for variations in inclination and declination over the study area (Baranov, 1957). Declination, inclination, and magnitude of the modern Earth's magnetic field can be taken according to the IGRF field at the studied location (Thebault et al., 2015) (Figure 2-9a, b).

2.3.5 Forward magnetic anomaly modelling

Interpretation of magnetic anomalies can be done by matching observed and modelled values of the anomalous magnetic field (EMAG2-v3). This forward modelling approach involves creating a hypothetical geologic model and calculating the geophysical response to that Earth model. Seismic interpretation can be used to provide the initial constraints for the magnetized crustal bodies for the geological model (e.g., Rippington et al., 2015). The choice of a forward modelling in this study,

instead of an inverse approach, was due to data limitations from the study area (see Chapter 4, section 4.2.2).

Data from the magnetic anomaly grid EMAG2-v3 (Meyer et al., 2017) for the EBSB region are used in this study. The anomaly grid is reduced-to-pole (RTP) setting the inclination and declination of the Earth's field to 90° and 0°, respectively. For the correction, values of declination, inclination, and the magnitude of the modern Earth's magnetic field at the study area were taken according to IGRF (Thebault et al., 2015) (Chapter 4).

The forward modelling approach used in this study is performed in Geosoft software Oasis Montaj, using GM-SYS modelling program. This program allows the interactive manipulation of the geologic model and a real-time calculation of the magnetic response based on user-defined values of magnetic susceptibility. The software forward-calculates the magnetic model response of the resulting susceptibility models using techniques outlined in Talwani and Heirtzler (1964) and makes use of the algorithms described in Won and Bevis (1987). Seismically defined horizons and susceptibility values of pre-defined crustal blocks can be modified until the forward-calculated response of the model satisfies all the available datasets. For model creation, a two-dimensional, flat-earth model for the magnetic calculations is used; that is, each structural unit or block extends to plus and minus infinity in the direction perpendicular to the profile. The Earth is assumed to have topography but no curvature. The model also extends plus and minus 30,000 km along the profile to eliminate edge effects.

Magnetic models are not unique, i.e. several Earth models can produce the same magnetic response, and many solutions may not be geologically realistic. Furthermore, the 2D model assumed implies that changes occur in depth (the Z direction) and in the direction of the profile (X direction; perpendicular to strike), but not in the strike direction (Y direction). This means that the resulting model may not be representative for the real, 3D distribution of the magnetic anomalies observed. The forward modelling approach, the model creation, the parameters used for this study and the method limitations are further discussed in Chapter 4 (section 4.2).

2.4 Gas hydrate modelling

This section describes the two modelling approaches used in Chapter 5: (i) the modelling of the BGHSZ under steady-state conditions (2.4.1) and (ii) the effective-medium modelling used to estimate gas and gas hydrate content in the pore space (2.4.2).

2.4.1 Modelling of the BGHSZ

2.4.1.1 Gas hydrate phase boundary

The methane hydrate phase boundary can be calculated from the intersections of methane gas solubility and methane hydrate solubility curves (Henry et al., 1999; Liu and Flemings, 2007). It has also been calculated using other methods, such as a statistical thermodynamic approach (Sloan and Koh, 2008) or empirical equations that fit experimental measurements (e.g., Moridis et al., 2008). The methane hydrate phase boundary is a pressure versus temperature (P-T) plot that depicts stable phases in different P-T zones at a fixed salinity and pore size (Figure 2-10, see also section 1.3.1).

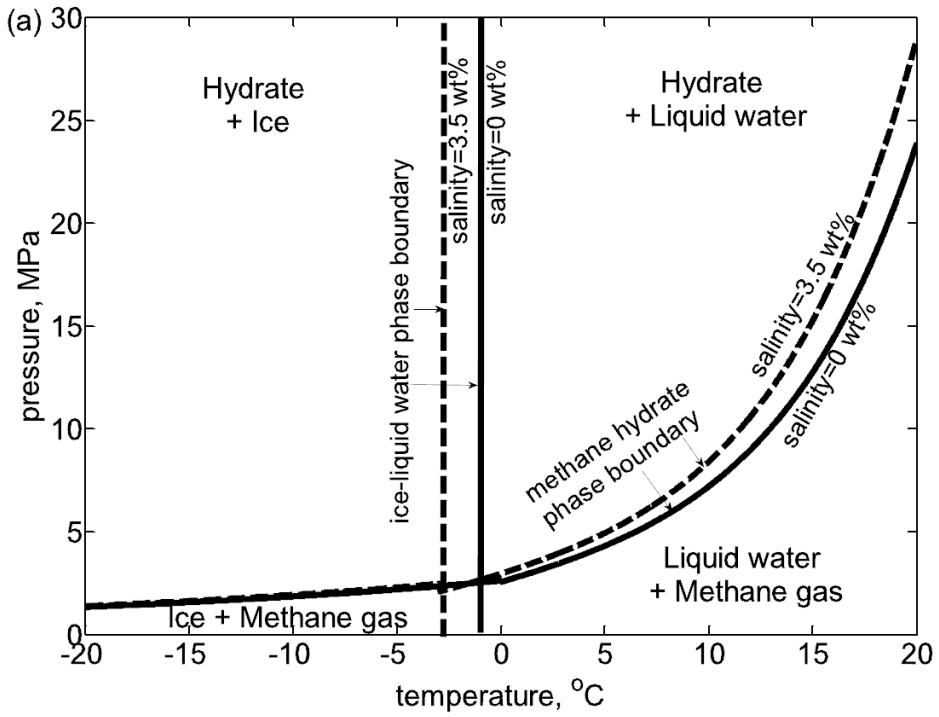

Figure 2-10. Methane hydrate phase boundary under bulk conditions in the pressure-temperature (P-T) space. Plot uses the model presented in Sun and Mohanty (2006) and Moridis (2002). Image from You et al. (2019).

Methane hydrate and liquid water are stable at high pressure and low temperature, whereas methane gas and liquid water are stable at low pressure and high temperature (Figure 2-10). Under the same P-T conditions, different compositions (fractions of methane and water) of the system lead to the presence of different phases. Under methane hydrate stability conditions, for example, if enough water is present in the system, formation of methane hydrate occurs. However, there will be only liquid water with dissolved methane if the amount of methane is below the methane solubility. In contrast, if there is insufficient water, only free methane gas is present.

Increasing salinity shifts the methane hydrate phase boundary toward higher pressure and/or lower temperature (Figure 2-10). The pore size also shifts the phase boundary due to the impact of capillary pressures. In the small pores of fine-grained sediments, hydrate-liquid capillary pressure becomes a significant component of pressure and shifts the methane hydrate phase boundary to lower temperatures and higher pressures (Clennell et al., 1999; Rempel, 2011).

2.4.1.2 Gas hydrate stability zone

Factors controlling the GHSZ have been introduced in section 1.3.1 (Figure 1-12), and include temperature and pressure conditions, pore-water salinity and the molecular composition of the hydrate forming gas. Here, the BGHSZ under steady state and hydrostatic pressure conditions is defined as the depth of the intersection between the temperature structure of the sediment with a hydrate phase boundary (Figure 1-12). This intersection, and so the thickness of the GHSZ below the seafloor, is found using a Matlab code.

This study uses the empirical methane hydrate phase boundary for pure water defined in the Tough+Hydrate code (Moridis et al., 2012), and the Dickens and Quinby-Hunt (1997) equation (Eq. 7) to convert the methane hydrate stability curve from pure water to a saline water. Fitting parameters to the methane hydrate phase boundary and the parameters used for the conversion to the saline water case are shown in Table 2-2.

*Table 2-2. Parameters and equations used to calculate the pure methane hydrate (GH) phase stability conditions and for the salinity correction. * is a standard value for seawater, which has been adapted to the EBSB case (see Chapter 5). T and P are the equilibrium hydration temperature and pressure for methane hydrate in a pure water system.*

Parameters for the methane hydrate phase boundary	
Pure water fusion temperature (ToK)	$273.2; (K)$
Pure water fusion enthalpy from pure water to ice at $273.2\ K$ (AHf)	$6008;\ (J/mol)$
Enthalpy of GH dissociation (AHd)	$54.200;\ (J/mol)$

Hydration number (N)	$6;\ (CH_4\ x\ 6H_2O)$
Water molar mass (M_{H_2O})	$18.015;\ (g)$
Pure water fusion temperature ($Tf\ =\ ToK$)	$273.2;\ (K)$
Water cryoscopic constant (Kf)	$1853;\ (K \times g/mol)$
Standard atmospheric pressure (atm)	$101{,}325;\ (Pa)$
Gravitational acceleration (g)	$9.81;\ (m/s^2)$
Methane hydrate phase boundary for pure water *(Moridis et al., 2012)*	For $T \geq 2.73.2°K$ $P = \exp.(-C(1) + C(2) \times T - C(3) \times (T^2) + C(4) \times (T^3) - C(5) \times (T^4) + C(6) \times (T^5)$ Fitting parameters by an empirical solution: $C(1) = 1.94138504464560E^5;$ $C(2) = 3.31018213397926E^3;$ $C(3) = 2.25540264493806E^1;$ $C(4) = 7.67559117787059E^{-2};$ $C(5) = 1.30465829788791E^{-4};$ $C(6) = 8.86065316687571E^{-8}$
Parameters for salinity correction	
Salt molar mass (M_{NaCl})	$58.44;\ (g)$
Blagden's law for ice fusion temperature in saltwater *(Ladd, 1998)* (Tfs)	$Tfs = Tf - Kf \times n(NaCl) \times vHf;\ (K)$
Van't Hoff factor for $NaCl$ (vHf)	2
Standard seawater salinity *(Miles, 1995)* (So)*	$3.5;\ (wt\ \%)$
Moles of $NaCl$ ($n(NaCl)$)	$So/100/MNaCl;\ (mol)$
Seawater density (ρ_{sw})	$1030;\ (kg/m^3)$
Temperature offset between GH stability curve for pure water and saltwater *(Dickens and Quinby-Hunt, 1997)* (Ts)	$Ts = (1/T - (N \times AHf./AHd) \times (1/ToK - 1/Tfs))^{-1});\ (K)$

2.4.2 Effective-medium modelling

An important aspect of the studies related to gas hydrate is the estimation of gas and/or hydrate concentration in the pore space. Attempts to obtain properties of the gas hydrate-bearing sediments directly from cores can be affected by the high instability of hydrates at normal pressure and temperature conditions. Consequently, the elastic properties of sediments are also inferred from seismic reflection data (Hyndman and Spence, 1992; Singh et al., 1993; Ecker et al., 1998). This is possible because the presence of both free gas and gas hydrate in marine sediments alters their physical properties, affecting the velocity of P- and S-wave propagation in the composite medium (section 1.3.3). Thus, the amount of gas and/or gas hydrate in sediments can be estimated by using

rock physics models linking seismic velocity to the internal rock structure (e.g., Chand et al., 2004; Westbrook et al., 2008).

In Chapter 5, the Hydrate-Bearing Effective Sediment (HBES) model described by Marin-Moreno et al. (2017) is presented and used to calculate the P-wave velocity based on a sediment frame comprising mineral grains, solid hydrate, water (brine) and gas in the pore space. The calculated velocities are compared with velocities obtained from travel-time analysis (observed velocities). Based on the best-fitting parameters, ranges of hydrate or gas saturation within sediments are provided.

The following sections introduce the modelling approach adopted in Chapter 5, including: (i) an introduction to the theory used to link physical and elastic properties of the sediment to their seismic response (Biot, 1956) via a rock physics analytical model (2.4.2.1), (ii) how gas hydrate is incorporated into the rock physics analytical model and the impact of different hydrate morphologies on velocity estimates (2.4.2.2).

2.4.2.1 Rock physics analysis

The rock physics analysis used in this study provides a link between the physical parameters (lithology, porosity, and pore phase saturation) and the elastic properties of the rock (elastic moduli and densities), which are ultimately related with its seismic properties (V_P and V_S).

Biot (1956) developed the first published comprehensive theory of wave propagation in single-phase fluid saturated poro-elastic media. He showed that the relative movement of pore fluid within the rock's elastic frame and the viscous coupling between them result in velocity dispersion and associated attenuation as a function of frequency. This theory considers a homogeneous rock saturated with a single-phase fluid, in which a passing seismic wave excites the fluid creating a relative fluid movement due to the peaks and troughs of the elastic wave. One of the main considerations of this theory is that the pore size is considered smaller than the elementary volume of the rock and this is considered smaller than the wavelength of the elastic wave.

Biot's theory provides a general framework for modelling wave propagation in a porous medium (e.g., Mavko et al., 2009). However, it only considers one attenuation mechanism, macroscopic inertial fluid flow, which is mostly relevant at frequencies greater than ultrasonic. At the microscopic scale (i.e., scale of each pore and grain) and lower frequencies, local wave-induced fluid flow or "*squirt flow*" (Mavko and Nur, 1975), can occur due to local pore pressure gradients that develop depending on the compressibility of the individual pores, which depend on pore shape and the fluid occupying the pores. Pores with high aspect ratio or "spherical" pores are stiffer than low-aspect ratio pores or "penny-shaped" (i.e., elliptic/fracture-like) pores.

2.4.2.2 Including gas hydrate in the formulation

The P- and S-wave velocities of sediments hosting gas hydrate are generally higher than those of the sediment without gas hydrate because the hydrate contributes to support any pressure loading (section 1.3.3). This information can be used to infer the saturation of hydrate using rock physics modelling and idealized representations of the hydrate morphology in the pores.

Different hydrate morphologies can be associated with different seismic velocity changes in the host sediment. In the following, only the effects of hydrate habits associated with non-grain displacing morphologies (pore-invasive) are described. In general, cementing hydrate habits generate a greater increase in P- and S-wave velocities than pore floating hydrate for the same amount of hydrate in the pores (Figure 2-11; (A), (C)). This is because cementing hydrates increase the number of grain contacts and thereby the elastic moduli of the host sediment whereas pore-floating/filling hydrate is suspended within the water and hence only increases the bulk modulus of the effective pore fluid. For pore-filling hydrate saturations above 25-40%, hydrate starts bridging sediment grains (i.e., becoming load bearing) and the elastic frame moduli and associated P- and S-wave velocities progressively increase (Waite et al., 2009; Dai et al., 2012) (Figure 2-11; (D), (E)).

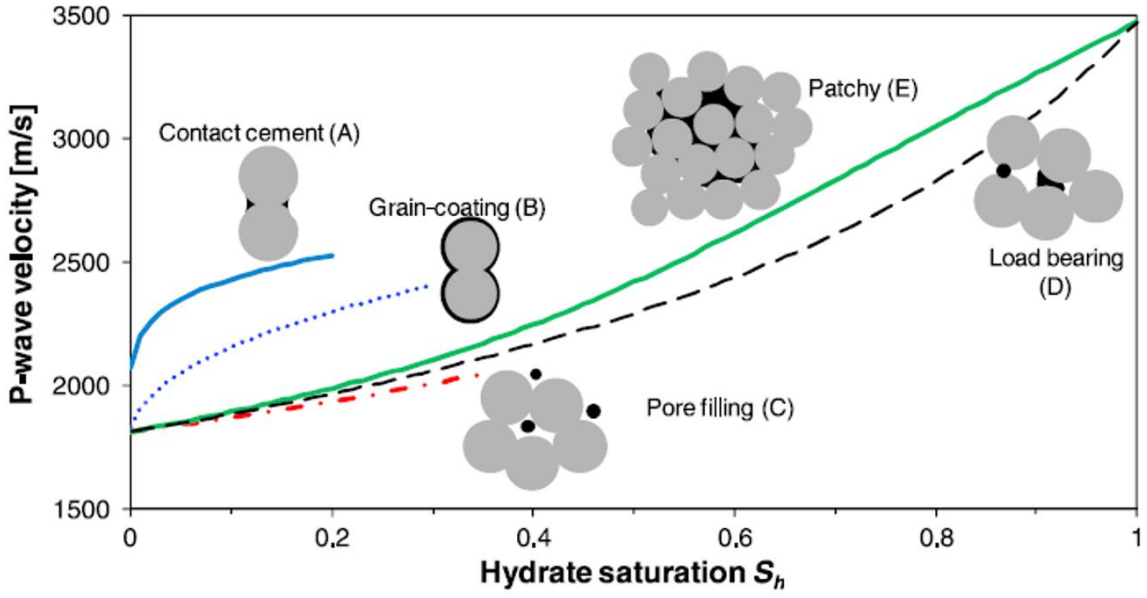

Figure 2-11. Predicted dependence of compressional, P wave velocity on gas hydrate saturation. P wave velocity increases rapidly even at very low hydrate saturations when hydrate forms at sediment grain contacts (A, B). When hydrate forms away from grain contacts (C, D), the velocity increases more rapidly at high hydrate saturation when hydrate begins bridging between multiple sediment grains across a pore or fully hydrate-saturated patches become large and numerous enough to begin interacting (E) (modified from Dai et al., 2012).

To account for the effect of gas hydrate formation in the rock physics model used in this study, three idealised habits are considered: pore-floating hydrate, cementing hydrate at grain contacts only and cementing hydrate enveloping the grains (Figure 2-12). The general mathematical formulation used here to represent these morphologies is described below and in Ecker et al. (1998). For more details on how these models are introduced into the HBES model refer to Marin-Moreno et al. (2017).

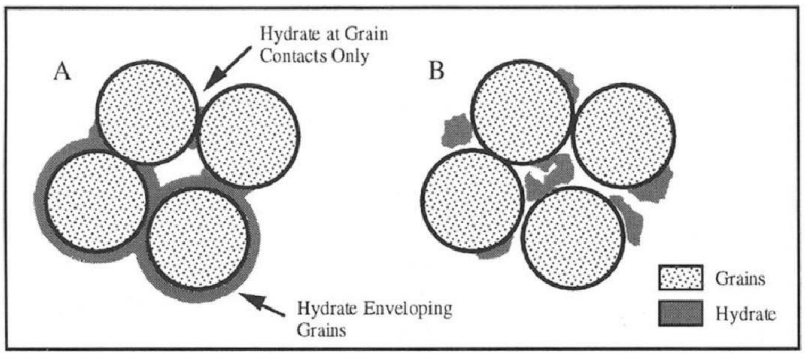

Figure 2-12. Two models of hydrate deposition among the grains: (a) the contact-cement model; (b) no-contact-cement model (Ecker et al., 1998).

Cemented sand model

The cemented-sand model allows to calculate the bulk and shear moduli of dry sand with spherical grains in which a cement is deposited at grain contacts. The cement is elastic, and its properties may differ from those of the sand. It is assumed that the starting framework of the cemented sand is a dense, random pack of identical spherical grains with initial porosity ϕ_0 and an average number of contacts per grain n = 9 (this parameter usually varies between 6 and 15). Adding cement to the grains reduces porosity and increases the effective elastic moduli of the aggregate. Then, these effective dry-rock bulk (K_{eff}) and shear (G_{eff}) moduli are (Dvorkin and Nur, 1996):

$$K_{eff} = \frac{n(1-\phi_0)}{6}\left(K_H + \frac{4}{3}\,G_H\right) S_n, \tag{2-9}$$

$$G_{eff} = \frac{K_{eff}}{5} + \frac{3n\,(1-\phi_0)}{20} G_H S_T, \tag{2-10}$$

where K_H and G_H are the cement (hydrate) bulk and shear moduli, respectively. These are linked with V_P and V_S as explained by Equations 1-2 and 1-3 (section 1.3.3). Parameters S_n and S_T are proportional to the normal and shear stiffnesses of a cemented two-grain combination, respectively, and they depend on the amount of contact cement and on the elastic properties of the cement and the grains (Ecker et al., 1998).

Uncemented sand model

The uncemented-sand (or "soft-sand") model allows to calculate the bulk and shear moduli of dry sand in which cement (hydrate) is deposited away from grain contacts. It is assumed that the starting framework of uncemented sand is a dense random pack of identical spherical grains with critical porosity ϕ_c of 0.36 and average number of contacts per grain n = 5 to 9. At this porosity, the contact Hertz–Mindlin (HM) theory (Mindlin, 1949) gives the following expressions for the effective bulk (K_{HM}) and shear (G_{HM}) moduli of a dry, dense, random pack of identical spherical grains subject to an effective stress σ':

$$K_{HM} = \left[\frac{n^2(1-\phi_c)^2G^2}{18\pi^2(1-\nu)^2}\sigma'\right]^{1/3} \quad (2\text{-}11)$$

$$G_{HM} = \frac{5-4\nu}{5(2-\nu)}\left[\frac{3n^2(1-\phi_c)^2G^2}{2\pi^2(1-\nu)^2}\sigma'\right]^{1/3} \quad (2\text{-}12)$$

where ν is the grain Poisson's ratio (sensitive to the fluid) and G is the grain shear modulus. To find the effective moduli (K_{eff} and G_{eff}) at a different porosity ϕ_0, a heuristic modified Hashin–Shtrikman lower bound is used (Dvorkin and Nur, 1996):

$$K_{eff} = \left[\frac{\phi/\phi_0}{K_{HM}+\frac{4}{3}G_{HM}} + \frac{1-\phi/\phi_0}{K+\frac{4}{3}G_{HM}}\right]^{-1} - \frac{4}{3}G_{HM} \quad (2\text{-}13)$$

$$G_{eff} = \left[\frac{\phi/\phi_0}{G_{HM}+\frac{G_{HM}}{6}\left(\frac{9K_{HM}+8G_{HM}}{K_{HM}+2G_{HM}}\right)} + \frac{1-\phi/\phi_0}{G+\frac{G_{HM}}{6}\left(\frac{9K_{HM}+8G_{HM}}{K_{HM}+2G_{HM}}\right)}\right]^{-1} - \frac{G_{HM}}{6}\left(\frac{9K_{HM}+8G_{HM}}{K_{HM}+2G_{HM}}\right) \quad (2\text{-}14)$$

where K is the grain bulk modulus.

This model can also be used for sediments with porosities above the critical porosity (Dvorkin et al., 1999) and for intermediate stiffness sands (Mavko et al., 2009).

Chapter 3 Spatial and temporal evolution of rifting and continental breakup in the Eastern Black Sea Basin revealed by long-offset seismic reflection data

Abstract

The age and distribution of the syn-rift and early post-rift infill records the spatial and temporal distribution of extension and breakup processes in a rift basin. The Eastern Black Sea Basin (EBSB) is thought to have formed by back-arc extension during Cretaceous to lower Cenozoic time. However, a lack of direct constraints on its deep stratigraphy leaves uncertainties over the time, duration and location for rifting and breakup processes in the basin. Here we use the enhanced imaging provided by 2D long-offset seismic reflection profiles to analyse the deep structural and stratigraphic elements of the EBSB. Based on these elements, we infer the presence of two distinct Upper Cretaceous syn-rift units, recording initial extension (rift stage 1) over the continental highs (Shatsky Ridge and the Mid Black Sea High), followed by strain localization along the major basin-bounding faults and rift migration towards the basin axis (rift stage 2). Overlying these units, Palaeocene(?)-Eocene and Oligocene units show a syn-kinematic character in the NW, with evidence for ongoing extension until Oligocene time. Towards the SE, these sequences are instead post-kinematic, directly overlaying a basement emplaced during breakup. We interpret the Palaeocene(?)-Oligocene units to record the time spanning from the initiation of breakup (Upper Cretaceous-Palaeocene, in the SE) to the end of extension (Oligocene, in the NW). The first ubiquitous post-rift infill is the Oligocene-lower Miocene Maykop Formation. Our results highlight the spatial and temporal variability of extension and breakup processes in the EBSB.

3.1 Introduction

Classical rifting models imply that rifting and continental breakup occur as processes well defined in time and space and recorded by distinct sedimentary sequences (e.g., Driscoll et al., 1995). However, these models are based on the interpretation of isolated transects across margins, so cannot be expected to explain the 3D distribution of structures and sedimentary sequences along a rift system. More recently, the availability of more comprehensive datasets has allowed the documentation of the along-strike evolution at rifted margins, showing that continental rifting and

breakup processes are more complex and variably distributed in time and space (e.g., Alves & Cunha, 2018; Muirhead et al., 2016; Nixon et al., 2016; Péron-Pinvidic et al., 2007; Soares et al., 2012).

In the context of intra-continental back-arc rifting, the Eastern Black Sea Basin (EBSB) is one of the most studied and yet most controversial basins in the world (Figure 3-1). It consists of a narrow NW trending linear trough underlain by oceanic or proto-oceanic crust, bounded by the continental domains of the Mid Black Sea High (MBSH) and the Shatsky Ridge (Figure 3-1a). The thickness of the sedimentary infill in the EBSB is approximately 8-9 km (Scott et al., 2009), including Cenozoic and Upper Mesozoic sediments (Shillington et al., 2008). However, the deep part of the EBSB is yet to be drilled and little is known about the age and distribution of its syn-rift and early post-rift infill. Early insights into the geological evolution of the Black Sea came from regional seismic lines (Belousov et al., 1988; Finetti et al., 1988; Tugolesov et al., 1985). Since then, researchers have attempted to unravel the kinematics, mechanisms and timing for the opening of the EBSB (e.g., Finetti et al., 1988; Görür, 1988; Graham et al., 2013; Nikishin et al., 2003; Okay et al., 1994; Rangin et al., 2002; Robinson et al., 1996; Shillington et al., 2008; Stephenson & Shellart, 2010). In addition, crustal-scale industry seismic datasets have been acquired due to the growing interest in the EBSB as a region with high hydrocarbon potential, related to the presence of a regionally distributed source-rock, the Maykop Formation (e.g., Graham et al., 2013; Robinson et al., 1996; Stovba et al., 2009).

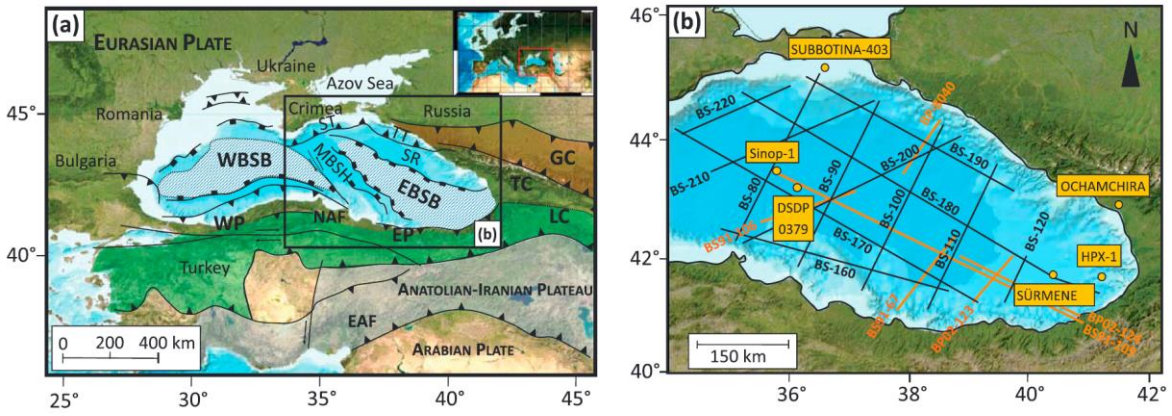

Figure 3-1. (a) Topographic and structural map of the Black Sea and Caucasus region (www.emodnet-bathymetry.eu). Black box represents the study area (b). Structural elements highlighted are: EBSB/WBSB —Eastern/Western Black Sea Basins; SR—Shatsky Ridge; MBSH—Mid Black Sea High; TT/ST—Tuapse/Sorokin Troughs; GC/LC - Greater/Lesser Caucasus; TC—Transcaucasus; EP/WP—Eastern/Western Pontides; NAF/EAF—North/East Anatolian Fault. (b) Bathymetry and topography map of the EBSB. Black lines mark the long-offset seismic reflection profiles. Orange lines mark other profiles used. Yellow dots mark deep-water and onshore wells in the area.

Surmene-1, Sinop-1, HPX-1 and Subbotina-403 wells locations are from Kitchka et al. (2014), Sydorenko et al. (2017) and Tari & Simmons (2018). The location for the onshore well Ochamchira is from Banks et al. (1997).

The identification of syn-rift stratigraphic intervals is essential to understand the evolution of rifted margins, as they record the early stage processes in a rift system. However, the determination of these syn-rift sequences is often complicated by a lack of data and of direct constraints (e.g., Péron-Pinvidic et al., 2007). In the EBSB, wells penetrating the entire Cenozoic and part of the Mesozoic sections are located along the margins or onshore, while strata of this age lie at depths ≥ 8 km in the center of the basin. Therefore, stratigraphic sections at well locations are comparatively condensed, and there are uncertainties in tracing major horizons from well locations into the basin center (Shillington et al., 2008). Also, most of the wells have been drilled in the Western Black Sea Basin (WBSB), and tracing horizons from the WBSB to the EBSB is challenging because of the presence of the MBSH, which prevents direct correlation of horizons older than upper Eocene (Banks et al., 1997).

Seismic data have also been used to define the presence and distribution of the syn-rift in the EBSB, but imaging is often limited by attenuation through the thick basin infill (e.g., Finetti et al., 1988; Rangin et al., 2002; Shillington et al., 2008). In fact, in most studies, syn-rift geometries (e.g., fanning reflector geometry toward fault planes) are not clearly observed in seismic data (e.g., Nikishin et al., 2015a; Shillington et al., 2008). Therefore, syn-rift units may be mistaken for pre-rift or post-rift strata because of the lack of obvious growth beds (Withjack et al., 2002). This ambiguity may explain the small thickness of syn-rift deposits identified in the EBSB (e.g., Görür & Tüysüz, 1997; Görür et al., 1993).

Here, we interpret and discuss the deep seismo-stratigraphic framework of the EBSB using long-offset seismic reflection profiles acquired in 2011 by *Geology Without Limits* (GWL) and ION GXT, which provide enhanced imaging at depth, combined with published litho-stratigraphy and well correlated seismic data. Isopach maps, seismic facies and examples of seismic profiles are presented to illustrate the characteristics, areal distribution, and thickness of each unit. The aim of this study is to present the distribution and ages of the syn-rift, early post-rift, and post-rift sequences, to analyse their stratigraphic contacts and their interaction with the structural features of the basin. These elements are used to define rift onset, propagation, and breakup stages in the EBSB.

Unravelling the rifting and breakup processes controlling EBSB formation has a key role in understanding the geodynamic evolution of this area and of similar rift systems. Furthermore, this study provides fundamental insights into (i) how deformation is accommodated in space and time,

and (ii) how stratigraphic and structural elements track strain distribution and localization during the process of continental extension.

3.2 Geological framework

3.2.1 Geological evolution of the EBSB region

The EBSB is a deep sedimentary basin lying between the Eastern Pontides and the Great Caucasus mountain ranges (Figure 3-1a). Rifting is the first-order geodynamic process responsible for the tectonic evolution of the EBSB and is related to the northward subduction of the Neotethys Ocean below the Eurasian Plate (Finetti et al., 1988; Görür, 1988; Nikishin et al., 2003; Okay et al., 1994; Robinson et al., 1996; Stephenson & Schellart, 2010; Zonenshain & Pichon, 1986). The basin opened in a back-arc setting behind the Pontides magmatic arc (Finetti et al., 1988; Görür, 1988; Okay et al., 1994; Zonenshain & Pichon, 1986). Back-arc extension was generated by the counter-clockwise rotation of the Shatsky Ridge away from the MBSH, as evidenced by paleo-magnetic data (Westphal et al., 1986). Compressional forces and tectonic inversion, due to the northward movement of the Arabian Plate, started along the Pontides in the Upper Cretaceous, reaching the Greater Caucasus possibly in the Palaeocene and becoming regionally widespread during the upper Eocene and Oligocene (Espurt et al., 2014; Hippolyte et al., 2017; Munteanu et al., 2011; Robinson et al., 1996; Vincent et al., 2016). The syn-collisional (orogenic) stage is generally considered to have started in the Oligocene, forming the Caucasus mountain range and causing the uplift of some areas within tectonic units as well as the reactivation of older fault systems and the formation of inverted structures (Stovba et al., 2009). Compressive deformation is concentrated around the edges of the EBSB, as shown by seismic reflection data, earthquake locations, and subsidence analysis (e.g., Edwards et al., 2009; Shillington et al., 2008).

3.2.2 Available data on the basin stratigraphy

Detailed analyses of the thicknesses and distribution of the sedimentary deposits in the EBSB are based on the most updated interpretation of seismic data (e.g., Kazmin et al., 2000; Nikishin et al., 2001, 2003, 2015a; Scott et al., 2009; Sydorenko et al., 2017) and estimates on the age and lithology of the sedimentary units generally come from seismic stratigraphic horizons tied to well control at the edges of the basin and to onshore outcrops (e.g., Greater and Lesser Caucasus, and Crimean Mountains - Nikishin et al., 2003, 2015a, 2015b; Okay et al., 2013; Robinson et al., 1996; Saintot et al., 2006; Stephenson & Schellart, 2010; Stovba et al., 2009). More reliable information comes from dredged sequences from the Archangelsky Ridge (Rudat & Macgregor, 1993) and from a complete Mesozoic to lower Palaeocene stratigraphy in wells drilled over the Shatsky Ridge in Georgia

(Robinson et al., 1996). These stratigraphic interpretations have fed into paleo-geographic reconstructions of the mechanisms and timing of basin opening (e.g., Egan & Meredith, 2007; Nikishin et al., 2015b; Okay et al., 1994; Robinson et al., 1996; Stephenson & Schellart, 2010).

Extensive deep-water drilling has occurred in the WBSB, whereas only four deep wells have been drilled in the EBSB to date (e.g., Stovba et al., 2009; Sydorenko et al., 2017; Tari & Simmons, 2018) (Figure 3-1b). Subbotina-403 reaches 4300 m below seabed and terminates in the lower Eocene succession (Stovba et al., 2009; Sydorenko et al., 2017) (Figure 3-1b). Sinop-1, 5531 m deep, was drilled on a structural high of Andrusov Ridge, targeting a syn-rift of Aptian to Albian age (e.g., Tari & Simmons, 2018) (Figure 3-1b). The sediment cover above the MBSH and the Shatsky Ridge has been described by using extensive academic and industry seismic reflection data (e.g., Belousov et al., 1988; Nikishin et al., 2015a, 2015b; Rangin et al., 2002; Robinson et al., 1996; Tari et al., 2018), crustal scale wide-angle seismic data (e.g., Shillington et al., 2017; Yegorova et al., 2010) and seafloor dredging (Rudat & MacGregor, 1993). Chronostratigraphic charts have been compiled to illustrate the different ages and litho-stratigraphy elements of the Black Sea region and EBSB (Adamia et al., 2017; Shillington et al., 2008; Sydorenko et al., 2017; Tari & Simmons, 2018).

Figure 3-2 and Table 3-1 summarize previous attempts to estimate the timing of rifting in the EBSB. Note that the definition of rift duration changes from author to author: it can be either the time from rift initiation to breakup (e.g., Nikishin et al., 2015a), or the time from rift initiation to the end of oceanic spreading (e.g., Okay et al., 1994). Some studies assume that the EBSB opened at the same time as the WBSB and provide age estimates which are mostly based on data coming from the WBSB region (e.g., Hsü et al., 1977; Tüysüz, 1999). Based on different data, rifting has been considered to be Jurassic (e.g., Zonenshain & Pichon, 1986), Cretaceous (e.g., Adamia et al., 1974; Görür, 1988; Nikishin et al., 2003; Okay et al., 1994), Lower Cretaceous to Palaeocene (e.g., Finetti et al., 1988; Sydorenko et al., 2017), Palaeocene to lower Eocene (e.g., Banks et al., 1997; Robinson et al., 1995b), or Eocene (e.g., Kazmin et al., 2000; Yilmaz et al., 2000) in age. From the analysis of the Crimean Mountains onshore outcrops, and from micro-paleontological dating (nanno-plankton) in the same region, studies infer similar timing for the EBSB rift (starting in Lower Cretaceous), breakup (Albian-Cenomanian) and oceanic spreading (Cenomanian to Santonian/Campanian) (e.g., Hippolyte et al., 2018; Nikishin et al., 2003; Sheremet et al., 2016). Conversely, studies based on Georgia and Eastern Pontides onshore outcrops generally infer an Upper Cretaceous-lower Cenozoic basin opening (e.g., Okay et al., 1994; Yilmaz et al., 2000). Similarly, studies integrating well data from the Shatsky Ridge and dredging from the Archangelsky Ridge, infer a Palaeocene-Eocene age for rifting (e.g., Banks et al., 1997; Rudat & Macgregor, 1993; Spadini et al., 1996). Depending on the location of the sampling, there are different outcomes in terms of timing for rifting and breakup in the EBSB.

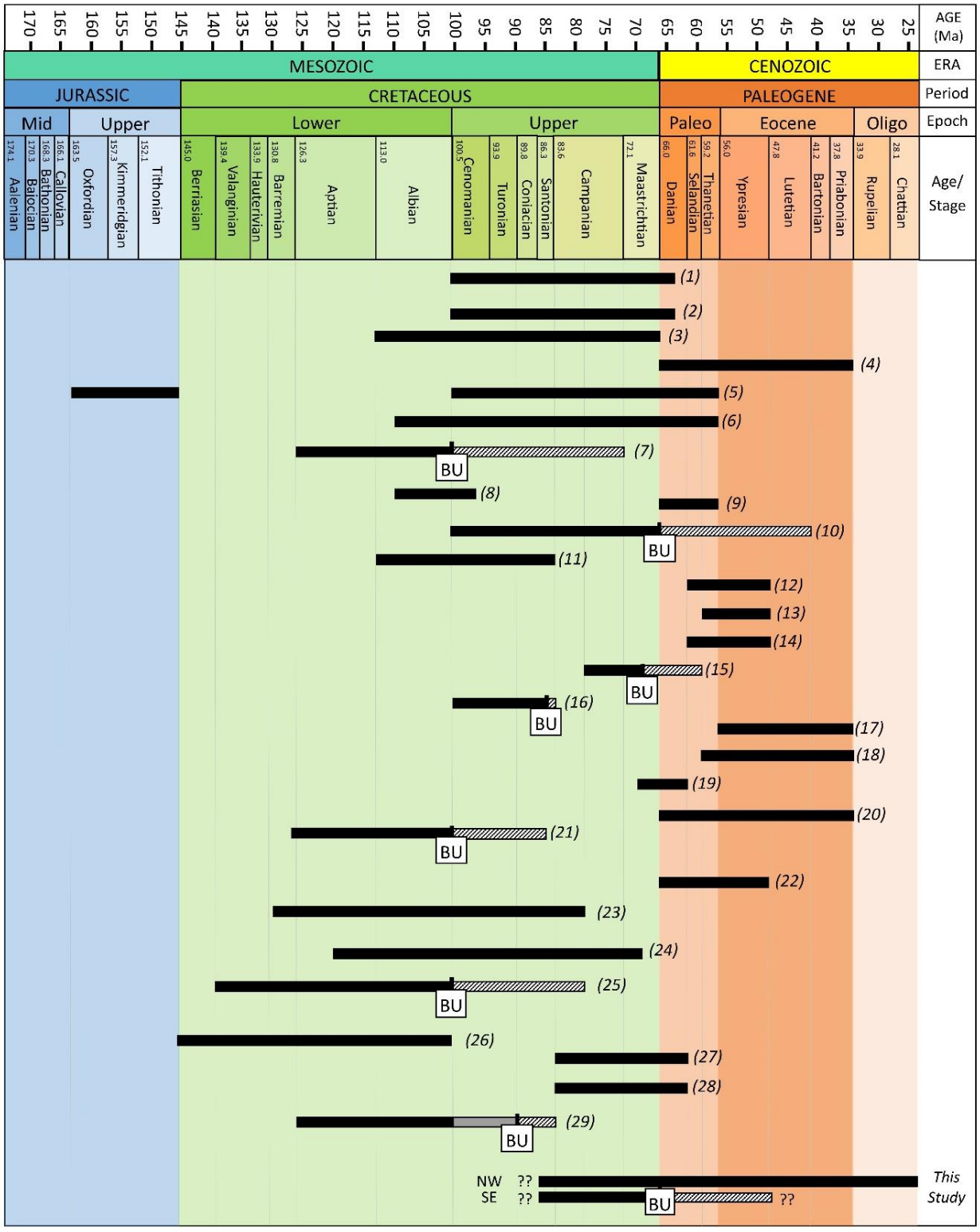

Figure 3-2. Timing of rift and breakup in the EBSB from previous studies.The black bar indicates rift duration. The grey bar indicates the age of a second syn-rift deposit identified by Tari & Simmons (2018). When available, timing of breakup (BU) and oceanic spreading are shown (hashed bar). Numbers correspond to the studies listed in Table 3-1. The geological timescale is adapted from Cohen et al. (2016).

Table 3-1. Table listing in chronological order the studies used as a reference for the previous estimated time of rifting and breakup in the EBSB. Numbers in the left column refer to the time-bar shown in Figure 3-2. For each of the studies, the methodology used to determine the time-constraints is briefly described.

#	List of authors	Data used to constrain timing of rifting
(1)	Adamia et al., 1974	Structural relationships from EBSB coastline, ages of magmatism, plate reconstruction.
(2)	Letouzey et al., 1977	Geological observations, seismic reflection data analysis.
(3)	Hsü et al., 1977	Plate reconstruction.
(4)	Tugolesov et al., 1985	Seismic data interpretation.
(5)	Zonenshain & Le Pichon, 1986	Seismic evidences and subsidence history analysis.
(6)	Finetti et al., 1988	Seismic reflection data and onshore observations.
(7)	Görür, 1988; Görür & Tüysüz, 1997; Görür et al., 1993	Paleogeography based on geological observations and stratigraphy Central Pontides.
(8)	Golmshtok et al., 1992	Seafloor heat-flow measurements and multichannel data.
(9)	Rudat & Macgregor, 1993	Wells data from Shatsky Ridge in Georgia and dredging from Archangelsky Ridge.
(10)	Okay et al., 1994; Okay & Şahintürk, 1997; Okay &Tüysüz, 1999	Structural/stratigraphic evidences, age of magmatic products of Eastern Pontides.
(11)	Bektas & Güven, 1995	Age of magmatism in Eastern Pontides.
(12)	Robinson et al., 1995a, b, 1996	Seismo-stratigraphic interpretation and well data.
(13)	Spadini et al., 1996	Kinematic modelling and thermal structure analysis.
(14)	Banks et al., 1997	Onshore outcrops, well data and seismic interpretation onshore Georgia.
(15)	Shreider et al., 1997; Shreider, 2005	Magnetic anomaly studies.
(16)	Tüysüz 1999; Tüysüz et al., 2012	Analysis of volcanogenic rocks in north Turkey.
(17)	Yilmaz et al., 2000	Structural correlations (Transcaucasus and Eastern Pontides), and age of magmatism.
(18)	Kazmin et al., 2000	Thickness and distribution of Palaeocene-Eocene sedimentary units from seismic data.
(19)	Verzhbitsky et al. 2002	Heat-flow analysis and seismic data interpretation.
(20)	Cloetingh et al., 2003	Thermo-mechanical modelling.
(21)	Nikishin et al., 2003, 2011, 2013, 2015b, 2015c	Correlation of Crimean onshore geology and regional seismic reflection profiles.
(22)	Shillington et al., 2008	Integration of onshore geological mapping, well data and seismic reflection data.
(23)	Stovba et al., 2009	Seismic data interpretation and correlation with Subbotina-403, -1 wells.
(24)	Stephenson & Schellart, 2010	Geo-dynamic modelling of back-arc extension.
(25)	Hippolyte et al., 2010, 2017, 2018	Structural and stratigraphic analysis in Crimes and Pontides, and nannoplankton ages.

(26)	Sheremet et al., 2016	Micro-paleontological dating sampled on the Crimean Mountains.
(27)	Vincent et al., 2016	Subsidence analysis.
(28)	Sydorenko et al., 2017	Seismic interpretation offshore Crimea, and correlation with Subbotina-403 well.
(29)	Tari, 2015; Tari & Simmons, 2018	Stratigraphic compilation of published information and well data.

3.3 Data and methods

3.3.1 Seismic data

We used twelve post-stack time-migrated long-offset seismic reflection profiles, acquired in 2011 by GWL and ION GXT (Figure 3-1b). Seismic profiles were acquired using an airgun array with total volume of 5680 cu. in, 816 channels, a 10,200 m long streamer and an 18-second (TWTT) record length. Processing was carried out by GWL and consisted of editing, low-cut filtering, spherical divergence correction, multiple suppression (predictive deconvolution and radon de-multiple), amplitude balancing, normal move-out correction, muting and stacking, post-stack Kirchhoff time migration and post-stack/post-migration band-pass filtering, coherent filtering and amplitude balancing. Long-offset profiles were integrated with six time-migrated multichannel seismic reflection profiles, acquired by BP and TPAO during the years 1991-1992 and 2002 (Figure 3-1b). These profiles were acquired with streamer lengths of 3600 to 6000 m, allowing 8 to 15-second (TWTT) record length, and they were used to constrain the shallower seismo-stratigraphic interpretation.

We converted the time migrated profiles to depth using interval velocities derived from the stacking velocities provided by GWL, combined with velocities from wide-angle seismic data (Shillington et al., 2009, 2017). A comparison between the GWL velocities and those from wide-angle seismic profiles, which have a sufficiently large aperture to constrain the velocities of deep sediments, showed that the two velocity functions are very similar in the shallow section (above basement reflection), while wide-angle seismic velocities are faster in the deeper section. In order to provide the most accurate velocity model for time-depth conversion, we combined these two velocity fields. Further information on the time-depth conversion steps is given in section 2.1.2 (Chapter 2).

3.3.2 Seismic interpretation: Method and Terminology

Regionally distributed prominent reflectors, characterized by discordant stratigraphic contacts and variations in seismic character, extend across the EBSB. These reflectors were used to identify the top and base of separate sedimentary sequences (S1-S7). We used the internal geometries and seismic facies variation of these sequences (Figure 3-3 – Figure 3-7; see also Appendix A), as well as their interaction with structural elements across the basin, to identify their pre-, syn- or post-rift character (e.g., Franke, 2013; Williams, 1993). Seismic horizons interpreted in depth were gridded using a Convergent Interpolation algorithm (e.g., Haecker, 1992) and a cell size of 250x250m to generate horizon structural surfaces. Thickness maps for each sedimentary sequence (isopach maps) were calculated from the difference between the horizon surfaces representing top and base of that sequence. Isopach maps are presented to illustrate the depo-center distribution and their spatial and temporal migration (Figure 3-8).

Normal fault systems were mapped and interpolated across seismic profiles, where possible. The resulting fault polygons were overlain on isopach maps to help to define fault-related depo-center development (Figure 3-8). Fault planes have been picked from discontinuities in reflections, from residual diffractions and from sedimentary infill geometries.

In this paper we classify the identified unconformities based on the stratigraphic models of Bond et al. (1995), Falvey (1974) and Franke (2013), which recognise two key unconformities that develop during rifting and continental breakup: the *rift-onset unconformity*, which separates pre-rift and syn-rift strata, and the *breakup unconformity*, which separates syn-rift from post-rift strata at the time of crustal breakup and onset of oceanic crust accretion (e.g., Falvey, 1974; Withjack et al., 1998). The breakup unconformity is defined as an erosional surface characterizing the uplifted margins during rifting stage, often truncating wedge-shaped syn-rift sediments and separating them from younger post-rift sequences that show little/no evidence of extension controlling their deposition (Franke, 2013). Basinward, this unconformity merges with an angular unconformity and terminates onto the top of the igneous crust (Franke, 2013). However, a clear definition of this unconformity as a single stratigraphic surface, together with the identification of distinct syn-rift and post-rift stratigraphic sequences, is complicated by the fact that rifting and continental breakup processes are variably distributed in time and space (e.g., Péron-Pinvidic et al., 2007). In this study we define the presence of a breakup unconformity of regional extent, which is the principal stratigraphic feature related to continental breakup along the continental highs. Downslope and in the central basin this unconformity becomes a stratigraphic contact between distinct sedimentary sequences and/or the contact between the top of the inferred oceanic crust and the overlying sequence.

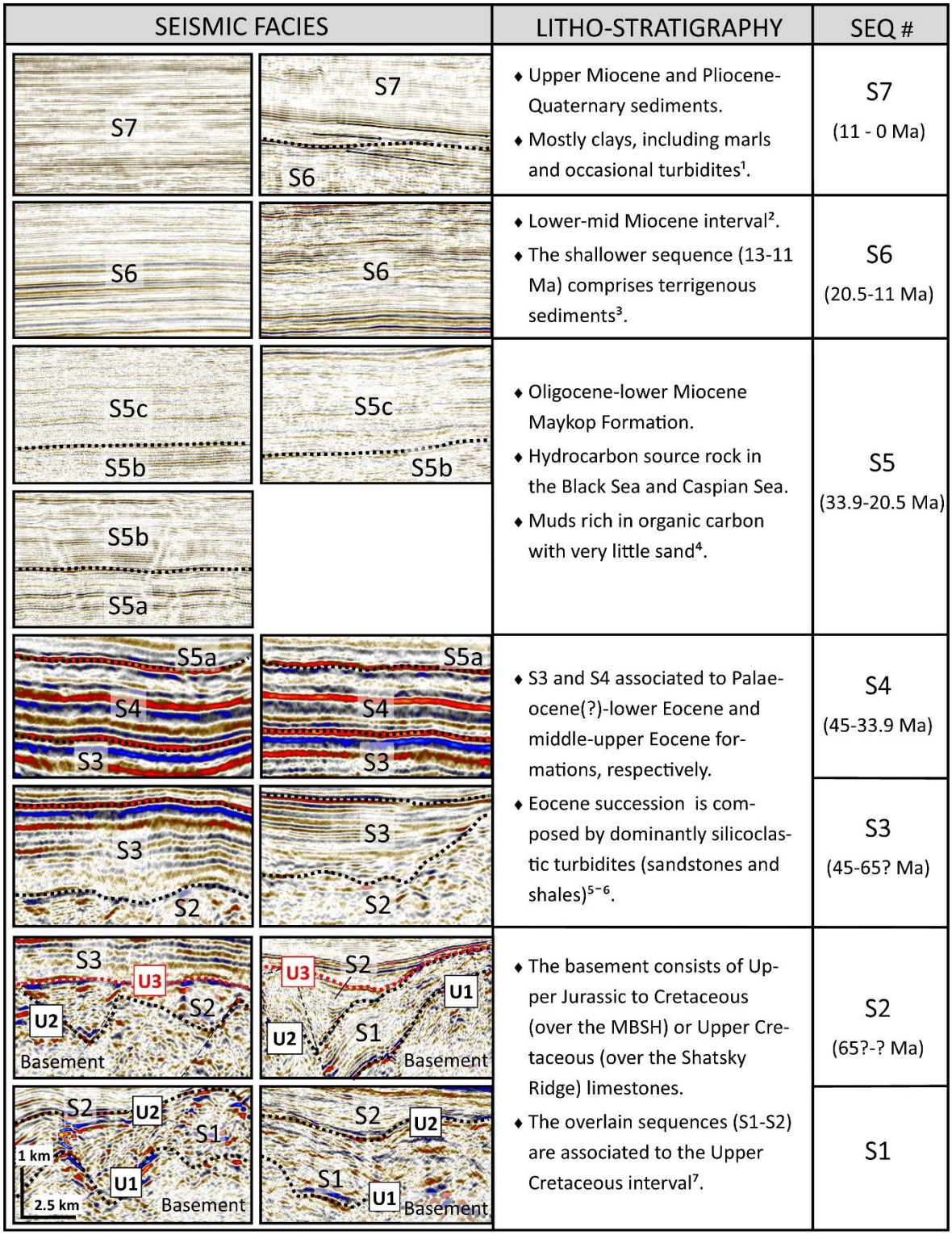

Figure 3-3. Summary of the interpreted seismo-stratigraphic units (S1—S7). From left to right: seismic examples for each sequence; litho-stratigraphy information from previous studies; sequence number and age estimated from correlation with previous studies. References: [1]Ross (1978); [2]Robinson et al. (1995a); [3]Nikishin et al. (2003); [4]Robinson et al. (1996); [5]Görür & Tüysüz (1997); [6]Sydorenko et al. (2017); [7]Robinson et al. (1995b).

Due to the complex definition of rift and breakup processes, previous studies introduced the idea of a *transition sequence* recording the gradual transition from syn-rift to post-rift stage (e.g., Moore, 1992). This idea has been further developed by more recent studies, acknowledging breakup as a prolonged event identified by a discernible unconformity-bounded stratigraphic sequence of regional extent, showing distinct depositional architectures compared to older (syn-rift) strata and younger (post-rift) units: the *breakup sequence* (e.g., Alves & Cunha, 2018; Soares et al., 2012). Here, we refer to a recent definition of *breakup sequence* by Soares et al. (2012), which describes the character of some sedimentary units deposited from the onset of lithospheric breakup to the establishment of thermal relaxation as the main process controlling the subsidence of the basin.

3.4 Seismic data analysis

3.4.1 Structural elements

The main rift-related structural elements of the EBSB are illustrated in profile bs-90 (Figure 3-4a). To the NE, the Shatsky Ridge is a basement high bounded to the south by one or more large normal faults (Shatsky Ridge fault), with a northern flank that is flexed beneath the Greater Caucasus, generating a small foreland basin, the Tuapse Trough (Figure 3-4a). On the western and south-western side of the basin are the Archangelsky and Andrusov Ridges (MBSH). Various evidence for extensional tectonics is visible, with normal faults generally showing a NW-SE to WNW-ESE trending direction and bounding graben and half-graben structures (Figure 3-4a,b, Figure 3-5a-c, Figure 3-6a, b, Figure 3-8). Basinward, normal fault arrays are organized in closely spaced domino faults (Figure 3-5c). All the identified faults cut the basement (pre-rift) and the deep sedimentary sequences (S1 and S2). The main fault systems, interpolated across the seismic profiles, are the basin-bounding faults also representing the flanks of Shatsky Ridge and MBSH (Figure 3-4a,b, Figure 3-8). The sedimentary sequences immediately overlying faulted basement blocks allow us to estimate the age and duration of fault activity. The faults affecting the basement highs generally show a variable but mostly high dip angle (30-70°; Figure 3-5a), whereas basinward faults arrays have quite a uniform and low dip angle (15-25°; Figure 3-5c). The velocity model used for seismic depth conversion affects the dip angle of the interpreted faults. Below basement, time-depth conversion using wide-angle velocities results in faults with dip angles up to 4-5° steeper than those from using stacking velocities. This difference in fault dip angle is similar to the 1-2° dip angle uncertainty from the standard deviation in wide-angle velocities (see section 2.1.2). Another change from the structural highs to the central basin, is represented by the different stratigraphic contacts with the top of the faulted basement blocks. Over the ridges, S1 is the dominant infill, whilst S2 is the prevalent infill within basinward half-graben structures (Figure 3-4a, Figure 3-5a, c, Figure 3-6a, b).

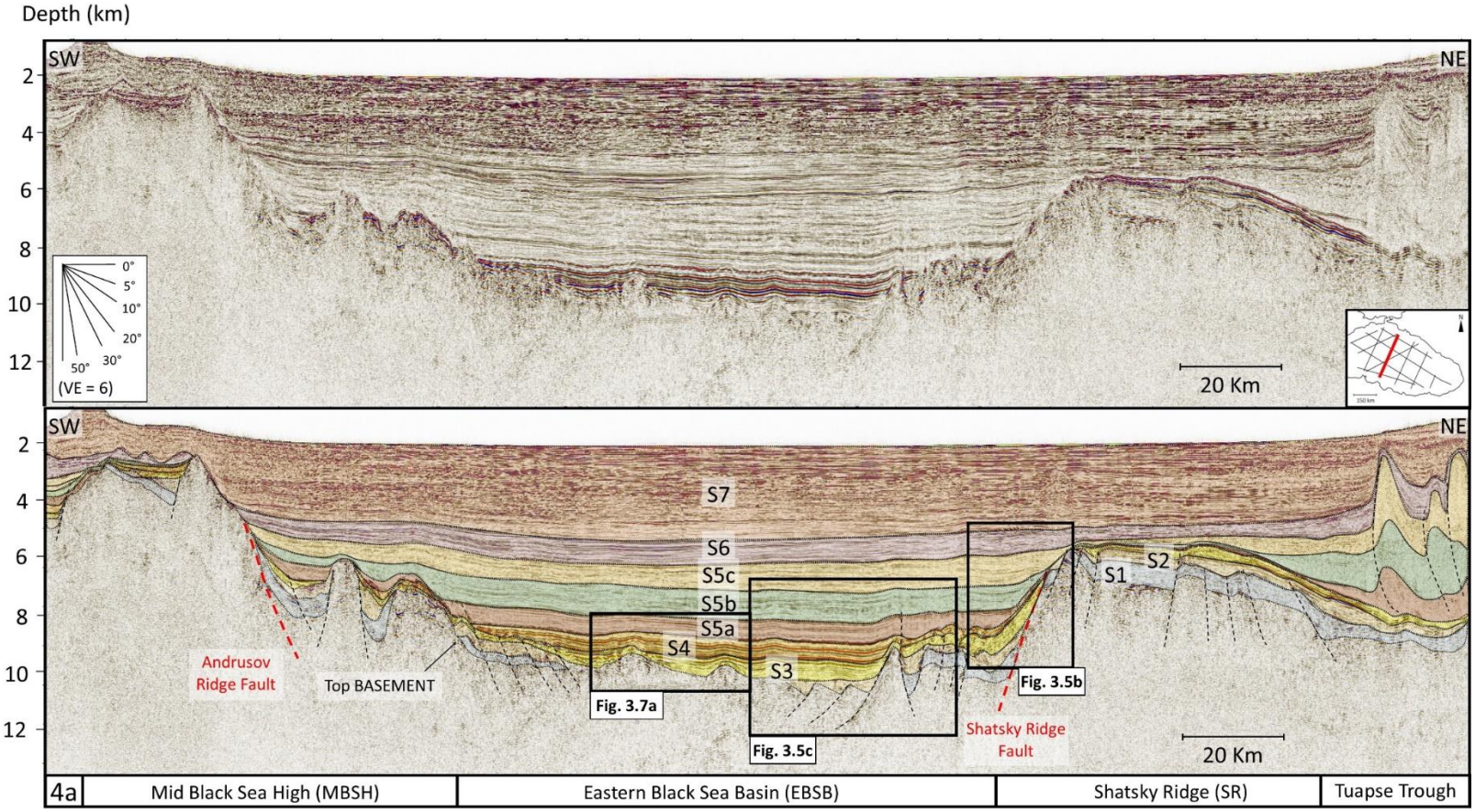

Figure 3-4. Continued...

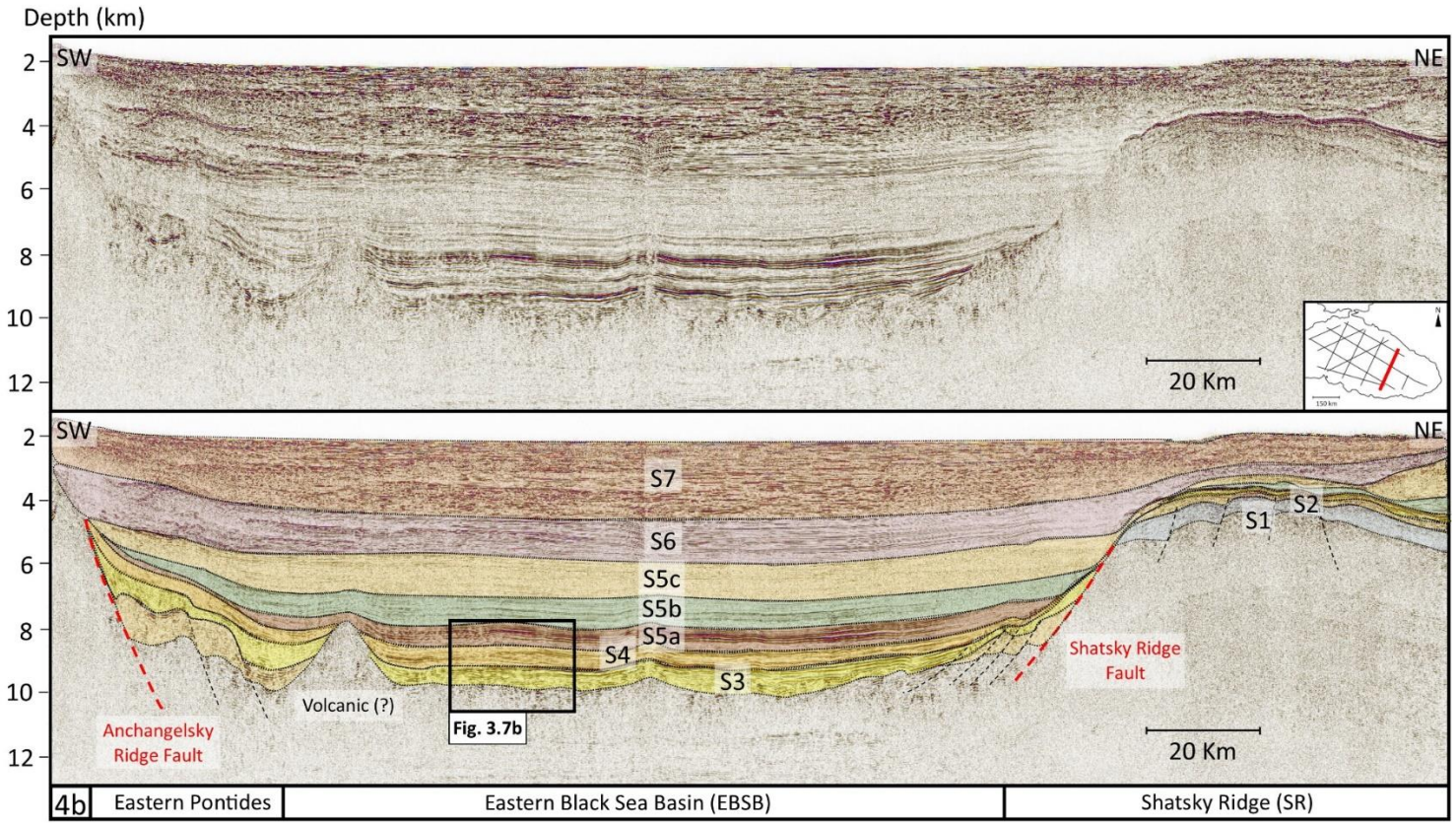

Figure 3-4. (a) Profile bs-90. The MBSH and the Shatsky Ridge bound the central EBSB. Colors mark interpreted stratigraphic sequences (S1 to S7). The top basement is affected by normal faults (dashed lines) generating tilted crustal blocks. Normal faults over the structural highs generally show higher dip angle (30°-70°), whereas downslope they show lower dip angle (15°-25°). Syn-kinematic deformation is mainly visible within units S1 and S2, but it affects also shallower units S3-S4 and S5a, at locations. The main fault planes are interpreted in continuity across NE-SW trending profiles (red dotted lines): Shatsky Ridge fault and Andrusov Ridge fault. Black boxes show the locations of Figure 3-5b, c and Figure 3-7a. (b) Profile bs-110. A major change in the character of the deep

sedimentary infill is visible: no clear syn-kinematic deformation affects sequences S3 and S4, which have instead a clear post-rift character, directly overlying the central EBSB basement. The Shatsky Ridge fault is mapped across from profile bs-90, showing here a lower dip angle. The Andrusov Ridge fault is also mapped across nearby profiles. A volcanic body has been interpreted at the SW end of this profile by previous studies (e.g., Nikishin et al., 2015a). Black box shows the location of Figure 3-7b. (VE = 6:1).

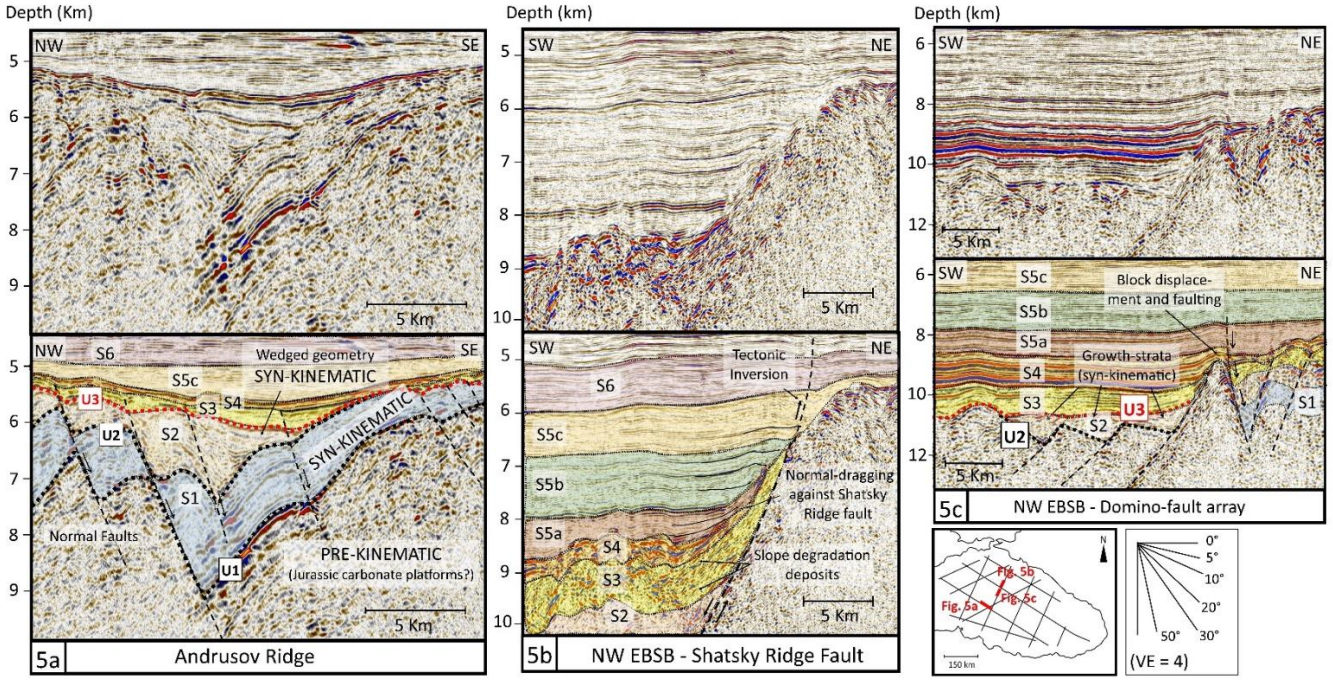

Figure 3-5. (a) Part of profile bs-170, showing syn-rift wedged geometries (S1-S2).The contact between S1 and the basement is defined by unconformity U1. S2 overlies S1 in angular discordance, defining unconformity U2. Horizon U3 identifies the top of S2 and the base of sequence S3. Sequences S3 and S4 are a thinner sedimentary cover over the structural highs. (b) Part of profile bs-90. The Oligocene Maykop Formation (S5a) shows strata dragging along the Shatsky Ridge fault. The Oligocene-lower Miocene Maykop Formation (S5b-S5c) pinches-up over the same fault plane, indicating compressive reactivation along this fault.

S3 and S4 units resemble the character of chaotic slope degradation deposits (VE = 4:1). (c) Part of profile bs-90. Downslope, wedged S2 deposits represent the main syn-rift infill, overlying tilted fault-blocks. S1 is generally absent. The base of the well layered S3 unit truncates the S2 wedges, defining unconformity U3. (VE = 3:1).

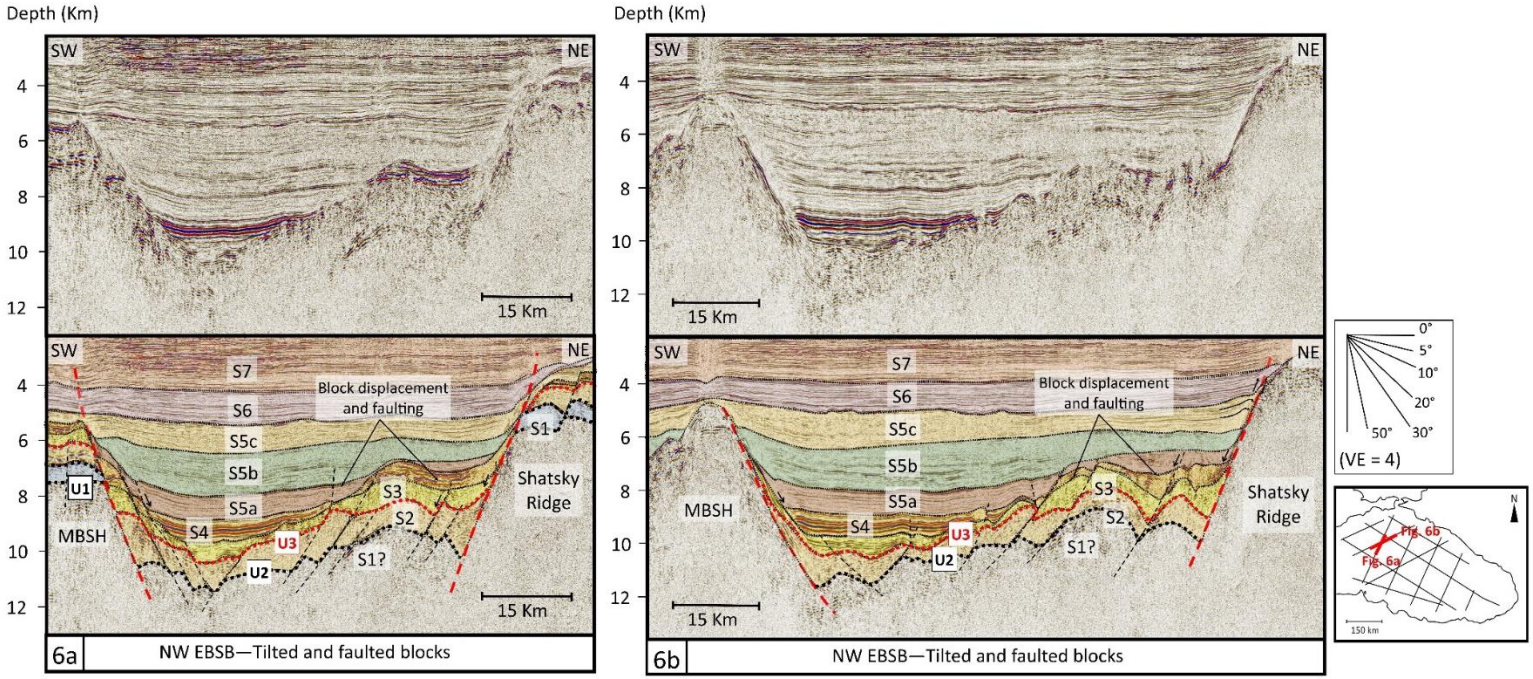

Figure 3-6. Profiles showing fault activity through S3, S4 and S5a units: (a) part of profile bs-80; (b) part of profile bs-210. In both examples, faulting and tilting of continental blocks occur up to the Oligocene Maykop Formation (S5a). The resulting syn-kinematic topography is then progressively smoothed out by the Oligocene-lower Miocene Maykop Formation (S5b and S5c). Red dashed lines are the Shatsky Ridge fault (NE) and the Andrusov Ridge fault (SW). Mapped unconformities U1, U2, and U3 are also shown. Evidence for S5c pinching-up over the Shatsky Ridge fault (b) indicates compressive reactivation along this fault (see also Figure 3-5b). (VE = 4:1).

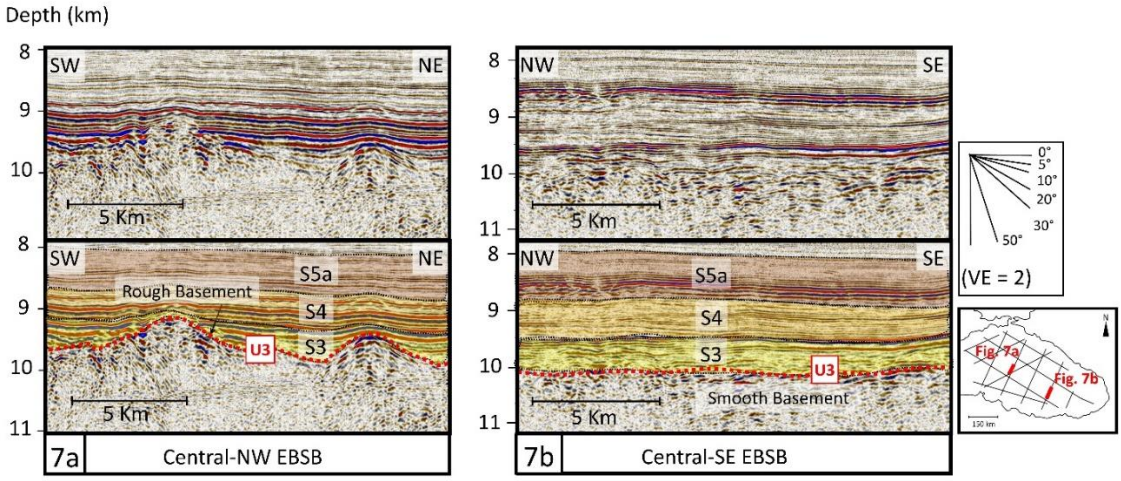

Figure 3-7. (a) Part of profile bs-90 where there is no evidence for syn-rift deposits (location in Figure 3-4a). S3 directly overlies the top of a rough basement, which morphology affects S3 thickness distribution (Figure 3-8c). (b) Part of profile bs-110 (location in Figure 3-4b). No evidence for syn-rift deposits in this area. S3 directly overlies a smooth basement, which is considered to have formed due to breakup and spreading in this area.

In the central and SE part of the basin, there is no evidence for normal faults (Figure 3-4a, b). The top basement is a corrugated surface becoming progressively smoother to the SE (Figure 3-7a, b). In this area, faults affecting the basement generate basement scarps that have been described in previous studies as the result of interpreted ENE-WS trending trans-tensional faulting (Shillington et al., 2009).

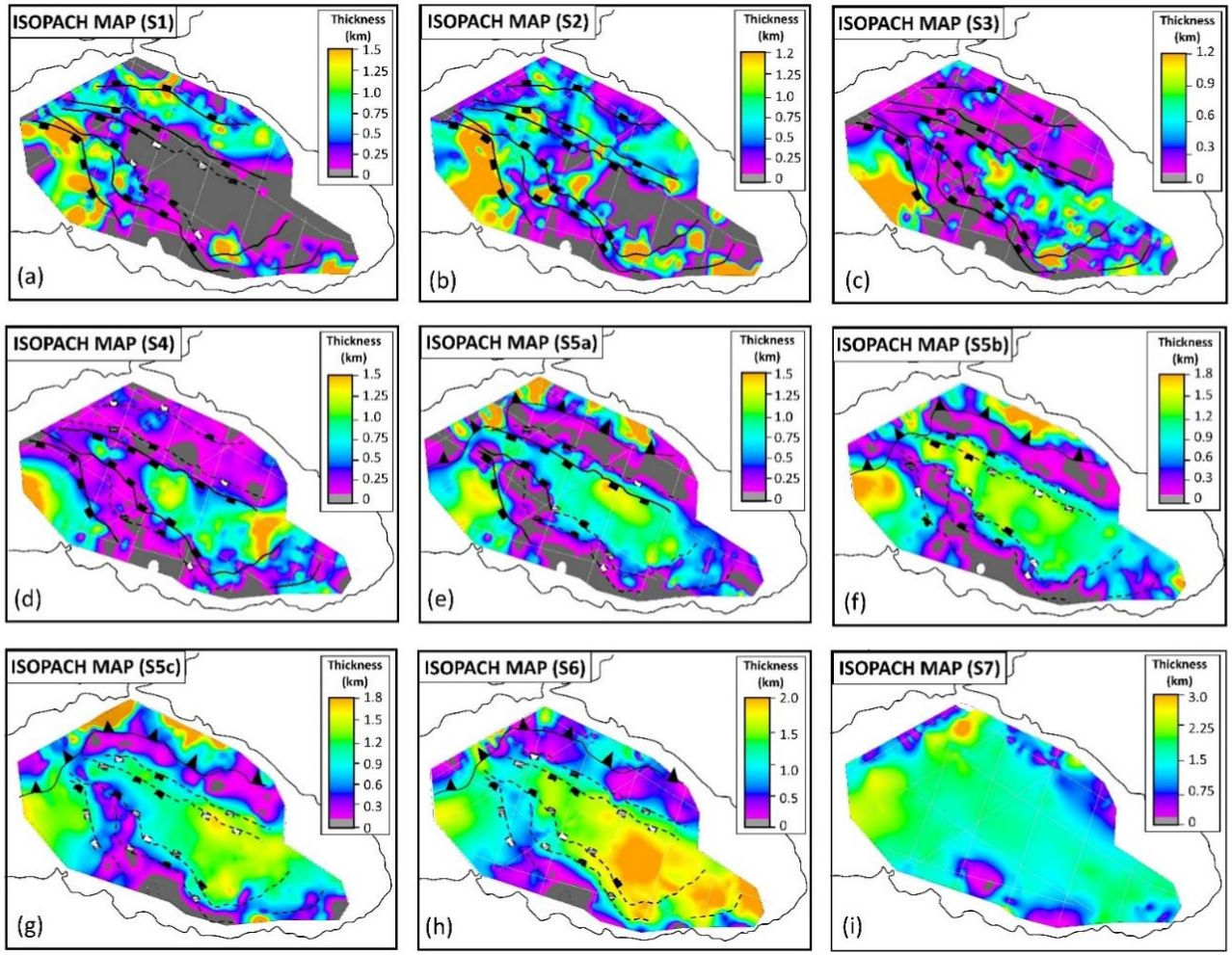

Figure 3-8. Isopach maps. (a) S1 – visible over the structural highs and rapidly thinning basinward (Rift stage 1); (b) S2 – visible basinward (NW), records strain migration towards the basin axis (Rift stage 2); (c) S3 – Palaeocene(?)-lower Eocene sequence, progressively infilling the central EBSB; (d) S4— middle-upper Eocene; (e) S5a—lower Maykop Formation. S3, S4 and S5a record ongoing extension in the NW, and a localized breakup in the SE; (f) S5b—intermediate Maykop Formation, showing the end of extension and the beginning of a regionally spread post-rift subsidence; (g) S5c—upper Maykop Formation. Thickness changes along basin-bounding faults are linked to compressional reactivation; (h) S6— Lower-mid Miocene, showing a greater amount of sediment supply in the SE, and (i) S7—Upper Miocene, Pliocene-Quaternary, progressively filling the all basin. Fault systems have been tentatively interpreted with a continuous black line (the fault was active during the time represented by that sequence), or with a dashed line (ceased/not started fault activity at that time).

3.4.2 Seismo-stratigraphic elements

We mapped the acoustic basement and seven sedimentary sequences across the EBSB, based on their seismic facies, internal geometries and interaction with structural elements (Figure 3-3). Some of the deepest and thus oldest, fault-bounded sequences are discontinuous throughout the basin. This lack of continuity, together with the presence of gaps between seismic profiles, prevents a clear correlation of these sequences at a regional scale. This point has to be considered when looking at isopachs for these sequences (especially S1 and S2), particularly in areas where seismic coverage is low. With this point in mind, we describe the interpreted sequences below, starting from the oldest, S1 (deepest), and moving to the youngest, S7 (shallowest):

S1 is a low amplitude seismic unit with isolated higher-amplitude reflections (Figure 3-3). Despite the general lack of coherency of its seismic facies, it can be present as a well layered infill of graben and half-graben structure (Figure 3-3, Figure 3-4a, Figure 3-5a). The S1 isopach map shows that S1 is present over the tops of the MBSH and the Shatsky Ridge, where it is 250 to 1500 m thick (Figure 3-8a). It then rapidly thins downslope, to disappear towards the central basin (Figure 3-4a, b, Figure 3-5c). S1 is bounded by two unconformities (horizons U1 and U2), marking the discordant contact at its base and top with the underlying basement and the overlying S2 sequence. Horizon U1 is, in some places, a very high reflectivity boundary (Figure 3-5a). In contrast, horizon U2 is a low amplitude reflection (Figure 3-5a). S1 is a tectonically controlled sedimentary infill, with strata thickness changes and wedged geometries bounded by normal fault planes (Figure 3-4a, Figure 3-5a).

S2 is a medium to low amplitude sequence, showing layered packages organized into sedimentary wedges bounded by normal faults (Figure 3-3, Figure 3-4a, Figure 3-5a,c). Along the main basin-bounding faults, S2 is sometimes a chaotic and semi-transparent package resembling detrital material deposited downslope and subsequently onlapped by chaotic to well layered younger sedimentary sequences (S3-S4) (Figure 3-4a, Figure 3-5b, Figure 3-6a,b). S2 is up to ~ 1500 m thick and is often confined within small depo-centers (Figure 3-8b). S2 occurs as secondary infill above S1, on the top of Shatsky Ridge and the MBSH, whilst it is a primary infill of basinward half-graben structures (Figure 3-4a, Figure 3-5c). Within these half-graben structures, S1 may be still present below S2, although not properly imaged. The top of S2 is defined by unconformity U3 (Figure 3-4a,b, Figure 3-5a,c, Figure 3-6a,b). The progressive basinward thinning of S1 and S2 causes the related unconformities U1 and U2 to merge in the basin center, and here only the top U2 horizon is interpreted (Figure 3-5c). Further basinward thinning of S2 causes the coalescence of horizons U2 with U3, leaving horizon U3 as the contact between S3 and the top basement (Figure 3-5c, Figure 3-7a,b). The S2 isopach map shows the uneven distribution of this unit through the basin (Figure

3-8b). Compared to S1, which is mostly interpreted over the Shatsky Ridge, the MBSH and the Tuapse and Sorokin Troughs, S2 exists further basinward, in the NW (Figure 3-8b). In the SE, S2 is interpreted along the basin-bounding faults, but it is absent in the central basin (Figure 3-4b, Figure 3-8b).

S3 is generally a well layered sequence, with low amplitude reflections at its base and higher amplitudes towards its top (Figure 3-3). In the NW, down the Shatsky Ridge slope, this sequence has the character of a chaotic detrital deposit (Figure 3-5b, Figure 3-6a,b). Seismic profiles and isopach map show that this unit is preferentially distributed in the central basin (with maximum thickness up to 1200 m), whilst it is < 500 m thick over the MBSH and the Shatsky Ridge (Figure 3-8c). Thickness changes are partly a response to the underlying basement topography (Figure 3-4a, Figure 3-7a), affecting the distribution of S3 in the central basin, but also a response to tectonic activity visible in the NW part of the basin and along the main basin-bounding faults (Figure 3-4a, Figure 3-5c, Figure 3-6a,b). In these areas normal faults cross-cut S3, indicating a syn-kinematic deposition (Figure 3-5c, Figure 3-6a,b).

S4 is characterized by sub-parallel, high to low amplitude reflections (Figure 3-3). The top and base of this sequence are identified by high acoustic impedance contrasts with the base of S5a (lower Maykop Formation) and the top of S3, respectively (Figure 3-3). Tectonic control is less visible within this sequence, but some normal faults propagate through S4 generating small thickness changes (Figure 3-5c, Figure 3-6a,b). S4 is deposited mainly in the central basin (500 to 1250 m thick), whilst it is a drape of sedimentary cover over the continental highs (≤ 250 m thick) (Figure 3-8d). S4 is generally more uniformly distributed in the central basin compared with the older sequence S3.

S5a, S5b and S5c units are associated to the regionally distributed Maykop Formation characterized by a semi-transparent seismic layer (e.g., Robinson et al., 1996; Sydorenko et al., 2017; Zonenshain & Pichon, 1986). S5 is indeed a low amplitude package with homogeneous appearance, generally linked to uniformity in its lithological character. This sequence is up to ~ 4500 m thick in the central basin, thinning over Shatsky Ridge and the MBSH (≤ 500 m thick), and thickening again along the compressed margins of the EBSB (Tuapse and Sorokin Troughs), where it can reach thicknesses of 2500 to ≥ 5000 m (Figure 3-8e,f,g). Although the Maykop Formation is usually interpreted as a single sedimentary package, we subdivide it into three layers: S5a, S5b and S5c (Figure 3-3, Figure 3-4a,b, Figure 3-5b, Figure 3-6a,b). This sub-division is marked by the presence of weak but laterally continuous reflectors, probably linked to lithological variation within the unit. Within the lower Maykop Formation (S5a) some high reflectivity layers are probably related to the intercalation of sandier interbeds (e.g., Stovba et al., 2009). Extensional faults propagate through S5a sequence generating small thickness changes (Figure 3-5c, Figure 3-6a,b). Furthermore, the lateral

termination of S5a on the Shatsky Ridge fault shows evidence of normal-drag (the hanging-wall beds dip away from the normal fault – Withjack et al., 2002) along the fault plane (Figure 3-5b, Figure 3-6b). In contrast, S5b and S5c show no particular evidence for extensional tectonics, and their strata onlap in reverse-drag (the hanging-wall beds dip towards the normal fault – Withjack et al., 2002) onto the basin-bounding faults (Figure 3-5b, Figure 3-6b). S5a, S5b and S5c isopach maps show depo-center migration through time (Figure 3-8e,f,g). S5a has quite a uniform distribution in the central basin, with visible thickness changes controlled by normal fault activity along the Shatsky Ridge fault, and thrust fault activity along the NE margin of the EBSB (Figure 3-8e). The compressional tectonics is associated with the folding and thrusting visible in the seismic data, also affecting the shallower units S5b and S5c (Figure 3-4a, Figure 3-5b). The S5b main depo-center is located in the NW corner of the basin (Figure 3-8f), whereas S5c main depo-center migrates towards the SE (Figure 3-8g). No clear tectonic control is visible within these units, so depo-center migration is probably due to a change in the main source of sediment supply. Furthermore, small thickness changes along fault planes, visible in the S5b and S5c isopach maps, may be related to the compressive reactivation of the basin-bounding faults (Figure 3-5b, Figure 3-6b, Figure 3-8g).

S6 and S7 are well layered and sub-parallel, medium to high reflectivity units with alternating semi-transparent strata (Figure 3-3). They represent the shallowest and youngest sequences filling the basin. Our interpretation matches previous seismic interpretation and well data correlation (e.g., Nikishin et al., 2015a; Shillington et al., 2008). The thickness of sequence S6 is up to 2500 m in the central basin, whilst sequence S7 reaches a thickness of 100-2000 m across the EBSB (Figure 3-8h,i). S6 is thicker towards the SE part of the basin, perhaps related to the main source of sediment supply in that area (Figure 3-8h).

3.5 Discussion

3.5.1 Character and distribution of the EBSB sedimentary infill

3.5.1.1 Age of the interpreted sequences

There are no new well data available for this study, so we rely on published information to define the age and litho-stratigraphy of the interpreted sequences. The Palaeocene(?)-Eocene to Recent EBSB infill is generally well known and considered to be post-rift, based on onshore and offshore drilling (e.g., Ross, 1978; Sydorenko et al., 2017), whereas the age and distribution of the syn-rift sequences is much less constrained. Syn-rift units interpreted on seismic data rely mostly on onshore observations (e.g., in Turkey, Crimea and Georgia). However, correlation of the syn-rift

laying in the central basin with its approximate onshore equivalent, requires the assumption that the timing of rifting is synchronous across this region.

The age of the interpreted sequences S1 and S2 is difficult to constrain, for the reasons stated above. Sequences overlying S2 are, in contrast, within depths investigated by some of the offshore drilling, especially in areas where those sequences have been uplifted by Eocene compression (e.g., Hippolyte et al., 2018; Sydorenko et al., 2017). In the N-NE part of the EBSB, offshore Crimea, the Subbotina-403 and -1 wells reached the Neogene and Oligocene-Eocene sequence (Stovba et al., 2009; Tari & Simmons, 2018). The oldest sequence identified consists of sediments of lower Eocene age. Above them, lies the Oligocene-lower Miocene Maykop Formation (corresponding to S5 units). Seismic data from the northern EBSB, correlated to Subbotina-403 well, are presented by Stovba et al. (2009) and Sydorenko et al. (2017). These profiles cross some of our seismic lines (bs220, bs180, bs210 and bs80), so we can correlate our interpreted sequences with this well stratigraphy. Sydorenko et al. (2017) interpreted a single sequence beneath the Maykop Formation, which includes the Palaeocene-Eocene deposits and corresponds to our S3-S4 units. Below that sequence, they interpreted an undifferentiated Cretaceous sequence, probably including our S1 and S2 units, which overlies an Upper Jurassic pre-rift in the northern part of the Shatsky Ridge.

Comparing the stratigraphic information from Subbotina-403 with the seismic facies of our interpreted sequences, we further subdivide the Palaeocene-Eocene unit. The S3 medium to low reflectivity facies, with high reflectivity towards the top (Figure 3-3), corresponds to the lower Eocene sequence litho-stratigraphy sampled by Subbotina-403, which is made of marls interlayered with clay and sandy layers towards the top (Sydorenko et al., 2017). The seismic character of sequence S4 (Figure 3-3) matches well with the middle-upper Eocene sequences sampled by Subbotina-403, showing alternating shale and sandy units, with sandy layers dominating top and base of the sequence, which would generate strong acoustic-impedance contrasts. Based on this evidence, we define S3 to be a Palaeocene(?)-lower Eocene (45-65 Ma) unit and S4 to be a middle-upper Eocene (45-33.9 Ma) unit. Consequently, the underlying sequences S1 and S2 represent an undifferentiated Upper Cretaceous infill, in agreement with other studies (e.g., Shillington et al., 2008; Sydorenko et al., 2017; Tari & Simmons, 2018).

From published litho-stratigraphy it is possible to define sequences S5a, S5b and S5c as the Oligocene-lower Miocene Maykop Formation, while S6 and S7 correspond to the lower-mid Miocene and upper Miocene-Plio-Quaternary, respectively (e.g., Hippolyte et al., 2018; Sydorenko et al., 2017). The presence of regional, medium-low reflectivity boundaries within the Maykop Formation (Figure 3-3, Figure 3-4a,b, Figure 3-6a,b) may be related to a change in the sedimentary character and physical properties of the sequence. The Maykop Formation is considered to be an

over-pressured layer (e.g., Scott et al., 2009), so this subdivision may alternatively imply a compartmentalisation of the overpressure within the sequence. A previous subdivision of the Maykop Formation is described by Jones & Simmons (1997). This layering within the Maykop Formation is not only representative for the potential variability in its physical and lithological properties, but it also associates to a different syn-kinematic (S5a) to post-kinematic (S5b-S5c) character of the sequence.

3.5.1.2 Rift stage

Although some studies have interpreted the presence of a syn-rift infill in the EBSB (e.g., Shillington et al., 2008; Sydorenko et al., 2017; Tari & Simmons, 2018), most authors tend to agree on the absence/near absence of syn-rift deposits in the central EBSB (e.g., Görür & Tüysüz, 1997; Görür et al., 1993), due to the lack of strong evidence for syn-rift sedimentary geometries on seismic profiles (e.g., Nikishin et al., 2015a).

In our seismic profiles, syn-tectonic growth structures and wedge geometries bounded by normal faults are clear features over the Shatsky Ridge and the MBSH (Figure 3-4a, Figure 3-5a). Here, overlying a faulted pre-rift (basement), sequences S1 and S2 (Upper Cretaceous) are interpreted as two distinct syn-rift deposits with a combined thickness up to 3 km (Figure 3-4a, Figure 3-5a,c, Figure 3-8a,b). Studies based on onshore observations also identified the presence of two syn-rift sequences in the region (e.g., Hippolyte et al., 2018; Nikishin et al., 2015a; Tari & Simmons, 2018). We define the contact between pre-kinematic (basement) and S1 as unconformity U1, which we interpret as a rift-onset unconformity (Franke, 2013; Withjack et al., 2002), marking the initial rifting event affecting the structural highs (Rift stage 1; Figure 3-9a). This unconformity progressively merges basinwards with the stratigraphically younger unconformity U2 (base of S2 unit) forming a composite unconformity (Figure 3-4a, Figure 3-5a,c). The merging of these unconformities is due to the gradual thinning of S1 towards the basin center, where half-graben structures are mostly filled by the younger syn-rift (S2) instead (Figure 3-4a, Figure 3-5a,c). The presence of an unconformity like U2, separating the early syn-rift strata from the later syn-rift strata, is a common feature in other rift basins (e.g., Buckley et al., 2015; Olsen, 1997; Lei et al., 2019). This unconformity shows the basinward migration of extension in the EBSB, associated with a progressive younging of the syn-rift infill towards the rift axis (Rift stage 2; Figure 3-9b). This two-stage rifting is visible in S1 and S2 isopach maps, where there is a clear basinward propagation of the main depo-center location (Figure 3-8a,b).

Rift migration is also recorded by a change in the character and age of the extensional faulting. Faults interpreted over the structural highs generally show higher dip angles (30°-70°). Here, the faulted basement is covered by the older S1 unit, and fault activity continues through the S1 and

S2 units, stopping at the base of S3 unit (Figure 3-4a, Figure 3-5a). Downslope, faults are organized into more closely spaced domino-fault arrays, characterized by lower dip angles (15°-25°) (Figure 3-4a, Figure 3-5c). In this area, the faulted basement is directly overlain by the younger syn-rift sequence (S2), and faults propagate sometimes into shallower units (up to S5a) steepening upwards (Figure 3-5c, Figure 3-6a,b). Fault initiation and duration can be constrained by the age of the syn-kinematic infill, so basinward faults formed later than those interpreted over the ridges. Similar evidence for syn-kinematic units recording the formation of faults that young oceanward is observed along other rift basins and rifted margins (e.g., Nixon et al., 2016; Péron-Pinvidic et al., 2007; Ranero & Pérez-Gussinyé, 2010; Reston, 2005). Various observational studies and numerical models show that rifting starts within a network of isolated normal fault segments generating a moderate crustal thinning (low β) and distributing deformation across the area (e.g., Cowie et al., 2000; Nagel & Buck, 2004; Péron-Pinvidic et al., 2017). As stretching continues, some faults grow laterally and coalesce into dominant basin-bounding single faults (e.g., Cowie et al., 2000). Deformation focuses along these few active, larger faults, whereas smaller faults along the less thinned rift flanks become inactive (e.g., Cowie et al., 2000; Ranero & Pérez-Gussinyé, 2010). As strain progressively migrates and focuses towards the future basin center, sequentially active normal faults form to accomplish rift migration (e.g., Brune et al., 2014; Nagel & Buck, 2004; Ranero & Pérez-Gussinyé, 2010). During this stage, further crustal thinning (high β) and increasing accommodation space occurs. In the EBSB, we consider high angle normal faults to record the initial stage of distributed faulting (Figure 3-9a), followed by subsequent fault linkage and generation of the master faults bounding the structural highs (Figure 3-9b). Continued extension then causes the border faults to experience more strain and basinward focusing of crustal thinning accompanied by the generation of new, lower angle sequential faults accommodating the basinward propagation of stretching (Figure 3-9b,c). The seaward decrease in fault dips is predicted by the “rolling hinge” model of Buck (1988) and Lavier et al. (1999). Evidence for normal faults initiating at higher dip angles and then rotating to lower angles during progressive extension is visible at other rifted margins (e.g., Ranero & Pérez-Gussinyé, 2010; Reston, 2005), and back-arc basins (e.g., Lei & Ren, 2016). This model may explain the progressive change in fault dip observed in the EBSB. Based on both stratigraphic and structural elements in the EBSB, we recognize a two-stage rifting process, initiating by widespread extension (Figure 3-9a), and followed by rift migration and strain focusing towards the basin axis (Figure 3-9b).

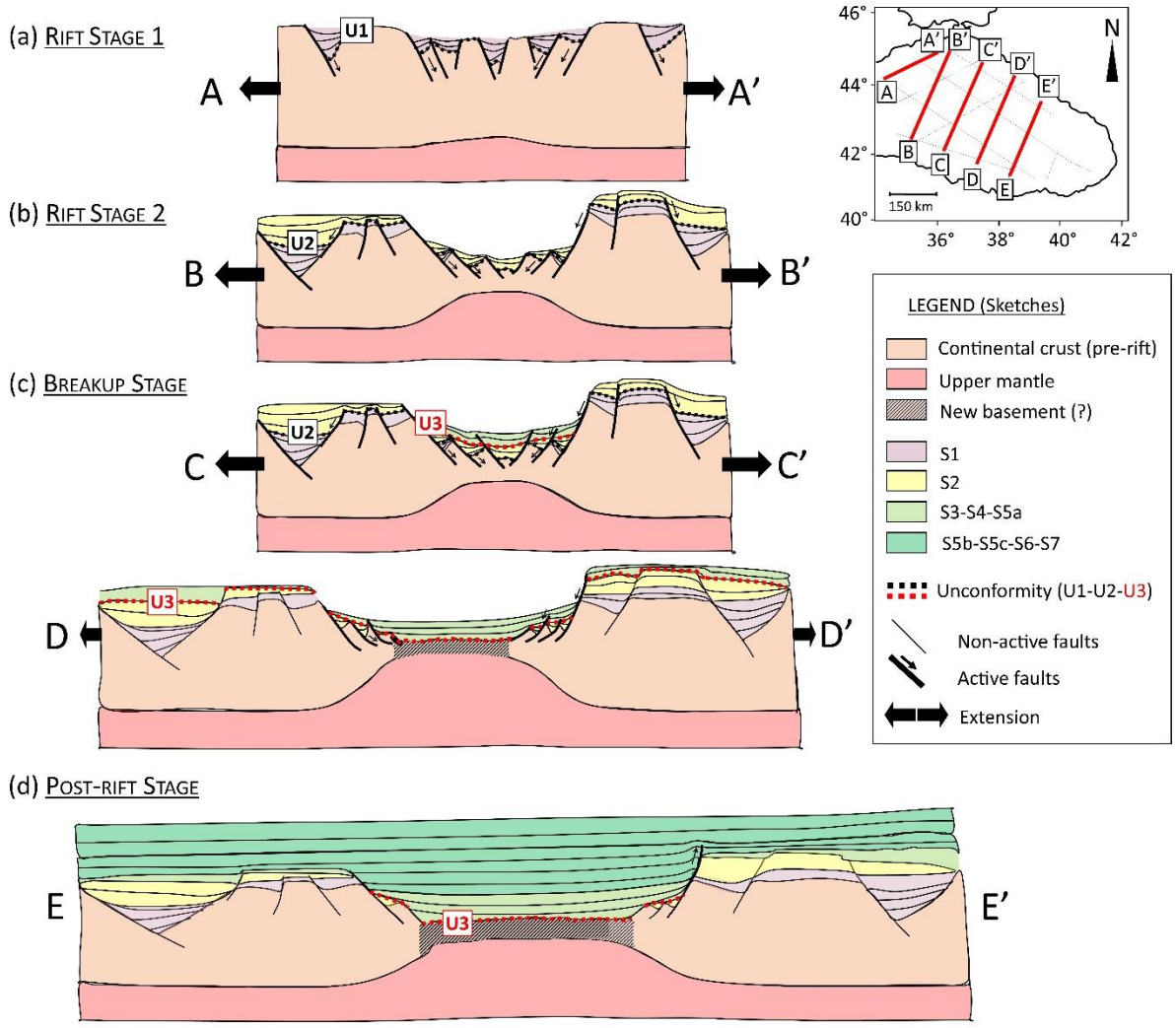

Figure 3-9. A summary of the EBSB evolution, with sketches based on seismic reflection profiles from different parts of the basin (sketches not in scale). (a) Rift Stage 1: Crustal stretching (low β) forming isolated depo-centers (Rift Onset Unconformity - U1), bounded by high-angle normal faults (30-70° dip). Graben and half-grabens are filled by syn-rift (S1) (b) Rift Stage 2: Isolated faults coalesce forming main basin-bounding faults and extension migrates towards the basin axis, where increased crustal thinning (high β) is accommodated by lower angle (15-25° dip) fault arrays. Half-grabens are filled by the younger syn-rift (S2). Unconformity U2 records the basinward migration of rifting. (c) Breakup Stage: Its onset is marked by unconformity U3. Units S3, S4, and S5a show extension up to Oligocene time (S5a) in the NW, synchronous to localized breakup and spreading in the SE, where these units show a clear post-rift character (d). (d) Post-rift Stage: The lower Miocene Maykop Formation represents the first widespread post-rift infill. Sketch profiles locations are plotted on the survey map on the top right corner.

Our observations from the EBSB are similar to those from other rift basins and rifted margins such as the Bay of Biscay (e.g., Tugend et al., 2015), the Iberia-Newfoundland margin (e.g., Brune et al.,

2017; Ranero & Pérez-Gussinyé, 2010; Reston, 2005), the Brazil-Angola margin (e.g., Brune et al., 2017), the Gulf of Corinth (e.g., Nixon et al., 2016), and the northern margin of the South China Sea (e.g., Lei & Ren, 2016; Lei et al., 2019).

3.5.1.3 Breakup stage

In our seismic interpretation, S3 lies in angular unconformity over the tilted and faulted blocks, covering the S1-S2 wedged geometries on the structural highs and cross-cutting, basinward, the tops of the S2 wedges (Figure 3-5a,c). The angular contact between S3 (Palaeocene(?)-Eocene) and S2 (Upper Cretaceous) defines unconformity U3 (Figure 3-5a,c). Based on the geometrical relationship of the contact between S2 and S3, U3 can be interpreted as a breakup unconformity (Falvey, 1974; Franke, 2013). Basinward, U3 becomes instead the stratigraphic contact between S3 and the underlying basement (Figure 3-4b, Figure 3-7a,b). Previous studies interpreted the Palaeocene(?)-Eocene units as a post-rift infill (e.g., Nikishin et al., 2015a; Sydorenko et al., 2017). However, there is evidence for normal fault propagation within these units in the NW part of the basin (Figure 3-5c, Figure 3-6a,b), together with evidence for strata terminations dragged upward along the main basin-bounding fault planes, indicating extensional activity during their deposition (Figure 3-5b, Figure 3-6b). Similarly, S5a (Oligocene Maykop Formation) shows evidence for active extension in the NW (Figure 3-5c, Figure 3-6a,b). Isopach maps highlight the irregularity of the S3 and S4 infills (Figure 3-8c,d). These irregularities partly result from the topography of the underlying basement affecting the distribution of the infill (Figure 3-7a), and/or may be related to differential compaction processes. However, observations along NW seismic profiles show clear evidence for active faulting during S3-S4 deposition (Figure 3-5c, Figure 3-6a,b). The S5a sequence appears to be more uniformly distributed across the basin, but fault activity observed along NW seismic profiles (Figure 3-5c, Figure 3-6a,b), together with thickening towards the Shatsky Ridge fault visible on the isopach map, suggest fault activity during the time of S5a deposition (Figure 3-8e).

Moving towards the central and SE part of the basin, there is no clear evidence of active extension in the S3 to S5a units. Here, these sequences appear like a typical post-rift infill overlying a basement reflection (Figure 3-4b, Figure 3-7a,b). The crustal velocity structure, determined from ocean bottom seismometer (OBS) data, suggests that the SE part of the EBSB is underlain by thick oceanic crust (Shillington et al., 2009). This interpretation agrees with the lack of evidence for extension, and with the post-rift character of S3-S5a sequences in this part of the basin. Therefore, S3-S5a probably consist of marine sediments deposited during and after breakup in the SE of the basin. The S3-S4-S5a units show an along-strike change in stratigraphic character that appears to be intermediate between syn-rift and post-rift sequences. The seismic character of these units shows similarities with the definition of breakup sequences given by Soares et al. (2012) and Alves

& Cunha (2018). Similarl to this definition, S3 to S5a units record the transitional period between the onset of breakup (SE) and the end of extension (NW), followed by the establishment of thermal relaxation as the main process controlling subsidence in the basin. Based on seismic evidence along the west Iberia-Newfoundland margins, Alves & Cunha (2018) identified within the breakup sequence distinct seismic intervals of chaotic to partly continuous seismic reflections terminating against the slope fault system and interpreted these intervals as mass-wasting and turbiditic deposits associated to the breakup stage. These units are then gradually draped by wavy to sub-parallel, low amplitude seismic reflections interpreted to reflect the spreading conditions on a fully developed margin. Similarly, we recognize that S3 and S4 units are locally organized in chaotic deposits linked to slope degradation processes, overlain by the younger and semi-transparent units of the Maykop Formation (Figure 3-5b, Figure 3-6a,b). This may be seen as a further evidence of the comparable character between our S3, S4 and S5a units and the breakup sequence defined by Soares et al. (2012), both recording the diachronous evolution of breakup processes at extensional settings. Based on these considerations, and on similarities with observations coming from other studies (e.g., Péron-Pinvidic & Manatschal, 2009; Soares et al., 2012), S3 to S5a units are interpreted to record a diachronous breakup stage across the EBSB (Figure 3-9c).

These considerations imply that the defined breakup unconformity (U3) cannot be considered representative for a widespread end of rifting and breakup initiation across the EBSB, as we need to acknowledge for the temporal and spatial variability of these processes across the basin (e.g., Péron-Pinvidic et al., 2007). The breakup stage (Figure 3-9c) is therefore time constrained by the ages of S3 to S5a infills, which show that extension continued up to Oligocene time in the NW, whereas breakup started before the deposition of S3 (Palaeocene(?)-lower Eocene time) in the SE, synchronous with the NW ongoing extension. The total thickness of S3 to S5a sequences ranges from 1.8 km to 4-4.5 km in the central basin. Because these units form part of the syn-kinematic infill in areas where extension was active up to Oligocene time, they are considered to contribute to the overall thickness of the syn-rift deposits of the EBSB.

3.5.1.4 Post-rift stage

Seismic data show no evidence for extensional tectonics within S5b, S5c, S6 and S7 units (Figure 3-6a,b). As these sequences all show a ubiquitous post-rift character, we consider the onset of thermal relaxation to be represented by the Oligocene-lower Miocene Maykop Formation (S5b) (Post-rift Stage – Figure 3-9d). Isopach maps show that these post-rift sequences progressively infill the pre-existing topography, while compression starts deforming the sediments accumulated along the NE margin (Tuapse and Sorokin Troughs) (Figure 3-8f,g,h). Thickness changes within these sequences are associated with depo-center migration related to a change in the source of sediment

supply through time, probably partially controlled by compressional deformation along the peripheral regions of the basin.

3.5.2 Final considerations

The identification of syn-rift stratigraphic intervals is a very important aspect in the study of rifted margins (e.g., Péron-Pinvidic et al., 2007). In the EBSB, we defined the presence of two clear syn-rift units (S1, S2), which are ascribed to two separate Upper Cretaceous extensional stages (Figure 3-9a,b). S3 to S5a units (Palaeocene(?) to Oligocene) are also interpreted to represent part of the syn-kinematic infill along the NW part of the basin, where active tectonics affects their deposition (Figure 3-6a,b). Previous studies suggested various timings for the syn-rift and thus for the basin opening, such as Aptian-Albian (e.g., Görür, 1988; Hippolyte et al., 2018), Cenomanian-Turonian-mid Santonian (e.g., Tari & Simmons, 2018; Tüysüz, 1999), or Palaeocene-lower Eocene or Eocene (e.g., Banks et al., 1997; Kazmin et al., 2000; Robinson et al., 1995a, 1995b), based on onshore data and well data acquired at different locations across the EBSB region. Similarly, breakup process has been estimated to be either Albian-Cenomanian (e.g., Görür, 1988: Hippolyte et al., 2018; Nikishin et al., 2015b), Turonian-Coniacian (e.g., Tari & Simmons, 2018), mid-Santonian (e.g., Tüysüz, 1999), or Maastrichtian-Danian (e.g., Okay et al., 1994, 2013; Shreider, 2005). Our study highlights the variable distribution of rifting and breakup processes at different locations and times in the basin. This distribution is recorded within the variable architecture and stratigraphic character of the identified sequences, showing either a syn-kinematic or post-kinematic character. With this observation in mind, the definition of rifting and breakup ages would be strictly dependent on the location of the study, and not really representative of the timing of the process on a regional scale. This complexity may explain such a variety of results and the general disagreement between different studies.

The EBSB is a multi-stage narrow rift formed by initial widespread stretching (Figure 3-9a), followed by rift migration towards the basin axis (Figure 3-9b), and progressive strain localization into the area of the future breakup (Figure 3-9c). Once breakup and spreading initiated along the more extended SE segment, extension continued along the less extended NW segment. This is well expressed by the Palaeocene(?)-Eocene and Oligocene sequences, which have both a syn-kinematic character in the area where extension continued up to Oligocene (NW) (Figure 3-9c), and a post-kinematic character in the area where breakup and “new” basement was generated (SE) (Figure 3-9d). Together with the along-axis variability in sedimentary ages and architecture, the change in character of the extensional faulting records the different rifting stages (e.g., Lavier & Manatschal, 2006; Moore, 1992; Péron-Pinvidic et al., 2007; Sutra et al., 2013). Starting as isolated high angle normal faults, some of these systems merged to form the main basin-bounding faults.

Strain then migrated towards the basin axis forming younger, low angle domino-fault arrays, associated with the progressive localization of rifting into the area of the future breakup (Figure 3-9a,b,c). This along-strike variability in fault geometry and sedimentary architecture reflects specific kinematics of basin opening. Several studies have proposed models to explain formation and evolution of V-shaped basins (e.g., Le Pourhiet et al., 2018; Lundin et al., 2014; Nirrengarten et al., 2018; Taylor et al., 1995; Zhou et al., 1995). Some models refer to a "scissor-like" opening (e.g., Hey et al., 1980), whereas other invoke a rift propagation or "zipper-slider" opening style, where the tip point of extension initiates in one area to then "jumps" (e.g., Taylor et al., 1995) or progressively migrate along with further rift propagation (e.g., Martin, 1984; Vink, 1982). The analysis of oceanic crust magnetic isochrons provides key information for the identification of propagation mechanisms, as it may reveal the diachronous development of oceanic crust younging towards the pole of rotation, thus allowing the reconstruction of its evolutional pattern (e.g., Franke, 2013; Lundin et al., 2014). The three-dimensional modelling of Le Pourhiet et al. (2018) simulates various scenarios for the opening mechanism of the V-shaped South China Sea basin, showing that a "scissor-like" model contradicts evidence from magnetic isochrons and conjugate margin structure, whereas previous studies invoked such a mechanism for this back-arc opening (e.g., Zhou et al., 1995). Recent studies have investigated the Southern North Atlantic basins to understand the partitioning and propagation of deformation, proposing a modified version to the model of oceanic propagation (e.g., Martin, 1984) by introducing the idea of segmented propagation controlled by the presence of transform faults (Nirrengarten et al., 2018).

Our observations of along-strike variations in temporal and spatial patterns of extension show clear evidence for rift propagation, associated with progressive basin opening. Although it is generally assumed that the EBSB opened around a "fixed" rotation pole located in Crimea (e.g., Okay et al., 1994), thus implying a "scissor-like" opening kinematic, sediment distribution and fault patterns seem to indicate that the tip of the propagator could have migrated in time from SE to NW. To test this idea, detailed three-dimensional mapping of the fault distribution and of the deep sedimentary sequences is required in order to date the migration of deformation across the basin (e.g., Péron-Pinvidic et al., 2007). The sparse coverage of our dataset in some areas precludes such mapping. A lack of clear seafloor spreading anomalies over the inferred oceanic domain (e.g., Graham et al., 2013; Spadini et al., 1996) also limits our ability to constrain the timing of propagation in this area. Our observations provide initial spatiotemporal markers to constrain models of EBSB rifting and continental breakup, but ultimately more closely spaced profiles of similar quality, or even 3D seismic datasets, will be required to determine exactly how the rift propagated.

This study highlights the similarity of EBSB evolution to that of rifted margins (e.g., Iberia-Newfoundland and Brazil-Angola margins - Brune et al., 2017; Reston et al., 1996; Tucholke &

Sibuet, 2007), back-arc basins (e.g., Tyrrhenian basin - Prada et al., 2015; Aegean Sea, Japan Sea and Yamato Basin - Jolivet et al., 1994, 1999; South China Sea - Lei & Ren, 2016; Woodlark Basin - Taylor et al., 1995), and rift basins elsewhere (e.g., Gulf of Suez - Gawthorpe et al., 2003; North Sea - Cowie et al., 2005), making the EBSB a case study for understanding the processes driving the evolution of extensional basins on a global scale.

3.6 Conclusions

Based on the interpretation of long-offset seismic reflection profiles, we conclude:

- Overlying the EBSB rifted basement, up to 3 km of Late Cretaceous syn-rift deposits (S1 and S2) record an initial localised extension over the structural highs (S1), followed by rift migration towards the basin axis (S2).
- Strain initiated along isolated high angle normal faults (30-70° dip) over the structural highs. Some faults coalesced forming the large systems bounding the ridges (Rift Stage 1). Strain then propagated downslope towards the basin axis, forming closely spaced domino-style fault arrays characterised by lower dip angles (15°-25°). Stratigraphic contacts show that these fault arrays are younger and they sometimes affect shallower stratigraphic levels (up to S5a), recording the process of strain localisation and basinward propagation (Rift Stage 2).
- Three main unconformities are identified: i) the rift-onset unconformity (U1) represents the initiation of Upper Cretaceous extension, ii) an intermediate rift unconformity (U2) records the migration of strain and the basinward younging of the syn-rift infill and normal faulting, iii) the breakup unconformity (U3) (Upper Cretaceous-Palaeocene(?)) records breakup initiation and spreading in the SE.
- Above the breakup unconformity (U3), up to 4-4.5 km of Palaeocene(?)-Eocene and Oligocene deposits (S3-S4 and S5a) show an intermediate character between syn-rift and post-rift, recording the diachronous distribution of syn-kinematic and breakup processes across the EBSB. Stratigraphic and structural evidence within these units shows extension up to Oligocene time, in the NW area and along the main basin-bounding faults. In the central and SE part of the EBSB, the post-rift character of these units confirms that localised breakup may have occurred before their deposition, and thus at the Upper Cretaceous-Palaeocene (?) boundary, synchronous with extension in the NW.
- The diachronous evolution of the EBSB is typical of well-studied rifted margins worldwide and provides further evidence for the need to consider continental breakup as a fully three-dimensional process that is poorly represented by a single transect.

Chapter 4 Integrated geophysical characterization of crustal domains in the Eastern Black Sea

Abstract

Rifting may lead ultimately to continental breakup, but the identification and characterization of the resulting crustal distribution remains challenging. Also, spatial and temporal changes in breakup magmatism may affect the geophysical character of the newly formed oceanic crust, resulting in contrasting interpretations of crustal composition and distribution. In the Eastern Black Sea Basin (EBSB), the evolution from rifting to breakup has been long debated, with several interpretations for the distribution of stretched continental and oceanic crust. We interpret basement morphological variations from long-offset seismic reflection profiles, highlighting a NW-SE transition from faulted and tilted continental blocks, to a rough and then smoother basement. We model magnetic anomalies to constrain further the various basement domains, and infer the presence of a weakly-magnetized, stretched continental crust in the NW, and a 0.4-3.8 A/m layer coinciding with the smooth basement in the central and SE area. We conclude that the EBSB oceanic crust extends further to the NW than was suggested previously from an abrupt change in crustal thickness and lower-crustal velocity. The apparent discrepancy between these different types of geophysical evidence may result from changes in magma supply during breakup, affecting thickness and velocity structure of the resulting oceanic crust.

4.1 Introduction

Observations of the structure and composition of the basement underlying rifted margins can unravel the geodynamic processes driving their formation. High-quality, 2D/3D regional seismic datasets provide insights into basement structures and sediment filling within the distal part of the margin, thus helping geodynamic reconstruction (e.g., Tucholke et al., 2007; Haupert et al., 2016). In deep-water and thick sedimentary infill settings, and when the basement is neither exposed nor sampled by well data, our ability to interpret rifting and breakup features and basement structures is limited. Particularly in these cases, refraction seismic (e.g., Dunn and Martinez, 2011) and potential field data (e.g., Ball et al., 2013) can be used to investigate the nature of the crust, its thickness and velocity structure, and the amount of magmatism contributing to its formation (e.g., Franke, 2013). Only a few studies integrate these approaches (e.g., Prada et al., 2014; Tugend et al., 2015).

In the Eastern Black Sea Basin (EBSB), interpretations of different datasets commonly disagree. Crustal thickness and lower-crustal velocities from wide-angle seismic data define a small area of oceanic crust to the SE of the basin (Shillington et al., 2009). Evidence for hummocky basement structures along seismic reflection profiles suggest a narrow and elongated oceanic crust extending further NW (Nikishin et al., 2015). Gravity modeling has also been used to define crustal boundaries, with different results (e.g., Graham et al., 2013) (Figure 4-1). Therefore, although it is generally agreed that the EBSB formed as an Upper Cretaceous-lower Cenozoic back-arc basin (e.g., Finetti et al., 1988; Okay et al., 1994), its crustal distribution is still debated.

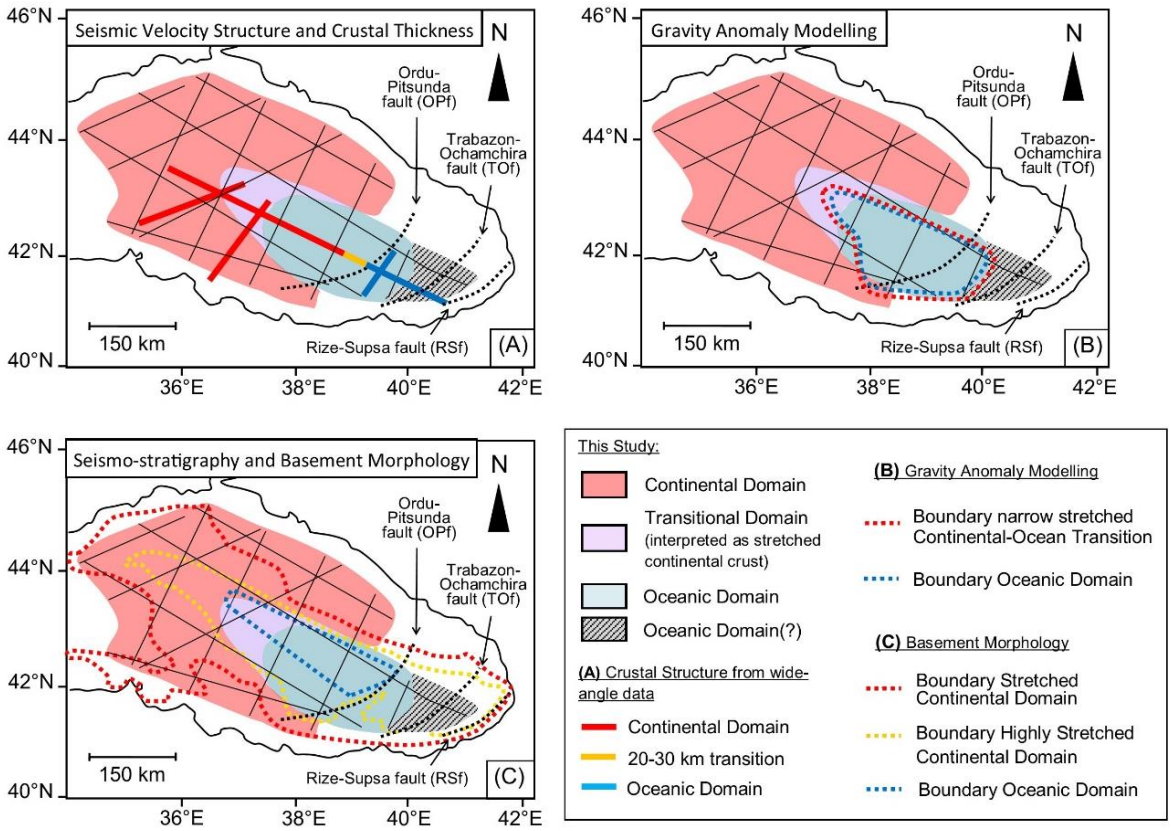

Figure 4-1. Comparison between crustal domain boundaries inferred in this study and crustal distribution from other studies using: (A) crustal thickness and lower crustal velocities from wide-angle seismic data (Shillington et al., 2009); (B) gravity anomaly modelling constrained by 2D long-offset seismic reflection profiles (Graham et al., 2013); (C) 2D long-offset seismic reflection profiles interpretation (Nikishin et al., 2015). Note that the extent of oceanic and transitional domains, and the nature of the transition, varies from study to study. In (A), an abrupt, 20-30 km transition from stretched continental to thick oceanic crust is attributed to an along-axis change from magma-poor to magma-rich margin (Shillington et al., 2009); in (B), an extremely abrupt transition zone surrounds the interpreted oceanic domain, and is associated to a ribbon of continental crust intruded by magmatic rocks (Graham et al., 2013); in (C), a wide area

of highly-stretched continental crust constitutes the transition to a narrow and elongated, NW-SE-trending oceanic domain (Nikishin et al., 2015). Background colors and colors used to plot crustal distribution/boundaries are explained in the legend. Black lines on each map represent the GWL seismic profiles used in this study and used also by Graham et al. (2013) and Nikishin et al. (2015).

New long-offset seismic reflection profiles, acquired in 2011 by *Geology Without Limits* (GWL) and ION GXT (Figure 4-1-Figure 4-2; section 2.1), allowed Monteleone et al. (2019) to define the spatial and temporal distribution of extension and breakup processes in the EBSB (Chapter 3). Here, we build on that analysis using additional data to untangle the lack of consensus on the EBSB crustal distribution. We first differentiate crustal domains based on basement morphological changes and the interaction between basement structures, stratigraphic and structural elements visible from long-offset seismic reflection profiles. We then apply magnetic anomaly modeling constrained by our seismic interpretation to investigate the magnetisation character of the seismically identified domains, using the Earth Magnetic Anomaly Grid (EMAG2-v3) over the EBSB region (Meyer et al., 2017) (Figure 4-2; see Appendix B, Figure B- 1 to Figure B- 6), and assuming a 1 km-thick magnetized layer below the top of the interpreted seismic basement (see section 4.2.2). Magnetic data have been previously used in the Black Sea to define the age of basin opening (Kazmin et al., 2007), crustal scale structures and faulting (Starostenko et al., 2015), and the thermal structure of the lithosphere (Starostenko et al., 2014), but no modeling has been attempted yet to define crustal composition.

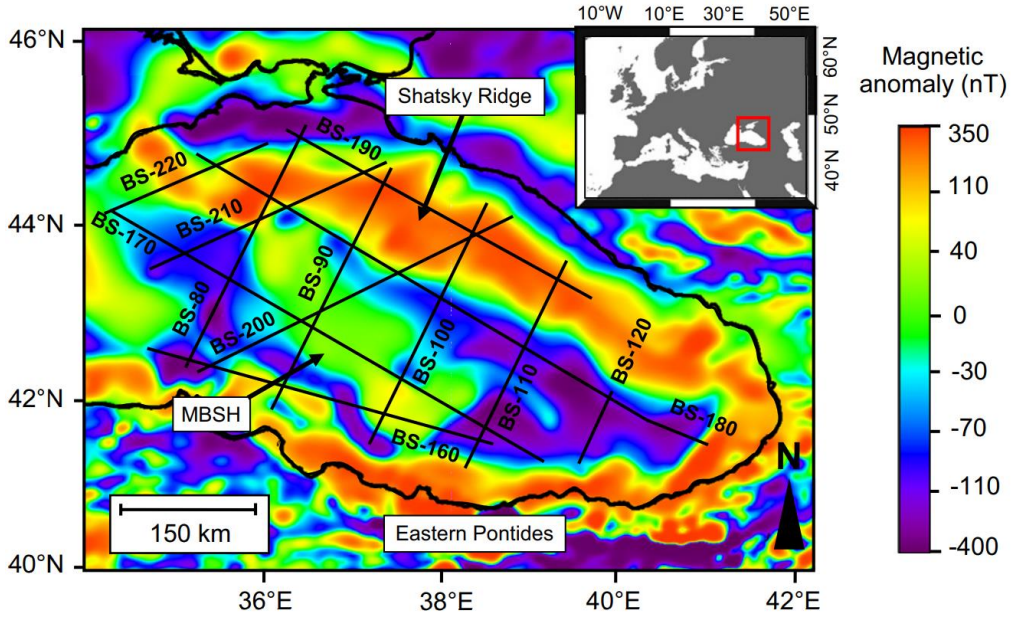

Figure 4-2. Reduced-to-pole magnetic anomaly map (EMAG2-v3; Meyer et al., 2017) for the EBSB region. Black lines mark GWL seismic profiles. Prominent positive anomalies

correspond to the Shatsky Ridge, the Mid Black Sea High (MBSH), the Eastern Pontides magmatic arc, and contrast with the negative anomaly of the central basin.

Our results show a NW-SE change in morphological and magnetic character of the EBSB basement. Our inferred oceanic domain extends into a region where the presence of thinned continental crust was previously inferred from the seismic velocity structure. We relate our new interpretation to along-axis changes in breakup kinematics and magma supply during spreading.

4.2 Method

4.2.1 Magnetic anomaly data

We used the Earth Magnetic Anomaly Grid (EMAG2-v3, www.NOAA.gov) over the EBSB region (Figure 4-2, Figure B- 1), which is specified as a 2-arc-minute resolution grid of the total intensity magnetic anomaly at an altitude of 4 km above mean sea level, and it is compiled from satellite, marine, aero-magnetic and ground magnetic surveys (Meyer et al., 2017).

A reduction-to-pole (RTP) transform was applied to the magnetic anomaly grid. RTP reduces the magnetic anomalies to the pole and corrects for variations in inclination and declination over the study area (Baranov, 1957). Declination, inclination, and magnitude of the modern Earth's magnetic field were taken according to IGRF field (Thebault et al., 2015). RTP was applied to the total intensity magnetic map using a declination of 6° and an inclination of 61° at the center of the EBSB.

4.2.2 Magnetic anomaly modelling

Inverse modeling of magnetic anomalies is generally used when well-defined constraints are available (e.g., Parker and Huestis, 1974; Russell and Whitmarsh, 2003). Such inverse models result in calculated anomalies that match closely those observed, including those resulting from 3D effects, and inverse models of 2D profiles will not normally match at profile crossings. To avoid over-fitting the data, and to ensure that models of crossing profiles are consistent with each other, we use a forward modeling approach. Due to the inherent non-uniqueness of such forward models, we kept them simple and made no attempt to produce perfect fits of the observed anomalies. Such a forward modeling approach has been used commonly along continental margins elsewhere (e.g., Bronner et al., 2011; Rippington et al., 2015).

Forward modelling was undertaken using Geosoft software, Oasis Montaj V9.4 along the seismic profiles. These models were built from SEG-Y files of the seismic data and modelled against the gridded potential field data sampled along the corresponding sections. Our 2D models assume that

there are no variations perpendicular to the profiles. However, because the observed anomaly results from 3D effects, we include the anomaly variations within about 15 km either side of the magnetic profiles (grey bands; Figure 4-3 and Appendix B). The choice of a 15 km range is due to the high geological variability perpendicular to the magnetic profiles. Ranges > 15 km would introduce anomaly trends from different crustal structures domains, especially along the NW-SE-trending profiles.

Magnetic anomaly profiles were extracted from the RTP EMAG2-v3 grid and used to complement seismic sections (Appendix B). Modelling was constrained by the top basement reflection interpreted from seismic data. Because the sedimentary cover has a very low magnetisation in the Black Sea region (e.g., Ross, 1978), modelling was done considering the upper boundary of the magnetized layer to coincide with the top basement. Crustal layers and magmatic bodies modelled along the top basement were assumed to have attained their magnetisation during the Upper Cretaceous and/or lower Cenozoic (e.g., Nikishin et al., 2015) at approximately their present latitude, so no paleo-latitude correction was applied in this study. No susceptibility data are available for the central EBSB, and little information is available from values of magnetic susceptibility of adjacent onshore samples (e.g., Rangin et al., 2002; Hippolyte et al., 2010). Thus, we were guided by average values of magnetisation estimated for different type of magnetized rocks (e.g., Hunt et al., 1995).

We started with the simplest possible model characterized by a non-magnetized sedimentary layer and a uniformly and weakly-magnetized crustal layer (0.05 A/m). For crustal thickness (top basement to Moho depth), we used results from both wide-angle data (Shillington et al., 2009) (Figure B- 7) and gravity modelling (Graham et al., 2013). Studies of the Curie temperature (578° C - temperature above which magnetite loses its magnetic properties) in the Black Sea region show that the Curie depth is reached mainly below Moho but sometimes above it, in a depth range of 24-36 km (e.g., Starostenko et al., 2014; Aydin et al., 2005; Maden, 2013). Since we are mostly concerned with regions where the Moho is shallower than 24 km, we assumed in this initial model that all the EBSB crust is magnetized.

A crustal magnetisation of 0.05 A/m had a limited contribution to the calculated anomaly and the observed anomaly was mostly determined by higher magnetisations near the top of basement. Magnetic modeling is usually performed either assuming a fixed value of magnetisation and a variable thickness for the magnetized layer, or a fixed layer thickness and variable magnetisation intensities along it (e.g., Banerjee, 1984). In the EBSB, there are no available independent constraints on the thickness or the intensity of magnetic sources. Our strategy was to find a simple model that could be mechanistically justified and was able to simulate the observed magnetic

anomaly. We limited the magnetisations to values representative of felsic to mafic igneous rocks (0.2-5.0 A/m; e.g., Hunt et al., 1995) and assumed a constant-thickness magnetized layer subdivided into bands/blocks of variable magnetisation, with its top coinciding with the seismically-inferred basement. This type of approach is common, particularly at rifted continental margins (e.g., Banerjee, 1984; Bronner et al., 2011; Collier et al., 2017). In oceanic domains, magnetic layer thicknesses of 0.5 km (e.g., Hussenoeder et al., 1996; Searle et al., 2010), 1.0 km (e.g., Ozima et al., 1974; Searle et al., 1998), 1.5 km (e.g., Bronner et al., 2011), or 2.0 km (e.g., Collier et al., 2017) are generally used. Changes in magnetized layer thickness will affect the intensity of the magnetisation inferred (almost inversely proportional to thickness) but will change little the overall trend of the modeled anomaly (e.g., Parker and Huestis, 1974). In this study, we exclude thin magnetized layers of a few hundred meters that would require anomalously high magnetisations to model the observed anomaly. We use a 1 km-thick layer in the oceanic domain because it is consistent with similar work elsewhere and allows us to generate a model with reasonable magnetisations.

Since no independent constraints are available on the thickness of the magnetized layer over the structural highs (Shatsky Ridge and MBSH), and because these areas are only modeled to provide lateral constraints for the central basin magnetic model, we decided to keep the same constant layer thickness in order to generate a simple and consistent model along the profiles.

Volcanic bodies imaged in seismic reflection data (e.g., Nikishin et al., 2003, 2015), and high-density bodies interpreted from gravity modelling (e.g., Starostenko et al., 2004), helped to constrain the distribution of these magnetized bodies and those along the basin margins during the main rifting phase. Based on these assumptions, we updated the starting model to fit adequately the observed field.

4.2.3 Magnetic anomaly filtering

A low-pass filter was applied to the calculated anomaly to remove wavelengths shorter than a specified cut-off, thus removing the result of a short-wavelength crustal anomalies such as those caused by local variations of the top basement horizon picked along seismic profiles. We chose a low-pass wavelength cut-off of 25 km. This cut-off allows us to remove some short-period oscillations from the calculated anomaly without removing lateral variations that fall within the wavelength of the observed anomaly. A cut-off > 25 km was observed to remove information resolved by the magnetic anomaly grid (Figure 4-3).

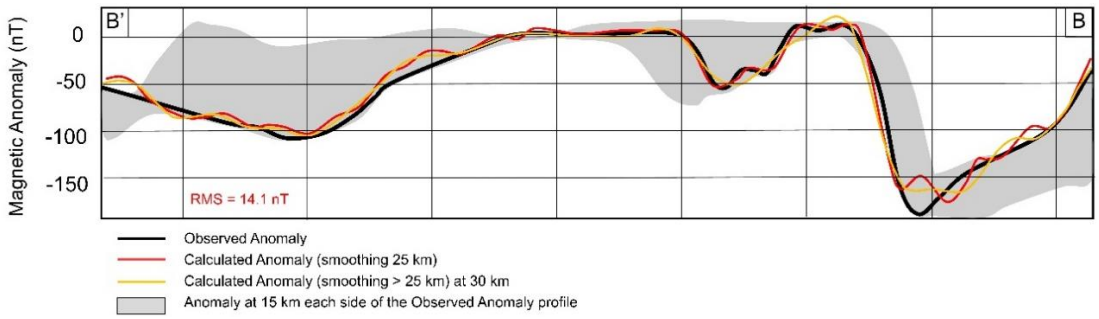

Figure 4-3. Magnetic anomaly modelling along seismic profile bs-170 (Figure B- 1; B-B'). A smoothing > 25 km over the calculated anomaly removes some of the features resolved by the observed anomaly.

4.2.4 Method limitations and data dependency

The non-uniqueness of the potential field problem requires introducing assumptions such as simplification of geometry, limits to size or depth, and range limits on susceptibility/magnetisation values (Paterson and Reeves, 1985). Interpretation of magnetic anomaly may be ambiguous, as any given anomaly could be caused by several possible sources. For example, the amplitude and shape of an anomaly produced by a large body at great depth can be similar to that of a small body closer to the surface. Changes in depth, shape, and position of the top basement horizon picked from seismic profiles and used as top boundary for the model creation can also affect the resulting calculated anomaly. In addition, attempting to model gridded magnetic data in 2D neglects the fact that the observed data could be affected by features out of the plane of the modeled section (3D effects) that make fitting these data very difficult at some locations (e.g., Rippington et al., 2015).

Despite all its limitations, 2D forward magnetic anomaly modeling can provide a quantitative perspective to features visible on seismic data and aid the interpretation in areas where seismic imaging is difficult. The non-uniqueness of the magnetic problem can be reduced in several ways. For example, having an even distribution of seismic lines across the area helps ensuring that any interpretation made on either the seismic or magnetic datasets can be calibrated to and constrained by the other. By interpreting features that fit both independent datasets we can increase the confidence in that interpretation. Also, geological knowledge and literature information is required to produce a reasonable set of modelling parameters.

Here, magnetic anomaly modelling allows us to estimate regional scale variations in the magnetisation character of crustal elements without specifically correlating small wavelength anomalies to a precise causative body. Although any conclusion inferred from magnetic modelling is strongly model dependent, because of the ambiguity in crustal affinity at the center of the EBSB

shown by seismic reflection and refraction data, our magnetic modelling results provide additional and effective insights into crustal affinity and distribution in the center of the EBSB.

4.3 Results and discussion

4.3.1 Seismic interpretation and magnetic anomaly modelling

We identify the EBSB basement as the most continuous seismic reflection underlying the sedimentary infill, showing a variable morphological and structural character (Figure 4-4). Over the structural highs (Shatsky Ridge and MBSH) and within the narrow NW rift, the basement is affected by normal faults generating half-graben structures bounded by faulted and tilted crustal blocks overlain by clear wedge-shaped syn-rift deposits (Figure 4-4B). These elements are typically associated with stretched continental basement (Domain I; Figure 4-4A, B). In this area, the observed magnetic anomaly is best fit by a weakly-magnetized layer (< 0.4 A/m), also suggesting a continental nature for Domain I, bounded by two highly magnetized layers corresponding to mafic magmatism over the Shatsky Ridge and MBSH (Starostenko et al., 2004; Nikishin et al., 2015) (Figure B- 1). Previous results from wide-angle seismic data support this interpretation (Figure 4-4A).

Seaward of Domain I, the basement has relief of similar magnitude but with no evidence for extensional faulting, nor clear syn-rift deposits (Figure 4-4C). This basement extends 70-80 km along-axis, and from its distinctive morphological character we interpret it as a separate crustal domain (Domain II; Figure 4-4A, C). This rough basement was interpreted by Nikishin et al. (2015) as having oceanic affinity. Rough basement may result from slow seafloor spreading (e.g., Malinverno, 1991), or mantle exhumation processes (e.g., Sauter et al., 2018). The observed magnetic anomaly along Domain II is best fit by a weakly-magnetized layer, suggesting a continental rather than oceanic nature (Figure 4-4C; Figure B- 2, Figure B- 3, Figure B- 4). Although we cannot rule out the presence of exhumed mantle, which also may have rather weak magnetisation (e.g., Sibuet et al., 2007), seismic velocities suggest the presence of highly stretched continental crust in this area (Figure 4-4A).

The rough basement of Domain II becomes smoother towards the central and SE part of the EBSB where well-layered, post-rift deposits are predominant (Domain III; Figure 4-4D, E; Figure B- 5, Figure B- 6). No extensional faults are visible from seismic data, although high-angle NE-SW-trending transform faults are present (Figure 4-4A, E). Along some profiles, volcano-like structures have been interpreted as evidence for enhanced magmatism in this area (Nikishin et al., 2015) (Figure 4-4A; Figure B- 6). Smooth basement with extrusive volcanic material may relate to anomalously thick and/or fast spreading oceanic crust (e.g., Small, 1994; Searle et al., 2010),

exhumed mantle (e.g., Pickup et al., 1996), or thinned continental crust overlain by basaltic flows (e.g., Zhao et al., 2016). At Domain III, magnetic anomaly data are best fit with negatively magnetized layers with intensity bands between 0.4 and 3.8 A/m, in contrast to the weakly magnetized Domain II (< 0.4 A/m) (Figure 4-5; Figure B- 1), thus providing evidence against continental crust or exhumed mantle. Serpentinized exhumed mantle may be significantly magnetized (e.g., Sibuet et al., 2007), but its presence is excluded based on crustal seismic velocities (Shillington et al., 2009).

Our seismic interpretation and magnetic anomaly modeling results support the presence of smooth and magnetized oceanic crust along Domain III (Figure 4-4, Figure 4-5; Figure B- 1 to Figure B- 6). However, wide-angle data (Shillington et al., 2009) indicate the presence of a thin crust (7-9 km) with low lower-crustal velocities (6.4-6.6 km/s) in the NW, and of a thick crust (11-13 km) with high lower-crustal velocities (6.8-7.2 km /s) in the SE. This change in crustal structure occurs close to the Ordu-Pitsunda transform fault (OPf) (Tari et al., 2018), within Domain III (Figure 4-4A, E). Shillington et al. (2009) interpreted this change as a transition from highly stretched continental (NW) to thick oceanic (SE) crust (Figure 4-4A), an interpretation inconsistent with the uniform magnetisation character of Domain III.

Our results show that a good fit along profile bs-110 (Figure 4-2), over crust interpreted as continental by Shillington et al. (2009), is obtained with magnetisations of 0.8-3.2 A/m over the Shatsky Ridge and 0.16 A/m towards the Pontides magmatic arc (Figure 4-5; Figure B- 6). In the central EBSB, the observed anomaly is best fit by a ~ 125 km-wide, negatively magnetized layer, with intensity bands between 1.1 and 3.8 A/m (Figure 4-5; Figure B- 6Figure B- 6). Similar results are obtained along profile bs-100 at the NW end of Domain III, and profile bs-120 at the SE end of Domain III where the velocity structure is clearly oceanic (Figure 4-4A; Figure B- 1, Figure B- 5). NW-SE profiles also show negative magnetisation of 0.4-2.8 A/m along Domain III (Figure B- 1). Although it is possible that magnetic anomalies NW of the OPf are caused by syn-rift magmatic intrusions through thinned continental crust (Starostenko et al., 2004), their intensity, overall continuity, and similarity to anomalies in the oceanic domain to the SE, support their formation by seafloor spreading. Thus, Domain III has a smooth and highly magnetized basement resembling that of oceanic crust, extending the EBSB oceanic domain farther NW than previously inferred from wide-angle data (Figure 4-4A; Shillington et al., 2009). Gravity modeling also supports a more extended oceanic domain, with boundaries comparable to those from our results (Graham et al., 2013) (Figure 4-1B). Crustal thickness and velocity structure are usually reliable parameters to discriminate crustal composition in extensional settings (e.g., Prada et al., 2014). However, observations from wide-angle data and magnetic anomaly modeling suggest contradicting results

on crustal distribution in the EBSB. Here we explain this apparent contradiction based on the tectono-magmatic evolution of the EBSB.

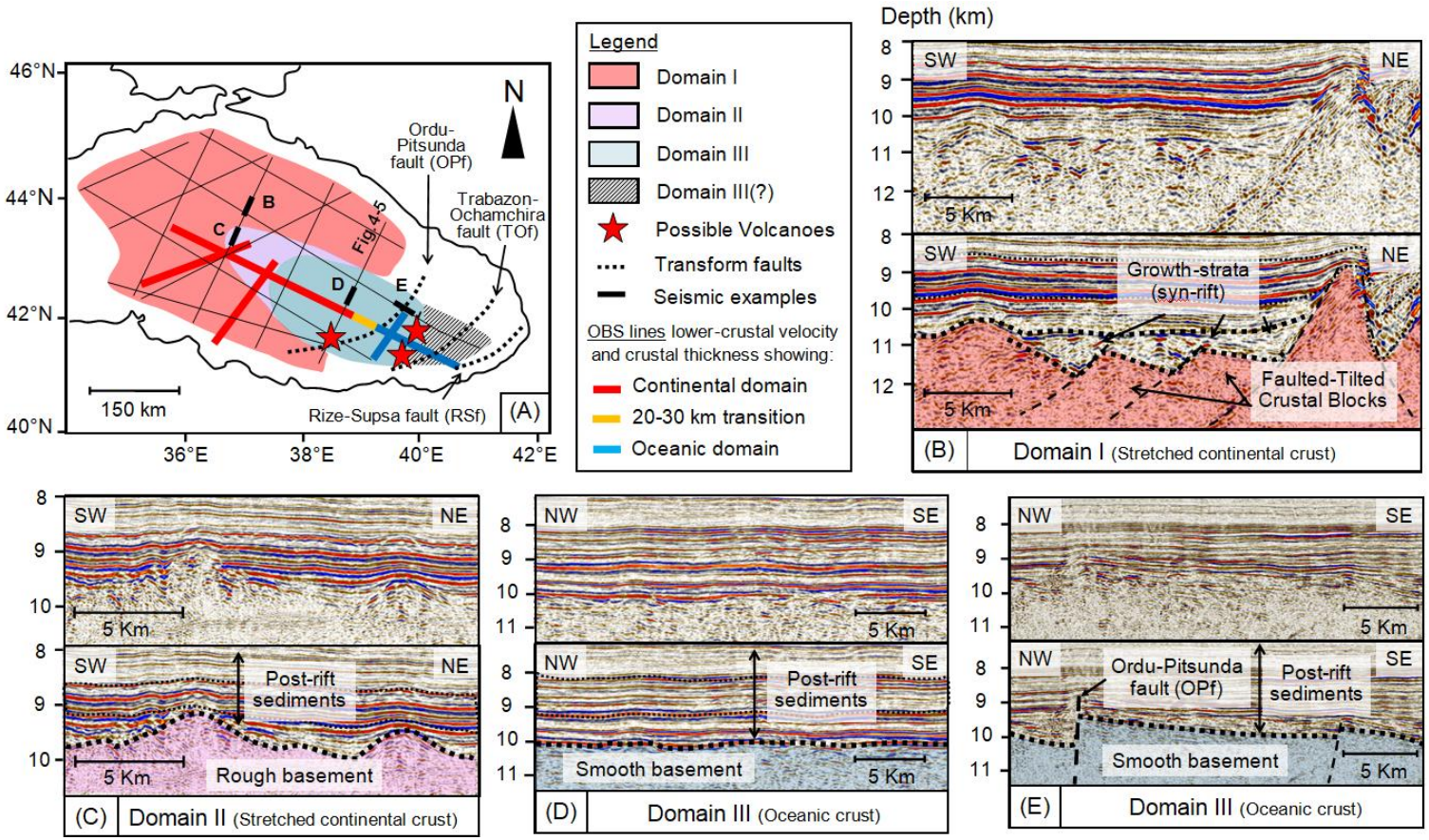

Figure 4-4. Summary of the basement morphology and distribution across the EBSB based on seismic interpretation. (A) Map of the identified crustal domains (Domain I, II and III). Overlain on map are the locations of GWL seismic profiles (thin black lines), the sections shown in B-E (thick black segments), and wide-angle seismic profiles (thick coloured lines) (Shillington et al., 2009). Color code for the wide-angle lines shows the crustal distribution interpreted by Shillington et al. (2009).

OBS – ocean-bottom seismometer. Possible volcanoes (red stars) are identified within Domain III (Nikishin et al., 2015). Transform faults interpreted in the SE of the basin are named after Tari et al. (2018). To the SE, we have insufficient data to constrain the seismic character in Domain III(?). (B) Domain I - tilted and faulted crustal blocks. (C) Domain II - rough basement with no extensional faulting nor syn-rift deposits. (D) Domain III - smooth basement with no extensional faulting. (E) Domain III - smooth basement affected by high-angle transform faults; thick vertical dashed line shows the location of the Ordu-Pitsuda fault (OPf).

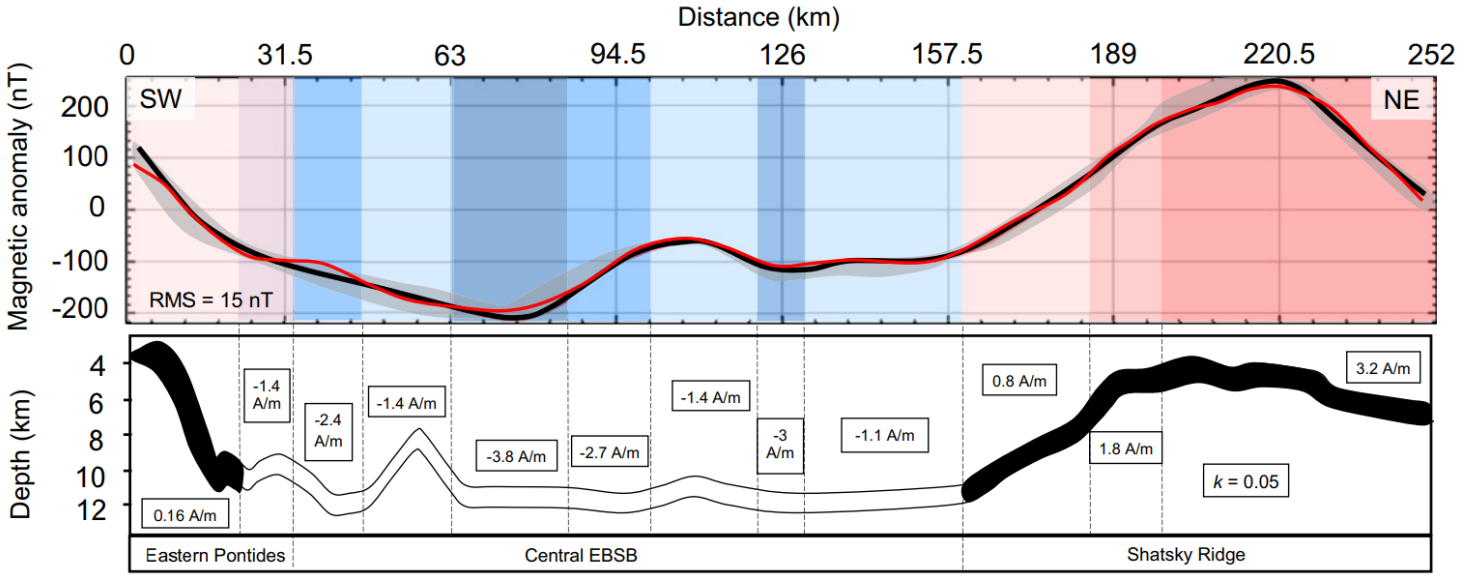

Figure 4-5. Magnetic anomaly modeling along profile bs-110 (location shown in Figure 4-2, Figure 4-4A and Figure B- 1). Top panel displays a comparison between calculated (red line) and observed (black line) anomalies. Root-mean-squared (RMS) error between observed and calculated anomaly is shown at the bottom left corner. Grey band represents anomaly variations 15 km to either side of the profile. Colored backgrounds show the lateral extent and intensity (dark - high intensity; pale - low intensity) of magnetized layers: pink - continental domain; blue - oceanic crust. Bottom panel shows model generating the calculated anomaly and the magnetisation for each layer. The source of the magnetic anomalies was assumed to lie within a 1 km-thick layer with the given intensity of magnetization (in A/m). Black blocks are normally magnetized. The susceptibility (k) value used for the continental crust is also shown.

4.3.2 Tectono-magmatic evolution

The EBSB rotational opening resulted in a V-shaped basin with increased extension to the SE (Okay et al., 1994; Shillington et al., 2008). Analytical and numerical models of V-shaped basins show that, as rifting propagates, stretching increases with distance from the pole of rotation, and breakup initiates away from the pole, propagating towards it and into stretched continental lithosphere (e.g., Vink, 1982; Le Pourhiet et al., 2018). As spreading progresses, spatial and temporal variations in magmatic crustal accretion driven by mantle temperature, strain localization, and spreading rates can influence the emplaced crustal structure and its geophysical character (Franke, 2013). Changes in crustal structure within Domain III may reflect along-axis changes in magmatism (e.g., Muller et al., 1999; Hooft et al., 2000), and/or variations in melt supply over time (e.g., Tucholke et al., 1997; Cannat et al., 2003). Such changes would mainly cause variations in oceanic Layer 3 thickness (e.g., Mutter and Mutter, 1993; Grevemeyer et al., 2018). Oceanic Layer 2, characterized by lower seismic velocities (e.g., Mutter and Mutter, 1993) and considered to be the main source of oceanic magnetic anomalies (e.g., Talwani et al., 1971), would not be much affected. An enhanced melt supply, driven by the advection of warm asthenosphere during lithospheric thinning or by the presence of a hot mantle plume (e.g., Hopper et al., 2003), can form atypically thick oceanic crust with a well-developed, high-velocity Layer 3. Lower melt supply, due to an initially cool lithosphere or conductive cooling at slow extension rates suppressing partial melting (Bown and White, 1995), would result in a thinner oceanic crust mostly characterized by Layer 2 velocities. Models of rotational basin opening suggest that a decrease in extension rates toward the rotational pole results in an along-axis reduction in the volumes of decompression melt (Franke, 2013), but do not explain the abrupt change in crustal structure at the OPf (Figure 4-4A, yellow line, Figure 4-6).

Discontinuities and/or transform faults can control magma supply along spreading segments (e.g., Fox and Gallo, 1984; Georgen and Lin, 2003), and thermal perturbation by transforms often results in a reduction in crustal thickness near the transforms (e.g., Hooft et al., 2000), resulting in anomalous oceanic crustal structure (e.g., Dunn and Martinez, 2011). Numerical models show that transfer/transform faults can act as rift propagation barriers delaying the opening of consecutive rift segments (Koopmann et al., 2014). Rift delay can affect both mantle and melt flow between segments, limiting the propagation of low-viscosity mantle across the segment boundary, and favoring melt accumulation at the opening segment (Koopmann et al., 2014). Koopmann et al.'s model predicts rift-parallel flow and concomitant magmatic peaks near the propagation barrier caused by the lateral pressure gradient between sequentially opening segments. This flow may result in abrupt changes in crustal thickness at segment boundaries matching observations from the EBSB. Thus, the OPf may have acted as a rift propagation barrier between SE and NW segments,

resulting in pooling of melt to the SE. Such a model would explain the abrupt transition from a thick oceanic crust SE of the fault, with a well-developed Layer 3, to a thin oceanic crust NW of the fault, with a thin or absent Layer 3 and velocities similar to those of thinned continental crust, but still with a distinctive magnetic character (Figure 4-6).

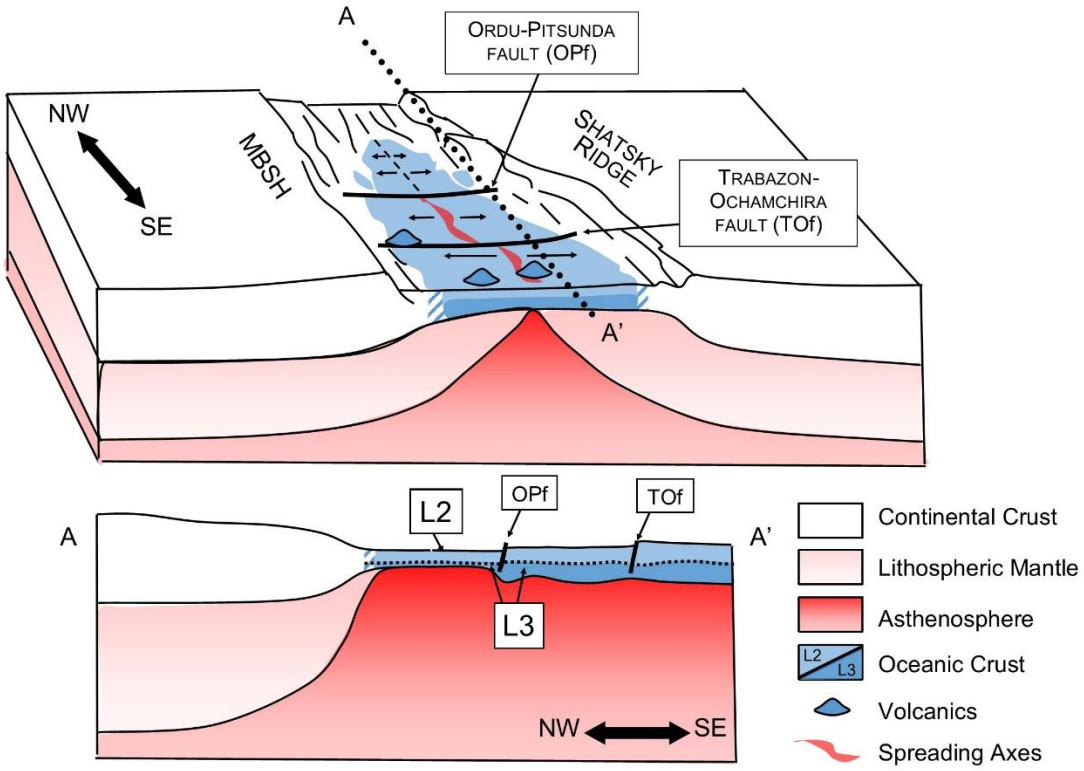

Figure 4-6. Conceptual 3D and 2D models for oceanic crustal accretion in the EBSB. After back-arc extension, breakup focused in the wider SE rift where higher amount of decompression melt and melt focusing favored the emplacement of a thick oceanic crust with a well-developed Layer 3 (L3). Some volcanoes are also visible in this area, probably extruded along fracture zones separating different spreading segments. Transform faults, particularly the OPf, acted as barriers limiting melt propagation towards the NW. In this area, a reduced supply of decompression melt and a limited melt migration from the SE segment, caused the emplacement of a thinner oceanic crust characterized mostly by the upper oceanic Layer 2 (L2). The main geophysical difference between the SE and the NW oceanic domains is the change in oceanic crustal thickness and velocity structure, related to the absence/near absence of L3 along the NW segment.

Based on these factors, we propose that the observed variations in crustal thickness and lower-crustal velocities in Domain III result from changes in oceanic crustal accretion rather than a change in crustal type. Variations in magma supply driven by the geometry of the opening rift, and the

effect of segmentation, were major controls on the basin architecture and the crustal structure at the newly emplaced EBSB crust.

4.4 Conclusions

Our results show a NW-SE change in the morphological and magnetic character of the EBSB basement. Our inferred oceanic domain extends into a region where the presence of thinned continental crust was previously inferred from the seismic velocity structure. Changes in crustal thickness and velocity structure from wide-angle seismic data within this oceanic domain (Shillington et al., 2009), previously interpreted to show oceanic crust only to the southeast of the basin, are here interpreted instead as evidence of changes in magma supply during spreading. Rift segmentation and transform faults may have played an important role in controlling the along-axis flow of mantle and melt. Initial spreading focused in the wider SE rift segment, where enhanced decompression melting and melt pooling caused the emplacement of thick oceanic crust with a well-developed layer 3. Melt propagation to the northwest was limited by transform faults, particularly the Ordu-Pitsunda fault, and/or by rift narrowing suppressing partial melting, resulting in the emplacement of a thinner oceanic crust lacking a well-developed layer 3.

This study highlights the ambiguity in the geophysical characterization of crustal type and distribution in rifted margin settings. Although large amounts of data are available, different and perhaps contradicting interpretations are possible, especially where geophysical evidence deviates from what is “normally” expected for continental and oceanic crusts. In such cases, to avoid contradicting interpretations, data comparison and integration are essential.

Chapter 5 Seismic characterisation of multiple BSRs in the Eastern Black Sea Basin

Abstract

Multiple Bottom-Simulating Reflectors (BSRs) are often interpreted as remnants of an older BSR that no longer marks the hydrate stability limit following temperature and/or pressure changes perturbing the hydrate equilibrium system, or as marking stability limits for different hydrate-forming gas compositions or different over-pressured zones. Nevertheless, their origin and formation mechanisms are not yet fully understood. Using long-offset seismic reflection data, we have identified up to four multiple BSRs (BSR0-3) within the folded sediments of the Tuapse Trough, along the NE margin of the EBSB. Here, we analyse the seismic character and extract the physical properties of these BSRs, aiming to assess their formation mechanisms. We applied downward continuation to the data, which improved refracted arrivals bringing them to closer offsets. However, the presence of a complex seafloor topography and sub-seafloor stratigraphy generates near offset noise and complicates phase recognition across lateral shot gather locations, thus limiting travel-time picking. Furthermore, downward continued first arrival refractions still result from deeper and faster events, probably obscuring shallower and slower BSR-related refractions. We developed a 2D travel-time velocity model of the sub-seafloor sediments using combined non-downward continued reflected and downward continued refracted travel-times.

The velocity model shows that the physical properties of sediments at the BSRs differ from nearby sediments. In the BSR area, the P-wave velocity (V_P) increase between seafloor and BSR0 (1.55-1.72 km/s) could be related to normal compaction, whereas the V_P increase between BSR0 and BSR1 (1.75-1.83 km/s) is higher than the V_P for sediments outside the BSR area at that depth. Beneath BSR1, a 70-80 m-thick layer including BSR2 and extending to BSR3 is associated with a V_P decrease from 1.83 km/s to 1.61-1.62 km/s. Beneath BSR3, V_P increases again. Based on an analytical model linking seismic velocity to physical properties, these V_P trends can be explained by a gas hydrate saturation of 0-4% in sediments from seafloor down to BSR0 and of 1-6% within the 100 m-thick layer of sediments with higher V_P between BSR0 and BSR1. A free gas saturation of up to 20-25% is estimated within the low-velocity zone between BSR1 and BSR3. Based on the higher hydrate saturation at BSR1 and on the free gas accumulation underneath it, we interpret this BSR to represent the present-day base of the gas hydrate stability zone (BGHSZ), consistent with the depth of the BGHSZ calculated assuming a geothermal gradient of 26-30˚C/km. The increasing hydrate saturation toward BSR1, and the free gas accumulation beneath it, can be explained by mechanisms

of methane recycling following hydrate dissociation due to pressure-temperature changes, with deeper BSRs indicating relics of past stability conditions and/or intermediate stages in GHSZ vertical shift. The localised nature of the BSR reflection and related physical properties are considered to result from combined structural and stratigraphic control favouring focused free gas flow and hydrate generation at the top of the crest structure where multiple BSRs are observed, similarl to the free gas and hydrate dynamics observed in other depositional and compressional settings.

5.1 Introduction

Gas hydrate is an “ice-like” crystalline solid composed of a cage of water molecules enclosing a gas molecule (e.g., Sloan and Koh, 2008). In the marine environment, the hydrate-forming gas primarily consists of methane generated by biogenic degradation, although heavier molecular hydrocarbons of thermogenic origin (i.e., methane, ethane, propane, butane) may also contribute to hydrate formation (e.g., Brooks et al., 1986; Sloan, 1998). Abiogenic mantle-derived methane may also provide a source of gas for hydrate formation (e.g., Hensen et al., 2015; Rusakov and Kutas, 2018). Hydrates can form where water and methane are present under medium to high pressure and low temperatures (Sloan and Koh, 2008), given the presence of sufficient water and of methane in excess of its solubility in surrounding pore waters (e.g., Klauda and Sandler, 2005; Xu and Ruppel, 1999). The maximum depth at which gas hydrate is stable, which is referred to as the base of the gas hydrate stability zone (BGHSZ), will be therefore controlled by parameters such as pressure, temperature (bottom-water temperature and geothermal gradient in the sedimentary column), salinity, gas composition (Shipley et al., 1979; Dickens and Quinby-Hunt, 1994), and pore size (e.g., Østergaard et al., 2002).

The presence of a Bottom-Simulating Reflector (BSR) in seismic reflection data is commonly interpreted as an indicator for the presence of gas hydrates in marine sediments (e.g., Shipley et al., 1979). The BSR is a distinct reflector generally characterised by a negative impedance contrast resulting from the contrast between high-velocity gas hydrate-bearing sediments above, and low-velocity non-hydrate-bearing or gas-bearing sediments directly underneath (Singh et al., 1993; Holbrook et al., 1996; Hyndman and Davis, 1992). As BSRs generally follow the BGHSZ, they are consequently sub-parallel to the seafloor, frequently crosscutting reflectors and stratigraphic sequences (Shipley et al., 1979). However, the relationship between BSRs and the presence of gas hydrate is not always clear, as changes in lithology, over-compaction of the sediments (e.g., Cook and Tost, 2014), or chemical changes during diagenesis (e.g., Berndt et al., 2004) may also result in a BSR-like reflection.

Multiple BSR-like reflections, subparallel to the seafloor but at different sub-bottom depths, have been observed along both active and passive margins (i.e., Tumbes basin offshore Peru, Auguy et al., 2017; Hydrate Ridge on Cascadia margin, Bangs et al., 2005; Nankai margin, offshore Japan, Foucher et al., 2002; North Atlantic margins, Posewang and Mienert, 1999; Four-Way-Closure Ridge off SW Taiwan, Kunath et al., 2020; Storegga Slide area on the Norwegian margin, Posewang and Mienert, 1999; Andreassen et al., 2000). These studies have presented different possible explanations for the origin of multiple BSRs. These are either considered to represent (i) remnants of an older BSR that no longer marks the hydrate stability limit and is in the process of dispersion/dissociation (transient state) following pressure and/or temperature changes (i.e., climatic, tectonic, and/or sedimentation rate variations) perturbing the hydrate equilibrium system (e.g., Foucher et al., 2002; Zander et al., 2017; Popescu et al., 2006; Bialas et al., 2020), (ii) the base of hydrate layers of different gas composition (e.g., Geletti and Busetti, 2011), (iii) top and base of the free gas zone or of the hydrate-bearing zone (e.g., Tinivella and Giustiniani, 2013; Posewang and Mienert, 1999), (iv) the boundary between overpressure compartments, which are generally observed at greater depths compared to the typical thickness of the GHSZ (e.g., Tinivella and Giustiniani, 2013), (v) resulting from a combination of recent sedimentation, tectonic uplift and/or fluid activities at subduction margins (e.g., Crutchley et al., 2019; Han et al., 2021), or (vi) unrelated to gas and gas hydrate and related to lithological and/or geochemical changes such as opal-A to opal CT transition (e.g., Berndt et al., 2004; Cook and Tost, 2014). When multiple BSRs are linked to past hydrate stability conditions, a physical explanation is needed for the paleo-BGHSZ remaining visible. It could be that gas or gas hydrate is left behind (e.g., Bangs et al., 2005; Popescu et al., 2006), or that the remnants are diagenetically induced permeability barriers that formed when the active BSR existed stably at that level for an extended period (e.g., Clennell et al., 1999).

In the Black Sea region, thermodynamic conditions combined with the semi-isolation of the basin from marine circulation and the cyclic periods of anoxia, and with the high sedimentation rates depositing large amounts of terrestrially sourced, organic-rich deposits, make this area favourable for gas hydrate generation (Vassilev and Dimitrov, 2002; Egorov et al., 2011). Abundant seepage and mud volcanoes are present along the basin's margins, and evidence of fluid accumulation and escape features on regional seismic reflection profiles (i.e., seismic blacking, gas pipes and chimneys, bright spots) are associated with the presence of biogenically sourced gas and hydrates within the shallow stratigraphic units of the Black Sea (e.g., Starostenko et al., 2010; Pape et al., 2011, 2021; Popescu et al., 2007; Egorov et al., 2011). Furthermore, thermogenic gas may be sourced from deeper stratigraphic levels, particularly from the Oligocene-lower Miocene organic-rich Maykop Formation (e.g., Simmons et al., 2018). Many previous studies have also identified the presence of seismic BSRs, most of which are located within the Danube and Dnieper delta and deep-

water fans in the Western Black Sea Basin (WBSB) (Figure 5-1). In these same locations, multiple BSRs have also been identified as mostly discontinuous seismic events limited to few areas (e.g., Popescu et al., 2007; Zander et al., 2017) (Figure 5-1). These features are predominantly interpreted to result from climatic changes (i.e., sea-level and/or temperature variations) following the LGM (e.g., Popescu et al., 2006). Borehole data analysis has shown that, at the end of the LGM (9 kyrs), the Black Sea paleo-environmental conditions consisted of a 4-5˚C cooler seafloor temperature, with a sea-level approximately 100-150 m lower than at the present-day, a 0.8-1.5 % bottom-water salinity (instead of the present-day 2.23 %), and in a slightly higher geothermal gradient of about 35 ± 5˚C/km (e.g., Zander et al., 2017; Ker et al., 2019; Bialas et al., 2020). Thus, sea level, water temperature and/or geothermal gradient changes are considered to have driven gas hydrate dissociation, causing a vertical shift in the BGHSZ and leaving behind the previous BSRs. Other factors, such as sedimentation rate/fill, with consequent re-equilibration of the sediments' temperature structure following increased lithostatic pressure due to enhanced sediment deposition, have also been considered to have contributed to multiple BSR generation (e.g., Zander et al., 2017). These perturbations have therefore resulted in a shift of the BGHSZ towards shallower depths, thus, the deeper BSRs have been interpreted as "*relics*" of the past pressure and temperature conditions, whereas the topmost BSR is associated with the present-day stability field.

In the EBSB, studies have identified the presence of single seismic BSRs along the offshore margins of Crimea, Georgia, and Turkey (Figure 5-1). The only mention of the presence of possible multiple BSRs come from a prospect by Rosneft Company and Moscow State University researchers on gas hydrates in the Tuapse Trough (Shnyukov, 2013). According to Shnyukov (2013), oil-bearing cores were recovered at several sites in the Tuapse Trough and along their sections "*three repetitive BSR boundaries of controversial nature*" have been identified. However, no other information is available on these BSRs.

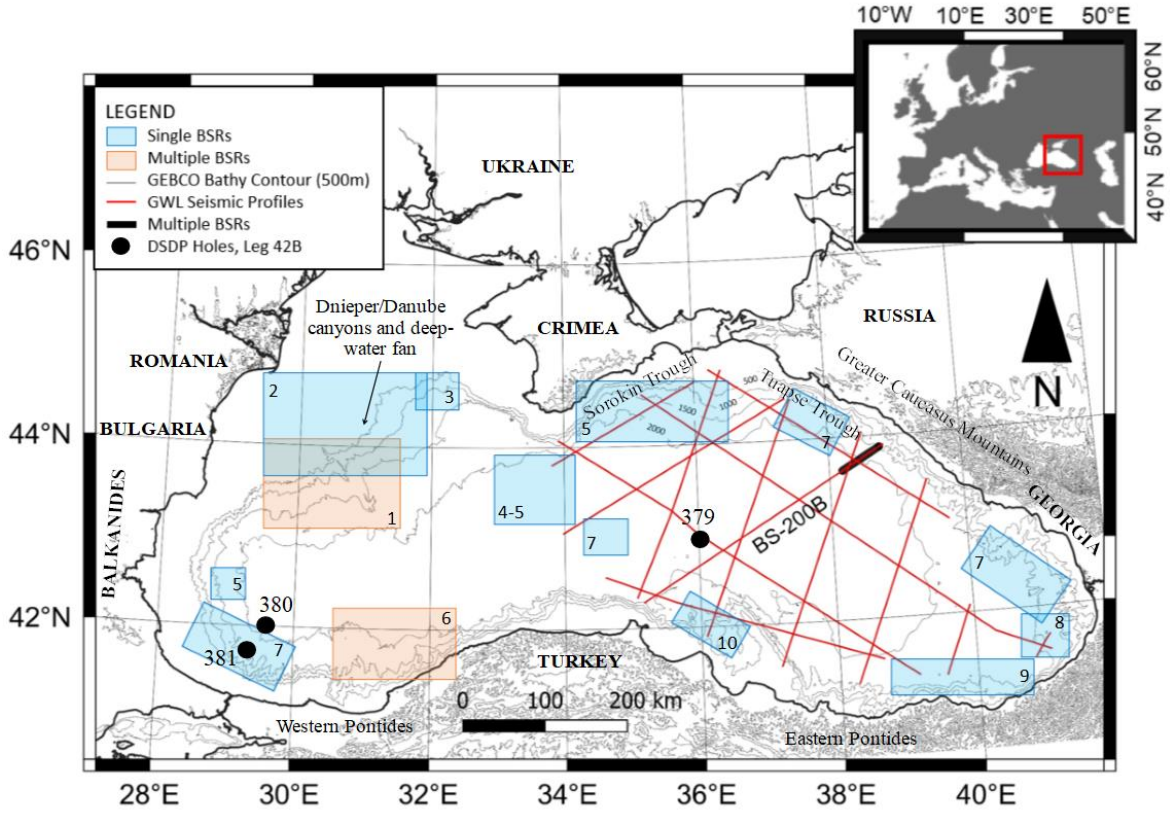

Figure 5-1. Map of the Black Sea region. Topographic and bathymetric contour lines are shown at 500 m interval (GEBCO bathymetry). A single profile (BS-200B), part of a regional seismic survey from GWL (red lines), is used in this study (Figure 5-2, Figure 5-3). The thick black segment to the NE-end of the profile shows the location of the multiple BSRs identified in this study. Numbered black circles show the DSDP Holes 379, 380 and 381 location (from Muratov et al., 1978). Boxes overlaid on map represent the locations of studies previously identifying single BSRs (blue boxes) and multiple BSRs (orange boxes) across the whole Black Sea region ([1]Zander et al., 2017, Bialas et al., 2020, Popescu et al., 2006, Gassner et al., 2019; [2]Riedel et al., 2020, Ker et al., 2019, Hillman et al., 2018; [3]Zillmer et al., 2005, Lüdmann et al., 2004; [4]Xing and Spiess, 2015; [5]Merey and Sinayuc, 2016; [6]Dondurur et al., 2013, Menlikli et al., 2009; [7]Vassilev and Dimitrov, 2002; [8]Minshull and Keddie, 2010; [9]Çifçi et al 2012; [10]Dondurur and Çifçi, 2009).

This study aims to investigate the nature of four BSRs observed, for the first time to our knowledge, within the upper Miocene-Quaternary sedimentary section of the Tuapse Trough, on the Russian margin of the EBSB (Figure 5-1, Figure 5-3). Previous work has focused on explaining the cause(s) of the shift in the BGHSZ and correspondent BSR, rather than on understanding the physical parameters making the paleo-BGHSZ still reflective. However, there are different implications for polarity/velocity contrasts depending on the mechanism responsible for the presence of multiple

BSRs on seismic data. Here, we look more closely at the physical properties associated with the seismic evidence of multiple BSRs, aiming to constrain the mechanisms linked with their generation.

The physical properties of BSR reflectors can be obtained from multichannel seismic reflection data. These are used to define a 2D compressional wave (V_P) velocity model for the shallow sediments using the travel-time forward modelling approach described by Zelt and Smith (1992). The 10.2 km-long offset recording of the seismic reflection profile used in this study, allows refracted arrivals to be imaged at far offsets within shot gathers. We apply downward continuation of streamer data to a datum closer to seafloor (Berryhill, 1979, 1984; Harding et al., 2007) aiming to bring refractions from shallower stratigraphic levels (i.e., BSRs depths) at closer offsets, thus providing valuable travel-time information for velocity modelling. Then, we compare the BSRs depths constrained by travel-time analysis against the expected depth for the present-day BGHSZ, calculated from a compilation of regional data (i.e., seafloor temperature, geothermal gradient, pore water salinity). Finally, velocities defined form travel-time analysis are used to provide an estimate of free gas and gas hydrate saturation, if any, in sediments using the gas hydrate effective-media model by Marin-Moreno et al. (2017).

Based on our results, we discuss: (i) the advantages and limitations of applying downward continuation to streamer data for shallow targets in the top few hundred meters below seafloor, (ii) the link between seismic BSRs and the physical properties of sediments and (iii) the possible nature and formation mechanisms that can explain multiple BSRs in the EBSB.

5.2 Geological setting

The Black Sea is a semi-isolated basin located between the Pontide Mountains in Turkey to the south, the Caucasus Mountains to the east, and the relatively low coastal regions of Ukraine and Balkan countries to the west (Figure 5-1). The basin is underlain by a flat, 2.0-2.2 km-deep abyssal plane that obscures two separate depocenters, the Western Black Sea Basin (WBSB) and the Eastern Black Sea Basin (EBSB). These two sub-basins formed by rifting in the hinterland of the Pontides magmatic arc as result of the subduction of Neotethyan lithosphere below the southern part of the Eurasian continental margin (e.g., Okay et al., 1994; Robinson end Kerusov, 1997; Nikishin et al., 2003; Stephenson and Schellart, 2010).

Following rifting, the Black Sea underwent rapid thermal subsidence accompanied by high sedimentation rates, which resulted in the deposition of thick sequences of mainly Tertiary sediments reaching up to 14 km in the central WBSB and up to 8-9 km in the central EBSB (e.g., Okay et al., 1994; Nikishin et al., 2003; Shillington et al., 2008). At present, the Black Sea is undergoing compressional deformation that has been active since the Eocene (Saintot et al., 2006),

or possibly the Palaeocene (Sheremet et al., 2016) time, and is related to the convergence of the Eurasian and Arabian plates. The Oligocene period is traditionally considered as the beginning of the syn-collisional (orogenic) stage forming the Caucasus mountain range to the east of the Black Sea basin, causing the uplift of some areas within tectonic units as well as the reactivation of older fault systems and the formation of inverted structures (Figure 5-2, Figure 5-3). This time also represents the onset of deposition of the Oligocene-lower Miocene organic-rich shale, formally the regional source-rock of the Black Sea basin: the Maykop Formation (Tari and Simmons, 2018). Compressive deformation has predominantly concentrated around the EBSB margins, as shown by seismic reflection data and earthquake locations (Reilinger et al., 2006). This has resulted in the folding and thrusting of the upper Miocene to Quaternary infills of the Tuapse and Sorokin troughs, which have thrusted over the shoulders of the Shatsky Ridge favoured by the presence of the more ductile Maykop units at their bottom (Figure 5-2).

This study focuses on the folded, upper Miocene-Quaternary successions of the Tuapse Trough, a 40 km-wide and 270 km-long, NW-SE-oriented trough representing the foreland basin of the Greater Caucasus thrust belt (e.g., Adamia et al., 2010; Tari et al., 2018; Vincent et al., 2007; Meisner et al., 2009; Sydorenko et al., 2017) (Figure 5-3). Its stratigraphy mainly consists of a thick sequence of Maykop shale, located at the base and squeezed in between the folded-and-thrusted upper Miocene-Quaternary units. These have been transported and deposited within the trough during the uplift of the Greater Caucasus (e.g., Meisner et al., 2009; Adamia et al., 2010; Tari et al., 2018; Vincent et al., 2007). The Tuapse Trough formed under marine conditions in lower Eocene to upper Eocene times (e.g., Tugolesov et al., 1985). Compressional uplift started at ~ 10 Ma during the upper Miocene, with the most intensive folding taking place in the last 5 Myr (Pliocene) (Milanovsky, 1991). The more ancient folds are located in the back part of the Tuapse Trough (NE), in a zone where the Tuapse Trough joins with the southern slope of the Greater Caucasus, while the youngest folds are located in the western frontal part of the trough (SW), where the Tuapse Trough joins with the Shatsky Ridge (Tugolesov et al., 1985). The sedimentary section of Tuapse Trough is, therefore, dominated by active growth of the fold system, with folds that are usually expressed as anticlines generating relief as submarine ridges up to 400–600 m high (Almendinger et al., 2011) (Figure 5-2). Growth of anticlines continues at present, with erosion of the ridges and sedimentation in isolated mini-basins (Almendinger et al., 2011).

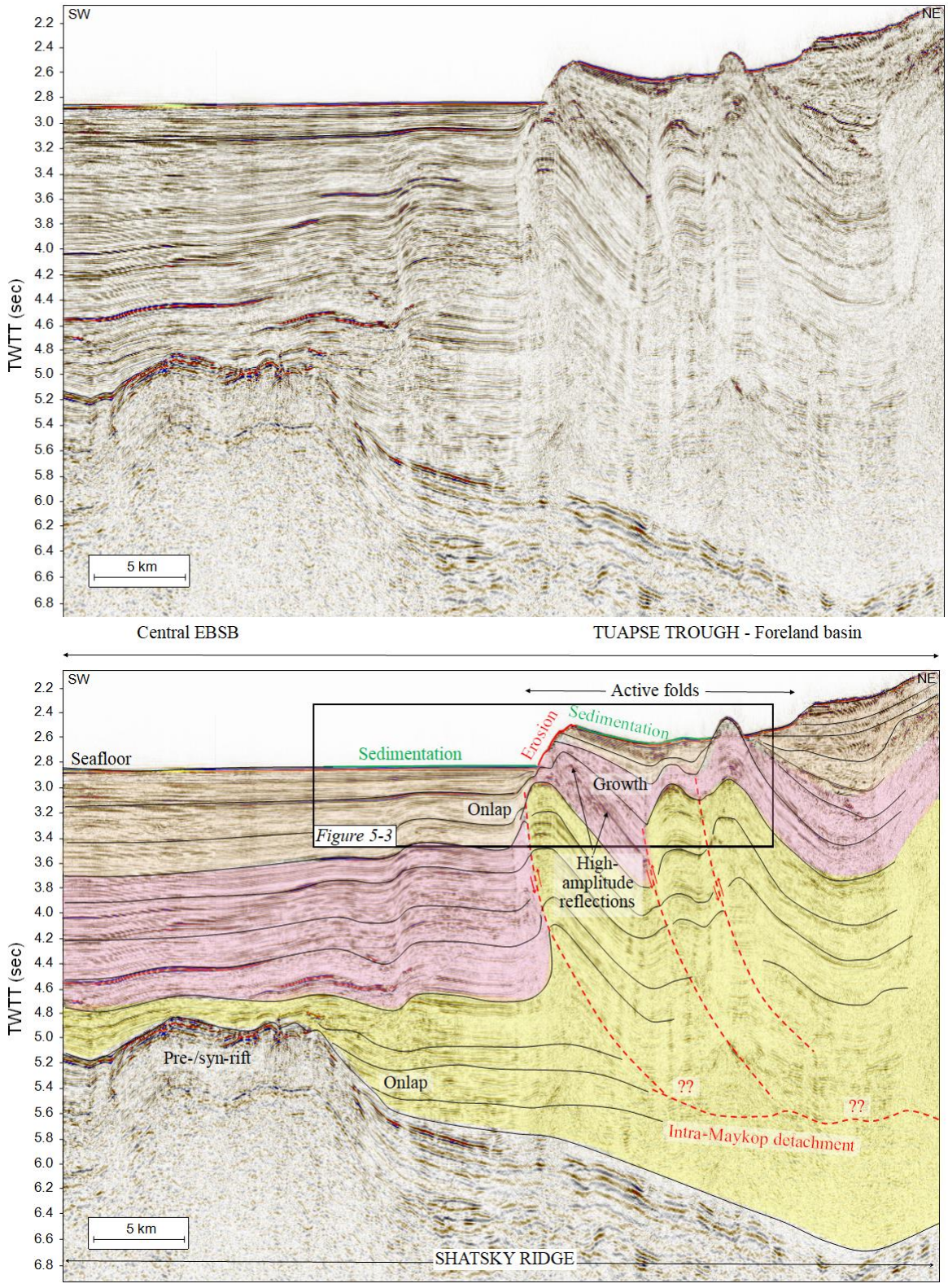

Figure 5-2. Profile BS-200B, showing the thrusted and folded sediments of the Tuapse Trough foreland basin building on top of the Shatsky Ridge shoulder. The main structural and stratigraphic features interpreted are: the Maykop Formation (yellow), middle-upper Miocene (pink) and Pliocene-Quaternary units (light brown), the main thrust faults and their intra-Maykop basal detachment (red dashed lines), onlaps and growth strata,

erosional and depositional domains at the seafloor topography. The black box shows the location of the zoomed section in Figure 5-3.

5.3 Seismic dataset

This study uses a single, post-stack time-migrated seismic reflection profile acquired as part of a 2D long-offset seismic reflection survey in 2011 by *Geology Without Limits* (GWL) and ION GXT (Figure 5-1). Data were acquired using an 816-channel hydrophone streamer with a maximum offset of 10.2 km, a receiver spacing of 12.5 m, and a towing depth of 9 ± 0.5 m. The source was a 5680 cubic-inch array towed at a depth of 8 ± 0.5 m and the source interval was 50 m. Profile BS-200B was acquired in a NE to SW direction, with a 200° heading direction. Further information on acquisition parameters and on the processing sequence applied by GWL is provided in Chapter 2 (section 2.1).

Here, we focus on a 53.1 km-long section of profile BS-200B, extending from the Tuapse Trough (NE) to the central basin (SW) (Figure 5-1, Figure 5-2, Figure 5-3).

5.4 Distribution and character of the multiple BSRs

Up to four, vertically stacked BSRs are identified within the folded sediments of the Tuapse Trough (Figure 5-2, Figure 5-3). The topmost BSR (BSR0) laterally pinches out to its SW-end on the crest of a folded structure, and it shows a weak seismic amplitude and seafloor-like signal polarity (Figure 5-3). Despite showing a weak signal amplitude on the stack profile, BSR0 appears as a clear event on shot gathers, where it is visible at offsets ranging from zero to 3.8 km (channel no. 1-300; Figure 5-4). Second from the top, BSR1 appears as a reflection characterised by stronger amplitude and a predominantly reversed polarity compared to the seafloor (Figure 5-3), which may be indicative of the acoustic impedance contrast arising from a lithological change or from the presence of free gas in sediments underneath. BSR1 appears as a stronger reflection on both the stacked profile and within a wide range of offsets (from near offset to ~ 4.5 km) along shot gathers (channel no. 1-350; Figure 5-4). A third, weak seismic reflection, BSR2, seems to show a predominantly reversed polarity (Figure 5-3). However, BSR2's waveforms are more complex than that of BSR1, likely reflecting the complex impedance structure within that layer as well as interference with reflections from background sedimentary strata. This aspect makes it difficult to clearly identify the BSR2 reflection event on shot gathers, where it is visible only within a narrow range of offsets (from zero to ~ 1.4 km offset; channel no. 1-110; Figure 5-4). Finally, the deepest BSR, BSR3, is characterised also by a stronger amplitude reflection, which is more clearly identified on shot gathers from near- to mid-offset ranges (~ 3.5 km offset; channel no. 1-280; Figure 5-4). Although signal polarity seems predominantly reversed to the SW-end of the BSR, it seems to be changing to a normal polarity

toward its NE-end (Figure 5-3). The different apparent polarity, and the discontinuous character of this seismic reflector, leaves uncertainty in linking the SW part of BSR3 with its NE part. Thus, BSR3 could be interpreted as two different reflectors.

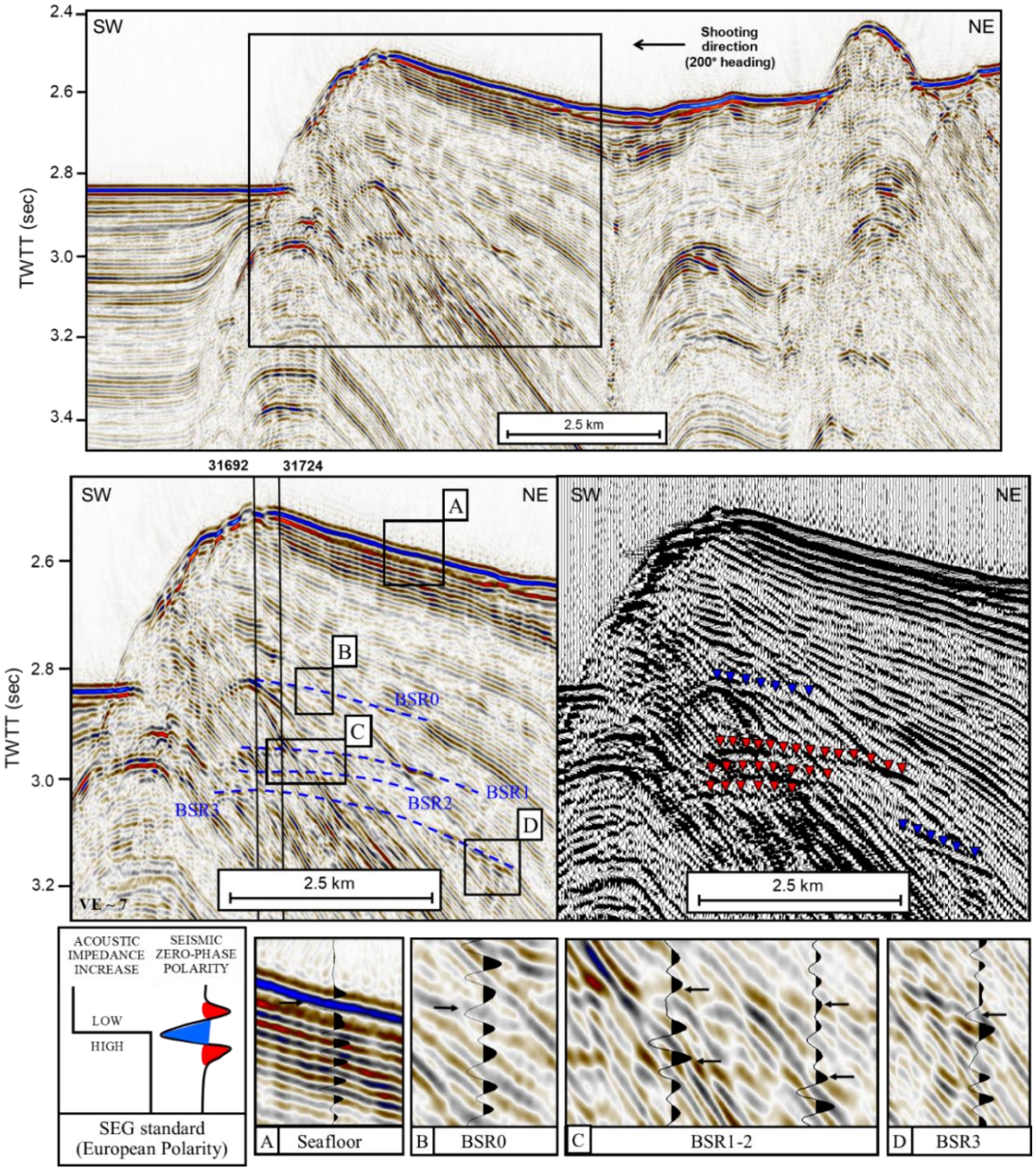

Figure 5-3. Seismic reflection profile BS-200B, crossing the upper Miocene-Quaternary folded sediments of the Tuapse Trough. Non-interpreted profile and zoomed, interpreted profile showing up to four seismic reflections sub-parallel to seafloor and cross cutting the background stratigraphy, which are interpreted as BSRs. Colour and wiggle displays are shown for the interpreted version. Also, coloured signal polarity for each BSR, compared to seafloor polarity (SEG European Polarity; increase in acoustic impedance shown as a trough with blue colour), is shown in the zoomed images (A, B, C, and D). Blue and red triangles on the wiggle display are used to highlight troughs and peaks

associated with the coloured BSR polarity. Vertical black segments on the interpreted stack profile show the location of FFID 31692 and 31724 shown in Figure 5-4.

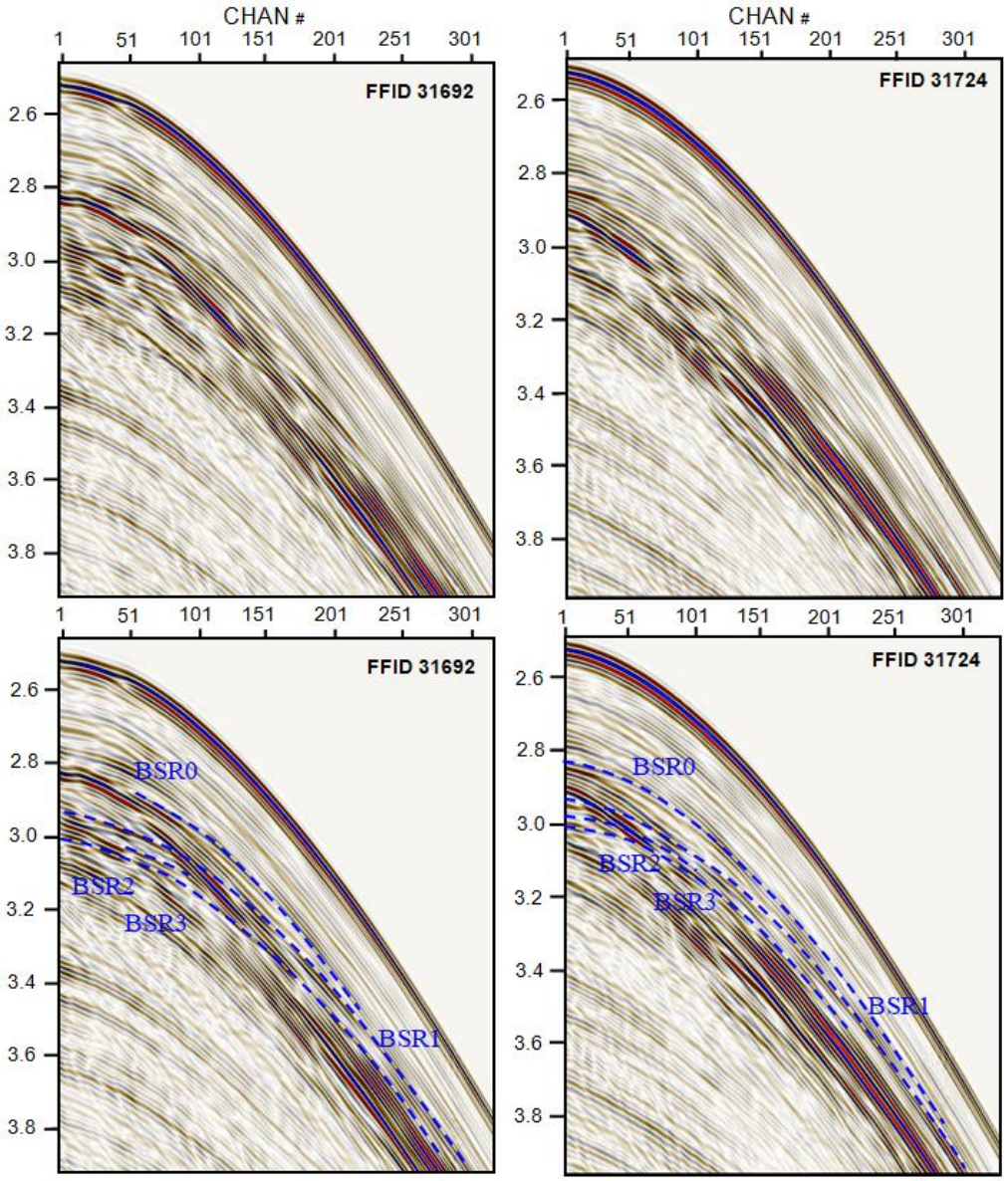

Figure 5-4. FFID 31692 and 31724 (location in Figure 5-3). Top) Non-interpreted shot gathers. Bottom) Interpreted shot gathers, showing an example of phase identification for all four BSRs. Offsets along the shot gathers are provided as channel number (CHAN #), where channel is a consecutive number with 12.5 m spacing.

5.5 Methodology

The time stacked profile was used to pick seismic horizons, including seafloor, BSRs and other main sedimentary layer reflections. Seafloor was converted into depth using a constant water velocity of 1.49 km/s, whereas all other picked horizons were initially converted into depth using a uniform velocity gradient of 0.42 s^{-1} (Monteleone et al., 2019; see section 2.1.2). Depth converted horizons

were used to define the initial velocity model layer boundaries for travel-time analysis (see section 5.5.2). Reflected travel-times, corresponding to the horizons picked on the time stacked profile, were picked on raw shot gathers and used in a forward travel-time modelling approach (Zelt and Smith, 1992) to constrain the velocity model structure and layers depths. In order to define a well-constrained velocity model, both reflected and refracted travel-times need to be considered. The long-offset nature of the seismic acquisition allows refracted signals to be imaged as first arrivals at far offsets. However, given the few hundred meters sub-seafloor depth of our target, key velocity information is provided by refractions from shallower stratigraphic levels. Picking travel-times for these phases is difficult because they are obscured by earlier direct and reflected signals. Therefore, to achieve the best result from travel-time analysis, downward continuation (Berryhill, 1979, 1984; Harding et al., 2007) was applied to streamer data (section 5.5.1) prior to travel-time analysis (section 5.5.2). The resulting velocity model was then used to compare BSR depths with the expected BGHSZ (section 5.5.3), and to provide estimates of gas and hydrate saturation in sediments (section 5.5.4).

5.5.1 Downward Continuation

Downward continuation is an efficient technique to extrapolate the recorded wave-field to an arbitrary surface, bringing refracted arrivals as first arrivals (Berryhill, 1979, 1984; Harding et al., 2007; Arnful et al., 2011). It can be carried out in the frequency domain, using pre-stack phase-shift methods (Gazdag, 1978), or in the time domain (Berryhill, 1979), applying Kirchhoff's integral method and solving the wave equation using the finite difference method (Claerbout, 1976). Here we apply downward continuation to the streamer data using a pre-stack Kirchhoff integral extrapolation technique in the time domain (Berryhill, 1984), which is formulated by convolving the recorded wavefield at the water surface with the time lagged delta functions and summing these convolved results over all receiver locations for all shot gathers (Harding et al., 2007). The time lags are estimated by dividing the distance between the surface locations of the shot gathers and their extrapolated positions on seafloor by a constant water velocity. In the absence of more detailed constraints on the water column velocity structure, we use a constant water velocity of 1.49 km/s.

The downward extrapolation has several advantages. First, it collapses the seafloor diffractions, improving the imaging condition. Second, there is the advantage of exposing more of the shallow turning refractions as first arrivals that can be accurately picked for tomography, improving vertical resolution of the resulting velocity model (Harding et al., 2016). Furthermore, the differential move-out of reflected arrivals is enhanced near to the seafloor, leading to improved velocity analysis and imaging (Arnulf et al., 2011).

Downward continuation can be performed moving both source and receivers down to the real seafloor topography or moving them to a constant datum above seafloor or below sea-level. Here, we apply downward continuation to a constant datum below sea-level. Since our seismic profile shows seafloor depth ranges from a minimum to 1.53 km (bsl) to the NE to a maximum depth of 2.13 km (bsl) to the SW, we tested model response to different downward continuation depths. Initially, both source and receivers were relocated to a depth of 1.8 km (bsl), based on seafloor depth ranges within the BSR area (~1.87-1.97 km bsl). However, the shot gathers sample structure beyond the BSR area, including areas of seabed shallower than 1.8 km, so this approach introduced noise and artefacts where a 1.8 km downward continuation depth was bringing sources and/or receivers beneath the seafloor. After further testing, sources and receivers were finally extrapolated at a shallower depth of 1.6 km (bsl), which provided a trade-off between avoiding the introduction of artefacts while allowing refracted signals to become first arrivals at sufficiently closer offsets (Figure 5-5). A deeper downward continuation depth (i.e., ≥ 1.9 km) could be applied for shot gathers in the central basin, where seafloor is almost flat and around 2.00-2.13 km deep. However, this area was not of primary interest for this study.

Downward continuation was carried out in two steps: 1) the extrapolation of each set of 816 traces of the receiver gathers (corresponding to a single shot point) vertically down to 1.6 km (bsl) and, after sorting of the extrapolated shot gathers into Common Receiver Point (CRP) gathers, 2) the extrapolation of each source wave field, corresponding to 204 shots per CPR gather, to the same depth. Finally, the data were sorted back into shot gathers before travel-time analysis (see Appendix C). The 53.1 km-long profile was pre-conditioned prior to downward continuation of both common-shot (step 1) and CRP gathers (step 2). Before step 1, shot gathers were cut down to 8 seconds (from the original 18 seconds) record length to eliminate unnecessary data. Noise attenuation was performed on the data in preparation for downward continuation (Figure C- 1), including: a minimum phase band-pass filter with cut-off frequency corners of 2-5-30-60 Hz, a top-mute cutting traces above first arrivals, and an FK filter to remove diffracted energy improving the signal-to-noise (S/N) ratio. An Automatic Gain Control (AGC) of 2000 ms was applied to reduce the signal amplitude decay caused by attenuation or spherical divergence, and thus, to balance amplitudes and improve the visibility of seismic events. An amplitude reduction (taper) has also been applied to near and far offset traces to avoid the introduction of edge effects artefacts from nearby gathers during downward continuation. We tested taper lengths of 5, 10, 20 and 50 traces. A final taper of 5 traces was applied to the near offsets, to avoid edge effects creation while maintaining the amplitudes of the near-offset reflection events, whereas a wider taper consisting of 20 traces was applied to the far offsets. Finally, data were re-sampled from 2 ms to 4 ms to reduce computational time.

The output from the first pass downward continuation was then re-sorted into CRPs (Figure C- 1). Only full-fold CRP gathers can be used for the second pass of downward continuation. Given the geometry of the data, with every 4th shot gather contributing to a CRP, 816 low-fold CRPs are present during resorting. This resorting results in a 10.2 km offset loss during re-sorting into CRPs. The resulting full-fold CRPs include 204 traces at 50 m spacing. At 50 m trace spacing, signal aliasing occurred at frequencies around 16 Hz. To avoid aliasing at such low frequencies, a trace interpolation (anti-aliasing FK trace interpolation) was applied to double the amount of traces, thus resulting in 407 traces per CRP with a 25 m trace interval (Figure C- 1). Interpolation and FK filtering allowed to preserve frequencies up to 20-25 Hz, which are representative of the refracted events. A top mute was also applied to remove excessive noise present above the first arrivals, previously introduced during the first pass downward continuation, as this could generate smearing artefacts during the second pass downward continuation.

Downward continuation parameters have also been tested to provide the best result. Testing included slowness value ranges (p-range) and dominant frequency (f_D) of the signal to be preserved during downward continuation. The p-range, or dip range of Kirchhoff operator (s/km), is the range of data dips to be included in downward continuation. This can be the same as the dip range of the data. However, it is often useful to discriminate against unwanted dips in the extrapolation process to avoid artefacts being introduced (i.e., bigger slowness value includes seismic events aliased at lower frequencies). The dominant frequency of the data is used to estimate the Fresnel zone padding for the summation hyperbola to ensure that the requested range of dips is accurately extrapolated (Harding et al., 2007). A p-range (slowness) between 0.625000 and 0.66667 (1/1600 m/s and 1/1500 m/s, respectively) and up to 0.00066667 (approximate infinite velocity) has been chosen to preserve all reflection and refraction events (Figure C- 2). However, a p-range of 0.55556 (1/1800 m/s) to 0.00066667 (approximate infinite velocity) was also considered to remove lower-velocity (compared to refractions), strong amplitude linear events visible at near- to mid-offsets and masking refracted arrivals (Figure C- 2). A dominant frequency (f_D) of 20 Hz, representative of refraction events, was used for downward continuation in both shot and CRP domains. This choice enabled removal of higher frequencies which were responsible for the generation of artefacts during downward continuation, maintaining the fundamental refracted signal information.

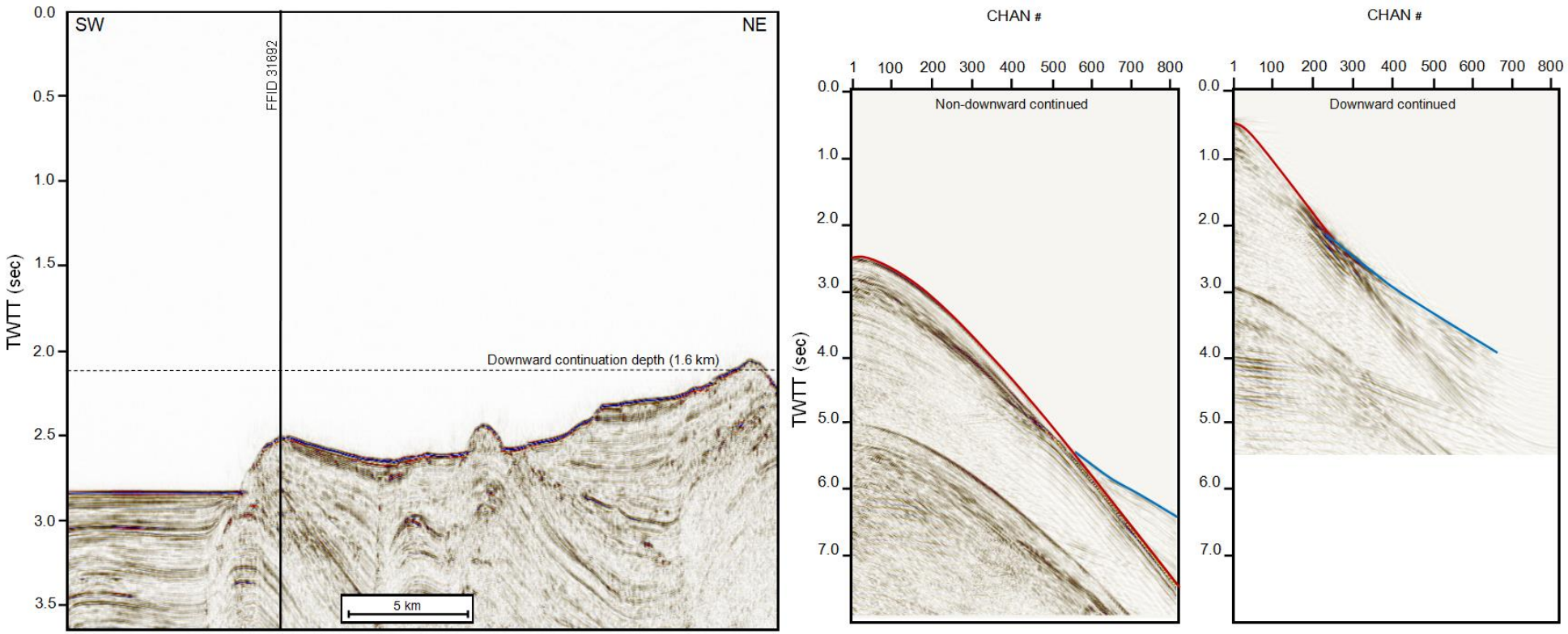

Figure 5-5. Downward continuation applied to streamer data. Left) seismic profile BS-200B; the original datum at 0 km (bsl) and the downward continued datum at 1.6 km depth (bsl) are shown. The vertical line represents the location of the shot gather (FFID 31692) shown to the right. Right) FFID 31692 is compared before and after downward continuation. Seafloor reflection (red), and first arrival refraction (blue), are also shown. The comparison highlights that downward continuation allows refracted events, originally visible from ~ 6.8 km offset (channel 550) on non-downward continued data, to be visible as first arrivals at ~ 2.7 km offset (channel 220).

After stage 2 extrapolation, interpolated traces were discarded, and the data were re-sorted into shot gathers in preparation for travel-time picking (Figure 5-5; Figure C- 1, Figure C- 2). Due to re-sorting, another 10.2 km profile length was lost into low-fold shot gathers, thus reducing the original length of 53.1 km down to 32.7 km. The final output of the downward continuation shows refracted arrivals at offsets as close as 2.75 km (channel no. 220) compared to the 5.5-6 km (channel no. 440-480) within non-downward continued shot gathers (Figure 5-5). The extent of the extrapolated arrivals depends on the distance between the extrapolation datum and the seafloor, the underlying velocity function, and local topography; therefore, the source-receiver range of extrapolated first arrivals changes slightly from one location to another (Arnulf et al., 2014). Whereas refracted arrivals have been improved by downward continuation, reflected arrivals are much less distinguishable on downward continued data. For this reason, non-downward continued data were used to pick reflected travel-times, whereas downward continued data were primarily used to pick refracted travel-times.

5.5.2 Travel-time analysis

Seismic travel-time analysis aims to reconstruct the seismic velocity structure of the subsurface from measurements of the seismic wavefield. In a forward approach, a defined model (i.e., seismic velocity model) is used to calculate the arrival times for reflection and/or refraction events using ray theory (Červený el al. 2001). The aim is to obtain a model for which the misfit between calculated and observed travel-time data is minimal (Scales et al., 1994).

Different tomographic approaches are available, which differ in terms of the velocity model parametrisation (i.e., equidistant grid, user-defined arbitrary grid, adaptive grid, etc.) for predefined layers separated by velocity discontinuities, and travel-time data used for modelling (i.e., first arrivals only or all observed arrivals, including reflections). First-arrival tomographic approaches, i.e., FAST (Zelt and Barton, 1998), only allow first-arrival refracted phases to be used, and they are not easily modified to model reflections, thus they were discarded because both reflections and later arrival refractions were needed for modeling. Layered reflection/refraction tomography, i.e., Tomo2D (Korenaga et al., 2000), can't deal with layers constrained by reflections only and codes that can, which also allow the use of later refracted phases as well as reflected arrivals apart from refracted first arrivals to build a layered model., i.e., JIVE 3D (Hobro et al., 2003), struggle with large numbers of layers, some of which are poorly constrained. We decided to use a forward modelling approach since this is better able to deal with complex structures and with large numbers of layers. Travel-time data were modelled using RAYINVR, the forward 2D ray-tracing approach of Zelt and Smith (1992), which allows all reflected and refracted phases to be used. Forward modelling has the advantage of being a good tool for checking the phase identification,

which is key for obtaining a correct model, and it allows to build a detailed model using most of the information contained in the record sections.

5.5.2.1 Travel-time phase definition

The first stage in the data modelling is travel-time picking and the assignment of phase to different arrivals, where a phase corresponds to energy that has the same propagation history, and thus, to a set of rays that have all turning and/or reflection points in the same layer or layers (Zelt and Smith, 1992). Layer boundaries were mapped in time domain on the stack profile. The depth-converted horizons were used to construct the initial layered model in which seismic velocities as well as layer depths were tested and adjusted manually to provide a better fit between calculated and observed travel-times (see section 5.5.2.2). Phases corresponding to the defined layer boundaries were then picked in the shot domain, where visible. Comparison with the stacked profile and with common channel domains was used to help identify each phase at near offsets and to provide guidance for phase recognition and picking at increasing offsets along the shot gathers. For reasons of practicality, we could not include every shot gather in the model. Given that travel-times showed good lateral continuity and that nearby shot gathers were providing redundancy of traces at the distance of interest along the profile, picking every 8^{th} shot was considered sufficient for this analysis. A total of ten reflected phases were picked at 13 shot locations at 400 m spacing (corresponding to every 8^{th} shot gather). The selected shots cover a distance from 19.45 km to 24.25 km along the 33 km-long profile, which includes the multiple BSRs area (Figure 5-6). The choice of multiple phases associated with stratigraphic reflectors beneath the BSRs is due to the geological complexity of this area, with folded structures present as steeping-dipping events often cross-cutting the BSRs (Figure 5-3, Figure 5-6). Thus, the choice of multiple horizons was necessary to constrain the velocity structure beneath the BSRs and within the surrounding sediments. Also, a simple model with flat, horizontal layers required unrealistic and abrupt lateral velocity variations to fit calculated and observed travel-times at the picked reflection events. Therefore, the real geometry of the reflection events was adopted for modelling (Figure 5-6).

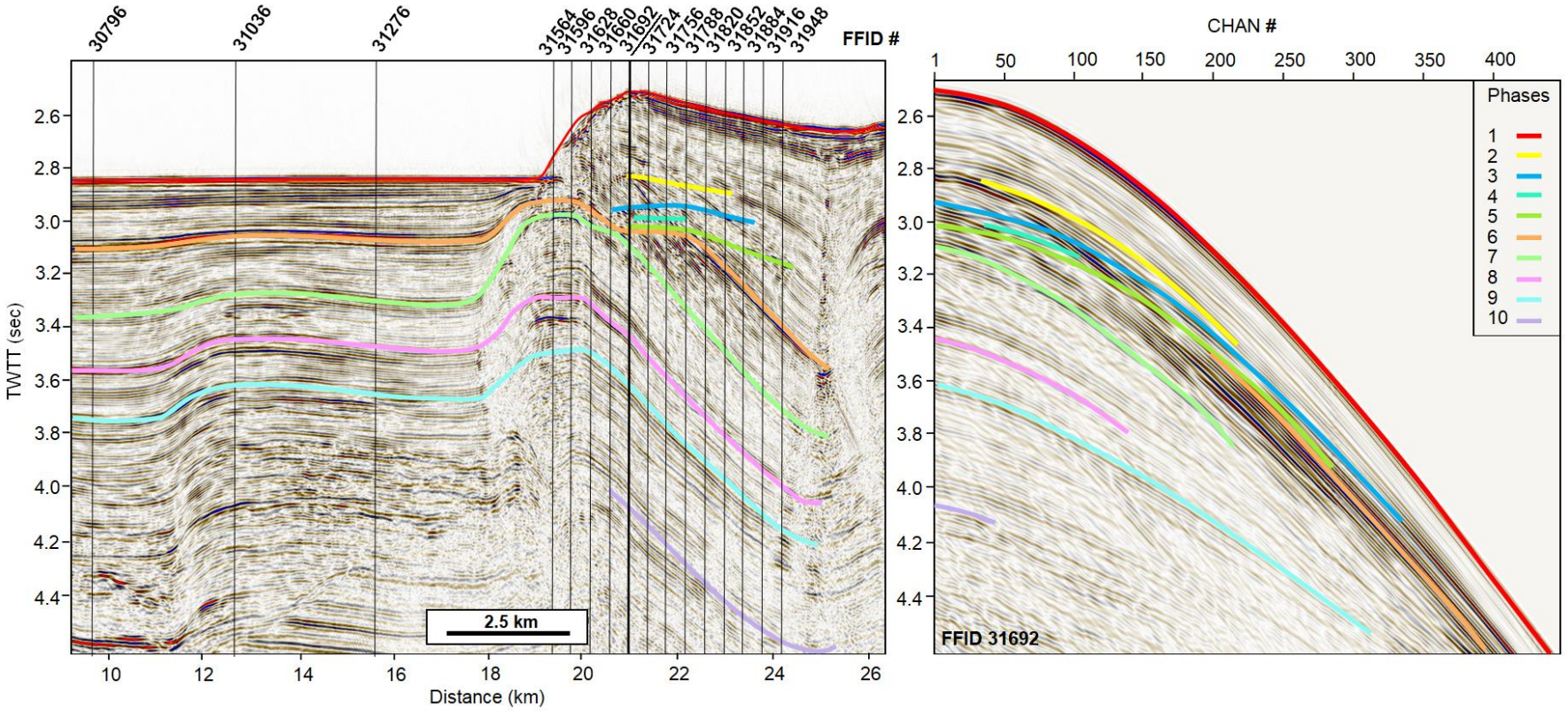

Figure 5-6. Seismic reflection profile showing the interpreted seismic phases used for the velocity model construction (coloured lines), and the location of the shot gathers picked for travel-time analysis (vertical black segments). Phase 1 - seafloor reflection; phases 2, 3, 4 and 5 - BSR0, BSR1, BSR2 and BSR3, respectively; phases 6 to 10 - stratigraphic horizons beneath BSR3. Three shot locations in the central basin (FFID 30796-31276) were used to compare shallow sedimentary velocities against those modelled at the BSR area. A total of 16 shot gathers (13 covering the BSR area and 3 within the central basin domain) were used to pick reflected and refracted travel-times. The thick black segment is the location of the shot gather to the right (FFID 31692) where interpreted phases are overlaid.

The model was extended basinward (to the SW of the profile) to allow a comparison between velocity trends in the shallow sedimentary section along the profile and, in particular, to define whether seismic velocity ranges defined in the BSRs area were representative for the shallow sedimentary section in other parts of the basin. Because of the complex geology in the NE part of the profile, phase picking on shot gathers in this area was difficult as no clear seismic events were recognised. In contrast, phase picking was easier in the central basin, to the SW part of the profile, where sub-horizontal sediments are present (Figure 5-3, Figure 5-6). We therefore chose this location instead. Given the lateral continuity of sedimentary layers in this area, only three shot gathers at 3 km offset spacing (from 9.85 km to a 15.85 km offset along the profile) were used for phase picking (Figure 5-6). At these shot locations, five phases were picked, which are laterally continuous on stack data. These layer boundaries can be followed into the north-eastern part of the profile (BSR area) as boundaries 1 (seafloor), 6, 7, 8, and 9.

Downward continued shot gathers were used mainly to pick refracted events, although some reflections were also picked to check the reliability of the downward continuation procedure (Figure 5-7). Three reflected phases were recognised: phase 1 (seafloor), and phase 2 and 3 (linked to BSR1 and BSR3 events) (Figure 5-7). Three refracted events were identified and picked: phases 4, 5 and 6 (Figure 5-7).

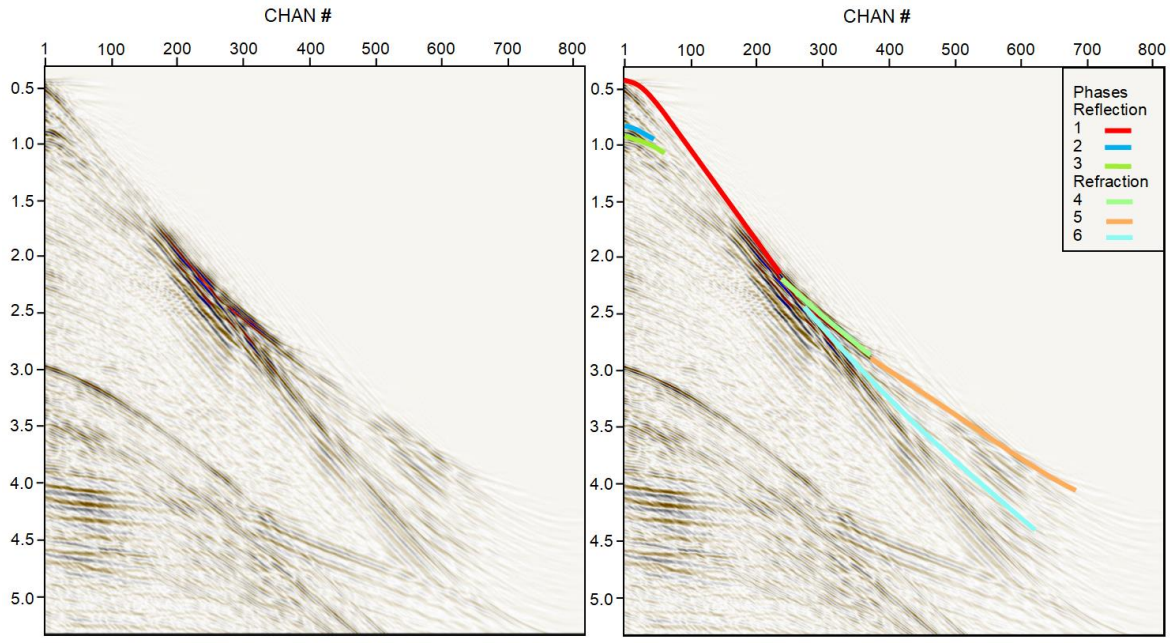

Figure 5-7. Phase identification on downward continued shot gather (FFID 31692). The shot location is shown in Figure 5-6. Three reflected phases were identified: phase 1 - seafloor, phase 2 - BSR1 and phase 3 - BSR3. Three refractions from mid- to far-offsets were picked (phases 4, 5 and 6).

Over 27500 reflected travel-time picks were made, on both non-downward continued and downward continued shot gathers. Picking uncertainty was assigned in the range of 5 ms to 10 ms, less than half of the predominant period (30 ms), to all near-normal incidence reflections picked on non-downward continued data. An uncertainty of 20 ms was instead assigned to reflected events picked on downward continued data, due to the deterioration in the reflected signal and the loss of high frequencies. Over 3300 refracted travel-time picks were made on downward continued data and assigned an uncertainty from 20 ms increasing to 25 ms at far-offsets, corresponding to approximately half of a wave cycle (50 ms).

5.5.2.2 Travel-time modelling

The model was parameterised to have limited velocity variations in the horizontal direction, compared to the vertical, and to allow rougher interfaces as opposed to more rapid velocity changes. The broad structure was modelled first, followed by the progressive introduction of more detailed structure until a satisfactory fit to the observed travel-times was achieved. By following this approach, the final model contains the minimum structure required to fit the observed data within their uncertainties.

Structure was defined from the stacked reflection profile and introduced in the model building. Modelling was carried out in a layer-stripping approach using non-downward continued travel-time picks (see Appendix D, Figure D- 1), where progressively deeper phases are modelled while holding the overlying layers fixed until all data have been fitted. The resulting model was then integrated with refracted and reflected travel-times picked on downward continued data (Figure 5-8, Figure D- 2 to Figure D- 6). At this stage, the velocity model was adjusted where necessary, with only minor adjustments to the layer boundaries.

The number and position of boundary nodes was adapted to the geology of the area and picked along the seismic reflection profile, whereas velocity node spacing was adjusted to fit the observed data with the minimum necessary changes in depth nodes. Stopping criteria for the normalised misfit (χ^2) of 1-1.5 were desired, with all layers fitting within this range for the selected shots (see section 5.6.1).

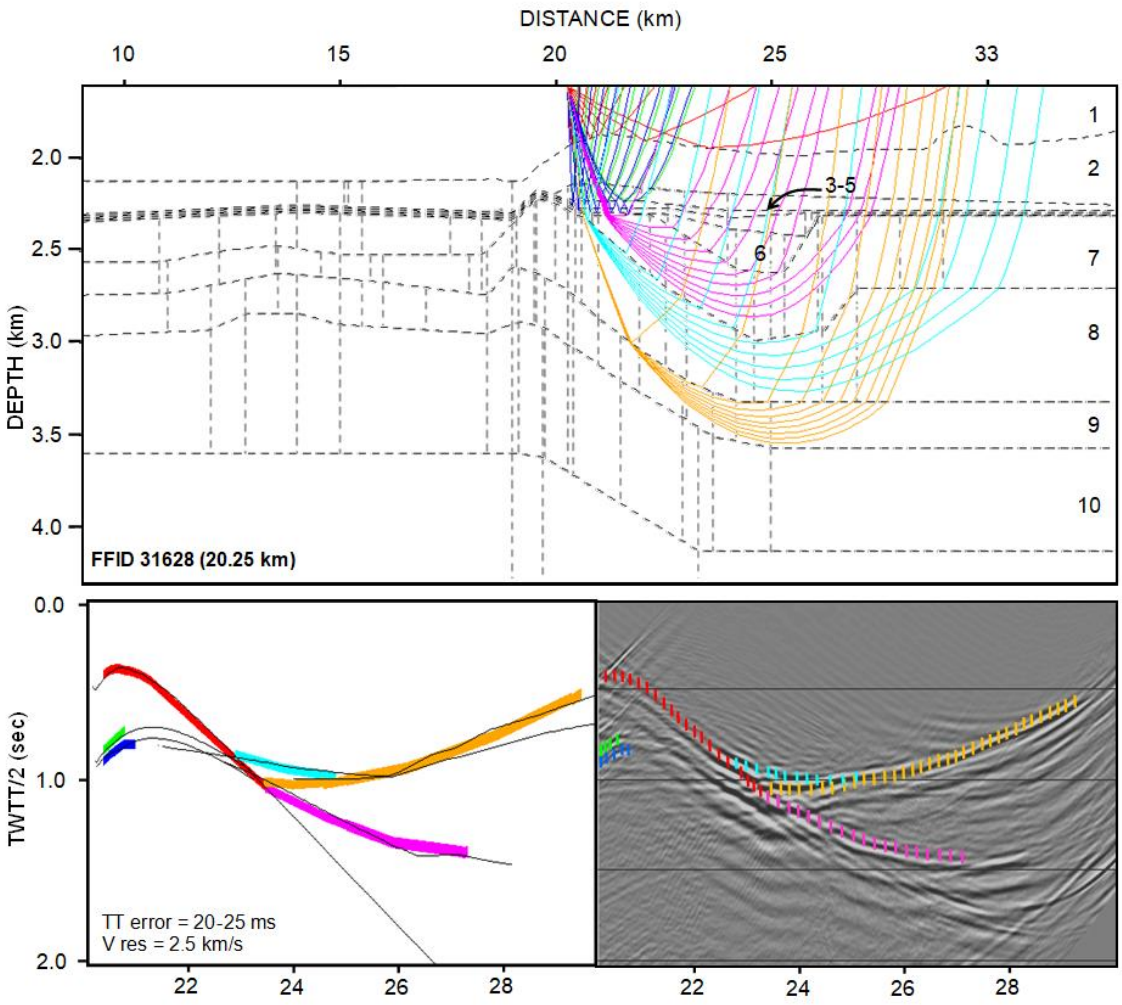

Figure 5-8. Travel-time analysis on a representative downward continued shot gather (FFID 31628). Top) velocity model showing the depth node positions initially defined by layer stripping approach using reflected travel-time phases picked on non-downward continued gathers (see Appendix D). Travel-time rays traced in the plot belong to refracted and reflected phases picked on FFID 31628 and used to complement model definition. Phases 1, 2 and 3 in the modelling represent reflections from layer 1 (seafloor), layer 3 (BSR1) and layer 5 (BSR3), respectively (see Figure 5-6). Three refractions, phases 4, 5 and 6, are associated with layers 7, 8 and 9, respectively. Bottom) To the left, observed and calculated travel-times are compared. To the right, observed travel-times are displayed on the shot gather as vertical segments (line length represents the travel-time uncertainty). A velocity reduction of 2.5 km/s applied to make travel-time identification easier. Further examples of travel-time analysis on downward continued shot gathers are shown in Appendix D (Figure D- 2 to Figure D-6).

Travel-time analysis allowed us to link refractions visible on downward-continued data with stratigraphic layers defined based on reflected travel-times. Although downward continuation has

improved refracted signal bringing it to closer offsets, the refractions still appear to come from beneath the BSRs (Figure 5-8; Figure D- 2 to Figure D- 6). Nevertheless, refracted arrivals bear information on the velocity structure of the layers they have travelled through, as these would also impact their resulting travel-times. The integration of refracted travel-times allowed, therefore, to prove the validity of the velocity model defined using reflected travel-times, to better constrain the deeper stratigraphic layers, and to evaluate the impact that velocity changes in shallower layers may have on the refracted arrival estimation.

5.5.3 Modelling of the base of the gas hydrate stability zone under steady state conditions

We compared the depth of the interpreted BSRs with the expected depth for the BGHSZ. The GHSZ thickness below seafloor is given by the distance between the seafloor and the intersection of the temperature profile with a hydrate phase boundary (e.g., Marin-Moreno et al., 2016; Tinivella and Giustiniani, 2013) (Figure 5-9). Assuming hydrostatic pore fluid pressure and constant temperature conditions, this calculation depends upon parameters such as bathymetry, geothermal gradient, seafloor temperature, pore-water salinity, and molecular composition of the hydrate forming gas (e.g., Sloan, 1998). Other parameters affecting hydrate stability such as pore size (e.g., Østergaard et al., 2002) are not considered here.

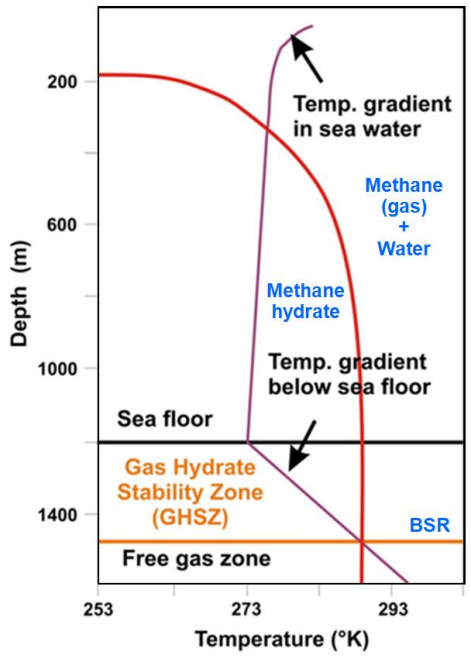

Figure 5-9. Plot showing the hydrate phase boundary for pure methane (red curve) and the estimated thickness for the GHSZ (orange line) for a given value of seafloor depth (black line) and water/geothermal gradients (purple line). The BSR should match the estimated depth for the base of the GHSZ (modified from Tinivella and Giustiniani, 2013).

We compiled temperature, salinity, and geothermal gradient data from published literature to define the parameters for the GHSZ modelling. Bathymetry is defined by the seafloor horizon picked along the time-migrated stack profile, which was converted from time to depth assuming a constant water velocity of 1.49 km/s. The geothermal gradient in this part of the EBSB is expected to vary between 20 and 42˚C/km, based on heat-flow measurements and other estimates (Vassilev, 2006;

Minshull and Keddie, 2010). Results from the DSDP 42B Hole 379A (see location in Figure 3-1 and Figure 5-1), provide a narrower range of geothermal gradients between 32 and 38˚C/km (Erickson and Von Herzen, 1978). The same DSDP cores (i.e., DSDP 379A; Muratov, 1978; Ross, 1978) and salinity analyses of pore water samples show that today's salinity decreases rapidly from ~ 2.23% wt at the seafloor (Özsoy and Ünlüata, 1997) to ~ 0.2-0.5% wt in shallow sub-bottom depths (Calvert and Batchelor, 1978), as geochemical conditions within the sediments change to lacustrine values (e.g., Manheim and Schug, 1978; Riboulot et al., 2018; Riedel et al., 2020). In particular, DSDP Hole 379A shows that within 25-350 m-deep sediments the pore-water salinity value is about 0.5% wt, with low salinity related to the dominant fresh-water stages during Quaternary deposition (Manheim and Schug, 1978). These corresponded to limnic conditions that occurred during LGM with sea-level low stands, when Mediterranean salt water could not pass the Bosporus inlet causing phases of isolation in the Black Sea (Manheim and Schug, 1978).

A seafloor temperature of 9 ± 0.1°C is well constrained by numerous studies and is generally uniform across the whole basin (Degens and Ross, 1974; Xing and Spiess, 2015; Ker et al., 2019; Vassilev, 2006). Finally, based on the analysis of methane isotope signatures from cores and seeps, the primary hydrate-forming gas composition for the Black Sea hydrate is considered to be 99.1-99.9% methane (e.g., Ginsburg and Soloviev, 1998; Vassilev and Dimitrov, 2002; Poort et al., 2005; Merey and Sinayuk, 2016; Zander et al., 2020; Chazallon et al., 2021), although some studies from the central Black Sea and the northern upper slope have reported the presence of thermogenic gasses (e.g., Merey, 2017; Limonov et al., 1997; Kruglyakova et al., 2004; Mazzini et al., 2004).

Here we consider 100% methane hydrate (Moridis, 2003), 0.5 % wt pore water salinity (e.g., Soulet et al., 2010; Riboulot et al., 2018; Bohrmann et al., 2018; Bialas et al., 2020), seafloor temperature of 9˚C (e.g., Degens and Ross, 1974; Vassilev and Dimitrov, 2002), constant geothermal gradient varying between 20 and 42˚C/km (e.g., Erickson and Von Herzen, 1978; Vassilev, 2006; Minshull and Keddie, 2010), water density of 1030 kg/m^3, and hydrostatic pressure. We use Dickens and Quinsby-Hunt's (1997) relationship to consider pore water salinity effects in Moridis (2003) freshwater methane hydrate stability curve.

5.5.4 Effective-medium modelling

Knowledge of the compressional (V_P) and shear (V_S) wave velocity can be used to estimate gas hydrate and free gas content in the pore space (e.g., Ecker et al., 1998; Jacobsen et al., 2000; Waite et al., 2009). Higher velocities than those expected for water-filled, normally compacted marine sediments within the GHSZ can often be attributed to the presence of gas hydrate (e.g., Chand et al., 2004). This is reflected in an increase of the composite's bulk and shear moduli (Ecker et al.,

1998) even for low hydrate saturations (Priest et al., 2009; Waite et al., 2009; Dai et al., 2012). The presence of small concentrations (i.e., only few percent) of free gas in the pore space can attenuate the propagation of seismic waves and reduce considerably the P-wave velocity, and thus, this can be used to define gas content in low-velocity zones (e.g., Singh et al., 1993).

Here we used the Hydrate-Bearing Effective Sediment (HBES) model described by Marin-Moreno et al. (2017). The model mathematically represents the concept of hydrate bearing sediment being an effective medium comprised by sediment grains, solid hydrate, water, and gas. It is based on the Biot-Stoll formulation (Biot, 1956; Stoll and Bryan, 1970) and predicts the P and S-wave velocity and corresponding attenuation of hydrate bearing sediments. In the HBES model the hydrate's habit is considered as either pore-floating, cementing hydrate at grain contact, or cementing hydrate enveloping the grains (Ecker et al., 1998, 2000) and load bearing (Sahoo et al., 2019). Different hydrate habits can affect P- and S-wave velocities differently and, generally, sediments with pore-floating hydrate result in small changes in elastic wave velocities, whereas load-bearing and cementing hydrate-bearing sediments show significantly higher P- and S-wave velocities than those of the host sediment velocities (Priest et al., 2009; Dai et al., 2012). This different velocity response depending on hydrate habit is represented in the HBES model by considering that pore-floating hydrate only modifies the bulk modulus of the pore fluid, whereas cementing hydrate increases the dry bulk and shear moduli of the sediment (Ecker et al., 1998, 2000).

The physical properties of the composite sediment with or without hydrate are modelled by mixing the various components in different ways (see section 5.5.4.1). To quantify the saturation of the different components that can explain the P-wave velocities obtained from travel-time analysis, we impose the shear and bulk modulus of the mineral grains, methane hydrate, methane gas and brine and test different fractions of these components and porosities. For simplicity, we do not consider cases in which free methane coexists with methane hydrate, although we recognise that hydrate and gas can co-exist (e.g., Sahoo et al., 2018). We therefore consider two models, one with variable amounts of methane hydrate and brine, and the other one with variable amounts of methane gas and brine in the pore space. When modelling methane gas, this is assumed to have a uniform distribution in the pore space. The calculated V_P from the HBES model is compared with the observed V_P from travel-time modelling at two locations, one in the flat-lying sediments of the central basin and the other in the BSRs area. This is because sediment velocities in the central basin differ from the ones at the BSRs, and they are considered representative for background V_P ranges (i.e., non-hydrate-bearing sediments). This is done at the stratigraphic depths of ~ 258, 360 and 438 mbsf, corresponding to BSR0, BSR1 and BSR3, respectively. BSR2 depth is not considered for the modelling, as only minor velocity variation has been detected at this reflector. We note that in the

following we only present P-wave velocities from the HBES model as this is the constraint we have from travel-time analysis.

5.5.4.1 Modelling parameters

The youngest sediments in the EBSB have been sampled by gravity cores, onshore geological mapping (i.e., NE Turkey) and existing well control. Samples recovered at these locations consistently demonstrate that the uppermost sediments contain mostly clays, although they also include marls and occasional turbidites (Ross, 1978; Hsü and Giovanoli, 1980; Aksu et al., 2002; Hiscott and Aksu, 2002). Sediment cores obtained during the DSDP Leg 42B in 1975 in the eastern-central Black Sea (Hole 379A) and at the entrance of the Bosphorus in the WBSB (Holes 380, 381), show sediments consisting of approximately 55% clay, 30% sand (quartz) and 15% Ca-Mg carbonate on average (Muratov et al., 1978; Ross et al., 1978). Previous studies in Black Sea have also assumed similar compositions to quantify gas hydrate and free gas saturation in sediments where BSRs have been identified (e.g., Lüdmann et al., 2004; Zillmer et al., 2005).

Here, we use previous estimates of the sediment's physical parameters (i.e., shear and bulk moduli, K_s and G_s, grain density, ρ_s) from Zillmer et al. (2005), that assumed a sediment composition of 60% clay, 20 % sand (quartz) and 20% Ca-Mg carbonate lithology. Based on shear and bulk moduli, and density values presented by Mavko et al. (2009), Zillmer et al. (2005) estimated average values of $K_s \approx 32 \pm 5\ GPa$, $G_s \approx 16\ GPa$ and $\rho_s \approx 2.63 \pm 0.05\ g/cm3$. Based on the density values assumed, these authors calculated that porosity (ϕ_0) decrease between the seafloor and 205-270 mbsf from 78 ± 1% to 57 ± 7%. Other studies have reported porosities of ~ 60% for the shallow sediments of the Black Sea, decreasing down to 50% at sediments around 150 mbsf (e.g., Vassilev, 2006, Riboulot et al., 2018; Merey, 2017). At DSDP Hole 379A, the ~ 70% porosity within shallow sediments decreases to 38% at ~ 350 mbsf depth (Ross et al., 1978). We therefore considered a porosity range of 30 to 60% for the deepest (~ 600 mbsf) to the shallowest (~ 258 mbsf) modelling depth used in this study (Table 5-1, Table 5-2).

Pore pressure and temperature are needed to calculate the density, viscosity and bulk modulus of the fluids (methane gas and liquid water) and the effective pressure is required for the calculation of the dry moduli in the presence of pore-floating hydrate (see Marin-Moreno et al., 2017). Hence, at the four BSR depths below seafloor (258 m, BSR0; 360 m, BSR1; 438 m, BSR3; Table 5-1) we calculated the pore pressure (P_p) and confining pressure (P_{conf}), so effective pressure assuming hydrostatic conditions, using grain (ρ_s) and water (ρ_w) densities of 2630 kg/m^3 and 1030 kg/m^3, respectively, and a porosity (ϕ_0) of 50%. For the temperature, we used a seabed temperature of 9˚C (Degens and Ross, 1974), and an average geothermal gradient of 31˚C/km based on the range considered in this study (20-42˚C/km) (e.g., Erickson and Von Herzen 1978; Vassilev, 2006).

Reference values used for the calculations, their error estimates, and the resulting error in calculated velocities (ΔV_P) are shown in Table 5-1.

For consistency with the modelling of the GHSZ presented above, we consider a salinity of 0.5 wt% and pure methane gas and hydrate. The pore-water salinity (s) is specified based on representative values for the EBSB.

Physical parameters for the gas hydrate solid phase occupying the pore space assume values for pure methane (structure I) hydrate, which is observed to occur more widely in nature (e.g., Kvenvolden, 2000) and in the Black Sea (Michaelis et al., 2002; Poort et al., 2005; Bialas, 2014; Merey and Sinayuk, 2016). Other relevant modelling parameters are presented in Table 5-2.

Table 5-1. Test conditions: confining *pressure (P_{conf}), pore pressure (P_p) and temperature (T) of sediments at the chosen stratigraphic depths. Error estimates are also shown*: ΔZ_s *= error in stratigraphic depth from travel-time analysis;* ΔTs *= error in sediment temperature;* $\Delta T/km$ *= error in geothermal gradient value assuming the range of 20-42˚C/km;* $\Delta\phi_0$ = error *in sediment porosity;* $\Delta\rho_s$ *= error in solid grain density;* $\Delta\rho$ *= error* in *bulk density of the sediment (calculated as* $\rho = \rho_s(1-\phi_0) + \phi_0(\rho_w)$*);* ΔP_p *= error in pore pressure calculated as* $P_p = \rho_w \cdot g \cdot Z_s$*;* ΔP_{conf} *= error in confining pressure calculated as* $P_{conf} = \rho \cdot g \cdot Z_s$*;* ΔV_P *= error in seismic velocity estimate*.

	Depth (mbsf)	**Pp (Pa)**	**Pconf (Pa)**	**T (°C)**
BSR0	258	$2.6\text{x}10^6$	$4.6\text{x}10^6$	17
BSR1	360	$3.6\text{x}10^6$	$6.5\text{x}10^6$	20
BSR3	438	$4.4\text{x}10^6$	$7.9\text{x}10^6$	23
-	600	$6.1\text{x}10^6$	$1.1\text{x}10^7$	28
Error estimates				
ΔZ_s	± 10 m			
ΔTs	± 3-5 ˚C	ΔZ_s and $\Delta T/km$		
$\Delta T/km$	± 11°C/km			
$\Delta\phi_0$	± 5%			
$\Delta\rho_s$	± 0.05 g/cm^3			
$\Delta\rho$	± 0.105 g/cm^3	$\Delta\phi_0, \Delta\rho_s$		
ΔP_p	± 0.1 x 10^6 Pa	ΔZ_s		
ΔP_{conf}	± 0.4-0.7 x 10^6	$\Delta\rho, \Delta Z_s$		
ΔV_P	± 27-37 m/s	$\Delta P_{conf}, \Delta P_p, \Delta Z_s, \Delta\phi_0, \Delta\rho_s$		

Table 5-2. Input parameters for the HBES model [[1]Best et al., 2013; [2]Helgerud et al., 2009; [3]Setzmann and Wagner, 1991; [4]Reagan and Moridis, 2008; [5]Zillmer et al., 2005; [6]Ecker

et al., 2000; [7]Millero et al., 1980; [8]Daigle et al., 2015; [9]Mavko et al., 2009]. Note: we present all the modelling parameters for completeness and reproducibility purposes. However, some of these parameters, e.g. fluid flow related parameters, are relevant primary for attenuation and velocity dispersion analysis which is not within the scope of this work. For more detailed information refer to Marin-Moreno et al. (2017).

Components properties	
Hydrate bulk modulus (K_H)[1]	7.9 x 10^9 Pa
Hydrate shear modulus (G_H)[1]	3.3 x 10^9 Pa
Hydrate Poisson's ratio (v_H)	0.32
Hydrate density (ρ_H)[2]	925 kg/m^3
Methane bulk modulus (K_{CH_4})[3]	K_{CH_4} (P_p,T)
Methane density (ρ_{CH_4})[3]	ρ_{CH_4} (P_p,T) [kg/m^3]
Methane viscosity (μ_{CH_4})[3]	μ_{CH_4} (P_p,T) [Pa s]
Methane irreducible saturation ($S_r\ CH_4$)[4]	0.02
Solid composition[5]	60% clay, 20% quartz, 20% Ca-Mg
Solid grain bulk modulus (K_S)[5]	32 x 10^9 Pa
Solid grain shear modulus (G_S)[5]	16 x 10^9 Pa
Solid grain Poisson's ration (v_S)[5]	0.29
Solid grain density (ρ_S)[5]	2630 kg/m^3
Solid grain diameter (d_S)	1 x 10^{-5} m
Solid grain coordination number (n)[6]	9
Water bulk modulus (K_w) [7]	K_w (P_p,T) [Pa]
Water density (ρ_w)[7]	ρ_w (P_p,T) [kg/m^3]
Water viscosity (μ_w)[7]	μ_w (P_p,T) [Pa s]
Water salinity (s)	0.5 %wt
Water irreducible saturation (S_{rw})[4]	0.2
Parameters	
Porosity without hydrate (ϕ_0)	0.5
Critical porosity (ϕ_c)[1]	0.38
Intrinsic permeability without hydrate (k_0)[8]	10^{-13} m^2
Intrinsic permeability exponent for cementing hydrate (n_{kc})	3
Intrinsic permeability exponent for pore-filling hydrate (n_{kPF})	2
Tortuosity (t)[9]	3

Capillary pressure fitting parameter $(m)^4$	0.45
Capillary pressure gas entry parameter $(P_0)^4$	2000 Pa

5.6 Results and Interpretation

5.6.1 Travel-time analysis: model fit and resolution

Uncertainty estimates need to account for the bias introduced by the interpreter (i.e. phase identification and picking), as well as the bias associated with the modelling approach (i.e. model parameterisation). The final model selected is that which provides the desired trade-off between RMS travel-time residual and parameter resolution, and which allows rays to be traced to all observation points (Zelt and Smith, 1992).

The final model from non-downward continued data has an overall RMS misfit of 9 ms between all observed and calculated travel-times, ranging from 4–14 ms for individual phases and a χ^2 of 0.755 (Table 5-3). The final model from downward continued data has an overall RMS misfit of 15 ms between all observed and calculated travel-times ranging from 9–24 ms for individual phases and a χ^2 of 0.663. The model is well constrained in the area of interest with dense ray coverage between 19.45 and 24.25 km (Figure 5-6). The F-test (variance-ratio test) statistical analysis (Press et al. 1992) was applied to model parameters to provide an estimate of the uncertainty in the final velocity model for both interfaces and velocities. Layer depth and velocities were tested by moving the entire boundary and adjusting velocities for individual parameters. Perturbed models are considered different from the final model when the variation in χ^2 is significant at the 95 per cent confidence limit. The velocity uncertainty is estimated at ±0.02 km s^{-1} for layer 2 and ±0.01 km s^{-1} for layer 3, corresponding to BSR0 and BSR1, respectively. For layers 4 and 5, corresponding to BSR2 and BSR3, the velocity uncertainty is estimated to be between +0.03 km s^{-1} and -0.02 km s^{-1}. Layer 6 shows a velocity uncertainty of +0.05 km s^{-1} and -0.03 km s^{-1}. The velocity uncertainty in the lower sedimentary layers (i.e., layers 9 and 10) is estimated up to ±0.07-0.10 km s^{-1}. Based on this statistical test the uncertainty of BSR0, BSR2 and BSR3 depth is less than ± 0.01 km, whereas it is estimated to be between < +0.01 km and -0.010-0.015 km at BSR1. For deeper sedimentary layers uncertainty in depth is also less than ± 0.01 km.

Table 5-3. Model fit to data for individual reflected and refracted phases and for the whole model.

Non-Downward Continued data					
Layer	Phase (Reflection)	No. shots	No. picks	RMS misfit (s)	χ^2
L1	Phase 1 (seafloor)	16	9503	0.004	0.808
L2	Phase 2 (BSR0)	9	1946	0.01	0.459
L3	Phase 3 (BSR1)	11	2465	0.007	0.542
L4	Phase 4 (BSR2)	3	273	0.007	0.432
L5	Phase 5 (BSR3)	11	1884	0.009	0.759
L6	Phase 6	11	2878	0.007	0.516
L7	Phase 7	11	1958	0.009	0.637
L8	Phase 8	14	2379	0.014	1.357
L9	Phase 9	14	2659	0.012	0.853
L10	Phase 10	5	367	0.011	0.524
	Overall model		26312	0.009	0.755
Downward Continued data					
Layer	Phase (Reflection)	No. Shots	No. picks	RMS misfit (s)	χ^2
L1	Phase 1 (seafloor)	4	841	0.012	0.388
L2	Phase 2 (BSR1)	4	163	0.012	0.372
L3	Phase 3 (BSR3)	4	197	0.009	0.222
	Phase (Refraction)				
L7	Phase 4	4	1380	0.024	1.028
L8	Phase 5	4	589	0.018	0.805
L9	Phase 6	4	1383	0.017	0.504
	Overall model		4553	0.015	0.663

5.6.2 Velocity model

Based on travel-time analysis, we constrain the depth of the picked seismic phases (Figure 5-6) and the velocity structure between them (Figure 5-10). BSR0, BSR1, BSR2 and BSR3 are inferred at an average depth of 258, 360, 395 and 438 ± 10 mbsf, respectively, where seafloor depth is around 1920 m. V_P increases from 1.55 km/s to 1.72 ± 0.02 km/s between seafloor and BSR0, from 1.75 km/s to 1.83 ± 0.01 km/s between BSR0 and BSR1 (Figure 5-10), and a V_P decrease from 1.83 km/s to 1.61-1.62 ± 0.03 km/s is modelled beneath BSR1. This low-velocity zone, which includes BSR2, is defined as a 70-80 m-thick layer bounded by BSR1 and BSR3 at its top and bottom, respectively. Within the low-velocity zone, the reduction in V_P of about 12% with respect to the V_P at BSR1 may be indicative of the presence of free gas. V_P then increases rapidly underneath BSR3, starting from values of 1.82-1.90 km/s (Figure 5-10).

The velocity model shown in Figure 5-10 is poorly constrained to the NE part of the profile, where modelling of travel-time arrivals was complicated by the geological setting characterised by the dominant presence of folded structures. Here, the complexity of the compressional tectonics

limited our ability to pick travel-time events consistently across shot gathers. Thus, layer depths and velocity structure of the travel-time model in this area is approximated to be laterally continuous with the layer defined in the area of the multiple BSRs (Figure 5-10). To the SW of the profile, within the almost flat sedimentation of the central basin, modelling is better constrained and layer boundaries can be traced in lateral continuity with the ones defined in the BSRs area (Figure 5-10). However, at the front of the compressional folding marking the transition from the BSRs area to the central basin domain, seismic events are also poorly imaged. As a result, this area has also to be considered poorly constrained in terms of the defined velocity model.

We focused on the definition of the shallow sediment velocity structure for the area where BSRs are identified (NE) and, as a comparison, for the sediments at similar sub-seafloor depths in the central basin (SW) (Figure 5-10). These two areas show seismic velocities with different trends. Sediments up to 258 mbsf in the central basin have a V_P range of 1.55-1.64 km/s, so Vp values lower than the range of 1.55-1.72 km/s modelled in sediments above and at BSR0 (Figure 5-10). Similarly, sediments up to 360 mbsf in the central basin have a V_P range of 1.72-1.75 km/s, also with V_P values lower than the range of 1.75-1.83 km/s modelled above and at BSR1 (Figure 5-10). An interesting additional observation is that, whereas a low-velocity zone is modelled between BSR1 and BSR3, velocities increase in sediments of the central basin (Figure 5-10). The presence of higher velocities in sediments between the seafloor and the imaged BSRs may indicate lithological changes and/or the presence of hydrate-bearing sediments. The lower velocities of sediments in the central basin may be representative for the background values assuming no hydrate in sediments.

Previously published tomographic seismic experiments (Scott et al., 2009) and information from well-data (Ross et al., 1978; Muratov et al., 1978) have shown that the top 2-3 km of sediments in the EBSB have a relatively homogeneous seismic velocity structure with a high velocity gradient and velocity increasing from 1.6 to 2.0 km/s, whereas velocities typically increase more gradually at greater sub-seafloor depths, reaching ~ 3.5 km/s at 5.0 km (Edwards et al., 2009). Scott et al. (2009), based on a travel-time analysis in the central-SW part of the EBSB, found that the seismic velocity in shallow sediments steadily increases with depth by a vertical gradient of $\sim$0.7 s^{-1}. Generally, the velocity gradient expected for shallow sub-seafloor sediments dominated by a shale lithology is $\sim$0.55 s^{-1} and by a sand lithology is ~1–1.15 s^{-1} (Japsen et al. 2007). Scott et al. (2009) interpreted their $\sim$0.7 s^{-1} gradient to suggest a shale-dominated lithology, in agreement with the DSDP Hole 379A lithostratigraphy (Ross, 1978). Given the lateral uniformity of sediments across the whole basin, we assume the same lithology in our study area.

Based on this knowledge of the EBSB shallow lithology, we compare the velocity trends observed in sediments above BSR1 with the expected velocity trends assuming standard velocity gradients

for shale and sand lithology (Japsen et al. 2007), and with the expected velocity trends assuming the intermediate shale gradient estimated by Scott et al. (2009). This comparison allows us to evaluate whether seismic velocities modelled in shallow sediments at the BSRs location may be considered anomalously high. The same comparison is also done for the velocity trend estimated within shallow sediments in the central basin, where velocities are generally lower than those above BSR1 (Figure 5-10, Figure 5-11).

The comparison between V_P profiles shows that shallow sediment velocities in the central basin have a similar gradient to that estimated by Scott et al. (2009), which is representative of a shale-dominated lithology (Figure 5-11). This agrees with the sediments expected within the top few hundred mbsf in the Black Sea (e.g., Ross, 1978; Tari and Simmons, 2018). Sediments in the BSRs area are instead characterised by higher V_P gradients and, in particular, sediments above BSR0 show a velocity gradient similar to the one of sand-dominated lithology (Japsen et al. 2007), and sediments between BSR0 and BSR1 have an even higher gradient (Figure 5-11). This comparison highlights the anomalous velocities within sediments up to BSR1, where gradients are outside the estimates corresponding to the expected lithology for this area. Below BSR1, the low-velocity zone represents another velocity anomaly (Figure 5-10, Figure 5-11). Although our tomographic approach cannot reveal the internal structure of the low-velocity zone, its thickness and mean velocity are well constrained by travel-times from a reflector marking its base.

The combined lateral and vertical variation in V_P is also linked to the variation in amplitude and polarity of the BSRs, which indicate a heterogeneous distribution of sediment properties and, more specifically, a variable distribution of potential hydrate and free gas at different stratigraphic levels. The observed V_P is used to model the effects that different concentrations of free gas and gas hydrate may have on the seismic properties of a shale-dominated sediment host (section 5.6.4).

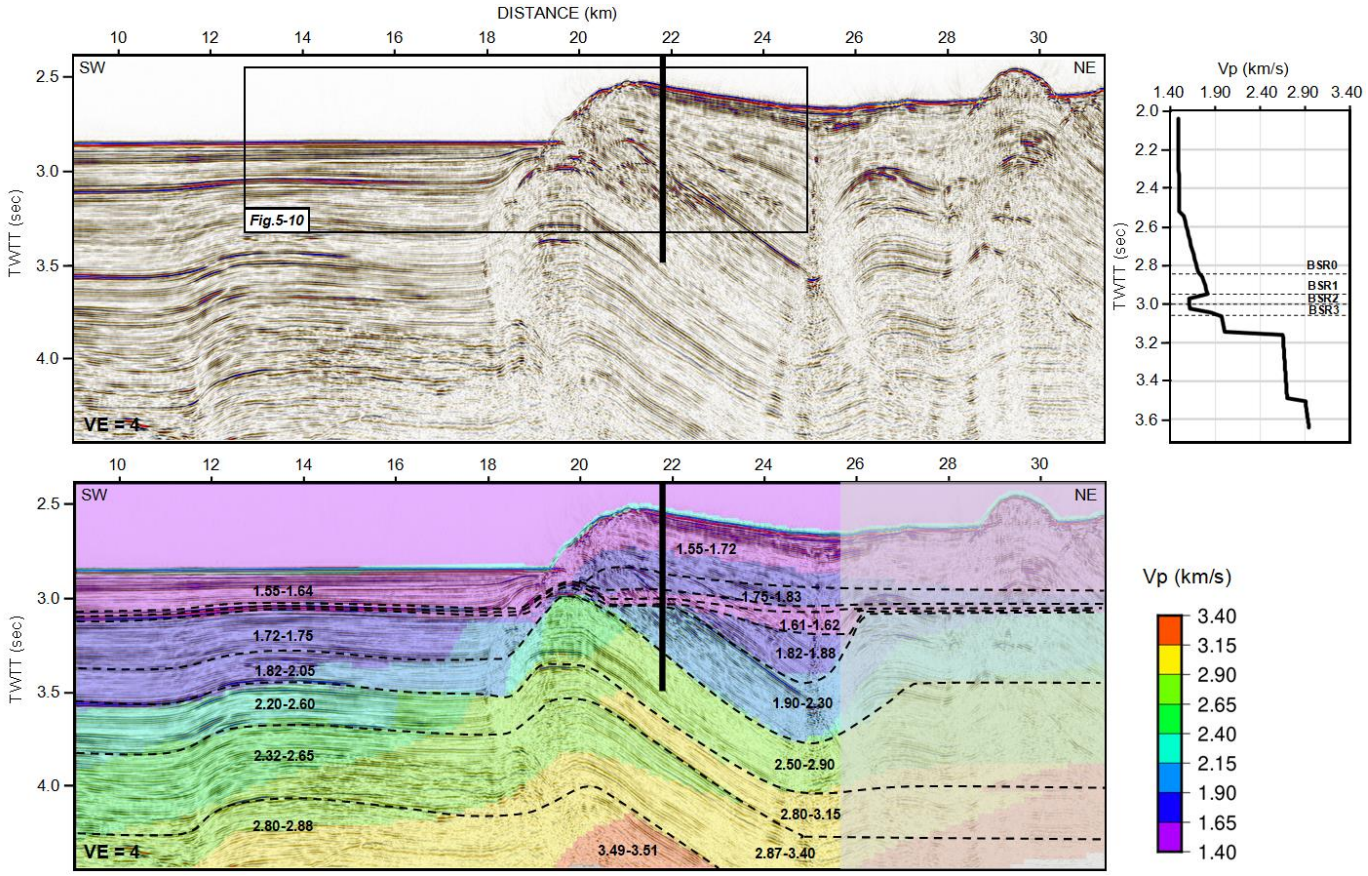

Figure 5-10. Stack profile of the seismic data used for velocity modelling (top), and the 2D velocity model resulting from the combined reflected and refracted travel-time analysis overlaid on top of the seismic section (bottom). The model is poorly constrained to the NE (shaded area), due to the geological complexity of the area. Good constrain on the velocity model exist between 9.85 km and 24.25 km distance along the profile. The thick black segment on the seismic sections show the location of the 1D velocity profile shown to the top right. V_P values are in km/s. The black box in the top section refers to the zoom image in Figure 5-11.

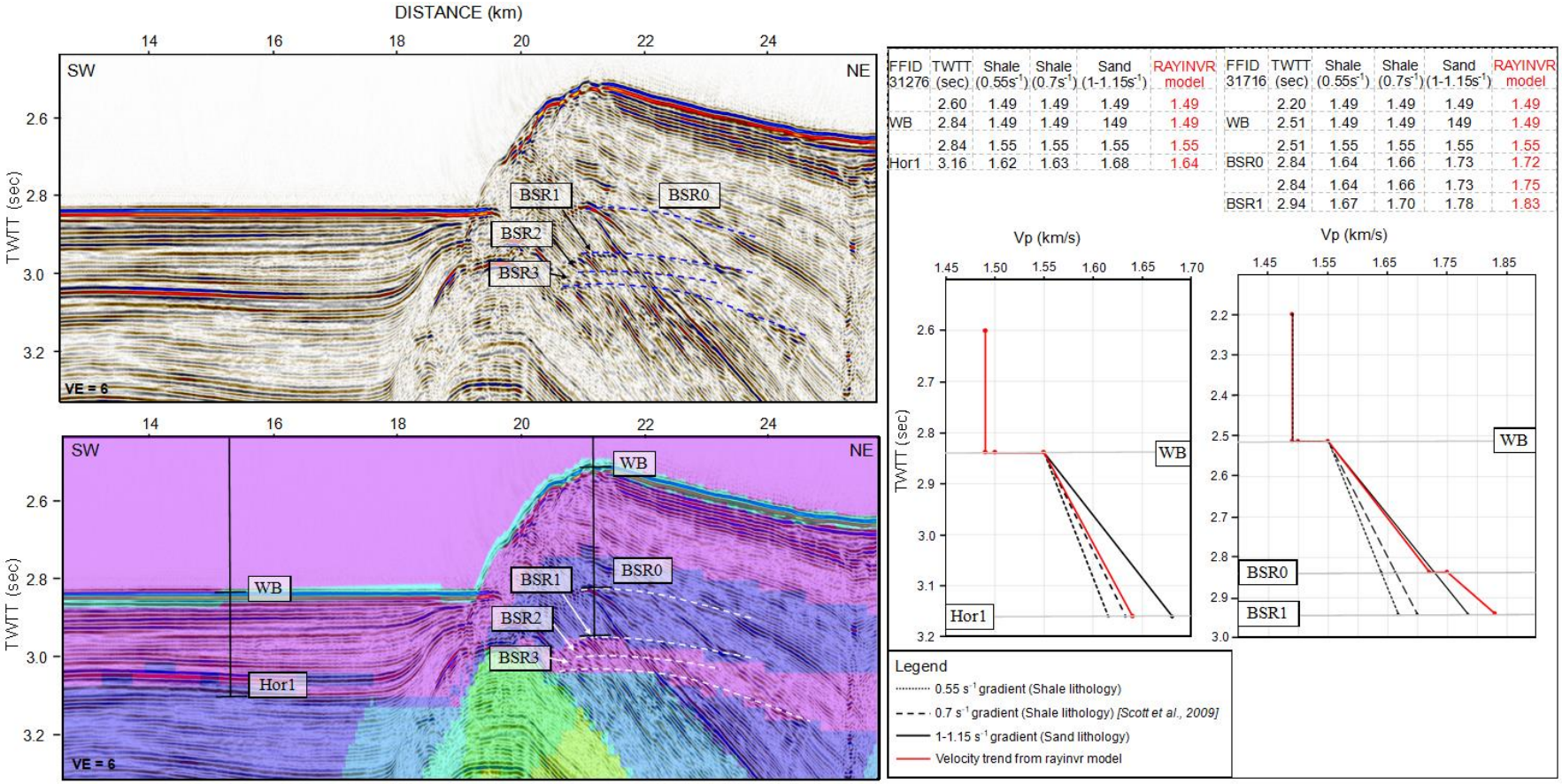

FFID 31276	TWTT (sec)	Shale (0.55s^{-1})	Shale (0.7s^{-1})	Sand (1-1.15s^{-1})	RAYINVR model
	2.60	1.49	1.49	1.49	1.49
WB	2.84	1.49	1.49	149	1.49
	2.84	1.55	1.55	1.55	1.55
Hor1	3.16	1.62	1.63	1.68	1.64

FFID 31716	TWTT (sec)	Shale (0.55s^{-1})	Shale (0.7s^{-1})	Sand (1-1.15s^{-1})	RAYINVR model
	2.20	1.49	1.49	1.49	1.49
WB	2.51	1.49	1.49	149	1.49
	2.51	1.55	1.55	1.55	1.55
BSR0	2.84	1.64	1.66	1.73	1.72
	2.84	1.64	1.66	1.73	1.75
BSR1	2.94	1.67	1.70	1.78	1.83

Figure 5-11. Comparison between shallow sediment velocity trends in the central basin and in the BSRs area, from seafloor (WB) down to ~ 360 mbsf (Hor1) and from seafloor (WB) down to BSR1, respectively. V_P trends are also calculated assuming velocity gradients expected for shale or sand dominated lithology (0.55 s^{-1} and 1-1.15 s^{-1}; Japsen et al. 2007 - note that a gradient value of 1.1 s^{-1} is assumed for calculating V_P trend for sand lithology), and the velocity gradient estimated by Scott et al. (2009), which was interpreted as representative for the shale lithology of the Black Sea shallow sediments (0.7 s^{-1}).

5.6.3 Modelling of the base gas hydrate stability zone

The comparison between the depths of the BSRs, calculated by travel-time analysis, and the calculated BGHSZs shows that a geothermal gradient of 38°C/km provides a better fit with the depth of BSR0. The BSR1 depth is instead best fitted by geothermal gradients between 26 and 30°C/km. Lower geothermal gradients need to be assumed for the deeper BSRs (BSR2 and BSR3) (Figure 5-12).

Parameters such as salinity, seafloor temperature and hydrate-forming gas composition are well-constrained across the Black Sea and they are not expected to vary in this area. Furthermore, any of the expected variations, except hydrate-forming gas composition, will only have a little impact on the estimated BGHSZ. The main uncertainty is here represented by the geothermal gradient values. Previous studies have showed that geothermal gradient in this particular area may be greater than 42 °C/km due to potentially deeply sourced heat-flow rising along the fault systems dominating the folded sediments of the Tuapse Trough (Vassilev, 2006). Overall, this analysis shows that, with the exception of BSR0, none of the other BSRs closely follow the calculated phase boundary.

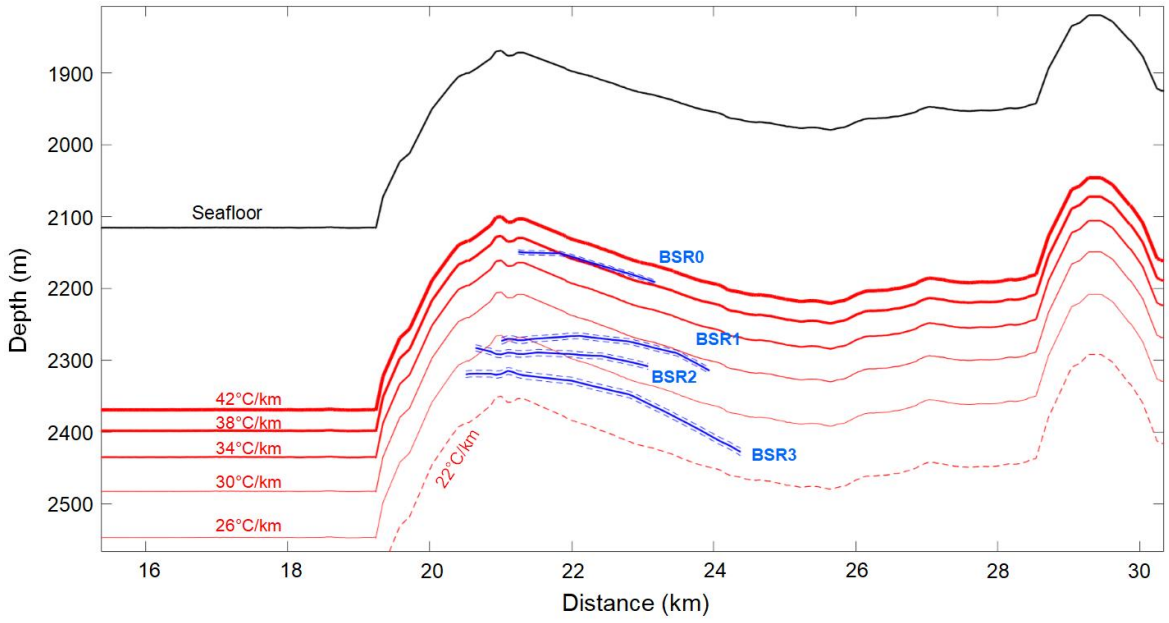

Figure 5-12. 2D plot showing results from the modelling of the BGHSZ assuming 100% methane gas composition, 0.5% wt pore-water salinity, 22-42°C/km geothermal gradient, and 9°C near seafloor temperature. Black lines represent seafloor depth obtained from seismic data; continuous blue lines are seismic BSR depths, and dashed blue lines show BSR depth error for a ± 20 m/s velocity variation estimated from travel-time analysis; red lines represent the calculated BGHSZ. Vertical axis is depth in metre (m) below sea-level. Horizontal axis is distance in km along the 33km-long profile.

5.6.4 Effective-medium modelling

We have used the effective-medium modelling approach described by Marin-Moreno et al. (2017) to calculate V_P and compare it with the V_P obtained from travel-time analysis (hereafter named as *observed* V_P). We model depths associated with main changes in V_P, which are related to the depth of the identified BSRs. Similar sub-seafloor depths are assumed in the central basin. This comparison allows to define which ranges of hydrate (S_H) or gas (S_G) saturation in the pore space can explain the observed V_P. To calculate the V_P we use the modelling parameters summarised in Table 5-1 and Table 5-2. The hydrate habit (i.e. pore-floating or cementing) has a strong influence on physical properties of sediments (e.g., Spangenberg et al., 2014), with cementing hydrate highly increasing V_P even at low (below 1%) hydrate saturation. Here, V_P values calculated assuming cementing hydrate were much higher and non-comparable with the observed V_P in our study area. Thus, we assumed a pore-floating hydrate morphology.

At the BSR0 depth of 258 mbsf, the observed V_P reaches a value of 1640 m/s in the central basin and of 1720 m/s at BSR0 location (Figure 5-11, Figure 5-13a). Assuming a 50% porosity of the sediment, the calculated Vp for a fully water saturated (S_w of 100%) sediment is 1671 m/s, close to the observed V_P in the central basin (Figure 5-13a). For porosities below 50%, the calculated V_P would be higher than the observed one. For a porosity of 60%, the calculated V_P matches the observed V_P assuming a S_H of about 1% (Figure 5-13a). At BSR0, the observed V_P is around 1720 m/s. To match the calculated and observed V_P, a S_H below 2% has to be assumed with 50% porosity, increasing to 4% saturation for 60% porosity (Figure 5-13a). Porosity slightly less than 50% could instead explain the observed V_P considering only water-saturated sediment. As previously reported porosities at a similar stratigraphic depth to the BSR0 depth are in the range of 50% (e.g., Zillmer et al., 2005), we assume this value to be the most representative.

At the BSR1 depth of 360 mbsf, the observed V_P reaches a value of 1720 m/s in the central basin and of 1830 m/s at the BSR1 location (Figure 5-11, Figure 5-13b). The calculated V_P matches the observed V_P in the central basin assuming a S_H below 1% with 50% porosity and below 3% with 60% porosity (Figure 5-13b). For porosity values slightly lower than 50%, a water-saturated sediment may be considered. At BSR1, observed V_P is around 1830 m/s. In order to match calculated and observed V_P, a S_H below 1% at 40% porosity, or a S_H below 4% at 50% porosity, or a S_H below 6% at 60 % porosity needs to be assumed (Figure 5-13b).

At the BSR3 depth of 438 mbsf, the observed V_P reaches a value of up to 1820 m/s in the central basin, while a velocity inversion is visible within a 70-80 m-thick layer just above BSR3 with associated V_P of 1610-1620 m/s (Figure 5-11, Figure 5-13c). The calculated V_P matches the observed V_P in the central basin either assuming a water-saturated sediment at 40 % porosity, or a S_H below

4% with 50% porosity and below 6% with 60% porosity (Figure 5-13c). For values of porosity slightly lower than 40%, the calculated V_P would be higher than the observed V_P. In the low-velocity zone above BSR3, the observed V_P is 1610-1620 m/s. In order to match calculated and observed V_P, a water-saturated porosity above 60% would be needed, although such a high porosity in sediments at depth greater than 400 mbsf is excluded (Figure 5-13c). As the velocity inversion observed may indicate the presence of free gas in sediments (Singh et al., 1993), we modelled the expected V_P for a brine and gas saturated sediment (Figure 5-13d). Assuming a 40-50% porosity, a S_G below 1% may explain the observed V_P. Assuming a porosity of 30%, a S_G up to 20-25% provides a match between calculated and observed V_P (Figure 5-13d). The presence of even small amounts of gas (i.e., below 1%) has a large impact on the calculated V_P, decreasing it by ~ 270 m/s. For higher values of gas saturation (i.e., above 1%), the impact on the calculated V_P is lower, with velocities decreasing by less than 40 m/s (see Appendix E). At both locations, estimates of gas hydrate saturation may vary by ± 1% according to the error estimates and resulting ΔV_P (Table 5-1). Gas saturation estimates may instead vary by up to ± 10% when considering S_G > 1% and up to 20-25% (see Appendix E).

As a final test, we model a V_P response at a deeper stratigraphic depth of ~ 600 mbsf. This depth corresponds to an average observed V_P of about 2020 m/s for both the central basin and BSRs area (Figure 5-10). The calculated V_P matches the observed velocity assuming a fully water-saturated sediment with a porosity of 30%, which is in good agreement with the porosity and lithology expected at that depth. This confirms the absence of anomalous velocities that may be associated with hydrate or gas in the pore space at that depth.

Modelling results show that the V_P ranges observed in the central basin may be explained by the assumed shale-dominated lithology, with a porosity decreasing from 60% to 40% from 258 m to 438 m depth bsf. Lower porosities ~ 30% may be assumed at greater depths (~600 mbsf). Generally, a S_w of 100% or a S_w above 99% with S_H up to 1%, provides a good match between observed and calculated V_P in the basin area at depths of ~258 mbsf. Given the uncertainty on sediment composition in this area, lithological changes (i.e., higher amounts of quartz or other minerals), rather than the presence of hydrate in the pore space, may explain the differences between calculated and observed V_P. A similar ambiguity can be assumed for differences in V_P at BSR0. However, while an S_H up to 1% is required for sediments in the central basin for a porosity of 60% at a similar depth to the BSR0 depth, at the BSR0 location an S_H up to 4% is required for the same 60% porosity. Similarly, whereas for depths of ~ 360 mbsf in the central basin a S_H below 3% may be assumed, at BSR1 location, an S_H up to 6% generates a better match between calculated and observed V_P. Finally, the low-velocity zone imaged above BSR3 seems to be best described by a S_G up to 1% and up to 20-25%, for porosities between 40-60% and 30-40%, respectively.

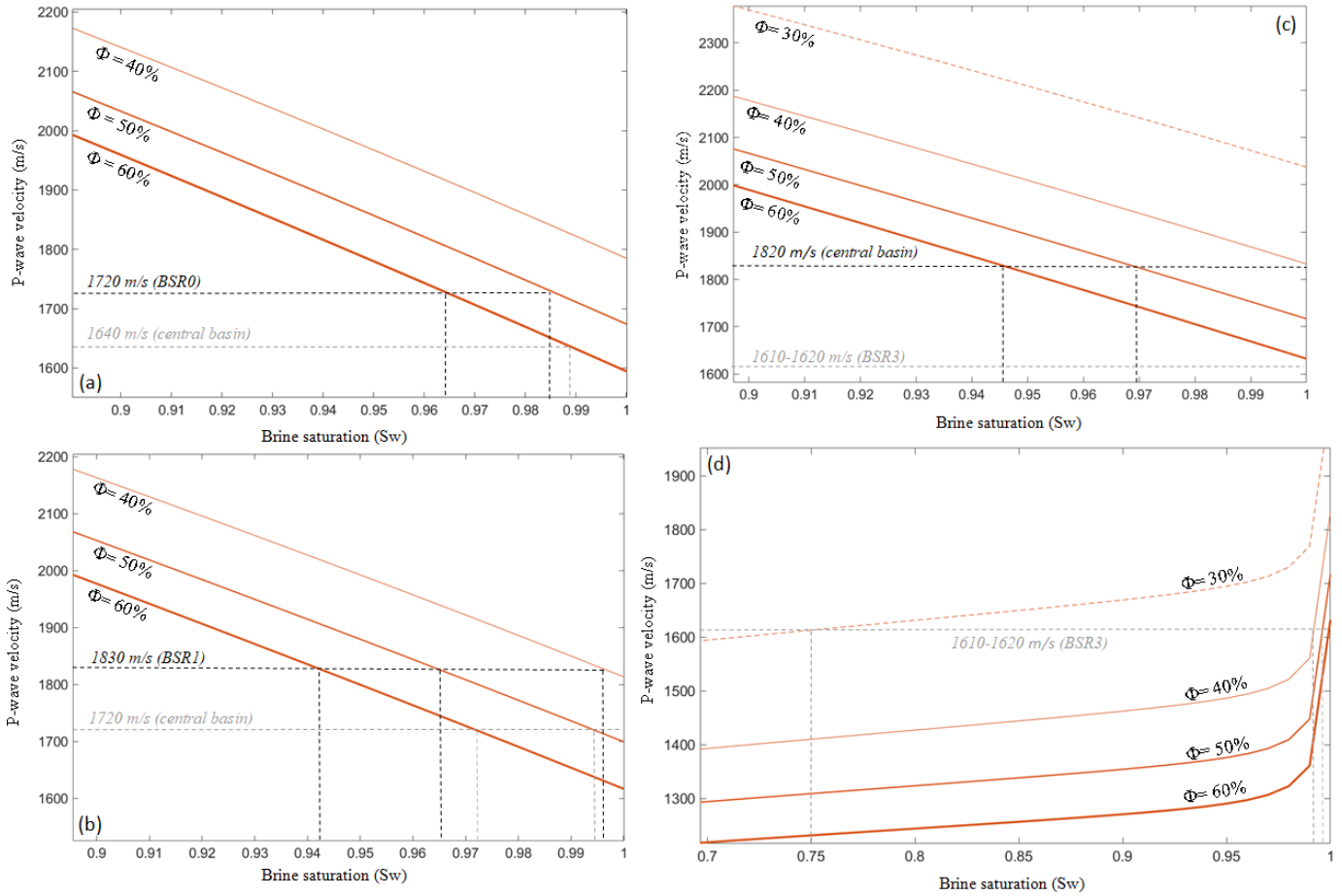

Figure 5-13. Plot of V_P trends at different percentages of brine saturation (Sw) versus hydrate saturation (S_H) or gas saturation (S_G) in the pore space, and as function of porosity (ϕ). A S_w of 1 means fully water-saturated sediment. V_P trends are shown at (a) 258 mbsf, (b) 360 mbsf and (c)-(d) 438 mbsf. V_P values are summarised in Figure E- 1 (Appendix E).

Overall, modelling results show that little S_H between 0-4% may be present in the shallow sediments of the central basin and at BSR0. Higher amounts of pore-floating hydrate may be expected within the 100 m-thick layer between BSR0 and BSR1, where modelling results suggest a S_H between 1-6%, depending on the sediment porosity assumed. Finally, the low-velocity zone between BSR1 and BSR3 seems to be associated with the presence of free gas in the pore space, which concentration may be as high as 20-25% for a 30-40% sediment porosity.

5.7 Discussion

Geophysical data are often used to constrain the physical properties of sediments. The long-offset nature of the seismic data used in this study allows refracted arrivals to be imaged at far offsets. Streamer data pre-conditioning can help to improve this travel-time information, making it comparable with a seafloor or near-seafloor refraction experiment (e.g., Harding et al., 2007; Henig et al., 2008). We therefore tested the ability of the downward continuation technique, generally used for targets at kilometre-scale depths within the sedimentary section and at crustal levels, to enhance far offset travel-times and thereby constrain velocity information within the top few hundred meters of sediments.

Downward continuing the seismic field improved the first arrival refraction, collapsing the seafloor reflection towards a point at zero offset and bringing out refractions from shallower structures as first arrivals at nearer offsets. However, downward continued data also contain strong linear artefacts at near offsets, which come before the first arrivals. These artefacts limited the refracted arrival offsets that could be used for travel-time analysis. Also, we were not able to recover refracted information between the multiple BSRs. This limitation may be due to the small spacing between seismic phases and their shallow position in the sub-seafloor sediments implying that, although refractions may be generated at such levels, they will not be first arrivals on shot gathers but instead they are masked by other refractions from deeper and faster layers (e.g., Qin and Singh, 2018). These elements limit the downward continuation technique when applied to shallow stratigraphic targets, thus impacting refracted travel-time analysis. Another element that affected our results is the geological complexity of the study area. This complexity not only impacted on the results of downward continuation generating a series of noise and artefacts, but also limited our ability to sample refracted, and some reflected, events in lateral continuity along shot gathers. Finally, since refracted arrivals are not generated by low-velocity zones, refracted travel-times provide little constraint over gas-bearing zones. For all these reasons, reflected travel-times were essential for velocity model construction and definition, whereas only few refracted arrivals could be used to improve the velocity field. Nevertheless, these travel-times allowed us to check model consistency and to better constrain the lateral variation of the velocity field. Such constraints were possible because, although refractions observed on downward continued data still come from layers deeper than the observed BSRs, their travel-times bear information of the shallow layer's velocity structure.

Multiple BSRs that are not representative of the present-day BGHSZ in an otherwise static hydrate system may derive from: (i) variations in gas compositions (Andreassen et al., 2000; Geletti and

Busetti, 2011) or (ii) variations in the subsurface pressure field (Pecher et al., 2017; Tinivella and Giustiniani, 2013). The presence of different hydrate-forming gases, stable at different pressure-temperature conditions, may generate multiple BSRs also characterised by a positive signal polarity (Andreassen et al., 2000). However, there is little evidence for the presence of relevant quantities of hydrate-forming gases other than methane in the Black Sea (e.g., Vassilev and Dimitrov, 2002; Poort et al., 2005; Zander et al., 2020). Overpressure compartments may also be present in sub-seafloor sediments, whose top and base may be imaged by seismic data as BSR-like reflections (e.g., Tinivella and Giustiniani, 2013). Overpressure compartments may lead to low-frequency events in seismic data, since high-frequency components of the seismic energy are absorbed by gas (e.g., Geletti and Busetti, 2011). However, our seismic data do not show evident blanking effects that may be associated with the presence of high amounts of gas. Furthermore, previous calculations from the WBSB where multiple BSRs have similar spacing in depth between them as the ones observed in this study, have shown that the presence of overpressure compartments can be excluded because the necessary gas column would exceed the vertical distance between two overlying BSRs (Zander at al., 2017). We therefore exclude that multiple BSRs identified in this study result from either changes in gas composition or from the presence of overpressure compartments.

Our results showed that P-wave velocities increase from 1.55 km/s to 1.72 km/s in sediments from seafloor down to BSR0 depth, with a velocity gradient resembling more that of a sand-dominated lithology (Figure 5-11). Within the approximately 100 m-thick sequence between BSR0 and BSR1, P-wave velocities range from 1.75 to 1.83 km/s, showing a velocity gradient higher than that expected for both a shale-dominated and sand-dominated lithology (Figure 5-11). An increase in seismic velocity beneath BSR0 is further indicated by the positive polarity of BSR0 (Figure 5-3). Sediments beneath BSR1 show a velocity decrease of approximately 12%, from 1.83 to 1.61-1.62 km/s. This low-velocity zone is 70-80 m thick and extends to BSR3. This velocity decrease is further evidenced by the negative polarity of the BSR1 reflector (Figure 5-3). BSR2 lies within the low-velocity zone, whereas BSR3 represents the base of the low-velocity zone, beneath which seismic velocities increase again. Free gas concentrations of only a few percent of the pore volume beneath the hydrate-bearing zone are sufficient to create a distinct BSR (e.g., Andreassen et al., 2007; Haacke et al., 2007). Gas trapped beneath a low-permeability layer that is not associated with the presence of hydrate (i.e., less permeable lithology or compacted layer), can also generate a BSR-like reflection. Thus, the presence of free gas may explain BSR1 even considering very low or absent gas hydrate saturation in the sediments above it, as this would still result in a reversed polarity reflection at BSR1. However, effective-medium modelling showed that the observed velocities may be expected for sediments at these depths assuming a pore-floating gas hydrate saturation of less than 4% at BSR0, and of less than 6% at BSR1 (Figure 5-13a, b). These values agree with observations

from fine-grained muddy sediments, where if gas supply to the system is modest, hydrate saturation is usually less than 10% and hydrate is disseminated in the pore space (i.e., pore-floating; e.g., Boswell et al., 2012; Collett et al., 2014; Holland et al., 2008).

Sediments in the central basin show different V_P trends compared to the BSR area, assuming similar stratigraphic depths. For sediments down to ~ 258 mbsf velocities up to 1.64 km/s could imply the presence of hydrate saturation of less than 2% (Figure 5-13a). Approximately 100 m deeper, velocities of 1.72 km/s point towards a gas hydrate saturation of less than 3% (Figure 5-13b). However, these hydrate saturation estimates assume a sediment porosity of 60%, which is higher than what is expected at such depths based on previous drilling results such those at DSDP Hole 379A, where the approximately 70% porosity within shallow sediments was found to decrease down to 38% at around 350 m depth bsf (Ross et al., 1978). Other estimates, assuming the average shear and bulk moduli and density for the Black Sea sediments, have also suggested that porosity in sediments between seafloor and 205-270 m bsf decreases from 78 ± 1% to 57 ± 7% (Zillmer et al., 2005). Further studies have also reported a porosity of approximately 60% for the shallow sediments of the Black Sea, decreasing down to 50% at sediments around 150 m bsf (e.g., Vassilev, 2006, Riboulot et al., 2018; Merey, 2017). Lower porosities (~ 50%) can, alone, produce the expected velocity range assuming water saturated sediment in the central basin. Similarly, the maximum estimated gas hydrate saturation above BSR0 and BSR1 is based on a 60% sediment porosity. Here, although assuming a lower porosity (~50%) decreases the expected hydrate saturation, a pore-floating gas hydrate saturation of less than 2% and 4% still needs to be considered to explain the observed velocities at BSR0 and BSR1, respectively (Figure 5-13a, b). Finally, sediments up to 438 m depth in the central basin, show increasing velocity trends which do not match the low velocities observed above BSR3. Sediments in the central basin are therefore considered to show the background velocity trend for sediments, whereas the velocity trends at the BSRs define a change in the physical properties of sediments. Although the velocity model has limited constraint over the lateral extent of these physical changes visible at the BSRs, these changes seem to be focused at the crest of the folded structure where BSRs are imaged (Figure 5-10, Figure 5-11).

The higher hydrate saturation estimates at BSR1, and the presence of gas beneath it, suggests that it marks the present-day BGHSZ. Conversely, BSR0 may be interpreted as an acoustic boundary between lower (at the top) and higher (at the bottom) hydrate saturation, or as the upper limit for the presence of hydrate in the pore space (e.g., Boswell et al., 2016; Taladay et al., 2017), i.e., the top of the gas hydrate occurrence zone (GHOZ; Wood and Ruppel, 2000; Riedel and Collett, 2017). BSR-like reflections associated with the top of the GHOZ are rarely observed (e.g., Posewang and Mienert, 1999). If BSR1 represents the BGHSZ, this would correspond to the BGHSZ modelled

assuming a 26-30˚C/km geothermal gradient (Figure 5-12). These values are slightly lower than that observed at DSDP Hole 379A (32–38˚C/km; Erickson and Von Herzen, 1978), which would generate a BGHSZ fitting BSR0 instead (Figure 5-12), but within ranges calculated/measured at other locations in the EBSB (e.g., Vassilev and Dimitrov, 2002; Minshull and Keddie, 2010). Nevertheless, constraints on the local geothermal gradient are limited and often show high degree of variability (Riedel et al., 2021). For instance, geothermal gradient measurements in the area have recorded values greater than 42˚C/km, which have been interpreted to result from local heat-flow focused along deep faults related to the compressional sediments folding in the Tuapse Trough (Vassilev, 2006). Localised tectonic deformation may therefore play a significant role in controlling fluid and heat-flow.

The presence of a low-velocity zone, typically a few meters to many tens of meters thick, in which there is a small proportion of free gas within the pore space is commonly observed below the BGHSZ (e.g., Singh et al., 1993; MacKay et al., 1994; Hovland et al., 1997). This free gas layer may have different origins. For instance, (i) it may be related to deeply sourced fluids that have migrated upwards along folded sediments or along fractures/faults (e.g., Crutchley et al., 2019), (ii) it may be related to in-situ biogenic gas generation (e.g., Schneider et al., 2016), (iii) it may be gas formed by hydrate dissociation which may still be in a transient state and has not migrated upward into the new GHSZ (e.g., Zander et al., 2017), or (iv) it may be a combination of these origins. When free gas flow takes place along permeable pathways, such as permeable or fractured fault systems or coarse-grained sediment layers (Collett et al., 2009; Nole et al., 2016), it may focus toward topographic or structural highs by buoyancy (e.g., crests of ridges or anticlines; Boswell et al., 2012; Flemings et al., 2003; Frederick and Buffett, 2011). Such permeable pathways are commonly observed in concentrated gas hydrate accumulations (e.g., Crutchley et al., 2019). The presence of potentially deep faults associated with folding and thrusting in the Tuapse Trough, together with the dipping geometries of the stratigraphic layers alternating fine- and coarse-grained material (Figure 5-2), provide plausible pathways for the focused migration and accumulation of gas at this level. Bedding-parallel fluid flow at anticlinal ridges and fluid upward migration along thrust faults have been inferred at a few other gas hydrate locations, i.e., offshore Taiwan (Lin et al., 2008), Hikurangi Margin offshore New Zealand (Crutchley et al., 2019; Han et al., 2021), Nankai Margin (Ashi et al., 2002). Free gas fluid flow from beneath the BGHSZ would also explain the higher hydrate saturation between BSR0 and BSR1. However, local free gas flow often results in high hydrate saturation values (e.g., up to or more than 90%; You and Flemings, 2018), whereas our results point towards hydrate saturations of less than 6% at BSR1. Rising fluids could have migrated through the GHSZ. Although numerous mud volcanoes and seeps related to fluid expulsion have been reported in this same area (e.g., Vassilev and Dimitrov, 2002; Meisner et al., 2009), no evidence for fluid

expulsion (i.e., pipes, chimneys) or clear faults/fractures through the GHSZ are visible on our seismic profile. Thus, we exclude focused fluid flow to represent the main mechanism driving free gas accumulation beneath BSR1 and gas hydrate formation just above BSR1. Nevertheless, given the high organic content characterising the Miocene, Pliocene and Quaternary units of the EBSB (Tari and Simmons, 2018), it is possible that free gas beneath BSR1 could derive from microbial biogenesis of organic-rich material buried beneath the BGHSZ (e.g., Schneider et al., 2016). If this biogenic gas was to contribute to hydrate formation at the BGHSZ, it would also result in low methane hydrate saturations, in the range of 1–10% (e.g., Malinverno, 2010). Given the localised nature of the free gas accumulation, this free gas may still have migrated laterally through permeable pathways, focusing at the anticlinal structure beneath BSR1.

Methane recycling can also explain the presence of both enriched methane hydrate at the BGHSZ and free gas beneath it. This process occurs when previously formed hydrate within sediments passes through the BGHSZ (i.e., sediment burial and/or climatic changes) where it dissociates into free gas and water. The free gas generated upon dissociation flows upward as a separate phase and reforms hydrate immediately above the BGHSZ (e.g., You et al., 2019). This mechanism also explains the presence of higher hydrate concentrations at the BGHSZ, although generally above 10% (i.e., Blake Ridge, Flemings et al., 2003; South China Sea, Wang et al., 2014).

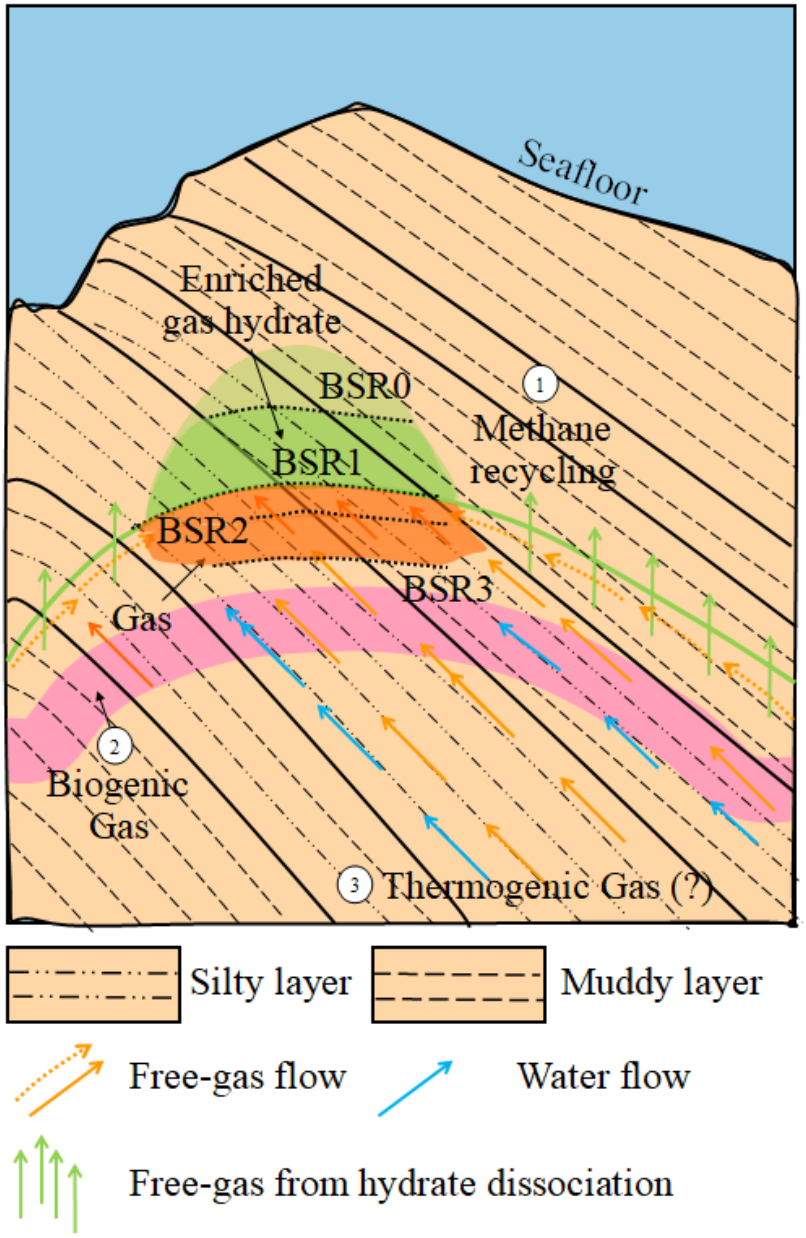

Figure 5-14. Schematic diagram showing the most likely mechanisms for generating multiple BSRs in the EBSB: (1) methane recycling and (2)-(3) free gas flow from beneath the BGHSZ, which may include microbial gas generated from beneath the BGHSZ (pink zone, (2)) and/or thermogenic gas coming from deeper sources (3). The folded stratigraphy favours a focused free gas migration along permeable layers and gas accumulation and gas hydrate formation at the crest structure. BSR0 is interpreted as the boundary between a lower gas hydrate concentration above (light green) and a higher gas hydrate concentration beneath (dark green). BSR1 represents the present-day BGHSZ, and the boundary between concentrated gas hydrate above (dark green) and free gas beneath (orange). BSR 2 and BSR3 are considered relics of previous BGHSZs; following gas hydrate destabilisation, a vertical shift of the BGHSZ has resulted in the release and upward migration of free gas (above BSR3). Note that the lateral extent of free gas and

gas hydrate accumulations reflects the lateral uncertainty in the velocity model. Diagram modified from You et al. (2019).

When resulting from dissociation processes, multiple BSRs are considered to record both the shifted modern and relic base(s) of the hydrate stability zone, indicating the presence of dynamic hydrate systems (Figure 5-14). Similar considerations come from studies on multiple BSRs in the WBSB (e.g., Bialas et al., 2020; Zander et al., 2017; Popescu et al., 2006, 2007). In the WBSB, as in other multiple BSRs areas, various processes are considered to explain the vertical shift in the BGHSZ. These may include (i) the ascent of warm and/or high-salinity fluids toward the seafloor (Boswell et al., 2012; Taladay et al., 2017), or (ii) sudden increases in water-bottom temperature and/or decrease in pressure, rapid sedimentation and tectonic uplift (Bangs et al., 2005, 2010; Foucher et al., 2002; Zander et al., 2017; Riedel et al., 2021). Most studies on paleo-environmental conditions of the Black Sea come from the Danube Fan, and are supported by information from litho-facies analysis from DSDP Holes 380 and 381 (Figure 5-1) (i.e., Zander et al., 2017). These well data have shown that the paleogeographic environment of the basin during Quaternary was determined mainly by climatic and tectonic phenomena (Muratov et al., 1978). During the Holocene, after the LGM, sea-level gradually rose, with the maximum level of transgression exceeding the recent one of some meters reached during middle Holocene (Muratov et al., 1978). At that time (9000 years ago) the last salinization of the Black Sea began due to the resumption of water exchange with the Mediterranean Sea. During upper Holocene (0-3000 years), judging by the sediment composition, the sea level in the basin was essentially the same as that of the present (Muratov et al., 1978). Therefore, since the LGM, the paleo-environmental conditions of the Black Sea resembled that of a “lake” in which marine ingression caused an eustatic sea-level increase of 100-150 m (e.g., Popescu et al., 2006, 2007; Zander et al., 2017; Ker et al., 2019; Vassilev, 2006; Ryan et al., 2003) and a seafloor temperature increase of 4-5 ˚C (e.g., Zander et al., 2017; Ker et al., 2019; Soutlet et al., 2010). A pressure increase due to the sea level rise would cause a downward shift of the BGHSZ, whereas a seafloor temperature increase would cause an upward shift of the BGHSZ. Typically, the hydrate system should respond more rapidly to pressure field changes in the subsurface, while temperature changes might require more time to reach the BGHSZ (Foucher et al., 2002; Pecher et al., 2017; Zander et al., 2017). WBSB paleo-BSRs depths have also been used to infer that geothermal gradient has changed since the LGM, decreasing from 32.5-37.5 ˚C/km to the present-day 24.5-30 ˚C/km (Zander et al., 2017). A geothermal gradient decrease from the LGM would have resulted in a downward shift of the BGHSZ, whereas the present-day stability field seems to be associated primarily to the topmost BSR. Beside the effects of these climatic changes, enhanced sediment loading due to rapid deposition is considered a major element that controlled heat conduction from below the BGHSZ and the pressure field in sediments, thus affecting the

hydrate system and contributing to their destabilisation and multiple BSR formation (Zander et al., 2017). Zander et al. (2017) noted that the sediment load above the multiple BSRs grew during the past glacial cycles and was not constant as stated by other studies (i.e., Popescu et al., 2006), thus leading to large errors when the BSRs are linked to ranges of lower bottom-water temperatures during stable cold climate periods. These authors also suggested that the thermal regime in the Danube Fan is in transient state and still adapting to the increase of the bottom water temperature from about 4-5˚C to today's 9˚C since the LGM. This implies that the BGHSZ will probably become shallower over the next tens of thousands of years as the geothermal gradient increases due to thermal diffusion (Poort et al., 2005; Zander et al., 2017).

A similar post-glacial evolution could be assumed for the nearby EBSB based on similar litho-facies analysis from DSDP Hole 379A (Figure 5-1), therefore, changed environmental conditions from the LGM may have affected our study area. Nevertheless, little is known about the influence and interaction of sedimentation/erosion processes in the EBSB, which are also important elements contributing to a shift the in the gas hydrate stability field. Our evidence suggests that multiple BSRs in the EBSB are most probably related to mechanisms of methane recycling following hydrate dissociation, although a contribution by microbial biogenesis beneath the BGHSZ cannot be excluded. Pressure field changes related to sea-level rise following the LGM would have resulted in a downward shift of the BGHSZ. Tectonic uplift in this compressional area would have instead resulted in an upward shift of the BGHSZ. Our evidence points towards an upward shift in the BGHSZ, forming a concentrated gas hydrate accumulation at the top of a crest structure. A temperature increase and/or an increase in sedimentation rates controlling heat conduction and the pressure field in sediments could be considered instead as primary factors controlling the upward shift of the BGHSZ. Temperature changes may have been driven by a combination of climatic changes, as for the WBSB multiple BSRs, tectonic processes (i.e., folding and thrusting) with differently distributed erosion and sedimentation processes, resulting in different shoaling and deepening of the BGHSZ and related BSR, and by changes in thermal conductivity and thus geothermal gradient within the folded sediments. The ascent of warm fluids from beneath the BGHSZ, which may be supported by the presence of faults running from the base of the folded structure up to the shallow sedimentary section, may also be considered to explain a vertical shift in the BGHSZ. Following gas hydrate dissociation, focused free gas may have migrated upward towards the new gas hydrate stability field and, given the folded sediments characterising this part of the EBSB, resulting in a focused gas hydrate formation (Figure 5-14). Free gas accumulation beneath the current BGHSZ may have therefore been controlled by the anticlinal shape of the sediments where BSRs are visible and, consequently, by lithology, with the coarser grained deposits favouring accumulation and migration of free gas along the folded structure. Similar

stratigraphic/structural control over the hydrate system has been inferred from multiple BSRs in the WBSB, although control elements are linked to the channel-levee depositional settings encountered in that area (Popescu et al., 2006; Riedel et al., 2021). In the EBSB, the stratigraphic/structural control over multiple BSRs generation shows a closer similarity with the dynamics occurring at compressional settings (i.e., offshore Panama, Reed et al., 1990; Hikurangi Margin, Crutchley et al., 2019). Assuming gas hydrate dissociation processes and upward migration of the BGHSZ, then BSR3 and BSR2 represent relics of past stability conditions still visible because of the presence of gas in the sediment pore space and/or because of their lithification following a long period of hydrate stability (e.g., Popescu et al., 2006). BSR2, within the low-velocity zone, could represent an intermediate stage in GHSZ upward shift.

5.8 Conclusions

- A long-offset seismic reflection profile reveals, for the first time, evidence for multiple BSR reflections along the NE margin of the EBSB. This profile was used to extract the physical parameters of sediments in the area, thus constraining the nature of the observed BSRs.
- Downward continuation was used to pre-condition seismic data before reflection and refraction travel-time analysis, resulting in improved first arrival refractions. Nevertheless, refracted events still come from layers deeper than the observed BSRs, and artefacts and noise at near offsets limit first arrival refraction picking. The close spacing between the BSR layers, the presence of a low-velocity zone, and the geological complexity of the area, pose limitations for the downward continuation technique and for picking of first arrivals related to the BSRs. Thus, the velocity model also strongly relies on reflected travel-time information from non-downward continued data.
- Combined travel-time analysis and effective-medium modelling show that the two topmost BSRs, BSR0 and BSR1, are associated with up to 2% and up to about 4 ± 2% pore-floating gas hydrate saturation respectively, assuming a 50% sediment porosity. Based on these estimates, we infer that BSR0 may represent the top of the GHOZ, or the acoustic boundary between sediments showing different amounts of hydrate saturation, whereas BSR1 represents the base of enriched hydrate accumulation directly above the BGHSZ. The depth of BSR1 shows good agreement with the depth of the modelled BGHSZ for a geothermal gradient between 26 and 30˚C/km, consistent with heat-flow estimates in the EBSB. Beneath BSR1, a 70-80m-thick low-velocity zone with up to 25 ± 10% of free gas includes BSR2 and extends down to the depth of BSR3.
- We infer that the higher gas hydrate concentration above BSR1, and evidence for free gas beneath BSR1, may be explained by mechanisms of methane recycling following primarily

temperature driven gas hydrate dissociation, although a contribution from biogenic (and/or thermogenic) free gas beneath the BGHSZ cannot be excluded. Differential erosion/deposition at the crest structure may have also played an important role in altering the sediments pressure field, thus causing an upward shift in the BGHSZ. However, more knowledge/constraints on the amounts of uplift, erosion and sediment deposition in this area is needed to assess the impact of pressure driven vertical shifts of the BGHSZ.

- The deeper BSRs are interpreted as relics of past hydrate stability conditions, defining the base of the gas layer (BSR3) and an intermediate level of the BGHSZ upward shift (BSR2). The localised nature of the hydrate and free gas accumulations are linked to the tectono-stratigraphic setting of the area, resulting in a focused gas and hydrate accumulation at the crest of the folded structure where BSRs are visible.

Given the limited constraints on the model parameters, saturation estimates strongly depend on the assumed sediment composition and porosity values. For a more robust estimate of hydrate and gas saturation in our study area, further constraints on the physical and chemical properties of the sediments (i.e., borehole measurements) are needed.

A more complex interaction between climatic events, tectonic uplift and consequent erosion and sedimentation processes, may have controlled gas hydrate stability changes in our study area. To assess the impact of tectono-sedimentary processes on the gas hydrate system in this part of the EBSB, a knowledge of rates of uplift and rates of sediment deposition is needed. Also, more densely spaced seismic profiles are necessary to better understand the interaction of the gas hydrate system with the tectonic setting and to constrain the presence and relevance of potential fluid migration pathways and flows.

Chapter 6 Conclusions and future work

6.1 Conclusions

The primary findings from this thesis can be summarised as follows:

- Long-offset seismic reflection data provided new insights into depositional geometries of the EBSB sedimentary infill, giving a broad picture of the depositional environments, facies distribution and, based on correlation with litho-stratigraphic information, on the distribution and age of deformation. The relationship between the age and architecture of the sedimentary units and their interaction with fault systems indicates that rifting initiated during Upper Cretaceous time, developing widespread extension and forming half-graben structures bounded by isolated high-angle normal faults along the margins of the basin. As extension migrated towards the basin axis, the main basin-bounding fault systems formed to accommodate the increase and focusing of extension. The progression from distributed to focused continental extension is recorded by two non-conformal syn-rift units. Fault geometry (i.e., dip angle) also indicates the progressive migration of extension towards the basin axis, changing from high-angle normal faults to low-angle, domino-fault arrays younging basinwards. As faulted and tilted blocks disappear to the SE, a transition from rough (NW) to smooth (SE) basement is related to an early Tertiary breakup followed by oceanic spreading. The age of breakup is constrained by sedimentary packages overlying the clear syn-rift to the NW and the top basement to the SE. These packages, previously interpreted as a post-rift infill, appear as post-kinematic (i.e., parallel or sub-parallel) in the central and SE part of the basin, and as syn-kinematic (i.e., fault displacement and wedge geometries) to the NW, where they indicate that extension may have continued until possibly Oligocene time. Their basal erosional unconformity is associated with the breakup stage, whereas their angular stratal relationship (i.e., downlap) with the underlying basement in the central and SE part of the basin is linked to oceanic spreading processes in this area. Results highlight the diachronous nature of rifting and breakup processes in the EBSB, similarly to other well-developed passive continental margins and extensional basins.
- Magnetic anomaly modelling was integrated to complement and guide seismic interpretation, helping to define the nature of morphologically and magnetically different basement domains in the central EBSB. Results showed a similar magnetisation character for both the rough (NW) and smooth (SE) basement morphologies, for which polarity and susceptibility values generally differ from the nearby continental crustal blocks. Thus, the

smooth and rough basement domains were interpreted to be both of mafic origin. Previous results from a wide-angle seismic experiment (Shillington et al., 2009) showed that changes in crustal thickness and velocity structure occur within the smooth and magnetised basement domain, which were interpreted to indicate the transition from a thin continental crust to a thick, magma-rich oceanic crust. Differences in melt distribution between the SE and NW rift segments, controlled by the presence of transform faults acting as rift propagation barriers delaying the opening of consecutive segments, are inferred to explain these apparent contradictions. Rift propagation delay can affect both mantle and melt flow between segments, thus limiting the propagation of low-viscosity mantle across the segment boundary and favouring melt accumulation at the opening segment. Varying melt supply can cause variations in crustal accretion that mostly affect oceanic layer 3, explaining both the changes in crustal thickness and velocity structure and the still uniformly magnetised character of the crust, which would result mainly from the upper oceanic layer (layer 2). Results from this study highlight the close magma-fault interaction driving oceanic spreading in the EBSB, and emphasise the ambiguity in the geophysical characterization of crustal type and in the definition of the continent-ocean transition (COT) at extensional settings, especially where geophysical evidence deviates from what is “normally” expected for continental and oceanic crusts. Only data integration and combined evidence from independent datasets can provide an interpretation of the crustal structure that can reconcile observations.

- Multiple BSRs, identified along the NE margin of the EBSB, provide a new case study to investigate the physical nature and the mechanisms driving the formation of these unusual features. Downward continuation was used to improve the refracted wavefield within shallow sub-seafloor depth targets, aiming to extract both reflected and refracted travel-times at the BSRs. However, a limited number of refractions could be picked and input for travel-time analysis. This was due to seafloor topography and the complex sub-seafloor stratigraphy causing noise and artefacts at near offsets, and to the shallow depth and close spacing of the BSR reflections limiting the ability of downward continuation to enhance those layers’ refracted arrivals making them first arrivals. Thus, travel-time velocity modelling had to rely mostly on reflection travel-times. The 2D velocity model obtained from travel-time analysis and results from an effective-medium modelling approach, showed that the uppermost BSR (BSR0) is associated with a subtle increase in seismic velocity that can be linked with an increase in the amount of gas hydrate in the pore space. The maximum predicted hydrate saturation (4 ± 2%) occurs directly above BSR1. BSR1 marks the boundary between this high-velocity interval (above) and a distinct low-velocity interval (below). Based on these results, BSR1 is linked with the present-day BGHSZ,

corresponding to the BGHSZ calculated assuming a local geothermal gradient of 26-30˚C/km, in good agreement with regional estimates. Beneath the BSR1, a 70-80 m-thick low-velocity zone is associated with the presence of up to 25 ± 10% of free gas in the pore space of sediments between BSR1 and BSR3. The higher gas hydrate concentrations above BSR1 and the accumulation of free gas beneath it are associated with mechanisms of hydrate re-cycling controlled by hydrate dissociation due to changes in pressure-temperature conditions, although free gas input from local biogenesis beneath the BGHSZ cannot be excluded. BSR2 and BSR3 are interpreted as relicts of previous gas hydrate stability conditions, and their existence may be linked to a lithological change in sediments at the old (BSR3) and intermediate (BSR2) BGHSZ, or to the presence of residual hydrate/gas left behind following vertical shift of the BGHSZ, or a combination of these elements.

6.2 Limitations of this study

Uncertainties and assumptions affect the results presented in Chapters 3, 4 and 5. In Chapters 3 and 4:

- The 3D nature of the investigated tectono-stratigraphic setting is poorly constrained by the sparse grid of 2D seismic lines, and by the intrinsic limitations of the seismic imaging technique suffering from signal attenuation at depth. 3D side effects from nearby geological structures can be present on seismic profiles, which may be interpreted as geological features belonging to the plane of the seismic section. This would introduce errors in the spatial definition of structural and stratigraphic elements. Also, the strike of the interpreted profiles can affect the recognition of fundamental geometrical relationships along the basin's flanks and in the central basin, thus impacting the characterisation of fault dip and geometry and the definition of syn- and post-kinematic stratal relationships.
- Unless clear constraints (i.e., densely spaced seismic data and/or direct sampling) are available, seismic interpretation can be highly subjective and the interpreter's view can play an important role in the identification and correlation of stratigraphic sequences. Sequence boundaries were here traced in lateral continuity across the basin based on similarity of seismic reflectivity patterns and stratal termination, thus defining regionally distributed features which are nevertheless affected by the above limitations. Uncertainties therefore exist in the definition of their time-correlative nature throughout their extent. Similarly, bias and uncertainties may exist in the definition of kinematic elements (faults) and their vertical and lateral extents. All these elements impact the three-dimensional definition of

the geometry and distribution of sedimentary and structural features, as well as their age definition.

- Temporal constraints are affected by the scarcity of deep well data in the area. Where a correlation between the interpreted units and published litho-stratigraphy is instead possible, the age attribution to distant units interpreted in regional continuity with the correlated ones is affected by uncertainties discussed above. As a result, this study cannot provide absolute age constraints, nor can it provide a constrained model for rift propagation and oceanic spreading dynamics. Ultimately, more closely spaced profiles of similar quality or 3D seismic datasets, together with new direct sampling of the basin's sedimentary sequences are required to determine more accurately how rifting has evolved in this area.
- The presence of a 2 km-thick water column and of a 9-10 km-thick sedimentary infill overlying the EBSB basement, makes drilling down to basement levels not possible with current technology. Therefore, the nature of the basement in this area has to be constrained using indirect methods (i.e., seismic, and potential field data). In this study, the unequivocal definition of crustal domains and their boundaries was hampered by the limited imaging at the top basement, and by the lack of a dense grid of seismic profiles. This translated into a poorly constrained definition of the extent of morphologically different domains. As crustal-scale features (i.e., Moho) are not resolved by the stacked seismic reflection profiles, velocity analysis at basement depths and beneath could not be considered reliable for the definition of the crustal structure. Refraction studies were needed to constrain crustal thickness as well as velocity structure at basement and crustal levels. However, previously published wide-angle seismic refraction data only consists of four profiles located to the SW and central part of the basin, thus they equally could not provide a regional constraint on crustal domain distribution.
- Seismic interpretation of basement morphology (smooth versus rough) is commonly performed at oceanic or transitional crustal settings and is used to discriminate between crustal type and/or spreading dynamics (e.g., Malinverno, 1991; Prada et al., 2014; Sauter et al., 2018). Nevertheless, besides the limited imaging at depth which may have affected the interpretation of the top basement morphology, rough or smooth morphologies can be the result of diverse and/or multi-stage processes, thus their interpretation must be supported by other evidence.
- 2D magnetic anomaly models are useful for quantitatively modelling features visible on the seismic data, to test models and aid with interpretation in areas where seismic imaging is difficult. However, the principal challenge with this method is distinguishing the source of magnetic anomalies, and whether they relate to superimposed geological features or a

single feature mappable across a large area. To avoid complicated models, and because this study investigated primarily the magnetisation character of the top basement, crustal magnetisation was assumed to occur within the topmost 1 km of the crust. However, such models may have failed to properly locate the source and to define the size and extent of the magnetic anomaly. Furthermore, as discussed in Chapters 2 and 4, magnetic models are non-unique, so that there are a multitude of susceptibility configurations that can produce the same amplitude and wavelength anomaly.

- Attempting to model gridded potential field data in 2D suffers from the fact that the gridded data could be affected by features that are out of plane of the profile. This means that the model could suffer from 3D effects, which make fitting the observed magnetic data in some places difficult. One way to reduce this uncertainty was to model very simple structures aiming to define a good-fitting model that was also possible to be justified considering the geological setting. Nevertheless, a better approach would be to generate a 2.5/3D model, where magnetised blocks are set to have a defined lateral extent outside the 2D plane of the seismic section (e.g., Rippington et al., 2015). This would allow, given enough constraints available, for a better definition of the spatial extent of magnetised crustal blocks. However, the limited seismic coverage restricts the knowledge on the spatial distribution of crustal blocks, thus requiring assumptions to be made. These considerations were also the reason for not choosing an inverse modelling approach in this study.
- Another assumption made for magnetic modelling is that all modelled magnetisation is parallel to the present-day field, although this may not be the case if magma emplaced during i.e., Upper Cretaceous-Palaeocene time (inferred time of breakup and oceanic spreading) cooled down at a different latitude from the present-day. However, paleomagnetism analysis on Cretaceous to Eocene rocks along the Turkish Pontides have shown paleolatitudes with little or insignificant variation compared with the present-day position (Meijers et al., 2010).
- Although magnetic anomaly data are often used to provide better constraints on the distribution of oceanic versus continental domains and to define the age of oceanic spreading, crustal magnetisation in the EBSB is anomalous compared to what normally expected at steady-state oceanic crust. At steady-state oceanic spreading areas, magnetic anomalies form clear positive and negative polarity stripes representative for the progressive age of oceanic emplacement. Magnetic lineations are therefore generally used to define the COB and to map the age of oceanic spreading (i.e., WBSB, Kazmin et al., 2007; East Antarctica, Davis et al., 2019). In the central and SE part of the EBSB, a mostly uniform and negative magnetic anomaly is present, with no clear evidence for such lineations. The record of magnetic anomalies by polarity changes of the Earth's magnetic field is complex

in domains that do not result from simple steady state seafloor spreading, causing debates on the nature, age, and significance of the magnetic anomalies (i.e., exhumed mantle or magma-starved domains; e.g., Sayers et al., 2001; Colwell et al., 2006; Bronner et al., 2013; Direen et al., 2011; Maffione et al., 2014). Furthermore, a lack of lineations can be indicative of spreading occurring during long geological time spans in which there has been no (or very few and limited in time) polarity reversals of the magnetic field or of an oceanic crust that has been emplaced during a time with short-duration reversals of the geomagnetic timescale (e.g., Tari and Simmons, 2018). Overall, the lack of magnetic lineation complicates the definition of clear boundaries between stretched continental and first oceanic crustal domains, of the spreading dynamics and relative age.

Different limitations affect results shown in Chapter 5:

- The complex seafloor topography and sub-seafloor stratigraphy generate near-offset noise during downward continuation. Far-offset wavefields are also deteriorated, thus, refracted travel-times could only be picked on limited ranges of offsets. Similar limitations have been presented by other studies applying this technique to long-offset streamer data (Qin and Singh, 2018). Downward continuation to a constant datum above seafloor, instead of to a datum following the actual seafloor topography, accounts for some of the noise/artefacts. This is true especially in areas (to the NE) where seafloor topography is shallowing at/across the chosen downward continuation depth. Downward continuation to a datum following seafloor topography would avoid the generation of those artefacts and allow to move both sources and receivers closer to/at the seafloor, improving further the refracted wavefield extrapolation. Other parameters, such as dominant frequency and slowness, may also be tested further to limit seismic frequencies and/or events which dip and velocity may be smeared/aliased during downward continuation causing poor signal to noise ratio.
- The limited spacing between the BSR seismic phases and their shallow sub-seafloor depth means that, although refractions may be generated at such levels, they will not be first arrivals on shot gather but masked by other refractions from deeper and faster layers (e.g., Qin and Singh, 2018). As a result, limited refracted arrivals could be input into travel-time analysis. Also, the geological complexity of the area means that seismic phases are not easy to recognise and trace between shot gathers, thus posing another limitation to the number of travel-times input.
- The choice of RAYINVR revealed to be efficient because: (i) the low computational times, (ii) it allowed to model first reflections then including the refracted arrivals information, and (iii) the number of model parameters to set was less compared to other tomographic codes (e.g., Gonçalves and Gabarito, 2021). These characteristics allowed for interactive,

arbitrary selection of model parameters (boundary and velocity nodes), which made modelling very flexible. On the other hand, areas with sparse model parametrisation resulted in a relatively low-resolution model. Moreover, the selection of parameters required interactive input and testing of several variants of the solution, thus, a manual trial-and-error process of attempting to fit the data for several shot points simultaneously was sometimes difficult and time-consuming. Nevertheless, it had the advantage that during modelling it allowed the identification of picked phases to be modified. This means that having problems in fitting some particular phase by a model fitting all the remaining data indicated that such a phase actually originated as, for instance, a side reflection or diffraction from some local structure. This trial-and-error phase identification helped to avoid significant model errors, bias or artefacts that could be introduced by the modelling of some incorrectly interpreted phases, whose nature was not initially obvious. Although this procedure allowed for better control of the modelling process, it also introduced some subjectivity into the final solution as model modifications depends on the interpreter's decision and phase picking.

- Travel-time analysis was affected by the limited number of picked travel-time phases from downward continued refractions. Refracted, and some reflected, travel-times were difficult to identify and follow laterally across shot gathers in areas where the geology was represented by complex wavefields. Forward travel-time modelling was helpful as it allowed for verification of the correspondence between calculated and observed travel-time phases. However, travel-times associated with shallow reflectors were still hard to follow due to the folded geology in this area, and correlation with the stacked profile was complicated by the poor-quality imaging within folded sequences. To increase the number of constraints, i.e., the number of seismic phases that were visible across a greater number of shot gathers, multiple layers were introduced during modelling to define the structure at and beneath the BSRs. However, increasing the number of layers can result in larger uncertainties in velocity estimation. Also, since limited phase picking was available at the sides of the BSRs, the velocity model at the two ends of the model domain was poorly constrained. Sensitivity analysis was performed for certain model parameters. However, there is no definitive method to evaluate the uncertainty as a slight change in the dip of a reflector, for example, may result in different ray coverage and the correspondence between model parameters and travel-time data is highly complex.
- The modelling of the BGHSZ also relied on a number of assumptions. Firstly, the assumption of a pure methane phase boundary. Although studies in the Black Sea generally agree on the presence of mainly biogenic methane, percentages of up to 4% of gases other than methane have been reported at different locations in the basin. The presence of even

1% of thermogenically sourced gases can significantly shift the hydrate phase boundary (Sloan and Koh, 2008). However, the real gas phase composition is not constrained in our study area. Another assumption is that the modelling was performed assuming steady state conditions, hydrostatic pressure, and a system in which the thermal properties of sediments are constant and uniform. In reality, and as expected considering the multiple BSRs formation mechanisms inferred in this study, the thermal structure and fluid pressure of the system might be more complex. For instance, different sediment types and/or the presence of gas and hydrate can provide different thermal conductivity; also, the presence of localised fluid flow can cause lateral changes in the thermal structure of sediments (e.g., Waite et al., 2009; You et al., 2019). Finally, sedimentation and erosion processes may have affected the temperature distribution at depth (Hornbach et al., 2008). Assumptions made in this model therefore neglect the presence of thermal property variations and lateral heat conduction, meaning that the calculated BGHSZ may differ significantly from the real one. Due to these uncertainties, the calculated BGHSZ cannot, on its own, be reliably used to define the present-day BGHSZ. This is the reason for adopting a range of geothermal gradient values and plotting different BGHSZs, which are then used for comparison with the BSR depths obtained from travel-time analysis.

- Effective-medium modelling assumed an isotropic, elastic, porous saturated media in which only water and gas, or water and gas hydrate can co-exist. Assuming a simple model helped to reduce the number of parameters and allowed to obtain simple solutions that could be used to explain the set of observed variables. However, these models are simplified definitions of a real, anisotropic system, where multiple phases (water, gas, and hydrate) often co-exist in the pore space, especially considering mechanisms of hydrate dissociation and a transient state of the hydrate system.
- The comparison between seismic velocity estimates in the central basin and at the BSRs, and the gas and gas hydrate saturation estimates in sediments at these two locations, is affected by the assumption of a similar compaction history for sediments in the central basin and in the thrust region. However, the compaction history beneath the thrust ridge might be quite different from the compaction history in the basin. Significant differences would have an influence on effective medium modelling and, ultimately, gas hydrate and free gas saturation estimates.
- The relations between seismic velocities and gas-hydrate concentration depend on how gas hydrates are distributed in their host sediments (Dai et al., 2012). Modelling performed in this study only considered one end-member hydrate morphology in which gas hydrates are disseminated throughout the sediment filling only the porous space, away from grain contacts, and so do not affect the dry mineral frame moduli of their host sediment (pore-

floating). As shown by laboratory experiments, hydrates distribution in sediments can vary widely and different models can be used to represent these different morphological scenarios (e.g., Waite et al., 2009).

- The accuracy of the saturation estimates depends mainly on velocity, porosity, and density data. Uncertainties exist over the set of physical parameters, especially the grain bulk and shear moduli, the bulk density and porosity of the host sediment without hydrate. Errors in estimates are especially affected by changing values of sediment porosity which may account for ±2% error in hydrate saturation estimates and makes gas saturation to shift from less than 1% to up to 25 ± 10%. Other parameters (i.e., bulk density, confining pressure, etc.) uncertainties are less important, and their errors have been estimated to result in V_P variation that lies within the travel-time analysis error estimates. An accurate velocity model is also needed as the effective-medium modelling estimates relied on the comparison with velocities provided by travel-time analysis, which were also affected by modelling errors. Thus, gas/gas hydrate saturations estimated are affected by the propagation of errors coming from travel-time analysis.
- Finally, although gas hydrate in the pore space of water-saturated sediments generally increases the compressional wave velocity, other minerals (i.e., limestone, opal, pyrite, etc.) can also cause a similar velocity increase, making it hard to distinguish gas hydrate from other minerals (Tian and Liu, 2020). Given the poor constraints on the local lithology, and the small amount of velocity variation showed by the travel-time model, effective-medium modelling results may simply suffer from poorly constrained parameters, and thus, they cannot be considered a robust discrimination between non-hydrate and hydrate-bearing sediments. Lithological changes may, alone, be able to explain the small velocity variations at the BSRs without implying the presence of gas hydrate (e.g., Cook and Tost, 2014).

Ultimately, a higher-resolution velocity model (i.e., from travel-time inversion) could provide a more robust velocity estimate and better constraints on the sediment's physical parameters (i.e., porosity, bulk density), subsequently balancing the lack of direct sampling from the study location and improving results from effective-medium modelling.

6.3 Wider implications of this study

Over the last decade, deep crustal seismic reflection data were acquired across a number of rifts and rifted margins, and integration of these data with additional well and previously acquired seismic data have shown that comparable architectural features can be found on many margins worldwide (i.e., the South China Sea, Yang et al., 2018; the Gulf of Aden, Autin et al., 2010; the

conjugate South Atlantic margins, Mohriak and Leroy, 2013; the Norwegian and Greenland margins, Osmundsen et al., 2016). Furthermore, onshore analogues of fossil margins preserved in collisional orogens, together with borehole data, enabled the translation of some of the seismic interpretations made at distal rifted margins (Andersen et al., 2012; Masini et al., 2012). Thus, the partitioning of the extensional systems into distinct structural domains can be interpreted to reflect a commonality of processes with regards to rifts and rifted margin formation (e.g., Franke, 2013; Peron-Pinvidic et al., 2013). Studies have also shown that rifting is fundamentally multiphase and that it results from the interaction of crustal and mantle processes, developing different rift scenarios, e.g. multiphase, propagation, sequential, migration (Reston, 2005; Lavier and Manatschal, 2006; Ranero and Perez-Gussinye, 2010; Huismans and Beaumont, 2011). These scenarios are recorded by the stratigraphic units deposited during the different stages of basin evolution and passive continental margin formation. Therefore, seismo-stratigraphic analysis is often used to identify and map the variably distributed rifting and breakup stages characterising an extensional basin, as well as the complex tectono-magmatic evolution along continental margins (e.g. Gillard et al., 2015; 2017; 2019; Peron-Pinvidic and Osmundsen, 2016; Tugend et al., 2020; Soares et al., 2012; Alves and Cunha, 2018; Alves et al., 2020). However, a clear definition of the classical syn- to early post-rift units is complicated by the fact that these units often show a spatio-temporal progression of rifting and breakup processes rather than a neat distinction. As such, new definitions for the previously defined syn- and post-rift stratigraphic sequences have been introduced to explain the “transitional” character of these stratigraphic units, as it is the case for the “breakup sequence” defined by Soares et al. (2012). Also, intermediate or transitional crustal types are often interpreted as a COT, which is recognised as the transition between stretched continental and oceanic crust. There are different interpretation on the nature and formation of the COT, which imply different mechanisms of extension and/or different amounts of decompression melting following breakup.

This thesis focuses on the seismo-stratigraphic reconstruction of rifting and breakup processes at extensional settings, as well as on the study of the often ambiguous nature and extent of different crustal domains resulting from extension, breakup and spreading, presenting the case study of the EBSB. Here, geodynamic reconstructions are complicated by the limited understanding on the deep stratigraphic record of the basin (e.g., Nikishin et al., 2015). Nevertheless, as at other rift settings (e.g., South China Sea; Porcupine Basin; Angola-Gabon margins; etc.), growing interest has been shown in the tectono-stratigraphic re-assessment of the EBSB evolution, aiming to constrain the geodynamic of basin opening (Stovba et al., 2020; Maynard and Erratt, 2020). Similar reviews of the tectono-stratigraphy at passive continental margins have been presented along most well-studied passive margins, such as the Atlantic margins, the W-Australian margin, New Zealand, South China

Sea, Barents Sea (Alves et al., 2019). Studies from these areas can therefore look at the EBSB case study presented in this thesis as a reference/comparison where similar observations on basin opening timing and kinematics are presented based on a developed understanding of the basin opening dynamics and on tectono-stratigraphic re-assessment efforts. These efforts run in parallel with the continuous interest in energy exploration targets, as is the case for the EBSB (Intawong and Went, 2020; Pape et al., 2021; Palabiyik et al., 2020). This is because a clear definition of the age and kinematics of basin opening and the presence and extent of the COT are essential to estimate the hydrocarbon potential of a basin.

A recent work from Maynard and Erratt (2020) investigates the age and dynamics of the EBSB basin opening using the same dataset as in Nikishin et al. (2015) and Monteleone et al. (2019) (Chapter 3). Maynard and Erratt's results agree with the presence of a Tertiary breakup in the EBSB, as presented in Monteleone et al. (2019), based on the identification of sediments younger than the Palaeocene-Eocene sitting on top of the oceanic/transitional crust. However, their interpretation of a basin-wide unconformity ("base of passive infill") separating syn-kinematic from post-kinematic section seems to show that the cessation of extension has occurred in Palaeocene time. According to this view, breakup would have followed the cessation of extensional processes, an interpretation that implies a different timing and kinematic of opening from the one shown in Chapter 3. Furthermore, Maynard and Erratt (2020) inferred that the lack of clear sedimentary onlap onto the oceanic basement along the axis of the rift, looking at strike seismic sections (NE-SW-trending lines), represented evidence against rift propagation as presented by Monteleone et al. (2019). However, for a propagating spreading centre, sediments deposited at the axis will show the same age as the older sediments carried away on both flanks. Thus, onlap is not expected to be seen on strike lines through the basin. Some onlap may be seen on the basin flanks, but there the stratal relationships can get complex. Results shown by Maynard and Erratt (2020) are affected by the same limitations as other studies and those presented in this thesis and highlight the ambiguity in a basin's geodynamic reconstruction at such complicated and poorly constrained settings. These contrasting observations also highlight the importance of understanding the link between rifting dynamics and the expected tectono-stratigraphic record associated with them. V-shaped basins can form by rotation or by rift propagation, or by a mixture of the two. This study has demonstrated that there is a component of rift propagation, but has also left open an important question: What is the dominant mechanism in creating the V-shape, rotation or propagation?

Research efforts in the EBSB show a great deal of similarity with studies looking for insights into the structure at the distal parts of the margins, considered preferential loci for magmatism, tectonism and mantle-crust processes (Gillard et al., 2019; Lei et al., 2019; Lymer et al., 2019; Gallahue et al., 2020; Nirrengarten et al., 2020; Tugend et al., 2020; Alves et al., 2021). One of the key elements for

the investigation of the disputed transition from continental rifting to potential seafloor spreading and of the resulting crustal configuration, is the use of combined methods (i.e., seismic reflection/refraction, magnetic anomaly data). Data integration is based on the recognition that each methodology/dataset can provide variable interpretations which, without further constraints, might not be valid on their own. Results from this study contribute not only to the understating of the Black Sea evolution, but to the understanding of rifting dynamics, breakup, oceanic spreading, and crustal accretion in a broader sense, proposing a model that can help the aim to reveal the thermal evolution, structure and sedimentary record of continental margins and spreading areas. The similarity of the EBSB evolution to that of rifted margins (i.e., Iberia-Newfoundland and Brazil-Angola margins), back-arc basins (i.e., Tyrrhenian basin; Aegean Sea, Japan Sea and Yamato Basin, South China Sea, Woodlark Basin), and rift basins elsewhere (i.e., Gulf of Suez, North Sea), makes it a case study which can provide valuable insights into the processes driving the evolution of the lithosphere at extensional settings.

Gas hydrate investigations are becoming another major research subject in the EBSB (e.g., Intawong and Went, 2020; Pape et al., 2021). This interest is growing in parallel with ongoing exploration targets, i.e. the Maykop Formation (e.g., Mayer et al., 2018; Vincent and Kaye, 2018; Tari and Simmons, 2018; Sachsenhofer et al., 2018; Intawong and Went, 2020), which are now also considered in light of their possible contribution to hydrocarbon gas accumulations within the Black Sea GHSZ (Pape et al., 2021). Investigations on the occurrence of prominent seepage sites within the GHSZ offshore Georgia (Pape et al., 2021) showed the presence of an active gas hydrate system in the EBSB which is still poorly known in comparison to the gas hydrate system in the WBSB. The evidence for multiple BSRs in the EBSB provide a new case study to investigate the physical nature and mechanism(s) for multiple BSRs generation, which can be compared to the WBSB and to other well-known areas. Since the presence of these unusual features is a subject of still growing research interest, results can provide valuable insights into a variety of subjects such as the relationship between gas hydrate dynamics and climatic changes, the effects of hydrate dissociation on slope stability, and the assessment of the global methane hydrate resources.

Geophysical prospecting is a widely used method for gas hydrate exploration, especially seismic exploration technology. Increasing importance has been given in recent years to the application of tomographic approaches to conventional streamer data (e.g., Harding et al., 2016), and growing interest lies in developing and testing techniques of data pre-conditioning that allow the enhancement of seismic wavefield provided by conventional streamer data, making it comparable with a tomographic experiment (e.g., Qin and Singh, 2018). Among the conventional seismic techniques, downward continuation is often used for the seismic signal enhancement aiming to extract refracted information from crustal scale levels or deep sedimentary units. Within these

target depths, results have been encouraging, thus showing that tomographic analysis is possible using streamer data alone, simulating a near-seafloor experiment with higher degree of resolution. This study provides an example of how downward continuation pre-conditioning works when applied to long-offset seismic reflection data within shallow (i.e., few hundred meters) sub-seafloor depths, and in areas with complex seafloor topography and/or sub-seafloor stratigraphy, providing an assessment of the method's benefits and limitations when applied to shallow (i.e., gas hydrate) studies. This same technique has the potential of being applied at different settings and for various shallow targets to obtain the physical properties of sediments, thus evaluating the presence and behaviour of fluids within sediments (e.g., reservoir monitoring during geological CO_2 storage).

Finally, analytical rock physics models are often used to support and add value to seismic data, providing a quantitative assessment for the presence, distribution and concentration of free gas and hydrate. This study analyses the different physical properties of unconsolidated marine sediments based on an effective medium theory. Although these methods are widely used, limitations and assumptions are always present and affect the reliability of the results. Discrepancies between some estimates of hydrate concentrations can partly be attributed to poor understanding of how gas hydrates are distributed in their host sediments. This study shows the challenge and ambiguity between seismic velocity changes and gas hydrate/lithological changes in sediments, and highlights the fact that estimates based on seismic measurements alone may not be sufficient without additional constraints from in-situ observations, i.e. borehole data.

6.4 Future work

- Some steps can be taken to tackle the weaknesses affecting downward continuation results and travel-time analysis in this study, including: (i) downward continue sources and receivers to a datum following seafloor topography or directly to the seafloor, aiming to reduce noises/artefacts introduced by laterally shallowing seafloor topography and to improve wavefield extrapolation bringing refractions to even closer offsets, (ii) increase the density of input phases allowing picking on more shot gathers and, in order to reduce picking time and to guide phase recognition, apply a semi-automatic picking based on the manually defined seismic phases and, finally, (iii) use the velocity field derived from forward travel-time analysis in an automated inversion approach, i.e., TOMO2D (Korenaga et al., 2000), which allows to handle bigger amounts of input travel-times and is able to produce final models that are more robust based on iterative input-fitting procedure; this procedure can provide a more robust estimate of the minimum structure required by the travel-time dataset than the RAYINVR forward models. Based on this refined velocity model, it would

be possible to compute the porosity of the sediments, and thus, better estimate the pore phases saturation along the BSRs area from effective-medium modelling.

- Results shown in Chapter 5 could be complemented by using another seismic profile, BS-100B. This profile also shows evidence for multiple BSRs at a similar location sampled by BS-200B and at another nearby location (Figure 6-1). Since seafloor topography is more complicated on this line, downward continuation needs to be improved first before being applied to enhance the refracted wavefield. Nevertheless, the acquisition direction for this line (20˚ heading) provides a better imaging of stratigraphic layers and it may help travel-time picking to improve the overall results from velocity modelling. Performing travel-time analysis and effective-medium modelling on profile BS-100B would complement results from line BS-200B, also providing a better understanding of the spatial distribution of the hydrate and/or gas-bearing zones.

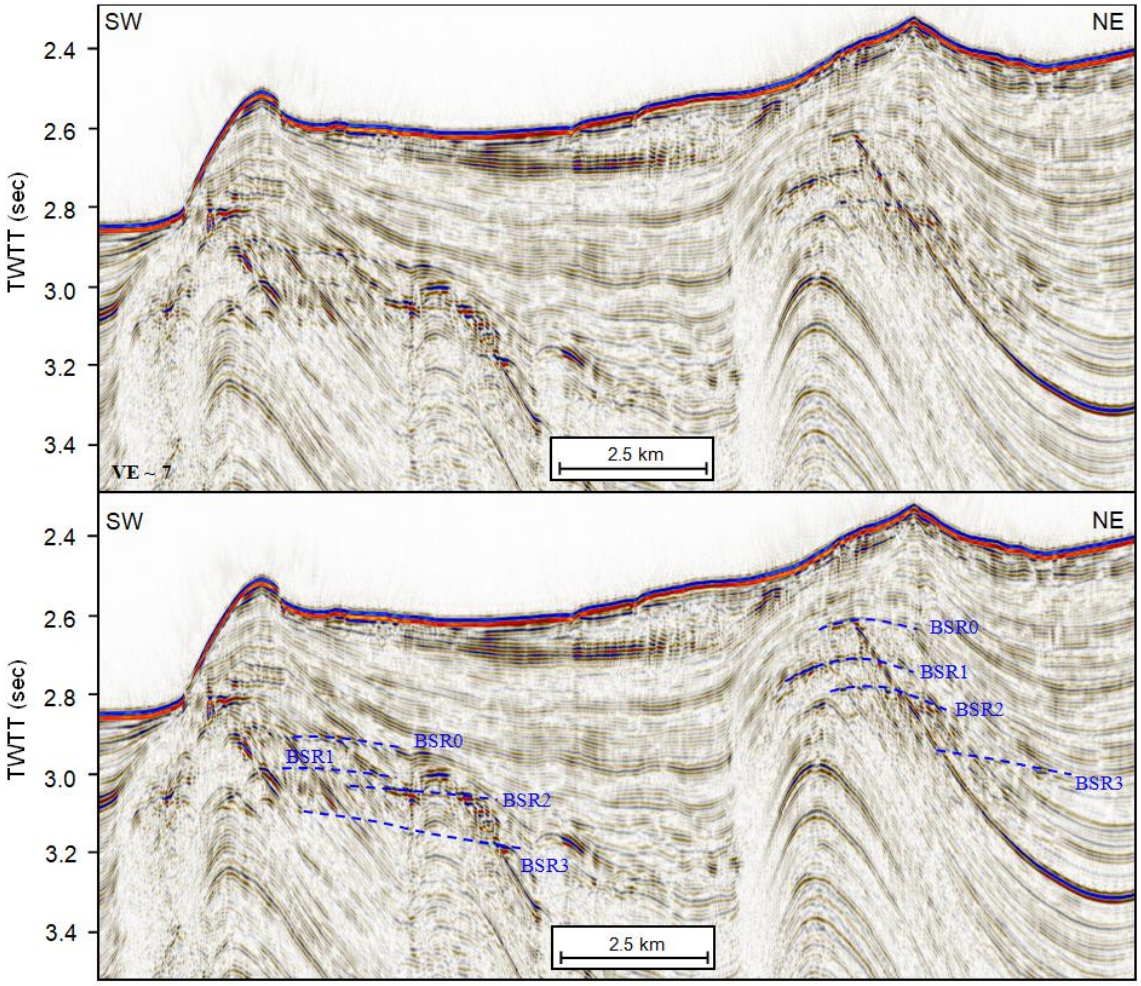

Figure 6-1. Seismic reflection profile BS-100B (location in Figure 2-1; NE-end of the profile). Top) Non-interpreted profile. Bottom) Interpreted profile showing two multiple BSRs locations. Multiple BSRs to the SW part of the section correspond laterally to the ones identified on profile BS-200B.

- Knowledge of the paleo-environmental, pressure-temperature conditions of the Black Sea basin following the LGM could be used to estimate the expected depth of the paleo-BGHSZ comparing it with the multiple BSRs depths. This type of analysis has already been performed in the WBSB (e.g., Popescu et al., 2006; Zander et al., 2017), providing useful insights on whether multiple BSRs reflect stages of stable sea-level lowstands, possibly during glacial times (Zander et al., 2017). For the EBSB case, estimates of the rates of sedimentation/tectonic uplift within the Tuapse Trough could also be integrated into the analysis. This analysis could provide further evidence on whether the vertical shift of the BGHSZ, inferred to result from mechanisms of hydrate re-cycling, was controlled by climatic (i.e., sealevel) changes and/or to sedimentation and tectonic processes in the area.
- Although long-offset seismic reflection profiles have presented some limitations in reconstructing the velocity field within shallow and complex geological areas, they could be used to achieve better results within deeper sedimentary layers. A subject of great interest in the Black Sea basin is the Oligocene-lower Miocene Maykop Formation, with the lowermost part of the sequence representing the most significant hydrocarbon source rock in the Black Sea region (Robinson et al. 1996). Wide-angle seismic data revealed the presence of a continuous low-velocity zone (LVZ) across the Maykop unit, which was interpreted as representing an under-compacted sedimentary layer with elevated pore pressure (Scott et al., 2009). However, Scott et al.'s results were limited to only four OBS profiles, and the top of the LVZ could not be clearly constrained because of the inability to identify a corresponding reflection. Thus, the regional distribution and magnitude of the overpressured and/or the presence of overpressure compartments in the EBSB sediments is still poorly constrained. Regional long-offset seismic reflection data could be used to provide a better definition of magnitude and extent of the LVZ. Downward continuation could be applied to further improve refracted arrivals visible on the long-offset seismic reflection data, enhancing seismic phases representative for the Maykop levels. Travel-time analysis would also be more densely sampled than that performed on OBS data, because of the nature of the streamer acquisition and the availability of more seismic profiles. Travel-time analysis of the long-offset seismic data can be therefore used to define a high-resolution P-wave velocity model within the Maykop Formation, providing pore-pressure estimates based on this velocity model. Results would complement previous studies (e.g., Scott et al., 2009), helping to define the magnitude and extent of the overpressured zone at a more regional scale.

Appendix A Seismic profiles interpretation

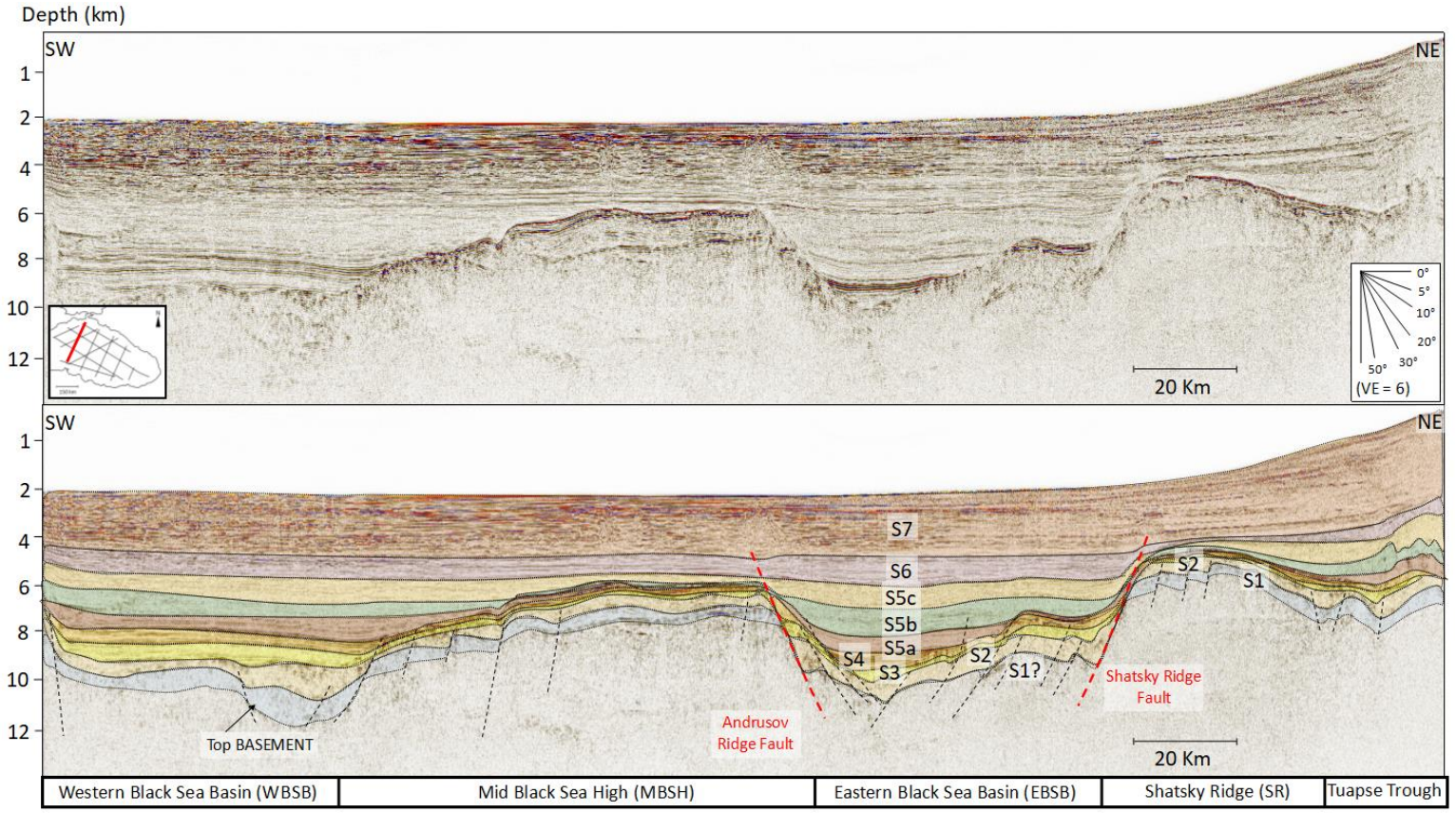

Figure A- 1. Profile bs-80. The MBSH and the Shatsky Ridge bound the central EBSB. Colors mark interpreted stratigraphic sequences (S1 to S7).

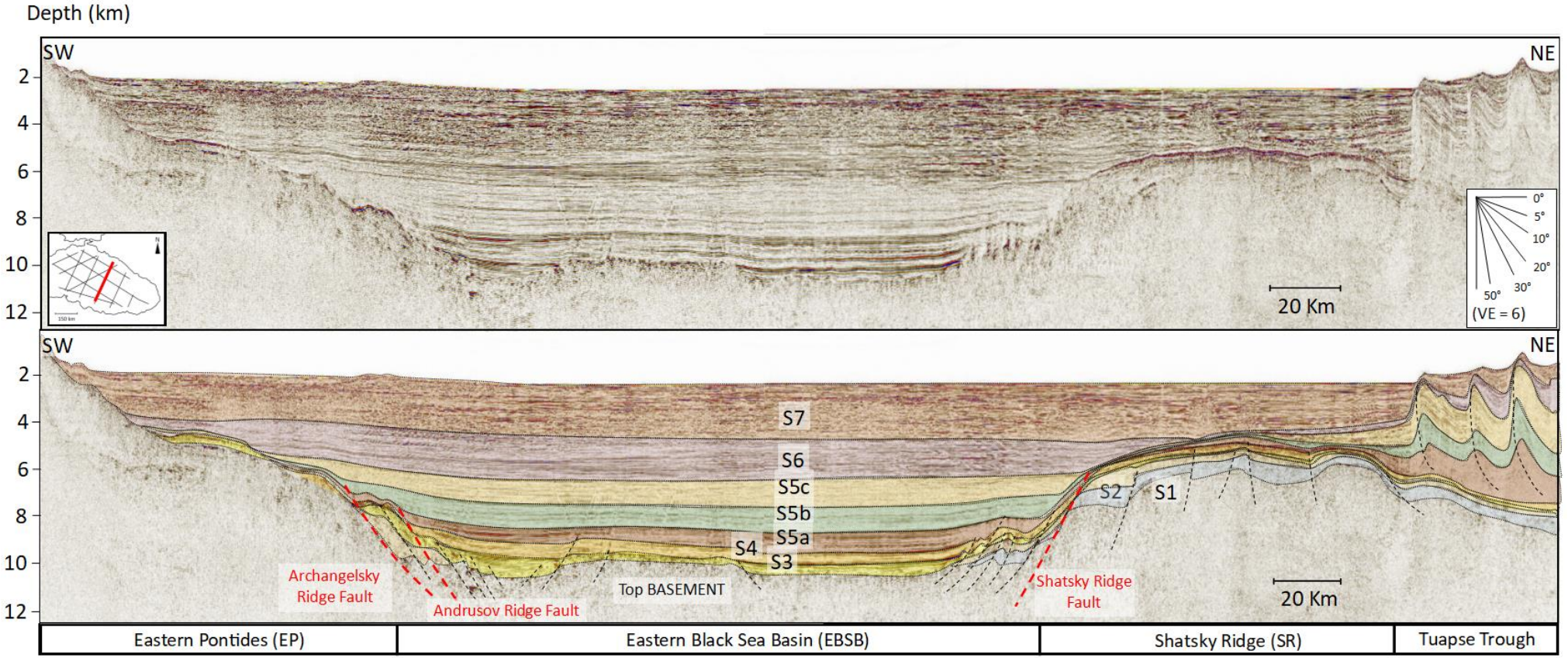

Figure A- 2. Profile bs-100. The MBSH and the Shatsky Ridge bound the central EBSB. To the NE of the profile, the folded and thrusted sediments of the Tuapse Trough. Colors mark interpreted stratigraphic sequences (S1 to S7).

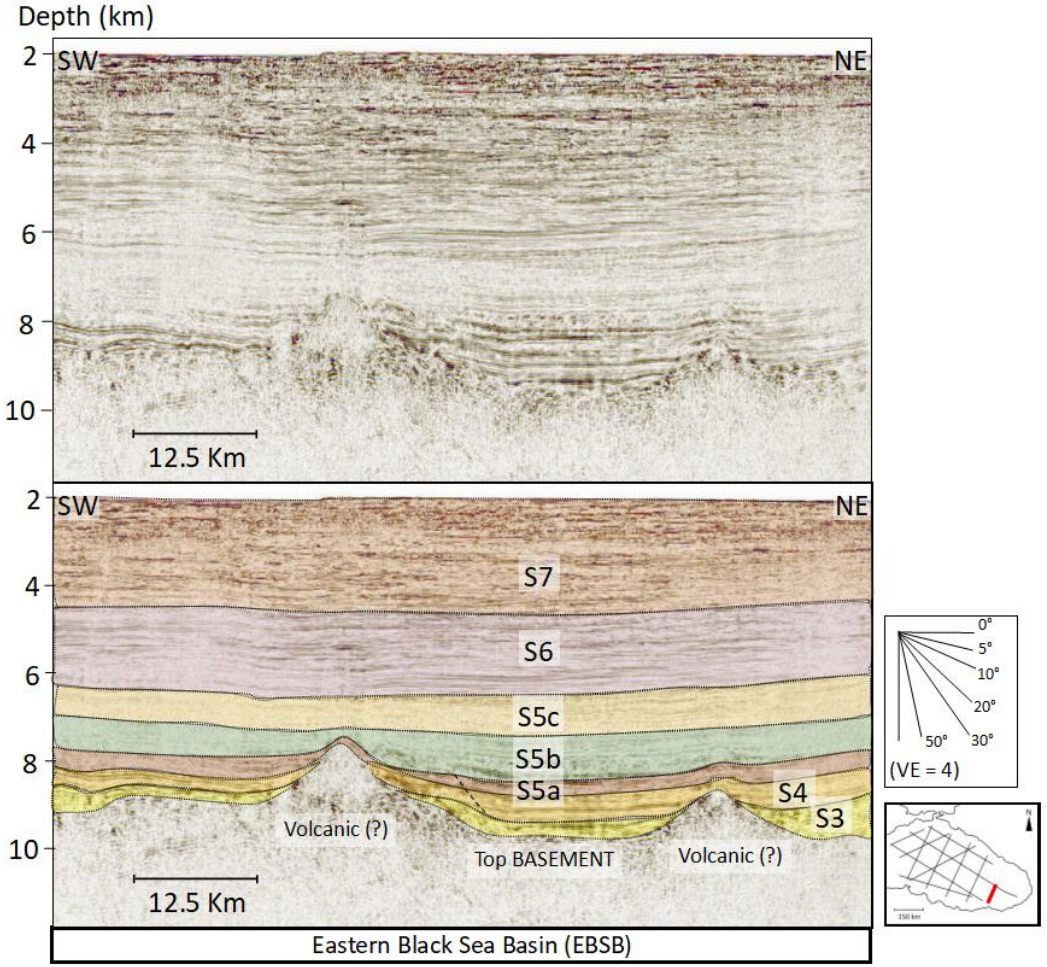

Figure A- 3. Profile bs-120, showing the SE part of the EBSB. A rough top basement is characterised by the presence of possible volcanic structures. Colors mark interpreted stratigraphic sequences (S1 to S7).

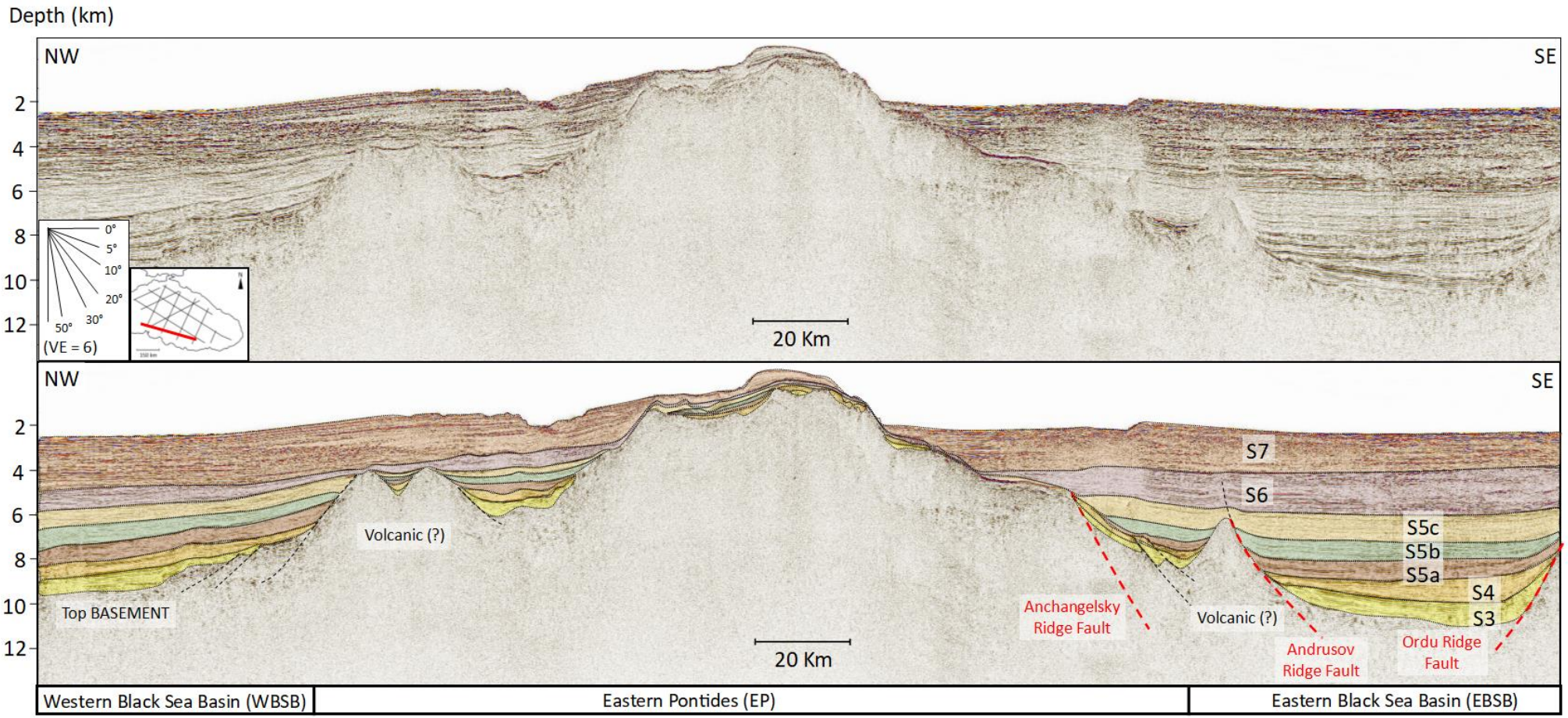

Figure A- 4. Profile bs-160. The volcanic arc of the Eastern Pontides (EP) separates the EBSB from the WBSB. A faulted and tilted block or a volcanic (?) structure bounded by the Andrusov Ridge fault is present in the SE part of the EBSB. Colors mark interpreted stratigraphic sequences (S1 to S7).

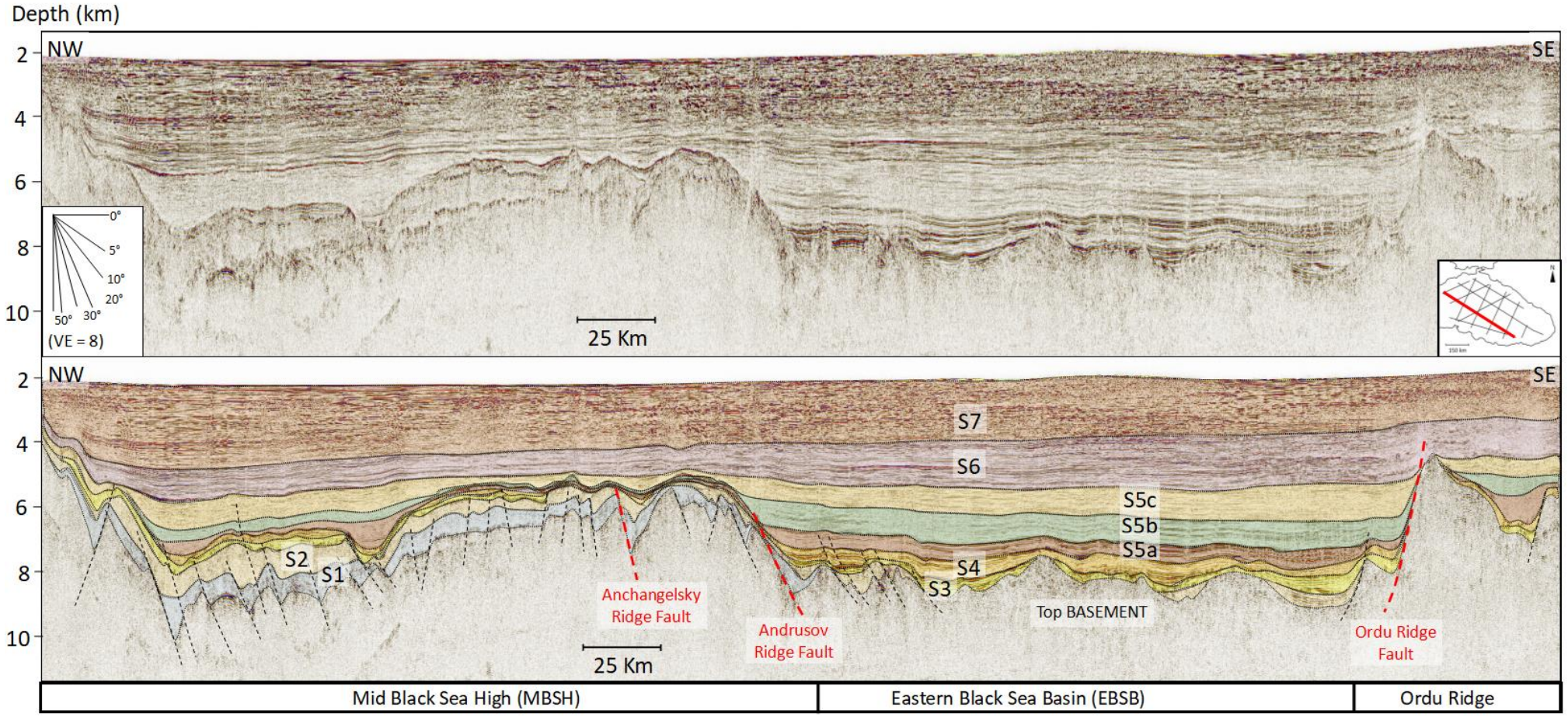

Figure A- 5. Profile bs-170. The MBSH (Archangelsky and Andrusov Ridges) are located to the NW of the profile, while the Ordu Ridge bounds the SE part of the EBSB. A rough basement characterises most of the central EBSB. Colors mark interpreted stratigraphic sequences (S1 to S7).

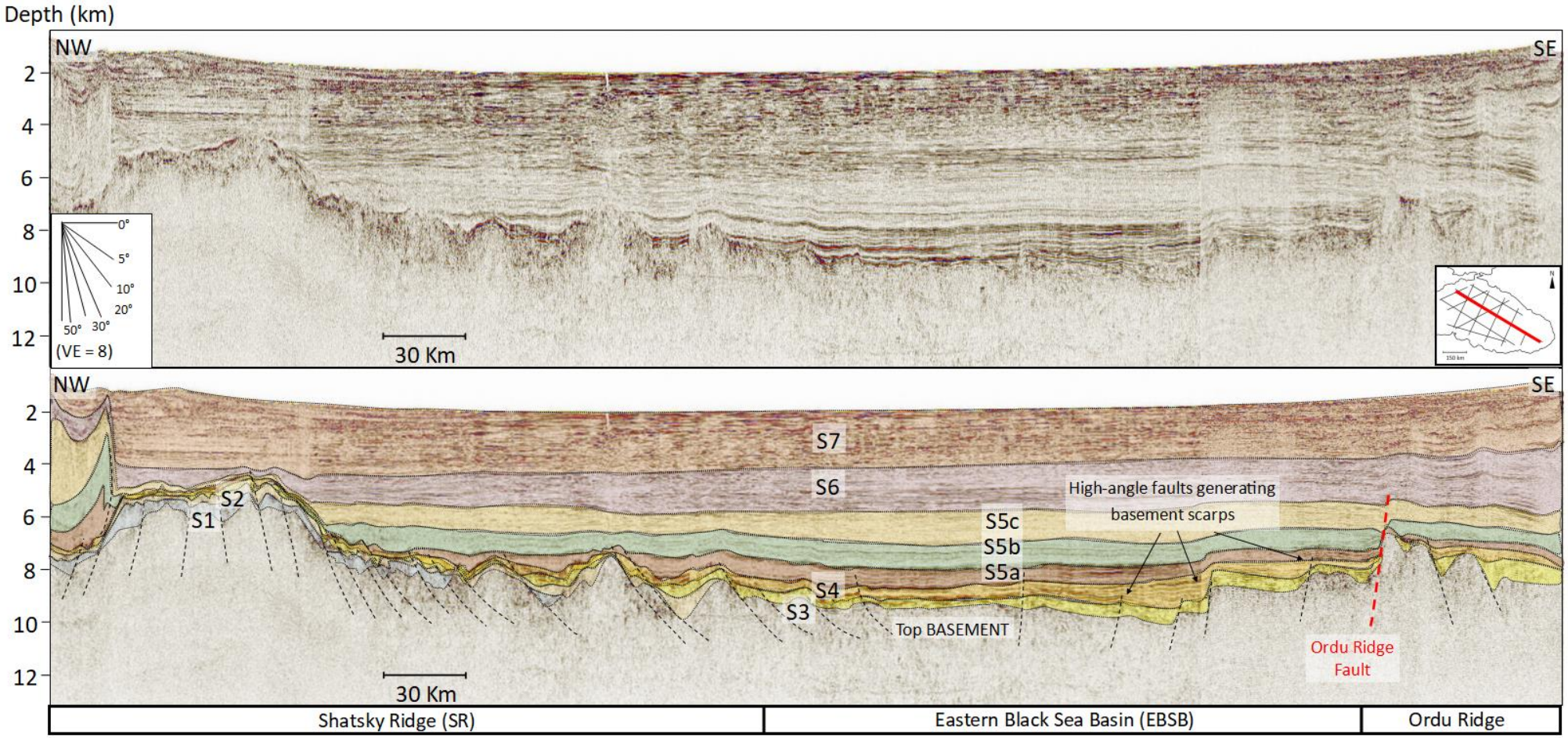

Figure A- 6. Profile bs-180. From NW to SE: the folds and thrusts of the Tuapse Trough sediments, the Shatsky Ridge, a rough basement with tilted and faulted crustal blocks, a smoother basement affected by high-angle faults, and the Ordu Ridge area. Colors mark interpreted stratigraphic sequences (S1 to S7)

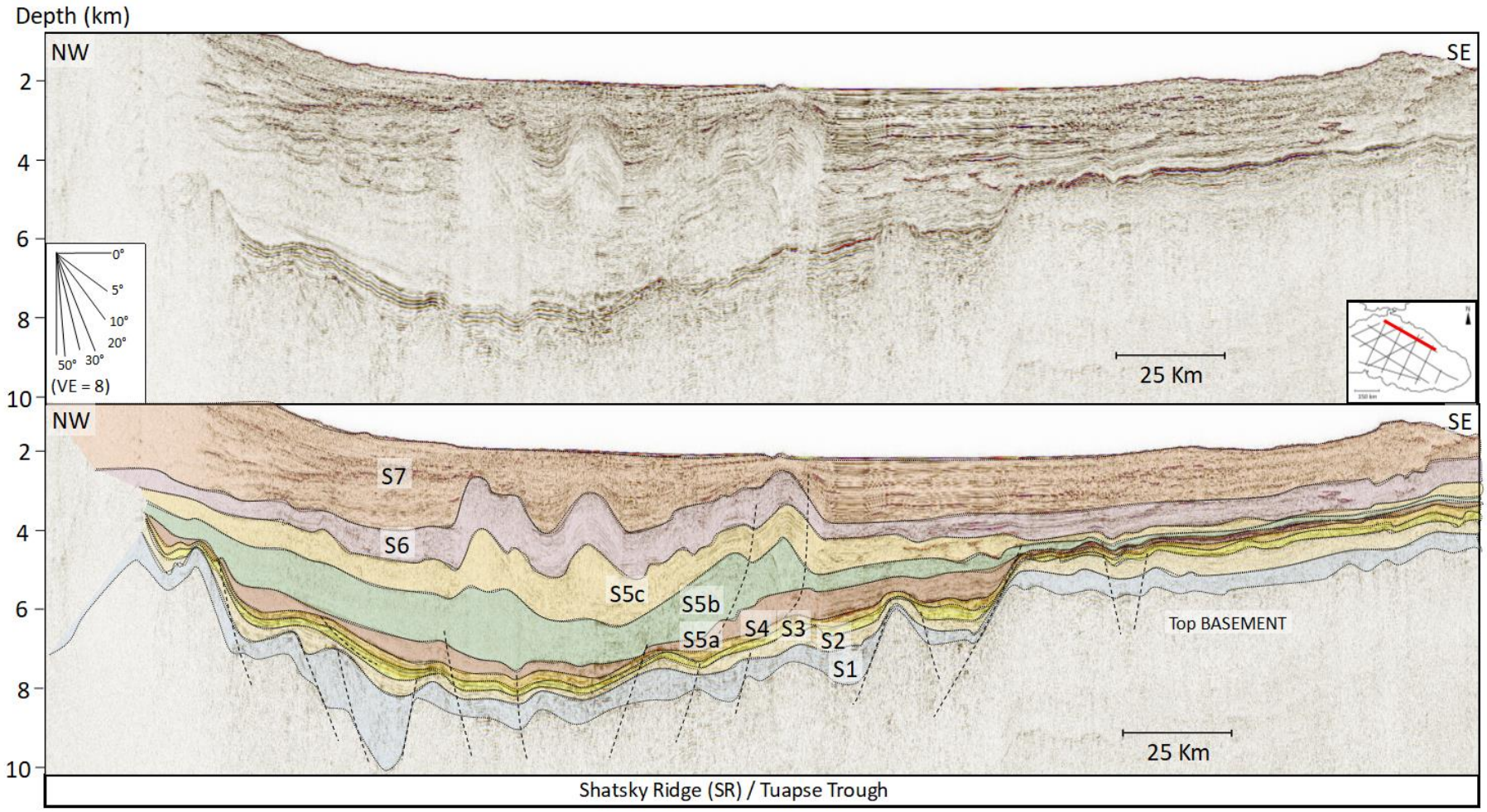

Figure A- 7. Profile bs-190 showing the Tuapse Trough sediments folded over the shoulders of the Shatsky Ridge. Colors mark interpreted stratigraphic sequences (S1 to S7).

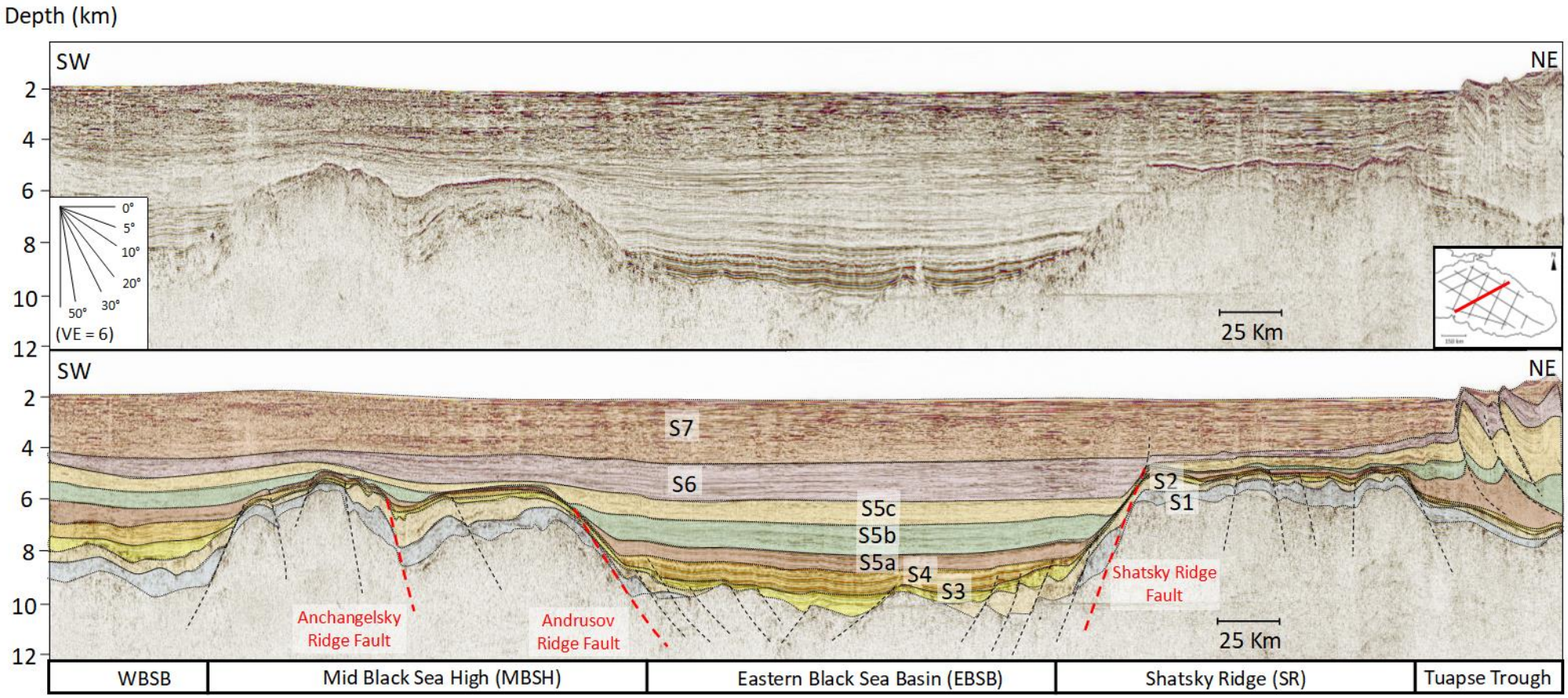

Figure A- 8. Profile bs-200. The MBSH (Archangelsky and Andrusov Ridges) and the Shatsky Ridge bound the central EBSB. A rough basement made of faulted and tilted crustal blocks characterises the central basin. Colors mark interpreted stratigraphic sequences (S1 to S7).

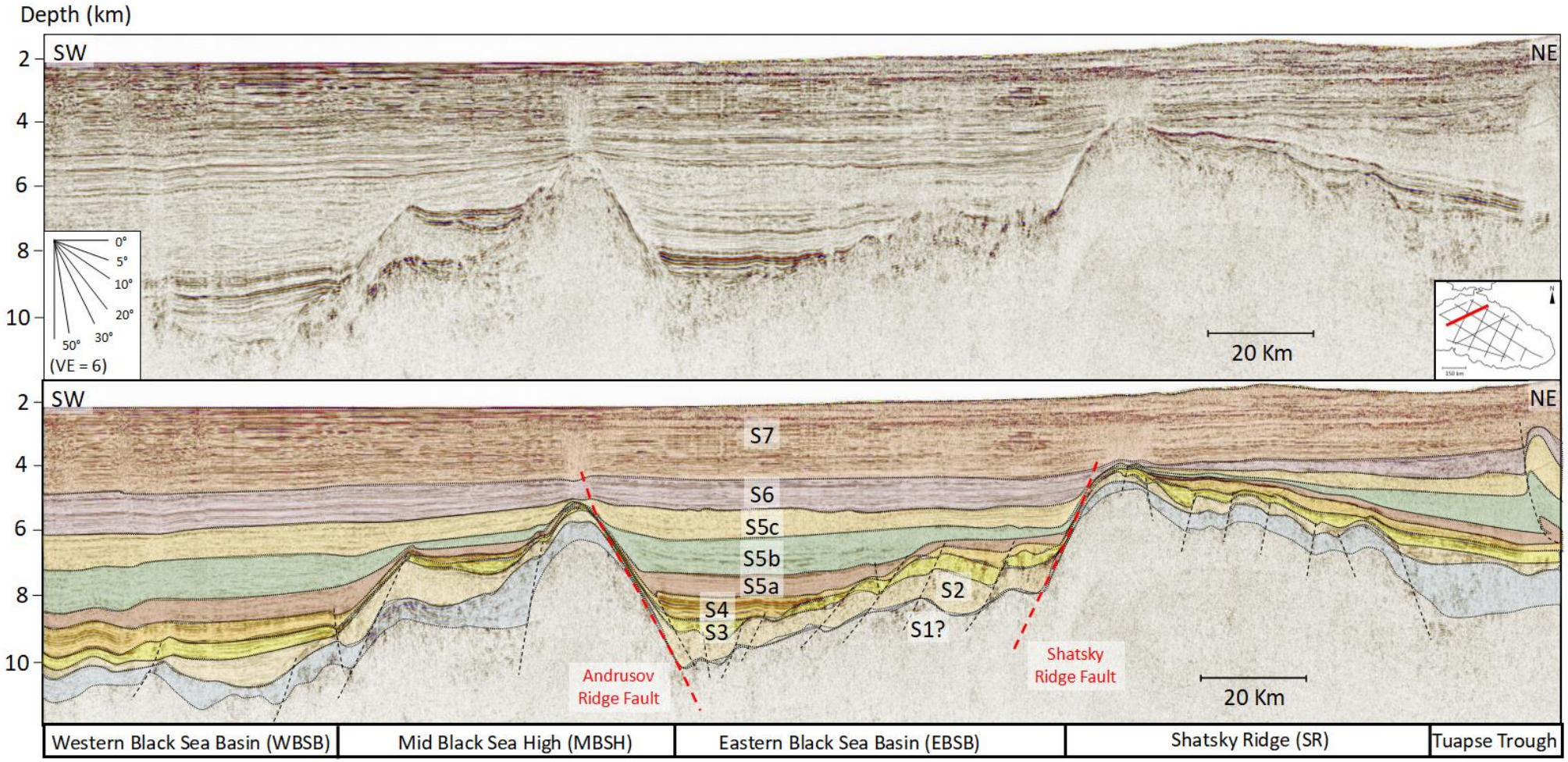

Figure A- 9. Profile bs-220. The MBSH (Andrusov Ridge) and the Shatsky Ridge bound the central EBSB. Colors mark interpreted stratigraphic sequences (S1 to S7)

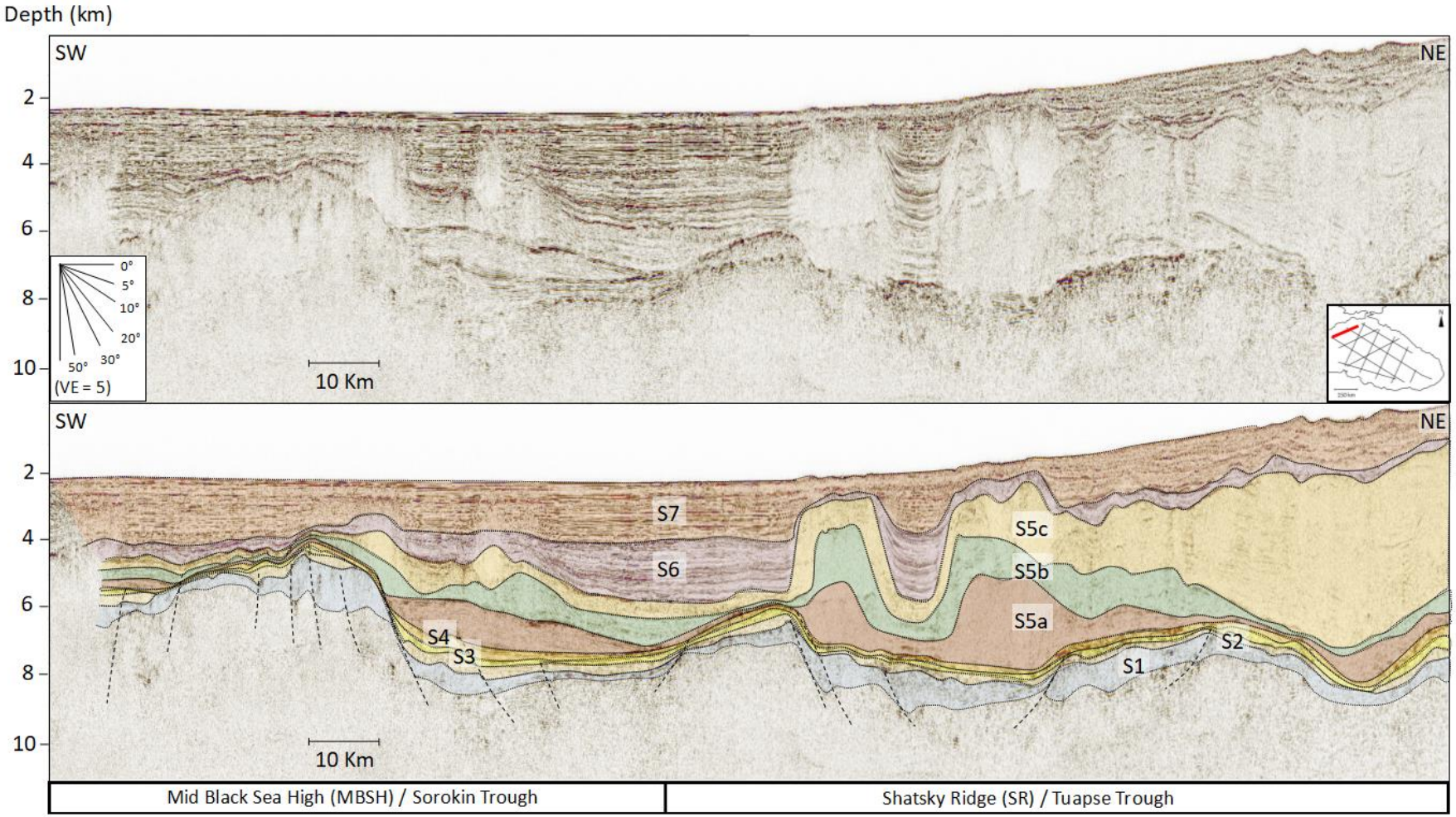

Figure A- 10.Profile bs-210. The north-western parts of the MBSH and the Shatsky Ridge, overlaid by the Tuapse and Sorokin Troughs sediments. Colors mark interpreted stratigraphic sequences (S1 to S7).

Appendix B Magnetic anomaly modelling

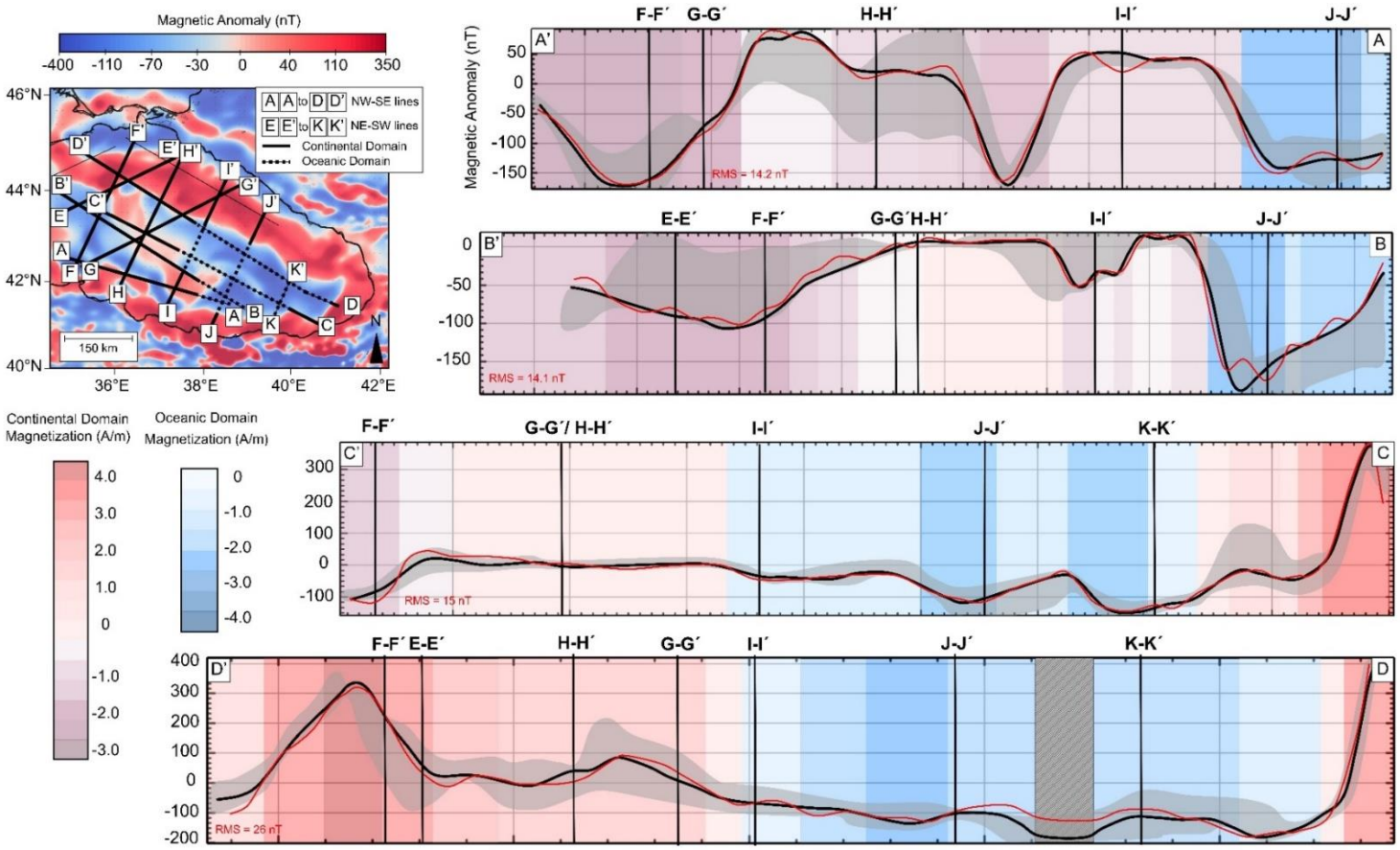

Figure B- 1. Continued…

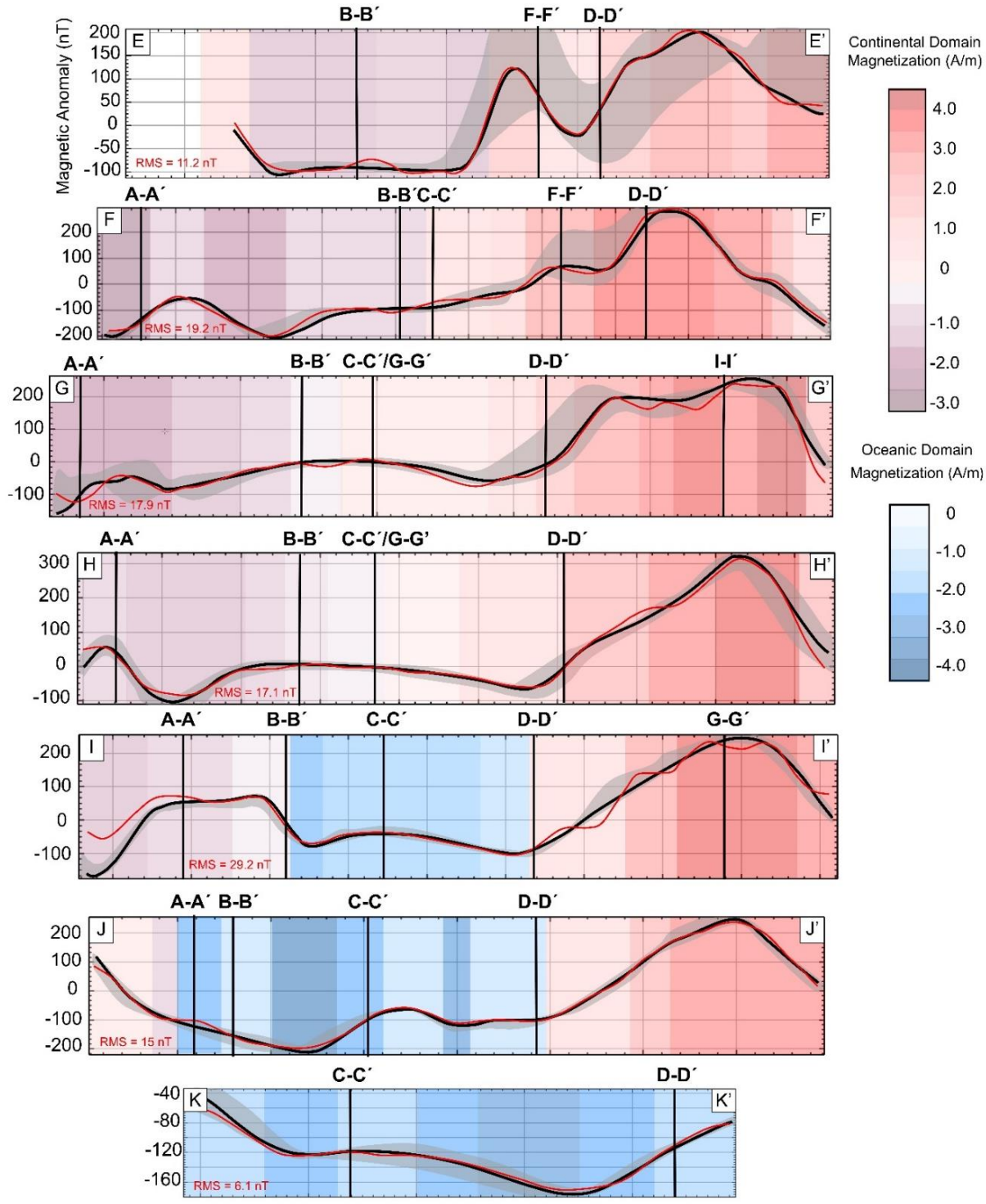

Figure B- 1. Magnetic anomaly models along each relevant seismic profile. On the top left corner, the magnetic anomaly map for the EBSB region (RTP EMAG2-v3), with seismic profiles in overlay: thick black lines are modelled profiles where continental crust has been interpreted; thick dotted lines are modelled profiles where oceanic crust has been interpreted. Profiles from A to D are NW-SE trending lines, whereas profiles from E to K are NE-SW trending lines. Each panel compares the calculated (red line) and observed (black line) anomalies. The grey band along the observed anomaly represents the

anomaly variations about 15 km either side of the profile. The root mean-squared (RMS) error, expressed in nT, between observed and calculated anomaly is shown at the bottom left corner of each panel. Colored backgrounds along displayed profiles show magnetisation intensities for the positively magnetized continental layers (pink), negatively magnetized continental layers (purple), and negatively magnetized oceanic layers (blue). Black vertical lines within each panel show profile intersections. The striped shading over the D-D' profile indicates a gap along the bs-180 seismic line.

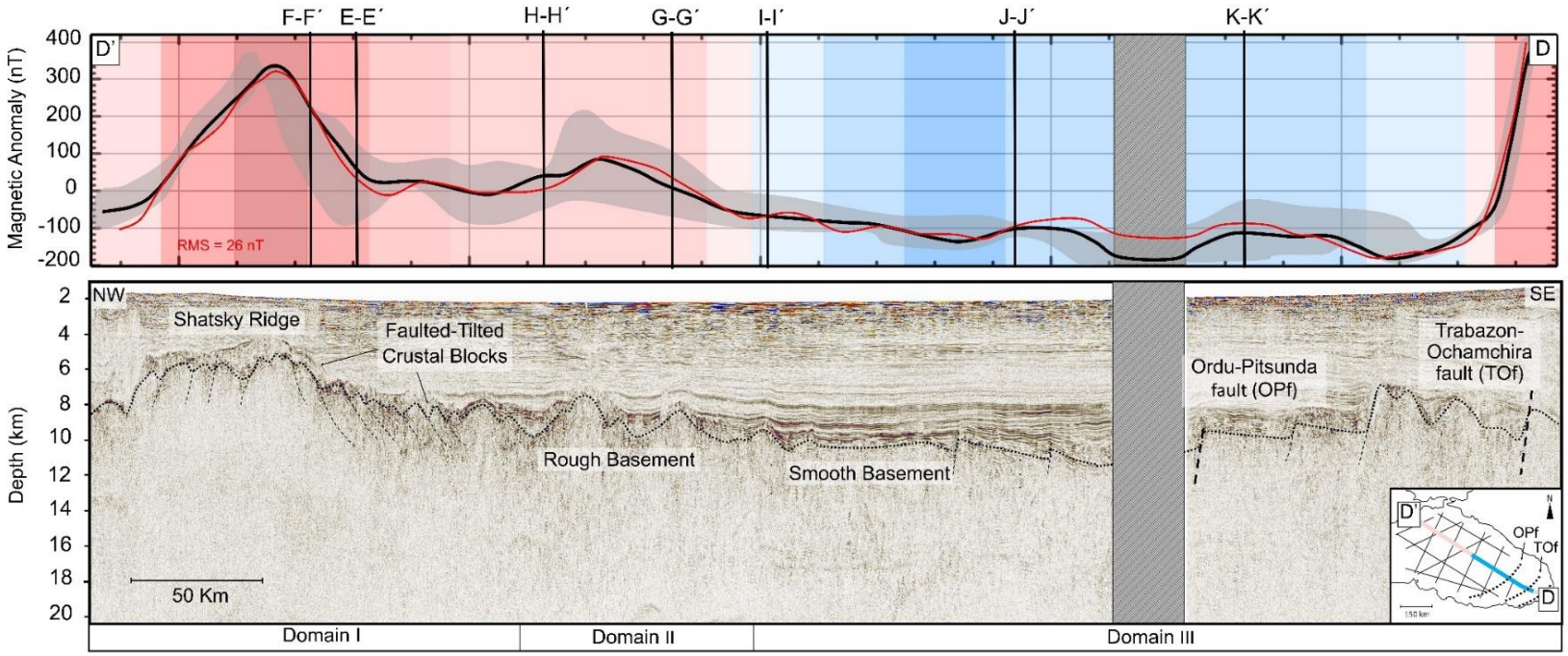

Figure B- 2. Magnetic anomaly modelling along seismic profile bs-180. Top panel (Figure B- 1 - D-D') shows the observed (black) and calculated (red) anomaly along this profile. Magnetic intensity is indicated with colored bands (color scale as shown in Figure B- 1). Bottom panel shows the bs-180 seismic profile. Top basement and fault systems interpreted are in overlay. This profile shows the transition from the tilted and faulted blocks of the stretched continental domain (Domain I), to the rough, non-faulted continental basement (Domain II), to the smooth oceanic basement affected by trans-tensional faults (Domain III). The striped shading over the two panels indicates a gap along the seismic profile. The location map at the bottom right corner shows the profile position, with colors associated to the interpreted continental (pink) and oceanic (blue) domains. Trans-tensional faults locations are also shown in the location map (OPf and TOf). (VE = 7)

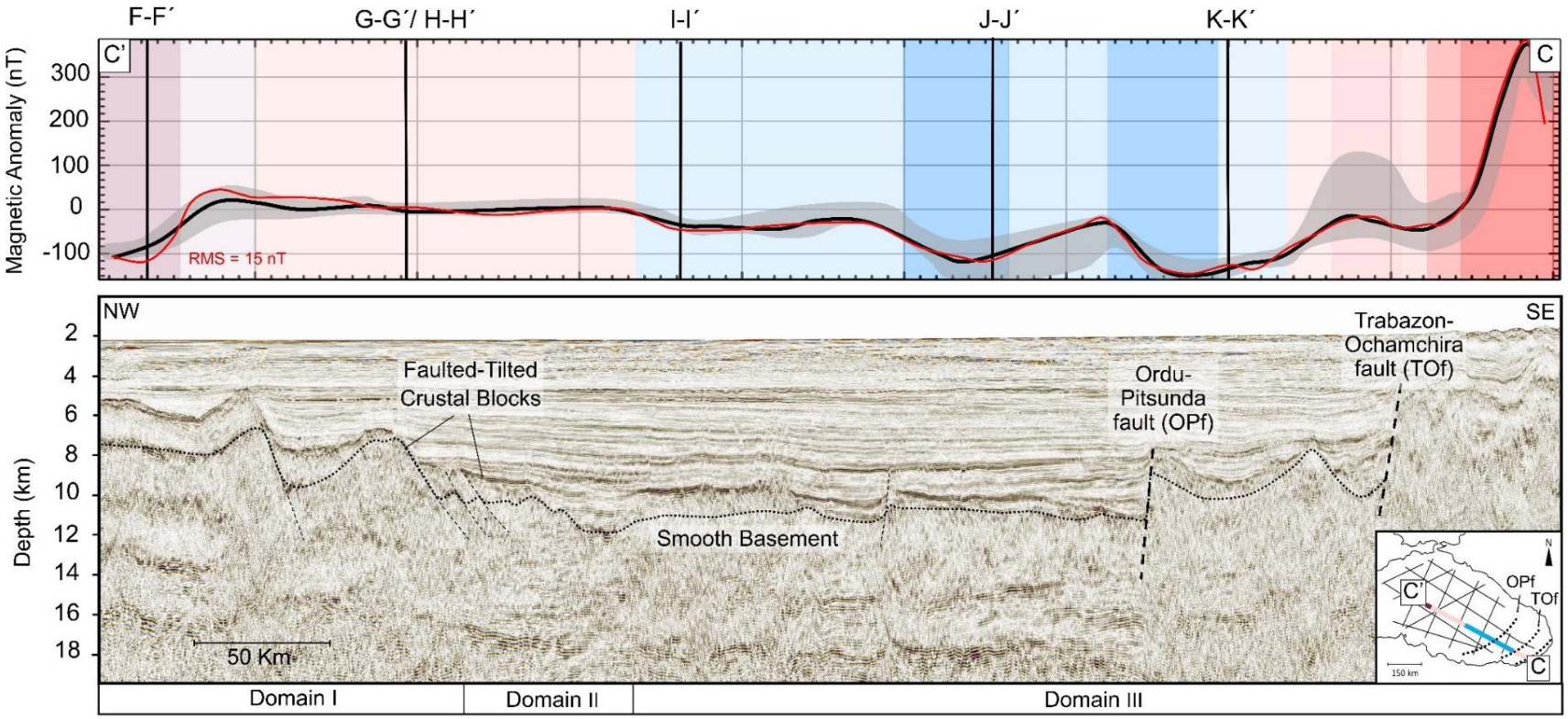

Figure B- 3. Magnetic anomaly modelling along seismic profile bp-91-109. Top panel (Figure B- 1 - C-C') shows the observed (black) and calculated (red) anomaly along this profile. Magnetic intensity is indicated with colored bands (color scale as shown in Figure B- 1). Bottom panel shows bp-91-109 seismic profile. Top basement and fault systems interpreted are in overlay. The location map at the bottom right corner shows the profile position, with colors associated to the interpreted continental (pink-purple) and oceanic (blue) domains. Trans-tensional fault locations are also shown in the location map (OPf and TOf). (VE = 7).

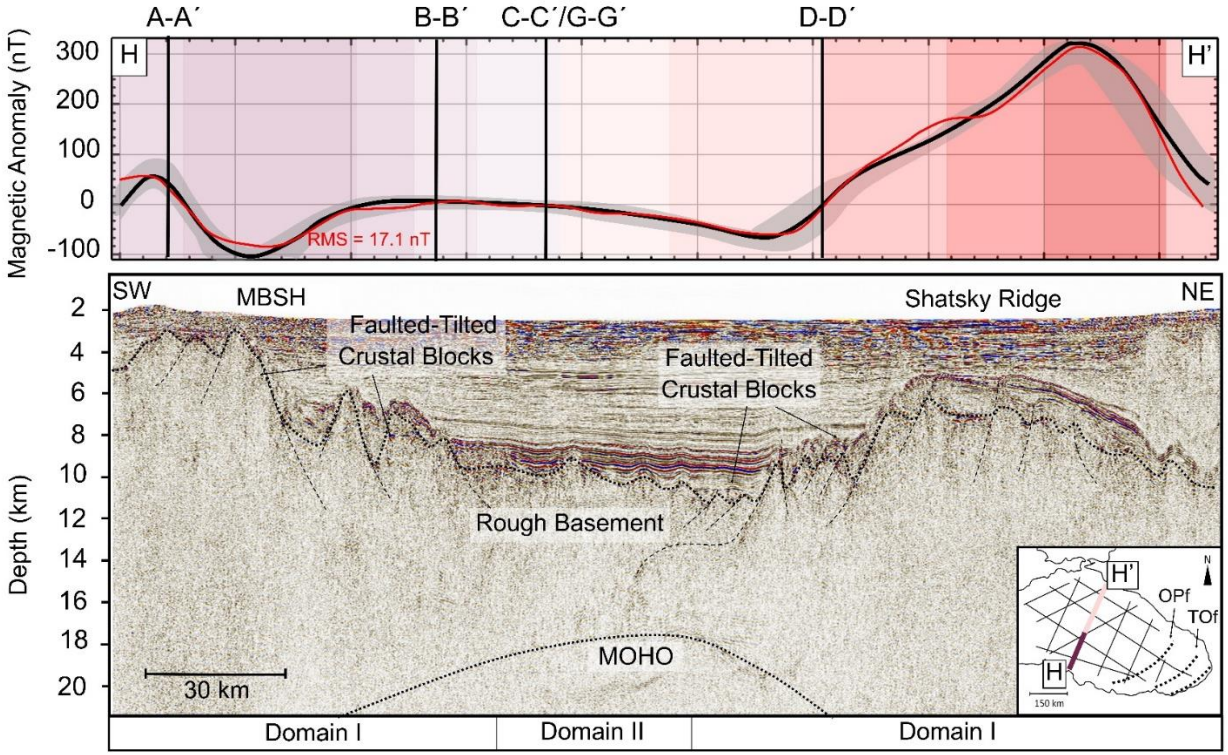

Figure B- 4. Magnetic anomaly modelling along seismic profile bs-90. Top panel (Figure B- 1 - H-H') shows the observed (black) and calculated (red) anomaly along this profile. Magnetic intensity is indicated with colored bands (color scale as shown in Figure B- 1). Bottom panel shows the bs-90 seismic profile. Top basement and fault systems interpreted are in overlay. Moho depth comes from Graham et al. (2013) gravity modelling. No oceanic crust is inferred in the central basin (Domain II), where a rough basement is instead associated with stretched continental crust based on the presence of weakly-magnetized layers. The location map at the bottom right corner shows the profile position, with colors marking the interpreted continental (pink-purple) domain. Trans-tensional fault locations are also shown in the location map (OPf and TOf). (VE = 5)

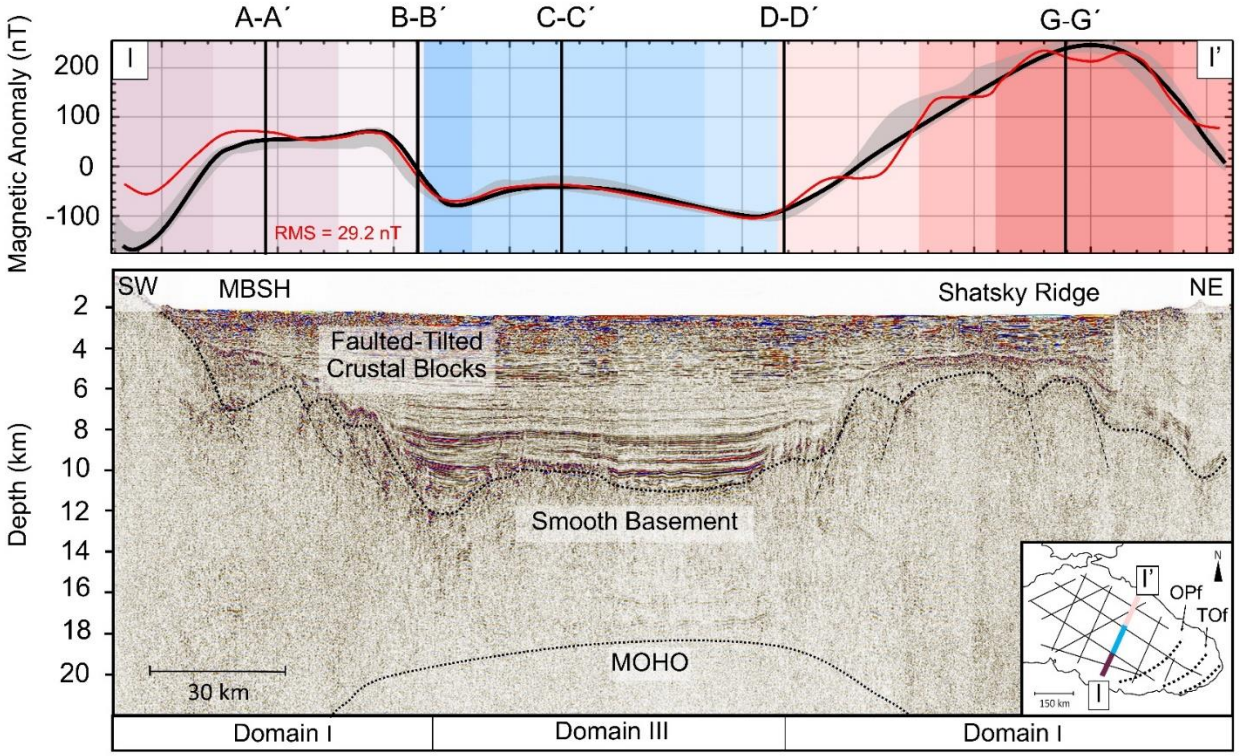

Figure B- 5. Magnetic anomaly modelling along seismic profile bs-100. Top panel (Figure B- 1 - I-I') shows the observed (black) and calculated (red) anomaly along this profile. Magnetic intensity is indicated with colored bands (color scale as shown in Figure B- 1). Bottom panel shows the bs-100 seismic profile. Top basement and fault systems are interpreted in overlay. Moho depth comes from Graham et al. (2013) gravity modelling. Domain III is interpreted as an oceanic type of crust, due to its smooth morphology and the strong and negative magnetisation character, with intensity between 1.6 and 2.4 A/m. The location map at the bottom right corner shows the profile position, with colors marking the interpreted continental (pink-purple) and oceanic (blue) domains. Trans-tensional fault locations are also shown in the location map (OPf and TOf). (VE = 5)

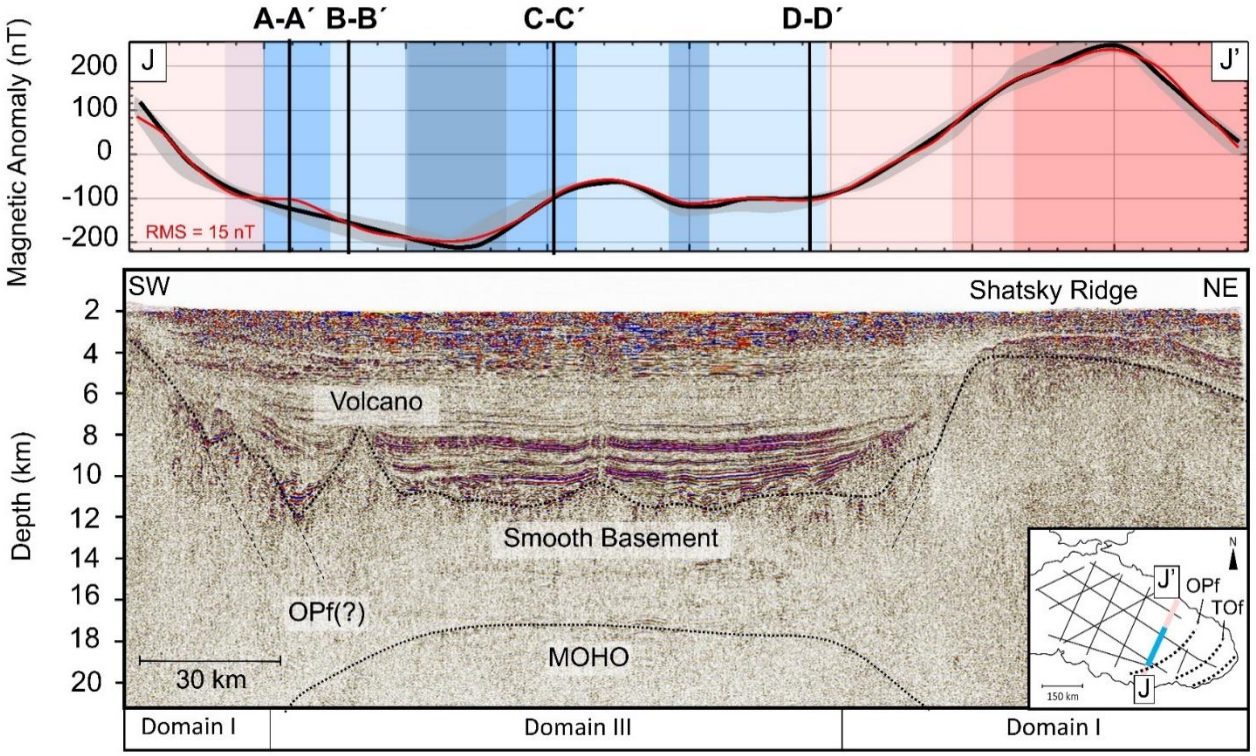

Figure B- 6. Magnetic anomaly modelling along seismic profile bs-110. Top panel (Figure B- 1- J-J') shows the observed (black) and calculated (red) anomaly along this profile. Magnetic intensity is indicated with colored bands (color scale as shown in Figure B- 1). Bottom panel shows the bs-110 seismic profile. Top basement and fault systems are interpreted in overlay. Moho depth comes from Graham et al. (2013) gravity modelling. Domain III is interpreted as oceanic crust, due to its smooth morphology and the strong and negative magnetisation character, with intensity between 1.1 and 3.8 A/m. The location map at the bottom right corner shows the profile position, with colors marking the interpreted continental (pink-purple) and oceanic (blue) domains. Trans-tensional fault locations are also shown in the location map (OPf and TOf). (VE = 5)

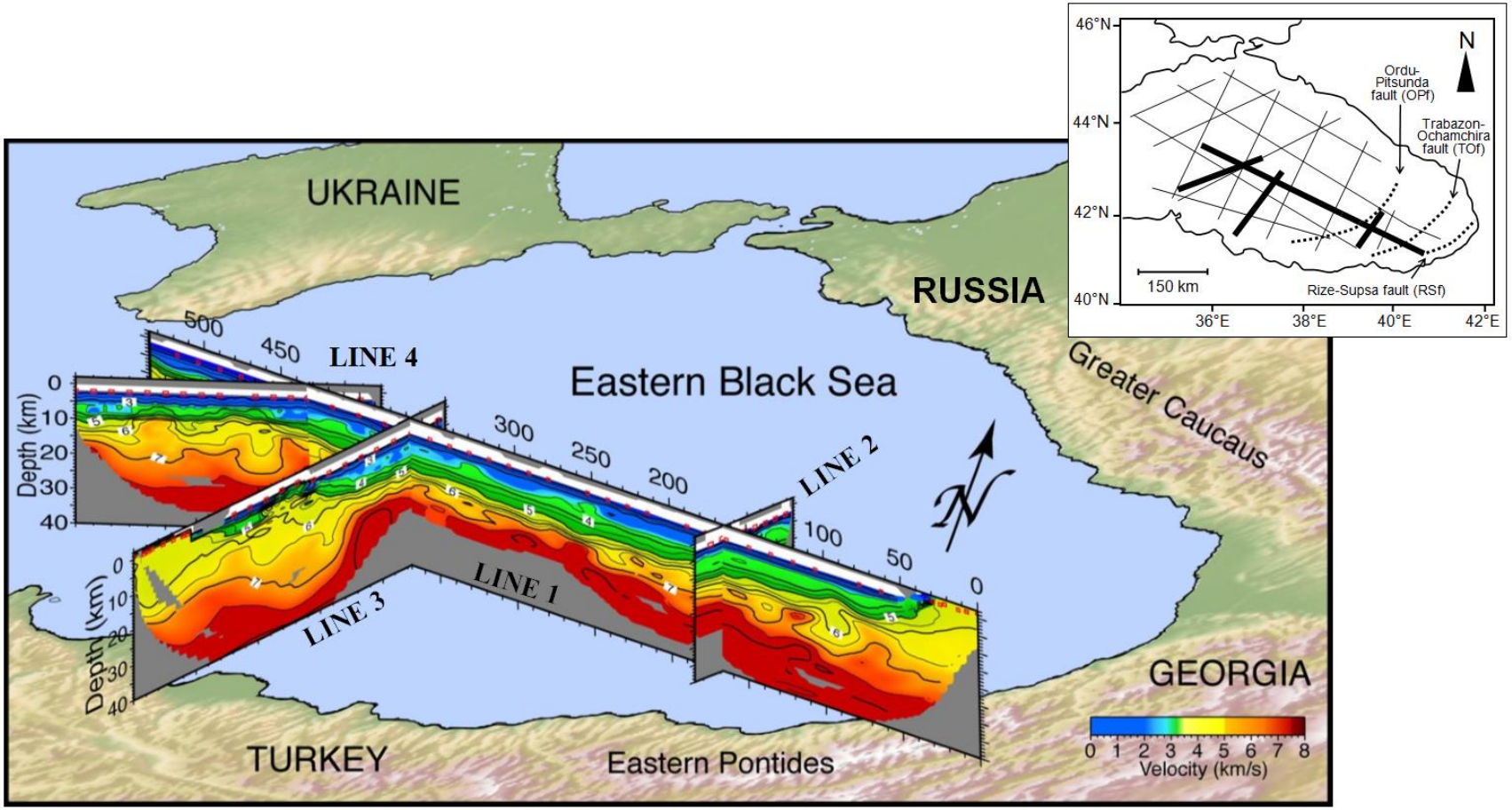

Figure B- 7. Wide-angle seismic data (OBS line 1, 2 3 and 4) from Shillington et al. (2009), with colour display showing crustal thickness and velocity. Wide-angle profiles location is shown along with the GWL profiles in the location map to the top right corner.

Appendix C Downward continuation

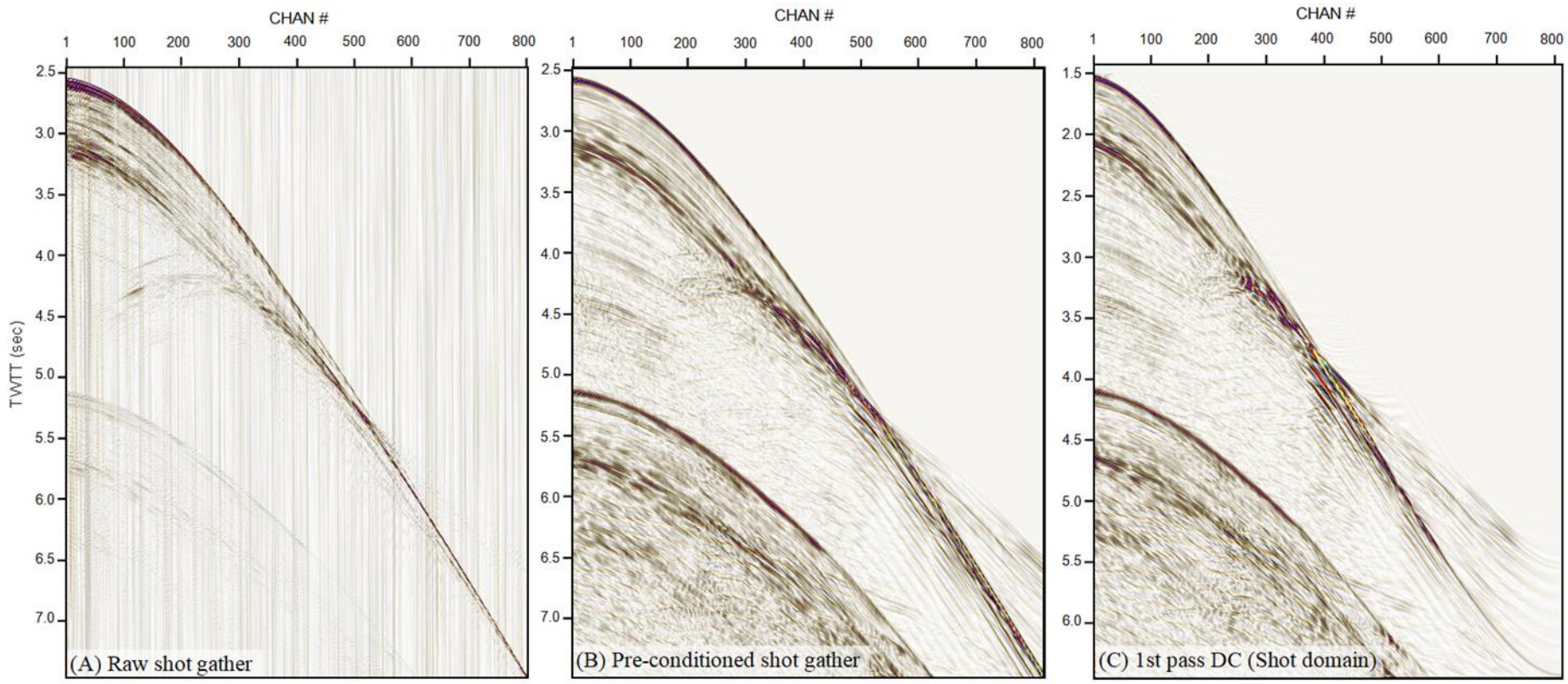

Figure C- 1. Continued...

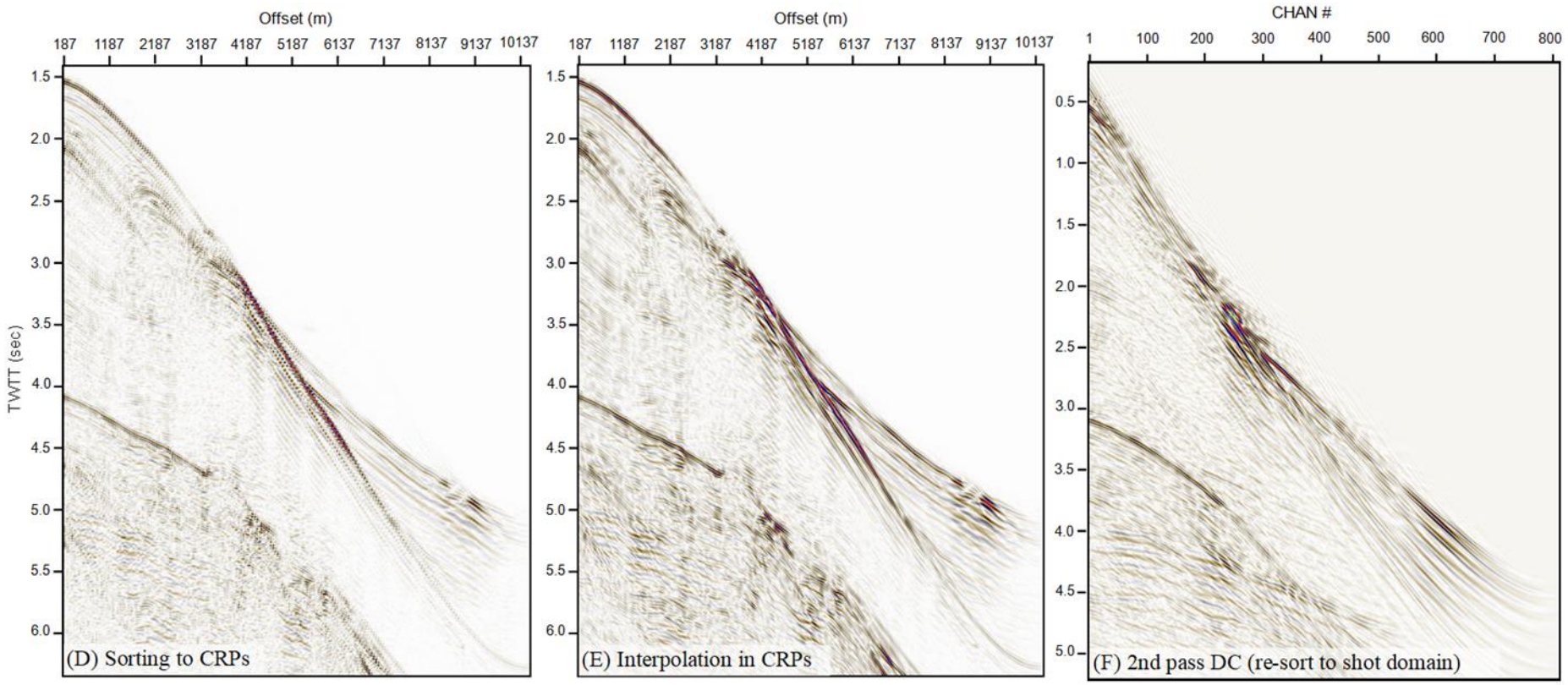

Figure C- 1 Example shot gather (FFID 31812) showing the different stages of downward continuation. (A) Raw shot gather, (B) pre-conditioned shot gather and (C) 1st pass downward continuation (DC) in shot domain. In (D), re-sorting to Common Receiver Points (CRPs) showed by an example shot (CRPs 31812, nearby FFID 31812) and (E) interpolation in CRPs. In (F), output of the 2nd pass DC after being re-sorted into shot domain (FFID 31812).

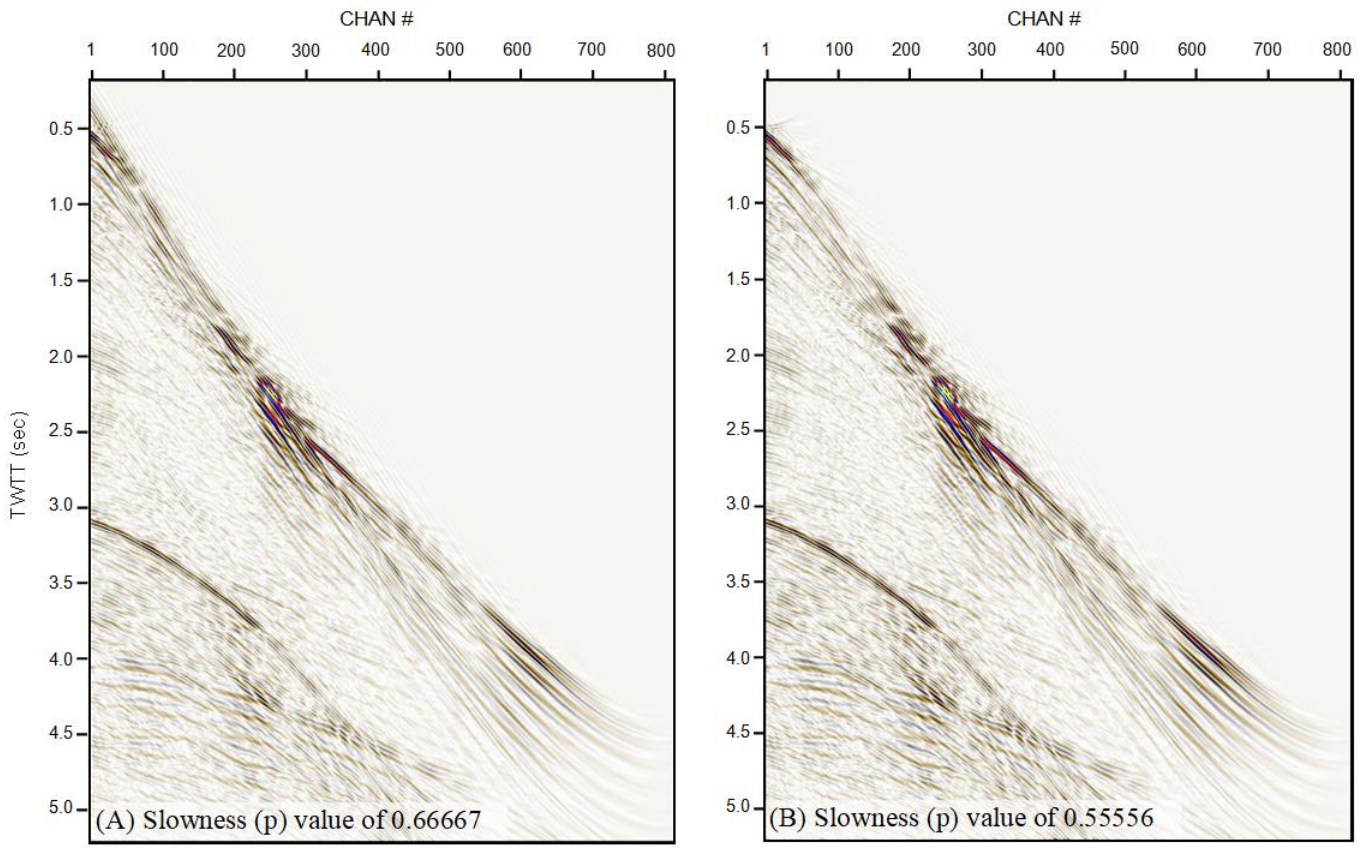

Figure C- 2. Example shot gather (FFID 31812) after downward continuation, comparing the output resulting from different ranges of slowness (p) applied during DC. (A) Slowness value of 0.66667, preserving all velocities up to ~ 1500 m/s. (B) Slowness value of 0.55556, preserving all velocities up to ~ 1800 m/s. Linear events near the seafloor reflection arrival in (A) are removed in (B).

Appendix D Travel-time analysis

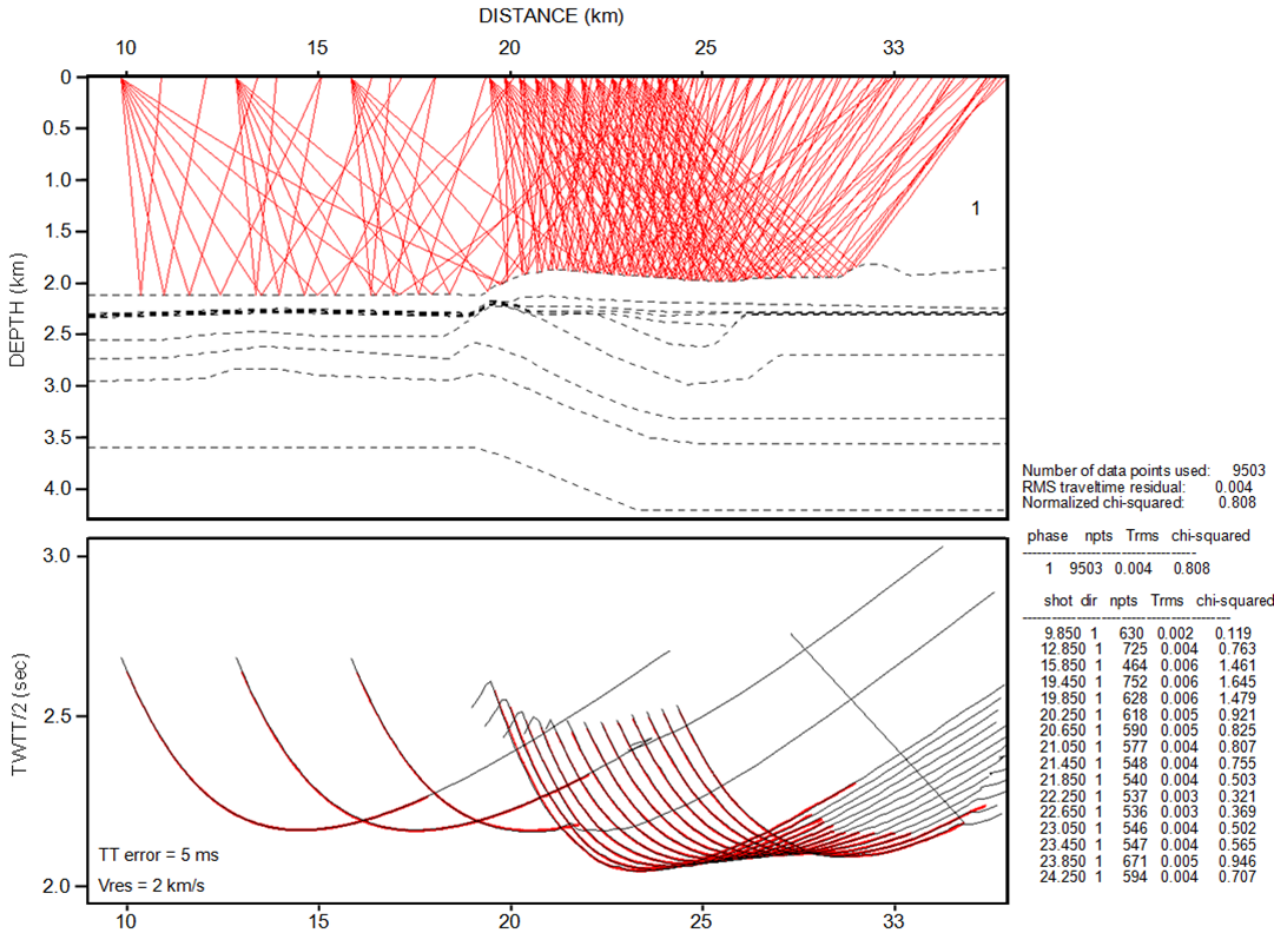

Figure D- 1. Continued…

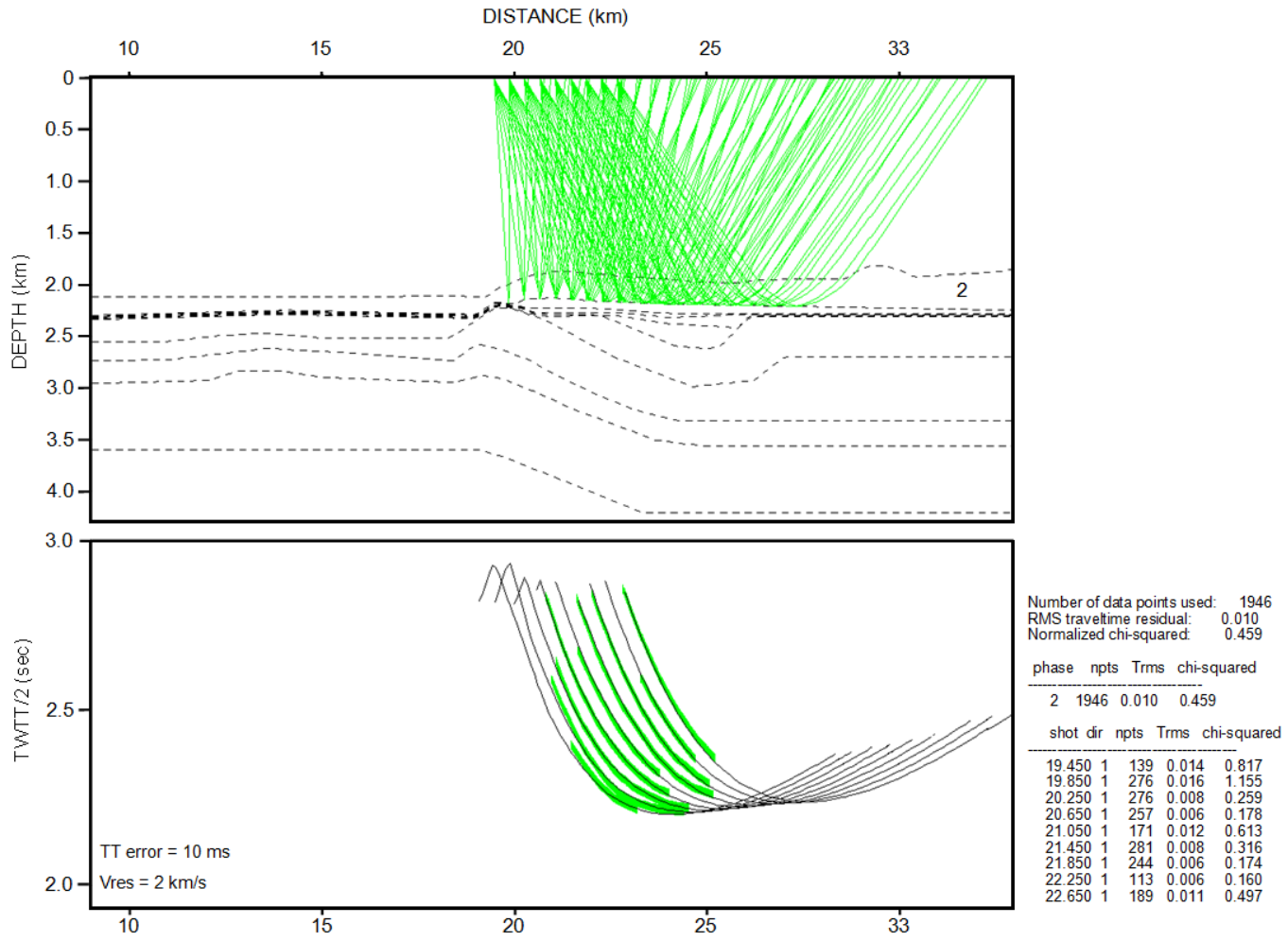

Figure D- 1. Continued…

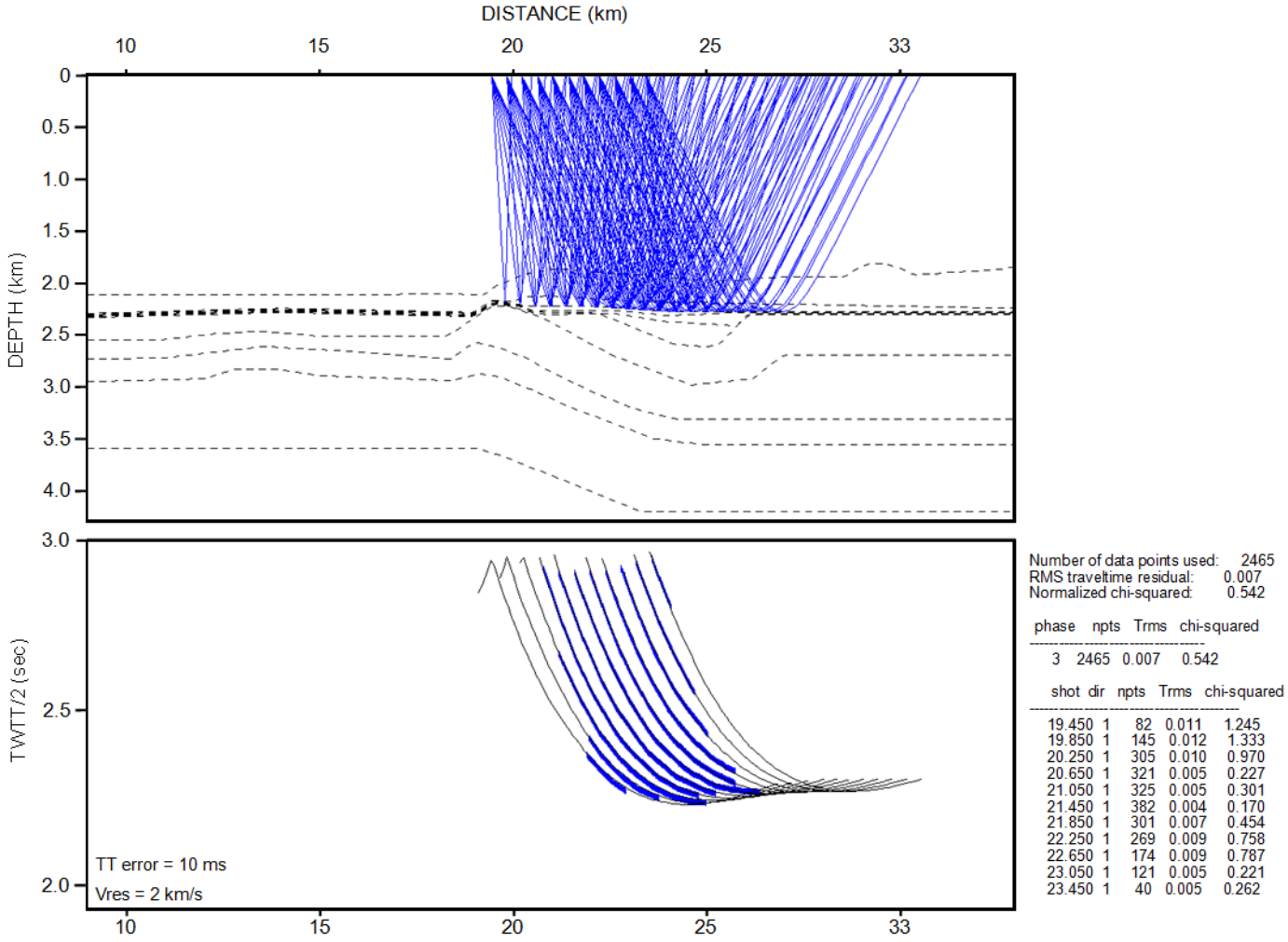

Figure D- 1. Continued…

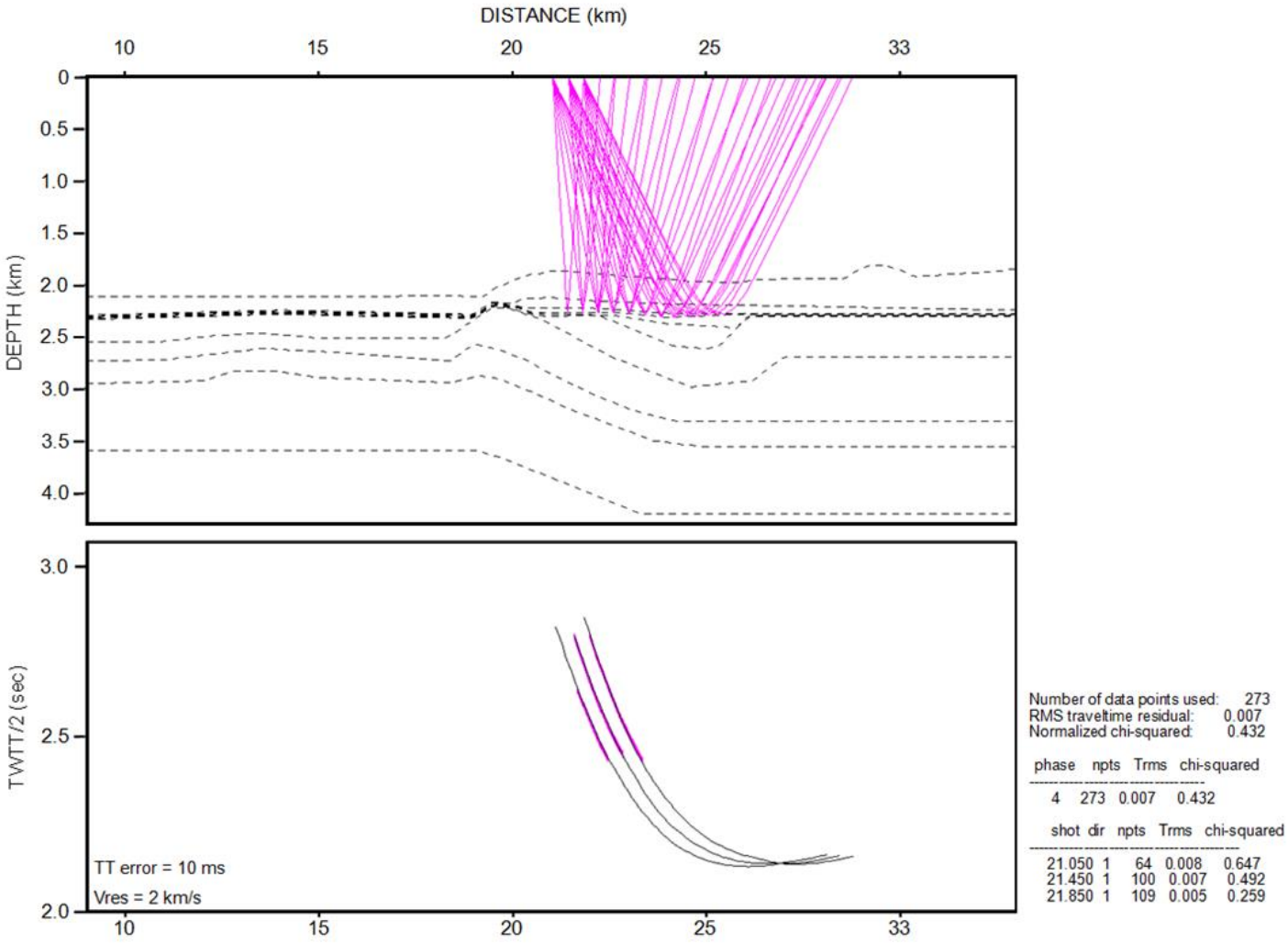

Figure D- 1. Continued…

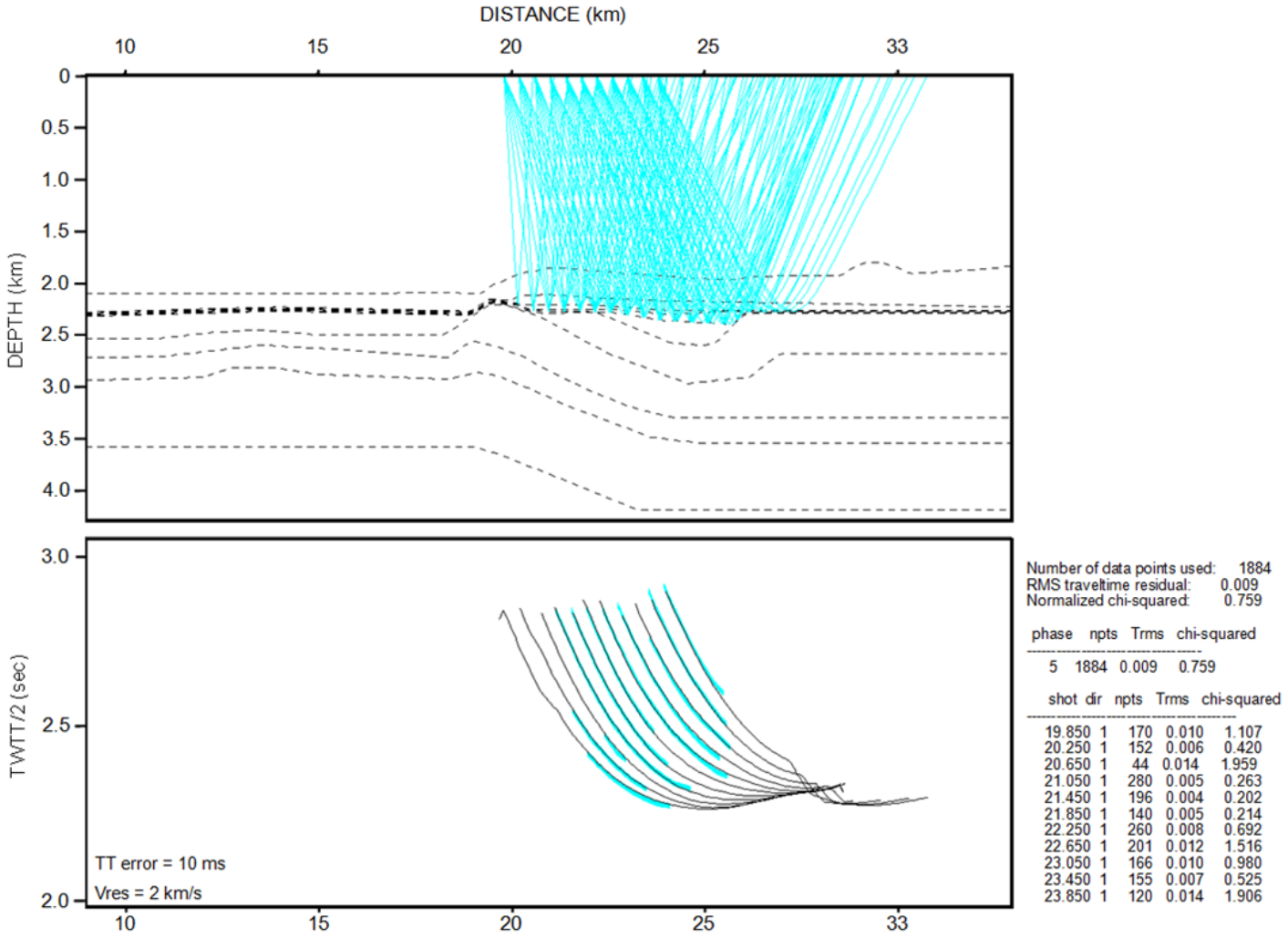

Figure D- 1. Continued…

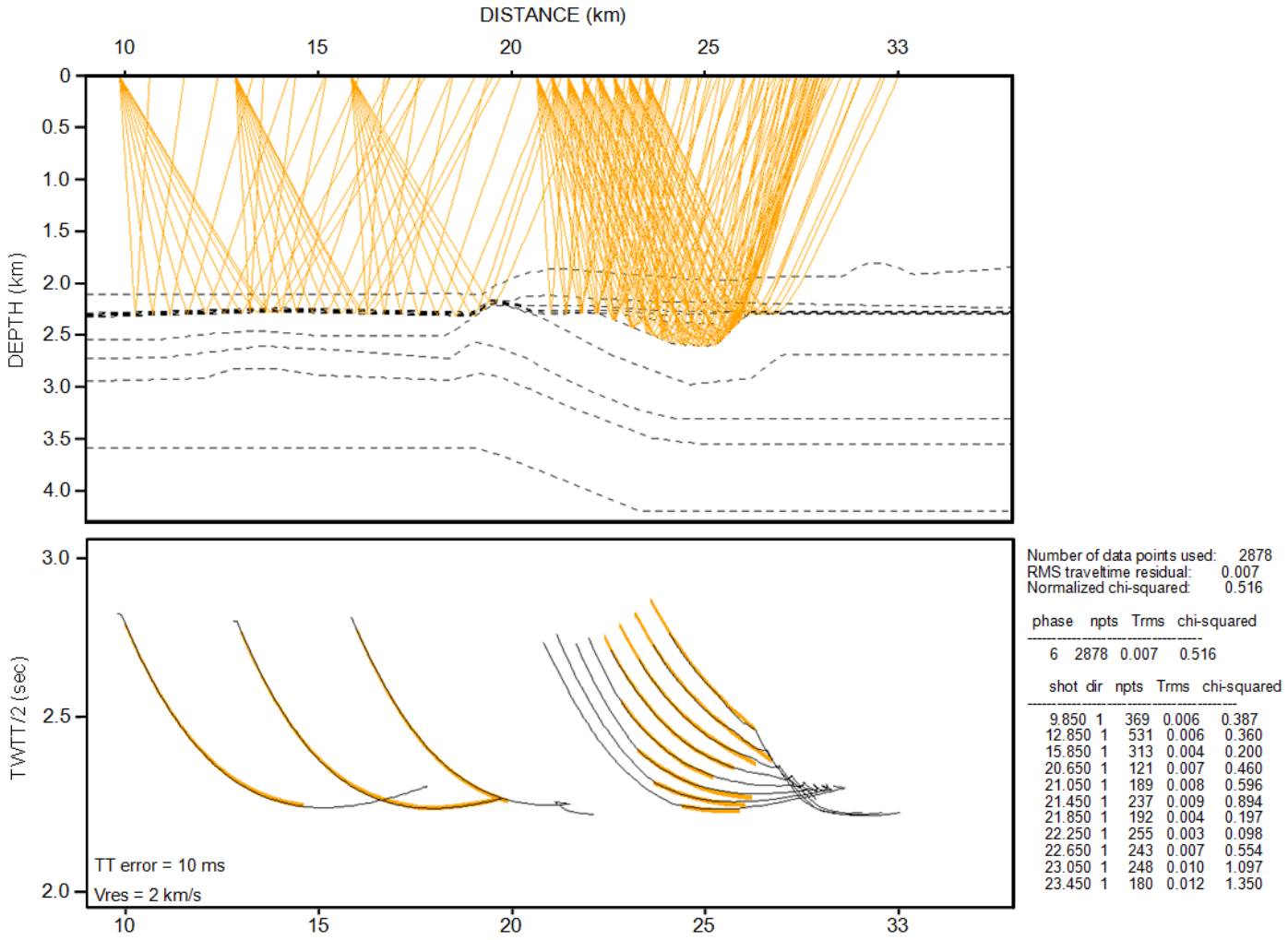

Figure D- 1. Continued…

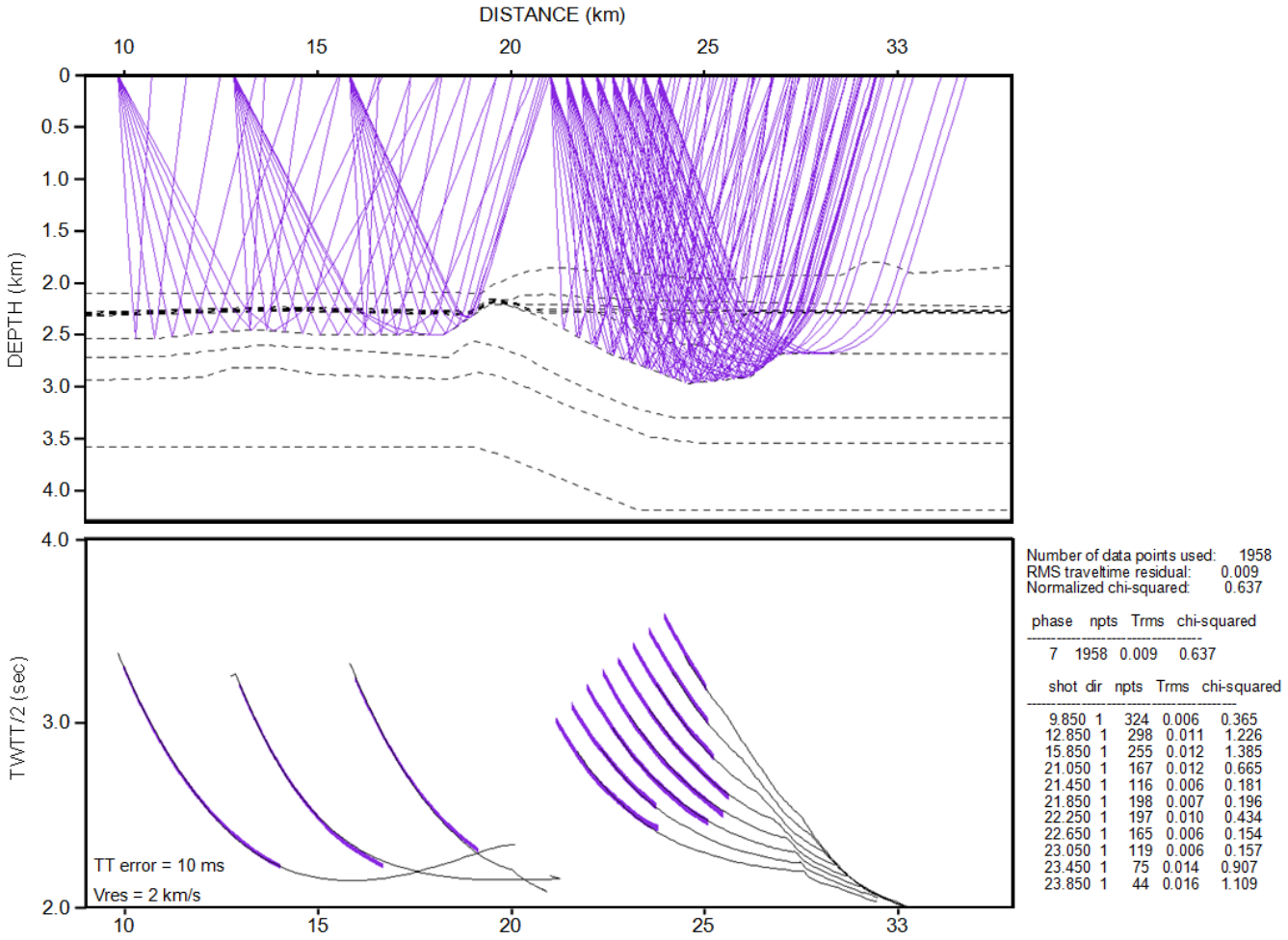

Figure D- 1. Continued…

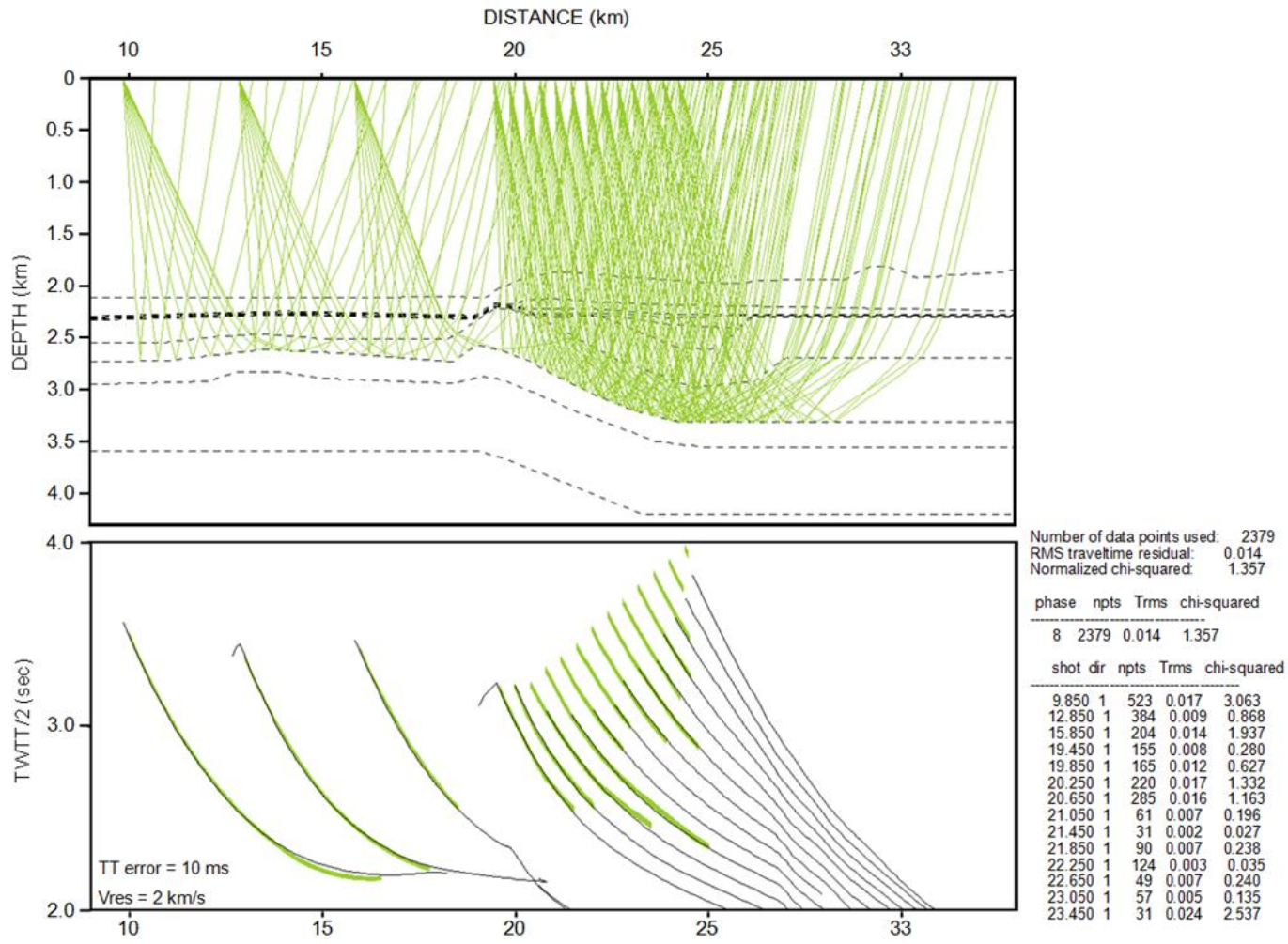

Figure D- 1. Continued…

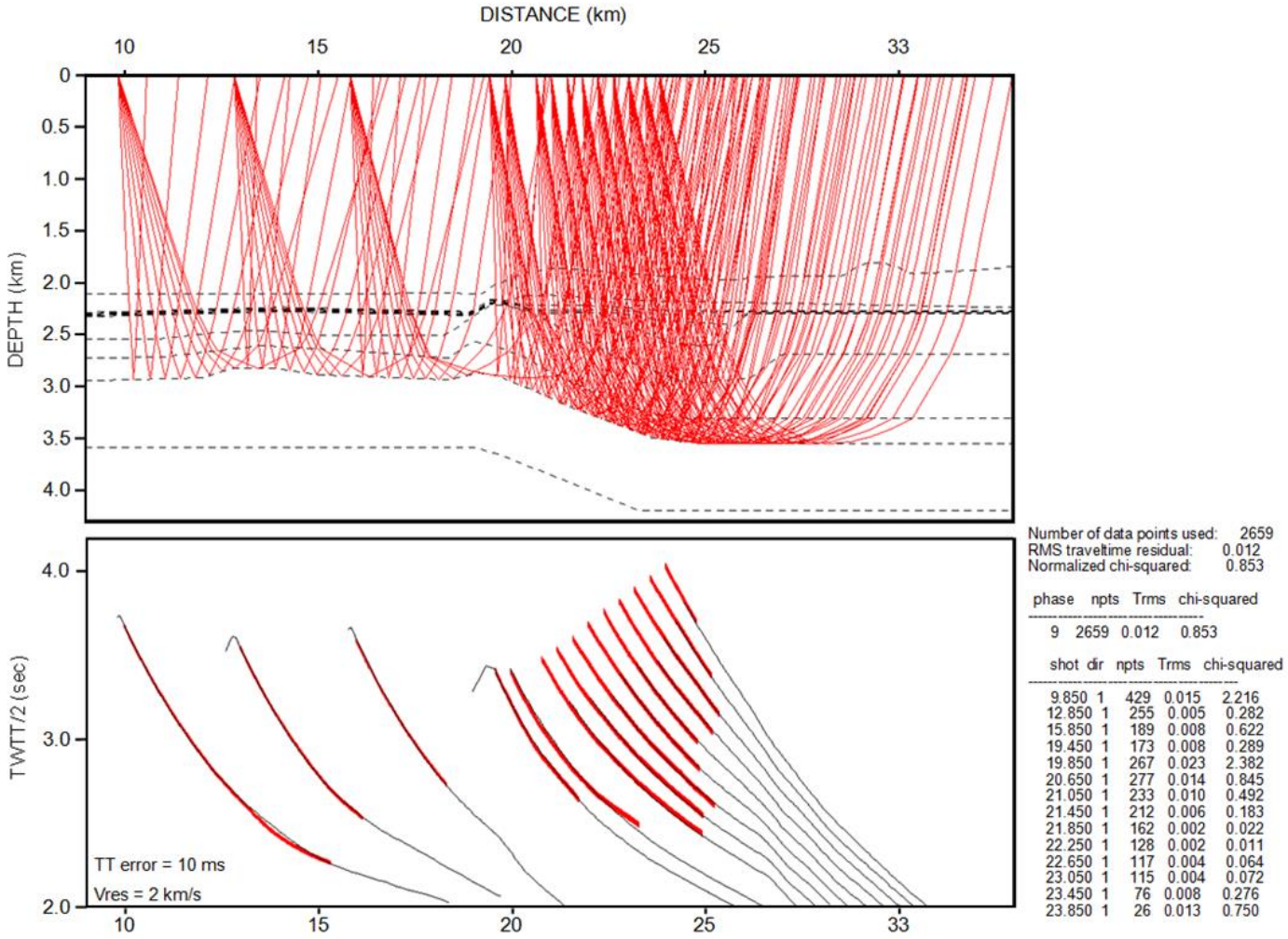

Figure D- 1. Continued…

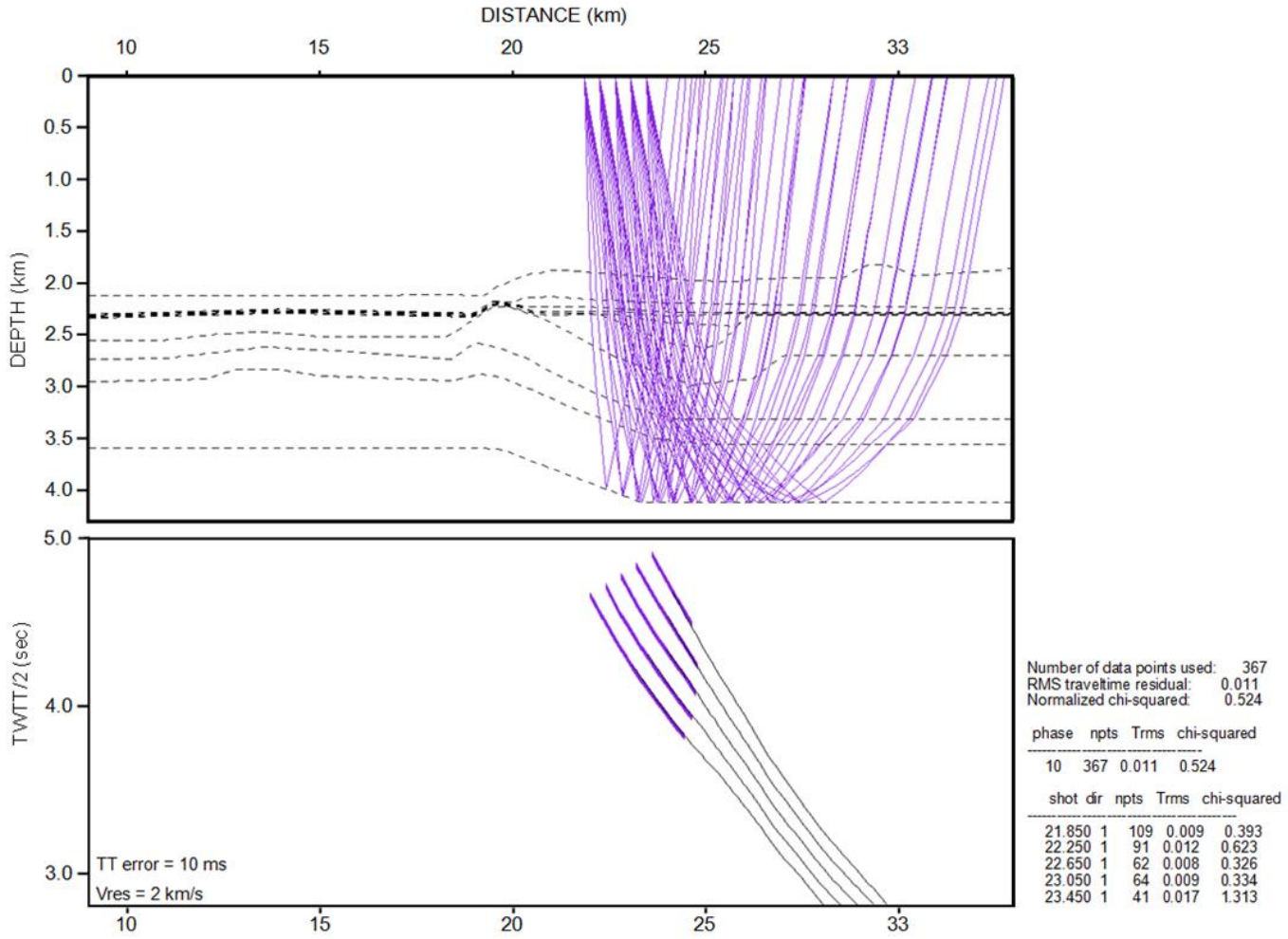

Figure D- 1. Layer-stripping approach using non-downward continued reflected travel-times. Progressively deeper phases are modelled while holding the overlying layers fixed until all data has been fitted. Phases used for the layer-stripping modelling approach are described in the main text (see section 5.5.2.2)

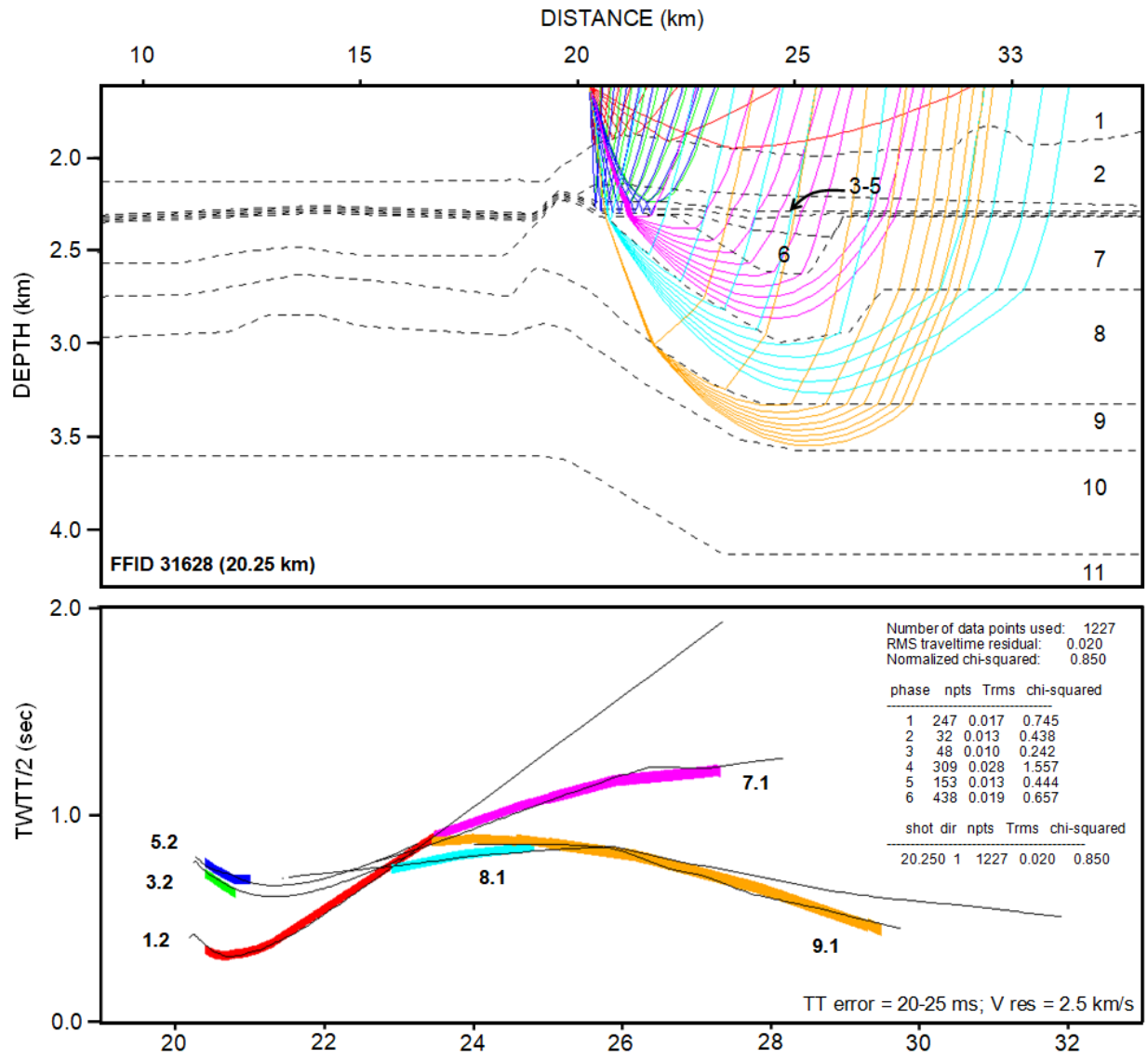

Figure D- 2. Reflected (1.2, 3.2 and 5.2) and refracted (7.1, 8.1 and 9.1) travel-time analysis on FFID 31628. Statistics for the model are shown to the bottom right. Modelling results show that refracted arrivals are associated with layers deeper than the ones associated with the BSRs.

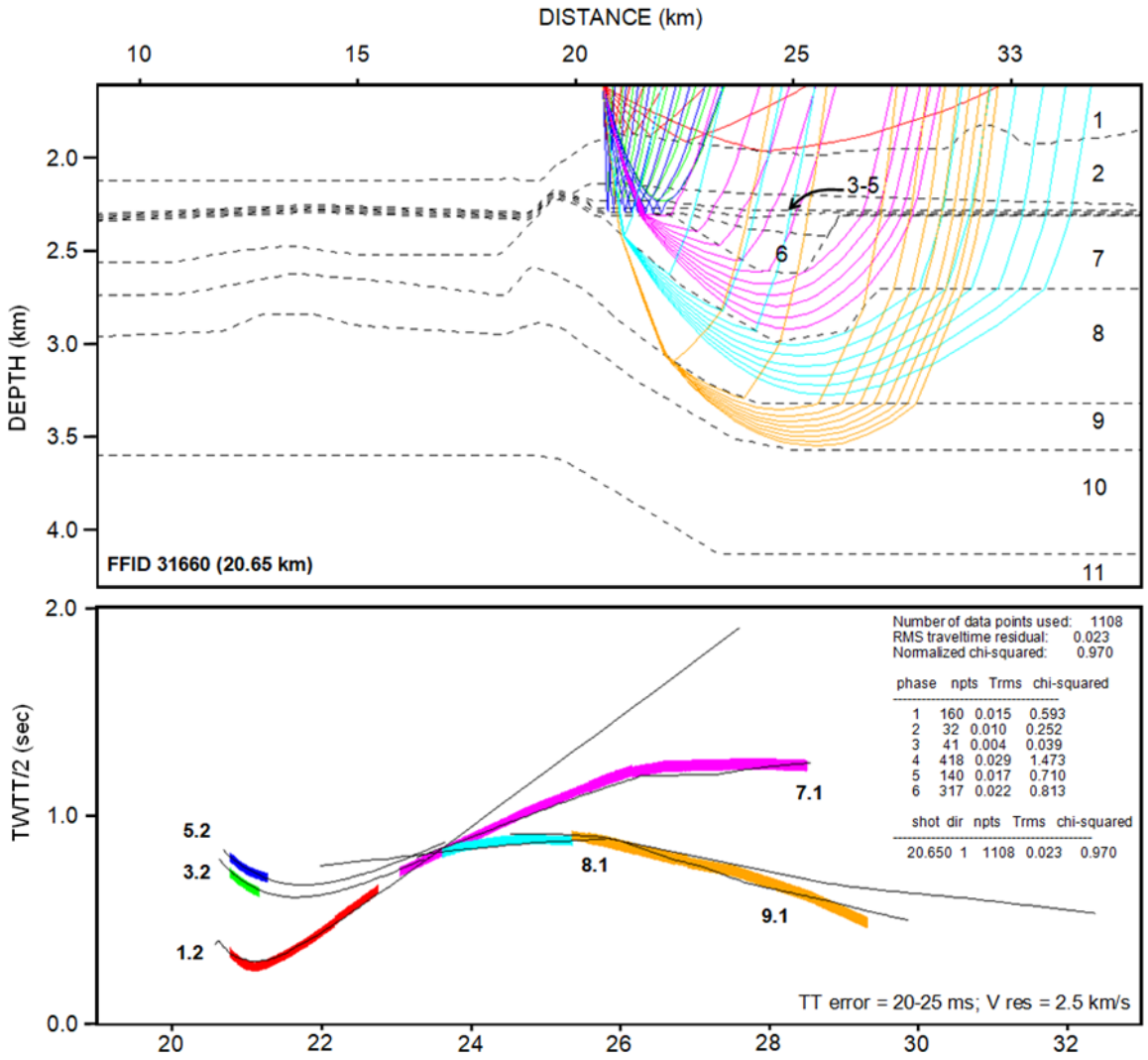

Figure D- 3. Reflected (1.2, 3.2 and 5.2) and refracted (7.1, 8.1 and 9.1) travel-time analysis on FFID 31660. Statistics for the model are shown to the bottom right. Modelling results show that refracted arrivals are associated with layers deeper than the ones associated with the BSRs.

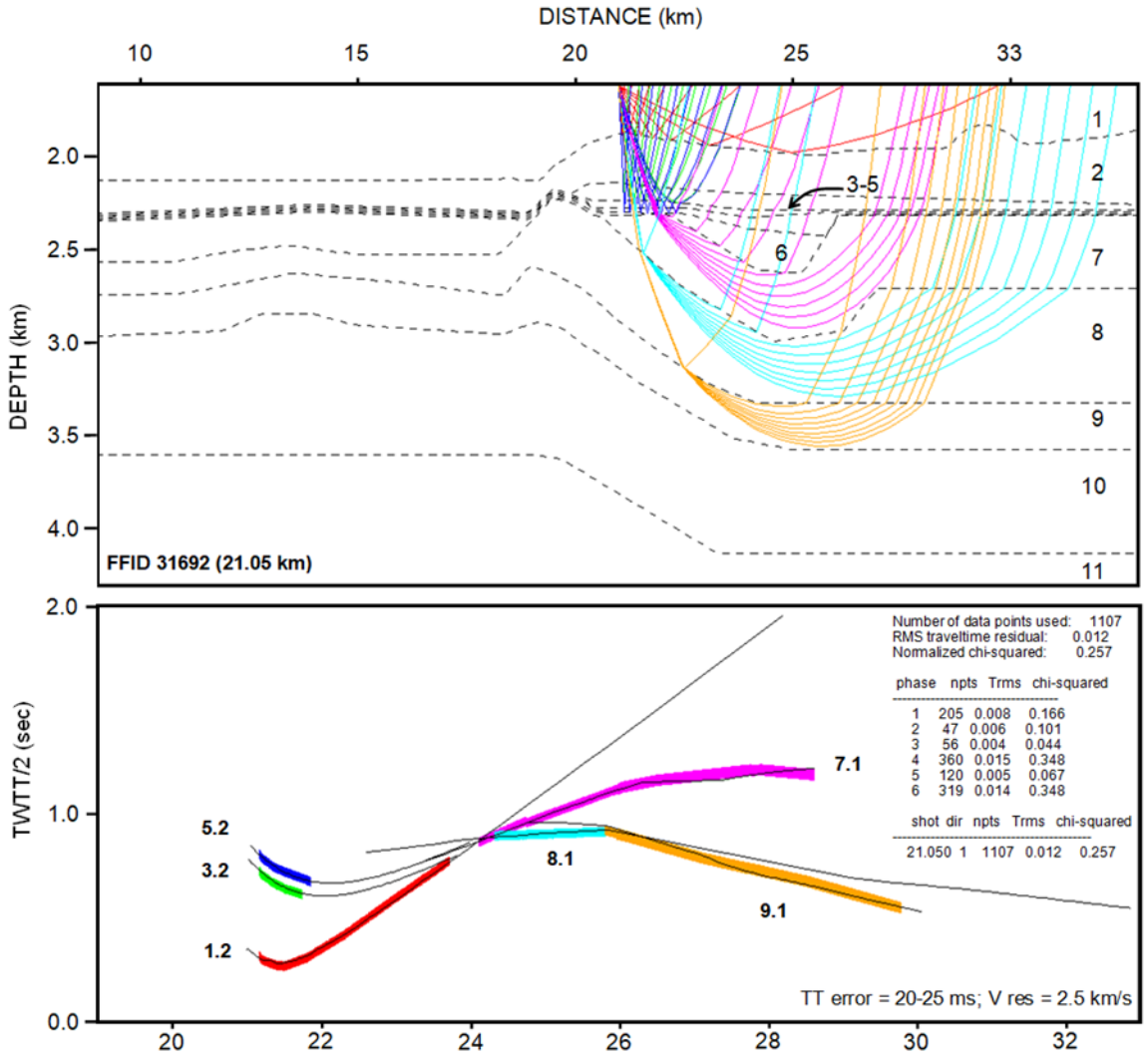

Figure D- 4. Reflected (1.2, 3.2 and 5.2) and refracted (7.1, 8.1 and 9.1) travel-time analysis on FFID 31692. Statistics for the model are shown to the bottom right. Modelling results show that refracted arrivals are associated with layers deeper than the ones associated with the BSRs.

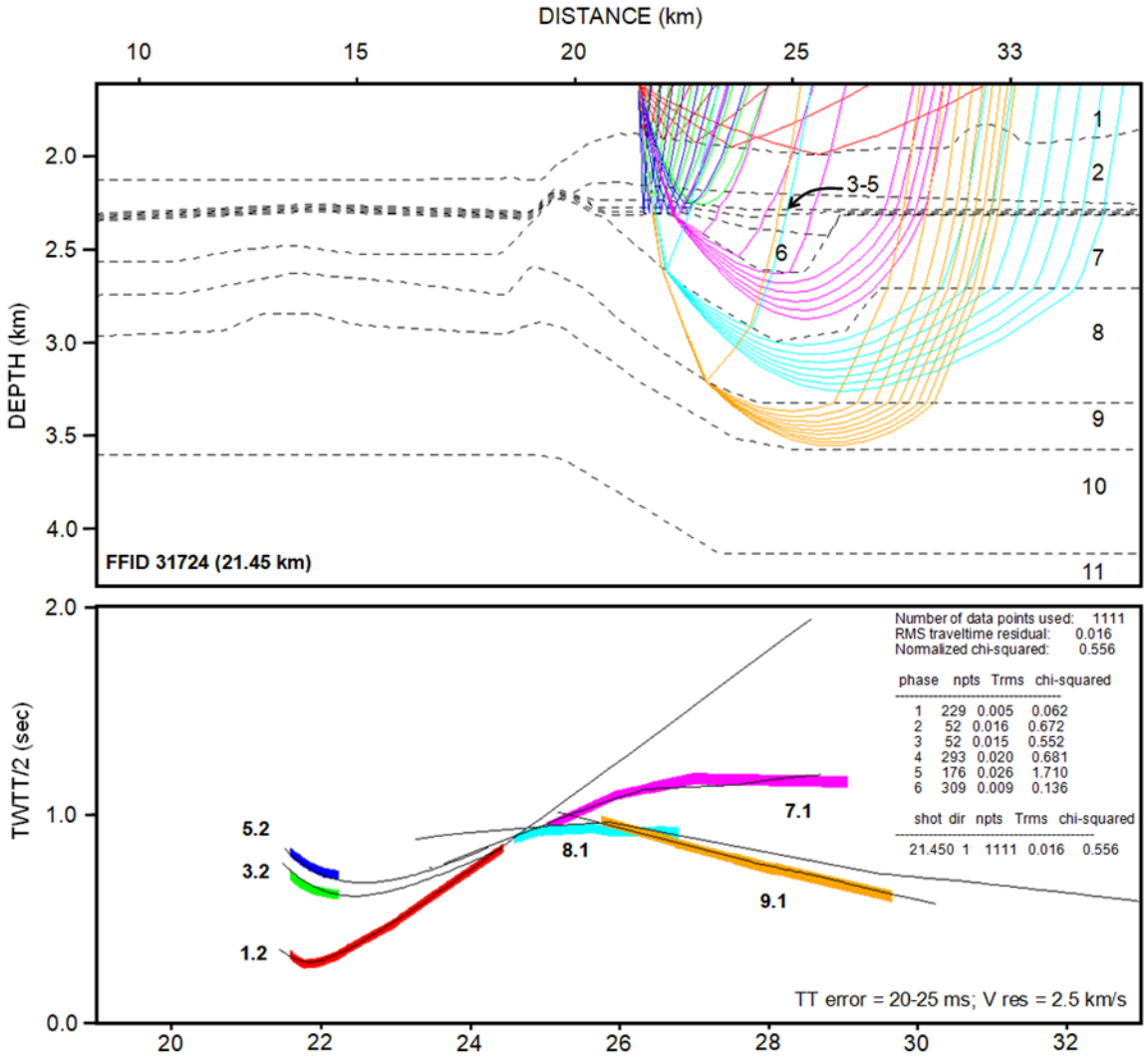

Figure D- 5. Reflected (1.2, 3.2 and 5.2) and refracted (7.1, 8.1 and 9.1) travel-time analysis on FFID 31724. Statistics for the model are shown to the bottom right. Modelling results show that refracted arrivals are associated with layers deeper than the ones associated with the BSRs.

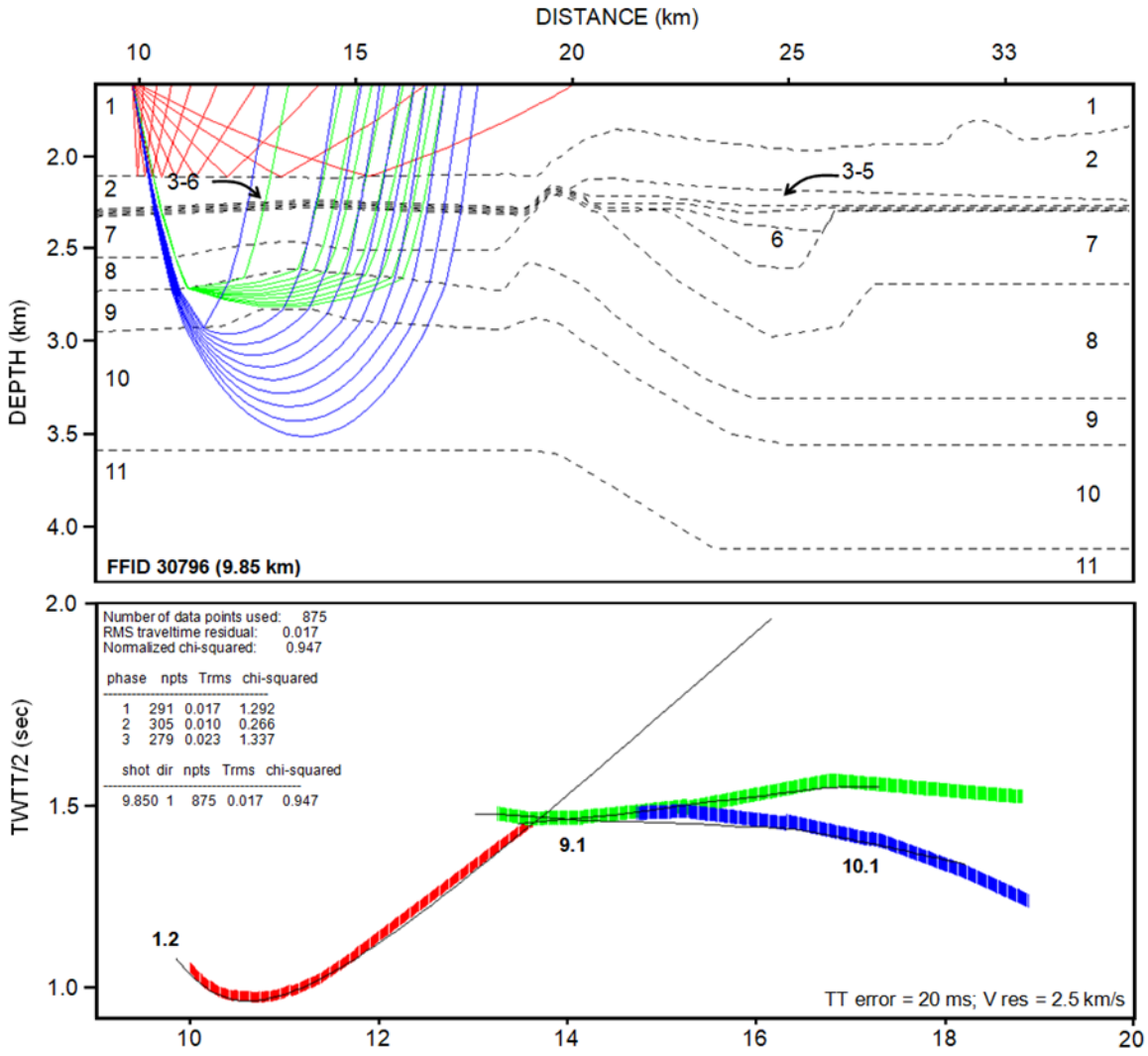

Figure D- 6. Reflected (1.2) and refracted (9.1 and 10.1) travel-time analysis on FFID 30796. Statistics for the model are shown to the top left. Modelling results show that refracted arrivals visible in the central basin are associated with layers deeper than the ones associated with the BSRs.

Appendix E Effective-medium modelling

		258 mbsf (central basin)					258 mbsf (BSR0)		
		ϕ (%)					ϕ (%)		
		40	50	60			40	50	60
S_H (%)	0	1782	1671	1592	S_H (%)	0	1782	1671	1592
	1	1819	1709	1630		1	1819	1709	1630
	2	1856	1746	1667		2	1856	1746	1667
	3	1893	1782	1704		3	1893	1782	1704
	4	1929	1819	1741		4	1929	1819	1741
	5	1965	1855	1778		5	1965	1855	1778
	6	2000	1890	1814		6	2000	1890	1814
	7	2035	1926	1850		7	2035	1926	1850

		360 mbsf (central basin)					360 mbsf (BSR1)		
			ϕ (%)					ϕ (%)	
		40	50	60			40	50	60
S_H (%)	0	1813	1699	1617	S_H (%)	0	1813	1699	1617
	1	1850	1736	1654		1	1850	1736	1654
	2	1886	1772	1690		2	1886	1772	1690
	3	1922	1808	1727		3	1922	1808	1727
	4	1957	1844	1763		4	1957	1844	1763
	5	1992	1879	1799		5	1992	1879	1799
	6	2027	1914	1835		6	2027	1914	1835
	7	2062	1949	1871		7	2062	1949	1871
	8	2096	1984	1906		8	2096	1984	1906

		438 mbsf (central basin)					438 mbsf (BSR3)			
		ϕ (%)					ϕ (%)			
		30	40	50	60		30	40	50	60
S_H (%)	0	2037	1832	1717	1632	S_G(%)	0	2037	1832	1717	1632
	1	2073	1869	1753	1669		1	1769	1561	1447	1361
	2	2107	1904	1789	1705		2	1730	1522	1409	1323
	3	2142	1940	1824	1742		3	1713	1505	1393	1307
	4	2175	1975	1860	1777		4	1702	1494	1383	1297
	5	2209	2009	1895	1813		5	1695	1486	1376	1290
	6	2242	2044	1930	1849		10	1669	1462	1354	1270
	7	2274	2078	1964	1884		15	1650	1444	1338	1257
	8	2306	2112	1998	1919		20	1631	1427	1323	1244
	9	2338	2145	2032	1954		25	1613	1410	1309	1231

Figure E- 1. Tables showing values of V_P (in m/s) obtained for different porosity (%) and S_H (or S_G) (%). V_P ranges highlighted show the match with the observed V_P.

Bibliography

Adamia, S. A., Chkhotua, T. G., Gavtadze, T. T., Lebanidze, Z. A., Lursmanashvili, N. D., Sadradze, N., et al. (2017). Tectonic setting of Georgia–eastern Black Sea: a review. *Geological Society, London, Special Publications*, 428(1), 11-40. https://doi.org/10.1144/SP428.6

Adamia, S. A., Gamkrelidze, I. P., Zakariadze, G. S., & Lordkipanidze, M. B. (1974). Adjara-Trialeti trough and the problem of the Black Sea origin. *Geotektonica*, 1, 78-94.

Adamia, S., Alania, V., Chabukiani, A., Chichua, G., Enukidze, O., & Sadradze, N. (2010). Evolution of the Late Cenozoic basins of Georgia (SW Caucasus): a review. *Geological Society, London, Special Publications*, 340(1), 239-259.

Ajay, K. K., Chaubey, A. K., Krishna, K. S., Rao, D. G., & Sar, D. (2010). Seaward dipping reflectors along the SW continental margin of India: Evidence for volcanic passive margin. *Journal of earth system science*, 119(6), 803.

Aksu, A.E., Hiscott, R.N., Yasar, D., Isler, F.I. & Marsh, S. (2002). Seismic stratigraphy of the Late Quatenary deposits from the southwestern Black Sea shelf: evidence for non-catastrophic variations in sea-level during the last ~10000 yr. *Mar. Geol.* 190, 61–94.

Almalki, K. A., Betts, P. G., & Ailleres, L. (2016). Incipient seafloor spreading segments: insights from the Red Sea. *Geophysical Research Letters*, 43(6), 2709-2715. https://doi.org/10.1002/2016GL068069

Almendinger, O. A., Mityukov, A. V., Myasoedov, N. K., & Nikishin, A. M. (2011). Modern erosion and sedimentation processes in the deep-water part of the Tuapse Trough based on the data of 3D seismic survey. *In Doklady Earth Sciences*, Vol. 439, 1, pp. 899-901. SP MAIK Nauka/Interperiodica.

Alves, T. M., & Cunha, T. A. (2018). A phase of transient subsidence, sediment bypass and deposition of regressive–transgressive cycles during the breakup of Iberia and Newfoundland. *Earth and Planetary Science Letters*, 484, 168-183. https://doi.org/10.1016/j.epsl.2017.11.054

Alves, T. M., Tugend, J., Holford, S., Bertoni, C., & Li, W. (2021). Continental margins unleashed-From their early inception to continental breakup. https://doi.org/10.1016/j.marpetgeo.2021.105097

Alves, T. M., Tugend, J., Holford, S., Bertoni, C., & Li, W. (2021). Continental margins unleashed-From their early inception to continental breakup. *Marine and Petroleum Geology*, 129. https://doi.org/10.1016/j.marpetgeo.2021.105097

Andreassen, K., Hart, P. E., & MacKay, M. (1997). Amplitude versus offset modeling of the bottom simulating reflection associated with submarine gas hydrates. *Marine Geology*, 137(1-2), 25-40. https://doi.org/10.1016/S0025-3227(96)00076-X

Andreassen, K., Mienert, J., Bryn, P., & Singh, S. C. (2000). A double gas-hydrate related bottom simulating reflector at the Norwegian continental margin. *Annals of the New York Academy of Sciences*, 912(1), 126-135.

Andreassen, K., Nilssen, E. G., & Ødegaard, C. M. (2007). Analysis of shallow gas and fluid migration within the Plio-Pleistocene sedimentary succession of the SW Barents Sea continental margin using 3D seismic data. *Geo-Marine Letters*, 27(2), 155-171.

Arnulf, A. F., Harding, A. J., Kent, G. M., Singh, S. C., & Crawford, W. C. (2014). Constraints on the shallow velocity structure of the Lucky Strike Volcano, Mid-Atlantic Ridge, from downward continued multichannel streamer data. *Journal of Geophysical Research: Solid Earth*, 119(2), 1119-1144.

Arnulf, A. F., Singh, S. C., Harding, A. J., Kent, G. M., & Crawford, W. (2011). Strong seismic heterogeneity in layer 2A near hydrothermal vents at the Mid-Atlantic Ridge. *Geophysical Research Letters*, 38(13).

Arora, A., Cameotra, S. S., & Chandrajit, B. (2015). Field testing of gas hydrates-an alternative to conventional fuels. *Journal of Petroleum & Environmental Biotechnology*, 6(05).

Ashi, J., Tokuyama, H., & Taira, A. (2002). Distribution of methane hydrate BSRs and its implication for the prism growth in the Nankai Trough. *Marine Geology*, 187(1–2), 177–191. https://doi.org/10.1016/S0025-3227(02)00265-7

Augustin, N., Devey, C. W., Van der Zwan, F. M., Feldens, P., Tominaga, M., Bantan, R. A., & Kwasnitschka, T. (2014). The rifting to spreading transition in the Red Sea. *Earth and Planetary Science Letters*, 395, 217-230. https://doi.org/10.1016/j.epsl.2014.03.047

Auguy, C., Calvès, G., Calderon, Y., & Brusset, S. (2017). Seismic evidence of gas hydrates, multiple BSRs and fluid flow offshore Tumbes Basin, Peru. *Marine Geophysical Research*, 38(4), 409-423.

Austin Jr, J. A., Stoffa, P. L., Phillips, J. D., Oh, J., Sawyer, D. S., Purdy, G. M., ... & Makris, J. (1990). Crustal structure of the Southeast Georgia embayment-Carolina trough: Preliminary results of a composite seismic image of a continental suture (?) and a volcanic passive margin. *Geology*, 18(10), 1023-1027. https://doi.org/10.1130/0091-7613(1990)018<1023:CSOTSG>2.3.CO;2

Autin, J., Leroy, S., Beslier, M. O., d'Acremont, E., Razin, P., Ribodetti, A., ... & Al Toubi, K. (2010). Continental break-up history of a deep magma-poor margin based on seismic reflection data (northeastern Gulf of Aden margin, offshore Oman). *Geophysical Journal International*, 180(2), 501-519. https://doi.org/10.1111/j.1365-246X.2009.04424.x

Aydın, İ., Karat, H. İ., and Koçak, A. (2005). Curie-point depth map of Turkey. *Geophysical Journal International*, 162(2), 633-640. https://doi.org/10.1111/j.1365-246X.2005.02617.x

Ball, P., Eagles, G., Ebinger, C., McClay, K., and Totterdell, J. (2013). The spatial and temporal evolution of strain during the separation of Australia and Antarctica. *Geochemistry, Geophysics, Geosystems*, 14(8), 2771-2799. doi: 10.1002/ggge.20160

Banerjee, S. K. (1984). The magnetic layer of the ocean crust—How thick is it?. Tectonophysics, 105(1-4), 15-27. https://doi.org/10.1016/0040-1951(84)90191-4

Bangs, N. L., Hornbach, M. J., Moore, G. F., & Park, J. O. (2010). Massive methane release triggered by seafloor erosion offshore southwestern Japan. *Geology*, 38(11), 1019-1022.

Bangs, N. L., Musgrave, R. J., & Tréhu, A. M. (2005). Upward shifts in the southern Hydrate Ridge gas hydrate stability zone following postglacial warming, offshore Oregon. *Journal of Geophysical Research: Solid Earth*, 110(B3).

Bangs, N. L., Sawyer, D. S., & Golovchenko, X. (1993). Free gas at the base of the gas hydrate zone in the vicinity of the Chile triple junction. *Geology*, 21(10), 905-908. https://doi.org/10.1130/0091-7613(1993)021<0905:FGATBO>2.3.CO;2

Banks, C. J., Robinson, A. G., & Williams, M. P. (1997). Structure and Regional Tectonics of the Achara-Trialet Fold Belt and the Adjacent Rioni and Kartli Foreland Basins, Republic of Georgia. In A. G. Robinson (Ed.), Regional and petroleum geology of the Black Sea and surrounding region: AAPG Memoir 68 (Chapter 17, pp. 331-346).

Baranov, V. (1957). A new method for interpretation of aeromagnetic maps: pseudo-gravimetric anomalies. *Geophysics*, 22(2), 359-382. https://doi.org/10.1190/1.1438369

Bassi, G., Keen, C. E., & Potter, P. (1993). Contrasting styles of rifting: Models and examples from the eastern Canadian margin. *Tectonics*, 12(3), 639-655. https://doi.org/10.1029/93TC00197

Bastow, I. D., & Keir, D. (2011). The protracted development of the continent–ocean transition in Afar. *Nature Geoscience*, 4(4), 248-250. https://doi.org/10.1038/ngeo1095

Bektaş, O., & Güven, İ. H. (1995). Alaskan Aphinitic Type Ultramafic and Mafic Complexes as the Root Zone of the Eastern Pontide Magmatic Arc (NE 48 Turkey), *Geology of the Black Sea Region*, 189-196.

Belousov, V. V., Volvovsky, B. S., Arkhipov, I. V., Buryanova, B. V., Evsyukov, Y. D., Goncharov, V. P., et al. (1988). Structure and evolution of the Earth's crust and upper mantle of the Black Sea. *Bollettino di Geofisica Teorica e Applicata*, 30(117-118), 109-196.

Berndt, C., Bünz, S., Clayton, T., Mienert, J., & Saunders, M. (2004). Seismic character of bottom simulating reflectors: examples from the mid-Norwegian margin. *Marine and Petroleum Geology*, 21(6), 723-733.

Berryhill, J. R. (1979). Wave equation datuming. *Geophysics*, 44(8), 1329–1344. https://doi.org/10.1190/1.1441010

Berryhill, J. R. (1984). Wave-equation datuming before stack. *Geophysics*, 49(11), 2064–2066. https://doi.org/10.1190/1.1441620

Berryman, J. G. (1992). Effective stress for transport properties of inhomogeneous porous rock. *Journal of Geophysical Research: Solid Earth*, 97(B12), 17409-17424. https://doi.org/10.1029/92JB01593

Best, A. I., J. A. Priest, C. R. I. Clayton, & E. V. L. Rees (2013). The effect of methane hydrate morphology and water saturation on seismic wave attenuation in sand under shallow sub-seafloor conditions, *Earth Planet. Sci. Lett*., 368, 78–87. doi:10.1016/j.epsl.2013.02.033.

Bialas, J., Bohlen, T., Dannowski, A., Eisenberg-Klein, G., Gassner, L., Gehrmann, R., ... & Zander, T. (2020). Joint interpretation of geophysical field experiments in the danube deep-sea fan, Black Sea. *Marine and Petroleum Geology*, 121, 104551.

Bialas, R. W., Buck, W. R., & Qin, R. (2010). How much magma is required to rift a continent?. *Earth and Planetary Science Letters*, 292(1-2), 68-78. https://doi.org/10.1016/j.epsl.2010.01.021

Bilim, F., Aydemir, A., Ateş, A., Dolmaz, M. N., Koşaroğlu, S., & Erbek, E. (2021). Crustal thickness in the Black Sea and surrounding region, estimated from the gravity data. *Marine and Petroleum Geology*, 123, 104735. https://doi.org/10.1016/j.marpetgeo.2020.104735

Biot, M. A. (1956). Theory of propagation of elastic waves in a fluid-saturated porous solid. II. Higher frequency range. *The Journal of the acoustical Society of America*, 28(2), 179-191. doi:10.1121/1.1908239.

Blaich, O. A., Faleide, J. I., & Tsikalas, F. (2011). Crustal breakup and continent-ocean transition at South Atlantic conjugate margins. *Journal of Geophysical Research: Solid Earth*, 116(B1). https://doi.org/10.1029/2010JB007686

Blakely, R. J. (1995). Potential theory in gravity & magnetic applications: *Cambridge University Press, New York*, 441p.

Bohrmann, G., Ahrlich, F., Bachmann, K., Bergenthal, M., Beims, M., Betzler, C., ... & Wunsch, D. (2018). R/V METEOR cruise report M142, Drilling Gas Hydrates in the Danube Deep-Sea Fan, Black Sea, Varna–Varna–Varna, 04 November–22 November–09 December 2017. Berichte, MARUM–Zentrum für Marine Umweltwissenschaften, Fachbereich Geowissenschaften, Universität Bremen, 320, 1-121.

Bohrmann, G., Ivanov, M.K., Foucher, J. P., Spiess, V., Bialas, J., et al. (2003). Mud volcanoes and gas hydrates in the Black Sea: new data from Dvurechenskii and Odessa mud volcanoes. *Geo Mar. Lett.* 23, 239–249.

Boillot, G., & Winterer, E. L. (1988). 45. DRILLING ON THE GALICIA MARGIN: RETROSPECT AND PROSPECT1. *In Proc. ODP, Scientific Results* (Vol. 103).

Boillot, G., Beslier, M. O., & Comas, M. (1992). Seismic image of undercrusted serpentinite beneath a rifted margin. *Terra Nova*, 4(1), 25-33. https://doi.org/10.1111/j.1365-3121.1992.tb00447.x

Boillot, G., Recq, M., Winterer, E. L., Meyer, A. W., Applegate, J., Baltuck, M., ... & Williamson, M. (1987). Tectonic denudation of the upper mantle along passive margins: a model based on drilling results (ODP leg 103, western Galicia margin, Spain). *Tectonophysics*, 132(4), 335-342. https://doi.org/10.1016/0040-1951(87)90352-0

Bond, G. C., Kominz, M. A., & Sheridan, R. E. (1995). Continental terraces and rises. *Tectonics of sedimentary basins: Oxford, Blackwell Science*, 149-178.

Boswell, R., & Collett, T. S. (2011). Current perspectives on gas hydrate resources. *Energy & environmental science*, 4(4), 1206-1215. DOI: 10.1039/C0EE00203H

Boswell, R., Collett, T. S., Frye, M., Shedd, W., McConnell, D. R., & Shelander, D. (2012). Subsurface gas hydrates in the northern Gulf of Mexico. *Marine and Petroleum Geology*, 34(1), 4-30.

Boswell, R., Hancock, S., Yamamoto, K., Collett, T., Pratap, M., & Lee, S. R. (2020). Natural Gas Hydrates: Status of Potential as an Energy Resource. *Future Energy*, 111-131. https://doi.org/10.1016/B978-0-08-102886-5.00006-2

Boswell, R., Shipp, C., Reichel, T., Shelander, D., Saeki, T., Frye, M., ... & McConnell, D. R. (2016). Prospecting for marine gas hydrate resources. *Interpretation,* 4(1), SA13-SA24.

Bourry, C., Chazallon, B., Charlou, J. L., Donval, J. P., Ruffine, L., Henry, P., ... & Moreau, M. (2009). Free gas and gas hydrates from the Sea of Marmara, Turkey: Chemical and structural characterization. *Chemical Geology*, 264(1-4), 197-206. https://doi.org/10.1016/j.chemgeo.2009.03.007

Bown, J. W., and White, R. S. (1995). Effect of finite extension rate on melt generation at rifted continental margins. *Journal of Geophysical Research: Solid Earth*, 100(B9), 18011-18029. https://doi.org/10.1029/94JB01478

Bradley, D. C. (2008). Passive margins through earth history. *Earth-Science Reviews*, 91(1-4), 1-26. https://doi.org/10.1016/j.earscirev.2008.08.001

Bronner, A. (2013). Exhumed mantle at ultra-slow spreading ridges and magma-poor rifted margins: what can we learn from marine magnetic anomalies? *(Doctoral dissertation, Université de Strasbourg).*

Bronner, A., Sauter, D., Manatschal, G., Péron-Pinvidic, G., and Munschy, M. (2011). Magmatic breakup as an explanation for magnetic anomalies at magma-poor rifted margins. *Nature Geoscience*, 4(8), 549. DOI: 10.1038/NGEO1201

Brooks, J. M., Cox, H. B., Bryant, W. R., Kennicutt Ii, M. C., Mann, R. G., & McDonald, T. J. (1986). Association of gas hydrates and oil seepage in the Gulf of Mexico. *Organic Geochemistry*, 10(1-3), 221-234.

Brown, H. E., Holbrook, W. S., Hornbach, M. J., & Nealon, J. (2006). Slide structure and role of gas hydrate at the northern boundary of the Storegga Slide, offshore Norway. *Marine geology*, 229(3-4), 179-186. https://doi.org/10.1016/j.margeo.2006.03.011

Brun, J. P. (2002). Deformation of the continental lithosphere: Insights from brittle-ductile models. *Geological Society, London, Special Publications*, 200(1), 355-370. https://doi.org/10.1144/GSL.SP.2001.200.01.20

Brune, S. (2016). Rifts and rifted margins: A review of geodynamic processes and natural hazards. *Plate Boundaries and Natural Hazards*, 219, 13.

Brune, S., Heine, C., Clift, P. D., & Pérez-Gussinyé, M. (2017). Rifted margin architecture and crustal rheology: Reviewing Iberia-Newfoundland, Central South Atlantic, and South China Sea. *Marine and Petroleum Geology*, 79, 257-281. https://doi.org/10.1016/j.marpetgeo.2016.10.018

Brune, S., Heine, C., Pérez-Gussinyé, M., & Sobolev, S. V. (2014). Rift migration explains continental margin asymmetry and crustal hyper-extension. *Nature Communications*, 5, 4014. https://doi.org/10.1038/ncomms5014

Buck, W. R. (1988). Flexural rotation of normal faults. *Tectonics*, 7(5), 959-973. https://doi.org/10.1029/TC007i005p00959

Buck, W. R. (2006). The role of magma in the development of the Afro-Arabian Rift System. *Geological Society, London, Special Publications*, 259(1), 43-54. https://doi.org/10.1144/GSL.SP.2006.259.01.05

Buck, W. R., Lavier, L. L., & Poliakov, A. N. (1999). How to make a rift wide. Philosophical Transactions of the Royal Society of London. *Series A: Mathematical, Physical and Engineering Sciences*, 357(1753), 671-693. https://doi.org/10.1098/rsta.1999.0348

Buckley, J. P., Bosence, D., & Elders, C. (2015). Tectonic setting and stratigraphic architecture of an Early Cretaceous lacustrine carbonate platform, Sugar Loaf High, Santos Basin, Brazil. *Geological Society, London, Special Publications*, 418, SP418-13. https://doi.org/10.1144/SP418.13

Burov, E., & Poliakov, A. (2001). Erosion and rheology controls on synrift and postrift evolution: Verifying old and new ideas using a fully coupled numerical model. *Journal of Geophysical Research: Solid Earth*, 106(B8), 16461-16481. https://doi.org/10.1029/2001JB000433

Calvert, S. E., & Batchelor, C.H. (1978). Major and Minor Element Geochemistry of Sediments from Hole 379A, Leg 42B, Deep-Sea Drilling Project Initial Reports of the Deep Sea Drilling Project 42, Part 2, pp. 527-541

Canales, J. P., Collins, J. A., Escartín, J., & Detrick, R. S. (2000). Seismic structure across the rift valley of the Mid-Atlantic Ridge at 23 20′(MARK area): Implications for crustal accretion processes at slow spreading ridges. *Journal of Geophysical Research: Solid Earth*, 105(B12), 28411-28425. https://doi.org/10.1029/2000JB900301

Canales, P. J., Detrick, R. S., Toomey, D. R., & Wilcock, W. S. (2003). Segment-scale variations in the crustal structure of 150–300 kyr old fast spreading oceanic crust (East Pacific Rise, 8 15′ N–10 5′ N) from wide-angle seismic refraction profiles. *Geophysical Journal International*, 152(3), 766-794. https://doi.org/10.1046/j.1365-246X.2003.01885.x

Cann, J. R., Blackman, D. K., Smith, D. K., McAllister, E., Janssen, B., Mello, S., ... & Escartin, J. (1997). Corrugated slip surfaces formed at ridge–transform intersections on the Mid-Atlantic Ridge. *Nature*, 385(6614), 329-332. https://doi.org/10.1038/385329a0

Cannat, M., Rommevaux-Jestin, C., and Fujimoto, H. (2003). Melt supply variations to a magma-poor ultra-slow spreading ridge (Southwest Indian Ridge 61° to 69° E). *Geochemistry, Geophysics, Geosystems*, 4(8). doi:10.1029/2002GC000480

Carbotte, S. M., Marjanović, M., Carton, H., Mutter, J. C., Canales, J. P., Nedimović, M. R., ... & Perfit, M. R. (2013). Fine-scale segmentation of the crustal magma reservoir beneath the East Pacific Rise. *Nature Geoscience*, 6(10), 866-870. https://doi.org/10.1038/ngeo1933

Carlson, R. L., & Jay Miller, D. (2004). Influence of pressure and mineralogy on seismic velocities in oceanic gabbros: Implications for the composition and state of the lower oceanic crust. *Journal of Geophysical Research: Solid Earth*, 109(B9). https://doi.org/10.1029/2003JB002699

Carmichael, R. S. (1982). Physical properties of rocks and minerals: *CRC Press, Inc*., 741p.

Červený, V. (2001). Seismic Ray Theory, pp. 53–73, *Cambridge Univ. Press*, New York.

Červeny, V., Molotkov, I. A., & Psenčík, I. (1977). Ray method in seismology: Prague. *Karlova University*.

Chabert, A., Minshull, T. A., Westbrook, G. K., Berndt, C., Thatcher, K. E., & Sarkar, S. (2011). Characterization of a stratigraphically constrained gas hydrate system along the western continental margin of Svalbard from ocean bottom seismometer data. *Journal of Geophysical Research: Solid Earth*, 116(B12). https://doi.org/10.1029/2011JB008211

Chalmers, J. A., & Pulvertaft, T. C. R. (2001). Development of the continental margins of the Labrador Sea: a review. *Geological Society, London, Special Publications*, 187(1), 77-105. https://doi.org/10.1144/GSL.SP.2001.187.01.05

Chand, S., Minshull, T. A., Gei, D., & Carcione, J. M. (2004). Elastic velocity models for gas-hydrate-bearing sediments—A comparison. *Geophysical Journal International*, 159(2), 573-590.

Chazallon, B., Rodriguez, C. T., Ruffine, L., Carpentier, Y., Donval, J. P., Ker, S., & Riboulot, V. (2021). Characterizing the variability of natural gas hydrate composition from a selected site of the Western Black Sea, off Romania. *Marine and Petroleum Geology*, 124, 104785.

Chen, Y. J. (1992). Oceanic crustal thickness versus spreading rate. *Geophysical Research Letters*, 19(8), 753-756.

Chian, D., Keen, C., Reid, I., & Louden, K. E. (1995). Evolution of nonvolcanic rifted margins: New results from the conjugate margins of the Labrador Sea. *Geology*, 23(7), 589-592. https://doi.org/10.1130/0091-7613(1995)023<0589:EONRMN>2.3.CO;2

Chorowicz, J. (2005). The east African rift system. *Journal of African Earth Sciences*, 43(1-3), 379-410. https://doi.org/10.1016/j.jafrearsci.2005.07.019

Chulliat, A., Macmillan, S., Alken, P., Beggan, C., Nair, M., Hamilton, B., ... & Thomson, A. (2015). The US/UK world magnetic model for 2015-2020. http://nora.nerc.ac.uk/id/eprint/510709

Cifci, G., Ozel, S., Okay, S., Atgin, O., Ozel, O., Barın, B., ... & Sung-Ho, B. (2012). Eastern Black Sea Gas Hydrate Related Structures In Eastern Black Sea. *In EGU General Assembly Conference Abstracts* (p. 10753).

Çınar, H., & Alkan, H. (2016). Crustal S-wave structure beneath Eastern Black Sea Region revealed by Rayleigh-wave group velocities. *Journal of Asian Earth Sciences*, 115, 273-284. https://doi.org/10.1016/j.jseaes.2015.10.014

Claerbout, J. F. (1976). Fundamentals of geophysical data processing (Vol. 274). McGraw-Hill, New York.

Clark, S. P. (1966). Handbook of physical constants: *Geological Society of America Memoir* #97, 587p.

Clennell, M. B., Hovland, M., Booth, P. H., & Winters, W. J. (1999). Formation of natural gas hydrates in marine sediments: 1. Conceptual model of gas hydrate growth conditioned by host sediment properties. *Journal of Geophysical Research*, 104(B10), 22,985–23,003. https://doi.org/10.1029/1999JB900175|

Cloetingh, S. A. P. L., Spadini, G., Van Wees, J. D., & Beekman, F. (2003). Thermo-mechanical modelling of Black Sea Basin (de) formation. *Sedimentary Geology*, 156(1-4), 169-184. https://doi.org/10.1016/S0037-0738(02)00287-7

Cohen, K. M., Harper, D. A. T., & Gibbard, P. L. (2016). International Chronostratigraphic Chart http://stratigraphy. org/ICSchart. ChronostratChart2016-12. jpg.

Colin, F., Ker, S., Riboulot, V., & Sultan, N. (2020). Irregular BSR: evidence of an ongoing reequilibrium of a gas hydrate system. *Geophysical Research Letters*, 47(20), e2020GL089906. https://doi.org/10.1029/2020GL089906

Collett, T. S., Boswell, R., Cochran, J. R., Kumar, P., Lall, M., Mazumdar, A., et al. (2014). Geologic implications of gas hydrates in the offshore of India: Results of the National Gas Hydrate Program Expedition 01. *Marine and Petroleum Geology*, 58, 3–28. https://doi.org/10.1016/j.marpetgeo.2014.07.021

Collett, T. S., Boswell, R., Waite, W. F., Kumar, P., Roy, S. K., Chopra, K., ... & Expedition, N. G. H. P. (2019). India National Gas Hydrate Program Expedition 02 summary of scientific results: gas hydrate systems along the eastern continental margin of India. *Marine and Petroleum Geology*, 108, 39-142. https://doi.org/10.1016/j.marpetgeo.2019.05.023

Collett, T. S., Johnson, A., Knapp, C., & Boswell, R. (2009). Natural gas hydrates: A review. In T. S. Collett, A. Johnson, C. Knapp, & R. Boswell (Eds.), Natural gas hydrates—Energy resource potential and associated geologic hazards, *AAPG Memoir*, Vol. 89, pp. 146–219.

Collett, T., Riedel, M., Cochran, J. R., Boswell, R., Kumar, P., & Sathe, A. V. (2008). Indian continental margin gas hydrate prospects: results of the Indian National Gas Hydrate Program (NGHP) expedition 01.

Collier, J. S., McDermott, C., Warner, G., Gyori, N., Schnabel, M., McDermott, K., and Horn, B. W. (2017). New constraints on the age and style of continental breakup in the South Atlantic from magnetic anomaly data. *Earth and Planetary Science Letters*, 477, 27-40. https://doi.org/10.1016/j.epsl.2017.08.007

Colwell, J. B., Stagg, H. M., Direen, N. G., Bernardel, G., & Borissova, I. (2006). The structure of the continental margin off Wilkes Land and Terre Adelie coast, east Antarctica. *In Antarctica* (pp. 327-340). Springer, Berlin, Heidelberg.

Contreras, J., Zühlke, R., Bowman, S., & Bechstädt, T. (2010). Seismic stratigraphy and subsidence analysis of the southern Brazilian margin (Campos, Santos and Pelotas basins). *Marine and Petroleum Geology*, 27(9), 1952-1980. https://doi.org/10.1016/j.marpetgeo.2010.06.007

Contrucci, I., Matias, L., Moulin, M., Géli, L., Klingelhofer, F., Nouzé, H., ... & Sibuet, J. C. (2004). Deep structure of the West African continental margin (Congo, Zaïre, Angola), between 5 S and 8 S, from reflection/refraction seismics and gravity data. *Geophysical Journal International*, 158(2), 529-553. https://doi.org/10.1111/j.1365-246X.2004.02303.x

Cook, A. E., & Tost, B. C. (2014). Geophysical signatures for low porosity can mimic natural gas hydrate: an example from Alaminos Canyon, Gulf of Mexico. *Journal of Geophysical Research: Solid Earth*, 119(10), 7458-7472. https://doi.org/10.1002/2014JB011342

Corti, G., Bonini, M., Innocenti, F., Manetti, P., Mulugeta, G., Sokoutis, D., & Cloetingh, S. (2003). Rift-parallel magma migration and localisation of magmatic activity in transfer zones. *Acta Vulcanologica*, 14(1/2), 17.

Cowie, P. A., Underhill, J. R., Behn, M. D., Lin, J., & Gill, C. E. (2005). Spatio-temporal evolution of strain accumulation derived from multi-scale observations of Late Jurassic rifting in the northern North Sea: A critical test of models for lithospheric extension. *Earth and Planetary Science Letters*, 234(3-4), 401-419. https://doi.org/10.1016/j.epsl.2005.01.039

Cowie, P.A., Gupta, S. & Dawers, N.H. (2000). Implications of fault array evolution for synrift depocenter development: insights from a numerical fault growth model. *Basin Research* 12, 241-261.

Crutchley, G. J., Kroeger, K. F., Pecher, I. A., & Gorman, A. R. (2019). How tectonic folding influences gas hydrate formation: New Zealand's Hikurangi subduction margin. *Geology*, 47(1), 39-42. https:// doi .org /10 .1130 /G45151.1.

Dai, S., J. C. Santamarina, W. F. Waite, & T. J. Kneafsey (2012). Hydrate morphology: Physical properties of sands with patchy hydrate saturation, *J. Geophys. Res.,* 117, B11205, doi: 10.1029/2012JB009667.

Daigle, H., A. Cook, & A. Malinverno (2015). Permeability and porosity of hydrate-bearing sediments in the northern Gulf of Mexico, *Mar. Pet. Geol.*, 68 (Part A), 551–564. doi:10.1016/j.marpetgeo.2015.10.004

Dangayach, S., Singh, D. N., Kumar, P., Dewri, S. K., Roy, B., Tandi, C., & Singh, J. (2015). Thermal instability of gas hydrate bearing sediments: some issues. *Marine and Petroleum Geology*, 67, 653-662. https://doi.org/10.1016/j.marpetgeo.2015.05.034

Dannowski, A., Grevemeyer, I., Phipps Morgan, J., Ranero, C. R., Maia, M., & Klein, G. (2011). Crustal structure of the propagating TAMMAR ridge segment on the Mid-Atlantic Ridge, 21.5 N. *Geochemistry, Geophysics, Geosystems*, 12(7). https://doi.org/10.1029/2011GC003534

Davis, J. K., Lawver, L. A., Norton, I. O., Dalziel, I. W., & Gahagan, L. M. (2019). The crustal structure of the Enderby Basin, East Antarctica. Marine Geophysical Research, 40(1), 1-16. https://doi.org/10.1007/s11001-018-9356-5

De Batist, M., Klerkx, J., Van Rensbergen, P., Vanneste, M., Poort, J., Golmshtok, A. Y., ... & Krinitsky, P. (2002). Active hydrate destabilization in Lake Baikal, Siberia?. *Terra Nova*, 14(6), 436-442. https://doi.org/10.1046/j.1365-3121.2002.00449.x

Dean, S. M., Minshull, T. A., Whitmarsh, R. B., & Louden, K. E. (2000). Deep structure of the ocean-continent transition in the southern Iberia Abyssal Plain from seismic refraction profiles: The IAM-9 transect at 40 20' N. *Journal of Geophysical Research: Solid Earth*, 105(B3), 5859-5885. https://doi.org/10.1029/1999JB900301

Degens, E. T., & Ross, D. A. (1974). Black Sea--geology, chemistry, and biology.

Delisle, G., Beiersdorf, H., Neben, S., & Steinmann, D. (1998). The geothermal field of the North Sulawesi accretionary wedge and a model on BSR migration in unstable depositional environments. *Geological Society, London, Special Publications*, 137(1), 267-274. https://doi.org/10.1144/GSL.SP.1998.137.01.21

Dewey, J. F., & JF, D. (1980). Episodicity, sequence and style at convergent plate boundaries.

Dick, H. J., & Zhou, H. (2015). Ocean rises are products of variable mantle composition, temperature and focused melting. *Nature Geoscience*, 8(1), 68-74. https://doi.org/10.1038/ngeo2318

Dickens, G. R., & Quinby-Hunt, M. S. (1994). Methane hydrate stability in seawater. *Geophysical Research Letters*, 21(19), 2115-2118.

Dickens, G. R., Castillo, M. M., & Walker, J. C. (1997). A blast of gas in the latest Paleocene: Simulating first-order effects of massive dissociation of oceanic methane hydrate. *Geology*, 25(3), 259-262. https://doi.org/10.1130/0091-7613(1997)025<0259:ABOGIT>2.3.CO;2

Direen, N. G., Stagg, H. M., Symonds, P. A., & Colwell, J. B. (2011). Dominant symmetry of a conjugate southern Australian and East Antarctic magma-poor rifted margin segment. *Geochemistry, Geophysics, Geosystems*, 12(2). https://doi.org/10.1029/2010GC003306

Dondurur, D., & Çifçi, G. (2009). Anomalous strong reflections on high resolution seismic data from the Turkish Shelf of the Eastern Black Sea: possible indicators of shallow hydrogen sulphide-rich gas hydrate layers. *Turkish Journal of Earth Sciences*, 18(2), 299-313. doi:10.3906/yer-0801-1

Dondurur, D., Küçük, H. M., & Çifçi, G. (2013). Quaternary mass wasting on the western Black Sea margin, offshore of Amasra. *Global and Planetary Change,* 103, 248-260.

Driscoll, N. W., & Karner, G. D. (1998). Lower crustal extension across the Northern Carnarvon basin, Australia: Evidence for an eastward dipping detachment. *Journal of Geophysical Research: Solid Earth*, 103(B3), 4975-4991. https://doi.org/10.1029/97JB03295

Driscoll, N. W., Hogg, J. R., Christie-Blick, N., & Karner, G. D. (1995). Extensional tectonics in the Jeanne d'Arc Basin, offshore Newfoundland: implications for the timing of break-up between Grand Banks and Iberia. *Geological Society, London, Special Publications*, 90(1), 1-28. https://doi.org/10.1144/GSL.SP.1995.090.01.01

Duan, Z., Li, D., Chen, Y., & Sun, R. (2011). The influence of temperature, pressure, salinity and capillary force on the formation of methane hydrate. *Geoscience Frontiers*, 2(2), 125–135. https://doi.org/10.1016/j.gsf.2011.03.009

Dunn, R. A., and Martinez, F. (2011). Contrasting crustal production and rapid mantle transitions beneath back-arc ridges. *Nature*, 469(7329), 198. doi:10.1038/nature09690

Dvorkin, J., & Nur, A. (1993). Rock physics for characterization of gas hydrates. *US Geological Survey Professional Paper*, 1570, 293-298.

Dvorkin, J., & Nur, A. (1996). Elasticity of high-porosity sandstones: Theory for two North Sea data sets. *Geophysics*, 61(5), 1363-1370. https://doi.org/10.1190/1.1444059

Dvorkin, J., Prasad, M., Sakai, A., & Lavoie, D. (1999). Elasticity of marine sediments: Rock physics modeling. *Geophysical research letters*, 26(12), 1781-1784. https://doi.org/10.1029/1999GL900332

Eagles, G., Pérez-Díaz, L., & Scarselli, N. (2015). Getting over continent ocean boundaries. *Earth-Science Reviews*, 151, 244-265. https://doi.org/10.1016/j.earscirev.2015.10.009

Ebbing, J., Lundin, E., Olesen, O., & Hansen, E. K. (2006). The mid-Norwegian margin: a discussion of crustal lineaments, mafic intrusions, and remnants of the Caledonian root by 3D density

modelling and structural interpretation. *Journal of the Geological Society*, 163(1), 47-59. https://doi.org/10.1144/0016-764905-029

Ebinger, C. J., & Casey, M. (2001). Continental breakup in magmatic provinces: An Ethiopian example. *Geology*, 29(6), 527-530. https://doi.org/10.1130/0091-7613(2001)029<0527:CBIMPA>2.0.CO;2

Ecker, C., J. Dvorkin, and A. M. Nur (2000). Estimating the amount of gas hydrate and free gas from marine seismic data, *Geophysics*, 65(2), 565–573, doi:10.1190/1.1444752.Edwards et al., 2009

Ecker, C., J. Dvorkin, and A. Nur (1998). Sediments with gas hydrates: Internal structure from seismic AVO, *Geophysics*, 63(5), 1659–1669, doi:10.1190/1.1444462.

Edwards, R. A., Scott, C. L., Shillington, D. J., Minshull, T. A., Brown, P. J., & White, N. J. (2009). Wide-angle seismic data reveal sedimentary and crustal structure of the Eastern Black Sea. *The Leading Edge*, 28(9), 1056-1065. https://doi.org/10.1190/1.3236375

Egan, S. S., & Meredith, D. J. (2007). A kinematic modelling approach to lithosphere deformation and basin formation: application to the Black Sea. *Geological Society, London, Special Publications*, 282(1), 173-198. https://doi.org/10.1144/SP282.9

Egorov, V. N., Artemov, Y. G., Gulin, S. B., & Polikarpov, G. G. (2011). Methane seeps in the Black Sea: discovery, quantification and environmental assessment. *J. Black Sea—Mediterranean Environment*, (2), 171-185.

Eldholm, O., & Grue, K. (1994). North Atlantic volcanic margins: dimensions and production rates. *Journal of Geophysical Research: Solid Earth*, 99(B2), 2955-2968. https://doi.org/10.1029/93JB02879

Ellis, P. G., & McClay, K. R. (1988). Listric extensional fault systems-results of analogue model experiments. *Basin Research*, 1(1), 55-70. DOI: https://doi.org/10.1111/j.1365-2117.1988.tb00005.x

Erickson, S. N., & Von Herzen, R. P. (1978). Downhole temperature measurements and heat flow data in the Black Sea—DSDP Leg 42B (1975). *Initial Report of the Deep Sea Drilling Project*, 42, 985-1103.

Escartín, J., Mevel, C., Petersen, S., Bonnemains, D., Cannat, M., Andreani, M., ... & Garcia, R. (2017). Tectonic structure, evolution, and the nature of oceanic core complexes and their detachment fault zones (13 20′ N and 13 30′ N, Mid Atlantic Ridge). *Geochemistry, Geophysics, Geosystems*, 18(4), 1451-1482. https://doi.org/10.1002/2016GC006775

Espurt, N., Hippolyte, J. C., Kaymakci, N., & Sangu, E. (2014). Lithospheric structural control on inversion of the southern margin of the Black Sea Basin, Central Pontides, Turkey. *Lithosphere*, 6(1), 26-34. https://doi.org/10.1130/L316.1

Falvey, D. A. (1974). The development of continental margins in plate tectonic theory. *The APPEA Journal*, 14(1), 95-106. https://doi.org/10.1071/AJ73012

Finetti, I., Bricchi, G., Del Ben, A., Pipan, M., & Xuan, X. (1988). Geophysical study of the Black Sea area. *Bollettino di Geofisica Teorica e Applicata*, 30(117), 197-324.

Flemings, P. B., Liu, X., & Winters, W. J. (2003). Critical pressure and multiphase flow in Blake Ridge gas hydrates. *Geology*, 31(12), 1057–1060. https://doi.org/10.1130/G19863.1

Foucher, J. P., Nouzé, H., & Henry, P. (2002). Observation and tentative interpretation of a double BSR on the Nankai slope. *Marine Geology*, 187(1-2), 161-175.

Fox, P. J., and Gallo, D. G. (1984). A tectonic model for ridge-transform-ridge plate boundaries: Implications for the structure of oceanic lithosphere. *Tectonophysics*, 104(3-4), 205-242. https://doi.org/10.1016/0040-1951(84)90124-0

Franke, D. (2013). Rifting, lithosphere breakup and volcanism: Comparison of magma-poor and volcanic rifted margins. *Marine and Petroleum Geology*, 43, 63-87. https://doi.org/10.1016/j.marpetgeo.2012.11.003

Franke, D., & Hinz, K. (2009). Geology of the shelves surrounding the New Siberian Islands, Russian Arctic. *Stephan Mueller Special Publication Series*, 4, 35-44. https://doi.org/10.5194/smsps-4-35-2009, 2009.

Franke, D., Neben, S., Ladage, S., Schreckenberger, B., & Hinz, K. (2007). Margin segmentation and volcano-tectonic architecture along the volcanic margin off Argentina/Uruguay, South Atlantic. *Marine Geology*, 244(1-4), 46-67. https://doi.org/10.1016/j.margeo.2007.06.009

Fraser, S. I., Fraser, A. J., Lentini, M. R., & Gawthorpe, R. L. (2007). Return to rifts–the next wave: fresh insights into the petroleum geology of global rift basins. *Petroleum Geoscience*, 13(2), 99-104. https://doi.org/10.1144/1354-079307-749

Frederick, J. M., & Buffett, B. A. (2011). Topography- and fracture-driven fluid focusing in layered ocean sediments. *Geophysical Research Letters*, 38, L08614. https://doi.org/10.1029/2010GL046027

Funck, T., Jackson, H. R., & Shimeld, J. (2011). The crustal structure of the Alpha Ridge at the transition to the Canadian Polar Margin: Results from a seismic refraction experiment. *Journal of Geophysical Research: Solid Earth*, 116(B12). https://doi.org/10.1029/2011JB008411

Gallahue, M., Stein, S., Stein, C. A., Jurdy, D., Barklage, M., & Rooney, T. (2020). A compilation of igneous rock volumes at volcanic passive continental margins from interpreted seismic profiles. *Marine and Petroleum Geology*, 104635. https://doi.org/10.1016/j.marpetgeo.2020.104635

Gallahue, M., Stein, S., Stein, C. A., Jurdy, D., Barklage, M., & Rooney, T. (2020). A compilation of igneous rock volumes at volcanic passive continental margins from interpreted seismic profiles. *Marine and Petroleum Geology*, 104635. https://doi.org/10.1016/j.marpetgeo.2020.104635

Galushkin, Y. I., Shreider, A. A., Bulychev, A. A., & Shreider, A. A. (2006). Heat flow and thermal evolution of the lithosphere of the Black Sea basin. *Oceanology*, 46(2), 274-291. https://doi.org/10.1134/S0001437006020147

Gassner, L., Gerach, T., Hertweck, T., & Bohlen, T. (2019). Seismic characterization of submarine gas-hydrate deposits in the Western Black Sea by acoustic full-waveform inversion of ocean-bottom seismic data. *Geophysics*, 84(5), B311-B324.

Gawthorpe, R. L., Jackson, C. A. L., Young, M. J., Sharp, I. R., Moustafa, A. R., & Leppard, C. W. (2003). Normal fault growth, displacement localisation and the evolution of normal fault populations: the Hammam Faraun fault block, Suez rift, Egypt. *Journal of Structural Geology*, 25(6), 883-895. https://doi.org/10.1016/S0191-8141(02)00088-3

Gazdag, J. (1978). Wave equation migration with the phase-shift method. *Geophysics*, 43(7), 1342-1351.

GEBCO Compilation Group (2019) GEBCO 2019 Grid (https://www.gebco.net/) doi:10.5285/836f016a-33be-6ddc-e053-6c86abc0788e

Geletti, R., & Busetti, M. (2011). A double bottom simulating reflector in the western Ross Sea, Antarctica. *Journal of Geophysical Research: Solid Earth*, 116(B4).

Geoffroy, L. (2005). Volcanic passive margins. *Comptes Rendus Geoscience*, 337(16), 1395-1408. https://doi.org/10.1016/j.crte.2005.10.006

Geoffroy, L., Burov, E. B., & Werner, P. (2015). Volcanic passive margins: another way to break up continents. *Scientific reports*, 5(1), 1-12. https://doi.org/10.1038/srep14828

Georgen, J. E., and Lin, J. (2003). Plume-transform interactions at ultra-slow spreading ridges: Implications for the Southwest Indian Ridge. *Geochemistry, Geophysics, Geosystems*, 4(9). doi:10.1029/2003GC000542

Gernigon, L., Lucazeau, F., Brigaud, F., Ringenbach, J. C., Planke, S., & Le Gall, B. (2006). A moderate melting model for the Vøring margin (Norway) based on structural observations and a

thermo-kinematical modelling: Implication for the meaning of the lower crustal bodies. *Tectonophysics*, 412(3-4), 255-278. https://doi.org/10.1016/j.tecto.2005.10.038

Gillard, M., Autin, J., Manatschal, G., Sauter, D., Munschy, M., & Schaming, M. (2015). Tectonomagmatic evolution of the final stages of rifting along the deep conjugate Australian-Antarctic magma-poor rifted margins: Constraints from seismic observations. *Tectonics*, 34(4), 753-783. https://doi.org/10.1002/2015TC003850

Gillard, M., Tugend, J., Müntener, O., Manatschal, G., Karner, G. D., Autin, J., ... & Ulrich, M. (2019). The role of serpentinization and magmatism in the formation of decoupling interfaces at magma-poor rifted margins. *Earth-Science Reviews*, 196, 102882. https://doi.org/10.1016/j.earscirev.2019.102882

Ginsburg, G. D., & Soloviev, V. A. (1998). Methane migration within the submarine gas-hydrate stability zone under deep-water conditions. *Marine Geology*, 137(1-2), 49-57.

Gobarenko, V. S., Murovskaya, A. V., Yegorova, T. P., & Sheremet, E. E. (2016). Collision processes at the northern margin of the Black Sea. *Geotectonics*, 50(4), 407-424. https://doi.org/10.1134/S0016852116040026

Goldsworthy, M., & Jackson, J. (2001). Migration of activity within normal fault systems: examples from the Quaternary of mainland Greece. *Journal of Structural Geology*, 23(2-3), 489-506. https://doi.org/10.1016/S0191-8141(00)00121-8

Golmshtok, A. Y., Zonenshain, L. P., Terekhov, A. A., & Shainurov, R. V. (1992). Age, thermal evolution and history of the Black Sea Basin based on heat flow and multichannel reflection data. *Tectonophysics*, 210 (3-4), 273-293. https://doi.org/10.1016/0040-1951(92)90326-2

Gonçalves, B. F., & Garabito, G. (2021). Flexible layer-based 2D refraction tomography method for statics corrections. *Journal of Applied Geophysics*, 185, 104254. https://doi.org/10.1016/j.jappgeo.2021.104254

Görür, N. (1988). Timing of opening of the Black Sea basin. *Tectonophysics*, 147(3-4), 247-262. https://doi.org/10.1016/0040-1951(88)90189-8

Görür, N., Tüysüz, O. (1997). Petroleum geology of the southern continental margin of the Black Sea. In A. G. Robinson (Ed.), Regional and petroleum geology of the Black Sea and surrounding region: *AAPG Memoir* 68 (Chapter 13, pp. 241-254).

Görür, N., Tüysüz, O., Aykol, A., Sakinç, M., Yiğitbaş, E. & Akkök, R. (1993) Cretaceous red pelagic carbonates of northern Turkey: their place in the opening history of the Black Sea. *Ecl. Geol. Helv*. 86, 819-838.

Graham, R., Kaymakci, N., & Horn, B. W. (2013). The Black Sea: something different. *Geo Expro*, 10(5), 57-62.

Grauls, D. (2001). Gas hydrates: importance and applications in petroleum exploration. *Marine and Petroleum Geology*, 18(4), 519-523. https://doi.org/10.1016/S0264-8172(00)00075-1

Greinert, J., McGinnis, D.F., Naudts, L., Linke, P., & De Batist, M. (2010). Atmospheric methane flux from bubbling seeps: spatially extrapolated quantification from a Black Sea shelf area. *J. Geophys. Res. Oceans* 115, C01002.

Grevemeyer, I., & Villinger, H. (2001). Gas hydrate stability and the assessment of heat flow through continental margins. *Geophysical Journal International*, 145(3), 647-660. https://doi.org/10.1046/j.0956-540x.2001.01404.x

Grevemeyer, I., Ranero, C. R., and Ivandic, M. (2018). Structure of oceanic crust and serpentinization at subduction trenches. *Geosphere*, 14(2), 395-418. doi:10.1130/GES01537.1

Gupta, S., Kanna, N., & Akilan, A. (2017). Volcanic passive continental margin beneath Maitri station in central DML, East Antarctica: constraints from crustal shear velocity through receiver function modelling. *Polar Research*, 36(1), 1332947. https://doi.org/10.1080/17518369.2017.1332947

Haacke, R. R., Westbrook, G. K., & Hyndman, R. D. (2007). Gas hydrate, fluid flow and free gas: Formation of the bottom-simulating reflector. *Earth and Planetary Science Letters*, 261(3-4), 407-420.

Haeckel, M., Bialas, J., Klaucke, I., Wallmann, K., Bohrmann, G., & Schwalenberg, K. (2015). Gas hydrate occurrences in the Black Sea–new observations from the German SUGAR project. *Fire in the Ice: Methane Hydrate Newsletter*, 15(2), 6-9.

Haecker, M. A. (1992). Convergent gridding: a new approach to surface reconstruction. *Geobyte*, 7(3), 48-53.

Haggerty, S. E. (1979). The aeromagnetic mineralogy of igneous rocks. *Canadian Journal of Earth Sciences*, 16(6), 1281-1293.

Hammond, J. O., Kendall, J. M., Stuart, G. W., Ebinger, C. J., Bastow, I. D., Keir, D., ... & Wright, T. J. (2013). Mantle upwelling and initiation of rift segmentation beneath the Afar Depression. *Geology*, 41(6), 635-638. ttps://doi.org/10.1130/G33925.1

Han, S., Bangs, N. L., Hornbach, M. J., Pecher, I. A., Tobin, H. J., & Silver, E. A. (2021). The many double BSRs across the northern Hikurangi margin and their implications for subduction processes. *Earth and Planetary Science Letters*, 558, 116743. https://doi.org/10.1016/j.epsl.2021.116743

Hanna, W. F. (1977). Weak-field magnetic susceptibility anisotropy and its dynamic measurement.

Harding, A. J., Arnulf, A. F., & Blackman, D. K. (2016). Velocity structure near IODP Hole U1309D, Atlantis Massif, from waveform inversion of streamer data and borehole measurements. *Geochemistry, Geophysics, Geosystems*, 17(6), 1990-2014.

Harding, A. J., Kent, G. M., Blackman, D. K., Singh, S., & Canales, J. P. (2007). A new method for MCS refraction data analysis of the uppermost section at a Mid-Atlantic Ridge core complex. *In AGU Fall Meeting Abstracts* (Vol. 2007, pp. S12A-03).

Harrison, C. G. A. (1987). Marine magnetic anomalies-the origin of the stripes. *Annual Review of Earth and Planetary Sciences*, 15, 505-543.

Haupert, I., Manatschal, G., Decarlis, A., and Unternehr, P. (2016). Upper-plate magma-poor rifted margins: Stratigraphic architecture and structural evolution. *Marine and Petroleum Geology*, 69, 241-261. http://dx.doi.org/10.1016/j.marpetgeo.2015.10.020

Heeschen, K. U., Haeckel, M., Klaucke, I., Ivanov, M. K., & Bohrmann, G. (2011). Quantifying in-situ gas hydrates at active seep sites in the eastern Black Sea using pressure coring technique. *Biogeosciences*, 8(12), 3555-3565. https://doi.org/10.5194/bg-8-3555-2011

Heezen, B. C. (1960). The rift in the ocean floor. Scientific American, 203(4), 98-114. https://www.jstor.org/stable/24940661

Helgerud, M. B., Waite, W. F., Kirby, S. H., & Nur, A. (2009). Elastic wave speeds and moduli in polycrystalline ice Ih, sI methane hydrate, and sII methane-ethane hydrate. *Journal of Geophysical Research: Solid Earth*, 114(B2).

Henig, A. S., Blackman, D. K., Harding, A. J., Canales, J. P., & Kent, G. M. (2012). Downward continued multichannel seismic refraction analysis of Atlantis Massif oceanic core complex, 30° N, Mid-Atlantic Ridge. *Geochemistry, Geophysics, Geosystems*, 13(5).

Henry, P., Thomas, M., & Clennell, M. B. (1999). Formation of natural gas hydrates in marine sediments: 2. Thermodynamic calculations of stability conditions in porous sediments. *Journal of Geophysical Research: Solid Earth*, 104(B10), 23005-23022. https://doi.org/10.1029/1999JB900167

Hensen, C., Scholz, F., Nuzzo, M., Valadares, V., Gracia, E., Terrinha, P., Liebetrau, V., et al. (2015). Strike-slip faults mediate the rise of crustal-derived fluids and mud volcanism in the deep sea. *Geology,* 43, 339-342.

Hess, H. H., Engel, A. E. J., James, H. L., & Leonard, B. F. (1962). History of ocean basins.

Hesse, R., & Schacht, U. (2011). Early diagenesis of deep-sea sediments. *Developments in Sedimentology*, 63, 557-713. https://doi.org/10.1016/B978-0-444-53000-4.00009-3

Hester, K. C., Peltzer, E. T., Walz, P. M., Dunk, R. M., Sloan, E. D., & Brewer, P. G. (2009). A natural hydrate dissolution experiment on complex multi-component hydrates on the sea floor. *Geochimica et Cosmochimica Acta*, 73(22), 6747-6756. https://doi.org/10.1016/j.gca.2009.08.007

Hey, R., Duennebier, F. K., & Morgan, W. J. (1980). Propagating rifts on midocean ridges. *Journal of Geophysical Research: Solid Earth*, 85(B7), 3647-3658. https://doi.org/10.1029/JB085iB07p03647

Hillman, J.I.T., Burwicz, E., Zander, T., et al. (2018). Investigating a gas hydrate system in apparent disequilibrium in the Danube Fan, Black Sea. *Earth Planet Sci*. Lett. 502, 1–11. https://doi.org/10.1016/j.epsl.2018.08.051.

Hinze, W. J., Von Frese, R. R., Von Frese, R., & Saad, A. H. (2013). Gravity and magnetic exploration: Principles, practices, and applications. *Cambridge University Press*.

Hippolyte, J. C., Müller, C., Kaymakci, N., & Sangu, E. (2010). Dating of the Black Sea Basin: new nannoplankton ages from its inverted margin in the Central Pontides (Turkey). *Geological Society, London, Special Publications*, 340(1), 113-136. https://doi.org/10.1144/SP340.7

Hippolyte, J. C., Müller, C., Sangu, E., & Kaymakci, N. (2017). Stratigraphic comparisons along the Pontides (Turkey) based on new nannoplankton age determinations in the Eastern Pontides: geodynamic implications. *Geological Society, London, Special Publications*, 428(1), 323-358. https://doi.org/10.1144/SP428.9

Hippolyte, J. C., Murovskaya, A., Volfman, Y., Yegorova, T., Gintov, O., Kaymakci, N., & Sangu, E. (2018). Age and geodynamic evolution of the Black Sea Basin: Tectonic evidences of rifting in Crimea. *Marine and Petroleum Geology*, 93, 298-314. https://doi.org/10.1016/j.marpetgeo.2018.03.009

Hiscott, R. N., & Aksu, A. E. (2002). Late Quaternary history of the Marmara Sea and Black Sea from high-resolution seismic and gravity-core studies. *Marine Geology*, 190(1-2), 261-282.

Hobro, J. W., Singh, S. C., & Minshull, T. A. (2003). Three-dimensional tomographic inversion of combined reflection and refraction seismic traveltime data. *Geophysical Journal International*, 152(1), 79-93. https://doi.org/10.1046/j.1365-246X.2003.01822.x

Holbrook, W. S., Hoskins, H., Wood, W. T., Stephen, R. A., & Lizarralde, D. (1996). Methane hydrate and free gas on the Blake Ridge from vertical seismic profiling. *Science*, 273(5283), 1840-1843. DOI: 10.1126/science.273.5283.1840

Holland, M., Schultheiss, P., Roberts, J., & Druce, M. (2008, July). Observed gas hydrate morphologies in marine sediments. In *6th International Conference on Gas Hydrates*, Chevron, Vancouver, BC, Canada (pp. 6-10).

Hooft, E. E. E., Detrick, R. S., Toomey, D. R., Collins, J. A., and Lin, J. (2000). Crustal thickness and structure along three contrasting spreading segments of the Mid-Atlantic Ridge, 33.5–35 N. *Journal of Geophysical Research: Solid Earth*, 105(B4), 8205-8226. https://doi.org/10.1029/1999JB900442

Hopper, J. R., Dahl-Jensen, T., Holbrook, W. S., Larsen, H. C., Lizarralde, D., Korenaga, J., Kent, G., M., and Kelemen, P. B. (2003). Structure of the SE Greenland margin from seismic reflection and refraction data: Implications for nascent spreading center subsidence and asymmetric crustal accretion during North Atlantic opening. *Journal of Geophysical Research: Solid Earth*, 108(B5). doi:10.1029/2002JB001996

Hopper, J. R., Mutter, J. C., Larson, R. L., & Mutter, C. Z. (1992). Magmatism and rift margin evolution: Evidence from northwest Australia. *Geology*, 20(9), 853-857. https://doi.org/10.1130/0091-7613(1992)020<0853:MARMEE>2.3.CO;2

Hornbach, M. J., Harris, R. N., & Phrampus, B. J. (2020). Heat Flow on the US Beaufort Margin, Arctic Ocean: Implications for Ocean Warming, Methane Hydrate Stability, and Regional Tectonics. *Geochemistry, Geophysics, Geosystems*, 21(5), e2020GC008933. https://doi.org/10.1029/2020GC008933

Hornbach, M. J., Saffer, D. M., Holbrook, W. S., Van Avendonk, H. J., & Gorman, A. R. (2008). Three-dimensional seismic imaging of the Blake Ridge methane hydrate province: Evidence for large, concentrated zones of gas hydrate and morphologically driven advection. *Journal of Geophysical Research: Solid Earth*, 113(B7). https://doi.org/10.1029/2007JB005392

Hovland, M., Gallagher, J. W., Clennell, M. B., & Lekvam, K. (1997). Gas hydrate and free gas volumes in marine sediments: Example from the Niger Delta front. *Marine and Petroleum Geology,* 14(3), 245-255. https://doi.org/10.1016/S0264-8172(97)00012-3

Hsü, K. J., Nachev, I. K., & Vuchev, V. T. (1977). Geologic evolution of Bulgaria in light of plate tectonics. *Tectonophysics*, 40(3-4), 245-256. https://doi.org/10.1016/0040-1951(77)90068-3

Hsü, K.J., & Giovanoli, F. (1980). Messian event in the Black Sea. *Palaeogeogr. Palaeoclimatol. Palaeoecol*. 29, 75–83.

Huismans, R. S., & Beaumont, C. (2007). Roles of lithospheric strain softening and heterogeneity in determining the geometry of rifts and continental margins. *Geological Society, London, Special Publications*, 282(1), 111-138. https://doi.org/10.1144/SP282.6

Huismans, R., & Beaumont, C. (2011). Depth-dependent extension, two-stage breakup and cratonic underplating at rifted margins. *Nature*, 473(7345), 74-78. https://doi.org/10.1038/nature09988

Hunt, C. P., Moskowitz, B. M., and Banerjee, S. K. (1995). Magnetic properties of rocks and minerals. Rock physics & phase relations: a handbook of physical constants, 3, 189-204. https://doi.org/10.1029/RF003p0189

Hussenoeder, S. A., Tivey, M. A., Schouten, H., and Searle, R. C. (1996). Near-bottom magnetic survey of the Mid-Atlantic Ridge axis, 24°–24° 40′ N: Implications for crustal accretion at slow spreading ridges. *Journal of Geophysical Research: Solid Earth*, 101(B10), 22051-22069. https://doi.org/10.1029/96JB01890

Hyndman, R. D., & Dallimore, S. R. (2001). Natural gas hydrate studies in Canada. *CSEG Recorder*, 11, 12-20.

Hyndman, R. D., & Davis, E. E. (1992). A mechanism for the formation of methane hydrate and seafloor bottom-simulating reflectors by vertical fluid expulsion. *Journal of Geophysical Research: Solid Earth*, 97(B5), 7025-7041. https://doi.org/10.1029/91JB03061

IFM-GEOMAR (https://www.geomar.de/en/centre/central-facilities/bibliothek/publications-at-geomar/ifm-geomar-reports)

Intawong, A., & Went, D. (2020). Eastern Black Sea Foreland Basin Architectures and Play Concepts. In 82nd EAGE Annual Conference & Exhibition (Vol. 2020, No. 1, pp. 1-5). *European Association of Geoscientists & Engineers*. https://doi.org/10.3997/2214-4609.202011124

Jackson, H. R., Reid, I., & Falconer, R. K. H. (1982). Crustal structure near the Arctic mid-ocean ridge. *Journal of Geophysical Research: Solid Earth*, 87(B3), 1773-1783. https://doi.org/10.1029/JB087iB03p01773

Jain, A. K., & Juanes, R. (2009). Preferential mode of gas invasion in sediments: Grain-scale mechanistic model of coupled multiphase fluid flow and sediment mechanics. *Journal of Geophysical Research: Solid Earth*, 114(B8). https://doi.org/10.1029/2008JB006002

Jakob, J., Andersen, T. B., & Kjøll, H. J. (2019). A review and reinterpretation of the architecture of the South and South-Central Scandinavian Caledonides—A magma-poor to magma-rich transition and the significance of the reactivation of rift inherited structures. *Earth-science reviews*, 192, 513-528. https://doi.org/10.1016/j.earscirev.2019.01.004

Jakobsen, M., Hudson, J. A., Minshull, T. A., & Singh, S. C. (2000). Elastic properties of hydrate-bearing sediments using effective medium theory. *Journal of Geophysical Research: Solid Earth*, 105(B1), 561-577. https://doi.org/10.1029/1999JB900190

Jammes, S., & Lavier, L. L. (2019). Effect of contrasting strength from inherited crustal fabrics on the development of rifting margins. *Geosphere*, 15(2), 407-422. https://doi.org/10.1130/GES01686.1

Japsen, P., Mukerji, T. & Mavko, G. (2007). Constraints on velocity-depth trends from rock physics models. *Geophys. Prospect.,* 55, 135–154.

Jeanniot, L., & Buiter, S. J. (2018). A quantitative analysis of transtensional margin width. *Earth and Planetary Science Letters*, 491, 95-108. https://doi.org/10.1016/j.epsl.2018.03.003

Johnson, C. L., Constable, C. G., Tauxe, L., Barendregt, R., Brown, L. L., Coe, R. S., ... & Stone, D. B. (2008). Recent investigations of the 0–5 Ma geomagnetic field recorded by lava flows. *Geochemistry, Geophysics, Geosystems*, 9(4). https://doi.org/10.1029/2007GC001696

Jokat, W., & Schmidt-Aursch, M. C. (2007). Geophysical characteristics of the ultraslow spreading Gakkel Ridge, Arctic Ocean. *Geophysical Journal International*, 168(3), 983-998. https://doi.org/10.1111/j.1365-246X.2006.03278.x

Jolivet, L., Faccenna, C., D'Agostino, N., Fournier, M., & Worrall, D. (1999). The kinematics of back-arc basins, examples from the Tyrrhenian, Aegean and Japan Seas. *Geological Society, London, Special Publications*, 164(1), 21-53. https://doi.org/10.1144/GSL.SP.1999.164.01.04

Jolivet, L., Labrousse, L., Agard, P., Lacombe, O., Bailly, V., Lecomte, E., ... & Mehl, C. (2010). Rifting and shallow-dipping detachments, clues from the Corinth Rift and the Aegean. *Tectonophysics*, 483(3-4), 287-304. https://doi.org/10.1016/j.tecto.2009.11.001

Jolivet, L., Tamaki, K., & Fournier, M. (1994). Japan Sea, opening history and mechanism: A synthesis. *Journal of Geophysical Research: Solid Earth*, 99(B11), 22237-22259. https://doi.org/10.1029/93JB03463

Jones, C. H., Wernicke, B. P., Farmer, G. L., Walker, J. D., Coleman, D. S., McKenna, L. W., & Perry, F. V. (1992). Variations across and along a major continental rift: An interdisciplinary study of the Basin and Range Province, western USA. *Tectonophysics*, 213(1-2), 57-96. https://doi.org/10.1016/0040-1951(92)90252-2

Jones, R. W., & Simmons, M. D. (1997). A review of the stratigraphy of Eastern Paratethys (Oligocene-Holocene), with particular emphasis on the Black Sea. In A. G. Robinson (Ed.),

Regional and petroleum geology of the Black Sea and surrounding region: *AAPG Memoir* 68 (Chapter 4, pp. 39-52).

Joshi, R. K., Mazumdar, A., Peketi, A., Ramamurty, P. B., Naik, B. G., Kocherla, M., ... & Ramana, M. V. (2014). Gas hydrate destabilization and methane release events in the Krishna–Godavari Basin, Bay of Bengal. *Marine and petroleum geology*, 58, 476-489. https://doi.org/10.1016/j.marpetgeo.2014.08.013

Kazmin, V. G., Schreider, A. A., & Bulychev, A. A. (2000). Early stages of evolution of the Black Sea. *Geological Society, London, Special Publications*, 173(1), 235-249. https://doi.org/10.1144/GSL.SP.2000.173.01.12

Kazmin, V. G., Shreider, A. A., and Shreider, A. A. (2007). Age of the western Black Sea basin according to an analysis of the anomalous magnetic field and geological data. *Oceanology*, 47(4), 571-578. doi:10.1134/S0001437007040145

Keen, C. E., & Potter, D. P. (1995). The transition from a volcanic to a nonvolcanic rifted margin off eastern Canada. *Tectonics*, 14(2), 359-371. https://doi.org/10.1029/94TC03090

Keller, G. R., & Baldridge, W. S. (1999). The Rio Grande rift: A geological and geophysical overview. *Rocky Mountain Geology*, 34(1), 121-130. https://doi.org/10.2113/34.1.121

Kelso, P. R., Banerjee, S. K., & Teyssier, C. (1993). Rock magnetic properties of the Arunta Block, Central Australia, and their implication for the interpretation of long-wavelength magnetic anomalies. *Journal of Geophysical Research: Solid Earth*, 98(B9), 15987-15999. https://doi.org/10.1029/93JB01158

Kent, G. M., Harding, A. J., & Orcutt, J. A. (1993). Distribution of magma beneath the East Pacific Rise near the 9 03' N overlapping spreading center from forward modeling of common depth point data. *Journal of Geophysical Research: Solid Earth*, 98(B8), 13971-13995. https://doi.org/10.1029/93JB00706

Ker, S., Thomas, Y., Riboulot, V., Sultan, N., Bernard, C., Scalabrin, C., ... & Marsset, B. (2019). Anomalously deep BSR related to a transient state of the gas hydrate system in the western Black Sea. Geochemistry, Geophysics, Geosystems, 20(1), 442-459. https://doi.org/10.1029/2018GC007861

Kitchka, A. A., Dovzhok, T. I., Vakarchuk, S. G., Orach, S. V., & Orach, I. A. (2014). Advancing in the Black Sea Basin Hydrocarbon Exploration-Geological Achievements vs. Industry Pitfalls. *In 76th EAGE Conference and Exhibition 2014*.

Klapp, S. A., Klein, H., & Kuhs, W. F. (2009). Gas hydrate crystallite size investigations with high-energy synchrotron radiation. *Geological Society, London, Special Publications*, 319(1), 161-170. https://doi.org/10.1144/SP319.13

Klauda, J. B., & Sandler, S. I. (2003). Predictions of gas hydrate phase equilibria and amounts in natural sediment porous media. *Marine and Petroleum Geology*, 20(5), 459-470. https://doi.org/10.1016/S0264-8172(03)00064-3

Klauda, J. B., & Sandler, S. I. (2005). Global distribution of methane hydrate in ocean sediment. *Energy & Fuels*, 19(2), 459-470.

Knopoff, L., & Gangi, A. F. (1959). Seismic reciprocity. *Geophysics*, 24(4), 681-691. https://doi.org/10.1190/1.1438647

Koopmann, H., Brune, S., Franke, D., and Breuer, S. (2014). Linking rift propagation barriers to excess magmatism at volcanic rifted margins. *Geology*, 42(12), 1071-1074. doi:10.1130/G36085.1

Korenaga, J., Holbrook, W. S., Kent, G. M., Kelemen, P. B., Detrick, R. S., Larsen, H. C., ... & Dahl-Jensen, T. (2000). Crustal structure of the southeast Greenland margin from joint refraction and reflection seismic tomography. *Journal of Geophysical Research: Solid Earth*, 105(B9), 21591-21614. https://doi.org/10.1029/2000JB900188

Korenaga, J., Kelemen, P. B., & Holbrook, W. S. (2002). Methods for resolving the origin of large igneous provinces from crustal seismology. *Journal of Geophysical Research: Solid Earth*, 107(B9), ECV-1. https://doi.org/10.1029/2001JB001030

Krastel, S., Spiess, V., Ivanov, M., Weinrebe, W., Bohrmann, G., Shashkin, P., & Heidersdorf, F. (2003). Acoustic investigations of mud volcanoes in the Sorokin Trough, Black Sea. *Geo-Marine Letters*, 23(3-4), 230-238. DOI 10.1007/s00367-003-0143-0

Kretschmer, K., Biastoch, A., Rüpke, L., & Burwicz, E. (2015). Modeling the fate of methane hydrates under global warming. *Global Biogeochemical Cycles*, 29(5), 610-625. https://doi.org/10.1002/2014GB005011

Kruglyakova, R. P., Byakov, Y. A., Kruglyakova, M. V., Chalenko, L. A., & Shevtsova, N. T. (2004). Natural oil and gas seeps on the Black Sea floor. *Geo-Marine Letters*, 24(3), 150-162. DOI 10.1007/s00367-004-0171-4

Küçük, H. M., Goldberg, D. S., Haines, S. S., Dondurur, D., Guerin, G., & Çifçi, G. (2016). Acoustic investigations of shallow gas and gas hydrates: comparison between the Black sea and the Gulf of Mexico. *In Gordon Research Seminars-Natural Gas Hydrate Systems* (Vol. 28).

Küçük, H.M., Dondurur, D., Özel, O., Atgun, O., Sınayuç, Ç., Merey, Ş. & Çifçi, G. (2015). Acoustic Investigations of Gas and Gas Hydrate Formations, Offshore Southwestern Black Sea, *American Geophysical Union Fall Meeting, San Francisco, USA*.

Kunath, P., Chi, W. C., Berndt, C., Chen, L., Liu, C. S., Kläschen, D., & Muff, S. (2020). A shallow seabed dynamic gas hydrate system off SW Taiwan: Results from 3-D seismic, thermal, and fluid migration analyses. *Journal of Geophysical Research: Solid Earth*, 125(11), e2019JB019245-T.

Kvenvolden, K. A. (1993). Gas hydrates—geological perspective and global change. *Reviews of geophysics*, 31(2), 173-187. https://doi.org/10.1029/93RG00268

Kvenvolden, K. A. (1998). A primer on the geological occurrence of gas hydrate. *Geological Society, London, Special Publications*, 137(1), 9-30. https://doi.org/10.1144/GSL.SP.1998.137.01.02

Kvenvolden, K. A. (2000). Natural gas hydrate: Background and history of discovery. *In Natural Gas Hydrate* (pp. 9-16). Springer, Dordrecht.

Kvenvolden, K. A., & Lorenson, T. D. (2001). The global occurrence of natural gas hydrate. Natural Gas Hydrates: Occurrence, Distribution, and Detection: Occurrence, Distribution, and Detection, 124, 3-18. https://doi.org/10.1029/GM124p0003

Ladd, M. F. C., & Ladd, M. (1998). Introduction to physical chemistry. *Cambridge University Press*.

Lavier, L. L., & Manatschal, G. (2006). A mechanism to thin the continental lithosphere at magma-poor margins. *Nature*, 440(7082), 324-328. doi:10.1038/nature04608

Lavier, L. L., Roger Buck, W., & Poliakov, A. N. (1999). Self-consistent rolling-hinge model for the evolution of large-offset low-angle normal faults. *Geology*, 27(12), 1127-1130. https://doi.org/10.1130/0091-7613(1999)027<1127:SCRHMF>2.3.CO;2

Le Pourhiet, L., Chamot-Rooke, N., Delescluse, M., May, D. A., Watremez, L., & Pubellier, M. (2018). Continental break-up of the South China Sea stalled by far-field compression. *Nature Geoscience*, 11(8), 605. https://doi.org/10.1038/s41561-018-0178-5

Lee, J. Y., Francisca, F. M., Santamarina, J. C., & Ruppel, C. (2010). Parametric study of the physical properties of hydrate-bearing sand, silt, and clay sediments: 2. Small-strain mechanical properties. *Journal of Geophysical Research: Solid Earth*, 115(B11). https://doi.org/10.1029/2009JB006670

Lee, M. W. (2007). Velocities and attenuations of gas hydrate-bearing sediments (p. 11). *US Department of the Interior, US Geological Survey*.

Lee, M. W., Collett, T. S., & Inks, T. L. (2009). Seismic-attribute analysis for gas-hydrate and free-gas prospects on the North Slope of Alaska. DOI:10.1306/13201123M893359

Lei, C., & Ren, J. (2016). Hyper-extended rift systems in the Xisha Trough, northwestern South China Sea: Implications for extreme crustal thinning ahead of a propagating ocean. *Marine and Petroleum Geology*, 77, 846-864. https://doi.org/10.1016/j.marpetgeo.2016.07.022

Lei, C., Alves, T. M., Ren, J., Pang, X., Yang, L., & Liu, J. (2019). Depositional architecture and structural evolution of a region immediately inboard of the locus of continental breakup (Liwan Sub-basin, South China Sea). *Geological Society of America Bulletin*. https://doi.org/10.1130/B35001.1

Lei, C., Alves, T. M., Ren, J., Pang, X., Yang, L., & Liu, J. (2019). Depositional architecture and structural evolution of a region immediately inboard of the locus of continental breakup (Liwan Sub-basin, South China Sea). *GSA Bulletin*, 131(7-8), 1059-1074. https://doi.org/10.1130/B35001.1

Lei, L. (2017). Gas hydrate in fine-grained sediments—Laboratory studies and coupled processes analyses (Doctoral dissertation, Georgia Institute of Technology). http://hdl.handle.net/1853/58215

Lei, L., Seol, Y., Choi, J. H., & Kneafsey, T. J. (2019). Pore habit of methane hydrate and its evolution in sediment matrix–Laboratory visualization with phase-contrast micro-CT. *Marine and Petroleum Geology, 104, 451-467*. https://doi.org/10.1016/j.marpetgeo.2019.04.004

Leroy, S., d'Acremont, E., Tiberi, C., Basuyau, C., Autin, J., Lucazeau, F., & Sloan, H. (2010). Recent off-axis volcanism in the eastern Gulf of Aden: implications for plume–ridge interaction. *Earth and Planetary Science Letters*, 293(1-2), 140-153. https://doi.org/10.1016/j.epsl.2010.02.036

Letouzey, J., Biju-Duval, B., Dorkel, A., Gonnard, R., Kristchev, K., Montadert, L., & Sungurlu, O. (1977). The Black Sea: a marginal basin; geophysical and geological data. *In International Symposium on the Structural History of the Mediterranean Basins. Technip*, Paris (pp. 363-376).

Levell, B., Argent, J., Doré, A. G., and Fraser, S. (2010). "Passive margins: overview," in Petroleum Geology: FromMature Basins to New Frontiers – *Proceedings of the 7th Petroleum Geology Conference*, Vol. 7, eds B. A. Vining and S. C. Pickering (London: Geological Society), 823–830. doi: 10.1144/0070823

Limonov, A. F., Van Weering, T. C., Kenyon, N. H., Ivanov, M. K., & Meisner, L. B. (1997). Seabed morphology and gas venting in the Black Sea mudvolcano area: observations with the MAK-

1 deep-tow sidescan sonar and bottom profiler. *Marine Geology,* 137(1-2), 121-136. https://doi.org/10.1016/S0025-3227(96)00083-7

Lin, A. T., Liu, C. S., Lin, C. C., Schnurle, P., Chen, G. Y., Liao, W. Z., et al. (2008). Tectonic features associated with the overriding of an accretionary wedge on top of a rifted continental margin: An example from Taiwan. *Marine Geology*, 255(3–4), 186–203. https://doi.org/

Lister, G. S., Etheridge, M. A., & Symonds, P. A. (1986). Detachment faulting and the evolution of passive continental margins. *Geology*, 14(3), 246-250. https://doi.org/10.1130/0091-7613(1986)14<246:DFATEO>2.0.CO;2

Liu, X., & Flemings, P. B. (2007). Dynamic multiphase flow model of hydrate formation in marine sediments. *Journal of Geophysical Research: Solid Earth*, 112(B3). https://doi.org/10.1029/2005JB004227

Lizarralde, D., Axen, G. J., Brown, H. E., Fletcher, J. M., González-Fernández, A., Harding, A. J., ... & Umhoefer, P. J. (2007). Variation in styles of rifting in the Gulf of California. *Nature*, 448(7152), 466-469. https://doi.org/10.1038/nature06035

Lorenson, T. D., & Collett, T. S. (2018). National Gas Hydrate Program Expedition 01 offshore India; gas hydrate systems as revealed by hydrocarbon gas geochemistry. *Marine and Petroleum Geology*, 92, 477-492. https://doi.org/10.1016/j.marpetgeo.2017.11.011

Lundin, E. R., & Doré, A. G. (2011). Hyperextension, serpentinization, and weakening: A new paradigm for rifted margin compressional deformation. *Geology*, 39(4), 347-350. https://doi.org/10.1130/G31499.1

Lundin, E. R., Redfield, T. F., Péron-Pindivic, G., & Pindell, J. (2014). Rifted continental margins: geometric influence on crustal architecture and melting. In: Pindell, J., Horn, B. et al. (eds) Sedimentary Basins: Origin, Depositional Histories, and Petroleum Systems, 33rd Annual GCSSEPM Foundation Bob F. Perkins Conference. Gulf Coast Section SEPM (GCSSEPM), Houston, TX, 18-53.

Lymer, G., Cresswell, D. J., Reston, T. J., Bull, J. M., Sawyer, D. S., Morgan, J. K., ... & Shillington, D. J. (2019). 3D development of detachment faulting during continental breakup. *Earth and Planetary Science Letters*, 515, 90-99. https://doi.org/10.1016/j.epsl.2019.03.018

MacKay, M. E., Jarrard, R. D., Westbrook, G. K., & Hyndman, R. D. (1994). Origin of bottom-simulating reflectors: geophysical evidence from the Cascadia accretionary prism. *Geology*, 22(5), 459-462. https://doi.org/10.1130/0091-7613(1994)022<0459:OOBSRG>2.3.CO;2

Maden, N. (2013). Geothermal structure of the eastern Black Sea basin and the eastern Pontides orogenic belt: Implications for subduction polarity of Tethys oceanic lithosphere. *Geoscience Frontiers*, 4(4), 389-398. https://doi.org/10.1016/j.gsf.2013.02.001

Maffione, M., Morris, A., Plümper, O., & van Hinsbergen, D. J. (2014). Magnetic properties of variably serpentinized peridotites and their implication for the evolution of oceanic core complexes. *Geochemistry, Geophysics, Geosystems*, 15(4), 923-944. https://doi.org/10.1002/2013GC004993

Maillard, A., Malod, J., Thiébot, E., Klingelhoefer, F., & Réhault, J. P. (2006). Imaging a lithospheric detachment at the continent–ocean crustal transition off Morocco. *Earth and Planetary Science Letters*, 241(3-4), 686-698. doi:10.1016/j.epsl.2005.11.013

Malinverno, A. (1991). Inverse square-root dependence of mid-ocean-ridge flank roughness on spreading rate. *Nature*, 352(6330), 58.

Malinverno, A. (2010). Marine gas hydrates in thin sand layers that soak up microbial methane. *Earth and Planetary Science Letters*, 292, 399–408. https://doi.org/10.1016/j.epsl.2010.02.008

Manatschal, G., Müntener, O., Lavier, L. L., Minshull, T. A., & Péron-Pinvidic, G. (2007). Observations from the Alpine Tethys and Iberia–Newfoundland margins pertinent to the interpretation of continental breakup. *Geological Society, London, Special Publications*, 282(1), 291-324. https://doi.org/10.1144/SP282.14

Manheim, F. T., & Schug, D. M. (1978). INTERSTITIAL WATERS OF BLACK SEA CORES.

Manighetti, I., Tapponnier, P., Courtillot, V., Gruszow, S., & Gillot, P. Y. (1997). Propagation of rifting along the Arabia-Somalia plate boundary: The gulfs of Aden and Tadjoura. *Journal of Geophysical Research: Solid Earth*, 102(B2), 2681-2710. https://doi.org/10.1029/96JB01185

Marín-Moreno, H., Giustiniani, M., Tinivella, U., & Piñero, E. (2016). The challenges of quantifying the carbon stored in Arctic marine gas hydrate. *Marine and Petroleum Geology*, 71, 76-82. http://dx.doi.org/10.1016/j.marpetgeo.2015.11.014

Marín-Moreno, H., Minshull, T. A., Westbrook, G. K., Sinha, B., & Sarkar, S. (2013). The response of methane hydrate beneath the seabed offshore Svalbard to ocean warming during the next three centuries. *Geophysical Research Letters*, 40(19), 5159-5163. https://doi.org/10.1002/grl.50985

Marín-Moreno, H., S. K. Sahoo, & A. I. Best (2017). Theoretical modeling insights into elastic wave attenuation mechanisms in marine sediments with pore-filling methane hydrate, *J. Geophys. Res. Solid Earth*, 122, 1835–1847. doi: 10.1002/2016JB013577.

Martin, A. K. (1984). Propagating rifts: Crustal extension during continental rifting. *Tectonics*, 3(6), 611-617.

Marzoli, A., Callegaro, S., Dal Corso, J., Davies, J. H., Chiaradia, M., Youbi, N., ... & Jourdan, F. (2018). The Central Atlantic magmatic province (CAMP): A review. *The Late Triassic World*, 91-125. https://doi.org/10.1007/978-3-319-68009-5_4

Maslin, M., Owen, M., Day, S., & Long, D. (2004). Linking continental-slope failures and climate change: Testing the clathrate gun hypothesis. *Geology*, 32(1), 53-56. https://doi.org/10.1130/G20114.1

Maus, S., et al. (2009). EMAG2: A 2–arc min resolution Earth Magnetic Anomaly Grid compiled from satellite, airborne, and marine magnetic measurements. *Geochemistry, Geophysics, Geosystems*, 10(8). doi:10.1029/2009GC002471

Mavko, G., & Mukerji, T. (1998). A rock physics strategy for quantifying uncertainty in common hydrocarbon indicators. *Geophysics*, 63(6), 1997-2008. https://doi.org/10.1190/1.1444493

Mavko, G., & Nur, A. (1975). Melt squirt in the asthenosphere. *Journal of Geophysical Research*, 80(11), 1444-1448. https://doi.org/10.1029/JB080i011p01444

Mavko, G., T. Mukerji, & J. Dvorkin (2009). The Rock Physics Handbook, 2nd ed*., Cambridge Univ. Press*, New York.

Max, M. D., & Johnson, A. H. (2014). Hydrate petroleum system approach to natural gas hydrate exploration. *Petroleum Geoscience*, 20(2), 187-199. DOI: https://doi.org/10.1144/petgeo2012-049

Max, M. D., & Johnson, A. H. (2018). Exploration and production of oceanic natural gas hydrate: Critical factors for commercialization. *Springer* [book].

Mayer, J., Sachsenhofer, R. F., Ungureanu, C., Bechtel, A., Gratzer, R., Sweda, M., & Tari, G. (2018). Petroleum charge and migration in the Black Sea: Insights from oil and source rock geochemistry. *Journal of Petroleum Geology*, 41(3), 337-350. https://doi.org/10.1111/jpg.12706

Maynard, J. R., & Erratt, D. (2020). The Black Sea, a Tertiary basin: Observations and insights. *Marine and Petroleum Geology*, 118, 104462. https://doi.org/10.1016/j.marpetgeo.2020.104462

Mazzini, A., Ivanov, M. K., Parnell, J., Stadnitskaia, A., Cronin, B. T., Poludetkina, E., ... & van Weering, T. (2004). Methane-related authigenic carbonates from the Black Sea: geochemical characterisation and relation to seeping fluids. *Marine Geology*, 212(1-4), 153-181. https://doi.org/10.1016/j.margeo.2004.08.001

McCarthy, A., Falloon, T. J., Sauermilch, I., Whittaker, J. M., Niida, K., & Green, D. H. (2020). Revisiting the Australian-Antarctic ocean-continent transition zone using petrological and geophysical characterization of exhumed subcontinental mantle. Geochemistry, Geophysics, Geosystems, 21(7), e2020GC009040.

McClay, K. R., & Hammerstein, J. A. (2020). About this title-Passive Margins: Tectonics, Sedimentation and Magmatism. *Geological Society, London, Special Publications*, 476(1), NP-NP. https://doi.org/10.1144/SP476

McConnell, D. R., Zhang, Z., & Boswell, R. (2012). Review of progress in evaluating gas hydrate drilling hazards. *Marine and Petroleum Geology*, 34(1), 209-223. https://doi.org/10.1016/j.marpetgeo.2012.02.010

McKenzie, D. (1978). Some remarks on the development of sedimentary basins. *Earth and Planetary science letters*, 40(1), 25-32. https://doi.org/10.1016/0012-821X(78)90071-7

Meijers, M. J., Langereis, C. G., van Hinsbergen, D. J., Kaymakcı, N., Stephenson, R. A., & Altıner, D. (2010). Jurassic–Cretaceous low paleolatitudes from the circum-Black Sea region (Crimea and Pontides) due to True Polar Wander. Earth and Planetary Science Letters, 296(3-4), 210-226. https://doi.org/10.1016/j.epsl.2010.04.052

Meisner, A., Krylov, O., & Nemčok, M. (2009). Development and structural architecture of the Eastern Black Sea. *The Leading Edge*, 28(9), 1046-1055.

Menard, H. W. (1960). The east Pacific rise. *Science*, 132(3441), 1737-1746. https://www.jstor.org/stable/1707121

Menlikli, C., Demirer, A., Sipahioglu, O., Korpe, L., Aydemir, V. (2009). Exploration plays in the Turkish Black Sea. *Lead. Edge,* 28 (9), 1066-1075. http://dx.doi.org/10.1190/1.3236376

Merey, Ş. (2016). Drilling of gas hydrate reservoirs. *Journal of Natural Gas Science and Engineering*, 35, 1167-1179. https://doi.org/10.1016/j.jngse.2016.09.058

Merey, Ş. (2017). Analysis of the Black Sea gas hydrates [Thesis]

Merey, S., & Sinayuc, C. (2016). Investigation of gas hydrate potential of the Black Sea and modelling of gas production from a hypothetical Class 1 methane hydrate reservoir in the Black Sea conditions. *Journal of Natural Gas Science and Engineering*, 29, 66-79. https://doi.org/10.1016/j.jngse.2015.12.048

Merrill, R.T., McElhinny, M.W. & McFadden, P.L. (1996). The Magnetic Field of the Earth: Paleomagnetism, the Core, and the Deep Mantle. *Academic Press, San Diego*, 531 pp.

Meyer, B., Saltus, R. & Chulliat, A. (2017). EMAG2: Earth Magnetic Anomaly Grid (2-arc-minute resolution) Version 3. *National Centers for Environmental Information*, NOAA. Model. doi:10.7289/V5H70CVX

Michaelis, W., Seifert, R., Nauhaus, K., Treude, T., Thiel, V., Blumenberg, M., ... & Gulin, M. B. (2002). Microbial reefs in the Black Sea fueled by anaerobic oxidation of methane. *Science*, 297(5583), 1013-1015. DOI: 10.1126/science.1072502

Milanovsky, E. E. (1991). Geology of the USSR, Part 3.

Miles, P. R. (1995). Potential distribution of methane hydrate beneath the European continental margins. *Geophysical Research Letters*, 22(23), 3179-3182. https://doi.org/10.1029/95GL03013

Millero, F. J., C.-T. Chen, A. Bradshaw, & K. Schleicher (1980). A new high pressure equation of state for seawater, *Deep Sea Res.*, Part A, 27(3), 255–264, doi:10.1016/0198-0149(80)90016-3.

Mindlin, R.D. (1949). Compliance of elastic bodies in contact. *J. Appl. Mech.*, 16, 259–268.

Minshull, T. A., & Keddie, A. (2010). Measuring the geotherm with gas hydrate bottom-simulating reflectors: a novel approach using three-dimensional seismic data from the eastern Black Sea. *Terra Nova*, 22(2), 131-136.

Minshull, T. A., Marín-Moreno, H., Betlem, P., Bialas, J., Buenz, S., Burwicz, E., Cameselle, A. L., et al. (2020). Hydrate occurrence in Europe: A review of available evidence. *Marine and Petroleum Geology*, 111, 735-764. https://doi.org/10.1016/j.marpetgeo.2019.08.014

Mitchum Jr, R. M., Vail, P. R., & Sangree, J. B. (1977b). Seismic stratigraphy and global changes of sea level: Part 6. Stratigraphic interpretation of seismic reflection patterns in depositional sequences: Section 2. Application of seismic reflection configuration to stratigraphic interpretation.

Mitchum Jr, R. M., Vail, P. R., & Thompson III, S. (1977a). Seismic stratigraphy and global changes of sea level: Part 2. The depositional sequence as a basic unit for stratigraphic analysis: Section 2. Application of seismic reflection configuration to stratigraphic interpretation.

Mjelde, R., Sellevoll, M. A., Shimamura, H., Iwasaki, T., & Kanazawa, T. (1992). A crustal study off Lofoten, N. Norway, by use of 3-component ocean bottom seismographs. *Tectonophysics*, 212(3-4), 269-288.

Mohriak, W. U., & Leroy, S. (2012). Architecture of rifted continental margins and break-up evolution: insights from the South Atlantic, North Atlantic and Red Sea–Gulf of Aden conjugate margins. *Geological Society, London, Special Publications*, 369(1), 497-535. https://doi.org/10.1144/SP369.17

Monteleone, V., Minshull, T. A., & Marin-Moreno, H. (2020). Integrated geophysical characterization of crustal domains in the eastern Black Sea. *Geology*, 48(4), 405-409. https://doi.org/10.1130/G47056.1

Monteleone, V., Minshull, T. A., and Marin-Moreno, H. (2019). Spatial and temporal evolution of rifting and continental breakup in the Eastern Black Sea Basin revealed by long-offset seismic reflection data, *Tectonics*, 38, 2646-2667. https://doi.org/10.1029/2019TC005523

Moore, J. G. (1992). A syn-rift to post-rift transition sequence in the Main Porcupine Basin, offshore western Ireland. *Geological Society, London, Special Publications*, 62(1), 333-349. https://doi.org/10.1144/GSL.SP.1992.062.01.26

Moridis, G. J. (2002). Numerical studies of gas production from methane hydrates. *Paper presented at the SPE Gas Technology Symposium, Calgary, Alberta, Canada*. https://doi.org/10.2118/75691-MS

Moridis, G. J. (2003). Numerical studies of gas production from methane hydrates, *Soc. Pet. Eng. J.,* 32(8), 359–370. https://doi.org/10.2118/75691-MS

Moridis, G. J., Kowalsky, M. B. & Pruess, K. (2012). TOUGH+HYDRATE v1.2 user's manual: A code for the simulation of system behavior in hydrate-bearing geological media, Per. LBNL-0149E, *Lawrence Berkeley Natl. Lab., Berkeley, Calif*. https://escholarship.org/uc/item/3mk82656

Moridis, G. J., Kowalsky, M. B., & Pruess, K. (2008). TOUGH+Hydrate v1.0 user's manual: A code for the simulation of system behavior in hydrate-bearing geologic media. *Lawrence Berkeley National Laboratory* Retrieved from http://escholarship.org/uc/item/23p861p4

Moridis, G., & Collett, T. (2003). Strategies for gas production from hydrate accumulations under various geologic conditions.

Mortimer, E. J., Gouiza, M., Paton, D. A., Stanca, R., Rodriguez, K., Hodgson, N., & Hussein, A. A. (2020). Architecture of a magma poor passive margin–Insights from the Somali margin. *Marine Geology*, 428, 106269. https://doi.org/10.1016/j.margeo.2020.106269

Moser, T. J. (1991). Shortest path calculation of seismic rays, *Geophysics*, 56, 59–67.

Muirhead, J.D., Kattenhorn, S.A., Lee, H., Mana, S., Turrin, B.D., Fischer, T.P., et al. (2016). Evolution of upper crustal faulting assisted by magmatic volatile release during early-stage

continental rift development in the East African Rift. *Geosphere* 12, 1670-1700. https://doi.org/10.1130/GES01375.1

Muller, M. R., Minshull, T. A., and White, R. S. (1999). Segmentation and melt supply at the Southwest Indian Ridge. *Geology*, 27(10), 867-870. https://doi.org/10.1130/0091-7613(1999)027<0867:SAMSAT>2.3.CO;2

Munteanu, I., Matenco, L., Dinu, C., & Cloetingh, S. A. P. L. (2011). Kinematics of back-arc inversion of the Western Black Sea Basin. *Tectonics*, 30(5). https://doi.org/10.1029/2011TC002865

Muratov, M. V., Neprochnov, Y. P., Ross, D. A., & Trimonis, E. S. (1978). Basic features of the black sea late Cenozoic history based on the results of deep-sea drilling, leg 42B1.

Mutter, C. Z., and Mutter, J. C. (1993). Variations in thickness of layer 3 dominate oceanic crustal structure. *Earth and Planetary Science Letters*, 117(1-2), 295-317. https://doi.org/10.1016/0012-821X(93)90134-U

Nagel, T. J., & Buck, W. R. (2004). Symmetric alternative to asymmetric rifting models. *Geology*, 32(11), 937-940. https://doi.org/10.1130/G20785.1

Naudts, L., Greinert, J., Artemov, Y.G., Staelens, P., Poort, J., Van Rensbergen, P., & De Batist, M. (2006). Geological and morphological setting of 2778 methane seeps in the Dnepr paleo-delta, northwestern Black Sea. *Mar. Geol*.227, 177–199. http://dx.doi.org/10.1016/j.margeo.2005.10.005.

Nemčok, M., & Rybár, S. (2017). Rift–drift transition in a magma-rich system: the Gop Rift–Laxmi Basin case study, West India. *Geological Society, London, Special Publications*, 445(1), 95-117. https://doi.org/10.1144/SP445.5

Nikishin, A. M., Khotylev, A. O., Bychkov, A. Y., Kopaevich, L. F., Petrov, E. I., & Yapaskurt, V. O. (2013). Cretaceous volcanic belts and the evolution of the Black Sea Basin. *Moscow University Geology Bulletin*, 68(3), 141-154. DOI: 10.3103/S0145875213030058

Nikishin, A. M., Korotaev, M. V., Ershov, A. V., & Brunet, M. F. (2003). The Black Sea basin: tectonic history and Neogene–Quaternary rapid subsidence modelling. *Sedimentary Geology*, 156(1-4), 149-168. https://doi.org/10.1016/S0037-0738(02)00286-5

Nikishin, A. M., Okay, A. I., Tüysüz, O., Demirer, A., Amelin, N., & Petrov, E. (2015a). The Black Sea basins structure and history: New model based on new deep penetration regional seismic data. Part 1: Basins structure and fill. *Marine and Petroleum Geology*, 59, 638-655. https://doi.org/10.1016/j.marpetgeo.2014.08.017

Nikishin, A. M., Okay, A., Tüysüz, O., Demirer, A., Wannier, M., Amelin, N., & Petrov, E. (2015b). The Black Sea basins structure and history: New model based on new deep penetration regional

seismic data. Part 2: Tectonic history and paleogeography. *Marine and Petroleum Geology*, 59, 656-670. https://doi.org/10.1016/j.marpetgeo.2014.08.018

Nikishin, A. M., Wannier, M., Alekseev, A. S., Almendinger, O. A., Fokin, P. A., Gabdullin, R. R., et al. (2015c). Mesozoic to recent geological history of southern Crimea and the Eastern Black Sea region. *Geological Society, London, Special Publications*, 428, 241-264. https://doi.org/10.1144/SP428.1

Nikishin, A. M., Ziegler, P. A., Bolotov, S. N., & Fokin, P. A. (2011). Late Palaeozoic to Cenozoic evolution of the Black Sea-Southern Eastern Europe region: a view from the Russian platform. *Turkish Journal of Earth Sciences*, 20, 571-634. doi:10.3906/yer-1005-22

Nimblett, J., & Ruppel, C. (2003). Permeability evolution during the formation of gas hydrates in marine sediments. *Journal of Geophysical Research: Solid Earth*, 108(B9). https://doi.org/10.1029/2001JB001650

Nirrengarten, M., Gernigon, L., & Manatschal, G. (2014). Lower crustal bodies in the Møre volcanic rifted margin: geophysical determination and geological implications. *Tectonophysics*, 636, 143-157. https://doi.org/10.1016/j.tecto.2014.08.004

Nirrengarten, M., Manatschal, G., Tugend, J., Kusznir, N., & Sauter, D. (2018). Kinematic evolution of the southern North Atlantic: Implications for the formation of hyperextended rift systems. *Tectonics*, 37(1), 89-118. doi: 10.1002/2017TC004495

Nirrengarten, M., Mohn, G., Kusznir, N. J., Sapin, F., Despinois, F., Pubellier, M., ... & Ringenbach, J. C. (2020). Extension modes and breakup processes of the southeast China-Northwest Palawan conjugate rifted margins. *Marine and Petroleum Geology*, 113, 104123. https://doi.org/10.1016/j.marpetgeo.2019.104123

Nisbet, E. (1990). Climate change and methane. *Nature*, 347(6288), 23-23.

Niu, X., Ruan, A., Li, J., Minshull, T. A., Sauter, D., Wu, Z., ... & Singh, S. (2015). Along-axis variation in crustal thickness at the ultraslow spreading S outhwest I ndian R idge (50° E) from a wide-angle seismic experiment. *Geochemistry, Geophysics, Geosystems*, 16(2), 468-485. https://doi.org/10.1002/2014GC005645

Nixon, C.W., McNeill, L.C., Bull, J.M., Bell, R.E., Gawthorpe, R.L., Henstock, T.J., et al. (2016). Rapid spatiotemporal variations in rift structure during development of the Corinth Rift, central Greece. *Tectonics*, 35, 1225-1248. 8, doi:10.1002/2015TC004026.

Nole, M., Daigle, H., Cook, A. E., & Malinverno, A. (2016). Short-range, overpressure-driven methane migration in coarse-grained gas hydrate reservoirs. *Geophysical Research Letters*, 43, 9500–9508. https://doi.org/10.1002/2016GL070096

Okay, A. I., & Şahintürk, O. (1997). Geology of the Eastern Pontides. In A. G. Robinson (Ed.), Regional and petroleum geology of the Black Sea and surrounding region: AAPG Memoir 68 (Chapter 15, pp. 291-311).

Okay, A. I., & Tüysüz, O. (1999). Tethyan sutures of northern Turkey. *Geological Society, London, Special Publications*, 156(1), 475-515. https://doi.org/10.1144/GSL.SP.1999.156.01.22

Okay, A. I., Celal Sengor, A. M., & Görür, N. (1994). Kinematic history of the opening of the Black Sea and its effect on the surrounding regions. *Geology*, 22(3), 267-270.https://doi.org/10.1130/0091-7613(1994)022<0267:KHOTOO>2.3.CO;2

Okay, A. I., Sunal, G., Sherlock, S., Altiner, D., Tüysüz, O., Kylander-Clark, A. R., & Aygül, M. (2013). Early Cretaceous sedimentation and orogeny on the active margin of Eurasia: Southern Central Pontides, Turkey. *Tectonics*, 32(5), 1247-1271. https://doi.org/10.1002/tect.20077

Olsen, N., & Mandea, M. (2007). Investigation of a secular variation impulse using satellite data: The 2003 geomagnetic jerk. *Earth and Planetary Science Letters*, 255(1-2), 94-105. https://doi.org/10.1016/j.epsl.2006.12.008

Olsen, P. E. (1997). Stratigraphic record of the early Mesozoic breakup of Pangea in the Laurasia-Gondwana rift system. *Annual Review of Earth and Planetary Sciences*, 25(1), 337-401. https://doi.org/10.1146/annurev.earth.25.1.337

Østergaard, K. K., Anderson, R., Llamedo, M., & Tohidi, B. (2002). Hydrate phase equilibria in porous media: effect of pore size and salinity. *Terra Nova*, 14(5), 307-312. https://doi.org/10.1046/j.1365-3121.2002.00433.x

Oufi, O., Cannat, M., & Horen, H. (2002). Magnetic properties of variably serpentinized abyssal peridotites. *Journal of Geophysical Research: Solid Earth*, 107(B5), EPM-3. https://doi.org/10.1029/2001JB000549

Ozima, M., Joshima, M., and Kinosmta, H. (1974). Magnetic properties of submarine basalts and the implications on the structure of the oceanic crust. *Journal of geomagnetism and geoelectricity*, 26(3), 335-354. https://doi.org/10.5636/jgg.26.335

Özsoy, E., & Ünlüata, Ü. (1997). Oceanography of the Black Sea: a review of some recent results. *Earth-Science Reviews*, 42(4), 231-272.

Paganoni, M., King, J. J., Foschi, M., Mellor-Jones, K., & Cartwright, J. A. (2019). A natural gas hydrate system on the Exmouth Plateau (NW shelf of Australia) sourced by thermogenic hydrocarbon leakage. *Marine and Petroleum Geology*, 99, 370-392. https://doi.org/10.1016/j.marpetgeo.2018.10.029

Palabiyik, Y., Ozdemir, A., & Karataş, A. (2020). The potential targets and drilling locations suggested for hydrocarbon discovery of turkey in the black sea basin. *International Black Sea Coastline Countries Scientific Research Symposium-IV, Giresun, Turkey.*

Pape, T., Bahr, A., Klapp, S. A., Abegg, F., & Bohrmann, G. (2011). High-intensity gas seepage causes rafting of shallow gas hydrates in the southeastern Black Sea. *Earth and Planetary Science Letters*, 307(1-2), 35-46.

Pape, T., Blumenberg, M., Reitz, A., Scheeder, G., Schmidt, M., Haeckel, M., ... & Bohrmann, G. (2021). Oil and gas seepage offshore Georgia (Black Sea)–Geochemical evidences for a Paleogene-Neogene hydrocarbon source rock. *Marine and Petroleum Geology*, 128, 104995.

Pape, T., Kasten, S., Zabel, M., Bahr, A., Abegg, F., Hohnberg, H.J. & Bohrmann, G. (2010). Gas hydrates in shallow deposits of the Amsterdam mud volcano, Anaximander Mountains, Northeastern Mediterranean Sea. *Geo-Mar Lett,* 30, 187-206.

Park, T., Lee, J. Y., & Kwon, T. H. (2018). Effect of pore size distribution on dissociation temperature depression and phase boundary shift of gas hydrate in various fine-grained sediments. *Energy & Fuels*, 32(4), 5321-5330. https://doi.org/10.1021/acs.energyfuels.8b00074

Parker, R. L. (1994). Geophysical inverse theory (Vol. 1). *Princeton university press*.

Parker, R. L., and Huestis, S. P. (1974). The inversion of magnetic anomalies in the presence of topography. *Journal of Geophysical Research*, 79(11), 1587-1593. https://doi.org/10.1029/JB079i011p01587

Paterson, N. R., and Reeves, C. V. (1985). Applications of gravity and magnetic surveys: The state-of-the-art in 1985. *Geophysics*, 50(12), 2558-2594. https://doi.org/10.1190/1.1441884

Pecher, I. A., Villinger, H., Kaul, N., Crutchley, G. J., Mountjoy, J. J., Huhn, K., ... & Coffin, R. B. (2017). A fluid pulse on the Hikurangi subduction margin: Evidence from a heat flux transect across the upper limit of gas hydrate stability. *Geophysical Research Letters*, 44(24), 12-385.

Peng, X., Li, C. F., Shen, C., Li, K., Zhao, Z., & Xie, X. (2020). Anomalous lower crustal structure and origin of magmatism in the southeastern margin of the South China Sea. *Marine and Petroleum Geology*, 122, 104711. https://doi.org/10.1016/j.marpetgeo.2020.104711

Pérez-Gussinyé, M., Morgan, J. P., Reston, T. J., & Ranero, C. R. (2006). The rift to drift transition at non-volcanic margins: Insights from numerical modelling. *Earth and Planetary Science Letters*, 244(1-2), 458-473. https://doi.org/10.1016/j.epsl.2006.01.059

Péron-Pinvidic, G., & Manatschal, G. (2009). The final rifting evolution at deep magma-poor passive margins from Iberia-Newfoundland: a new point of view. *International Journal of Earth Sciences*, 98(7), 1581-1597. DOI 10.1007/s00531-008-0337-9

Péron-Pinvidic, G., & Manatschal, G. (2010). From microcontinents to extensional allochthons: witnesses of how continents rift and break apart?. *Petroleum Geoscience*, 16(3), 189-197. DOI 10.1144/1354-079309-903

Peron-Pinvidic, G., & Manatschal, G. (2019). Rifted margins: State of the art and future challenges. *Frontiers in Earth Science*, 7, 218. https://doi.org/10.3389/feart.2019.00218

Peron-Pinvidic, G., & Osmundsen, P. T. (2018). The Mid Norwegian-NE Greenland conjugate margins: Rifting evolution, margin segmentation, and breakup. *Marine and Petroleum Geology*, 98, 162-184. https://doi.org/10.1016/j.marpetgeo.2018.08.011

Peron-Pinvidic, G., Manatschal, G., & Osmundsen, P. T. (2013). Structural comparison of archetypal Atlantic rifted margins: A review of observations and concepts. *Marine and petroleum geology*, 43, 21-47. https://doi.org/10.1016/j.marpetgeo.2013.02.002

Péron-Pinvidic, G., Manatschal, G., Masini, E., Sutra, E., Flament, J. M., Haupert, I., & Unternehr, P. (2017). Unravelling the along-strike variability of the Angola–Gabon rifted margin: a mapping approach. *Geological Society, London, Special Publications*, 438(1), 49-76. https://doi.org/10.1144/SP438.1

Péron-Pinvidic, G., Manatschal, G., Minshull, T. A., & Sawyer, D. S. (2007). Tectonosedimentary evolution of the deep Iberia-Newfoundland margins: Evidence for a complex breakup history. *Tectonics*, 26(2). https://doi.org/10.1029/2006TC001970

Phrampus, B. J., Hornbach, M. J., Ruppel, C. D., & Hart, P. E. (2014). Widespread gas hydrate instability on the upper US Beaufort margin. *Journal of Geophysical Research: Solid Earth*, 119(12), 8594-8609. https://doi.org/10.1002/2014JB011290

Pickup, S. L. B., Whitmarsh, R. B., Fowler, C. M. R., and Reston, T. J. (1996). Insight into the nature of the ocean-continent transition off West Iberia from a deep multichannel seismic reflection profile. *Geology*, 24(12), 1079-1082. https://doi.org/10.1130/0091-7613(1996)024<1079:IITNOT>2.3.CO;2

Planke, S., Symonds, P. A., Alvestad, E., & Skogseid, J. (2000). Seismic volcanostratigraphy of large-volume basaltic extrusive complexes on rifted margins. *Journal of Geophysical Research: Solid Earth*, 105(B8), 19335-19351. https://doi.org/10.1029/1999JB900005

Poort, J., Vassilev, A., & Dimitrov, L. (2005). Did postglacial catastrophic flooding trigger massive changes in the Black Sea gas hydrate reservoir?. *Terra Nova*, 17(2), 135-140.

Popescu, I., De Batist, M., Lericolais, G., Nouzé, H., Poort, J., Panin, N., ... & Gillet, H. (2006). Multiple bottom-simulating reflections in the Black Sea: potential proxies of past climate conditions. *Marine Geology*, 227(3-4), 163-176.

Popescu, I., Lericolais, G., Panin, N., De Batist, M., & Gillet, H. (2007). Seismic expression of gas and gas hydrates across the western Black Sea. *Geo-Marine Letters*, 27(2-4), 173-183.

Posewang, J., & Mienert, J. (1999). The enigma of double BSRs: indicators for changes in the hydrate stability field?. *Geo-marine letters*, 19(1-2), 157-163.

Prada, M., Sallarès, V., Ranero, C. R., Vendrell, M. G., Grevemeyer, I., Zitellini, N., & de Franco, R. (2015). The complex 3-D transition from continental crust to backarc magmatism and exhumed mantle in the Central Tyrrhenian basin. *Geophysical Journal International*, 203(1), 63-78. https://doi.org/10.1093/gji/ggv271

Prada, M., Sallarès, V., Ranero, C. R., Vendrell, M. G., Grevemeyer, I., Zitellini, N., and de Franco, R. (2014). Seismic structure of the Central Tyrrhenian basin: Geophysical constraints on the nature of the main crustal domains. *Journal of Geophysical Research: Solid Earth*, 119(1), 52-70. https://doi.org/10.1002/2013JB010527

Press, W.H., Teukolsky, S.A., Vetterling, W.T., Flannery, B.P. (1992). Numerical Recipes in Fortran 77: the art of scientific computing. *Cambridge University Press, Cambridge*.

Priest, J.A., Best, A.I., & Clayton, C.R.I. (2009). Influence of gas hydrate morphology on the seismic velocities of sands, 114, B11205. https://doi.org/10.1029/2009JB006284

Qin, F., Luo, Y., Olsen, K. B., Cai, W., & Schuster, G. T. (1992). Finite-difference solution of the eikonal equation along expanding wavefronts, *Geophysics*, 57, 478–487.

Qin, Y., & Singh, S. C. (2018). Insight into frontal seismogenic zone in the Mentawai locked region from seismic full waveform inversion of ultralong offset streamer data. *Geochemistry, Geophysics, Geosystems*, 19(11), 4342-4365. https://doi.org/10.1029/2018GC007787

Railsback, B. (2010). The Black Sea IIIa: Variation with Depth. Retrieved from (Accessed on April 23, 2016): http://www. gly. uga. edu/railsback/Fundamentals/BlackSeaTSOProfile01.

Raitt, R. W. (1963). The crustal rocks. *In: M. N. HILL* (Editor), The Sea. Wiley, New York, N.Y., 3: 85-102.

Ranero, C. R., & Pérez-Gussinyé, M. (2010). Sequential faulting explains the asymmetry and extension discrepancy of conjugate margins. *Nature*, 468(7321), 294. 10.1038/nature09520

Rangin, C., Bader, A. G., Pascal, G., Ecevitoğlu, B., & Görür, N. (2002). Deep structure of the Mid Black Sea High (offshore Turkey) imaged by multi-channel seismic survey (BLACKSIS cruise) 1, 2. *Marine Geology*, 182(3-4), 265-278. https://doi.org/10.1016/S0025-3227(01)00236-5

Rawlinson, N., & Sambridge, M. (2003). Seismic traveltime tomography of the crust and lithosphere. *Advances in geophysics*, 46, 81-199.

Reagan, M. T., & Moridis, G. J. (2008). Dynamic response of oceanic hydrate deposits to ocean temperature change. *Journal of Geophysical Research: Oceans*, 113(C12).

Reeburgh, W.S. (2007). Oceanic methane biogeochemistry. *Chem. Rev*. 107, 486–513.

Reed, D. L., Silver, E. A., Tagudin, J. E., Shipley, T. H., & Vrolijk, P. (1990). Relations between mud volcanoes, thrust deformation, slope sedimentation, and gas hydrate, offshore north Panama. *Marine and Petroleum* Geology, 7(1), 44-54.

Reilinger, R., McClusky, S., Vernant, P., Lawrence, S., Ergintav, S., Cakmak, R., ... & Karam, G. (2006). GPS constraints on continental deformation in the Africa-Arabia-Eurasia continental collision zone and implications for the dynamics of plate interactions. *Journal of Geophysical Research: Solid Earth*, 111(B5). https://doi.org/10.1029/2005JB004051

Reitz, A., Pape, T., Haeckel, M., Schmidt, M., Berner, U., Scholz, F., Liebetrau, V., Aloisi, G., Weise, S.M., & Wallmann, K. (2011). Sources of fluids and gases expelled at cold seeps offshore Georgia, Eastern Black Sea. *Geochim. Cosmochim. Acta*, 75, 3250–3268.

Rempel, A. W. (2011). A model for the diffusive growth of hydrate saturation anomalies in layered sediments. *Journal of Geophysical Research*, 116, B10105. https://doi.org/10.1029/2011JB008484

Ren, X., Guo, Z., Ning, F., & Ma, S. (2020). Permeability of hydrate-bearing sediments. *Earth-Science Reviews*, 202, 103100. https://doi.org/10.1016/j.earscirev.2020.103100

Reshef, M. (1991). Depth migration from irregular surfaces with depth extrapolation methods. *Geophysics*, 56(1), 119-122. https://doi.org/10.1190/1.1442947

Reston, T. J. (2005). Polyphase faulting during the development of the west Galicia rifted margin. *Earth and Planetary Science Letters*, 237(3-4), 561-576.

Reston, T. J. (2009). The extension discrepancy and syn-rift subsidence deficit at rifted margins. *Petroleum Geoscience*, 15(3), 217-237. https://doi.org/10.1144/1354-079309-845

Reston, T. J., & McDermott, K. G. (2011). Successive detachment faults and mantle unroofing at magma-poor rifted margins. *Geology*, 39(11), 1071-1074. https://doi.org/10.1130/G32428.1

Reston, T. J., & Ranero, C. R. (2011). The 3-D geometry of detachment faulting at mid-ocean ridges. *Geochemistry, Geophysics, Geosystems*, 12(7). https://doi.org/10.1029/2011GC003666

Reston, T. J., Krawczyk, C. M., & Klaeschen, D. (1996). The S reflector west of Galicia (Spain): Evidence from prestack depth migration for detachment faulting during continental breakup. *Journal of Geophysical Research: Solid Earth*, 101(B4), 8075-8091. https://doi.org/10.1029/95JB03466

Riboulot, V., Cattaneo, A., Scalabrin, C., Gaillot, A., Jouet, G., Ballas, G., ... & Ker, S. (2017). Control of the geomorphology and gas hydrate extent on widespread gas emissions offshore Romania. La géomorphologie des fonds marins et la présence d'hydrates de gaz contrôlent les émissions de gaz dans la Mer Noire au large de la Roumanie. *Bulletin de la Société géologique de France*, 188(4). https://doi.org/10.1051/bsgf/2017182

Riboulot, V., Ker, S., Sultan, N., Thomas, Y., Marsset, B., Scalabrin, C., ... & Ion, G. (2018). Freshwater lake to salt-water sea causing widespread hydrate dissociation in the Black Sea. *Nature communications*, 9(1), 1-8. https://doi.org/10.1038/s41467-017-02271-z

Riedel, M., & Collett, T. S. (2017). Observed correlation between the depth to base and top of gas hydrate occurrence from review of global drilling data: Journal of Geochem. *Geochemistry, Geophysics, Geosystems*, 18, 2543–2561. https://doi.org/10.1002/2017GC006805

Riedel, M., Bialas, J., Villinger, H., Pape, T., Haeckel, M., & Bohrmann, G. (2021). Heat Flow Measurements at the Danube Deep-Sea Fan,Western Black Sea. *Geosciences*, 11, 240. https:// doi.org/10.3390/geosciences11060240

Riedel, M., Collett, T. S., & Shankar, U. (2011). Documenting channel features associated with gas hydrates in the Krishna–Godavari Basin, offshore India. *Marine Geology*, 279(1-4), 1-11. https://doi.org/10.1016/j.margeo.2010.10.008

Riedel, M., Freudenthal, T., Bergenthal, M., Haeckel, M., Wallmann, K., Spangenberg, E., ... & Bohrmann, G. (2020). Physical properties and core-log seismic integration from drilling at the Danube deep-sea fan, Black Sea. *Marine and Petroleum Geology*, 114, 104192.

Riedel, M., Novosel, I., Spence, G. D., Hyndman, R. D., Chapman, R. N., Solem, R. C., & Lewis, T. (2006). Geophysical and geochemical signatures associated with gas hydrate-related venting in the northern Cascadia margin. *GSA Bulletin*, 118(1/2), 23–38. https://doi.org/10.1130/B25720.1

Rippington, S., Mazur, S., and Warner, J. (2015). The crustal architecture of the Faroe–Shetland Basin: insights from a newly merged gravity and magnetic dataset. *Geological Society, London, Special Publications*, 421(1), 169-196. https://doi.org/10.1144/SP421.10

Robinson, A. G., & Kerusov, E. (1997). AAPG Memoir 68: Regional and Petroleum Geology of the Black Sea and Surrounding Region. Chapter 19: Stratigraphic and Structural Development of the Gulf of Odessa, Ukrainian Black Sea: Implications for Petroleum Exploration.

Robinson, A. G., Banks, C. J., Rutherford, M. M., & Hirst, J. P. P. (1995a). Stratigraphic and structural development of the Eastern Pontides, Turkey. *Journal of the Geological Society*, 152(5), 861-872. https://doi.org/10.1144/gsjgs.152.5.0861

Robinson, A. G., Rudat, J. H., Banks, C. J., & Wiles, R. L. F. (1996). Petroleum geology of the Black Sea. *Marine and Petroleum Geology*, 13(2), 195-223. https://doi.org/10.1016/0264-8172(95)00042-9

Robinson, A., Spadini, G., Cloetingh, S., & Rudat, J. (1995b). Stratigraphic evolution of the Black Sea: inferences from basin modelling. *Marine and Petroleum Geology*, 12(8), 821-835. https://doi.org/10.1016/0264-8172(95)98850-5

Rogers, R. (2015). Offshore gas hydrates: Origins, development, and production. Gulf Professional Publishing [book].

Römer, M., Sahling, H., Pape, T., Bahr, A., Feseker, T., Wintersteller, P., & Bohrmann, G. (2012). Geological control and magnitude of methane ebullition from a high-flux seep area in the Black Sea – the Kerch seep area. *Mar. Geol*.319–322, 57–74. http://dx.doi.org/10.1016/j.margeo.2012.07.005.

Ross, D. A. (1978). Summary of results of Black Sea drilling. Initial Reports of the Deep Sea Drilling Project, 42, 1149–1177 (Part 2).

Ross, D. A., & Degens, E. T. (1974). Recent Sediments of Black Sea: Sediments.

Ross, D.A., Neprchnov, Y.P., Hsu, K.J., Trimonis, E.S., Percival Jr., S.F., Erickson, A.J., Degens, E.T., Hunt, J.M., Manheim, F.T., Senalp, M., Traverse, A., Stoffers, P. (1978). Leg 42, Part 2, of the cruises of the drilling vessel Glomar Challenger; Istanbul, Turkey to Istanbul, Turkey, May–June 1975, DSDP.

Rudat, J. H., & MacGregor, D. S. (1993). Unconventional exploration techniques in a high cost deep water basin: a case study from the Black Sea. *Society of Exploration Geophysicists*. In Abstracts with Programs. https://doi.org/10.1190/1.1822382

Ruffine, L., Deusner, C., Haeckel, M., Kossel, E., Toucanne, S., Chéron, S., ... & Riboulot, V. (2021). Effects of postglacial seawater intrusion on sediment geochemical characteristics in the Romanian sector of the Black Sea. *Marine and Petroleum Geology*, 123, 104746. https://doi.org/10.1016/j.marpetgeo.2020.104746

Rüpke, L. H., Schmid, D. W., Perez-Gussinye, M., & Hartz, E. (2013). Interrelation between rifting, faulting, sedimentation, and mantle serpentinization during continental margin formation—including examples from the Norwegian Sea. *Geochemistry, Geophysics, Geosystems*, 14(10), 4351-4369. https://doi.org/10.1002/ggge.20268

Ruppel, C. (1997). Anomalously cold temperatures observed at the base of the gas hydrate stability zone on the U.S. Atlantic passive margin. *Geology*, 25(8), 699–702. https://doi.org/10.1130/0091-7613(1997)025<0699:ACTOAT>2.3.CO;2

Ruppel, C. (2015). Permafrost-associated gas hydrate: is it really approximately 1% of the global system?. *Journal of Chemical & Engineering Data*, 60(2), 429-436. https://doi.org/10.1021/je500770m

Ruppel, C. D. (2011). Methane hydrates and contemporary climate change. *Nature Eduction Knowledge*, 2(12), 12.

Ruppel, C. D., & Kessler, J. D. (2017). The interaction of climate change and methane hydrates. *Reviews of Geophysics*, 55(1), 126-168. https://doi.org/10.1002/2016RG000534

Rusakov, O., & Kutas, R. (2018). Mantle origin of methane in the Black Sea. *Geofizicheskiy Zhurnal*, 40(5), 191–207. https://doi.org/10.24028/gzh.0203-3100.v40i5.2018.147482

Russell, S. M., and Whitmarsh, R. B. (2003). Magmatism at the west Iberia non-volcanic rifted continental margin: evidence from analyses of magnetic anomalies. *Geophysical Journal International*, 154(3), 706-730. https://doi.org/10.1046/j.1365-246X.2003.01999.x

Saad, A. H. (1969). Magnetic properties of ultramafic rocks from Red Mountain, California. *Geophysics*, 34(6), 974-987.

Sachsenhofer, R. F., Popov, S. V., Coric, S., Mayer, J., Misch, D., Morton, M. T., ... & Tari, G. (2018). Paratethyan petroleum source rocks: an overview. *Journal of Petroleum Geology*, 41(3), 219-245. https://doi.org/10.1111/jpg.12702

Sahoo, S. K., Marín-Moreno, H., North, L. J., Falcon-Suarez, I., Madhusudhan, B. N., Best, A. I., & Minshull, T. A. (2018). Presence and consequences of coexisting methane gas with hydrate under two phase water-hydrate stability conditions. *Journal of geophysical research: solid earth*, 123(5), 3377-3390. https://doi.org/10.1029/2018JB015598

Sahoo, S. K., North, L. J., Marín-Moreno, H., Minshull, T. A., & Best, A. I. (2019). Laboratory observations of frequency-dependent ultrasonic P-wave velocity and attenuation during methane hydrate formation in Berea sandstone. *Geophysical Journal International*, 219(1), 713-723. https://doi.org/10.1093/gji/ggz311

Saintot, A., Brunet, M. F., Yakovlev, F., Sébrier, M., Stephenson, R., Ershov, A., ... & McCann, T. (2006). The Mesozoic-Cenozoic tectonic evolution of the Greater Caucasus. *Geological Society, London,* Memoirs, 32(1), 277-289. https://doi.org/10.1144/GSL.MEM.2006.032.01.16

Sato, T., No, T., Arai, R., Miura, S., & Kodaira, S. (2020). Transition from continental rift to back-arc basin in the southern Japan Sea deduced from seismic velocity structures. *Geophysical Journal International*, 221(1), 722-739. https://doi.org/10.1093/gji/ggaa006

Sauter, D., Cannat, M., Rouméjon, S., Andreani, M., Birot, D., Bronner, A., ... & Searle, R. (2013). Continuous exhumation of mantle-derived rocks at the Southwest Indian Ridge for 11 million years. *Nature Geoscience*, 6(4), 314-320. https://doi.org/10.1038/ngeo1771

Sauter, D., Tugend, J., Gillard, M., Nirrengarten, M., Autin, J., Manatschal, G., Cannat, M., Leroy, S. and Schaming, M. (2018). Oceanic basement roughness alongside magma-poor rifted margins: insight into initial seafloor spreading. *Geophysical Journal International*, 212(2), 900-915. doi: 10.1093/gji/ggx439

Sava, D., & Hardage, B. A. (2006). Rock physics characterization of hydrate-bearing deepwater sediments. *The Leading Edge*, 25(5), 616-619. https://doi.org/10.1190/1.2202666

Sayers, J., Symonds, P. A., Direen, N. G., & Bernardel, G. (2001). Nature of the continent-ocean transition on the non-volcanic rifted margin of the central Great Australian Bight. *Geological Society, London, Special Publications*, 187(1), 51-76. https://doi.org/10.1144/GSL.SP.2001.187.01.04

Scales, J. A., Smith, M. L., & Treitel, S. (1994). Introductory geophysical inverse theory. *Golden: Samizdat Press*.

Schmale, O., Haeckel, M., & McGinnis, D. F. (2011). Response of the Black Sea methane budget to massive short-term submarine inputs of methane. *Biogeosciences*, 8(4), 911-918. https://doi.org/10.5194/bg-8-911-2011

Schneider, F., Dubille, M., & Montadert, L. (2016). Modeling of microbial gas generation: Application to the eastern Mediterranean "Biogenic Play". *Geologica Acta*, 14, 403–417. https://doi.org/10.1344/GeologicaActa2016.1314.1344.1345

Schweller, W. J., Gidman, J., Reed, A. A., & Grant, C. W. (1987). Topographically restricted deep-sea fan deposits, Inglewood field, Los Angeles *Basin. AAPG (Am. Assoc. Pet. Geol.) Bull.;(United States),* 71(CONF-870606-).

Scott, C. L., Shillington, D. J., Minshull, T. A., Edwards, R. A., Brown, P. J., & White, N. J. (2009). Wide-angle seismic data reveal extensive overpressures in the Eastern Black Sea Basin.

Geophysical Journal International, 178(2), 1145-1163. https://doi.org/10.1111/j.1365-246X.2009.04215.x

Scott, D. L., Rawlings, D. J., Page, R. W., Tarlowski, C. Z., Idnurm, M., Jackson, M. J., & Southgate, P. N. (2000). Basement framework and geodynamic evolution of the Palaeoproterozoic superbasins of north-central Australia: an integrated review of geochemical, geochronological and geophysical data. *Australian Journal of Earth Sciences*, 47(3), 341-380. https://doi.org/10.1046/j.1440-0952.2000.00793.x

Searle, R. C., Cowie, P. A., Mitchell, N. C., Allerton, S., MacLeod, C. J., Escartin, J., Russell, S. M., Slootweg, P. A. and Tanaka, T. (1998). Fault structure and detailed evolution of a slow spreading ridge segment: The Mid-Atlantic Ridge at 29 N. *Earth and Planetary Science Letters*, 154(1-4), 167-183. https://doi.org/10.1016/S0012-821X(97)00160-X

Searle, R. C., Murton, B. J., Achenbach, K., LeBas, T., Tivey, M., Yeo, I., et al. (2010). Structure and development of an axial volcanic ridge: Mid-Atlantic Ridge, 45 N. *Earth and Planetary Science Letters*, 299(1-2), 228-241. https://doi.org/10.1016/j.epsl.2010.09.003

Seebeck, H., Nicol, A., Villamor, P., Ristau, J., & Pettinga, J. (2014). Structure and kinematics of the Taupo Rift, New Zealand. *Tectonics*, 33(6), 1178-1199. https://doi.org/10.1002/2014TC003569

Setzmann, U., & Wagner, W. (1991). A new equation of state and tables of thermodynamic properties for methane covering the range from the melting line to 625 K at pressures up to 100 MPa, *J. Phys. Chem. Ref. Data*, 20(6), 1061–1155, doi:10.1063/1.555898.

Sheremet, Y., Sosson, M., Ratzov, G., Sydorenko, G., Voitsitskiy, Z., Yegorova, T., ... & Murovskaya, A. (2016). An offshore-onland transect across the north-eastern Black Sea basin (Crimean margin): Evidence of Paleocene to Pliocene two-stage compression. *Tectonophysics,* 688, 84-100. https://doi.org/10.1016/j.tecto.2016.09.015

Sheriff, R. E., & Geldart, L. P. (1983). Data-processing and interpretation. *Cambridgge University Press*.

Sheriff, R. E., & Geldart, L. P. (1995). Exploration seismology. *Cambridge university press*.

Shillington, D. J., Minshull, T. A., Edwards, R. A., & White, N. (2017). Crustal structure of the Mid Black Sea High from wide-angle seismic data. *Geological Society, London, Special Publications*, 464, SP464-6. https://doi.org/10.1144/SP464.6

Shillington, D. J., Scott, C. L., Minshull, T. A., Edwards, R. A., Brown, P. J., & White, N. (2009). Abrupt transition from magma-starved to magma-rich rifting in the eastern Black Sea. *Geology*, 37(1), 7-10. https://doi.org/10.1130/G25302A.1

Shillington, D. J., White, N., Minshull, T. A., Edwards, G. R., Jones, S. M., Edwards, R. A., & Scott, C. L. (2008). Cenozoic evolution of the eastern Black Sea: A test of depth-dependent stretching models. *Earth and Planetary Science Letters*, 265(3-4), 360-378. https://doi.org/10.1016/j.epsl.2007.10.033

Shipley, T. H., Houston, M. H., Buffler, R. T., Shaub, F. J., McMillen, K. J., LAOD, J. W., & Worzel, J. L. (1979). Seismic evidence for widespread possible gas hydrate horizons on continental slopes and rises. *AAPG bulletin*, 63(12), 2204-2213. https://doi.org/10.1306/2F91890A-16CE-11D7-8645000102C1865D

Shishkina, O. V. (1978). Distribution of Bromine, Cl/Br Relationships and Iodine in Interstitial Water of the Black Sea, Based on DSDP Leg 42B. In Initial Reports of the Deep Sea Drilling Project (Vol. 42, pp. 631-635). *US Government Printing Office*.

Shive, P. N. (1986). Suggestions for the use of SI units in magnetism: *EOS Transactions of the American Geophysical Union*, 67, 25.

Shive, P. N., Blakely, R. J., Frost, B. R., & Fountain, D. M. (1992). Magnetic properties of the lower continental crust. *Continental lower crust*, 23, 145-177.

Shnyukov, E. F. (2013). Mud volcanoes of the Black Sea as a prospecting indicator of methane gas hydrates. *Lithology and Mineral Resources*, 48(2), 114. DOI:10.1134/S0024490213010045

Shreider, A. A. (2005). Opening of the deep-water basin of the Black Sea. *Oceanology*, 45(4), 560-571.

Shreider, A. A., Kazmin, V. G., & Lygin, V. S. (1997). Magnetic anomalies and age of the Black Sea Deep Basins. *Geotectonics*, 31(1), 54-64.

Sibuet, J. C., & Tucholke, B. E. (2013). The geodynamic province of transitional lithosphere adjacent to magma-poor continental margins. *Geological Society, London, Special Publications*, 369(1), 429-452. https://doi.org/10.1144/SP369.15

Sibuet, J. C., Hsu, S. K., Shyu, C. T., & Liu, C. S. (1995). Structural and kinematic evolutions of the Okinawa Trough backarc basin. In Backarc basins (pp. 343-379). *Springer, Boston, MA*. https://doi.org/10.1007/978-1-4615-1843-3_9

Sibuet, J. C., Srivastava, S., and Manatschal, G. (2007). Exhumed mantle-forming transitional crust in the Newfoundland-Iberia rift and associated magnetic anomalies. *Journal of Geophysical Research: Solid Earth*, 112(B6). doi:10.1029/2005JB003856

Simmons, M. D., Tari, G. C., & Okay, A. I. (2018). Petroleum geology of the Black Sea: introduction. *Geological Society, London, Special Publications,* 464(1), 1-18. https://doi.org/10.1144/SP464.15

Singh, S. C., Minshull, T. A., & Spence, G. D. (1993). Velocity structure of a gas hydrate reflector. *Science*, 260(5105), 204-207. DOI: 10.1126/science.260.5105.204

Skaarup, N., Jackson, H. R., & Oakey, G. (2006). Margin segmentation of Baffin Bay/Davis Strait, eastern Canada based on seismic reflection and potential field data. *Marine and Petroleum Geology*, 23(1), 127-144. https://doi.org/10.1016/j.marpetgeo.2005.06.002

Sloan, E. D. (1998). Gas hydrates: review of physical/chemical properties. *Energy & fuels*, 12(2), 191-196.

Sloan, E. D. (2003). Clathrate hydrate measurements: microscopic, mesoscopic, and macroscopic. *The journal of chemical thermodynamics*, 35(1), 41-53. https://doi.org/10.1016/S0021-9614(02)00302-6

Sloan, E.D., & Koh, C.A. (2008). Clathrate Hydrates of Natural Gases, Third Edition. *CRC Press-Taylor & Francis Group*, Boca Raton, Florida.

Slotnick, M. M. (1936). On seismic computations, with applications, *I. Geophysics*, 1(1), 9-22. https://doi.org/10.1190/1.1437084

Small, C. (1994). A global analysis of mid-ocean ridge axial topography. *Geophysical Journal International*, 116(1), 64-84. https://doi.org/10.1111/j.1365-246X.1994.tb02128.x

Soares, D. M., Alves, T. M., & Terrinha, P. (2012). The breakup sequence and associated lithospheric breakup surface: Their significance in the context of rifted continental margins (West Iberia and Newfoundland margins, North Atlantic). *Earth and Planetary Science Letters*, 355, 311-326. https://doi.org/10.1016/j.epsl.2012.08.036

Soulet, G., Delaygue, G., Vallet-Coulomb, C., et al. (2010). Glacial hydrologic conditions in the Black Sea reconstructed using geochemical pore water profiles. *Earth Planet Sci. Lett*. 296, 57–66. https://doi.org/10.1016/j.epsl.2010.04.045.

Spadini, G., Robinson, A., & Cloetingh, S. (1996). Western versus Eastern Black Sea tectonic evolution: pre-rift lithospheric controls on basin formation. *Tectonophysics*, 266(1-4), 139-154. https://doi.org/10.1016/S0040-1951(96)00187-4

Spangenberg, E., Priegnitz, M., Heeschen, K., Schicks, J.M. (2014). Are laboratory-formed hydrate-bearing systems analogous to those in nature? J. *Chem. Eng. Data*, 60, 258–268. https://doi.org/10.1021/je5005609

Stanev, E. V., He, Y., Staneva, J., & Yakushev, E. (2014). Mixing in the Black Sea detected from the temporal and spatial variability of oxygen and sulfide–Argo float observations and numerical modelling. *Biogeosciences*, 11(20), 5707-5732. https://doi.org/10.5194/bg-11-5707-2014

Stanton, N., Kusznir, N., Gordon, A., & Schmitt, R. (2019). Architecture and Tectono-magmatic evolution of the Campos Rifted Margin: Control of OCT structure by basement inheritance. *Marine and Petroleum Geology*, 100, 43-59. https://doi.org/10.1016/j.marpetgeo.2018.10.043

Starostenko, V. I., Dolmaz, M. N., Kutas, R. I., Rusakov, O. M., Oksum, E., Hisarli, Z. M., Okyar, M., Kalyoncuoglu, U. Y., Tununsatar, H. E. and Legostaeva, O. V. (2014). Thermal structure of the crust in the Black Sea: comparative analysis of magnetic and heat flow data. *Marine Geophysical Research*, 35(4), 345-359. doi: 10.1007/s11001-014-9224-x

Starostenko, V. I., Rusakov, O. M., Pashkevich, I. K., Kutas, R. I., Makarenko, I. B., Legostaeva, O. V., Lebed, T. V. and Savchenko, A. (2015). Heterogeneous structure of the lithosphere in the Black Sea from a multidisciplinary analysis of geophysical fields. *Geofizicheskiy zhurnal*, 37(2), 3-28.

Starostenko, V. I., Rusakov, O. M., Shnyukov, E. F., Kobolev, V. P., & Kutas, R. I. (2010). Methane in the northern Black Sea: characterization of its geomorphological and geological environments. *Geological Society, London, Special Publications*, 340(1), 57-75. https://doi.org/10.1144/SP340.5

Starostenko, V., Buryanov, V., Makarenko, I., Rusakov, O., Stephenson, R., Nikishin, A., Georgiev, M., Dimitriu, R., Legostaeva, O., Pchelarov, V. and Sava, C. (2004). Topography of the crust–mantle boundary beneath the Black Sea Basin. *Tectonophysics*, 381(1-4), 211-233. https://doi.org/10.1016/j.tecto.2002.08.001

Stephenson, R., & Schellart, W. P. (2010). The Black Sea back-arc basin: insights to its origin from geodynamic models of modern analogues. *Geological Society, London, Special Publications*, 340(1), 11-21. https://doi.org/10.1144/SP340.2

Stern, R. J., & Dickinson, W. R. (2010). The Gulf of Mexico is a Jurassic backarc basin. *Geosphere*, 6(6), 739-754. https://doi.org/10.1130/GES00585.1

Stoll, R. D., & Bryan, G. M. (1970). Wave attenuation in saturated sediments. *The journal of the acoustical society of America*, 47(5B), 1440-1447. doi:10.1121/1.1912054.

Stovba, S. M., Popadyuk, I. V., Fenota, P. O., & Khriachtchevskaia, O. I. (2020). Geological structure and tectonic evolution of the Ukrainian sector of the Black Sea. *Geofizicheskiy Zhurnal*, 42(5), 53-106. https://doi.org/10.24028/gzh.0203-3100.v42i5.2020.215072

Stovba, S., Khriachtchevskaia, O., & Popadyuk, I. (2009). Hydrocarbon-bearing areas in the eastern part of the Ukrainian Black Sea. *The Leading Edge*, 28(9), 1042-1045. https://doi.org/10.1190/1.3236373

Suess, E., Torres, M. E., Bohrmann, G., Collier, R. W., Greinert, J., Linke, P., ... & Zuleger, E. (1999). Gas hydrate destabilization: enhanced dewatering, benthic material turnover and large methane plumes at the Cascadia convergent margin. *Earth and Planetary Science Letters*, 170(1-2), 1-15. https://doi.org/10.1016/S0012-821X(99)00092-8

Sultan, N., Cochonat, P., Foucher, J. P., & Mienert, J. (2004). Effect of gas hydrates melting on seafloor slope instability. *Marine geology*, 213(1-4), 379-401. https://doi.org/10.1016/j.margeo.2004.10.015

Sultan, N., Marsset, B., Ker, S., Marsset, T., Voisset, M., Vernant, A. M., ... & Drapeau, D. (2010). Hydrate dissolution as a potential mechanism for pockmark formation in the Niger delta. *Journal of Geophysical Research: Solid Earth*, 115(B8). https://doi.org/10.1029/2010JB007453

Sun, X., & Mohanty, K. K. (2006). Kinetic simulation of methane hydrate formation and dissociation in porous media. *Chemical Engineering Science*, 61, 3476–3495. https://doi.org/10.1016/j.ces.2005.12.017

Sutra, E., Manatschal, G., Mohn, G., & Unternehr, P. (2013). Quantification and restoration of extensional deformation along the Western Iberia and Newfoundland rifted margins. *Geochemistry, Geophysics, Geosystems*, 14(8), 2575-2597. https://doi.org/10.1002/ggge.20135

Sydorenko, G., Stephenson, R., Yegorova, T., Starostenko, V., Tolkunov, A., Janik, T., et al. (2017). Geological structure of the northern part of the Eastern Black Sea from regional seismic reflection data including the DOBRE-2 CDP profile. *Geological Society, London, Special Publications*, 428(1), 307-321. https://doi.org/10.1144/SP428.15

Taladay, K., Boston, B., & Moore, G. F. (2017). Gas-in-place estimate for potential gas hydrate concentrated zone in the Kumano Basin, Nankai Trough Forearc, Japan. *Energies,* 10(10), 1552.

Talwani, M., & Abreu, V. (2000). Inferences regarding initiation of oceanic crust formation from the US East Coast margin and conjugate South Atlantic margins. *GEOPHYSICAL MONOGRAPH-AMERICAN GEOPHYSICAL UNION*, 115, 211-234.

Talwani, M., & Heirtzler, J. R. (1964). Computation of magnetic anomalies caused by two dimensional bodies of arbitrary shape, in Parks, G. A., Ed., Computers in the mineral industries, Part 1: *Stanford Univ. Publ., Geological Sciences*, 9, 464-480.

Talwani, M., Windisch, C., and Langseth, M. (1971). Reykjanes ridge crest: A detailed geophysical study, *J. Geophys. Res*., 76, 473-517.

Tarantola, A. (1987). Inversion of travel times and seismic waveforms. *Seismic tomography*, 135-157.

Tari, G. C. (2015). Is the Black Sea really a back-arc basin? In: Transactions of the GCSEPM Foundation Perkins–Rosen 34th Annual Research Conference 'Petroleum Systems in Rift Basins', 510–520.

Tari, G. C., & Simmons, M. D. (2018). History of deepwater exploration in the Black Sea and an overview of deepwater petroleum play types. *Geological Society, London, Special Publications,* 464(1), 439-475. https://doi.org/10.1144/SP464.16

Tari, G. C., Vakhania, D., Tatishvili, G., Mikeladze, V., Gogritchiani, K., Vacharadze, S., et al. (2018). Stratigraphy, structure and petroleum exploration play types of the Rioni Basin, Georgia. *Geological Society, London, Special Publications*, 464(1), 403-438. https://doi.org/10.1144/SP464.14

Taylor, B., Goodliffe, A. M., & Martinez, F. (1999). How continents break up: insights from Papua New Guinea. *Journal of Geophysical Research: Solid Earth*, 104(B4), 7497-7512. https://doi.org/10.1029/1998JB900115

Taylor, B., Goodliffe, A., Martinez, F., & Hey, R. (1995). Continental rifting and initial sea-floor spreading in the Woodlark Basin. *Nature*, 374(6522), 534. doi: 10.1038/374534a0

Thébault, E., Finlay, C. C., Beggan, C. D., Alken, P., Aubert, J., Barrois, O., ... & Zvereva, T. (2015). International geomagnetic reference field: the 12th generation. *Earth, Planets and Space*, 67(1), 1-19. https://doi.org/10.1186/s40623-015-0228-9

Tian, D., & Liu, X. (2020). A new approach for the identification of gas hydrate in marine sediments. *Marine Geophysical Research*, 41(3), 1-12. https://doi.org/10.1007/s11001-020-09412-y

Tinivella, U., & Giustiniani, M. (2013). Variations in BSR depth due to gas hydrate stability versus pore pressure. *Global and Planetary Change*, 100, 119-128. https://doi.org/10.1016/j.gloplacha.2012.10.012

Tolstoy, M., Harding, A. J., & Orcutt, J. A. (1993). Crustal thickness on the Mid-Atlantic Ridge: Bull's-eye gravity anomalies and focused accretion. *Science*, 262(5134), 726-729. DOI: 10.1126/science.262.5134.726

Tréhu, A. M., Torres, M. E., Moore, G. F., Suess, E., & Bohrmann, G. (1999). Temporal and spatial evolution of a gas hydrate–bearing accretionary ridge on the Oregon continental margin. *Geology*, 27(10), 939-942.

Tucholke, B. E., & Sibuet, J. C. (2007). Leg 210 synthesis: Tectonic, magmatic, and sedimentary evolution of the Newfoundland-Iberia rift. In Proceedings of the Ocean Drilling Program, scientific results (Vol. 210, pp. 1-56). *College Station, TX: Ocean Drilling Program*.

Tucholke, B. E., Lin, J., Kleinrock, M. C., Tivey, M. A., Reed, T. B., Goff, J., and Jaroslow, G. E. (1997). Segmentation and crustal structure of the western Mid-Atlantic Ridge flank, 25° 25′–27° 10′ N and 0–29 my. *Journal of Geophysical Research: Solid Earth*, 102(B5), 10203-10223. https://doi.org/10.1029/96JB03896

Tucholke, B. E., Sawyer, D. S., and Sibuet, J. C. (2007). Breakup of the Newfoundland–Iberia rift. *Geological Society, London, Special Publications*, 282(1), 9-46. doi: 10.1144/SP282.2

Tugend, J., Chamot-Rooke, N., Arsenikos, S., Blanpied, C., & Frizon de Lamotte, D. (2019). Geology of the Ionian basin and margins: A key to the East Mediterranean geodynamics. *Tectonics*, 38(8), 2668-2702. https://doi.org/10.1029/2018TC005472

Tugend, J., Gillard, M., Manatschal, G., Nirrengarten, M., Harkin, C., Epin, M. E., ... & Mcdermott, K. (2020). Reappraisal of the magma-rich versus magma-poor rifted margin archetypes. *Geological Society, London, Special Publications*, 476(1), 23-47. https://doi.org/10.1144/SP476.9

Tugend, J., Gillard, M., Manatschal, G., Nirrengarten, M., Harkin, C., Epin, M. E., ... & Mcdermott, K. (2020). Reappraisal of the magma-rich versus magma-poor rifted margin archetypes. *Geological Society, London, Special Publications*, 476(1), 23-47. https://doi.org/10.1144/SP476.9

Tugend, J., Manatschal, G., Kusznir, N. J., & Masini, E. (2015). Characterizing and identifying structural domains at rifted continental margins: application to the Bay of Biscay margins and its Western Pyrenean fossil remnants. *Geological Society, London, Special Publications*, 413(1), 171-203. https://doi.org/10.1144/SP413.3

Tugolesov D.A., Gorshkov A.S. et al. (1985). Tectonics of the Mesozoic Sediments of the Black Sea Basin. *Nedra*, Moscow, 215 [in Russian].

Tüysüz, O. (1999). Geology of the Cretaceous sedimentary basins of the Western Pontides. *Geological Journal*, 34(1-2), 75-93. https://doi.org/10.1002/(SICI)1099-1034(199901/06)34:1/2<75::AID-GJ815>3.0.CO;2-S

Tüysüz, O., Yilmaz, İ. Ö., Svabenicka, L., & Kirici, S. (2012). The Unaz formation: a key unit in the Western Black Sea region, N Turkey. *Turkish Journal of Earth Sciences*, 21(6), 1009-1028. doi:10.3906/yer-1006-30

Vail, P. R., Mitchum Jr, R. M., & Thompson III, S. (1977). Seismic stratigraphy and global changes of sea level: Part 3. Relative changes of sea level from Coastal Onlap: section 2. Application of seismic reflection Configuration to Stratigraphic Interpretation.

Valentine, D. L., Blanton, D. C., Reeburgh, W. S., & Kastner, M. (2001). Water column methane oxidation adjacent to an area of active hydrate dissociation, Eel River Basin. *Geochimica et Cosmochimica Acta*, 65(16), 2633-2640. https://doi.org/10.1016/S0016-7037(01)00625-1

Van Avendonk, H. J., Davis, J. K., Harding, J. L., & Lawver, L. A. (2017). Decrease in oceanic crustal thickness since the breakup of Pangaea. *Nature Geoscience*, 10(1), 58-61. https://doi.org/10.1038/ngeo2849

Vassilev, A. (2006). Black Sea gas hydrates stability zone model (Optimistic & Pessimistic Assessment). *In: CRIMEA Final Project Meeting*, January 19-21, 2006, Gent, Belgium.

Vassilev, A., & Dimitrov, L. (2002). Spatial and quantity evaluation of the Black Sea gas hydrates. *Russian Geology and Geophysics*, 43(7), 672-684.

Verzhbitsky, E., Kuzin, I., & Lobkovsky, L. (2002). Age and thickness of the lithosphere within the Western and Eastern basins of the Black Sea according to geophysical data. *Turkish Journal of Earth Sciences*, 11(3), 231-242.

Vidale, J. E. (1990). Finite-difference calculations of traveltimes in three dimensions, *Geophysics*, 55, 521–526.

Vincent, S. J., & Kaye, M. N. (2018). Source rock evaluation of Middle Eocene–Early Miocene mudstones from the NE margin of the Black Sea. *Geological Society, London, Special Publications*, 464(1), 329-363. https://doi.org/10.1144/SP464.7

Vincent, S. J., Braham, W., Lavrishchev, V. A., Maynard, J. R., & Harland, M. (2016). The formation and inversion of the western Greater Caucasus Basin and the uplift of the western Greater Caucasus: Implications for the wider Black Sea region. *Tectonics*, 35(12), 2948-2962. https://doi.org/10.1002/2016TC004204

Vincent, S. J., Morton, A. C., Carter, A., Gibbs, S., & Barabadze, T. G. (2007). Oligocene uplift of the Western Greater Caucasus: an effect of initial Arabia–Eurasia collision. *Terra Nova*, 19(2), 160-166.

Vine, F. J., & Moores, E. M. (1972). A model for the gross structure, petrology, and magnetic properties of oceanic crust. Studies in Earth and Space Sciences: *A Memoir in Honor of Harry Hammond Hess*, 195-205.

Vink, G. E. (1982). Continental rifting and the implications for plate tectonic reconstructions. *Journal of Geophysical Research: Solid Earth*, 87(B13), 10677-10688. https://doi.org/10.1029/JB087iB13p10677

Virieux, J., & Operto, S. (2009). An overview of full-waveform inversion in exploration geophysics. *Geophysics*, 74(6), WCC1-WCC26. https://doi.org/10.1190/1.3238367

Waite, W. F., Helgerud, M. B., Nur, A., Pinkston, J. C., Stern, L. A., Kirby, S. H., & Durham, W. B. (2000). Laboratory measurements of compressional and shear wave speeds through methane hydrate. *ANNALS-NEW YORK ACADEMY OF SCIENCES*, 912, 1003-1010.

Waite, W. F., Santamarina, J. C., Cortes, D. D., Dugan, B., Espinoza, D. N., Germaine, J., ... & Yun, T. S. (2009). Physical properties of hydrate-bearing sediments. *Reviews of geophysics*, 47(4).

Wallace, L. M., Ellis, S., & Mann, P. (2009). Collisional model for rapid fore-arc block rotations, arc curvature, and episodic back-arc rifting in subduction settings. *Geochemistry, Geophysics, Geosystems*, 10(5). https://doi.org/10.1029/2008GC002220

Wallmann, K., Pinero, E., Burwicz, E., Haeckel, M., Hensen, C., Dale, A., & Ruepke, L. (2012). The global inventory of methane hydrate in marine sediments: A theoretical approach. *Energies*, 5(7), 2449. https://doi.org/10.3390/en5072449

Walsh, J. J., Childs, C., Meyer, V., Manzocchi, T., Imber, J., Nicol, A., ... & Strand, J. (2001). Geometric controls on the evolution of normal fault systems. *Geological Society, London, Special Publications*, 186(1), 157-170. https://doi.org/10.1144/GSL.SP.2001.186.01.10

Wang, J., Zhang, L., Ge, K., Zhao, J., & Song, Y. (2020). Characterizing anisotropy changes in the permeability of hydrate sediment. *Energy*, 205, 117997. https://doi.org/10.1016/j.energy.2020.117997

Wang, X., Collett, T. S., Lee, M. W., Yang, S., Guo, Y., & Wu, S. (2014). Geological controls on the occurrence of gas hydrate from core, downhole log, and seismic data in the Shenhu area, South China Sea. *Marine Geology*, 357, 272–292. https://doi.org/10.1016/j.margeo.2014.09.040

Welford, J. K., Shannon, P. M., O'Reilly, B. M., & Hall, J. (2012). Comparison of lithosphere structure across the Orphan Basin–Flemish Cap and Irish Atlantic conjugate continental margins from constrained 3D gravity inversions. *Journal of the Geological Society*, 169(4), 405-420. https://doi.org/10.1144/0016-76492011-114

Wernicke, B. (1985). Uniform-sense normal simple shear of the continental lithosphere. *Canadian Journal of Earth Sciences*, 22(1), 108-125. https://doi.org/10.1139/e85-009

Wernicke, B. (2009). The detachment era (1977–1982) and its role in revolutionizing continental tectonics. *Geological Society, London, Special Publications*, 321(1), 1-8. https://doi.org/10.1144/SP321.1

West, M., Ni, J., Baldridge, W. S., Wilson, D., Aster, R., Gao, W., & Grand, S. (2004). Crust and upper mantle shear wave structure of the southwest United States: Implications for rifting and support for high elevation. *Journal of Geophysical Research: Solid Earth*, 109(B3). https://doi.org/10.1029/2003JB002575

Westbrook, G. K., Chand, S., Rossi, G., Long, C., Bünz, S., Camerlenghi, A., ... & Zillmer, M. (2008). Estimation of gas hydrate concentration from multi-component seismic data at sites on the continental margins of NW Svalbard and the Storegga region of Norway. *Marine and Petroleum Geology*, 25(8), 744-758.

Westphal, M., Bazhenov, M. L., Lauer, J. P., Pechersky, D. M., & Sibuet, J. C. (1986). Paleomagnetic implications on the evolution of the Tethys belt from the Atlantic Ocean to the Pamirs since the Triassic. *Tectonophysics*, 123(1-4), 37-82. https://doi.org/10.1016/0040-1951(86)90193-9

White, R. S., McKenzie, D., & O'Nions, R. K. (1992). Oceanic crustal thickness from seismic measurements and rare earth element inversions. *Journal of Geophysical Research: Solid Earth*, 97(B13), 19683-19715. https://doi.org/10.1029/92JB01749

White, R. S., Minshull, T. A., Bickle, M. J., & Robinson, C. J. (2001). Melt generation at very slow-spreading oceanic ridges: Constraints from geochemical and geophysical data. *Journal of Petrology*, 42(6), 1171-1196. https://doi.org/10.1093/petrology/42.6.1171

White, R. S., Smith, L. K., Roberts, A. W., Christie, P. A. F., & Kusznir, N. J. (2008). Lower-crustal intrusion on the North Atlantic continental margin. *Nature*, 452(7186), 460-464. https://doi.org/10.1038/nature06687

White, R. S., Spence, G. D., Fowler, S. R., McKenzie, D. P., Westbrook, G. K., & Bowen, A. N. (1987). Magmatism at rifted continental margins. *Nature*, 330(6147), 439-444. https://doi.org/10.1038/330439a0

Whitmarsh, R. B., Manatschal, G. & Minshull, T. A. (2001). Evolution of magma-poor continental margins from rifting to seafloor spreading. *Nature*, 413, 150–154. doi: 10.1038/35093085

Williams, G. D. (1993). Tectonics and seismic sequence stratigraphy: an introduction. *Geological Society, London, Special Publications*, 71(1), 1-13. https://doi.org/10.1144/GSL.SP.1993.071.01.01

Williams, S. E., Whittaker, J. M., & Müller, R. D. (2011). Full-fit, palinspastic reconstruction of the conjugate Australian-Antarctic margins. *Tectonics*, 30(6). https://doi.org/10.1029/2011TC002912

Wilson J.T. (1966). Did the Atlantic close and then re-open? *Nature*, 211, 676–681, https://doi.org/10.1038/211676a0

Wilson, D., Aster, R., Ni, J., Grand, S., West, M., Gao, W., ... & Semken, S. (2005). Imaging the seismic structure of the crust and upper mantle beneath the Great Plains, Rio Grande Rift, and Colorado Plateau using receiver functions. *Journal of Geophysical Research: Solid Earth*, 110(B5). DOI:10.1029/2004JB003430.

Windisch, C. C., Ewing, J. I., & Bryan, G. M. (1965). Basement structural trends associated with the Bermuda Rise. *EOS, Trans. Am. geophys. Union*, 136.

Withjack, M. O., Schlische, R. W., & Olsen, P. E. (1998). Diachronous rifting, drifting, and inversion on the passive margin of central eastern North America: an analog for other passive margins. *AAPG bulletin*, 82(5), 817-835.

Withjack, M. O., Schlische, R. W., & Olsen, P. E. (2002). Rift-basin structure and its influence on sedimentary systems. *SEPM Special Publication*, 73, 57-81.

Won, I. J., & Bevis, M. (1987). Computing the gravitational and magnetic anomalies due to a polygon: Algorithms and Fortran subroutines. *Geophysics*, 52, 232-238.

Wood, W. T., & Ruppel, C. (2000). Seismic and thermal investigations of the Blake Ridge gas hydrate area: a synthesis. Proceedings of the Ocean Drilling Program. *Scientific results. Ocean Drilling Program*, 253-264.

Xing, J., & Spiess, V. (2015). Shallow gas transport and reservoirs in the vicinity of deeply rooted mud volcanoes in the central Black Sea. *Marine Geology*, 369, 67-78.

Xu, W., & Ruppel, C. (1999). Predicting the occurrence, distribution, and evolution of methane gas hydrate in porous marine sediments. *Journal of Geophysical Research: Solid Earth*, 104(B3), 5081-5095.

Yang, L., Ai, L., Xue, K., Ling, Z., & Li, Y. (2018). Analyzing the effects of inhomogeneity on the permeability of porous media containing methane hydrates through pore network models combined with CT observation. *Energy*, 163, 27-37. https://doi.org/10.1016/j.energy.2018.08.100

Ye, Y., & Liu, C. (Eds.). (2012). Natural Gas Hydrates: Experimental Techniques and Their Applications. *Springer Science & Business Media*.

Yegorova, T., & Gobarenko, V. (2010). Structure of the Earth's crust and upper mantle of the West- and East-Black Sea Basins revealed from geophysical data and its tectonic implications. *Geological Society, London, Special Publications*, 340(1), 23-42. https://doi.org/10.1144/SP340.3

Yegorova, T., Baranova, E., & Omelchenko, V. (2010). The crustal structure of the Black Sea from the reinterpretation of deep seismic sounding data acquired in the 1960s. *Geological Society, London, Special Publications*, 340(1), 43-56. https://doi.org/10.1144/SP340.4

Yegorova, T., Gobarenko, V., & Yanovskaya, T. (2013). Lithosphere structure of the Black Sea from 3-D gravity analysis and seismic tomography. *Geophysical Journal International*, 193(1), 287-303. https://doi.org/10.1093/gji/ggs098

Yilmaz, A., Adamia, S., Chabukiani, A., Chkhotua, T., ErdoĞan, K., Tuzcu, S., & KarabiyikoĞlu, M. (2000). Structural correlation of the southern Transcaucasus (Georgia)-eastern Pontides (Turkey). *Geological Society, London, Special Publications*, 173(1), 171-182. https://doi.org/10.1144/GSL.SP.2000.173.01.08

You, K., & Flemings, P. B. (2018). Methane hydrate formation in thick sandstones by free gas flow. *Journal of Geophysical Research: Solid Earth*, 123, 4582–4600. https://doi.org/10.1029/2018JB015683

You, K., Flemings, P. B., Malinverno, A., Collett, T. S., & Darnell, K. (2019). Mechanisms of methane hydrate formation in geological systems. *Reviews of Geophysics*, 57(4), 1146-1196. https://doi.org/10.1029/2018RG000638

Yu, J., Yan, P., Qiu, Y., Delescluse, M., Huang, W., & Wang, Y. (2021). Oceanic crustal structures and temporal variations of magmatic budget during seafloor spreading in the East Sub-basin of the South China Sea. *Marine Geology*, 436, 106475. https://doi.org/10.1016/j.margeo.2021.106475

Yun, T. S., Francisca, F. M., Santamarina, J. C., & Ruppel, C. (2005). Compressional and shear wave velocities in uncemented sediment containing gas hydrate. *Geophysical Research Letters*, 32(10). doi:10.1029/2005GL022607

Zander, T., Haeckel, M., Berndt, C., Chi, W. C., Klaucke, I., Bialas, J., ... & Atgın, O. (2017). On the origin of multiple BSRs in the Danube deep-sea fan, Black Sea. *Earth and Planetary Science Letters,* 462, 15-25. . https://doi.org/10.1016/j.epsl.2017.01.006.

Zander, T., Haeckel, M., Klaucke, I., Bialas, J., Klaeschen, D., Papenberg, C., ... & Bohrmann, G. (2020). New insights into geology and geochemistry of the Kerch seep area in the Black Sea.

Marine and Petroleum Geology, 113, 104162. https://doi.org/10.1016/j.marpetgeo.2019.104162

Zatsepina, O. Y., & Buffett, B. A. (1998). Thermodynamic conditions for the stability of gas hydrate in the seafloor. *Journal of Geophysical Research*, 103(B10), 24,127–24,139. https://doi.org/10.1029/98JB02137

Zelt, C. A., & Barton, P. J. (1998). Three-dimensional seismic refraction tomography: A comparison of two methods applied to data from the Faeroe Basin. *Journal of Geophysical Research: Solid Earth,* 103(B4), 7187-7210. https://doi.org/10.1029/97JB03536

Zelt, C. A., & Ellis, R. M. (1988). Practical and efficient ray tracing in two-dimensional media for rapid traveltime and amplitude forward modeling. *Canadian journal of exploration geophysics*, 24(1), 16-31.

Zelt, C. A., & Smith, R. B. (1992). Seismic traveltime inversion for 2-D crustal velocity structure. *Geophysical journal international*, 108(1), 16-34.

Zhang, X. H., Lu, X. B., Shi, Y. H., & Xia, Z. (2015). Study on the mechanical properties of hydrate-bearing silty clay. *Marine and Petroleum Geology*, 67, 72-80. https://doi.org/10.1016/j.marpetgeo.2015.04.019

Zhao, F., Alves, T. M., Wu, S., Li, W., Huuse, M., Mi, L., Sun, Q., and Ma, B. (2016). Prolonged post-rift magmatism on highly extended crust of divergent continental margins (Baiyun Sag, South China Sea). *Earth and Planetary Science Letters*, 445, 79-91. http://dx.doi.org/10.1016/j.epsl.2016.04.001

Zhou, D., Ru, K., & Chen, H. Z. (1995). Kinematics of Cenozoic extension on the South China Sea continental margin and its implications for the tectonic evolution of the region. *Tectonophysics*, 251(1-4), 161-177. https://doi.org/10.1016/0040-1951(95)00018-6

Ziegler, P. A., & Cloetingh, S. (2004). Dynamic processes controlling evolution of rifted basins. *Earth-Science Reviews*, 64(1-2), 1-50. https://doi.org/10.1016/S0012-8252(03)00041-2

Zillmer, M., Flueh, E. R., & Petersen, J. (2005). Seismic investigation of a bottom simulating reflector and quantification of gas hydrate in the Black Sea. *Geophysical Journal International*, 161(3), 662-678.

Zonenshain, L. P., & Le Pichon, X. (1986). Deep basins of the Black Sea and Caspian Sea as remnants of Mesozoic back-arc basins. *Tectonophysics*, *123*(1-4), 181-211. https://doi.org/10.1016/0040-1951(86)90197-6

Zwaan, F., & Schreurs, G. (2020). Rift segment interaction in orthogonal and rotational extension experiments: Implications for the large-scale development of rift systems. *Journal of structural geology*, 140, 104119. https://doi.org/10.1016/j.jsg.2020.104119

Zwaan, F., Corti, G., Keir, D., & Sani, F. (2020). A review of tectonic models for the rifted margin of Afar: Implications for continental break-up and passive margin formation. *Journal of African Earth Sciences*, 164, 103649. https://doi.org/10.1016/j.jafrearsci.2019.103649